



FEUP Universidade do Porto
Faculdade de Engenharia

**NUMERICAL MODELLING FOR SAFETY
EXAMINATION OF EXISTING CONCRETE
BRIDGES**

Mário Jorge de Seixas Pimentel

A dissertation presented to the Faculty of Engineering of the University of Porto
for the degree of Doctor in Civil Engineering.

Supervisors: Joaquim Figueiras (Full Professor); Eugen Brüwhiler (Full Professor).



ABSTRACT

In the structural safety examination of an existing bridge, the adoption of a stepwise approach is generally recommended. As the economical impact of conservative calculations can be large and lead to unnecessary interventions, increasing level of refinement is introduced in the structural analysis as the assessment level progresses. This thesis aims at presenting a harmonized suit of models with different levels of complexity that can be used in this context.

Nonlinear finite element analysis (NLFEA) is adopted as the reference method for the accurate assessment of the load-carrying capacity of concrete structures. Since many structures can be thought as an assembly of membrane elements, a new model for cracked, orthogonally reinforced concrete panels subjected to a homogeneous state of stress is presented. Instead of using empirical spatially averaged stress-strain relations, the RC panel behaviour is obtained from the contributions of each of the physical phenomena taking place at the cracks and bond slip effects are dealt with using a stepped rigid-plastic constitutive law. The model was found to provide good estimates of the deformation capacity, failure loads and failure modes of a set of 54 RC panels tested under in-plane axial and shear stresses.

A new NLFEA model based on the previously developed RC membrane element is then developed, implemented, and validated through comparison with the results of experimental tests on large scale structural elements. Although the emphasis is placed on the analysis of shear critical elements, the model is also capable of predicting the rotational capacity of plastic hinges, being thereby generally applicable to the safety evaluation of existing bridges. Besides the ultimate loads, also crack spacing and crack widths can be estimated with good accuracy. The implementation revealed robust and efficient in terms of the required computational resources.

It is shown that the proposed RC membrane model can be reduced to a limit analysis formulation through the application of some simplifying assumptions. At the cost of the loss of some generality, the latter is more suitable for use in engineering practice and still presents good accuracy in the calculation of the shear capacity of both continuity and discontinuity regions via the finite element method. For the particular case of continuity regions, a sectional analysis procedure for shear strength assessment is derived which results in a set of equations similar to those of the well known variable angle truss model. By incorporating the longitudinal strains in the definition of the effective concrete strength, the proposed method allows for a wider range of values for the inclination of the struts and is suitable for an intermediate shear strength assessment of existing concrete bridges.

Finally, a case study is presented consisting of a post-tensioned box girder bridge exhibiting cracking related pathologies. The inspection and monitoring campaigns that were developed for establishing the bridge condition are described, as well as the numerical simulations aimed at explaining the causes for the observed cracking patterns. The application of developed models in the safety evaluation of the bridge is exemplified. In the case of the NLFEA, appropriate semi-probabilistic safety formats are discussed and further developed.

RESUMO

Na análise de estruturas existentes, nomeadamente no caso das pontes, a utilização de métodos de análise estrutural mais realistas pode ser decisiva na verificação de segurança. A abordagem que tem vindo a ser reconhecida na regulamentação mais recente preconiza a utilização de modelos de complexidade crescente em função das necessidades evidenciadas pelo caso em estudo. Neste âmbito, é de todo desejável que os modelos a usar nos diversos níveis de análise estejam interligados entre si de forma a tornar clara a sua aplicação. Esta dissertação apresenta um contributo neste domínio.

A análise não linear de estruturas é adoptada como ferramenta de referência para a avaliação do comportamento e da capacidade resistente de elementos em betão estrutural. Neste contexto, grande parte dos elementos estruturais podem ser idealizados como uma associação de painéis elementares cujo comportamento é governado pelos esforços actuantes no seu próprio plano. Desta forma, na primeira parte da dissertação é desenvolvido um novo modelo para a análise do comportamento de painéis ortogonalmente armados sujeitos a um estado de tensão uniforme. Em vez de recorrer a leis tensão-deformação empíricas estabelecidas com base na homogeneização das deformações medidas em ensaios experimentais, no modelo proposto o comportamento do painel é obtido directamente a partir da contribuição de cada um dos fenómenos que têm lugar ao nível das fendas. A aderência entre as armaduras e o betão é modelada através de uma relação rígido-plástica, permitindo reproduzir de forma consistente o fenómeno de retenção de tensões de tracção no betão tanto antes como após a cedência das armaduras e, conseqüentemente, a obtenção de estimativas realistas da sua capacidade de deformação. O modelo foi validado com uma base de dados contendo 54 ensaios experimentais.

Um novo modelo constitutivo de análise não linear de estruturas foi desenvolvido para acomodar o elemento de painel atrás mencionado. Este modelo foi implementado num código de elementos finitos e validado através da comparação com os resultados de ensaios experimentais em elementos estruturais de grandes dimensões. Embora tenha sido dado especial relevo à capacidade do modelo em reproduzir roturas por corte, o modelo é também capaz de modelar a capacidade de rotação de rótulas plásticas, não tendo portanto restrições importantes no que concerne à sua aplicabilidade. Para além das cargas e dos modos de rotura, também o espaçamento e a abertura de fendas podem ser reproduzidos com boa precisão. A implementação revelou ser robusta e económica em termos dos recursos computacionais requeridos.

Partindo da formulação geral do elemento de painel anteriormente mencionada, e após vários níveis de simplificação, chegou-se a um modelo de análise limite passível de ser utilizado na prática corrente de engenharia estrutural para a verificação de segurança em relação ao corte. Este modelo simplificado foi também implementado num programa de elementos finitos e permite estabelecer os campos de tensões em condições de rotura. No caso particular das regiões de continuidade, o modelo de análise limite foi degenerado numa formulação analítica de análise seccional. Embora seja formalmente análogo ao método das bielas de inclinação variável preconizado na regulamentação

actual, o modelo proposto permite considerar a influência do estado de deformação das almas na resistência ao esmagamento das bielas, e portanto na resistência ao corte.

Finalmente é apresentado um caso de estudo onde se ilustra a metodologia adoptada para efectuar a avaliação de segurança de uma ponte rodoviária existente. Trata-se de uma ponte em betão armado e pré-esforçado, com uma secção transversal em caixão bicelular e com um comprimento total de 250m. A ponte, com cerca de 30 anos, apresenta uma série de patologias relacionadas com a fissuração do tabuleiro. Descreve-se sucintamente a inspecção detalhada que foi efectuada, os principais resultados do ensaio de carga realizado e ainda os resultados das análises numéricas efectuadas com vista a aferir as causas para a fissuração observada. A verificação de segurança é efectuada recorrendo aos modelos desenvolvidos. Para o caso específico da análise não linear de estruturas, novos formatos de segurança de base semi-probabilística são discutidos e desenvolvidos.

RÉSUMÉ

Lors de l'examen de la sécurité structurale du pont existant, l'adoption d'une approche par étapes est généralement recommandée. Une fois que l'impact économique des calculs conservateurs peut être important et conduire à des interventions inutiles, modèles d'analyse structurale plus réalistes et détaillées devraient être utilisés à des étapes ultérieures. Dans ce contexte, il est souhaitable que ces modèles à utiliser dans chaque étape soient reliés entre eux afin de préciser son application. Cette thèse vise à présenter une ensemble harmonisé de modèles avec différents niveaux de complexité et qui peuvent être utilisés dans ce contexte.

L'analyse non linéaire par éléments finis est adoptée comme la méthode de référence pour l'évaluation précise de la capacité portante des structures en béton. Une fois que nombreuses structures peut être idéalisées comme un assemblage d'éléments de membrane, un nouveau modèle est présenté pour l'analyse de panneaux en béton orthogonalement armées et soumis à un état de contrainte uniforme. Au lieu d'utiliser les lois empiriques de contrainte-déformation établis après l'homogénéisation des déformations mesurées aux essais expérimentaux, le comportement du panneau est obtenu directement à partir de la contribution de chacun des phénomènes qui ont lieu au niveau des fissures. L'adhérence entre l'armature et le béton est modélisé par une relation de rigide-plastique, permettant la modélisation consistant du phénomène de rétention de contraintes de traction dans le béton et d'obtenir des estimations réalistes de la capacité de déformation de l'armature. Le modèle a été validé avec 54 essais expérimentaux.

Un nouveau modèle constitutif pour l'analyse non linéaire des structures destinées à accueillir l'élément de panneau mentionné ci-dessus est développé. Ce modèle est implémenté dans un code éléments finis et est validé par comparaison avec les résultats des essais sur éléments structurales de grande dimension. Bien que mettant l'accent sur les ruptures par effort tranchant, il est également capable de modéliser la capacité de rotation des rotules plastiques, et n'a donc pas d'importantes restrictions quant à leur applicabilité. Aussi l'espacement et l'ouverture des fissures sont reproduites avec une bonne précision. L'implémentation s'est avérée robuste et économique en termes de ressources de calcul nécessaires.

A partir de la formulation générale de l'élément de membrane mentionné ci-dessus, et après plusieurs niveaux de simplification, un modèle d'analyse limite est développé pour être utilisé dans la pratique du génie civil pour la vérification de sécurité contre effort tranchant. Ce modèle simplifié a été également implémenté dans un code éléments finis et permet l'obtention de champs de contraintes et des charges de rupture. Dans le cas particulier des régions de continuité, le modèle d'analyse limite a été dégénéré dans une formulation analytique d'analyse en section. Bien qu'il soit formellement analogue à la méthode des bielles d'inclinaison variable recommandé dans les règlements actuelles, le modèle proposé permet d'étudier l'influence de la déformation des âmes dans la résistance au cisaillement.

Pour terminer, on présente une étude de cas qui illustre la méthodologie adoptée pour faire l'évaluation de la sécurité d'un pont routier existant. Il s'agit d'un pont de béton armé et précontraint avec une longueur totale de 250m et qui présente fissuration dans le tablier. Il est décrit brièvement l'inspection qui a été menée, les principaux résultats du test de charge ainsi que les résultats de l'analyse numérique afin de déterminer les causes de la fissuration observée. La vérification de sécurité est effectuée en utilisant les modèles développés. Pour le cas spécifique de l'analyse non linéaire de structures, un nouvel format de sécurité basé sur une approche semi-probabiliste est discuté et développé.

ACKNOWLEDGMENTS

This research work was carried out at the Laboratory of Concrete Technology and Structural Behaviour (LABEST) of the Faculty of Engineering of the University of Porto under the supervision of Prof. Joaquim Figueiras. I wish to express my gratitude for his support, guidance and enthusiastic following of the work.

I would also like to thank Prof. Brühwiler, the co-supervisor of this thesis, for having welcomed me during a 6 month stay at the Laboratory of Maintenance and Safety of Structures (MCS), in the École Polytechnique Fédérale de Lausanne. As a result of our fruitful discussions I gained a new and valuable insight on maintenance of the existing infrastructure.

To Prof. Mariscotti I want to express my deep gratitude for his unrelenting cooperation during the gamma-ray inspection of the N. S. da Guia Bridge and for sharing his knowledge and experience concerning radiographic methods for non-destructive inspection of concrete structures.

The support given by the Portuguese Foundation for Science and Technology (FCT) through the PhD grant SFRH/BD/24540/2005 is also gratefully acknowledged.

For so many good moments spent relaxing and so many shared experiences, I would like to show my deepest appreciation to my friends and coworkers Andrin Herwig, António Topa Gomes, Carlos Sousa, Filipe Magalhães, Luis Borges, Luis Noites, Miguel Azenha, Miguel Castro, Miguel Ferraz, Nuno Raposo, Pedro Costa and Xavier Romão. The friendly environment at our workplace was very important for the success of this work.

I would also like express my profound gratitude for the unconditional love and support from my parents and sister.

Finally, I am deeply thankful to my beloved wife Marta and newborn son Nuno for their understanding, caring and nurturing.

Table of Contents

1	INTRODUCTION	1
1.1	MOTIVATION	1
1.2	OBJECTIVES	3
1.3	OVERVIEW	4
2	MATERIAL BEHAVIOUR.....	7
2.1	TENSILE FRACTURE.....	7
2.1.1	<i>Tensile strength</i>	7
2.1.2	<i>Deformational behaviour</i>	8
2.2	BOND STRESS TRANSFER AND TENSION STIFFENING.....	11
2.2.1	<i>The bond-slip relation and the differential equation of bond</i>	12
2.2.2	<i>Tension stiffening</i>	14
2.3	SHEAR TRANSFER THROUGH ROUGH CRACKS.....	16
2.4	COMPRESSIVE FRACTURE.....	19
2.4.1	<i>Uniaxial compression</i>	19
2.4.2	<i>Effect of multiaxial stresses</i>	22
2.4.3	<i>Cracked concrete</i>	24
3	THE RC CRACKED MEMBRANE ELEMENT	29
3.1	GENERAL.....	29
3.2	EQUILIBRIUM EQUATIONS	30
3.2.1	<i>Concrete contribution to shear strength</i>	33
3.2.2	<i>Relationship between average and local crack stresses</i>	33
3.3	COMPATIBILITY EQUATIONS	37
3.4	PARTICULAR CASES	38
3.5	REVIEW ON PREVIOUS WORK	39
3.6	CONSTITUTIVE RELATIONSHIPS.....	48
3.6.1	<i>Compressive behaviour</i>	48
3.6.2	<i>Tensile crack bridging stresses</i>	52
3.6.3	<i>Shear transfer through rough cracks</i>	52
3.6.4	<i>Reinforcement steel and tension stiffening</i>	55
3.7	CALCULATION EXAMPLE.....	62
3.7.1	<i>F-CMM</i>	65

3.7.2	<i>R-CMM</i>	68
3.8	VALIDATION.....	69
3.8.1	<i>The influence of the reinforcement content</i>	72
3.8.2	<i>The influence of prestressing</i>	75
3.8.3	<i>The influence of the concrete strength</i>	77
3.8.4	<i>Summary</i>	81
3.9	CONCLUDING REMARKS.....	83
4	IMPLEMENTATION IN A FINITE ELEMENT CODE	85
4.1	GENERAL.....	85
4.2	COMPUTATIONAL MODELLING OF THE NONLINEAR BEHAVIOUR OF STRUCTURAL CONCRETE.....	85
4.2.1	<i>Kinematic description of the displacement field</i>	85
4.2.2	<i>Constitutive models and constitutive laws</i>	87
4.2.3	<i>Discretization strategy</i>	89
4.2.4	<i>Discussion</i>	90
4.2.5	<i>Solution procedures for nonlinear systems</i>	91
4.3	TOTAL STRAIN BASED MODEL.....	98
4.3.1	<i>Uncracked concrete</i>	101
4.3.2	<i>Cracked concrete</i>	108
4.3.3	<i>Reinforcement steel</i>	123
4.4	EXTENSION TO SHELL ELEMENTS.....	133
4.5	CONCLUDING REMARKS.....	135
5	ANALYSIS OF SHEAR CRITICAL ELEMENTS	137
5.1	GENERAL.....	137
5.2	SHEAR IN CONTINUITY REGIONS.....	138
5.2.1	<i>Description and objectives</i>	138
5.2.2	<i>Results</i>	140
5.3	SHEAR IN DISCONTINUITY REGIONS WITH PLASTIC REINFORCEMENT STRAINS.....	145
5.3.1	<i>Description and objectives</i>	145
5.3.2	<i>Results</i>	148
5.4	HIGH STRENGTH CONCRETE GIRDERS CRITICAL IN SHEAR.....	155
5.4.1	<i>Description and objectives</i>	155
5.4.2	<i>Results</i>	158
5.5	ANALYSIS OF THE DEFORMATION CAPACITY OF PLASTIC HINGES WITH HIGH SHEAR STRESSES.....	164
5.5.1	<i>Description and objectives</i>	164
5.5.2	<i>Results</i>	167
5.6	CONCLUDING REMARKS.....	172

6	SIMPLIFIED MODELS FOR ENGINEERING PRACTICE.....	173
6.1	GENERAL	173
6.2	LIMIT ANALYSIS METHODS FOR STRUCTURAL CONCRETE ELEMENTS SUBJECTED TO IN-PLANE FORCES 174	
6.2.1	<i>Overview and general considerations</i>	174
6.2.2	<i>Yield conditions of reinforced concrete membranes</i>	176
6.2.3	<i>Yield conditions accounting for compression softening</i>	178
6.2.4	<i>Continuous stress fields</i>	183
6.2.5	<i>Discontinuous stress fields</i>	186
6.2.6	<i>Section-by-section analysis for continuity regions</i>	195
6.3	CODE-LIKE FORMULATION	197
6.3.1	<i>Proposed expressions</i>	198
6.3.2	<i>Sample calculations</i>	201
6.4	CONCLUDING REMARKS	206
7	CASE STUDY: N. S. DA GUIA BRIDGE	209
7.1	DESCRIPTION OF THE BRIDGE AND PROBLEM STATEMENT.....	209
7.2	AVAILABLE DATA	211
7.3	INSPECTION.....	213
7.3.1	<i>Mapping of the cracking patterns</i>	213
7.3.2	<i>Corrosion evidence</i>	217
7.3.3	<i>Verification of the reinforcement layout</i>	217
7.3.4	<i>Trial test using gamma rays</i>	218
7.4	MATERIAL CHARACTERIZATION	225
7.4.1	<i>Concrete</i>	225
7.4.2	<i>Reinforcing steel</i>	229
7.4.3	<i>Prestressing steel</i>	229
7.5	MONITORING CAMPAIGN.....	229
7.5.1	<i>Load test</i>	232
7.5.2	<i>Response to temperature variations</i>	236
7.6	INVESTIGATION OF THE CAUSES FOR THE OBSERVED CRACKING PATTERNS	237
7.6.1	<i>Stress analysis in serviceability conditions</i>	237
7.6.2	<i>Effect of local stress conditions</i>	252
7.7	DISCUSSION	261
8	SAFETY EVALUATION OF THE N. S. DA GUIA BRIDGE	263
8.1	GENERAL	263
8.2	SAFETY FORMAT FOR NONLINEAR ANALYSIS OF EXISTING BRIDGES.....	265
8.2.1	<i>Basic reliability concepts</i>	265

8.2.2	<i>Global resistance safety factor</i>	268
8.2.3	<i>Target reliability index</i>	273
8.2.4	<i>Application to NLFEA of existing bridges</i>	275
8.3	STRUCTURAL SAFETY EVALUATION OF THE N. S. DA GUIA BRIDGE	276
8.3.1	<i>Definition of the target reliability index</i>	276
8.3.2	<i>Updated examination values</i>	278
8.3.3	<i>Linear elastic analysis – member level approach</i>	279
8.3.4	<i>Nonlinear analysis</i>	280
8.3.5	<i>Continuous stress field analysis</i>	290
8.4	CONCLUDING REMARKS	292
9	SUMMARY AND CONCLUSIONS	295
9.1	RECOMMENDATIONS FOR FUTURE RESEARCH	301
	REFERENCES	305
	APPENDIX – DETAILED VALIDATION RESULTS	319
A1.1	ISOTROPICALLY REINFORCED CONCRETE PANELS	319
A1.1.1	<i>Series A</i>	319
A1.1.2	<i>Series VA</i>	320
A1.1.3	<i>Series PV</i>	321
A1.2	ORTHOTROPICALLY REINFORCED CONCRETE PANELS	322
A1.2.1	<i>Series B</i>	322
A1.2.2	<i>Series PP</i>	325
A1.2.3	<i>Series SE</i>	327
A1.2.4	<i>Series VB</i>	328
A1.2.5	<i>Series M</i>	330
A1.2.6	<i>Series PV</i>	332

1 Introduction

1.1 Motivation

The built infrastructure, of which bridges are an important component, is a hugely valuable economic and political asset. Its maintenance, repair and renewal constitute a heavy burden for society. For the existing highway bridge stock in all 27 countries of the European Union, the total expenditure was estimated at €400 billion [66] in 2004, which was roughly 4% of the Gross Domestic Product. Due to the large sums involved, the financing of maintenance, repair and renewal needs to be put on a rational basis. There is consensus regarding the need for specific procedures for the assessment of existing bridges and the importance of adequate bridge management strategies. This is crucial for minimizing and rationalizing the increasingly growing maintenance costs and associated traffic disturbances, for contributing to environmental sustainability and for ensuring the adequate safety levels to the infrastructure users.

In the final report of the BRIME research program [36], devoted to the development of a framework for the management of bridges on the European road network, it is proposed that a general Bridge Management System (BMS) should be constituted by 5 main components: (1) an inventory database; (2) a suite of procedures for assessing bridges condition; (3) methods for performing the structural safety assessment; (4) a decision making procedure for determining whether a sub-standard or deteriorated bridge should be repaired, strengthened or replaced; and (5) some prioritization criteria for deciding the best allocation of the limited financial resources. Structural engineering plays a major role in all these components and especially in components 2 and 3. In fact, the key for extending the service life of an existing bridge is a detailed examination of its condition and an accurate structural safety evaluation, thereby requiring a completely different approach than the traditionally adopted in the design of a new bridge.

In design and construction of new structures a great effort must be placed on the conceptual design, on the choice of the appropriate structural form and its aesthetics, on the analysis of the local conditions, on the selection of the construction methods and materials and on the feasibility of the proposed solution. Many solutions have to be tested until the

final design is achieved. The analytical work is only part of the process and usually simple methods are preferred, enabling quick estimates of the internal forces and conservative estimates of the actual resistance. Design codes are available for guiding the structural engineer throughout the required safety checks, indicating the load models to be adopted, the material properties, the design formulas and the appropriate safety format. The latter is usually based on a semi-probabilistic approach grounded on a uniform target safety level, independent of the structural element being designed. In most cases, the additional cost due to a conservative design is not very significant [155] and this procedure is shown to be adequate.

On the other hand, in the assessment of an existing bridge advantage must be taken from the fact that the bridge can be inspected, tested and monitored during load testing or under traffic and environmental actions. The structural engineer should resort to more detailed structural analysis methods since the economical impact of conservative calculations can be large and lead to unnecessary interventions, and because the structural condition can be established based on appropriate testing and inspection techniques. If necessary, the load models can be updated taken into account local traffic conditions and risk based approaches can be used to define the target safety level taking into account the identified hazard scenarios and the corresponding consequences with respect to damage and economic importance of the bridge. This process requires comprehensive knowledge of structural engineering beyond the scope of design codes and supplies sufficient motivation and economical benefits for the application of advanced numerical methods and the latest accepted scientific findings.

Whilst in recent decades considerable effort has been put into the development of new standards for the design of new structures, comparatively less has been done on the development of guidance documents addressing the assessment of existing structures. In the case of bridges, several research programmes funded by the European Commission have been undertaken for filling this gap [36; 66; 202; 258; 259]. In general a stepwise approach is recommended [36; 66; 259] to identify which bridges are at an unacceptably high level of risk so that appropriate remedial measures can be taken. In the case of the structural analysis, increasing level of refinement is introduced as the assessment level progresses. Although this line of thinking is already reflected in recent codes [87], there is still work to be developed regarding the establishment of suitable analysis methods that can be used in such a context. The simpler methods should preferably be based on the more detailed ones through transparent simplifying assumptions in order to keep clarity

and consistency between the results obtained in the successive levels of analysis. This thesis aims at presenting a contribution in this field.

1.2 Objectives

Nonlinear finite element analysis (NLFEA) is increasingly recognized as an effective tool for the accurate assessment of the load-carrying capacity of concrete structures [86]. By enabling the consideration of both equilibrium and compatibility conditions, and if appropriate constitutive laws are adopted, realistic force-deformation relationships and ultimate loads can be calculated. Within the NLFEA context, many structural concrete elements, such as bridge I-girders and box-girders, shear walls, transfer beams, containment structures and offshore oil platforms, to cite a few, can be idealized as an assembly of membrane elements subjected mainly to in-plane shear and axial forces. Therefore, the accurate representation of the structural concrete behaviour at the membrane element level is here taken as the starting point for the detailed analysis of structural concrete elements with arbitrary geometry via the finite element method.

In this context, the first objective of this thesis is the development of a strict reinforced concrete (RC) cracked membrane element formulation, in the sense that the mechanical phenomena taking place at the cracks, and which are known to govern the behaviour of cracked concrete elements, are taken into account in a transparent manner. The main features of the structural concrete behaviour, such as tensile cracking, compression softening, shear stress transfer between rough cracks and bond interaction with the reinforcement shall be explicitly considered in the formulation. The model shall describe the complex stress and strain fields developing in the membrane element, and retrieve useful information for the structural engineer, such as concrete and reinforcement failures as well as the crack spacing and crack widths.

The second objective of the thesis is the implementation of the above mentioned RC cracked membrane element formulation in a finite element code, thereby constituting an advanced analysis tool allowing detailed safety examinations of concrete structures. The implementation shall be robust in order to minimize the convergence difficulties that often discourage the use of nonlinear analysis methods. Short-term static loading is assumed, excluding dynamic or cyclic loads as well as long-term and material degradation effects.

The third objective is the development of simplified formulations suited for use in engineering practice. In fact, practitioner structural engineers are seldom familiar with nonlinear analysis concepts and do not have the vocation to deal with the great amount of information provided by nonlinear finite element analysis tools. These simplified formulations shall be traced back to the previously outlined detailed models through clear simplifying assumptions, so as to make them part of an integrated and stepwise structural assessment procedure. Since flexural strength can be considered to be satisfactorily predicted in current design methods, the focus of these simplified formulations shall be driven to shear dominated problems.

The last and fourth objective is the safety examination of a real bridge and the application of the developed structural analysis tools in a case study. The available safety formats suitable for nonlinear analysis shall be applied and further developed.

1.3 Overview

In Chapter 2 the fundamental concepts related with concrete behaviour under short term loading conditions and its interactions with the reinforcement are introduced. These concepts and terminology are used throughout the thesis, namely in Chapters 3, 4 and 6.

In Chapter 3 the development and validation of a new formulation describing the behaviour of RC cracked membrane elements is presented. Rather than using empirical and spatially averaged stress-strain relations, in the proposed formulation RC behaviour is described taking into account the individual contribution of the mechanical phenomena taking place at the cracks. Bond slip effects are dealt with using a stepped rigid-plastic constitutive law according to the Tension Chord Model [151] which allows for a consistent treatment of the tension stiffening effects and a proper evaluation of steel deformation capacity in the post-yielding stage. After having introduced the general equilibrium and compatibility equations governing the problem, and having analysed in detail the complex stress field developing at the cracks and in between the cracks, the relationship between the different existing approaches are clarified and the previous work on this field is critically reviewed. The adopted constitutive relationships are presented and the results obtained with the developed model are evaluated using a database of 54 experimental tests on RC panels under in-plane shear and axial forces. The influences of the reinforcement content, prestressing force and concrete strength on the behaviour of RC panels are examined in detail.

In Chapter 4, the RC cracked membrane element formulation is further developed to be used in the structural analysis via the finite element method. The concepts behind NLFEA of concrete structures are introduced and a short overview of the existing approaches is presented. In addition to the work described in Chapter 3, the implementation in a finite element code requires the formulation of concrete nonlinear behaviour in biaxial compression, the establishment of suitable loading/unloading conditions, the generalization of the shear stress transfer model to cases where two orthogonal cracks arise in the same integration point, the treatment of strain localization issues and the formulation of the tangent stiffness matrix to be used in the incremental-iterative solution procedure. The structure of the code is presented, as well as the implemented algorithms. Some single element validation examples are presented to clarify the model behaviour under complex loading histories. In order to enlarge the range of applicability of the proposed model, the formulation is extended to shell elements.

In Chapter 5 the analysis of large scale structural concrete elements is performed for validation purposes and for illustrating the model capabilities. The analysed examples were selected for evaluating the accuracy of the model in the: (1) calculation of shear failure loads and corresponding failure mechanisms; (2) determination of the load-deformation curves and of the deformation capacity of large scale beams; (3) simulation of the observed cracking patterns and calculation of the corresponding crack widths. Each of the selected test series represents a specific feature of the structural behaviour that should be properly modelled in order to allow improved structural analyses of existing concrete bridges.

In Chapter 6 the derivation of simplified formulations for engineering practice is presented. Starting from a particular case of the equilibrium equations of the RC cracked membrane element, neglecting the tensile strength and the bond stress transfer effects, and considering simple rigid-plastic relations for concrete and steel, the classical closed form limit analysis expressions for shear strength calculation of RC panels are derived. Following the work developed by Kaufmann [117], these expressions are then worked out to include the effect of the tensile strains in the effective concrete compressive strength, thus allowing to include strain compatibility conditions in shear strength calculations. Besides improving the accuracy of the classical limit analysis expressions, this formulation can be easily implemented in a finite element code in such a way that is more suitable to be used in engineering practice than the detailed models developed in Chapters 3 and 4. However, the relevant outcomes are simply the continuous stress field expressing the equilibrium at failure conditions and the corresponding ultimate load. A simple sectional analysis method

for beam continuity regions is derived from the same set of expressions but considering a constant shear stress distribution along the cross-section height, thus avoiding the resource to finite element analyses in cases where a sectional analysis approach is deemed sufficient.

In Chapter 7, a case study is presented consisting of a 30-years old and 250 m long post-tensioned box-girder bridge exhibiting cracking patterns with both longitudinal and transversal symmetry. The inspection and monitoring campaigns that were developed for establishing the structural condition of the bridge are described, as well as the numerical analyses aimed at explaining the origin of the observed cracking patterns.

In Chapter 8 the safety evaluation of the bridge with resource to the models developed in the present thesis is presented. The chapter begins by giving an overview on the applicable safety formats whenever nonlinear analysis concepts are adopted, and by showing how to define a global resistance factor based on semi-probabilistic concepts that can capture the resistance sensitiveness to the random variation of the input variables. A stepwise approach is adopted in the structural safety evaluation illustrating the applicability of the developed models in each assessment stage.

Finally, Chapter 9 summarises and discusses the results obtained in this thesis and concludes with a set of recommendations for future research.

2 Material behaviour

2.1 Tensile fracture

2.1.1 Tensile strength

Concrete tensile strength f_{ct} is relatively low when compared to the compressive strength f'_c , is subject to high scatter and is significantly affected by additional factors like restraining shrinkage stresses. Therefore, it is common practice to neglect it in strength calculations of properly reinforced concrete members. However, shear resistance of some structural elements, like girders or slabs without stirrups, relies on the existence of concrete tensile stresses [27; 63; 166]. The consideration of concrete tensile stresses allows explaining the strong size effects that have been reported in shear failures of beams without shear reinforcement [18; 62]. Concrete tensile behaviour also plays a key role in important aspects related with serviceability considerations, like the quantification of the deformations, assessment of crack spacing and crack widths. Moreover, the evaluation of the reinforcing steel deformation capacity – which is essential for an accurate calculation of the force-deformation curves, failure modes and, in case of statically indeterminate structures, of the failure loads – can only be evaluated if due consideration is given to the concrete tensile behaviour and to the bond shear stress transfer mechanics.

The tensile strength can be determined from direct tension tests or by means of indirect tests such as the split cylinder test, double punch test or bending test. While easier to perform these indirect tests require assumptions about the state of stress within the specimen in order to calculate the tensile strength from the measured failure load. For most purposes, the tensile strength of normal strength concrete can be estimated from [46],

$$f_{ct} = k \cdot 0.3 f'_c{}^{2/3} \quad [\text{MPa}] \quad (2.1)$$

where the parameter k varies between 0.65 and 1 and allows for the effect of non-uniform self equilibrating stresses leading to a reduction of the “apparent” tensile strength. This parameter introduces a structural effect on f_{ct} since it depends on the specimen thickness,

reinforcement content, etc. Alternatively, a lower bound estimate, already accounting for the self equilibrated residual stresses, can be obtained from [20; 240]:

$$f_{ct} = 0.33\sqrt{f'_c} \quad [\text{MPa}] \quad (2.2)$$

2.1.2 Deformational behaviour

The stress-strain response depicted in Figure 2.1 (a) can be typically obtained in a displacement controlled direct tension test. Until stress levels near the tensile strength the response is approximately linear elastic. Near the peak load the response becomes softer due to micro-crack growth at the interface between the aggregates and the cement paste. As the tensile strength is reached, deformations begin to appear heavily localized in a narrow band, the so called *fracture process zone (FPZ)* [17], and the micro-cracks start coalescing into a macroscopic crack. Tensile stresses can still be transmitted due to crack bridging effects [102] and a strain-softening behaviour can be observed. At this stage the deformations are highly localized, the specimen unloads outside of the FPZ and the measured softening branch can be more or less steep, depending on the base length that is used for averaging the deformations. At the macro-level, this behaviour cannot be explained by regular continuum mechanic models neither by linear elastic fracture mechanics (LEFM), requiring the application of nonlinear fracture mechanics (NLFM) concepts. It must be remarked that the softening behaviour does not exist in a heterogeneous material like concrete if its micro or meso-structure is considered with sufficient resolution, being only a mere homogenization product at the macro-level [9]. The NLFM models can be classified according to the assumed localization criteria for the deformations in the softening regime [75] (see Figure 2.1 (b)-(d)).

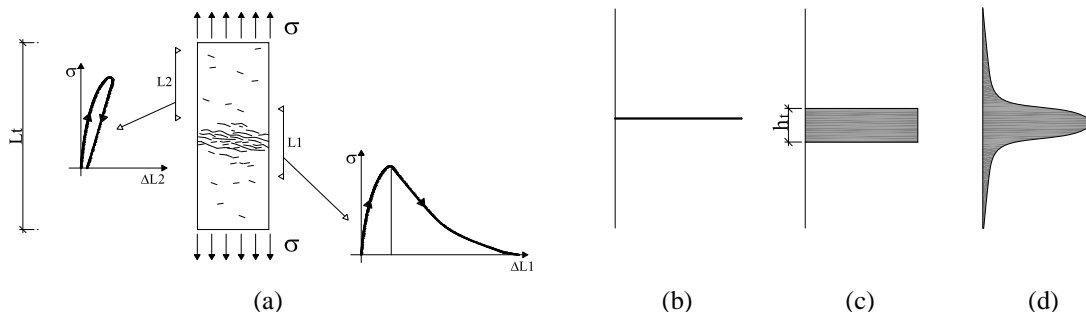


Figure 2.1 – Tension softening and localization criteria for the deformations in the softening regime: (a) behaviour of a tensioned concrete specimen; (b) FPZ lumped into a line – *fictitious crack model* [99]; (c) deformations localized in a band of finite length – *crack band model*; (d) continuous strain field - *non local continuum models*.

Hillerborg [99] introduced the *fictitious crack model* for describing the observed behaviour of concrete in tension. In this model the FPZ is lumped to a line, the *fictitious* or *cohesive crack*, which is still capable of transmitting stresses (Figure 2.2). According to the fictitious crack model the total elongation δ of a specimen subjected to pure tension is given by Eq. (2.3), where L_t is the total specimen length, ε_c is the concrete strain outside the FPZ and w is the elongation in the FPZ.

$$\delta = \varepsilon_c L_t + w \quad (2.3)$$

The average specimen strain ε_m can be calculated from:

$$\varepsilon_m = \varepsilon_c + w/L_t \quad (2.4)$$

As shown in Eq. (2.4) the fictitious crack model can successfully explain the size dependency of the σ - ε_m curve after the tensile strength is reached, i.e., when $w > 0$. After the beginning of strain localization the σ - ε_m curve is no longer a material property. The uniaxial tensile constitutive relationship is then expressed by two curves: (1) a stress-strain curve σ - ε_c for the concrete outside the FPZ; (2) a stress-elongation curve σ - w for the FPZ.

The consideration of the σ - w relation as a material property leads to the definition of a material parameter defined by the area of the σ - w diagram. This parameter, that Hillerborg named as fracture energy, G_F [$\text{N}\cdot\text{m}^{-1}$], corresponds to the energy required for the formation of a macroscopic crack with unit area,

$$G_F = \int_0^{w_c} \sigma dw \quad (2.5)$$

where w_c is the fictitious crack opening at which the tensile stress drops to zero.

The fracture energy depends primarily on water/cement ratio, maximum aggregate size D_{max} and age of concrete [84]. As a rough approximation G_F can be estimated from [84]:

$$G_F = G_{F0} \left(\frac{f'_c}{10} \right)^{0.7} \quad \text{for } f'_c \leq 80 \text{ MPa} \quad (2.6)$$

$$G_F = 4.30 G_{F0} \quad \text{for } f'_c > 80 \text{ MPa}$$

where $G_{F0} = 25, 30$ or $58 \text{ N}\cdot\text{m}^{-1}$ for $D_{max} = 8, 16$ or 32 mm respectively.

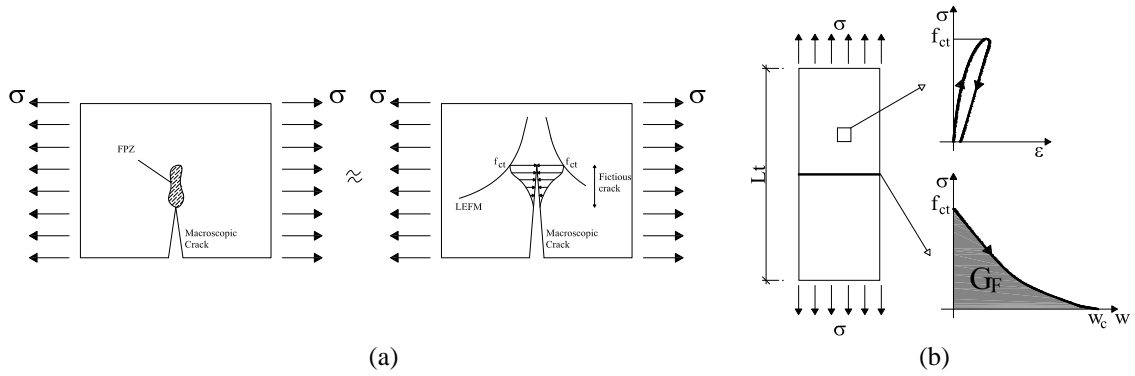


Figure 2.2 – Fictitious crack model: (a) crack bridging stresses in the fictitious crack; (b) components of the total deformation.

Bazant and Oh [17] introduced the *crack band model*. In this model strains are assumed to localize in a finite length FPZ, following a uniform distribution. The crack band model introduces the crack band width h_t as a new parameter, representing the width over which the FPZ deformations are averaged. This averaging process corresponds to the simplest homogenization procedure of the real strain distribution enabling treating a heterogeneous material like concrete as a continuum. The constitutive relationships for the crack band model are illustrated in Figure 2.3. For the concrete inside the FPZ the constitutive relationship is a function of f_{ct} , G_F and h_t . A parallelism with the fictitious crack model can be established by defining the crack strain as $\epsilon_{cr} = w / h_t$, being the fracture energy now defined by:

$$G_F = h_t \int_0^{\epsilon_u} \sigma d\epsilon - L_t \omega = h_t \int_0^{\epsilon_{cr,u}} \sigma d\epsilon_{cr} \quad (2.7)$$

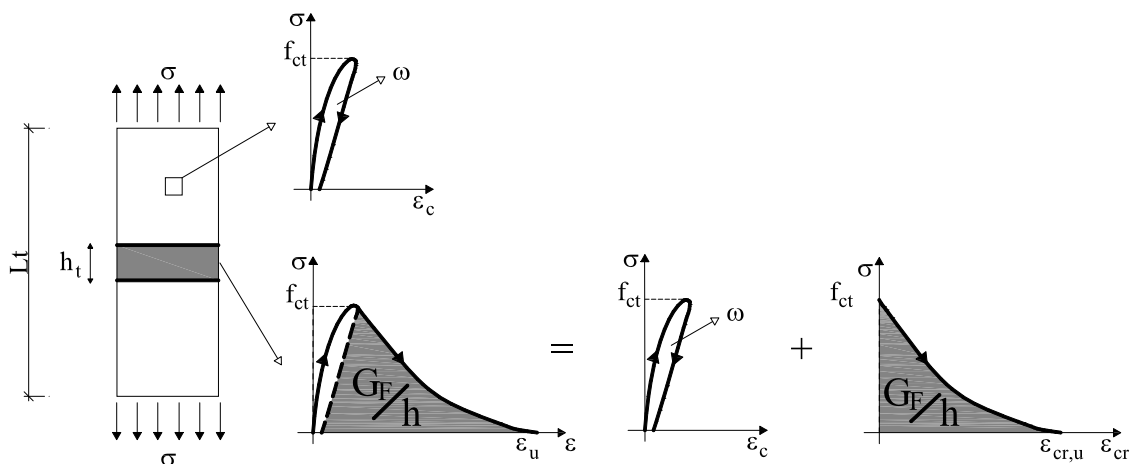


Figure 2.3 – Crack band model. Notation.

The crack band model supplies the theoretical background allowing the application of NLFM concepts within a continuum mechanics framework, thus enabling the use of standard continuum finite element models in cases where strain localization in a few narrow zones governs the structural behaviour. This will be discussed in more detail in Chapter 4. More powerful and generic continuum descriptions (see Figure 2.1(d)), which include a so called internal length defining the (non-zero) width of the localization zone, were developed after the crack band model. Such enhanced continuum theories include the Cosserat continuum (see e.g. [31]), the non-local continuum with integral averaging of strain (see e.g. [14; 16]) and the high order gradient continuum (see e.g. [33]). A detailed description of such theories is out of scope of the present work.

2.2 Bond stress transfer and tension stiffening

Bond between reinforcement and concrete is a fundamental issue in the study of structural concrete behaviour. After cracking, relative displacements between concrete and reinforcement occur leading to the development of bond stresses at the steel-concrete interface.

In the case of plain reinforcing bars, bond action is mainly governed by adhesion. After breakage of the adhesive forces, which occurs for very low relative displacements, force transfer is provided by dry friction. In the case of ribbed bars, bond action is primarily governed by bearing of the ribs against the surrounding concrete and forces are transmitted to concrete by inclined compressive forces radiating from the bars. These bearing forces can be decomposed in the parallel and radial directions to the bar axis. The sum of parallel components equals the bond force, whereas the radial components are balanced by circumferential tensile stresses in the concrete or by lateral confining stresses. The latter can be provided by circumferential reinforcement. If significant forces have to be transmitted over a short length from steel to the embedding concrete, splitting failures along the reinforcement will occur unless sufficient concrete cover or proper confinement is provided. This effect is called tension splitting. For a detailed discussion about the bond phenomenon refer to references [3; 84; 85; 214].

The complex mechanism of bond stress transfer can be studied at different levels with regard to the size of the control volume [137]. In the most common approach, the problem is simplified by considering a nominal bond shear stress uniformly distributed over the

nominal perimeter of the reinforcing bar. In this case, the control volume can be assumed to be the finite domain between two consecutive cracks.

2.2.1 The bond-slip relation and the differential equation of bond

Average bond shear stress-slip relationships, $\tau_b - \delta$, are normally obtained from pull-out tests, see Figure 2.4 (b) and (a), respectively. The average bond shear stress, τ_b , along the embedment length, l_b , can be determined from the pull-out force as $\tau_b = F / \emptyset \pi l_b$, where \emptyset is the nominal rebar diameter. In a pull-out test, bond shear stresses increase with the slip until the maximum bond shear stress $\tau_{b \max}$ is reached. This typically occurs at a slip $\delta = 0.5 \dots 1$ mm. If the slip is further increased, bond shear stresses decrease, as shown in the curve depicted in Figure 2.4 (b). In general this curve represents a structural behaviour since it depends on the concrete cover, on the existence of confinement stresses, type of reinforcing bar, etc.

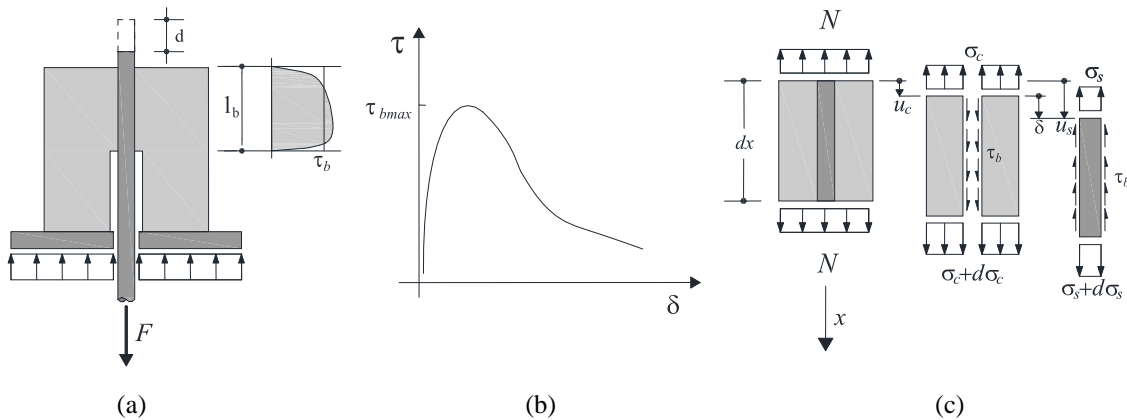


Figure 2.4 – (a) Pull-out test; (b) Average bond shear stress-slip curve; (c) Equilibrium of a differential element.

Consider a concrete element loaded in uniform tension, Figure 2.4 (c). For any section of the element, equilibrium requires that:

$$\frac{N}{A_s} = \sigma_s + \frac{1-\rho}{\rho} \sigma_c \quad (2.8)$$

where $\rho = A_s / A_c$ is the reinforcement ratio, A_s is the cross sectional area of reinforcement, A_c is the gross cross-section of concrete, and σ_c and σ_s are the concrete and steel stresses, respectively. Formulating the equilibrium of the differential element of length dx , see Figure 2.4 (c), one obtains the relations,

$$\frac{d\sigma_s}{dx} = \frac{4\tau_b}{\phi} \quad \frac{d\sigma_c}{dx} = -\frac{\rho}{1-\rho} \frac{d\sigma_s}{dx} \quad (2.9)$$

for the stresses transferred between concrete and reinforcement by bond. Noting that $\delta = u_s - u_c$, the kinematic condition is obtained:

$$\frac{d\delta}{dx} = \varepsilon_s - \varepsilon_c \quad (2.10)$$

The second order differential equation for the slip δ is obtained by differentiating (2.10) with respect to x , inserting (2.9) and substituting the stress-strain relationships for steel and concrete. For linear elastic behaviour, $\sigma_s = E_s \varepsilon_s$ and $\sigma_c = E_c \varepsilon_c$, the equation simplifies to:

$$\frac{d^2 \delta}{dx^2} = \frac{4\tau_b}{\phi E_s} \left(1 + \frac{n\rho}{1-\rho} \right) \quad (2.11)$$

where ρ is the geometrical reinforcement ratio and n is the modular ratio E_s/E_c .

Adopting a bond shear stress-slip relationship $\tau_b - \delta$, the differential equation (2.11) can be solved in an iterative numerical manner [3; 214], and the distributions of the stresses, strains and slip along the reinforcing bars can be obtained. Such distributions are qualitatively depicted in Figure 2.5 for the stabilized cracking stage. The dotted lines refer to the pre-yielding stage whereas the solid lines refer to the post-yielding stage. In the pre-yielding stage the steel stresses at the cracks σ_{sr} are below the steel yielding stress f_{sy} . After reinforcement yielding strong strain localizations are observed in the vicinity of the cracks.

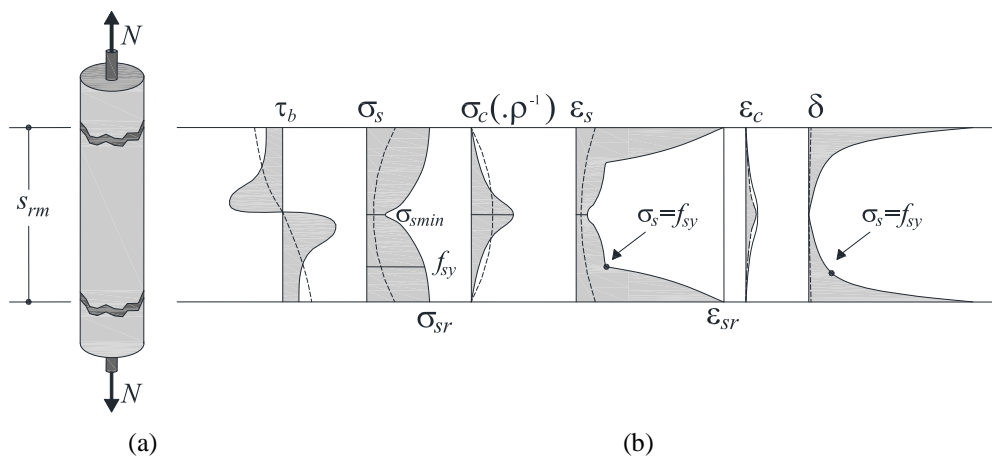


Figure 2.5 – (a) Tension chord element. (b) Qualitative distribution of bond shear stresses, steel and concrete stresses and strains, and bond slip.

The crack width w_r can be calculated by integrating Eq. (2.10) between two consecutive cracks

$$w_r = \int_0^{s_r} (\varepsilon_s - \varepsilon_c) dx \quad (2.12)$$

with s_r being the crack spacing.

2.2.2 Tension stiffening

In a cracked concrete cross-section, all tensile forces are resisted by the reinforcing bars. As discussed above, between adjacent cracks these forces are partially transmitted from the steel to the surrounding concrete by bond stresses. At the structural level, the effect of the concrete contribution between the cracks on the behaviour of a structural concrete tension chord is reflected by a stiffer load-displacement response than that of a naked steel bar of equal resistance, see Figure 2.6. This effect is called tension stiffening.

Tension stiffening is automatically accounted for if the slip between the reinforcing bars and the surrounding concrete is explicitly considered and proper bond shear stress-slip relationships are adopted, as outlined previously. In general, this procedure requires the solution of the second order bond-slip differential equation via an iterative numerical method. However, simpler formulations can be obtained if the bond stress-slip law is chosen such that the integration of the differential equation is simplified. A formulation of this type is going to be adopted in this work and will be further detailed in Chapter 3.

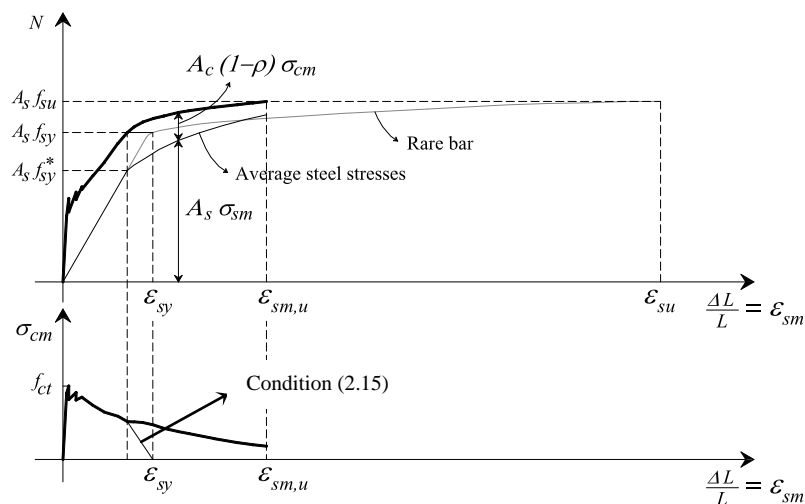


Figure 2.6 –Tension stiffening.

When the control volume over which the constitutive laws are established is enlarged to include several cracks, the so called tension stiffening curves are frequently used to directly relate the average concrete tensile stress σ_{cm} with the average tensile strains ε_{sm} , see Figure 2.6. In this case, both the stress and strain fields are spatially averaged within the control volume and the stress and strain distributions between the cracks are not explicitly considered. These spatially averaged relationships are valid if the reinforcement ratio is higher than the minimum, ensuring that yielding does not occur immediately after cracking. In these circumstances, a distributed stabilized cracking pattern is formed and the explicit consideration of the strain localization issues mentioned in Section 2.1 can be disregarded in the structural analysis.

The average tensile response of cracked reinforced concrete can be obtained directly from tests on tensioned structural concrete members [21] or from equilibrium considerations based on idealized concrete tensile stress distributions between the cracks [40; 84]. Other authors establish the tension stiffening curve from tests on RC panels subjected to in plane shear and axial stresses [25; 240]. However, the tension stiffening diagrams obtained in this way cannot be determined simply from equilibrium equations and are based on a series of assumptions, as will be shown in Chapter 3. Therefore, the obtained diagrams reflect the theory used in assessing the experimental results and may mask other mechanical effects.

When using a tension stiffening diagram for calculating the response of a tensioned structural concrete member, a suitably spatially averaged relationship for the reinforcement steel must be adopted. If Eq. (2.8) is written in terms of averaged quantities it is possible to conclude that:

$$\frac{N}{A_s} = \sigma_{sr} = \sigma_{sm} + \frac{1-\rho}{\rho} \sigma_{cm} \quad (2.13)$$

When the load is increased such that reinforcement yielding occurs at the crack location, i.e. $\sigma_{sr} = f_{sy}$, one obtains

$$f_{sy} = f_{sy}^* + \frac{1-\rho}{\rho} \sigma_{cm} \quad (2.14)$$

where f_{sy}^* is the average yield stress, i.e. the average stress in the reinforcing bars corresponding to the occurrence of the first yield at the cracks, see Figure 2.6. This average

yield stress depends on the adopted tension stiffening diagram. In references [21; 137] suitable averaged stress-strain relationships for the embedded bars are proposed.

Some authors use the bare bar stress-strain relationship. In these circumstances the adopted tension stiffening diagram must fulfil the condition:

$$\sigma_{cm} \leq \frac{\rho}{1-\rho} (f_{sy} - \sigma_{sm}) \quad (2.15)$$

In this case, tensile stresses carried by concrete in the post yielding stage are disregarded and the deformation capacity of the structural members is not properly evaluated, as can be seen in Figure 2.6.

The crack widths can still be calculated using this averaged approach by estimating the crack spacing s_r and expressing the integral relationship (2.12) in terms of the average strains and average concrete stresses:

$$w_r = s_r \left(\varepsilon_{sm} - \frac{\sigma_{cm}}{E_c} \right) \quad (2.16)$$

2.3 Shear transfer through rough cracks

The last stage of the tensile fracture process corresponds to the formation of a macroscopic crack that cannot transmit normal stresses. Shear transfer across these cracks cannot be simply formulated as a relation between shear stress and shear displacement, but is a more complex mechanism, in which shear stress, shear displacement, normal stress and crack width are involved. Several models have been proposed for reproducing the shear transfer mechanisms through the rough crack lips. Some of these models arise from a physical description of the material behaviour at the mesoscale level (via the mechanics of the crack surface contacts), while others result from more or less empirical fits to a set of experimental results. For a review of the existing proposals refer to references [13; 37; 41; 133; 251]. The experimental tests consist essentially in the application of shear forces along previously cracked surfaces – the *push off* test – varying the crack width, the confinement degree and the loading path (Figure 2.7).

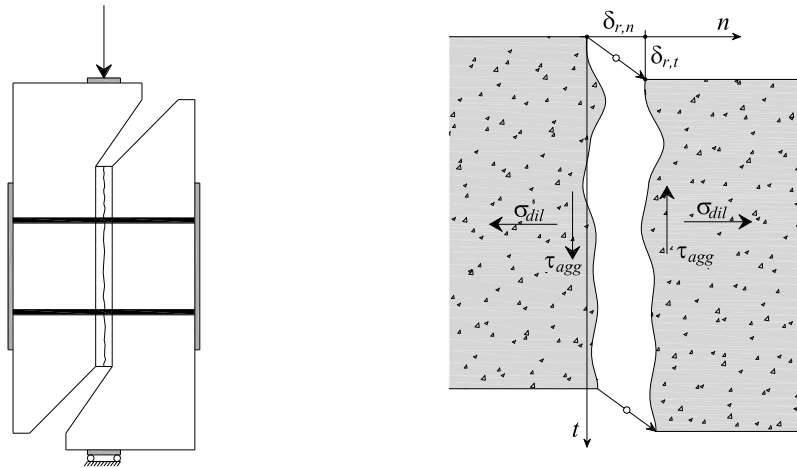


Figure 2.7 – Shear transfer through rough cracks: (a) push off test setup; (b) notation.

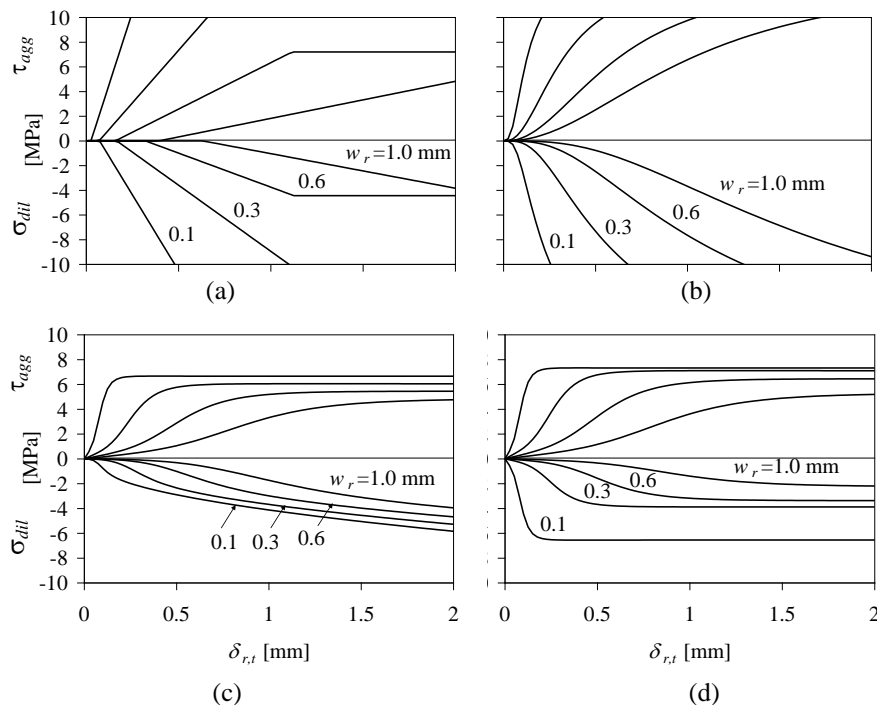


Figure 2.8 – Simulation of a push off test under controlled w_r : (a) Aggregate interlock relation by Walraven [251] combined with the crack shear capacity expression proposed by Vecchio and Collins [240]; (b) Contact density model by Li et al. [133]; (c) Rough crack model by Bazant and Gambarova [12]; (d) Rough crack model by Gambarova and Karakoç, according to [23; 257].

In normal strength concrete (NSC) cracks propagate essentially along the interface between the hardened cement paste and the aggregate particles, originating a highly irregular macroscopic fracture surface. When a crack is subjected to a shear displacement aggregates are pushed against its negative in the hardened cement paste and both normal and frictional forces can be transmitted in numerous contact surfaces. Aggregate particles are generally stiffer than the cement paste, which crushes locally at the contact surfaces,

producing a highly inelastic macroscopic behaviour. The crack roughness is also responsible for a dilating behaviour that is manifested as follows (see Figure 2.7 for notation): keeping the normal confinement stress σ_{dil} constant, a shear stress τ_{agg} will produce a shear displacement $\delta_{r,t}$ and an increase in the crack opening $\delta_{r,n}$ (or w_r); keeping $\delta_{r,n}$ constant, a shear stress τ_{agg} will produce a shear displacement $\delta_{r,t}$ and an increase of the confinement stress σ_{dil} . With increasing crack opening, the contact zones between the opposite crack faces will diminish and the transmitted shear force decreases with increasing $\delta_{r,n}$. For large values of $\delta_{r,t}$ large degradation of the crack surface may occur and the transmitted shear force tends to stabilize, or even decrease, after a certain $\delta_{r,t}$ threshold value. In Figure 2.8 the simulation of a push off test under controlled w_r according to several theoretical models is presented. A concrete strength of $f'_c = 30$ MPa and a maximum aggregate size $D_{max} = 16$ mm were adopted. From the theoretical models available in the literature, only the ones for which a closed form solution is possible, at least for the monotonic load path, were chosen.

For similar fracture surface typologies, the crack shear strength increases with the concrete strength. However, in high strength concrete, cracks propagate through the aggregate particles and the crack surfaces tend to be smoother. Although there is experimental evidence that shear transfer capacity may be reduced, still significant shear forces can be transmitted through high strength concrete cracks. Walraven [251] reported less shear dilatancy for high strength concrete specimens, which indicates higher preponderance of the frictional stresses as load carrying mechanisms, when compared to normal strength concrete.

Cracks crossed by bonded reinforcement exhibit a distinct behaviour, which cannot be solely attributed to dowel action effects. Compared to the results of similar tests in specimens with interrupted bond in the neighbourhood of the crack or in specimens with external restraints, Walraven [251] observed a stiffer response, more crack shear dilatancy and that the crack opening direction was almost independent of the reinforcement content. These differences were attributed to the reduction of the crack width near the reinforcements due to bond stress action, leading to the formation of compressive struts which are responsible for an additional load carrying mechanism (Figure 2.9 (a)). This effect was important for reinforcement contents larger than 0.56%. Walraven proposed a physical model for this effect involving the consideration of a system of stiff hinged struts connecting the crack lips. The polygon of forces expressing the equilibrium in the crack plane is represented in Figure 2.9 (b).

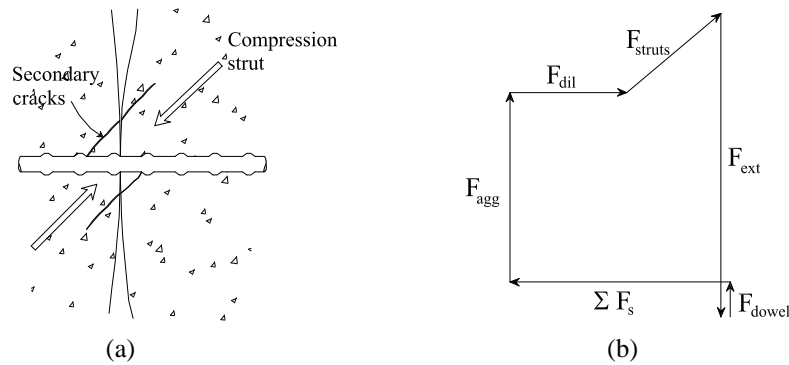


Figure 2.9 – Shear transfer through steel reinforced cracks: (a) expected additional cracking and load carrying mechanism in the case of bonded deformed bars; (b) equilibrium of forces (F_{ext} is the applied shear force, F_{dowel} is the force due to dowel action, F_s is the sum of the reinforcement forces, F_{agg} is the force due to aggregate interlock, F_{dil} is the corresponding dilatancy force and F_{struts} is the additional force required to close the polygon).

2.4 Compressive fracture

2.4.1 Uniaxial compression

Uniaxial compressive strength

The response of concrete in uniaxial compression is usually obtained from cylinders with a height to diameter ratio of 2. The standard cylinder is 300mm high by 150mm in diameter and the resulting compressive strength is here denoted by f'_c . Smaller cubes are commonly used for production control. The cube strength is higher than the obtained from standard cylinders since the end zones of the specimens are laterally constrained by the frame loading plates and the state of stress in the failure zone cannot be considered purely uniaxial.

Uniaxial compression tests on wall elements of plain concrete result in strengths about 10 to 20% lower than the obtained in tests on standard cylinders. This is attributed to the different failure modes, which change from sliding to laminar splitting, with cracks forming parallel to the compressive direction. The additional resistance against laminar splitting provided by the constraints at the specimen ends is responsible for the sliding failure mode that is observed in cylinders.

It was experimentally observed that the resistance to laminar splitting, i.e. the uniaxial compressive strength of unconstrained concrete panels or wall elements, f_{c1} , increases less

than proportionally with f'_c [261]. The relationship between the two compressive strengths can be expressed by

$$f_{c1} = \zeta_f f'_c \quad (2.17)$$

where ζ_f is a reduction coefficient expressing the dependency of the panel compressive strength on f'_c . There are three recognized proposals for this coefficient, one by Muttoni et al. [167], which assumes $f_{c1} \propto f_c'^{\frac{2}{3}}$,

$$\zeta_f = \left(\frac{20}{f'_c} \right)^{\frac{1}{3}} \leq 1 \quad (f'_c \text{ in MPa}) \quad (2.18)$$

another by Zhang and Hsu [261; 262], which assumes $f_{c1} \propto \sqrt{f'_c}$,

$$\zeta_f = \frac{5.8}{\sqrt{f'_c}} \leq 0.9 \quad (f'_c \text{ in MPa}) \quad (2.19)$$

and the third is the proposal in the Eurocode 2 [46],

$$\zeta_f = 1 - \frac{f'_c}{250} \quad (f'_c \text{ in MPa}) \quad (2.20)$$

These expressions are plotted in Figure 2.10 for comparative purposes.

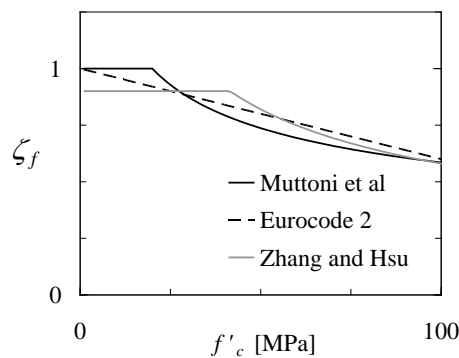


Figure 2.10 – Ratio between the panel and cylinder compressive strengths.

Deformational behaviour

The stress-strain curve of a concrete specimen under uniaxial compressive stresses is nonlinear and its shape is dictated by microcracking propagation at the interface between the aggregates and the cement paste [124; 233]. Near the peak load, lateral strains increase more rapidly and the volumetric strain becomes positive, i.e., the specimen dilates. In the post peak range the load carrying capacity decreases with increasing deformation - strain softening in compression. At this stage, similarly to uniaxial tension, the deformations localize in the fracture process zone. A size effect is observed as longer specimens exhibit a steeper softening branch than that of short specimens [108; 232].

The strain softening behaviour of concrete in compression is far more complicated than that in tension. Vonk [249] has shown, via micromechanical simulations, that the fracture process is not only determined by a local component but also by a continuum component, i.e., for small specimens, the energy dissipated in the post-peak regime – the compressive fracture energy, G_C – was found to increase with the specimen size. Markeset and Hillerborg [144] proposed a theoretical model – the Compression Damage Zone (CDZ) model - which can reasonably describe this behaviour. In the CDZ model, the softening branch of the stress-strain curve of uniaxially compressed cylinders is described by three curves, as depicted in Figure 2.11. The first curve reflects the unloading of concrete material and is valid for the whole specimen; the second curve shows the relationship between the stress and the average strain in the so called damage zone and is related to the formation of longitudinal cracks; the third curve is related to the localized deformations that take place in the inclined shear band, in the case of the specimen illustrated in Figure 2.11, or in other ways, in the case of other specimen shapes leading to different failure modes. According to the CDZ model, the total elongation δ of a specimen subjected to pure compression is given by Eq. (2.21), where L is the total specimen length, L_d is the length of the damage zone, ε_c is the concrete strain of the unloading concrete, ε_d is the concrete strain inside the damage zone and w is the elongation in the FPZ.

$$\delta = \varepsilon_c L + \varepsilon_d L_d + w \quad (2.21)$$

The average specimen strain ε_m can be calculated from:

$$\varepsilon_m = \varepsilon_c + \varepsilon_d \frac{L_d}{L} + \frac{w}{L}, \quad \frac{L_d}{L} \leq 1 \quad (2.22)$$

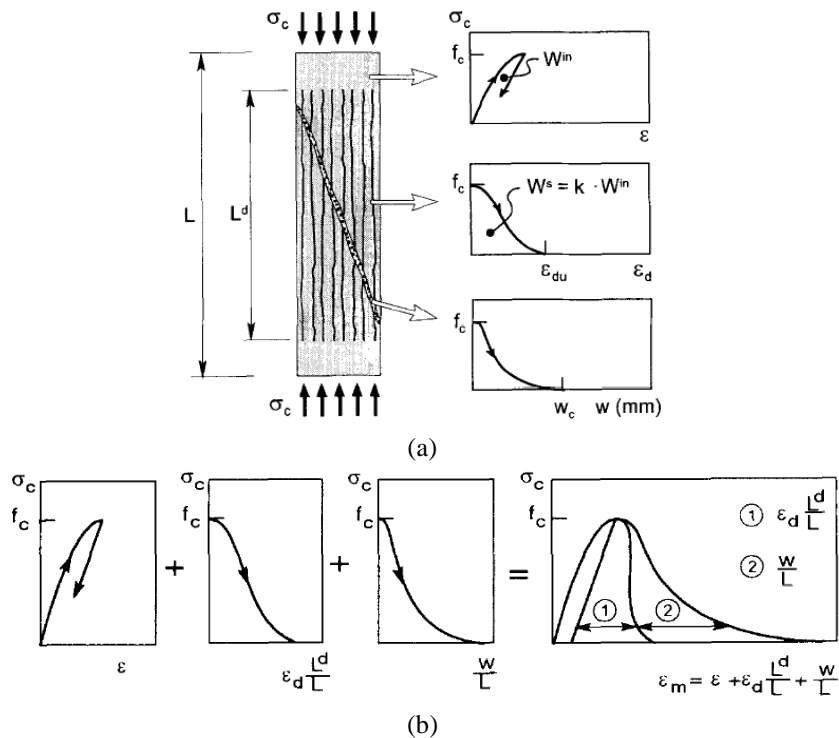


Figure 2.11 – Strain softening behaviour in compression (taken from reference [144]): (a) Illustration of the CDZ model; (b) Composition of the stress-strain curve.

It must be emphasized that the damage zone is not solely dependent on material properties, as it is commonly accepted to occur with the localization process in uniaxial tension. A structural behaviour is introduced because the localization band size depends on the element thickness, in the case of a panel, or on the diameter, in the case of a cylinder. Compressive failure is also a three-dimensional process, highly sensitive to the boundary restraint influences. It is easily understood that the degree of confinement provided by the structural shape strongly influences the development of this localized deformations region.

2.4.2 Effect of multiaxial stresses

In the stress space, the locus of all the stress combinations for which a proportionally loaded concrete specimen reaches its load carrying capacity is usually called the *failure surface*. This surface is commonly expressed as a function of the stress invariants. It is a convenient simplification to assume that a failure surface based on proportional loading tests can still be used for more general load cases. In these circumstances, provided the individual components of the stress tensor do not deviate too much from the monotonic path, the scatter of the available experimental tests is larger than any systematic variation of the failure surface attributable to different loading paths [124; 136].

The failure surface for axisymmetric stress states is depicted in Figure 2.12 (a). The hydrostatic component of the applied stress tensor inhibits the formation of oriented fracture processes in a compressed concrete specimen. Therefore, both strength and ductility increase with confinement degree. When lateral confinement increases beyond a certain level, indicated by the transition point TP in Figure 2.12 (a), failure becomes ductile and softening cannot be observed. Test results indicate that for moderate lateral compressive stresses of about $-\sigma_1 = -\sigma_2 \leq 2f_{c1}$, the triaxial compressive strength, f_{c3} , can be determined by the linear relationship [167]:

$$f_{c3} = f_{c1} - 4\sigma_1 \quad (2.23)$$

More accurate proposals for general 3D failure surfaces can be found in [58; 89; 103; 116; 124; 177; 181; 190].

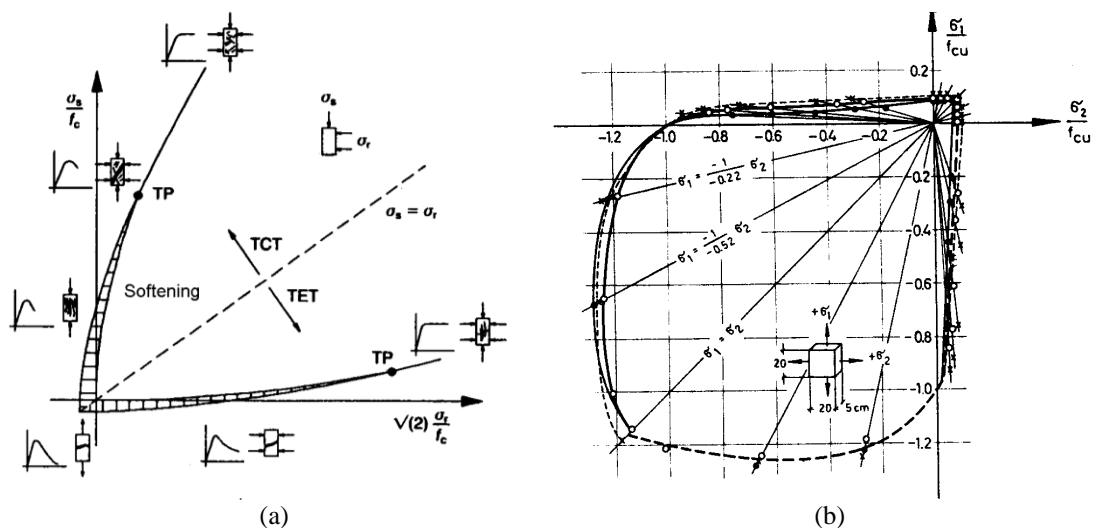


Figure 2.12 – Failure surface and failure modes under multiaxial stress conditions: (a) compressive and tensile meridians defining the failure surface for axisymmetric stress conditions [190]; (b) failure surface for biaxial stress conditions according to Kupfer and Gerstle [128].

The failure surface under biaxial stress states is depicted in Figure 2.12 (b). After tensile failure in biaxial tension-compression has occurred, compressive stresses parallel to the cracks can still be resisted. If the compressive stress is increased, the specimen will eventually fail in compression at a load approximately equal to the uniaxial compressive strength. For small tensile stresses, failure in the compression/tension region occurs for a compressive stress somewhat lower than f_{c1} . According to the failure surface proposed by Kupfer and Gerstle [128], in the biaxial compression region, the biaxial compressive strength f_{c2} can be 16% and 29% higher than the uniaxial panel strength f_{c1} , for the stress

trajectories $\sigma_1/\sigma_2 = 1/1$ and $\sigma_1/\sigma_2 = 0.52/1$, respectively. If confinement at the specimen ends is eliminated as far as possible, the failure modes vary between laminar splitting and tensile failure. In these circumstances the sliding failure mode is never observed.

2.4.3 Cracked concrete

The compression response of cracked concrete reinforced with deformed bars differs from that in the uncracked state. This effect was first reported in 1961 by Robinson [195] from tests in concrete beams failing by web crushing and was later elaborated on by several research groups, namely in Paris, Copenhagen, Zurich and Stuttgart. From this first set of research works it was found that the primary characteristic of cracked concrete compressive behaviour is the reduction of the peak stress in comparison to that of the standard cylinder. This effect is called compression softening¹. Neglecting it was found to lead to serious overestimations of the shear capacity of structural concrete elements, although it was not clear which were the parameters governing the softening effect. This was mainly due to the technical difficulties in the experimental arrangements involved in the study of the compressive response of cracked reinforced concrete. The effective concrete strength was expressed by $f_{c,ef} = \nu f'_c$, with ν being an effectiveness factor taken as a constant or as a function of f'_c . These formulations are still used today within plastic analysis of structural concrete elements and are implemented in many design codes. For a complete bibliographic review on this topic refer to reference [20].

Some of the above mentioned technical difficulties with the experimental arrangements were overcome by Vecchio and Collins in 1981 [234] after the construction of the “shear rig” at the University of Toronto. From tests on RC panels subjected to uniform in-plane shear and axial stresses they found the average principal tensile (lateral) strain as the primary variable influencing compression softening. Reductions up to only 20% of the reference value f'_c were reported. Since then numerous experimental studies have been undertaken to establish the relationship between the softening coefficient and the lateral tensile strains [242]. It is generally agreed that the effective compressive strength of cracked reinforced concrete can be conveniently expressed as:

$$f_{c,ef} = \zeta_e f_{c1} = \zeta_e \zeta_f f'_c \quad (2.24)$$

¹ In this context the term ‘softening’ is used for expressing the reduction of the compressive strength of cracked concrete in comparison to that of the standard cylinder and not the post peak behaviour.

where ζ_e is the softening coefficient expressing the influence of the lateral tensile strains and ζ_f is defined according to Eqs. (2.18), (2.19) or (2.20).

Gross differences can still be found between the several proposals for the softening effect, see Figure 2.13. Besides the inherent scatter due to the heterogeneous nature of concrete, this discrepancy can be partially explained by differences in the experimental arrangements, - including specimens size, reinforcement type and layout, load path and measuring techniques – different concrete strengths of the tested specimens and lateral strain ranges analysed in each experimental campaign.

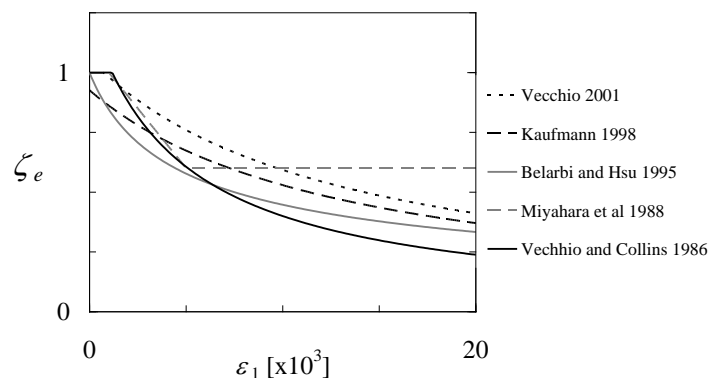


Figure 2.13 – Compression softening coefficient according to several authors [22; 117; 160; 240; 246].

The compression softening coefficient ζ_e should be determined based on biaxial tension-compression tests on RC panels with the external loading aligned with the reinforcement directions. In these tests concrete stresses can be calculated exclusively from equilibrium considerations. The specimens can be subjected to sequential or proportional loading in tension-compression. For tests with reinforcement bars inclined 45° with respect to the applied stresses and for equal reinforcement ratios in both diagonal directions, concrete stresses can still be determined exclusively from the equilibrium equations. However, due to bond stress transfer mechanisms, concrete compressive stresses between the cracks are smaller than at the cracks, see Chapter 3, and care must be taken in interpreting the experimental results. In shear tests of orthotropically reinforced panels, concrete and reinforcement stresses can only be determined based on a series of assumptions. Therefore, the expressions calibrated using these tests reflect the theory used in assessing the stresses and may be masking other mechanical effects. For example, calibration of the expressions for the compression response of cracked concrete adopted in the Modified Compression Field Theory (MFCT) [240; 242] was based on this type of tests (shear tests on orthotropically reinforced panels). Within the formulation of the more recent Disturbed

Stress Field Model (DSFM) [237], the same authors recognized that a significantly reduced amount of compressive softening was required for obtaining equivalent results and another expression was proposed for the softening coefficient, see Figure 2.13. Care must be taken when using compression softening relationships beyond the scope of the theory used in assessing the experimental results.

The systematic experimental study carried out by Hsu and co-workers [22; 262] at the University of Houston allowed a deeper understating on the compression softening phenomena. The tensile strain was confirmed as the main variable behind compressive softening, but a close inspection of the experimental results reveals that improved correlations can be obtained if the influences of the concrete strength, load path and of the reinforcement direction with respect to the cracks are taken into account, see Figure 2.14.

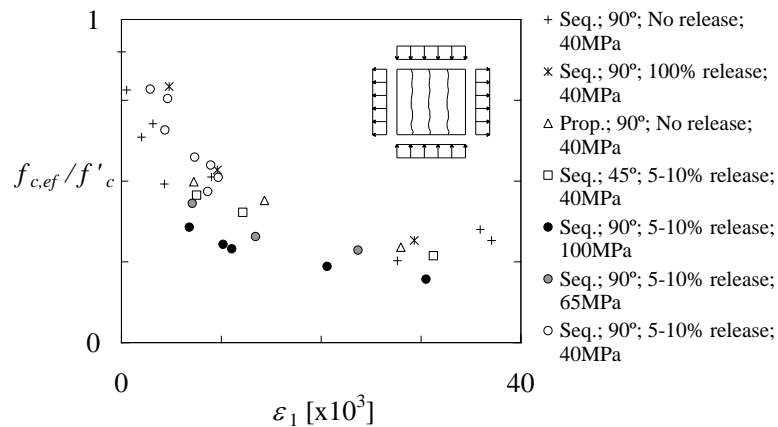


Figure 2.14 – Experimental data from RC panels tested in biaxial tension compression by Hsu and co-workers at the University of Houston [20; 178; 261]. Key for the legend: *Seq.* - sequential loading; *Prop.* - proportional loading; *90°* - compressive loading normal to the lateral reinforcement; *45°* - isotropic reinforcement at 45° with the loading directions; *5-10% or 100% release* – lateral tensile loading released during the compressive loading in order to maintain a predefined lateral strain value; *no release* – no release in the tensile lateral loading; *40/65/100 MPa* – f'_c value.

There are two physical phenomena underlying the strong correlation between the lateral tensile strains and the softening effect. Consider an RC panel subjected to in plane biaxial tension-compression stresses. Due to concrete heterogeneity, cracks present a crooked shape which is responsible for an eccentricity of the resultant force in each concrete strut. Eccentricities cause serious non-uniform stresses in the struts, leading to premature concrete failures in the zones where the stresses are higher and subsequent stress redistributions to the stronger zones in the middle of the struts. With increasing average tensile strain new cracks form and the stress distribution becomes even less uniform.

However, the crack spacing stabilizes before steel yielding and, according to the described above, no justification is given to the continuous reduction of the compressive strength at large lateral strains ($\varepsilon_1 \gg \varepsilon_{sy}$). This may be explained by the bond behaviour of deformed bars. As the slip between concrete and reinforcement increases, the ribs of the reinforcing bars tend to separate the surrounding concrete along the reinforcement. This effect is known as tension splitting and has been reported in RC panels subjected to in-plane tensile stresses [244; 261]. In-plane dilatation has been measured in the direction perpendicular to the tensile stresses, contradicting the expected contraction due to Poisson effect. This dilatation also occurs in the direction normal to the panel plane, and laminar splitting of concrete will occur at markedly lower compressive stresses than in uniaxial compression. While specimens with only one reinforcement layer will fail, spalling of concrete cover will occur for specimens reinforced with two or more reinforcement layers, and a further load increase is often possible (although the previous peak load can no longer be reached).

Following this line of thinking, it is expected that, at large tensile strains, larger values of the \emptyset/c ratio - where \emptyset is the rebar diameter and c is the concrete cover - will lead to larger strength reductions. This is confirmed by the experimental results of Belarbi and Hsu [22]. Also, if the transverse reinforcement is not normal to the compression field, additional concrete degradation can be attributed to the localized crushing in the vicinity of the reinforcing bars. Strictly speaking, compression softening is not a material property since it depends on the type and the layout of the reinforcement.

3 The RC cracked membrane element

3.1 General

For the past 30 years a strong investment has been made on the research of suitable constitutive laws for RC membranes. Nonetheless, shear dominated behaviours still remain a difficult problem to solve. Due to the multiplicity of the involved mechanical effects, the desired accuracy and complexity of the theoretical models had to be balanced in order to achieve a satisfactory engineering solution to the problem. One of the most striking aspects of structural concrete behaviour is that, after cracking, the slip between concrete and reinforcement leads to a highly irregular stress field. This aspect is commonly dealt with by treating reinforced concrete as a new material with its own stress-strain characteristics, which are valid only in spatially averaged terms. These laws are established based on experimental evidence resulting from extensive tests on RC panels subjected to in-plane shear and axial stresses. Although neither the strain nor the stress fields are uniform throughout each of these panels - local variations occur between the cracks as it will be discussed in this chapter -, up to the peak load it is licit to assume an averaged (or homogenised) state of strain. In fact, once the crack pattern is stabilized one can assume that these irregularities are repeated and that the stress and strain fields can be averaged. This is confirmed by the redundant measurements that are made in properly conducted experiments. The RC panel is thus considered as the basic unit, or the control volume, over which the constitutive laws are valid and no spatial discretization is required for calculating its force-deformation response.

Although this type of formulations has greatly contributed to improved accuracy in the analyses of the shear response of RC elements, they fail to give a quantitative description of both local and average stress/strain fields. Due to this fact it is not possible to quantify the steel strains in the vicinity of the cracks in the post yielding regime. Consequently, it is not possible to formulate a rational criterion for evaluating the deformation capacity of the reinforcement, which can be crucial for accurate safety evaluations of structural concrete elements reinforced with less ductile steel or corroded reinforcement. It is also commonly assumed that the direction of the principal average concrete stress coincides with that of the principal average strain. Even though this assumption greatly simplifies the resulting

theories, a lag between the two directions is observed in the experiments [237]. Moreover, this assumption is clearly violated in the case of a sliding shear failure in which part of a specimen is pushed up and away relative to the other. Additionally, the relationship between the adopted constitutive laws and the well established mechanical models for some specific phenomena taking place at the cracks and which are known to govern the behaviour of RC elements, such as the crack shear stress transfer mechanics (including crack shear dilatancy effects), is often not transparent.

The goal of the work presented in this chapter is the development of a more strict formulation for a spatially-averaged cracked membrane element, which: (1) eliminates the need to resort to empirical averaged stress-strain relations for the reinforced concrete material; (2) enables a rational quantitative description of the stress/strain fields both at the cracks and in between the cracks, allowing a deeper understanding of the complex mechanics involved in shear behaviour of cracked membrane elements; (3) provides proper consideration of bond shear stress transfer mechanisms in the post-yielding stage of the reinforcement steel and, consequently realistic estimates of its deformation capacity; (4) is sufficiently simple in order to allow its implementation in a robust formulation for finite element analysis of real scale structures.

Following this brief introduction, in Sections 3.2 and 3.3 the equilibrium and compatibility equations of the cracked membrane element are derived for the general case of fixed and interlocked cracks. Special attention is paid to the relationship between the stresses at the cracks and its spatially averaged counterparts. The formulation of rotating crack and limit analysis models is discussed in Section 3.4 as a particular case of the general formulation presented in 3.2 and 3.3. The existing models for the analysis of cracked RC membrane elements are reviewed in Section 3.5 in light of what has been previously exposed. The adopted constitutive relationships are introduced in Section 3.6 and a calculation example is detailed in Section 3.7 illustrating the response of the developed model. An extensive validation campaign using a wide database of RC panels tested under in-plane stress conditions is presented in Section 3.8. This chapter concludes with a brief review and some suggestions for further work.

3.2 Equilibrium equations

Consider an orthogonally reinforced RC panel with a set of parallel and uniformly spaced cracks as depicted in Figure 3.1. The panel is subjected to the external in plane

stresses $\boldsymbol{\sigma}_{xy} = \{\sigma_x \ \sigma_y \ \tau_{xy}\}^T$. For simplicity, the global coordinate system is aligned with the reinforcement directions. The sign convention is such that the stresses represented in the figure are positive. The local crack coordinates n and t are aligned with the crack direction. The angle θ_r defines the direction of the normal to the cracks.

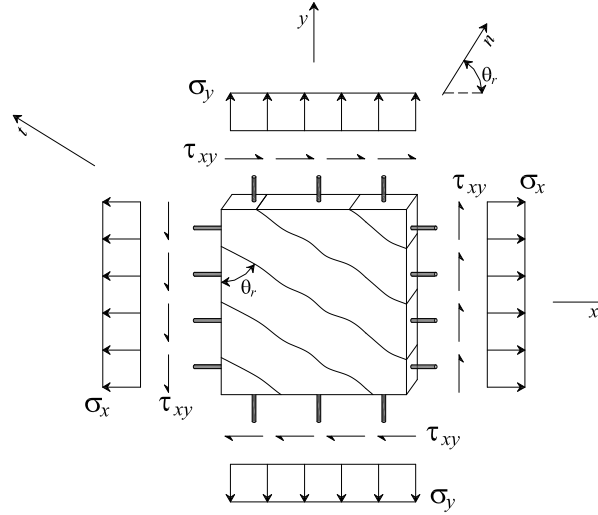


Figure 3.1 – Cracked membrane element.

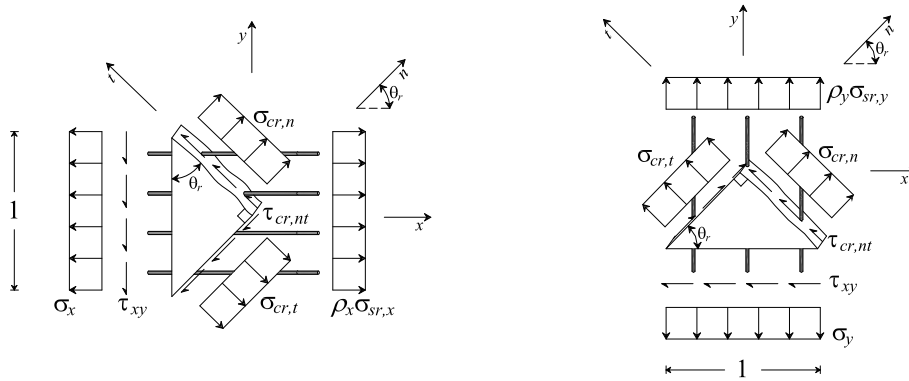


Figure 3.2 – Equilibrium expressed in terms of stresses at the crack.

In the general case of fixed and interlocked cracks, equilibrium of stresses at the cracks requires that (see Figure 3.2),

$$\begin{aligned}
 \sigma_x &= \sigma_{cr,n} \cos^2 \theta_r + \sigma_{cr,t} \sin^2 \theta_r - 2\tau_{cr,nt} \sin \theta_r \cos \theta_r + \rho_x \sigma_{sr,x} \\
 \sigma_y &= \sigma_{cr,n} \sin^2 \theta_r + \sigma_{cr,t} \cos^2 \theta_r + 2\tau_{cr,nt} \sin \theta_r \cos \theta_r + \rho_y \sigma_{sr,y} \\
 \tau_{xy} &= \sigma_{cr,n} \sin \theta_r \cos \theta_r - \sigma_{cr,t} \sin \theta_r \cos \theta_r + \tau_{cr,nt} (\cos^2 \theta_r - \sin^2 \theta_r)
 \end{aligned}
 \tag{3.1}$$

These relations can also be expressed in matrix form as:

$$\boldsymbol{\sigma}_{xy} = \mathbf{T}_{\sigma} \boldsymbol{\sigma}_{cr,nt} + \boldsymbol{\rho} \boldsymbol{\sigma}_{sr,xy}$$

$$\boldsymbol{\sigma}_{cr,nt} = \{\sigma_{cr,n} \quad \sigma_{cr,t} \quad \tau_{cr,nt}\}^T \quad \boldsymbol{\rho} \boldsymbol{\sigma}_{sr,xy} = \{\rho_x \sigma_{sr,x} \quad \rho_y \sigma_{sr,y} \quad 0\}^T \quad (3.2)$$

$$\mathbf{T}_{\sigma} = \begin{bmatrix} c^2 & s^2 & -2sc \\ s^2 & c^2 & 2sc \\ sc & -sc & c^2 - s^2 \end{bmatrix}, \quad \begin{matrix} s = \sin \theta_r \\ c = \cos \theta_r \end{matrix}$$

The local crack stresses have a clear physical meaning in light of the concrete mechanics and of what has been exposed in the previous chapter. The normal concrete stress component along the t coordinate, $\sigma_{cr,t}$, is related to the diagonal compressive field. The normal concrete stress component along the n coordinate, $\sigma_{cr,n}$, is obtained by summing the crack bridging stresses and the crack dilatancy stresses arising from the crack shear transfer mechanisms,

$$\sigma_{cr,n} = \sigma_{bri} + \sigma_{dil} \quad (3.3)$$

The crack shear stress, $\tau_{cr,nt}$, is given by the sum of the shear stresses arising from the aggregate interlock and dowel action effects,

$$\tau_{cr,nt} = \tau_{agg} + \tau_{dow} \quad (3.4)$$

The equilibrium can be visualized in the Mohr circle of stresses of Figure 3.3. In the right circle, the points $X=(\sigma_x, \tau_{xy})$ and $Y=(\sigma_y, -\tau_{xy})$ represent the applied stresses in the xy coordinate system. The concrete stresses at the cracks are represented by the left circle, with $X_{cr}=(\sigma_{cr,x}, \tau_{cr,xy})$, $Y_{cr}=(\sigma_{cr,y}, -\tau_{cr,xy})$ and $N_{cr}=(\sigma_{cr,n}, \tau_{cr,nt})$, $T_{cr}=(\sigma_{cr,t}, -\tau_{cr,nt})$ representing the concrete crack stress tensor in the global and local coordinate systems, respectively. Due to dilatancy stresses $\sigma_{cr,n}$ can be negative, as represented in the figure. The equilibrium between the applied stresses and the internal stresses is obtained by adding the reinforcement stress contribution at the cracks, $\rho_x \sigma_{sr,x}$ and $\rho_y \sigma_{sr,y}$. As the reinforcements are aligned with the xy coordinate system and as they carry only axial stresses, the equality $\tau_{xy} = \tau_{cr,xy}$ is valid and the points X_{cr}/X and Y_{cr}/Y have the same ordinate.

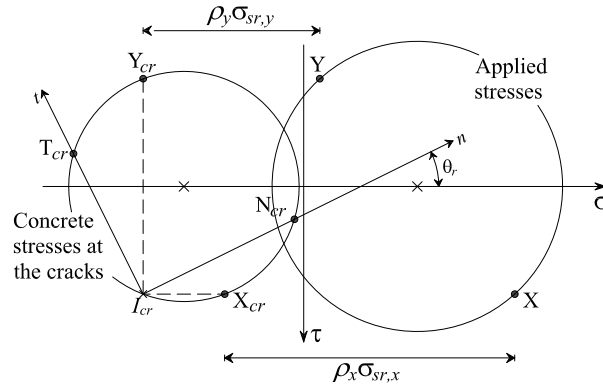


Figure 3.3 – Mohr circle of stresses expressing the equilibrium in terms of local crack stresses.

3.2.1 Concrete contribution to shear strength

The equilibrium equations (3.1) can be rearranged and the shear stress can be written as:

$$\tau_{xy} = \tau_{cr,nt} + \sigma_{cr,n} \tan \theta_r + (\rho_y \sigma_{sr,y} - \sigma_y) \tan \theta_r \quad (3.5)$$

Considering the particular case of having $\sigma_y = 0$, the equation above states that the applied shear stress is equilibrated by two components, $\tau_{xy} = \tau_{xy,cr} + \tau_{xy,sr}$, the first being attributed only to concrete and the second to the reinforcing steel:

$$\tau_{xy,cr} = \tau_{cr,nt} + \sigma_{cr,n} \tan \theta_r \quad (3.6)$$

$$\tau_{xy,sr} = \rho_y \sigma_{sr,y} \tan \theta_r$$

It is noted that in the concrete component the stress $\sigma_{cr,n}$ is usually compressive due to the crack dilatancy stresses arising from shear stress transfer mechanisms, thus having a negative contribution to the shear strength.

3.2.2 Relationship between average and local crack stresses

For unbonded reinforcement, steel and concrete stresses are constant within the membrane element. In the presence of bonded reinforcement, the bond stress transfer between reinforcement and concrete is activated as soon as crack is formed, as discussed in Section 2.2, leading to the existence of an irregular concrete stress field, as depicted schematically in Figure 3.4. The variation of the concrete stresses in the $n-t$ coordinate system can be observed in the upper left side of the figure. At the cracks, the normal concrete stress $\sigma_{c,n}$

can assume negative values due to crack dilatancy effects. Equilibrium requires that the compressive stress parallel to the t - direction, $\sigma_{c,t}$, has its maximum magnitude at the cracks. The same occurs with the shear stress $\tau_{c,nt}$. In the reinforcement x - and y - directions (right side and bottom of the figure) the steel stresses $\sigma_{s,x}$ and $\sigma_{s,y}$, the concrete stresses $\sigma_{c,x}$ and $\sigma_{c,y}$, and the tensile stresses transferred from steel to concrete $\Delta\sigma_{c,x}$ and $\Delta\sigma_{c,y}$ can be analysed. Steel tensile stresses are maximum at the cracks, gradually decreasing due to bond action towards the surrounding concrete. In order to maintain equilibrium concrete stresses vary accordingly. In general, the compressive stresses magnitude is higher at the cracks and lower between the cracks, the opposite occurring with the tensile stresses. It must be remarked that the concrete stresses in the reinforcement directions, $\sigma_{c,x}$ and $\sigma_{c,y}$, are generally compressive (see Figure 3.3). The spatially averaged (or homogenised) stress field can be obtained averaging the concrete and steel stress distributions. The average tensile stresses transferred from steel to concrete in the reinforcement directions, i.e., the tension stiffening stresses, are represented by $\Delta\sigma_{cm,x}$ and $\Delta\sigma_{cm,y}$. These stresses can be obtained from:

$$\begin{aligned}\Delta\sigma_{cm,x} &= \rho_x (\sigma_{sr,x} - \sigma_{sm,x}) \\ \Delta\sigma_{cm,y} &= \rho_y (\sigma_{sr,y} - \sigma_{sm,y})\end{aligned}\tag{3.7}$$

where $\sigma_{sr,x/y}$ are the steel stresses at the cracks for the x/y -reinforcements and $\sigma_{sm,x/y}$ are the corresponding average stresses.

The panel equilibrium can also be expressed in terms of average stresses, which can still be expressed by the equations (3.1) if the stresses at the cracks $\sigma_{cr,n}$, $\sigma_{cr,t}$, $\tau_{cr,nt}$, $\sigma_{sr,x}$ and $\sigma_{sr,y}$ are replaced by the corresponding average stresses $\sigma_{cm,n}$, $\sigma_{cm,t}$, $\tau_{cm,nt}$, $\sigma_{sm,x}$ and $\sigma_{sm,y}$.

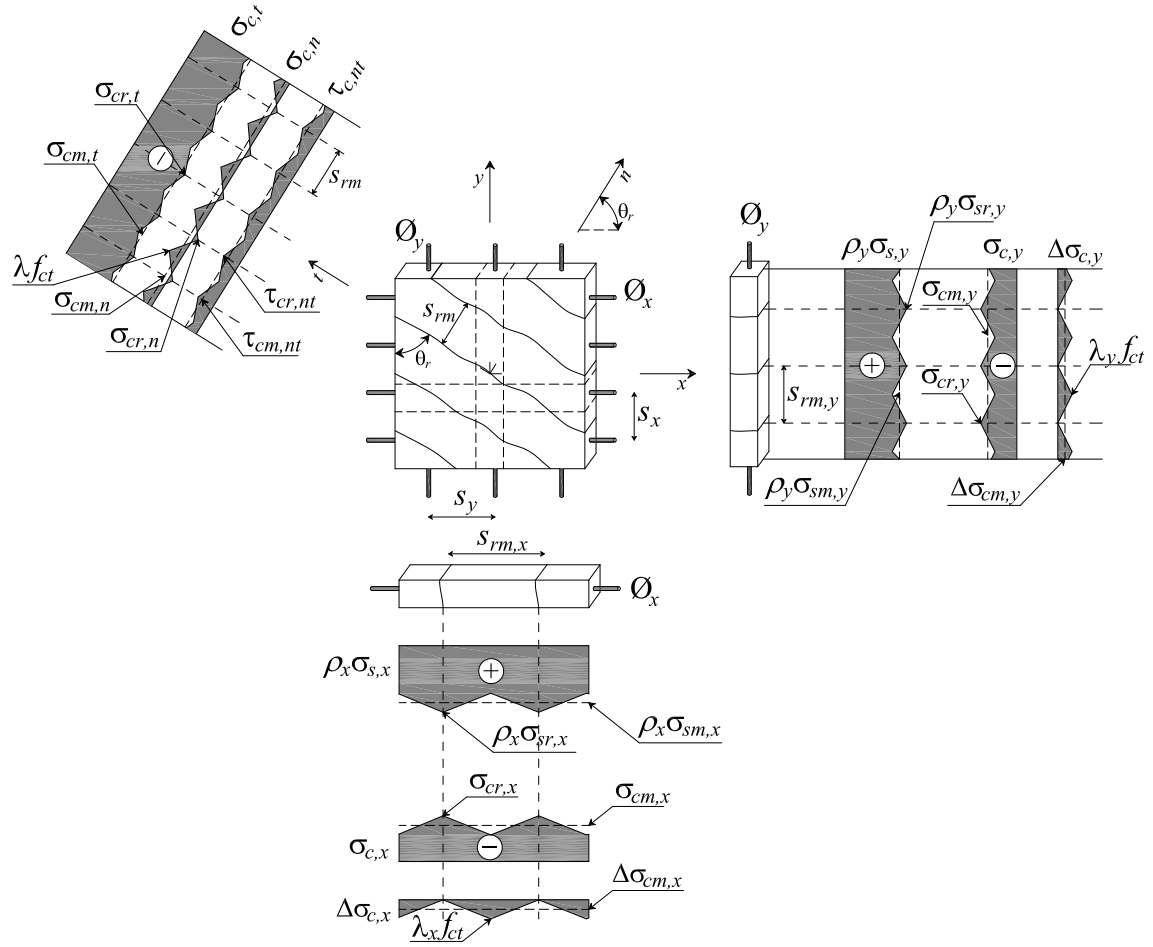


Figure 3.4 – Stress field in the cracked membrane element. Notation.

In the Mohr circle of stresses of Figure 3.5, the relationship between concrete average stresses and concrete stresses at the cracks is shown. The tension stiffening stresses are responsible for the deviation of the two circles, which can be expressed analytically as,

$$\boldsymbol{\sigma}_{cm,nt} = \boldsymbol{\sigma}_{cr,nt} + \mathbf{T}_{\sigma}^{-1} \left\{ \Delta\sigma_{cm,x} \quad \Delta\sigma_{cm,y} \quad 0 \right\}^T \quad (3.8)$$

or equivalently as,

$$\begin{aligned} \sigma_{cm,n} &= \sigma_{cr,n} + \Delta\sigma_{cm,x} \cos^2 \theta_r + \Delta\sigma_{cm,y} \sin^2 \theta_r \\ \sigma_{cm,t} &= \sigma_{cr,t} + \Delta\sigma_{cm,x} \sin^2 \theta_r + \Delta\sigma_{cm,y} \cos^2 \theta_r \\ \tau_{cm,nt} &= \tau_{cr,nt} + \left(-\Delta\sigma_{cm,x} + \Delta\sigma_{cm,y} \right) \sin \theta_r \cos \theta_r \end{aligned} \quad (3.9)$$

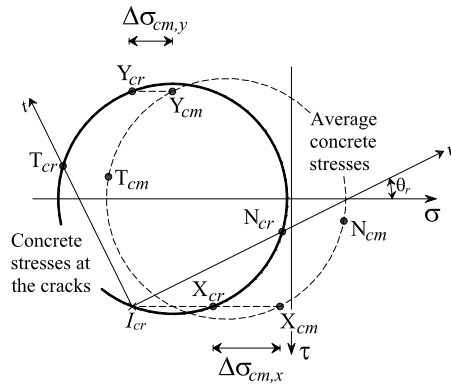


Figure 3.5 – Mohr circle of stresses showing the relationship between concrete average stresses and concrete stresses at the cracks.

In general, the principal stress directions of the two concrete stress tensors, θ_{cr} and θ_{cm} , do not coincide and the components of the average concrete stress tensor have a different meaning from their counterparts at the cracks (see Figure 3.6). Apart from the crack bridging stresses and whenever there is no crack shear slip, $\sigma_{cm,n}$ is the projection of the tension stiffening stresses in the n - direction, as shown in Eq. (3.9)₁. However, if shear slip at the cracks is activated, crack dilatancy stresses introduce an extra stress component along the n - axis. Whenever the tension stiffening stresses are different, a shear component is also introduced. Consequently the crack shear stress $\tau_{cr,nt}$ and the average shear stresses $\tau_{cm,nt}$ are not equal, which is reflected by the different ordinate of the points N_{cr} and N_{cm} .

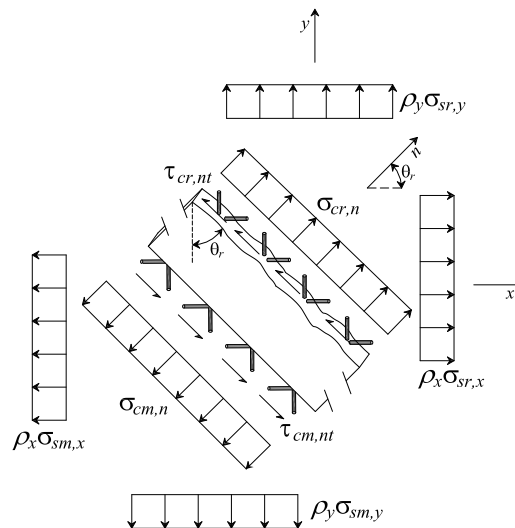


Figure 3.6 – Equilibrium in terms of local and average stresses.

3.3 Compatibility equations

In this work, an approach involving average, or smeared, strains is adopted. The bond shear stress-slip relationship is formulated in such a way that the slip between reinforcement and concrete does not need to be explicitly modelled. This concept agrees with the goal of formulating a material model suitable for implementation in a finite element code dedicated to the analysis of real scale structures.

The total average engineering strains, $\boldsymbol{\varepsilon}_{nt} = \{\varepsilon_n \quad \varepsilon_t \quad \gamma_{nt}\}^T$, can be divided into average strains due to deformation of the concrete between the cracks, $\boldsymbol{\varepsilon}_{nt}^{(c)}$, and average strains due to crack displacements, $\boldsymbol{\varepsilon}_{nt}^{(r)}$:

$$\boldsymbol{\varepsilon}_{nt} = \boldsymbol{\varepsilon}_{nt}^{(c)} + \boldsymbol{\varepsilon}_{nt}^{(r)} \quad (3.10)$$

In the local crack coordinate system, the smeared average strain components due to crack opening, $\delta_{r,n}$ (or simply w_r), and crack slip, $\delta_{r,t}$, are given by (Figure 3.7):

$$\varepsilon_n^{(r)} = \frac{\delta_{r,n}}{s_{rm}} \quad \varepsilon_t^{(r)} = 0 \quad \gamma_{nt}^{(r)} = \frac{\delta_{r,t}}{s_{rm}} \quad (3.11)$$

with s_{rm} being the average crack spacing.

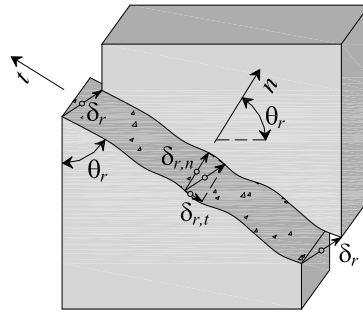


Figure 3.7 – Crack kinematics. Notation.

In order to avoid internal iterative loops at the constitutive level for performing the tensorial split given by Eq. (3.10), two simplifying assumptions are adopted regarding the concrete strains: (1) after cracking, the axial contraction of the struts due to transversal tensile stresses is neglected; (2) concrete shear deformation in between the cracks can be neglected when compared with the deformation corresponding to smearing the slip occurring between the crack lips, i.e., $\gamma_{nt}^{(c)} = 0$.

The average total engineering strains in the local crack coordinate system can be obtained from the total engineering strains in the global coordinate system using the strain transformation relationship [74],

$$\boldsymbol{\varepsilon}_{nt} = \mathbf{T}_\varepsilon \boldsymbol{\varepsilon}_{xy} \Leftrightarrow \begin{Bmatrix} \varepsilon_n \\ \varepsilon_t \\ \gamma_{nt} \end{Bmatrix} = \begin{bmatrix} c^2 & s^2 & sc \\ s^2 & c^2 & -sc \\ -2sc & 2sc & c^2 - s^2 \end{bmatrix} \begin{Bmatrix} \varepsilon_x \\ \varepsilon_y \\ \gamma_{xy} \end{Bmatrix}, \quad \begin{aligned} s &= \sin \theta_r \\ c &= \cos \theta_r \end{aligned} \quad (3.12)$$

3.4 Particular cases

The equilibrium equations (3.1) can be simplified if some additional assumptions are adopted. A commonly adopted simplification is to consider that the principal average strain axes and the principal concrete stress axes coincide. If the equilibrium equations are established in terms of stresses at the cracks, this means that the local crack stresses are co-linear with the correspondent average principal strains. An immediate consequence of the previous assumption is that no crack shear stress is admitted and that the cracks are able to rotate. In this case the angle θ_r ceases to be fixed and defines the direction of the current tensile principal average strain, being given by

$$\tan^2 \theta_r = \frac{\varepsilon_y - \varepsilon_2}{\varepsilon_x - \varepsilon_2} \quad (3.13)$$

where ε_2 is the compressive principal average strain.

The equilibrium equations simplify to

$$\begin{aligned} \sigma_x &= \sigma_{cr,1} \cos^2 \theta_r + \sigma_{cr,2} \sin^2 \theta_r + \rho_x \sigma_{sr,x} \\ \sigma_y &= \sigma_{cr,1} \sin^2 \theta_r + \sigma_{cr,2} \cos^2 \theta_r + \rho_y \sigma_{sr,y} \\ \tau_{xy} &= \sigma_{cr,1} \sin \theta_r \cos \theta_r - \sigma_{cr,2} \sin \theta_r \cos \theta_r \end{aligned} \quad (3.14)$$

where the indexes $(.)_n$ and $(.)_t$ are replaced by $(.)_1$ and $(.)_2$ since the local axes coincide with the principal directions. The crack stress $\sigma_{cr,1}$ is due to the crack bridging stresses and is only significant for poorly reinforced concrete elements. In this case, the concrete contribution to the shear strength identified in Eq. (3.6)₁ disappears and only the steel contribution remains. After reinforcement yielding, the applied shear stress can still be

increased due to crack rotation. This rotation can continue until steel rupture, in which case $\sigma_{sr,y} = f_{su,y}$ in Eq. (3.6)₂, or until concrete crushing. Considering that $\sigma_{cr,1}$ is exhausted, the latter failure mode is described by

$$\tau_{xy} = -\sigma_{cr,2} \sin \theta_r \cos \theta_r = -\frac{\sigma_{cr,2}}{\tan \theta_r + \cot \theta_r} \quad (3.15)$$

This equation, which is quite similar to the plasticity based code equations dealing with web crushing failure in beams, states that if stress free and rotating cracks are considered, the shear stress sustained by the panel depends only on the crack direction and on the current value of the diagonal compressive concrete stress.

The equilibrium equations can be even more simplified if the concrete tensile strength is neglected, which means that bond stress transfer effects are also disregarded. This is consistent with limit analysis assumptions. In this case, the index $(.)_r$ is dropped since no distinction can be made between the average stresses and stresses at the cracks:

$$\begin{aligned} \sigma_x &= \sigma_{c,2} \sin^2 \theta + \rho_x \sigma_{s,x} \\ \sigma_y &= \sigma_{c,2} \cos^2 \theta + \rho_y \sigma_{s,y} \\ \tau_{xy} &= -\sigma_{c,2} \sin \theta \cos \theta \end{aligned} \quad (3.16)$$

3.5 Review on previous work

For a better understanding of the differences amongst the existing constitutive models for RC cracked membranes it is useful to recall that, in general, in a RC panel subjected to in plane shear and axial stresses, for an arbitrary set of applied stresses and reinforcement contents, none of the following angles coincide:

- θ_r - direction of the normal to the cracks;
- θ_{cr} - principal direction of the concrete stress tensor at the cracks;
- θ_{cm} - principal direction of the average concrete stress tensor;
- θ_e - principal direction of the average strain tensor;

The direction of the local crack coordinate system θ_r is determined by the concrete stress conditions prior to cracking. For the first array of cracks it is sufficiently accurate to

assume that θ_r defines the principal direction of the applied stress tensor at impending cracking. Due to the existence of fixed interlocked cracks, the slip between the crack lips is responsible for the deviation of θ_e from θ_r . As explained in Section 3.2 (Figure 3.4 and Figure 3.5), due to the bond stress transfer between the reinforcing bars and the surrounding concrete, the angle defining principal direction of the concrete stress tensor at the cracks, θ_{cr} , does not coincide with that defining the principal direction of the average concrete stress tensor, θ_{cm} , if $\Delta\sigma_{cm,x} \neq \Delta\sigma_{cm,y}$, i.e., if the tension stiffening stresses in the reinforcement directions are different. On the other hand, crack shear and dilatancy stresses arising from aggregate interlock mechanisms allow the principal direction of the concrete compressive stress field to intersect the existing cracks, making $\theta_r \neq \theta_{cr}$. If sufficient reinforcement is present to avoid excessive crack openings, leading to steel ruptures or crack shear sliding failures, new cracks may occur at higher load levels, their orientation being determined by the principal direction of the concrete stress tensor between the existing cracks. These new cracks may govern the structural behaviour and previous cracks may close.

As discussed above, cracked concrete behaviour is highly complex and a set of simplifying assumptions is required for achieving a satisfactory engineering solution to the problem. In the following, the existing theoretical models are briefly described.

Compression field theory

Mitchell and Collins [159] and Collins [60] were the first to propose a method for calculating the response of a cracked RC panel over the full loading range. This procedure was called the Compression Field Theory (CFT). In the CFT fictitious rotating and stress free cracks are considered which opening is restricted to be perpendicular to their normal direction. The bond stress transfer mechanisms are neglected and therefore the variations in the concrete stress field are disregarded. This is equivalent to considering an array of cracks with vanishing spacing. According to the CFT, a uniform uniaxial compressive stress field exists in the concrete and no distinction is made between the stresses at the cracks and the average stresses. As the cracks are free to rotate, these assumptions lead to $\theta_e = \theta_r = \theta_{cm} = \theta_{cr}$ and to the simplified form of the equilibrium equations given by (3.16).

The required constitutive laws are only the stress-strain relationships for the reinforcing steel and for the cracked concrete in compression. The concrete constitutive laws are established in the local (rotating) crack coordinate system which defines the local axes of material orthotropy. Due to the rotating crack assumption, no crack shear stress-slip

relationship is required. Based on the results from a series of beam tests, it was suggested that the diagonally cracked concrete fails at lower compressive stress when compared to the peak stresses obtained from cylinder tests. The compressive strength of the diagonally cracked concrete was made a function of the diameter of the Mohr circle of strains: the larger the strain circle, the smaller the compressive strength. Using the nonlinear compressive field approach arbitrary stress-strain relationships for the steel and for the diagonally compressed concrete can be dealt with.

As remarked by Kauffman [120], besides allowing carrying out complete load deformation analysis, the original compressive field approaches are directly linked to limit analysis methods since the equilibrium equations (3.16) do not rely on the concrete tensile strength. Also, as evidenced by Crisfield and Wills [71], similarly to the no-tension rotating crack assumptions, the simple no-tension and no-crushing square concrete yield criterion that is often used for limit load calculations also leads to the coincidence of the principal stress and strain directions if the deformation theory of plasticity is used. However, the response predictions using the CFT typically overestimate the deformations since tension stiffening effects are disregarded and stress free rotating cracks are considered. Nonetheless, by first considering the equilibrium and compatibility conditions together with nonlinear constitutive laws treating cracked concrete as a new material, the CFT represented a major contribution to our understanding of the shear failure mechanisms.

Modified compression field theory

The Modified Compression Field Theory (MCFT) was proposed by Vecchio and Collins [240] to improve the original CFT by taking into account the tension stiffening effects. The constitutive laws of the MCFT were based on experiments involving RC panels subjected to uniform membrane stresses [234; 240; 242].

In the MFCT the principal direction of the average concrete stresses is considered to coincide with the principal direction of the average strains, i.e., $\theta_e = \theta_{cm}$. This was assumed as a reasonable simplification to the model, although a deviation between the two principal directions could be seen in the experimental results. Cracks are assumed to rotate freely and its direction is normal to the maximum principal average strains (or stresses), $\theta_r = \theta_e = \theta_{cm}$. In the MCFT a distinction is made between the average and local stresses at the cracks. The local values of the reinforcement stresses at the cracks are acknowledged to govern the ultimate capacity of biaxially stressed elements. At the cracks, concrete is assumed not to carry any significant normal stress. To transmit forces through the cracks,

the reinforcement stresses increase locally and local crack shear stresses are required if yielding of the reinforcement in one of the directions occurs [61]. This means that the average concrete stress tensor is assumed to deviate from the concrete stress tensor at the cracks and, therefore, $\theta_e = \theta_r = \theta_{cm} \neq \theta_{cr}$. In this case, the equilibrium equations expressed by (3.14) in terms of average stresses are:

$$\begin{aligned}\sigma_x &= \sigma_{cm,1} \cos^2 \theta_r + \sigma_{cm,2} \sin^2 \theta_r + \rho_x \sigma_{sm,x} \\ \sigma_y &= \sigma_{cm,1} \sin^2 \theta_r + \sigma_{cm,2} \cos^2 \theta_r + \rho_y \sigma_{sm,y} \\ \tau_{xy} &= \sigma_{cm,1} \sin \theta_r \cos \theta_r - \sigma_{cm,2} \sin \theta_r \cos \theta_r\end{aligned}\quad (3.17)$$

In the previous equilibrium equations, the axes 1-2 now refer to the rotating directions of maximum and minimum principal average stress (or strain), respectively, and θ_r is the angle of the normal to the rotating crack.

The required concrete constitutive laws consist of a uniaxial average stress-average strain relationship for the diagonally compressed cracked concrete ($\sigma_{cm,2}$ v.s. ε_2), including a softening term accounting for the compressive strength decrease with increasing principal average tensile strain, a tension stiffening formulation relating the tensile average strains with the average tensile concrete stresses ($\sigma_{cm,1}$ v.s. ε_1) and a criterion for the maximum interface shear stress capacity at the cracks, τ_{cr}^{MAX} . For the reinforcement, the constitutive laws of a bare bar are adopted to relate the average steel stresses with the average strains. As referred in Section 2.2, this last feature requires an additional equilibrium check in terms of local crack stresses which basically reduces the tension stiffening stress until equilibrium can be achieved between the average and the local stress fields (note that, in the limit, if the tension stiffening stress is null the two stress fields coincide). The equilibrium check at the crack is one of the less understood features of the MCFT [61]. Due to its importance and to explain some of the theory assumptions, this aspect will be further detailed in the following paragraphs.

According to the MCFT, the equilibrium in terms of local and average stresses can be obtained from Figure 3.6 if the average shear stress $\tau_{cm,nt}$ is neglected because the 1-2 coordinate axes are principal axes of average concrete stress. At the cracks, the crack dilatancy stresses $\sigma_{cr,n}$ (here $\sigma_{cr,1}$) are disregarded and only the crack shear stresses $\tau_{cr,nt}$ (here $\tau_{cr,12}$) are considered. As the local and average stress fields must be in equilibrium, the two following relations can be derived:

$$\rho_x (\sigma_{sr,x} - \sigma_{sm,x}) \cos^2 \theta_r + \rho_y (\sigma_{sr,y} - \sigma_{sm,y}) \sin^2 \theta_r = \sigma_{cm,1} \quad (3.18)$$

$$[\rho_x (\sigma_{sr,x} - \sigma_{sm,x}) - \rho_y (\sigma_{sr,y} - \sigma_{sm,y})] \sin \theta_r \cos \theta_r = \tau_{cr,12}$$

As there are three unknown stress components ($\sigma_{sr,x}$, $\sigma_{sr,y}$ and $\tau_{cr,12}$) and only two equilibrium equations, an additional condition is required in order to obtain the stresses at the cracks. The basic assumption behind the local equilibrium check performed in the MCFT is that the steel load resisting mechanism is stiffer than the crack shear mechanism, leading to a minimization of the crack shear stress. This has the effect of exhausting all the steel capacity in the weak direction before any shear on the crack is required. The two following conditions have then to be complied,

$$\rho_x (f_{sy,x} - \sigma_{sm,x}) \cos^2 \theta_r + \rho_y (f_{sy,y} - \sigma_{sm,y}) \sin^2 \theta_r \geq \sigma_{cm,1} \quad (3.19)$$

$$[\rho_x (f_{sy,x} - \sigma_{sm,x}) - \rho_y (f_{sy,y} - \sigma_{sm,y})] \sin \theta_r \cos \theta_r \leq \tau_{cr}^{MAX}$$

where $f_{sy,x}$ and $f_{sy,y}$ are the reinforcement yielding stresses in the x and y directions, respectively, and τ_{cr}^{MAX} is the maximum allowed crack shear stress, which is assumed to decrease with increasing average crack width. In reference [24] a suitable algorithm for performing this crack check is presented. The MCFT also predicts a concrete contribution to the shear strength. Considering $\sigma_y = 0$, the equilibrium equations (3.17) can be rearranged to give:

$$\tau_{xy} = \sigma_{cm,1} \tan \theta_r + \rho_y \sigma_{sy} \tan \theta_r \quad (3.20)$$

which also expresses the equilibrium of the applied shear stress as a sum of concrete and steel components. Considering that there is still enough strength reserve in the longitudinal steel, after yielding of the y -reinforcement, the inequalities (3.19) lead to the condition:

$$\sigma_{cm,1} \tan \theta_r \leq \tau_{cr}^{MAX} \quad (3.21)$$

Equations (3.20) and (3.21) are the basis of the shear design methods based on the MCFT adopted in the North America [26; 63].

The MFCT was formulated more than 20 years ago and the originally proposed constitutive laws have suffered some minor changes since its formulation [25; 242; 243]. The theory is widely spread among the scientific and technical community and it is

implemented in advanced analysis tools [24; 213; 235; 236; 241; 247]. Simplified versions were formulated for the shear design of beams elements and subsequently implemented into various design code procedures [1; 72].

Disturbed stress field model

The Disturbed Stress Field Model (DSFM) proposed by Vecchio [237] was formulated to eliminate some of the MCFT inaccuracies which were attributed to the forced alignment between the average strains and average concrete stresses. The DSFM is conceptually similar to the MCFT but extends the MCFT by incorporating the crack shear slip in the compatibility conditions.

In the DSFM a distinction is made between the average total strains, $\boldsymbol{\varepsilon}$, the average net concrete strains, $\boldsymbol{\varepsilon}^{(cm)}$, and the average strains arising from smearing the crack shear slip by the spacing between the cracks, $\boldsymbol{\varepsilon}^{(s)}$:

$$\boldsymbol{\varepsilon} = \boldsymbol{\varepsilon}^{(cm)} + \boldsymbol{\varepsilon}^{(s)} \quad (3.22)$$

The splitting of the total average strain tensor expressed by Eq. (3.22) is different in concept from that expressed by Eq. (3.10). In Eq. (3.22), besides the concrete deformations, the vector $\boldsymbol{\varepsilon}^{(cm)}$ also includes the smeared crack opening displacements $\delta_{r,n}/s_{rm}$ (see Figure 3.7), while in $\boldsymbol{\varepsilon}^{(s)}$ only the smeared shear slip $\delta_{r,t}/s_{rm}$ is included. In the crack local coordinate system, the strain vectors are given by:

$$\begin{aligned} \boldsymbol{\varepsilon}_{nt} &= \{\varepsilon_n \quad \varepsilon_t \quad \gamma_{nt}\}^T \\ \boldsymbol{\varepsilon}_{nt}^{(cm)} &= \{\varepsilon_{cm,n} \quad \varepsilon_{cm,t} \quad 0\}^T \\ \boldsymbol{\varepsilon}_{nt}^{(s)} &= \{0 \quad 0 \quad \delta_{r,t}/s_{rm}\}^T \end{aligned} \quad (3.23)$$

Cracks are assumed to rotate and to be perpendicular to the direction of the maximum average concrete stress, which in turn is assumed to coincide with the direction of maximum average net concrete strains. The n - t coordinate system is then a rotating principal system of average concrete stresses and average net concrete strains. These strains are employed in the constitutive relations to determine the average concrete stresses, while the total average strains are used to determine the average reinforcement stresses.

Similar to the MFCT, in the DSFM the equilibrium is expressed both in terms of average stresses using Eqs. (3.17) and in terms of local crack stresses using Eqs. (3.18), leading to

$\theta_e \neq \theta_r = \theta_{cm} \neq \theta_{cr}$. Additionally to the MCFT constitutive laws, in the DSFM a relationship between the crack shear slip $\delta_{r,t}$ and the crack shear stress $\tau_{cr,nt}$ is required. As the bare bar constitutive law is adopted for the reinforcements, the average tensile stresses must be limited according to (3.19)₁. Unlike the MCFT, however, the tensile stress is no longer subject to the limitation of shear stresses at a crack (3.19)₂, since the DSFM explicitly incorporates deformations due to shear slip rather than ascribing a limiting stress corresponding to shear slip failure.

The average reinforcement stresses $\sigma_{sm,x}$ and $\sigma_{sm,y}$ are directly computed from the average total strains. The local reinforcement stresses at the cracks $\sigma_{sr,x}$ and $\sigma_{sr,y}$ are obtained from equilibrium using Eq. (3.18)₁. As two stress components are to be determined from only one equation, an additional assumption is made regarding the direction of the local incremental reinforcement strain vector at the cracks, $\Delta\epsilon^{(r)}$. It is assumed that $\Delta\epsilon^{(r)}$ is co-linear with the principal stress direction (the n -direction). Once $\sigma_{sr,x}$ and $\sigma_{sr,y}$ are computed, the local crack shear stress can be determined from Eq. (3.18)₂ and the slip obtained from the constitutive relationship. An internal loop is necessary to divide the total strains as expressed by Eq. (3.22), i.e., giving the total average strain vector, the calculation of the average stresses requires an iterative procedure. A suitable algorithm is given in [238].

The DSFM was implemented into a finite element formulation and has been successfully applied to the analysis of structural elements subjected to shear failures [245; 246; 248].

Softened truss models

The so-called “softened truss models” were developed at the University of Houston by Hsu and co-workers. These are fully smeared models as equilibrium, compatibility and constitutive laws are established exclusively in terms of average quantities. The constitutive laws relating average stresses with the average strains were derived on the basis of a series of experimental tests on RC panels subjected to in plane stress conditions [21; 22; 104; 106; 179; 180; 262; 264]. Contrary to the compression field approaches developed at the University of Toronto by Collins and Vecchio, in these models an average stress-strain relationship is used for the reinforcement steel eliminating the need of performing an additional check in terms of local stresses at the cracks.

In the Rotating Angle Softened Truss Model (RA-STM) [178; 179] the cracks are assumed to rotate and are perpendicular to the principal directions of maximum average concrete stress and strain, implying $\theta_e = \theta_r = \theta_{cm}$. The equilibrium equations are given by (3.17) and the required constitutive laws consist of a softened stress-strain relationship for the

diagonally compressed concrete, a tension stiffening formulation and an average stress-strain relationship for the reinforcement steel.

The Fixed Angle Softened Truss Model (FA-STM) [178; 180] was proposed to extend the validity of the RA-STM to cases with very different amounts of reinforcement in orthogonal directions by allowing the existence of shear in the crack planes. In the FA-STM the cracks are fixed and the assumption of co-linearity between principal average concrete stresses and principal average strains is dropped, leading to $\theta_e \neq \theta_r \neq \theta_{cm}$. The equilibrium equations are given by (3.1) (but expressed in terms of average stresses) and an additional average concrete shear stress-average shear strain relationship ($\tau_{cm,nt} - \gamma_{nt}$) is required. Due to the form of the adopted constitutive equation for the average concrete shear stresses, the solution procedure is complex, requiring a two stage procedure [105].

The Softened Membrane Model (SMM) [106; 263] was proposed to overcome the complex solution procedure required by the FA-STM and to introduce the Poisson effect into the constitutive equations, which is claimed to improve the post-peak response of the model. The so-called Hsu-Zhu ratios [263; 264] characterize the Poisson effect after cracking. The SMM considers a fixed crack direction, but assumes that the principal direction of average concrete stresses coincides with that of average principal strains, leading to $\theta_\varepsilon = \theta_{cm} \neq \theta_r$. The assumption of co-linearity between average concrete stresses and total strains allows the derivation of a secant shear modulus depending only on the constitutive laws adopted for the average concrete compressive and tensile stresses and strains [265]. Except for the Hsu-Zhu ratios, the constitutive laws are essentially the same as for the RA-STM, although some refinements have been proposed [253] for the softened compressive concrete stress-strain relationship, as well as an extension of the steel constitutive laws to prestressed reinforcement.

The models from the University of Houston, namely the latest SMM, represent an alternative approach to the problem, are rooted in experimental evidence and are theoretically consistent with the fully smeared approach by establishing the constitutive laws purely in terms of average quantities.

Cracked membrane model

The Cracked Membrane Model (CMM) [117; 120] combines the basic concepts of the original CFT with the Tension Chord Model (TCM) [151]. The equilibrium equations are formulated in terms of stresses at the cracks and both the crack spacing and concrete stresses between the cracks are determined from first principles. The CMM considers rotating and stress free cracks which are assumed to be perpendicular to the principal

tensile direction of average strains. Due to bond stress transfer mechanisms, the principal directions of local and average concrete stresses may not coincide and therefore $\theta_e = \theta_r = \theta_{cr} \neq \theta_{cm}$. Contrary to the MCFT, the non-colinearity between the average and local stresses is explained by different tension stiffening components arising in the two reinforcement directions. The equilibrium equations are given by (3.14), where the stress component $\sigma_{cr,l}$ is neglected. As for the concrete constitutive laws, only a softened uniaxial compressive stress-strain relationship is required. The reinforcement constitutive laws are formulated according to the TCM, relating the local steel stresses at the cracks with the average strains both in pre- and post-yielding regimes.

The CMM is a simple model that proved to be as accurate as other compression field approaches. Since the equilibrium equations are directly formulated in terms of local crack stresses and by considering rotating stress free cracks perpendicular to the direction of the principal average strain, the CMM allows a direct link to limit analysis methods. The CMM differs from the previously mentioned compression field approaches due to the way the tension stiffening effects are accounted for. By combining the TCM relationships with the CFT concepts, the tension stiffening effects in the pre- and post yielding domains are accounted for in a rational manner. A quantitative description of the concrete and reinforcements stress fields is given, enabling its calculation both at the cracks and in average terms. As a major simplification stress-free rotating cracks are considered.

Models based on local crack stresses

In reference [120] a framework was proposed for calculating the response of a RC membrane under in plane stress conditions considering fixed interlocked cracks and the specific contribution of the individual mechanical effects at the crack level. However, this approach was not pursued and a set of simplifying assumptions were made leading to the formulation of the CMM. Since then various formulations have been presented that can be considered to follow the originally proposed framework, complying with the general requirement $\theta_e \neq \theta_r \neq \theta_{cr} \neq \theta_{cm}$.

Belleti *et al* [23] presented a fixed crack model that considers the specific contributions of the individual mechanic effects at the cracks. Tension stiffening effects are evaluated by means of an appropriate increment of the steel bars average strains. Sato and Fuji [207] proposed a formulation for the analysis of cracked RC membranes where compatibility conditions are extended to include bond slip. In this way, local and average stress and strain fields are accurately evaluated. Equilibrium is established at the cracks and the

individual mechanic effects can be accounted for in a rational manner. Soltani *et al* [224] further elaborated this type of formulation by including more sophisticated material constitutive laws. With the aid of this model a complete description of the size dependency in RC mechanics was presented [223]. Cerioni *et al* [52] extended the concept by formulating a comprehensive model allowing the formation of non-orthogonal cracks. These models allow a deeper understating of the complex mechanics involved in the shear behaviour of RC cracked membranes at the cost of more computational effort and complexity of the formulations. The explicit consideration of the slip between the reinforcements and concrete, although allowing a more rigorous treatment of the crack formation and bond stress transfer, introduces the need for performing inner loops to solve the bond stress-slip problem.

3.6 Constitutive relationships

A general model for complete load-deformation analysis of RC membrane elements subjected to in-plane shear and axial stresses needs to consider the general equilibrium conditions expressed by (3.1), the compatibility conditions (Section 3.3) and suitable constitutive laws for: (1) concrete nonlinear behaviour under compressive stresses; (2) crack bridging stress; (3) shear stress transfer between rough cracks; (4) bond-stress transfer between the reinforcing bars and surrounding concrete.

A formulation considering fixed interlocked cracks, which can be regarded as an extension of the CMM to the case of fixed and interlocked cracks, is proposed. Equilibrium is expressed in terms of crack stresses and compatibility is expressed in terms of average strains, according to Sections 3.2 and 3.3. Therefore, the adopted constitutive laws shall relate these stress and strain tensors. The proposed formulation will be hereby designated as F-CMM, where “F-“ stands for fixed and interlocked cracks. The CMM will be considered as a particular case, and referred to as R-CMM, where the “R-“ stands for rotating cracks.

In the following, compression is assumed negative. The superscript $(\cdot)'$ indicates a positive definite compression related variable.

3.6.1 Compressive behaviour

As discussed in Section 2.4.3 the compressive strength of plain concrete is reduced (or softened, as usually termed) in the presence of tensile strains in the orthogonal direction.

The softened compressive strength is here considered as the product of two coefficients, ζ_f and ζ_e , by the cylinder compressive strength:

$$f_{c,ef} = \zeta_e \zeta_f f'_c$$

$$\zeta_e = \frac{1}{C_m (1.08 + 81\varepsilon_n)} \leq 1 \quad (3.24)$$

$$\zeta_f = \left(\frac{f_{c0}}{f'_c} \right)^{\frac{1}{3}} \leq 1 \quad (f'_c \text{ in MPa})$$

where $f_{c0}=20\text{MPa}$, ε_n is the average tensile strain in the direction normal to the cracks, and C_m is a constant.

The coefficient ζ_f was defined according to Muttoni *et al.* [167] and expresses the dependency of the uniaxial compressive strength of unconstrained concrete panels or wall elements on f'_c . The expression for the softening coefficient ζ_e is based on the proposal of Kaufmann [117; 120]. The original expression was calibrated for the CMM, which is a rotating crack model, and is equivalent to considering $C_m=1.0$. However, as discussed by Vecchio [237], rotating crack models require more compression softening than models which explicitly account for the crack shear slip kinematics. The parameter C_m allows adjusting the expression for ζ_e in order to eliminate the slippage influence on the compression softening coefficient. As in the F-CMM both crack shear slip and crack dilatancy effects are taken into account by independent models, the compression softening relationship must be calibrated with experimental data obtained from tension-compression tests on RC panels. These tests allow for an independent calibration of the compressive softening law without any assumption regarding the tensile behaviour in the perpendicular direction or regarding the slip between the crack lips. In Figure 3.8(a) it can be seen that an improved fit to the experimental results can be obtained with the adoption of $C_m=0.9$.

As it was shown by Belarbi and Hsu [22], in cases of proportional loading the strain at peak stress is also reduced. In the present model, the same softening coefficient used for the compressive strength was also adopted for the uniaxial peak strain ε'_0 :

$$\varepsilon_{0,ef} = \zeta_e \zeta_f \varepsilon'_0 \quad (3.25)$$

The uniaxial peak strain can be related to the compressive strength by the following relationship [84]:

$$\varepsilon'_0 = 0.0017 + 0.0010 \frac{f'_c}{70} \quad (f'_c \text{ in MPa}) \quad (3.26)$$

In the case of the R-CMM, $\varepsilon_{0,ef} = \varepsilon'_0$ was adopted because overly too stiff force-deformation responses are obtained if $\varepsilon_{0,ef}$ is calculated according to Eq. (3.25). This is more noticeable in reinforced panels failing in shear after yielding of the weaker reinforcement and is due to the fact that the principal compressive average strain includes the contributions of both concrete deformations and smeared crack shear displacements. However, whenever shear slip does not occur (as for instance in isotropically reinforced panels), or it is not significant (over-reinforced panels in general), overly too soft load-deformation responses are to be expected from the R-CMM. Note that in the F-CMM shear slip is calculated using dedicated constitutive laws and, therefore, this does not pose a problem.

The stress-strain curve is defined on the basis of normalized values of the compressive stress and compressive strain:

$$S = -\frac{\sigma_{cr,t}}{f_{c,ef}} \quad E = -\frac{\varepsilon_t}{\varepsilon_{0,ef}} \quad (3.27)$$

The stress-strain relationships in the ascending and post-peak branches are given by:

$$S = \begin{cases} \frac{kE - E^2}{1 + (k-2)E} & , \quad E \leq 1 \\ \frac{1}{1 + \frac{\eta}{2}(1 - 2E + E^2)} & , \quad E > 1 \end{cases} \quad (3.28)$$

For the ascending branch, $E \leq 1$, the Sargin's law was adopted [84], while the descending branch was defined ensuring that S is continuously differentiable. The parameter k in the expression for the ascending branch controls the shape of the curve. With $k=2$, a parabolic relationship is obtained. In general,

$$k = \frac{E_{ci}}{f_{c,ef} / \varepsilon_{0,ef}} \quad (3.29)$$

with E_{ci} being the tangential modulus of elasticity at $\sigma_c = 0$, which can be estimated from [84]:

$$E_{ci} = \alpha_{agg} 21500 \left(\frac{f'_c}{10} \right)^{1/3} \quad (f'_c \text{ in MPa}) \quad (3.30)$$

The parameter α_{agg} depends on the type of aggregate, being equal to 0.9 for limestone, 1.0 for quartzitic aggregates and 1.2 for basalt or dense limestone.

It was shown experimentally [261; 262] that even high strength concrete exhibits a ductile behaviour when crushing in the presence of large lateral strains. In the proposed post-peak relationship this effect is taken into account by the parameter η , which was made dependent on the softening coefficients ζ_f and ζ_e :

$$\eta = \frac{\pi^2}{4} \left(\frac{f_{c,ef}}{f'_c} \right)^2 \left(\frac{\varepsilon_{0,ef}}{\varepsilon'_0} \right)^2 \quad (3.31)$$

The compressive stress-strain curves for varying softening coefficient values are depicted in Figure 3.8.

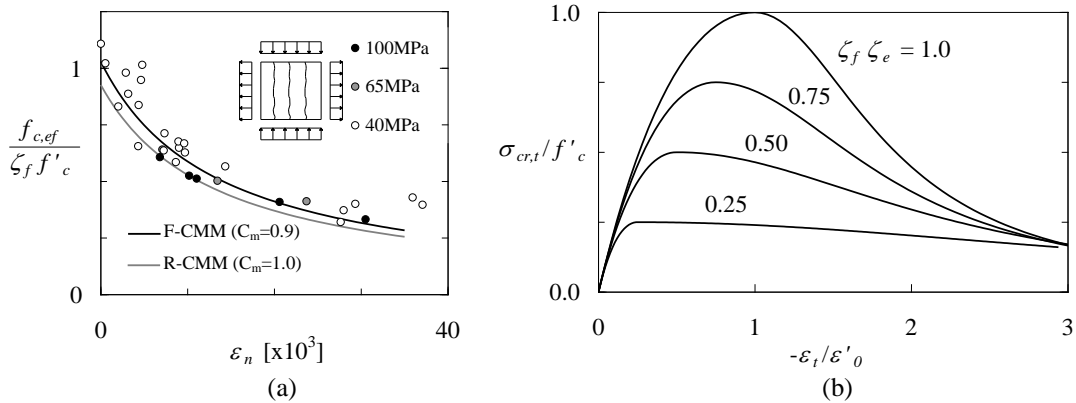


Figure 3.8 – Softened compressive stress-strain relationship for cracked concrete: (a) ratio $\zeta_e = f_{c,ef} / \zeta_f f'_c$ versus lateral strains (experimental data from references [20; 178; 261]); (b) compressive stress-strain curve for varying softening degrees in the F-CMM.

3.6.2 Tensile crack bridging stresses

Up to tensile strength, concrete is assumed to behave elastically. When the tensile strength is reached, the fracture process develops until a macroscopic crack is formed. Tensile stresses arising from crack bridging effects can still be transmitted during the fracture process and, although negligible for well reinforced structures, can play an important role when modelling poorly reinforced or plain concrete elements. In the present model, the relationship proposed in references [64; 101] is adopted for the post peak-branch:

$$\frac{\sigma_{cr,n}}{f_{ct}} = \left[1 + 27 \left(\frac{w_r}{w_c} \right)^3 \right] e^{-6.93 \frac{w_r}{w_c}} - 0.027384 \frac{w_r}{w_c} \quad (3.32)$$

$$w_c = 5.14 \frac{G_F}{f_{ct}} \quad , \quad w_r = h_t \varepsilon_n$$

where G_F is the fracture energy. The parameter h_t is the crack bandwidth, which in the case of finite element analysis depends on the finite element size [17]. In the calculations presented in this chapter, it was assumed to be equal to an estimate of the average crack spacing.

3.6.3 Shear transfer through rough cracks

As discussed in Section 2.3, the existing theoretical models for shear transfer through rough cracks are based on experimental tests in pre-cracked notched specimens – the push-off tests. In these tests a straight crack is formed along a predefined notch and the crack roughness is only due to the protruding aggregates. This can be defined as local crack roughness. However, due to concrete heterogeneity, in RC panels tested under in-plane stress conditions, as well as in real structures, cracks present a crooked shape. This global roughness is responsible for another interlocking mechanism in addition to aggregate interlock [167; 180]. Additionally, as reported by Walraven [251], cracks reinforced with deformed bars exhibit an extra shear stress transfer mechanism, which is mobilized due to the crack width reduction in the neighbourhood of the reinforcing bars. In conclusion, for given crack opening and shear displacements, larger shear and dilatancy stresses are to be expected across structural concrete cracks when compared to the ones obtained from push-off tests.

In the present model, a closed form solution based on the Contact Density Model [133] is adopted. The shear stress and the accompanying normal compressive component (the crack dilatancy stress) are given by:

$$\begin{aligned}\tau_{agg} &= \tau_{LIM} \frac{\beta^2}{1 + \beta^2} \\ \sigma_{dil} &= -\tau_{LIM} \left(\frac{\pi}{2} - \cot^{-1} \beta - \frac{\beta}{1 + \beta^2} \right)\end{aligned}\quad (3.33)$$

$$\tau_{LIM} = 3.83 f_c'^{1/3} g(\varepsilon_n, s_{rm\theta}) \quad , \quad g(\varepsilon_n, s_{rm\theta}) = \frac{0.5}{0.31 + 200 s_{rm\theta} \varepsilon_n} \leq 1$$

where $\beta = \delta_{r,t} / w_r$. If a regular array of cracks is formed then, from Eq. (3.11), it is possible to conclude that $\beta = \gamma_{nt} / \varepsilon_n$. In the previous expression, τ_{LIM} is the maximum attainable shear stress and $s_{rm\theta}$ is an estimate of the crack spacing:

$$s_{rm\theta} = \lambda \left(\frac{\cos \theta_r}{s_{rmx0}} + \frac{\sin \theta_r}{s_{rmy0}} \right)^{-1}\quad (3.34)$$

with s_{rmx0} and s_{rmy0} being the maximum uniaxial crack spacing in the reinforcement directions, which must be determined according to the expressions of Section 3.6.4. The parameter λ is comprised between 0.5 and 1, corresponding to the minimum and maximum crack spacing, respectively (see Section 3.6.4). In the original approximate closed form solution of the Contact Density Model a constant value $\tau_{LIM} = 3.83 f_c'^{1/3}$ was adopted. However, this value was found to overestimate the crack shear capacity for large crack openings. In the present formulation, a function $g(\varepsilon_n, s_{rm\theta})$ is defined which basically reduces the crack shear capacity when the normal strain, and therefore the crack opening, becomes large.

This function was developed modifying the expression proposed by Vecchio and Collins [240] for the crack shear capacity in order to take into account the crack width reduction in the neighbourhood of the rebars and the cracks meandering shape. For simplicity, the influence of the maximum aggregate size was neglected. It must be recalled that the parameter 200 in the denominator of $g(\varepsilon_n, s_{rm\theta})$ is closely related to how the uniaxial crack spacing is determined. This value was found to lead to good results for maximum uniaxial crack spacing determined according to Eq. (3.43) and with f_{ct} calculated with Eq. (2.2). The Eqs. (3.33) are plotted in Figure 3.9 (a) and (b).

A unique relation between shear and dilatancy compressive stresses at the crack can be derived from Eqs. (3.33). Its graphical representation is depicted in Figure 3.9 (c). It can be seen that, as the shear stress approximates the crack shear capacity, large confinement stresses are required to sustain the shear demand. In Figure 3.9 (c) the model response is depicted for a monotonic loading path with constant crack opening.

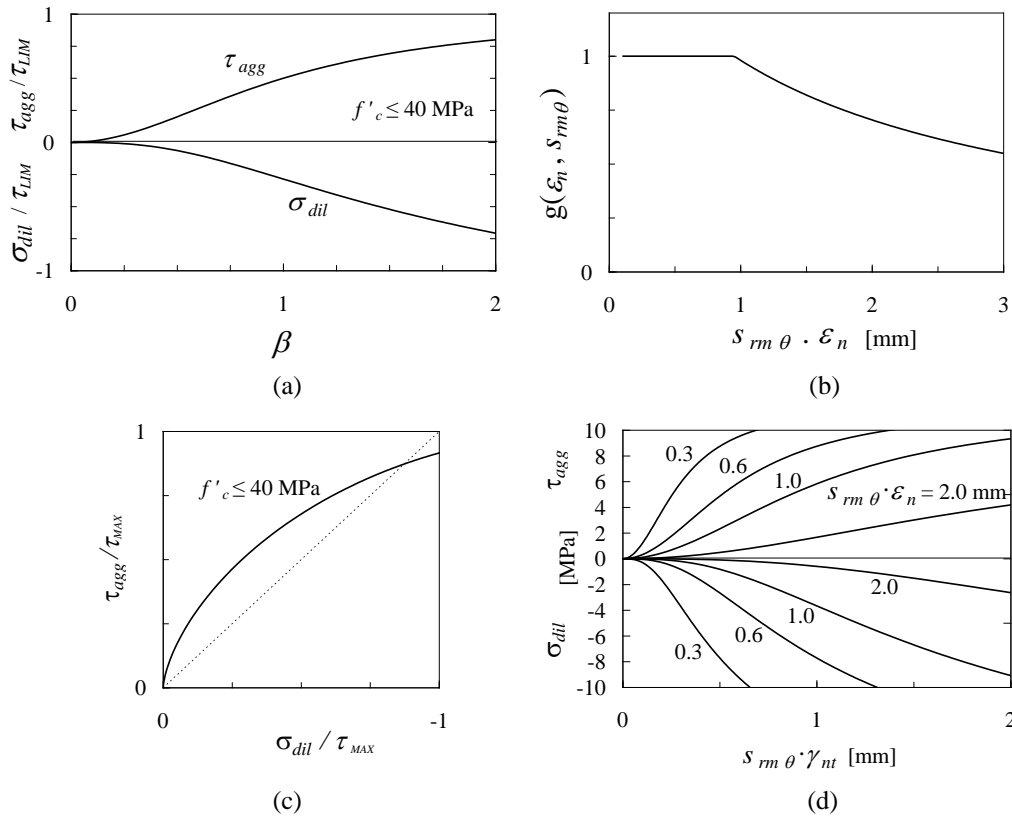


Figure 3.9 – Crack shear transfer model: a) Normalized shear and dilatancy stresses vs. normalized shear strain; b) Function $g(\varepsilon_n, s_{rm}\theta)$; c) Unique relation between shear and compressive stresses for $f'_c \leq 40 \text{ MPa}$; d) Simulation of four push-off tests with constant crack opening for $f'_c = 30 \text{ MPa}$

The Contact Density Model was originally formulated considering the crack surface geometry of normal strength concrete. As discussed in Section 2.3 in the case of high strength concrete (HSC) the crack surface geometry is smoother. This is attributable to the fact that the bond strength between the mortar and coarse aggregates is so high that these tend to break apart, rather than separate from mortar as in normal strength concrete. Due to this fact, in HSC less shear dilatancy is observed. In order to take this effect into account in a simplified manner f'_c is limited to 40MPa in the σ_{dil} equation (3.33)₂. However, also the crack shear stress law (3.33)₁ and crack shear capacity (3.33)₃ must be updated for HSC. Therefore, further research must be made in order to develop a suitable closed form

expression similar to Eqs. (3.33) that can be applicable for HSC, thus improving the generality of the model.

The dowel action effect is here assumed to be indirectly taken into account via the $g(\varepsilon_n, s_{rm\theta})$ function defined above. This function was calibrated with the results from RC panel tests and, therefore, indirectly considers dowel action effects. In the future, this subject could be object of further refinement of the proposed model.

3.6.4 Reinforcement steel and tension stiffening

As discussed in Section 2.2, the effect of bond on the behaviour of structural concrete members is reflected by the stiffer post-cracking response exhibited by the tension chord when compared to the obtained with a naked steel bar of equal resistance. This effect is called tension stiffening and its inclusion in the structural analysis is essential both in the pre- and post-yield regimes. In the present material model, tension stiffening is taken into account by calculating the reinforcement stresses at the cracks from the average strains. This is performed following the lines of the Tension Chord Model (TCM) [3; 117; 151; 216]. In the TCM, a simple stepped rigid-perfectly plastic bond stress-slip relationship is used, allowing the derivation of closed form solutions for the distribution of stresses and strains along the tension chord. Its extension to cracked panels [117; 120] eliminates the need for constitutive equations relating average strains and average stresses. The TCM assumptions have been extensively validated with experimental results and numerical simulations with more detailed bond stress-slip laws [3; 121; 122; 151; 216] and its applicability has been verified both in pre- and post-yield regimes.

3.6.4.1 Tension Chord Model – 1D stress conditions

For the bond stress-slip relationship of Figure 3.10 (a) and in the case of ordinary ribbed rebars, it was suggested by Sigrist [216] to assume $\tau_{b0} = 0.6f_c'^{\frac{2}{3}}$ (prior to reinforcement yielding) and $\tau_{b1} = 0.3f_c'^{\frac{2}{3}}$ (after reinforcement yielding). In the following, a bilinear stress-strain relationship is considered for the reinforcement, as depicted in Figure 3.10 (b).

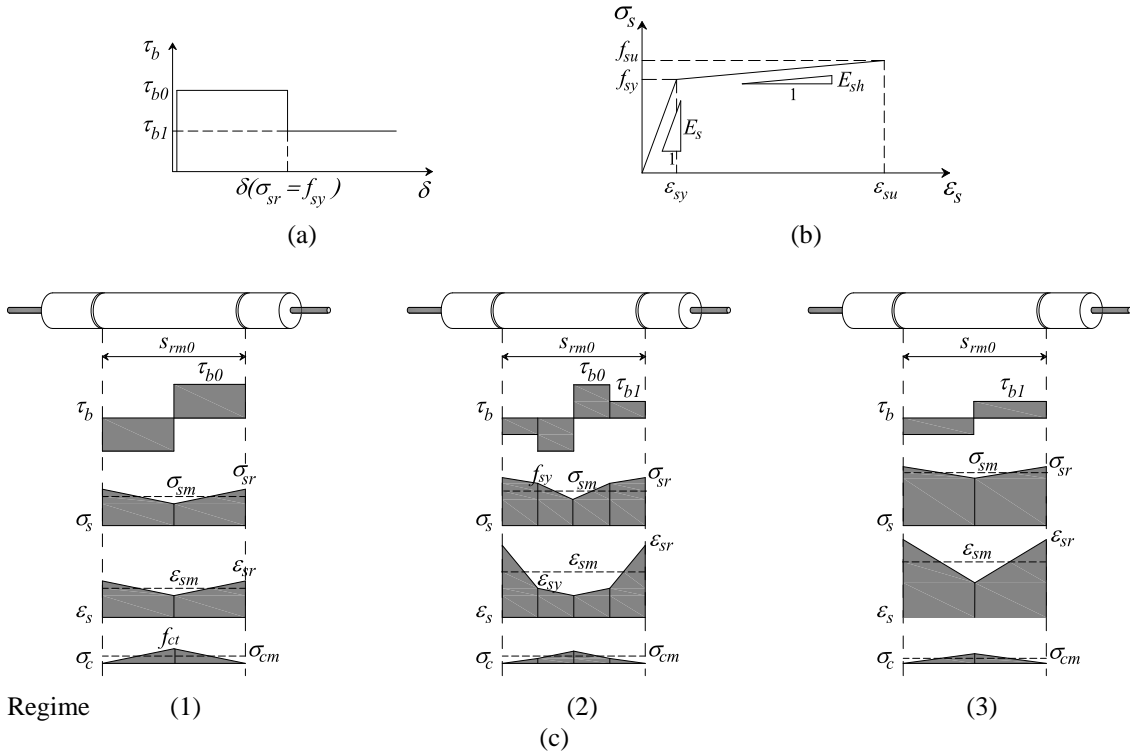


Figure 3.10 – Tension chord model: (a) Bond shear stress-slip relationship; (b) Stress-strain relation for the rebars; (c) Chord element for increasing load levels corresponding to regimes 1, 2 and 3.

Consider a tension chord element subjected to constant axial tensile forces inducing a symmetric bond stress distribution along the element. In Figure 3.10 (c) the stress and strain distributions along the chord element are presented for three different working conditions, corresponding to increasing applied load levels: (1) fully developed crack pattern with the reinforcement in the elastic range, i.e., $\sigma_{sr} \leq f_{sy}$; (2) partial reinforcement yielding along the chord element, i.e., $\sigma_{s,min} \leq f_{sy} \leq \sigma_{sr}$; (3) reinforcement yielding along the entire chord element, i.e., $f_{sy} \leq \sigma_{s,min}$. After reinforcement yielding, the reinforcement strain distribution becomes even more irregular exhibiting strong strain localizations in the vicinity of the cracks. This aspect can be successfully reproduced by the TCM and it is an important feature for an accurate calculation of the deformation capacity of RC members.

With the adopted bond stress-slip relationship, the equilibrium along the chord element (see Section 2.2.1) for the working regime 1 requires that the maximum crack spacing is given by:

$$s_{rm0} = \frac{f_{ct} \phi (1 - \rho)}{2 \tau_{b0} \rho} \quad (3.35)$$

where $\rho = A_s/A_c$ is the reinforcement ratio, A_c is the gross cross sectional concrete area and $A_s = \pi\phi^2/4$ is the rebar area. In general, in a fully developed crack pattern, the average crack spacing is smaller than s_{rm0} , and is given by

$$s_{rm} = \lambda s_{rm0} \quad 0.5 \leq \lambda \leq 1 \quad (3.36)$$

The factor λ takes into account that sections with the concrete stresses equal to f_{ct} can either crack ($\lambda = 0.5$) or remain uncracked ($\lambda = 1$), giving a lower and an upper limit to the tension stiffening effect, respectively. However, it must be remarked that the crack spacing is often dictated by the position of transverse reinforcing bars and not solely determined by the bond conditions.

In Figure 3.11 (a) the relationship between the crack spacing and the steel ratio according to TCM is depicted. In Figure 3.11 (b) a comparison between the crack spacing predicted by the TCM (with $\tau_{b0} = 2f_{ct}$) and by the Eurocode 2 [46] provisions for the maximum crack spacing is presented. A tension chord with Ø16mm high bond bars and 30mm of concrete cover were considered.

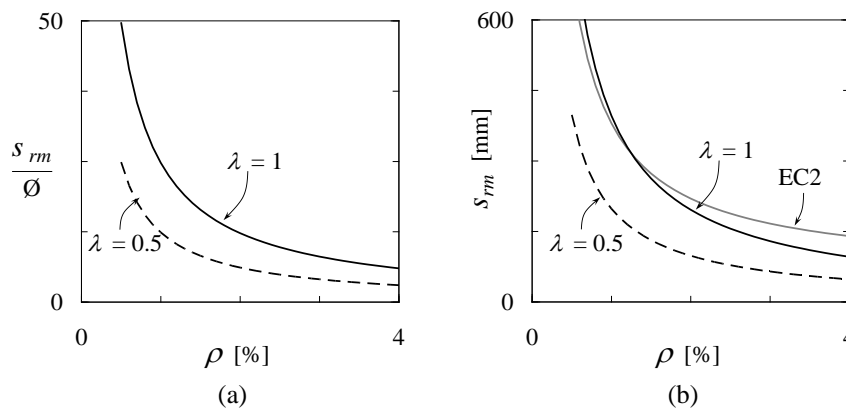


Figure 3.11 – (a) Crack spacing according to the TCM ($\tau_{b0} = 2f_{ct}$); (b) Comparison with the EC2 [46] expression for the maximum crack spacing (high bond bars, pure tension and 30mm of concrete cover).

Using the adopted constitutive laws and the equilibrium conditions along the tension chord, the relationships between stresses and strains, as well as their correspondent distribution between the cracks, namely its values at the cracks and in average terms, can be obtained in a closed form and without explicitly calculating the slip between reinforcements and concrete (see Figure 3.10 for notation):

$$\text{Regime 1 - } \sigma_{sr} \leq f_{sy} \Leftrightarrow \varepsilon_{sm} \leq \varepsilon_{sy} - \frac{\tau_{b0} S_{rm}}{E_s \phi}$$

$$\begin{aligned} \sigma_{sr} &= E_s \varepsilon_{sm} + \frac{\tau_{b0} S_{rm}}{\phi} \\ \sigma_{sm} &= \sigma_{sr} - \frac{\tau_{b0} S_{rm}}{\phi} \end{aligned} \quad (3.37)$$

$$\text{Regime 2 - } f_{sy} < \sigma_{sr} < f_{sy} + \frac{2\tau_{b1} S_{rm}}{\phi} \Leftrightarrow \varepsilon_{sy} - \frac{\tau_{b0} S_{rm}}{E_s \phi} < \varepsilon_{sm} < \varepsilon_{sy} + \left(\frac{\tau_{b1}}{E_{sh}} - \frac{\tau_{b0}}{E_s} \right) \frac{S_{rm}}{\phi}$$

$$\sigma_{sr} = f_{sy} + 2 \frac{\frac{\tau_{b0} S_{rm}}{\phi} - \sqrt{\left(f_{sy} - E_s \varepsilon_{sm} \right) \frac{\tau_{b1} S_{rm}}{\phi} \left(\frac{\tau_{b0}}{\tau_{b1}} - \frac{E_s}{E_{sh}} \right) + \frac{E_s}{E_{sh}} \tau_{b0} \tau_{b1} \left(\frac{S_{rm}}{\phi} \right)^2}}{\frac{\tau_{b0}}{\tau_{b1}} - \frac{E_s}{E_{sh}}} \quad (3.38)$$

$$\sigma_{sm} = f_{sy} - \frac{\tau_{b0} S_{rm}}{\phi} + \left(\sigma_{sr} - f_{sy} \right) \frac{\tau_{b0}}{\tau_{b1}} - \frac{\left(\sigma_{sr} - f_{sy} \right)^2 \phi \left(\frac{\tau_{b0}}{\tau_{b1}} - 1 \right)}{4 \tau_{b1} S_{rm}}$$

$$\text{Regime 3 - } f_{sy} + \frac{2\tau_{b1} S_{rm}}{\phi} \leq \sigma_{sr} \leq f_{su} \Leftrightarrow \varepsilon_{sy} + \left(\frac{\tau_{b1}}{E_{sh}} - \frac{\tau_{b0}}{E_s} \right) \frac{S_{rm}}{\phi} \leq \varepsilon_{sm} \leq \varepsilon_{su} - \frac{\tau_{b1} S_{rm}}{E_{sh} \phi}$$

$$\begin{aligned} \sigma_{sr} &= f_{sy} + E_{sh} \left(\varepsilon_{sm} - \varepsilon_{sy} \right) + \frac{\tau_{b1} S_{rm}}{\phi} \\ \sigma_{sm} &= \sigma_{sr} - \frac{\tau_{b1} S_{rm}}{\phi} \end{aligned} \quad (3.39)$$

In reference [3] similar expressions were derived for other $\sigma_s - \varepsilon_s$ relationships. The average concrete stresses σ_{cm} can easily be calculated from equilibrium using Eq. (3.40) and the reinforcement strains at the cracks can be obtained from the steel constitutive law.

$$\sigma_{cm} = \frac{\rho}{1-\rho} (\sigma_{sr} - \sigma_{sm}) \quad (3.40)$$

The evolution of the steel stresses at the crack of a tension chord under monotonically increasing applied load is schematically depicted in Figure 3.12. Immediately after cracking the steel stress at the crack jumps from $n f_{ct}$ (where n is the modular ratio E_s/E_c) to σ_{sr0} . Points C and E correspond to the end of the crack formation phase for $\lambda = 1$ or $\lambda < 1$, respectively. The implementation of the TCM in the present model is such that, in the crack formation phase, the dashed line ADC or ADE is followed, instead of the ABC or ABE trajectories. This is due to the numerical stability of the algorithm in the two-dimensional case.

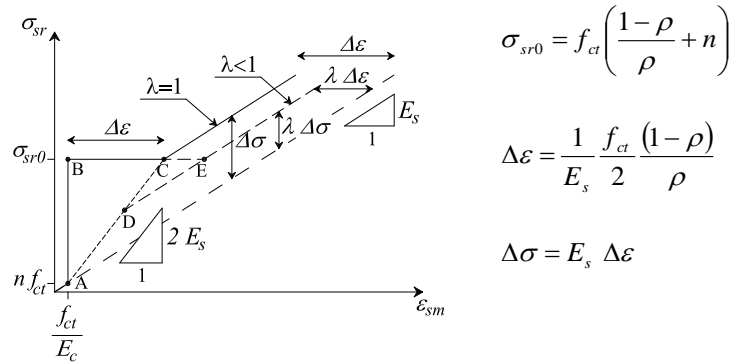


Figure 3.12 – Steel stresses for a monotonically increasing load according to the TCM.

In Figure 3.13 the behaviour of a tension chord according to the TCM is illustrated for four different reinforcement ratios, assuming $\lambda = 1$, $f_{sy} = 500\text{MPa}$, $f_{su} = 625\text{MPa}$, $E_s = 200\text{GPa}$, $\varepsilon_{su} = 0.05$, $\emptyset = 16\text{mm}$, $f'_c = 30\text{MPa}$, $f_{ct} = 0.3 f'_c{}^{2/3}$, $\tau_{b0} = 0.6 f'_c{}^{2/3}$, $\tau_{b1} = 0.3 f'_c{}^{2/3}$.

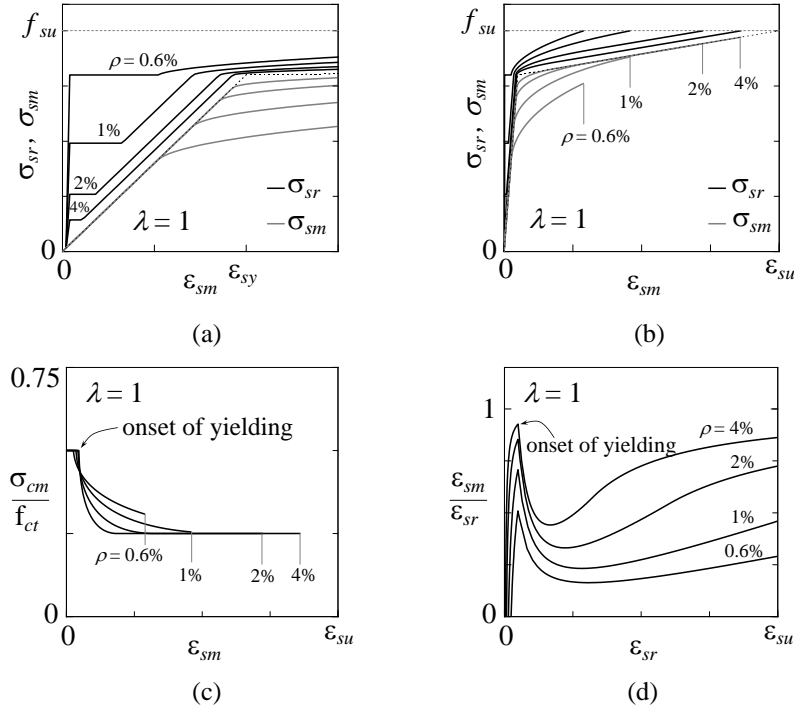


Figure 3.13 – Response of a tension chord according to the TCM: (a) and (b) steel stresses at the cracks and average steel stresses versus average strains; (c) average concrete stresses versus average strains; (d) strain localization versus steel strain at the cracks.

3.6.4.2 Tension Chord Model – generalization to 2D plane stress conditions

According to Figure 3.4, the crack spacings in the reinforcement directions are related to each other by

$$s_{rm} = s_{rmx} \cos \theta_r = s_{rmy} \sin \theta_r \quad (3.41)$$

where s_{rm} is the diagonal crack spacing. The stress distribution between the cracks is also illustrated in Figure 3.4. At the centre between two consecutive cracks the tensile stresses transferred to concrete by bond reach their maximum values $\Delta\sigma_{c,x} = \lambda_x f_{ct}$ and $\Delta\sigma_{c,y} = \lambda_y f_{ct}$, where

$$\lambda_x = \frac{\Delta\sigma_{c,x}}{f_{ct}} = \frac{s_{rmx}}{s_{rmx0}} = \frac{s_{rm}}{s_{rmx0} \cos \theta_r} \quad (3.42)$$

$$\lambda_y = \frac{\Delta\sigma_{c,y}}{f_{ct}} = \frac{s_{rmy}}{s_{rmy0}} = \frac{s_{rm}}{s_{rmy0} \sin \theta_r}$$

The maximum crack spacings s_{rmx0} and s_{rmy0} for uniaxial tension in the x- and y- directions, respectively, follow from Eq. (3.35):

$$s_{rmx0} = \frac{f_{ct} \phi_x (1 - \rho_x)}{2 \tau_{b0} \rho_x} \quad s_{rmy0} = \frac{f_{ct} \phi_y (1 - \rho_y)}{2 \tau_{b0} \rho_y} \quad (3.43)$$

The parameters λ_x and λ_y are no longer limited by the interval [0.5;1.0] as in the uniaxial tension case. Rather, the diagonal crack spacing s_{rm} follows from the observation that the maximum concrete tensile stress at the centre between the cracks cannot be greater than λf_{ct} :

$$\lambda f_{ct} = \frac{\sigma_{c,x} + \sigma_{c,y}}{2} + \sqrt{\left(\frac{\sigma_{c,x} - \sigma_{c,y}}{2}\right)^2 + \tau_{xy}^2} \quad (3.44)$$

which can be worked out to:

$$\lambda = a + \frac{\lambda_x + \lambda_y}{2} + \sqrt{\left(b + \frac{\lambda_x - \lambda_y}{2}\right)^2 + \left(\frac{\tau_{xy}}{f_{ct}}\right)^2} \quad (3.45)$$

where the parameters a and b can be expressed in terms of the local concrete stresses at the cracks as:

$$a = \frac{\sigma_{cr,n} + \sigma_{cr,t}}{2 f_{ct}} \quad b = \frac{(\sigma_{cr,n} - \sigma_{cr,t}) \cos 2\theta_r - 2\tau_{cr,nt} \sin 2\theta_r}{2 f_{ct}} \quad (3.46)$$

Equation (3.45) can be solved for the maximum diagonal crack spacing s_{rm0} . This equation was derived based on the equilibrium conditions of the cracked membrane element and on TCM bond stress-slip relationship, and includes the solution derived by Marti and Kauffman [117; 120] for the CMM as a particular case. If stress-free rotating cracks perpendicular to the principal tensile direction of average strains are considered, then $\sigma_{cr,n} = \tau_{cr,nt} = 0$ and $\sigma_{cr,t} = -\tau_{xy} (\tan \theta_r + \cot \theta_r)$. Substituting the previous relations in Eqs. (3.46) and (3.45) yields the crack spacing relation proposed for the CMM. Figure 3.14 provides polar representations of the solution, assuming $\rho_x = 2\%$, $\phi_x = 16\text{mm}$, $f_{ct} = 2.9\text{MPa}$, $\tau_{b0} = 2f_{ct}$ and both stress free ($\tau_{cr,nt} = 0$) and interlocked cracks ($\tau_{cr,nt} \neq 0$). For the cases where interlocked cracks are considered, shear and normal stresses at the cracks were determined according to the Contact Density Model (see Section 3.6.3). The

solid line corresponds to the crack spacing obtained from the expression proposed by Vecchio and Collins [240]:

$$s_{rm} = \frac{1}{\frac{\cos \theta_r}{s_{rmx}} + \frac{\sin \theta_r}{s_{rmy}}} \quad (3.47)$$

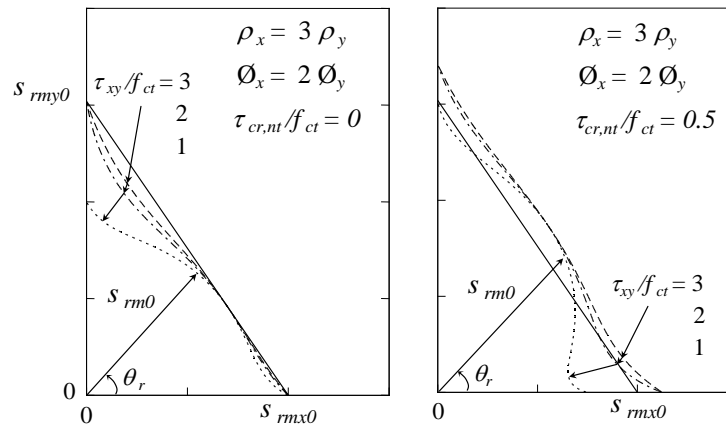


Figure 3.14 – Polar representations of the maximum diagonal crack spacing s_{rm0} .

Once s_{rm} is found, s_{rmx} and s_{rmy} are obtained from Eq. (3.41). The steel stresses in the x- and y- reinforcement are calculated from Eq. (3.37) to (3.39) replacing ε_{sm} and s_{rm} by ε_x and s_{rmx} , or by ε_y and s_{rmy} , respectively.

The crack width can be obtained from the general uniaxial equation (2.16). Although having almost negligible effect, the lateral expansion of the diagonally compressed concrete is accounted for in a simplified manner by adding the term $\nu \cdot \varepsilon_t$ to the average concrete tensile strain (note that ε_t is a negative value):

$$w_m = \lambda s_{rm0} \left(\varepsilon_n + \nu \varepsilon_t - \frac{\sigma_{cm}}{E_c} \right) \quad (3.48)$$

where ν is the Poisson ratio.

3.7 Calculation example

Both the R-CMM and the F-CMM were implemented in a stand-alone subroutine for the analysis of RC panels under in-plane shear and axial stresses. The panel responses were calculated with a stress-driven incremental iterative scheme using the Newton-Raphson

method together with an arc-length procedure [69] to constrain the norm of the incremental strain. This allows obtaining the local peaks as well as the softening branch of the response. The “updated normal plane” constraint [191] was adopted. Details are given in Section 4.2.5. The main steps for the calculation of the stresses corresponding to a given trial total strain vector are given by the flowchart in Figure 3.15. Prior to cracking, linear elastic behaviour is considered using the plane stress elasticity matrix. The formulation of the tangent stiffness matrix, of the unloading/reloading behaviour, and of the uncracked nonlinear behaviour of concrete is discussed in Chapter 4. While in the case of the R-CMM the crack angle θ , is determined from the principal tensile direction of the current total average strains, in the F-CMM this angle is set in the step where cracking occurs and kept in memory. In the R-CMM both the crack shear stress $\tau_{cr,nt}$ and the dilatancy stress σ_{dil} are null. A converged solution is found when the ratio between the norm of unbalanced stresses in iteration i and the norm of the calculated stresses in the first iteration is smaller than $tol = 10^{-4}$.

Three different failure modes can be distinguished with the F-CMM: (1) fracture of the reinforcement bars; (2) concrete crushing; and (3) shear sliding along a wide open crack. The first failure mode occurs mainly when the reinforcement ratios are small and low ductility steel is used. Depending on the reinforcement content, the second failure mode may occur after reinforcement yielding – either in one or in both directions – or before reinforcement yielding. In the latter, the panel is said to be over-reinforced. The third failure mode can be obtained when the reinforcement ratios in the two directions are markedly different. In general, the shear sliding failure mode occurs after yielding of the weaker reinforcement and with the stronger reinforcement still operating in the elastic range. The R-CMM can only distinguish between the first two failure modes. Due to the fact that fictitious rotating and stress free¹ cracks are considered, the sliding shear failure mode cannot be directly reproduced and is indirectly taken into account in the crushing failure mode.

The orthotropically reinforced panel PP1 tested by Marti and Meyboom [152] is here analysed in detail, thus exemplifying a typical load deformation response. The panel, with dimensions 1626x1626x286 mm³, was submitted to pure shear loading $\sigma_x:\sigma_y:\tau_{xy} = 0:0:1$. In the experiment, a slow sliding failure occurred along a crack that had formed in the early load stages. A strip was pushed up and away relative to the rest of the specimen. The y-reinforcement yielded, whereas the x-direction reinforcement remained elastic. Some

¹ The cracks are stress free apart from the crack bridging stresses.

localized cover spalling was observed. The adopted material properties are: $f'_c = 27$ MPa; $f_{sy,x} = 479$ MPa; $f_{su,x} = 667$ MPa; $\varepsilon_{su,x} = 0.090$; $\varnothing_x = 19.5$ mm; $\rho_x = 1.94\%$; $f_{sy,y} = 480$ MPa; $f_{su,y} = 640$ MPa; $\varepsilon_{su,y} = 0.091$; $\varnothing_y = 11.3$ mm; $\rho_y = 0.647\%$. The tensile strength of concrete was estimated according to Eq. (2.2).

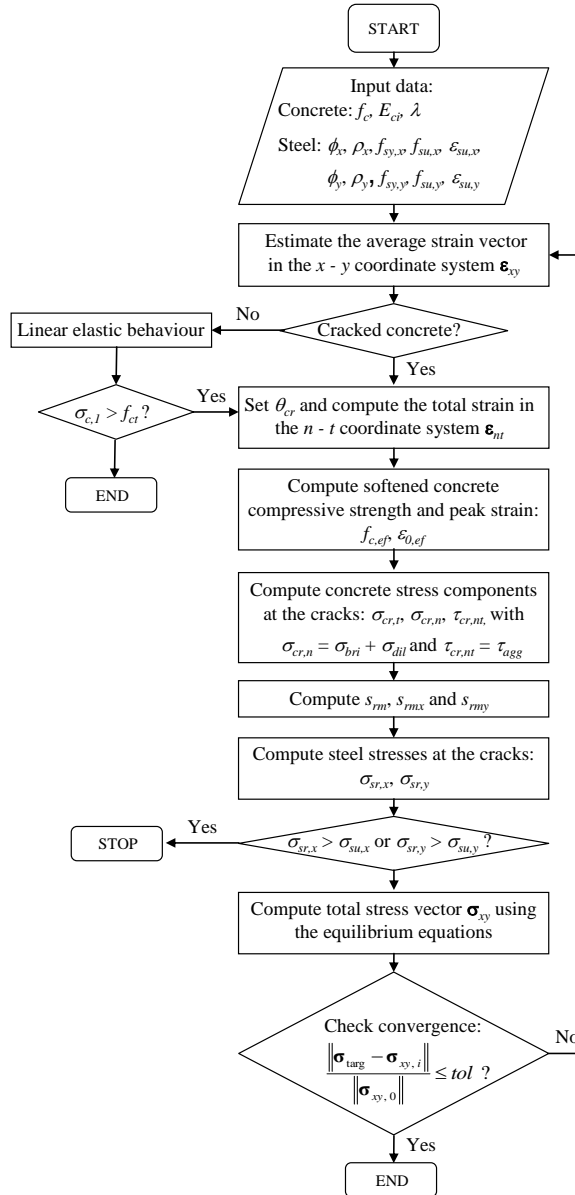


Figure 3.15– Flowchart of the main steps for the calculation of the stresses, given the total strain vector.

3.7.1 F-CMM

The calculated load-deformation relationships are presented in Figure 3.16 and, where available, experimental data is presented for comparison. The solid lines refer to the analysis considering bonded reinforcement ($\lambda = 1$), while the dashed lines refer to the analysis considering $\lambda = 0$, which is equivalent to disregarding tension stiffening effects.

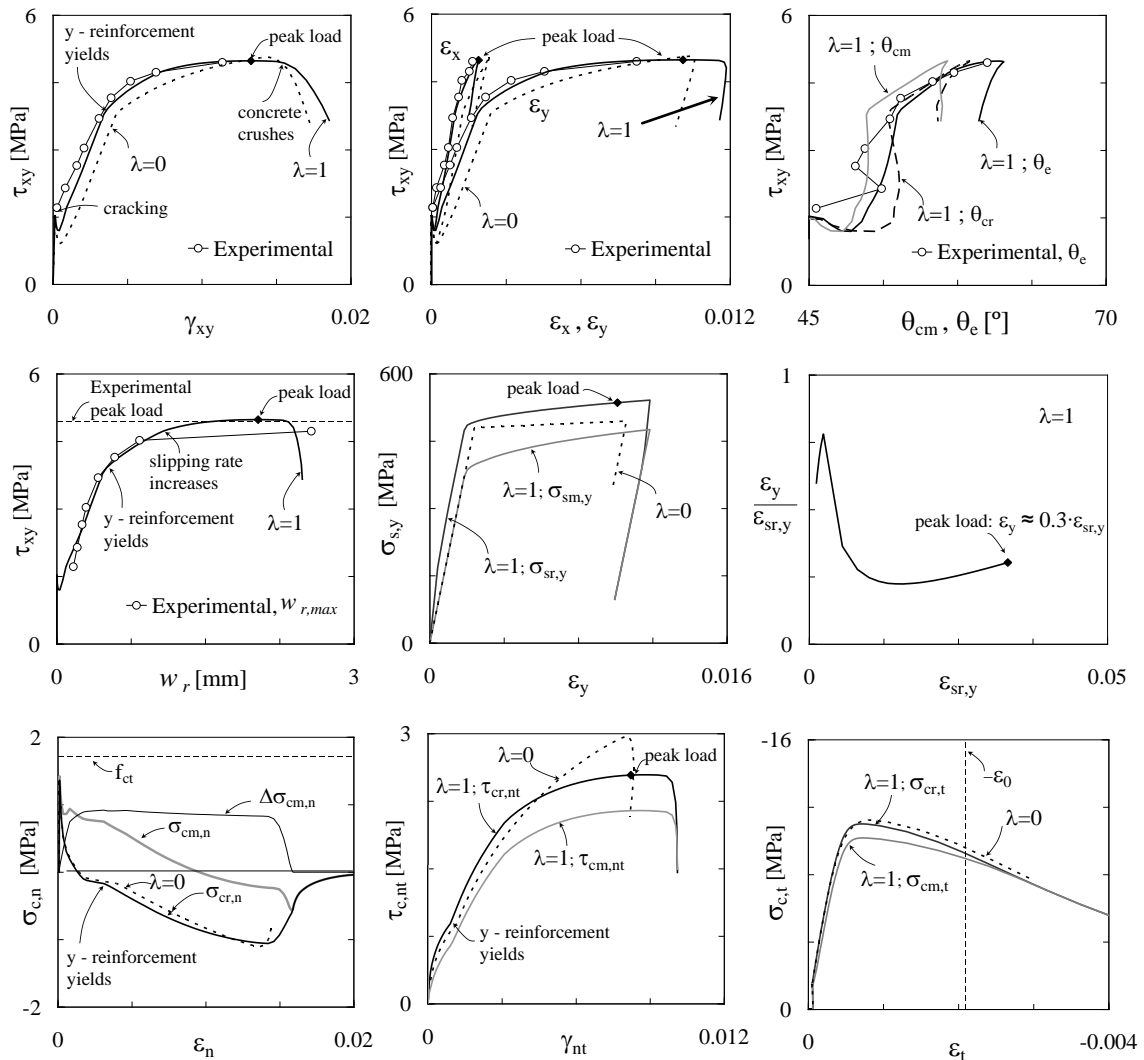


Figure 3.16– F-CMM: analysis of panel PP1 tested by Marti and Meyboom [152].

A markedly stiffer response can be observed in the shear stress-strain curve including the tension-stiffening effect. The stress-deformation curves compare favourably with the experimental results and the good fit exhibited by the τ_{xy} - ε_x and τ_{xy} - ε_y curves confirms the adequacy of the tension stiffening model. In the numerical analysis, the peak stress was achieved before concrete crushing and after extensive crack slipping. Therefore, the calculated failure mode can be deemed a shear sliding failure followed by concrete

crushing, which agrees with the experimental observations. In the analysis with $\lambda = 0$, the ultimate load is somewhat increased due to the fact that vanishing spacing cracks are considered. In this theoretical scenario the crack shear strength predicted by Eqs. (3.33) is higher because the crack widths are null. In this case, failure occurs due to diagonal concrete crushing.

The angle θ_e , – which defines the direction of the principal tensile average strains –, does not remain constant at 45° due to the crack slip. The crack shear slip increases sharply during the crack formation phase, after which follows a steady increase phase until the weaker reinforcement yields. At this point θ_e starts to increase faster. A good correspondence with the experimental measurements can also be observed here, which confirms that the model can reproduce the crack kinematics. The evolution of the angle defining the principal average concrete tensile stress direction, θ_{cm} , is also presented in Figure 3.16. It can be observed that the model can describe the lag between θ_{cm} and θ_e , as reported by Vecchio [237]. Also relevant is the evolution of the angle θ_{cr} , which defines the direction normal to the principal compressive concrete stresses at the cracks. After yielding of the weaker reinforcement, θ_{cr} and θ_e have similar values. However, near failure, a drift between the two angles is observed due to the increasing crack shear slip rate. This is a clear indication of a shear sliding failure.

A comparison between the predicted and measured maximum crack openings is also presented with a good match being obtained. Near failure, with the increasing shear slip, the accompanying opening movement due to crack dilatancy leads the crack width to increase more rapidly.

Regarding the reinforcement, the average steel stresses and the steel stresses at the cracks can be discerned. Due to crack kinematics, the stresses in the y-reinforcement kept increasing after the peak load was reached and only started to decrease after concrete crushing. The analysis of the local steel strains at the cracks reveals that, for the y-reinforcement, the local strain $\varepsilon_{sr,y}$ is more than three times the corresponding average strain ε_y .

In the analysis with $\lambda = 1$, the average stresses transmitted by bond action, $\Delta\sigma_{cm,x}$ and $\Delta\sigma_{cm,y}$, can be added to the concrete stresses at the cracks in order to obtain the average concrete stress field, as discussed in Section 3.2.2. Observing the stress components in the n - direction, it can be discerned the compressive stresses arising from crack shear transfer

mechanisms, $\sigma_{cr,n}$, the projection along the n - direction of the tension stiffening stresses, $\Delta\sigma_{cm,n}$, and the resulting “apparent” tension stiffening diagram $\sigma_{cm,n} - \varepsilon_n$. The onset of y - reinforcement yielding is reflected by changes in the slope of these diagrams. Also the concrete shear stress component in the local $n-t$ coordinate system is shown. The difference between the shear stress at the cracks and the average shear stress can be observed. Regarding the compressive concrete stresses in the t - direction, it can be confirmed that the compressive stresses at the cracks are higher than the average ones. The above description confirms that the proposed model allows a rational description of the complex stress field in a cracked membrane element.

Figure 3.17 shows the shear strength development of the panel. Up to first cracking all shear is resisted by tension in the uncracked concrete. Immediately after cracking, the F-CMM predicts that a fraction of the applied shear is carried by stress in the reinforcing steel while another is carried by shear stress on the cracks, according to Eqs. (3.5) and (3.6). Up to y -reinforcement yielding, the concrete component remains approximately constant, after which starts increasing. In this phase, the slope of the $\tau_{xy,cr}$ curve is somewhat lower than one due to the hardening behaviour of the reinforcing steel which is responsible for the slight increase of the $\tau_{xy,sr}$ component after yielding of the weaker reinforcement. Near failure, the concrete component stabilizes again. The concrete and steel components of the shear strength are represented in Figure 3.17 both in terms of stresses at the cracks and in terms of spatially averaged stresses. Bond stress transfer mechanisms are responsible for the existence of concrete tensile stresses in between the cracks. Consequently, the concrete contribution is higher if expressed in terms of average stresses.

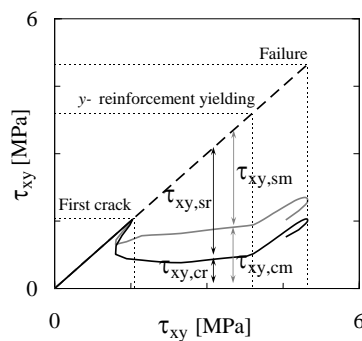


Figure 3.17– Contributions to the shear strength according to the F-CMM.

3.7.2 R-CMM

In the case of the R-CMM, the calculated load deformation relationships are presented in Figure 3.18. Once again, the solid lines refer to the analysis considering bonded reinforcement ($\lambda = 1$), while the dashed lines refer to the analysis considering $\lambda = 0$. The failure load is somewhat over-predicted and failure is predicted to occur by concrete crushing with the x -reinforcement operating in the elastic range.

Immediately after cracking, crack reorientation occurs such that the fictitious crack angle $\theta_r = \theta_e = \theta_{cr}$ does not coincide with principal tensile direction of the applied stresses. Up to y -reinforcement yielding, the crack angle remains approximately constant. After yielding of the weaker reinforcement, the fictitious cracks start rotating again. Although the angles θ_e and θ_{cr} are assumed to coincide, the lag between θ_e and θ_{cm} can be calculated and is represented in the top right plot of Figure 3.18. Regarding the concrete stress projection along the principal 1 – (or n –) direction (plot in the bottom left), it can be seen that the tension stiffening diagram is now governed by the stresses transmitted by bond action, given the fact that the crack bridging stresses are exhausted soon after cracking and that no crack dilatancy stresses are considered. The compressive stress-strain curve along the principal 2 – (or t) direction clearly shows that the softening coefficient is not applied to the peak strain, as discussed in Section 3.6.1. The plot in the lower right corner shows the shear stress decomposition in concrete and steel components, according to Eq. (3.6). In terms of stresses at the cracks, the concrete component is only due to the crack bridging stresses and is exhausted almost immediately after cracking. In terms of spatially averaged stresses, the R-CMM can predict a kind of concrete contribution to the shear strength due to the fact that tensile concrete stresses are assumed in between the cracks. The average concrete contribution does not decrease after steel yielding as could be expected. In fact, the decrease of the bond shear stress in post yield conditions is partially compensated by rotation of the cracks, thereby increasing the crack spacing along the x -reinforcement and, according to Eq. (3.42)₁, increasing the tensile stresses transferred in the x -direction

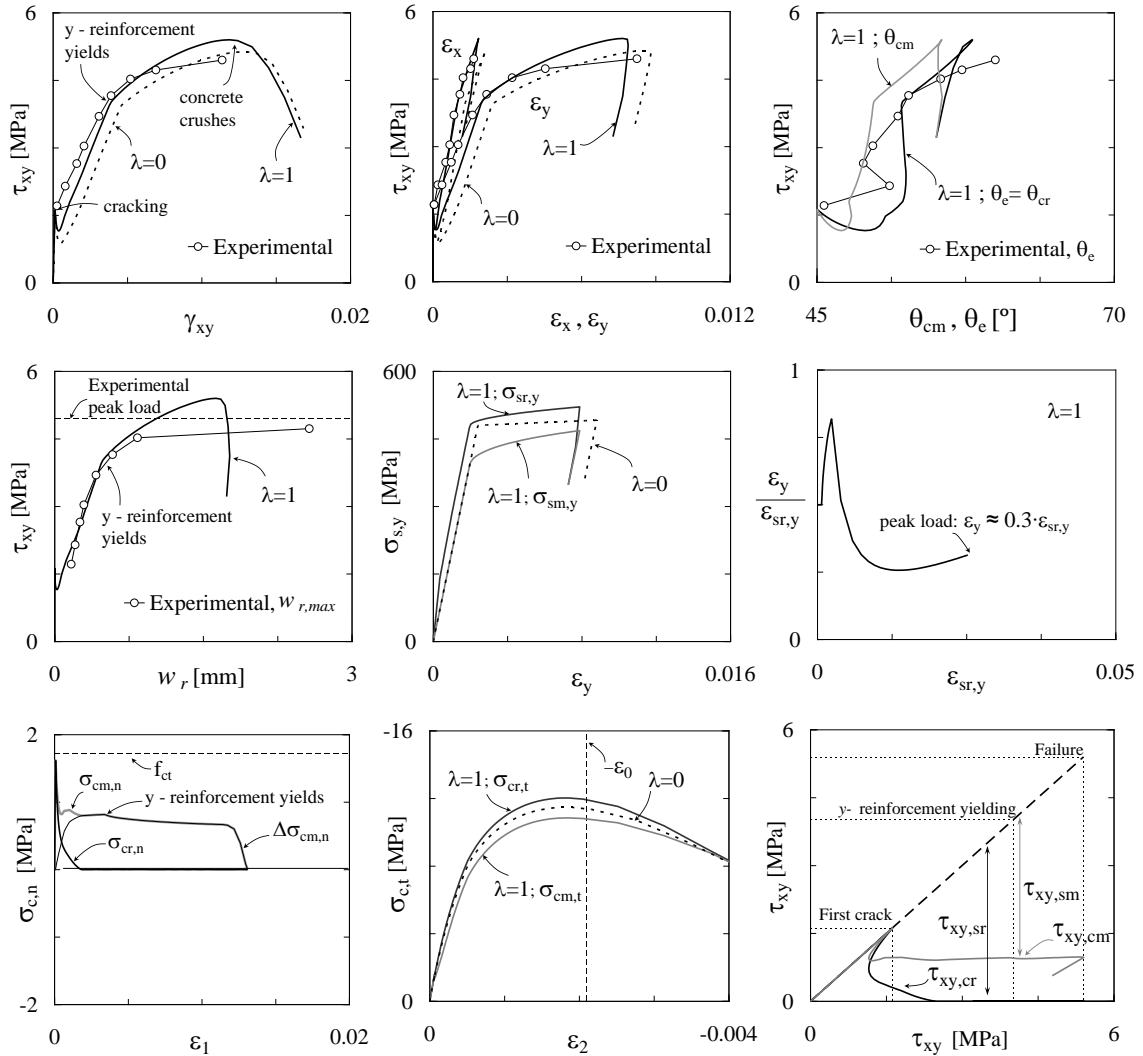


Figure 3.18– R-CMM: analysis of panel PP1 tested by Marti and Meyboom [152].

3.8 Validation

In this section, some validation examples are presented and the overall behaviour of both the F-CMM and R-CMM is discussed. A detailed comparison of the calculated force-deformation curves with the corresponding experimental measurements is presented in the Appendix. For all the calculations, concrete tensile strength was estimated according to Eq. (2.2) and $\alpha_{agg} = 1$ was considered in Eq. (3.30) for estimating the concrete Young modulus.

A distinction is made between isotropically and orthotropically reinforced panels. In isotropically reinforced panels under pure shear loading, or biaxial tension/compression proportional to the shear stress, shear slip is not activated at the crack interface. Due to

symmetry conditions, the angles $\theta_r = \theta_e = \theta_{cr} = \theta_{cm}$ are identical and remain constant at 45°. In the case of pure shear, the equilibrium at the cracks requires that:

$$\tau_{xy} = \rho_x \sigma_{sr,x} = \rho_y \sigma_{sr,y} = -0.5 \sigma_{cr,t} \quad (3.49)$$

The equation above shows that these panels can be used to check the reinforcement model according to the TCM and to check the compression model of cracked concrete. If the same constitutive law for compressed concrete was used, the results obtained with fixed and rotating crack models would be identical. Basic panel data is given in Table 3.1.

Table 3.1 – Isotropic panels properties

Panel	Ref.	Size [mm]	$\sigma_x: \sigma_y: \tau_{xy}$	f'_c [MPa]	$\rho_x = \rho_y$ [%]	f_{sy} [MPa]	f_{su} [MPa]	ε_{su} [%]	\emptyset [mm]
A2		1397 x 178	0:0:1	42.2	1.13 ^a	445	579 ^b	50 ^c	16.0
A3	[178]	1397 x 178	0:0:1	41.3	1.70 ^a	463	610 ^b	50 ^c	19.5
A4		1397 x 178	0:0:1	41.6	2.83 ^a	446	625 ^b	50 ^c	25.2
VA0		1397 x 178	0:0:1	98.8	0.57 ^a	445	579 ^b	50 ^c	11.3
VA1		1397 x 178	0:0:1	95.1	1.14 ^a	445	579 ^b	50 ^c	11.3
VA2	[261]	1397 x 178	0:0:1	98.2	2.28 ^a	409	534 ^b	50 ^c	16.0
VA3		1397 x 178	0:0:1	94.6	3.42 ^a	455	608 ^b	50 ^c	19.5
VA4		e	0:0:1	103.1	4.99 ^a	470	606 ^b	50 ^c	25.2
PV16			0:0:1	21.7	0.74	255	281 ^d	100 ^c	4.1
PV23		890 x 70	-.39:-.39:1	20.5	1.79	518	570 ^d	100 ^c	6.35
PV25	[234]	890 x 70	-.69:-.69:1	19.2	1.79	466	513 ^d	100 ^c	6.35
PV27		890 x 70	0:0:1	20.5	1.79	442	486 ^d	100 ^c	6.35
PV28			.32:.32:1	19.0	1.79	483	531 ^d	100 ^c	6.35

^a average over entire panel; values given in the test report apply only to the central portion of the panels and are 5% higher; ^b ultimate stress measured at a strain of 50%; ^c assumed value; ε_{su} not given in the test report; ^d f_{su} not given in the test report.; taken as $1.10f_{sy}$; ^e panel dimensions: 1397x1397x203 mm

In the case of RC panels with different amounts of reinforcement in the longitudinal and transversal directions, shear slip at the crack interface is activated and the shear transfer model plays an important role in the calculated response. Basic data for the analysed orthotropically reinforced panels is given in Table 3.2.

Table 3.2 – Orthotropic panels properties

Panel	Ref.	Size	f'_c	ρ_x	$f_{sy,x}$	$f_{su,x}$	$\varepsilon_{su,x}$	\emptyset_x	ρ_y	$f_{sy,y}$	$f_{su,y}$	$\varepsilon_{su,y}$	\emptyset_y
		[mm]	[MPa]	[%]	[MPa]	[MPa]	[%]	[mm]	[%]	[MPa]	[MPa]	[%]	[mm]
B1			45.2	1.13 ^a	463	609 ^b	50 ^c	16.0	0.57 ^a	445	579 ^b	50 ^c	11.3
B2			44.1	1.70 ^a	446	625 ^b	50 ^c	19.5	1.13 ^a	463	609 ^b	50 ^c	16.0
B3	[178]		44.9	1.70 ^a	446	625 ^b	50 ^c	19.5	0.57 ^a	445	579 ^b	50 ^c	11.3
B4			44.8	2.83 ^a	470	629 ^b	50 ^c	25.2	0.57 ^a	445	579 ^b	50 ^c	11.3
B5			42.8	2.83 ^a	470	629 ^b	50 ^c	25.2	1.13 ^a	463	609 ^b	50 ^c	16.0
B6			43.0	2.83 ^a	470	629 ^b	50 ^c	25.2	1.70 ^a	446	625 ^b	50 ^c	19.5
M2			48.3	1.70	446	629 ^b	50 ^c	19.5	0.42	420	630	80	6.3
M3	[59]		48.1	1.70	446	629 ^b	50 ^c	19.5	0.19	420	630	80	6.3
M4		1397	44.8	2.66	470	629 ^b	50 ^c	25.2	0.37	420	630	80	6.3
M5		1397	43.4	2.66	470	629 ^b	50 ^c	25.2	0.17	420	630	80	6.3
HB3	[260]	x 178	66.8	1.71 ^a	446	583 ^b	50 ^c	19.5	0.57 ^a	450	579 ^b	50 ^c	11.3
HB4			62.9	2.84 ^a	470	629 ^b	50 ^c	25.2	0.57 ^a	450	579 ^b	50 ^c	11.3
VB1			98.2	2.28 ^a	409	534 ^b	50 ^c	16.0	1.14 ^a	445	579 ^b	50 ^c	11.3
VB2	[261]		97.6	3.42 ^a	455	608 ^b	50 ^c	19.5	1.14 ^a	445	579 ^b	50 ^c	11.3
VB3			102.3	5.70 ^a	470	608 ^b	50 ^c	25.2	1.14 ^a	445	579 ^b	50 ^c	11.3
VB4			96.9	1.71 ^a	455	608 ^b	50 ^c	19.5	0.57 ^a	445	579 ^b	50 ^c	11.3
TA2			41.3	0.84 ^e	1670	1860	50 ^c	13.4 ^f	0.77	415	550 ^b	50 ^c	12.7
TA4	[253]		42.5	0.59 ^e	1670	1860	50 ^c	13.4 ^f	0.77	415	550 ^b	50 ^c	12.7
TA5			41.1	0.42 ^e	1670	1860	50 ^c	11.2 ^f	0.77	415	550 ^b	50 ^c	12.7
PP1			27.0	1.94	479	667	90	19.5	0.65	480	640	91	11.3
PP2	[152]	1626	28.1	1.30 ^g	486	630	100	19.5	0.65	480	640	91	11.3
PP3		x 1626	27.7	0.65 ^g	480	640	91	19.5	0.65	480	640	91	11.3
SE1	[123]	x 287	42.5	2.93	492	625 ^b	50 ^c	19.5	0.98	479	605 ^b	50 ^c	11.3
SE6			40.0	2.93	492	625 ^b	50 ^c	19.5	0.33	479	605 ^b	50 ^c	11.3
PV10			14.5	1.79	276	304 ^d	100 ^c	6.35	1.00	276	304 ^d	100 ^c	4.70
PV12		890	16.0	1.79	469	516 ^d	100 ^c	6.35	0.45	269	296 ^d	100 ^c	6.35
PV19	[234]	x 890	19.0	1.79	458	504 ^d	100 ^c	6.35	0.71	299	329 ^d	100 ^c	6.35
PV20		x 70	19.6	1.79	460	506 ^d	100 ^c	6.35	0.89	297	327 ^d	100 ^c	6.35
PV21			19.5	1.79	458	504 ^d	100 ^c	6.35	1.30	302	332 ^d	100 ^c	6.35
PV22			19.6	1.79	458	504 ^d	100 ^c	6.35	1.52	420	462 ^d	100 ^c	6.35

^a average over entire panel; values given in the test report apply only to the central portion of the panels and are 5% higher; ^b ultimate stress measured at a strain of 50‰; ^c assumed value; ε_{su} not given in the test report; ^d f_{su} not given in the test report and taken as $1.10 \cdot f_{sy}$; ^e The panels of the series TA are prestressed in the x-direction - 0.6” seven wire strands were provided in TA2 and T4 and 0.5” strands were provided in TA5 (no additional x-reinforcement was provided) with an initial prestress of 990 MPa; ^f Equivalent diameter; ^g additional unbonded prestress with an initial stress around 750MPa was provided in the x-direction: $\rho_{p,x} = 0.293$ and 0.586 for the panels PP2 and PP3, respectively, $f_{pyx} = 910\text{MPa}$, $f_{pux} = 1135\text{MPa}$ and $\varepsilon_{pux} = 100\%$;

3.8.1 The influence of the reinforcement content

The failure envelope given by the F-CMM is presented in Figure 3.19(a). The calculations were made varying the longitudinal and transversal reinforcement ratios and considering $f'_c = 45$ MPa, $f_{sy,x} = f_{sy,y} = 450$ MPa, $f_{su,x} = f_{su,y} = 580$ MPa, $\varepsilon_{su,x} = \varepsilon_{su,y} = 50\%$ and $\varnothing_x = \varnothing_y = 16$ mm. The dashed lines define the boundaries over which failure occurs with $\sigma_{sr,x} = f_{sy}$ or $\sigma_{sr,y} = f_{sy}$. In Figure 3.19(b)-(c), the four sections of the failure envelope identified in Figure 3.19(a) are presented for both the F-CMM and R-CMM and are compared to experimental failure loads of panels with similar properties. In general, good agreement can be found. In the case of over-reinforced panels, and due to the adoption of $C_m = 0.9$ in the compression softening coefficient, the F-CMM provides higher failure loads than those calculated with the R-CMM

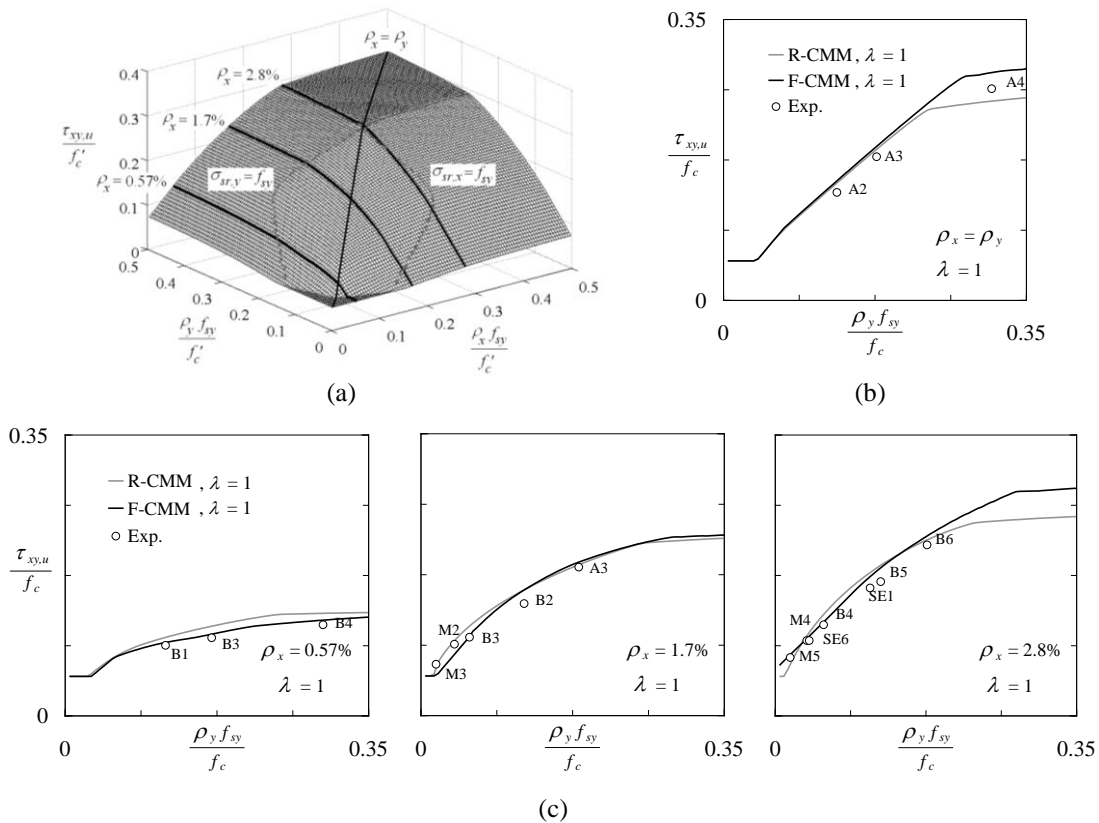


Figure 3.19 – Influence of the reinforcement content on the ultimate shear stress: (a) Failure envelope given by the F-CMM ($\lambda = 1$); (b) section by $\rho_x = \rho_y$; (c) sections by $\rho_x = 0.57\%$, 1.7% and 2.8% .

In Figure 3.20, the results of a series of panels is presented that allows the evaluation of the influence of increasing transversal reinforcement ratios in the shear stress-strain curves. Most of the panels belong to the series A, B and M, have f'_c values around 45MPa, and were tested in the “Universal Panel Tester” at the University of Houston. These panels

were 178mm thick and reinforced with deformed bars which spacing varied between 100 and 200mm. The orthotropically reinforced panels with $\rho_x \approx 2.8\%$ are partially over-reinforced in the x -direction while the panels with $\rho_x \approx 1.7\%$ are under-reinforced (except for the panel M3 which also fails with the x -reinforcement still operating in the elastic range¹). The experimental shear stress-strain curves are compared to the calculated responses with both the rotating and fixed crack models.

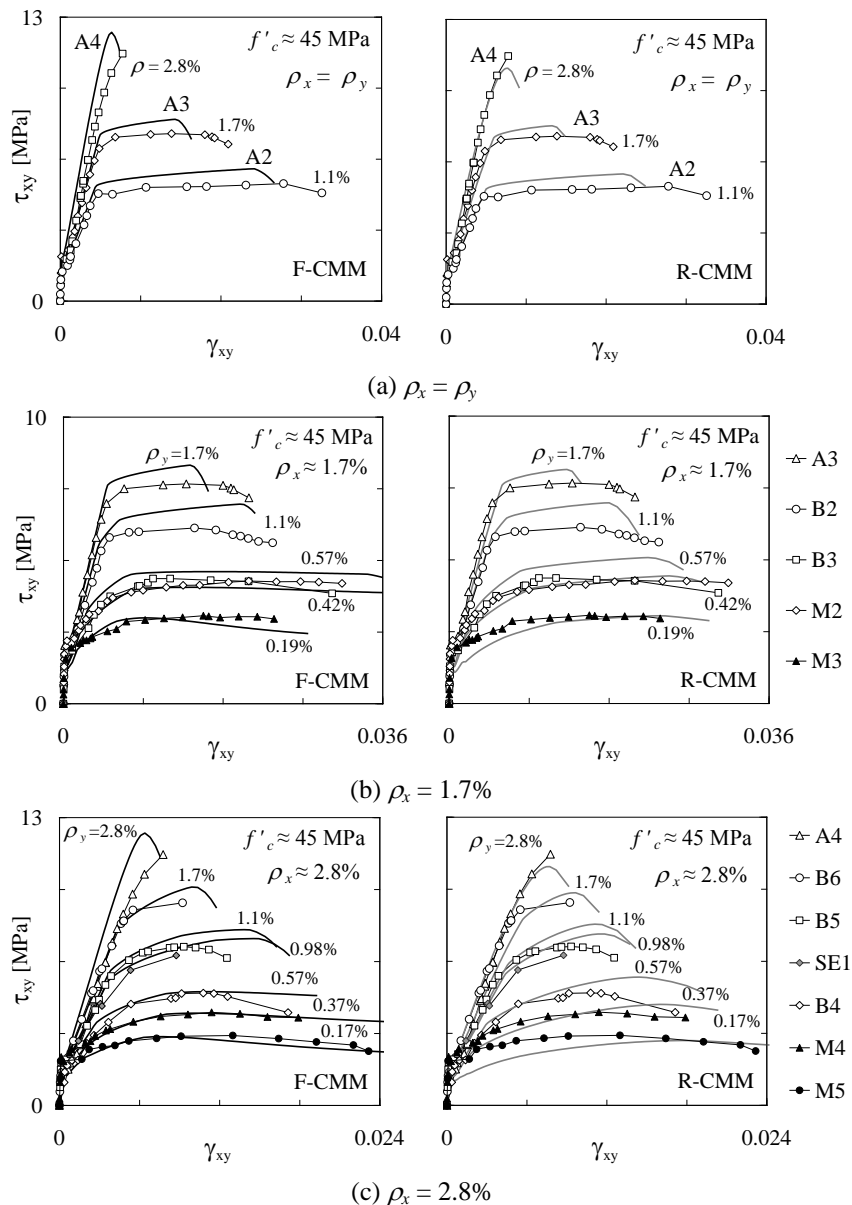


Figure 3.20 – Shear stress-strain curves for some of the panels referred in Figure 3.19. Experimental data is given by the curves with symbols.

¹ This can be confirmed by the stress-strain curves presented in the Appendix.

Regarding the isotropically reinforced panels (Figure 3.20(a)), the stiffness in the pre-yielding stage is well reproduced. However, the yielding stress of panels A2 and A3 is slightly over-predicted. The authors of the tests attributed this fact to flexure of the bars in the vicinity of the crack plane [178; 261]. Based on these tests they proposed a reduction in the steel “apparent” yield stress. This reduction is related to the rebars inclination relatively to the cracks and a maximum value of 10% was proposed for 45° cracks. However, this reduction factor was omitted in the most recent constitutive relations proposed by the same research group [263]. It is clear from Eq. (3.49) that either the steel yielded before the reported uniaxial yielding stress or some experimental procedure influenced the results. Panel A4 was reinforced to be close to the “balance point” and failure occurred due to concrete crushing when steel began to yield.

Concerning the orthotropically reinforced panels, the agreement between the experimental and calculated shear stress-strain curves is generally good. A slight overestimation of the yielding stress in some of the panels of the B series is also visible. As these panels belong to the same experimental campaign of the A series, the same remarks apply. The slight underestimation by the F-CMM of the failure loads for panels with very low amounts of y -reinforcement exhibited in the envelope section $\rho_x \approx 1.7\%$ of Figure 3.19(c) is due to the consideration of 16mm rebars in the weaker direction, while the real panels were reinforced with smaller rebars. As expected, in the cases where failure occurs by shear sliding, the ultimate shear strength was found to be highly dependent on the crack spacing. The shear stress-strain curves of Figure 3.20 were calculated with the rebar properties presented in Table 3.2 and good agreement can be found.

A measure of the panel orthotropy degree is given by

$$\chi = \frac{\rho_y f_{sy,y} - \sigma_y}{\rho_x f_{sy,x} - \sigma_x} \quad (3.50)$$

The orthotropy degree χ of the panels analysed in Figure 3.20 ranges between 0.06 and 1, covering a wide range of transversal reinforcement ratios. For very low values of χ it is expected that either large shear slips are observed at the cracks or, if the longitudinal reinforcement is strong enough to avoid a shear slip failure, new cracks arise with an orientation closer to the longitudinal (stronger) bars. These cracks may govern the behaviour, making the applicability of the fixed crack model in these circumstances questionable. In Figure 3.21 the evolution of the normal strains in the fixed crack $n-t$ coordinate system is presented for the panels of the B series. If the governing cracks are

indeed oriented 45° to the reinforcements, as predicted by the F-CMM, then ε_t would always be compressive. However, if the governing cracks are rotated with respect to the first array of cracks, the strain trajectories expressed in the local fixed crack coordinate system may diverge significantly from the predictions given by the F-CMM and ε_t may decrease or even become tensile. From the analysis of Figure 3.21 is clear that significant crack rotation has occurred in panels B1 and B4. Nonetheless, the F-CMM still does a good job in predicting the load-deformation responses in both cases (see Appendix).

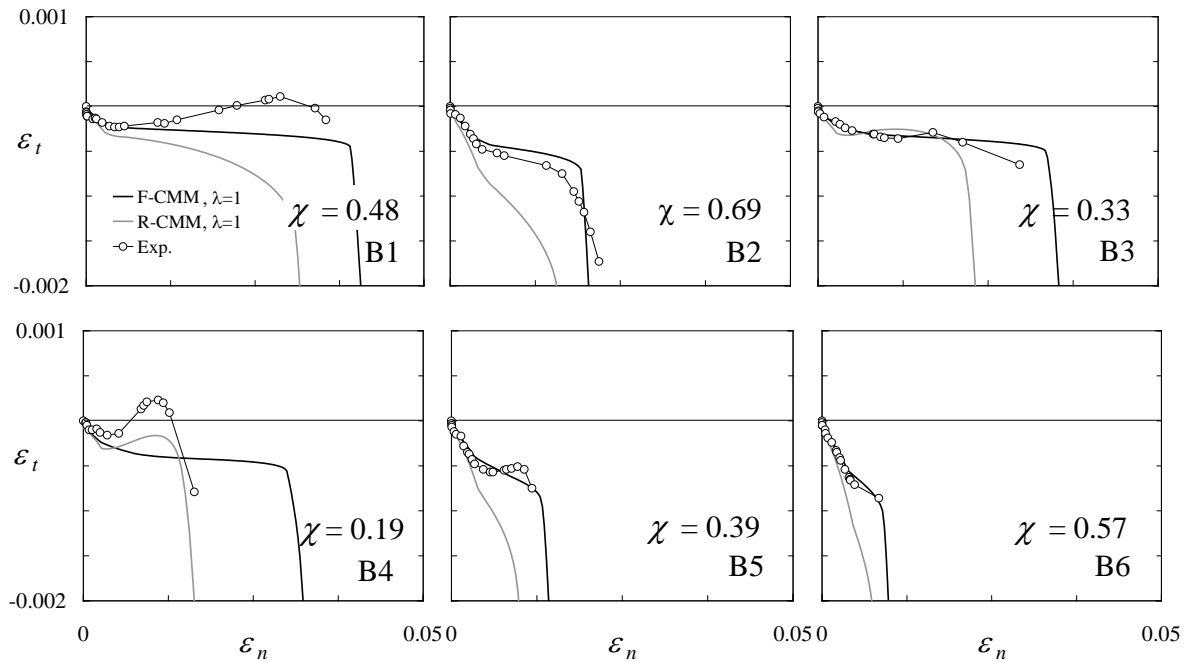


Figure 3.21 – Average normal strains in the fixed crack coordinate system.

3.8.2 The influence of prestressing

The panels from series PP [152] were tested in the “Shell Element Tester” at the University of Toronto. These panels were 287mm thick and contained the same amount of transversal reinforcement, $\rho_y = 0.647\%$. Panels PP2 and PP3 were prestressed in the x-direction along their middle planes with 16mm diameter, unbonded, high strength steel bars placed inside a PVC sheathing. The initial concrete compressive stress due to the prestress was equal to 2.07 and 4.40MPa for panels PP2 and PP3, respectively. The amount of ordinary and prestressing reinforcement in the x-direction was proportioned such that the total force that could be developed in yielding conditions was approximately the same for all panels.

The results are presented in Figure 3.22. Excellent agreement with the F-CMM calculations can be found for all panels, both for failure loads and for load-deformation

responses (see Appendix). The failure modes were also exactly predicted: shear sliding failure in the case of PP1 (see discussion in Section 3.7.1) with the x -reinforcement in the elastic range, and concrete crushing with yielded reinforcements for PP2 and PP3. It can be concluded that without prestress, failure was anticipated due to excessive crack shear slip. The R-CMM tends to overestimate the ultimate loads and the response stiffness after the y -reinforcement yielding of the non-prestressed panel, as discussed in 3.7.2. Therefore, the ultimate load increase due to the prestressing could not be precisely reproduced by the R-CMM because of its inability to distinguish between shear sliding and concrete crushing.

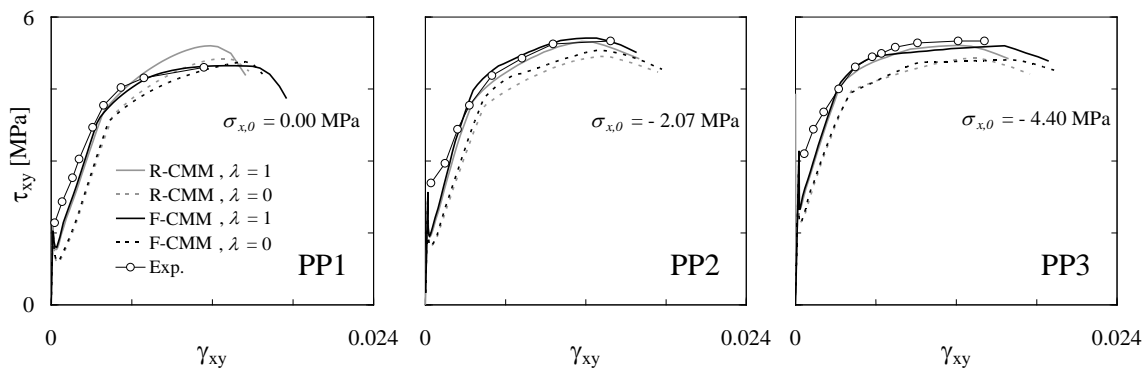


Figure 3.22 – Comparison with experiments of Series PP by Marti and Meyboom [152].

The panels of the TA series [253] were 178mm thick and were tested in the “Universal Panel Tester” at the University of Houston. The panels were post-tensioned using 7-wire strands placed inside flexible corrugated plastic ducts 32mm in diameter. After post-tensioning, the ducts were grouted with high-strength self compacting concrete grout ensuring that the bond condition of the post-tensioned strands was similar to that of pre-tensioned strands. The panels analysed here have the same amount of y -reinforcement ($\rho_y = 0.77\%$). In the x -direction, only prestressing steel was provided with an initial prestress of approximately 990MPa. The prestressed reinforcement ratios were 0.84, 0.59 and 0.42% for panels TA2, TA4 and TA5, respectively, which corresponds to initial concrete compressive stresses of 8.32, 5.70 and 4.16MPa.

It is well known that the presence of ducts in the web of a girder influences its strength. The same is expected to occur in panels such as the ones analysed here. This effect is discussed in detail by Muttoni *et al* [165]. According to these authors, for grouted plastic ducts the strength reduction can be given by

$$\zeta_D = 1 - 0.8 \cdot \delta \quad (3.51)$$

with δ being the ratio between the sum of the duct diameters and the thickness of the panel. In the case of panels TA2 and TA4, two layers of 32mm ducts were used, while only one layer was used in TA5. Therefore, $\zeta_D = 0.71$ for panels TA2 and TA4, and 0.86 for TA5. The compressive strength was determined using $f'_{c,ef} = \zeta_D \zeta_e \zeta_f f'_c$.

According to the CEB recommendations, the bond strength of the strands is approximately 60% of that of ordinary ribbed reinforcement [40; 46]. This reduction was applied to the bilinear bond shear stress-slip relation of the prestressed reinforcement.

The obtained shear stress-strain curves are presented in Figure 3.23. The behaviour of panels is accurately reproduced, although in the case of Panel TA5 concrete crushing occurred sooner than predicted by both models.

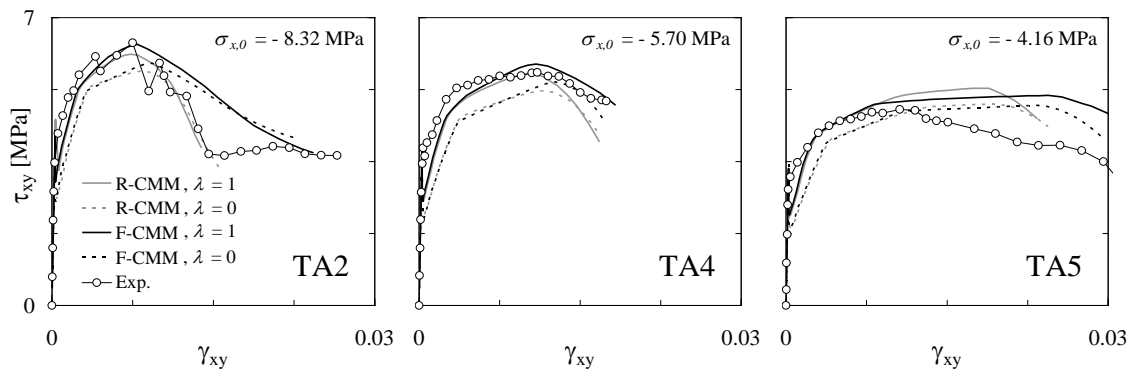


Figure 3.23 – Comparison with experiments of series TA by Wang [253]

3.8.3 The influence of the concrete strength

In Figure 3.24 the shear stress-strain curves for panels B3, B4, HB3 and HB4 are presented. The panels HB3 and HB4 are identical to the panels B3 and B4, respectively, except for the fact that medium high-strength concrete was used ($f'_c \approx 65\text{MPa}$) instead of normal strength concrete (NSC) ($f'_c \approx 45\text{MPa}$). The failure modes and the shear stress-strain responses were similar and could be satisfactorily reproduced by the F-CMM. The R-CMM overestimates the failure load in both situations. Panels B3 and HB3 failed with concrete crushing after yielding of both reinforcements. Although the F-CMM predicts a large amount of crack shear slip, the peak load is reached with concrete crushing. Panels B4 and HB4 failed with the longitudinal reinforcement in the elastic range. In this case, the F-CMM predicts a shear-sliding failure.

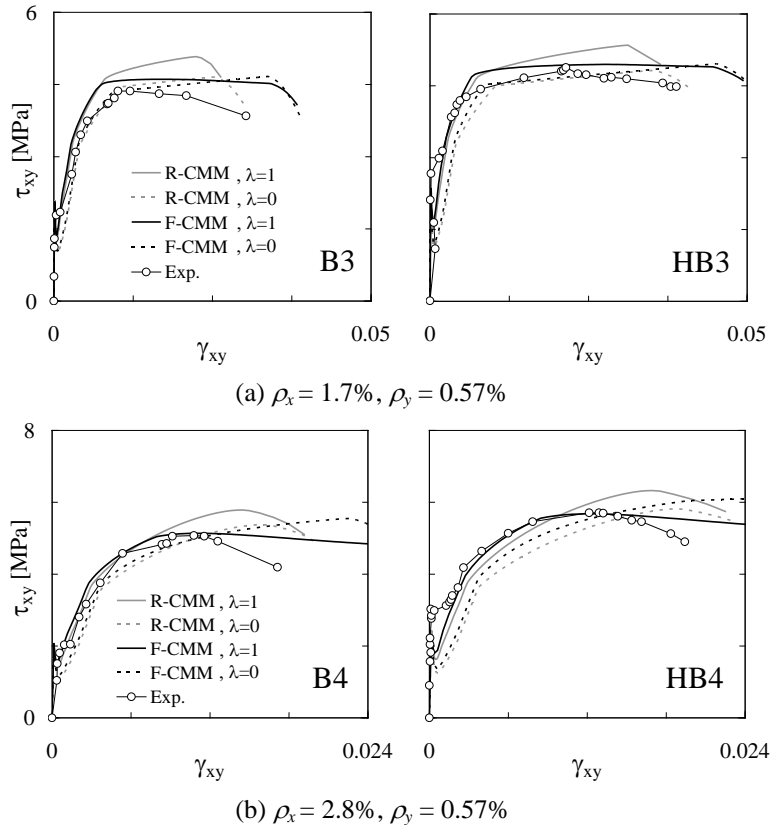


Figure 3.24 – Shear stress-strain curves of panels made with normal and medium-high strength concrete: series B by Pang [178] and series HB by Zhang [261]. Experimental data of the HB panels taken from [117].

In Figure 3.25(a) two sections of the failure surfaces of panels cast with normal strength and high strength concrete (HSC) are compared with experimental evidence. The HSC panels ($f'_c \approx 98\text{MPa}$) of the VA and VB series have the same dimensions and were tested in the same machine as the panels from the A and B series. The envelope section corresponding to panels with a mechanical reinforcement ratio of $\rho_x f_{sy} / f'_c = 0.055$ allows a comparison between the normalized failure shear stresses of HSC and NSC concrete panels with low amount of transversal reinforcement. Regarding the NSC panels, panels B1 and B3 are under-reinforced whereas panel B4 failed with elastic longitudinal reinforcement. The HSC panel VB2 is very close to the boundary dividing the under-reinforced and partially-under-reinforced region of the envelope, as can be inferred from the stress-strain curves presented in the Appendix. In the case of HSC panels, the transition between the two regions occurs for lower values of the mechanical reinforcement ratio. This effect is reasonably reproduced by both models. Moreover, the normalized shear stress at failure is lower for over-reinforced HSC than for NSC panels, as can be seen in the envelope section corresponding to $\rho_x = \rho_y$. This confirms once again that the compressive strength of cracked concrete increases less than proportionally with f'_c .

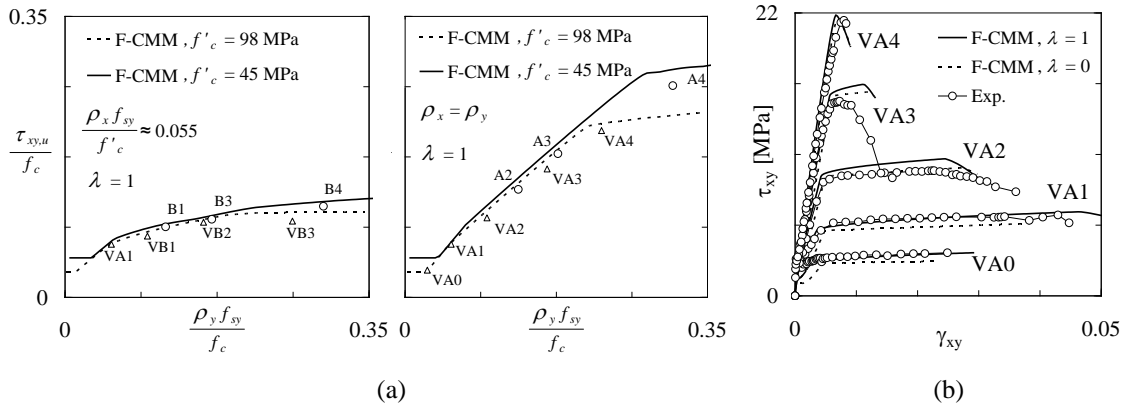


Figure 3.25 – Effect of the concrete strength: (a) Sections of the failure surface for normal and high strength concrete; (b) Shear stress-strain curves for isotropically reinforced panels cast with high strength concrete.

The shear stress-strain curves of the VA series panels are presented in Figure 3.25(b). In panels with low to moderate reinforcement content, the compressed concrete stress-strain relation plays a minor role on the global shear stress-strain curves. Hence, the results of panels VA0, VA1 and VA2 serve to check the suitability of the reinforcement formulation according to the TCM and the resulting tension stiffening effect. The post yielding response predictions are excellent for panels VA0 and VA1. Panel VA0 did not reach failure in the experiment, since the test had to be stopped due to the limited stroke of the actuators. Reinforcement yielded almost immediately after cracking. The numerical model predicts that failure would occur due to exhaustion of the steel deformation capacity. Panel VA4 is over-reinforced and failed by concrete crushing before yielding of the reinforcements. This panel serves mainly to check the softened compressed stress-strain curve of concrete. Concrete compressive softening is also important for accurate predictions of the ductility of the panels. In fact, even under-reinforced panels eventually fail by concrete crushing due to the large tensile strains that occur after reinforcement yielding. The results of panel VA1 and VA2 seem to confirm the adequacy of the softening coefficients $\zeta_f \zeta_e$, now for the case of large tensile strains.

In Figure 3.26(a) one section of the failure surfaces of NSC and low-strength concrete (LSC) panels ($f'_c \approx 20$ MPa) is presented, corresponding to a high mechanical reinforcement ratio in the longitudinal direction. The section corresponding to LSC panels has been calculated with the same material properties as mentioned above, except for the rebar diameters, which were taken as $\varnothing_x = \varnothing_y = 6$ mm.

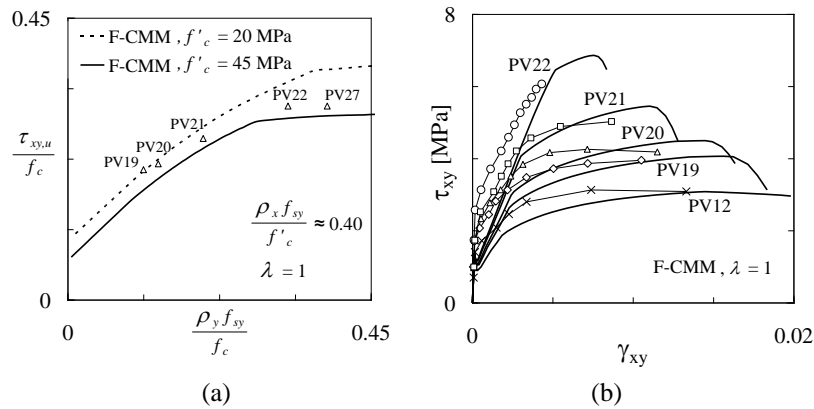


Figure 3.26 – Effect of the concrete strength: (a) Sections of the failure surface for normal and low strength concrete; (b) Shear stress-strain curves for the panels of the PV series.

The experimental data corresponds to the panels of the PV series, which were tested in the “Membrane element tester” at the University of Toronto. The panels were only 70mm thick and were reinforced with a welded wire mesh made of small diameter plain bars. The bar spacing was approximately 50mm. For the partially over-reinforced panels, the calculated and the observed ultimate shear stresses are in reasonable agreement. However, in the case of the over-reinforced panels PV22 and PV27, the F-CMM over-predicts the ultimate shear stress. As noticed by other authors [137], this can be attributed to the fact that the test panels had a small concrete cover that might have easily spalled off when subjected to high compression.

As shown in reference [222], the bond behaviour of this type of reinforcement is different from the one exhibited by deformed bars. In welded wire meshes with closely spaced wires, the crack spacing and the amount of steel stresses transferred to surrounding concrete do not depend on the type of surfacing of the rebars but mainly on the anchorage provided by transversal wires. In this case the tensile response of RC elements is stiffer and less ductile than the obtained using larger wire spacings or deformed bars. As the wire spacing increases, bond stress starts gaining importance as the main mechanism of stress transfer. The TCM considers the bond stress as the only mechanism of steel stress transfer to concrete. Thus the agreement of the calculated and the experimental stress-strain curves presented in Figure 3.26(b) is not as good for the PV series as the obtained with panels reinforced with normal size and widely spaced deformed bars. This effect is also recognized by other researchers and often the tension stiffening diagram is modified in order to fit the results from the PV series [25; 137; 171].

3.8.4 Summary

A summary of the results of the validation campaign is presented in Figure 3.27 and in Table 3.3. A total of 54 panels were analysed. The average values of the $\tau_{u,exp}/\tau_{u,calc}$ ratio are close to unity, which shows that both models can be used to calculate the shear strength of RC panels with good accuracy. The coefficients of variation are equal to 8% and 10.7% for the F-CMM and R-CMM, respectively, which is a good result having in mind the complexity of the problem and the diversity of the tested panels.

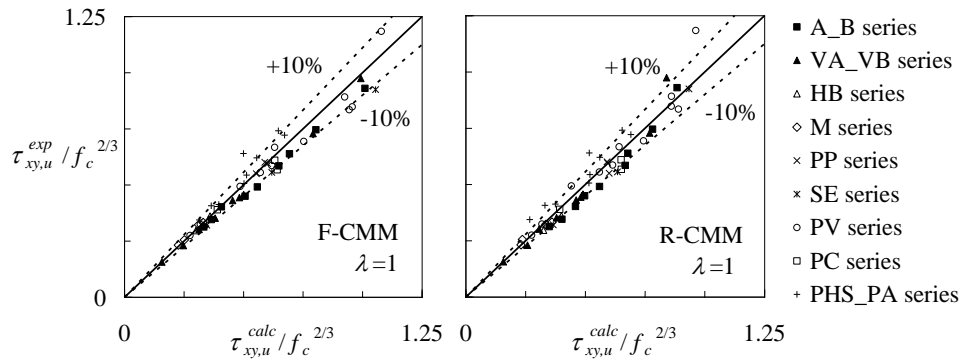


Figure 3.27 – Comparison of the calculated with the experimental shear strengths of RC panels tested under in plane shear and axial forces

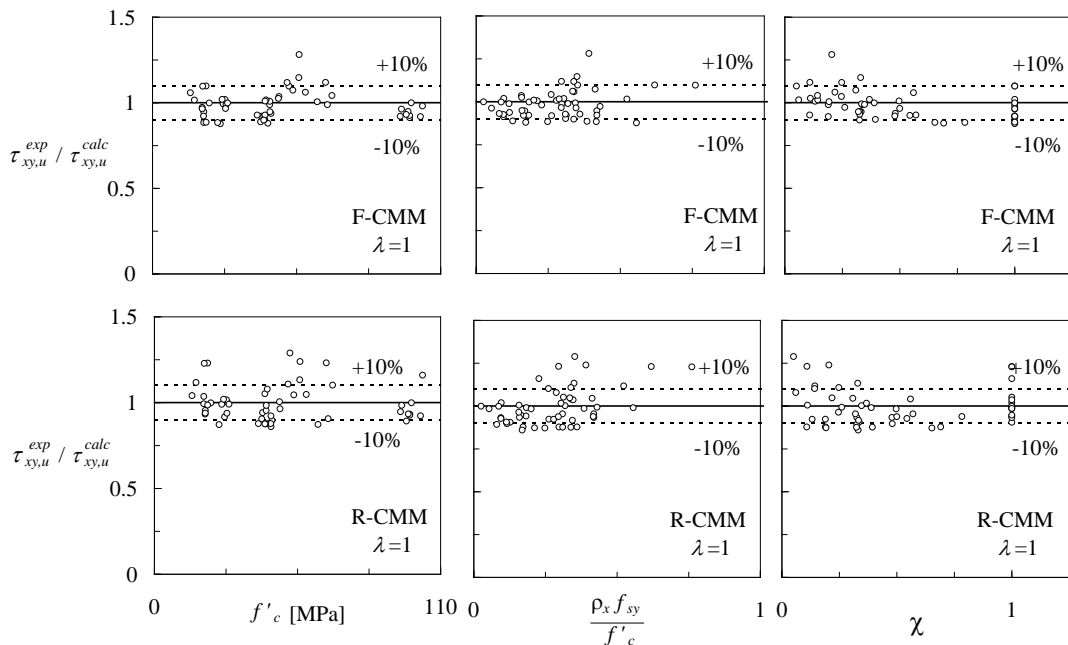


Figure 3.28 – $\tau_{xy,u}^{exp} / \tau_{xy,u}^{calc}$ ratio as function of the concrete uniaxial τ compressive strength, longitudinal mechanical reinforcement ratio and orthotropy indicator.

Table 3.3 – Summary of validation results.

Panel	Ref.	f'_c	ω_x^*	χ	$\tau_{u,exp}$	$\tau_{xy,u}^{exp} / \tau_{xy,u}^{calc}$				Limit An. Eq. (6.6)
		[MPa]	[MPa ^{1/3}]	[-]	[MPa]	F-CMM $\lambda=1$	F-CMM $\lambda=0$	R-CMM $\lambda=1$	R-CMM $\lambda=0$	
A2		41.3	0.44	1.00	5.38	0.89	0.96	0.91	0.97	1.03
A3		41.6	0.63	1.00	7.67	0.92	0.97	0.94	0.99	1.01
A4		42.5	1.09	1.00	11.33	0.92	0.94	1.05	1.07	1.08
B1	[178]	45.2	0.41	0.48	3.97	0.94	0.99	0.90	1.00	1.09
B2		44.1	0.61	0.69	6.13	0.88	0.94	0.88	0.93	0.97
B3		44.9	0.60	0.33	4.36	0.95	0.94	0.86	0.94	1.00
B4		44.8	1.06	0.19	5.07	0.99	0.91	0.88	0.94	0.98
B5		42.8	1.09	0.39	7.16	0.90	0.92	0.88	0.91	0.92
B6		43.0	1.08	0.57	9.15	0.93	0.96	0.95	0.98	0.98
HB3	[260]	66.8	0.46	0.34	4.89	0.99	1.09	0.91	1.01	1.11
HB4		62.9	0.84	0.19	5.71	1.01	1.09	0.87	0.94	1.01
VA0		98.8	0.12	1.00	3.35	1.00	1.08	1.00	1.08	1.32
VA1		95.1	0.24	1.00	6.29	0.96	1.07	0.98	1.10	1.24
VA2		98.2	0.44	1.00	9.73	0.91	0.98	0.93	1.00	1.05
VA3		94.6	0.75	1.00	15.13	0.92	0.95	0.95	0.97	0.97
VA4	[261]	103.1	1.07	1.00	21.42	0.98	0.99	1.16	1.18	1.13
VB1		98.2	0.44	0.54	7.50	0.92	1.00	0.93	1.01	1.09
VB2		97.6	0.73	0.33	9.14	0.95	0.99	0.93	0.99	1.03
VB3		102.3	1.22	0.19	9.71	0.92	0.95	0.92	0.98	0.99
VB4	96.9	0.37	0.33	4.86	0.93	1.01	0.89	1.02	1.09	
PP1		27.0	1.03	0.33	4.95	0.99	0.98	0.92	0.96	0.97
PP2***	[152]	28.1	0.97	0.35	5.50	0.99	1.04	1.00	1.06	1.07
PP3***		27.7	0.92	0.37	5.50	1.02	1.08	1.02	1.07	1.07
SE1		42.5	1.18	0.32	6.77	0.90	0.93	0.88	0.91	0.92
SE5	[123]	25.9	1.65	1.00	8.09	0.88	0.89	0.99	1.00	1.15
SE6		40.0	1.23	0.11	3.75	0.93	0.85	0.88	0.94	1.02
M2		48.3	0.57	0.25	4.28	1.05	1.04	0.96	1.08	1.14
M3	[59]	48.1	0.57	0.11	3.07	1.03	0.93	1.01	1.14	1.21
M4		44.8	0.99	0.13	4.20	1.01	0.91	0.92	1.03	1.07
M5		43.4	1.01	0.06	3.15	1.02	0.86	1.08	1.23	1.36
PV4		26.6	0.29	1.00	2.89	1.02	1.11	1.02	1.11	1.13
PV10		14.5	0.83	0.56	3.97	1.06	1.10	1.04	1.07	1.08
PV12		16.0	1.32	0.14	3.13	1.02	1.03	1.12	1.19	1.25
PV16		21.7	0.24	1.00	2.14	1.00	1.11	1.00	1.11	1.13
PV19		19.0	1.15	0.26	3.96	0.97	1.00	0.99	1.04	1.06
PV20	[234]	19.6	1.13	0.32	4.26	0.95	0.97	0.95	0.99	1.01
PV21		19.5	1.13	0.48	5.03	0.92	0.95	0.93	0.96	0.97
PV22		19.6	1.12	0.78	6.07	0.88	0.90	0.94	0.96	0.97
PV23**		20.5	1.70	1.00	8.87	1.10	1.12	1.23	1.25	1.37
PV25**		19.2	2.04	1.00	9.12	1.10	1.12	1.23	1.26	1.48
PV27		20.5	1.05	1.00	6.35	0.89	0.90	0.99	1.00	0.98
PV28**	19.0	0.93	1.00	6.35	0.96	0.97	1.04	1.05	1.03	
PC1A		27.9	0.90	0.50	5.61	0.97	1.00	0.94	0.96	0.96
PC4**	[239]	24.9	0.72	0.65	4.84	0.88	0.96	0.87	0.93	0.97
PC7**		28.7	0.56	0.39	3.65	1.00	1.06	0.99	1.05	1.11
PA2		43.0	0.70	0.50	6.22	1.01	1.06	0.98	1.02	1.02
PHS2		66.1	1.20	0.11	6.66	1.12	1.14	1.23	1.31	1.31
PHS3		58.4	1.30	0.22	8.19	1.06	1.10	1.05	1.09	1.07
PHS4**		68.5	1.07	0.14	6.91	1.04	1.08	1.10	1.16	1.20
PHS5**	[5]	52.1	1.32	0.05	4.81	1.10	1.11	1.29	1.37	1.73
PHS7**		53.6	1.56	0.31	10.26	1.07	1.11	1.05	1.08	1.07
PHS8		55.9	1.34	0.33	10.84	1.15	1.18	1.13	1.17	1.14
PHS9**		56.0	1.50	0.20	9.37	1.28	1.32	1.24	1.30	1.21
PHS10**		51.4	1.26	0.25	8.58	1.12	1.15	1.11	1.14	1.16
Average (54 panels)						0.99	1.01	1.00	1.06	1.10
Coefficient of variation [%]						8.0	9.1	10.7	10.8	14.7

* Mechanical x-reinforcement ratio defined as $\omega_x = \rho_x f_{sy,x} / f_c^{2/3}$; **Panels tested in biaxial tension or compression proportional to shear stress. In these cases $\omega_{x/y} = (\rho_{x/y} f_{sy,x/y} - \sigma_{x/y,u,exp}) / f_c^{2/3}$; *** Prestressed panels in the x-direction. In these cases $\omega_x = (\rho_x f_{sy,x} + \rho_{p,x} f_{py,x}) / f_c^{2/3}$.

An evaluation of the bias between the theoretical and the experimental shear strength is presented in Figure 3.28. It can be seen that the results are uncorrelated with the compressive strength, with the longitudinal reinforcement ratio and with the orthotropy indicator, which ensures that both models are generally applicable.

3.9 Concluding remarks

A fixed crack model is proposed for the analysis of RC cracked membrane elements subjected to in-plane shear and axial stresses. The present model complements the Cracked Membrane Model of Kaufmann and Marti by extending its concept to the case of fixed and interlocked cracks capable of transferring shear and normal stresses. This enabled a more consistent reproduction of shear sliding failures in orthotropically reinforced panels as well as a slight improvement in the overall accuracy. Equilibrium is formulated in terms of stresses at the cracks and compatibility is formulated in terms of average strains. The consideration of the local mechanical effects that take place at the cracks - such as aggregate interlock, crack bridging and softened compressed concrete behaviour - together with the bond stress transfer mechanics described according to the Tension Chord Model, allows a rational derivation of both local and average stress/strain fields and a deeper understanding of the complex mechanics governing the behaviour of cracked RC membranes. Nevertheless, the model was kept sufficiently simple for implementation in a robust finite element formulation for structural analysis.

A validation campaign was carried out using a database with the experimental results of 54 RC panels tested under in-plane shear and axial stress conditions. Good agreement was found between the predicted and the observed shear strengths, failure modes and deformational behaviour. The average ratio of the experimental-to-predicted shear strength of the 54 panels is 0.99, with a coefficient of variation of 8%. The database covered a wide range of reinforcement ratios and concrete strengths ensuring that the model is generally applicable.

The implementation of both the F-CMM and R-CMM in a finite element program is described in the next chapter.

4 Implementation in a finite element code

4.1 General

In this chapter, a constitutive model based on the previously presented RC cracked membrane element is developed for the analysis of structural concrete elements via the finite element method (FEM). The model is implemented in the general purpose finite element code DIANA (www.tnodiana.com). In this context, the F-CMM and R-CMM are further developed so as to deal with arbitrary load paths, leading to the formulation of the uncracked concrete nonlinear behaviour, suitable loading/unloading conditions, and equilibrium and compatibility conditions in cases of two orthogonal cracks arising in the same integration point. The tangent stiffness matrix of the constitutive model is also formulated to be used in the incremental-iterative solution procedure. Strain localization issues are dealt with using a description of the displacement field based on the “weak discontinuities” concept (see section 4.2.1), thus improving the objectivity of the results with respect to the size of the finite elements whenever strain localization phenomena occur.

This chapter begins with a brief presentation of the underlying concepts behind NLFEA of concrete structures and with a short overview of the different existing approaches, both introduced in Section 4.2. The developed model is presented in Section 4.3, where the implemented algorithms are explained and some simple examples are used for illustrating the response. In Section 4.4 the formulation is extended to shell elements. The chapter ends with some concluding remarks.

4.2 Computational modelling of the nonlinear behaviour of structural concrete

4.2.1 Kinematic description of the displacement field

The behaviour of quasi-brittle materials like concrete is characterized by the localization of strain and damage in relatively narrow zones. This process usually leads to the development of macroscopic cracks. Compressive stress states can also lead to damage

localization whenever the confining stresses are low, as discussed in Section 2.4. Despite the considerable progress made in the last three decades, the theoretical modelling and computational resolution of this localization process still remains a challenging issue in contemporary solid mechanics.

Three different types of kinematic description of the displacement field $\mathbf{u}(\mathbf{x})$ can be considered [112], as illustrated schematically in Figure 4.1.

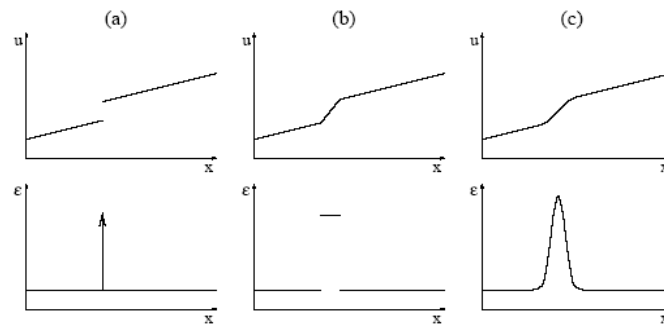


Figure 4.1 – Kinematic description of the displacement field: (a) Strong discontinuities; (b) Weak discontinuities; (c) No discontinuities.

The first case corresponds to the so-called *strong discontinuities* approach, where the displacement field is discontinuous and the strain field $\boldsymbol{\epsilon}(\mathbf{x})$ consists of a regular part obtained by differentiation of the displacement field and a multiple of the Dirac delta function. Physically this approach can be seen to reflect a sharp crack.

The *weak discontinuities* approach is characterized by a continuous displacement field and a discontinuous strain field. Strain is assumed to be constant inside the finite thickness of the so called *fracture process zone* (FPZ). Physically this approach reflects a band with a constant density of defects.

The third possible approach uses a description with a continuous differentiable displacement field, and subsequently the strain field remains continuous. Strain localization is manifested by high strains in the central part and by a gradual transition to the lower strains in the surrounding parts. Physically this approach can reflect a FPZ with a higher density of defects around its centre.

4.2.2 Constitutive models and constitutive laws

4.2.2.1 Types of constitutive models

A constitutive model can be thought as the mathematical description of the material behaviour which yields the relation between the stress and strain tensors in a material point \mathbf{x} of the body as a function of time t . The most general formulation is to consider the stress at point \mathbf{x} to be a functional of the deformation history of all points of the body [29]. This concept can be simplified if the stress is only influenced by the strain field in a neighbourhood of the material point. Formulations of this type constitute the so-called *non-local* constitutive models. Most macroscopic constitutive models used in concrete structures come into the class of *local* homogenous constitutive models, for which the stress tensor depends only on the local strain tensor, and for which the material properties do not depend upon the material point. Although an exhaustive classification of this particular type of constitutive models is out of scope of the present thesis, for which the reader is referred to [58; 254], a distinction is made between rate and total formulations. In a constitutive model of the rate type the stress tensor at time t ¹ is generically expressed by:

$$\boldsymbol{\sigma}(\mathbf{x}, t) = \int_0^t \dot{\boldsymbol{\sigma}} d\tau \quad (4.1)$$

where the stress rate $\dot{\boldsymbol{\sigma}}$ is generally given as a function of the strain rate $\dot{\boldsymbol{\epsilon}}$ and some internal (state) variables $\boldsymbol{\kappa}$, which keep track of the loading history:

$$\dot{\boldsymbol{\sigma}}(\mathbf{x}, t) = f(\dot{\boldsymbol{\epsilon}}, \boldsymbol{\kappa}) \quad (4.2)$$

Material models which comply with this description are, for instance, the ones based on the flow theory of plasticity. In this particular case the stress rate is given by $\dot{\boldsymbol{\sigma}} = \mathbf{D}_e \dot{\boldsymbol{\epsilon}}_e = \mathbf{D}_e (\dot{\boldsymbol{\epsilon}} - \dot{\boldsymbol{\epsilon}}_p)$, where \mathbf{D}_e is the fourth order elasticity tensor. The inelastic strain rate $\dot{\boldsymbol{\epsilon}}_p = \dot{\boldsymbol{\epsilon}}_p(\dot{\boldsymbol{\epsilon}}, \boldsymbol{\kappa})$ can be considered a function of the total strain rate $\dot{\boldsymbol{\epsilon}}$ and of the vector of state variables $\boldsymbol{\kappa}$.

In the constitutive models following a total formulation, the stress vector is directly computed from the total strain vector and can be most generally described by:

¹ In this work, the variable time attains the role of a parameter which merely orders the loading process. Although time-dependent effects are not going to be considered, a division of the loading process in a finite number of increments is required. This will be referred to as a temporal discretization.

$$\boldsymbol{\sigma}(\mathbf{x}, t) = f(\boldsymbol{\varepsilon}, \boldsymbol{\kappa}) \quad (4.3)$$

Among others, secant pseudo-elastic models and models based on the theory of continuum damage belong to this type of formulations. In these cases the stress tensor is given by $\boldsymbol{\sigma} = \mathbf{D}_{\text{sec}} \boldsymbol{\varepsilon}$, where \mathbf{D}_{sec} is a fourth-order secant stiffness tensor. In the particular case of continuum scalar damage models this tensor can be expressed as $\mathbf{D}_{\text{sec}} = (1 - d) \mathbf{D}_e$, being d the scalar damage variable(s) which keeps track of the previous loading history.

It must be realized that concrete is neither a plastic nor continuum damage like material. In computational modelling of concrete structures, plastic flow or continuum damage theories, to cite these two, are used to circumvent the lack of a realistic model for concrete and its interaction with the reinforcement. The choice between several constitutive models is often dictated by the availability of well established and sound numerical algorithms which allow obtaining converged solutions beyond the failure load and which guarantee the satisfaction of the basic thermodynamic requirements ensuring that meaningful structural responses can be obtained in complex loading scenarios. However, in simpler cases, such as the ones corresponding to plane stress conditions, sufficient experimental evidence on the behaviour of RC elements is available sustaining the direct implementation of phenomenological models such as the one developed in Chapter 3. As the number of possible stress trajectories is smaller than in the general three-dimensional case, the model can be validated for almost all the possible stress states, thereby eliminating the need for a sound theoretical background. The phenomenological approach is followed in the work presented in this chapter and the constitutive model is developed following a total formulation as expressed by Eq. (4.3).

4.2.2.2 Constitutive laws, control volume and kinematic description of the displacement field

A constitutive law (or relationship) is defined as the analytical expression relating two individual components of the stress and strain tensors. The constitutive laws are the core of a constitutive model and must be defined not only in close relation with the kinematic description of the displacement field but also with the control volume over which they are established. Regarding the latter, the work developed in the previous chapter represents an illustrative example. Spatially averaged relationships were developed for reproducing the behaviour of an array of cracks as a whole, thus efficiently reproducing the response of RC panels.

In some cases this spatially averaged approach may not be applicable and the behaviour of each individual crack must be tracked, for which fracture mechanics concepts must be applied. This being the case, the relation between the kinematic description of the displacement field and the constitutive laws for concrete in tension is very clear and is taken here as an illustrative example. Within the strong discontinuities approach, and in the simplest case, the crack faces may be assumed as stress free and the remaining material as elastic. This drives necessarily to a singularity in the stress field at the crack tip and the crack propagation criteria is based on energy considerations and stress intensity factors, according to the linear elastic fracture mechanics (LEFM) laws. This approach is rarely applicable with sufficient accuracy to concrete, and it is only valid when the FPZ dimensions are negligible compared with the structural size. In general, the size of the FPZ must be accounted for and *nonlinear fracture mechanics* (NLFM) laws must be applied. In the case of the strong discontinuities approach, the fictitious crack model of Hilleborg and co-workers [99] is the suited NLFM model (see Section 2.1.2). In the case of displacement fields with localization bands bounded by weak discontinuities, the constitutive laws must be formulated within the crack-band model [17]. Instead of lumping all the inelastic effects in a line, in the crack-band model they are assumed to be uniformly distributed along the FPZ. In the case of continuous displacement and strain fields, the appropriate constitutive laws must be formulated within the concepts of the non-local continuum mechanics [10; 14; 110; 182].

4.2.3 Discretization strategy

The finite element method is the most widely used numerical approach in the domain of solid mechanics. In this context, the discretization strategy to be adopted is closely related to the description of the displacement field. In the case of the strong discontinuities approach the simplest way is to allow crack propagation through the boundaries of the finite elements [2]. Also re-meshing techniques can be used [107]. If the crack pattern is known in advance another approach is to use special interface elements with zero thickness [77; 198]. More powerful approaches use a more elegant and efficient procedure using finite elements enriched with terms that can reproduce jumps in the displacement field. For an overview of the broad type of enriched formulations see [111; 112] and for comparative analysis of their performance refer to [174].

Regular finite elements can be used with the other two kinematic descriptions of the displacement field and corresponding constitutive laws. Within the weak discontinuities

concept the localized strain is assumed to be smeared along a length, the crack-band width, which must be somehow related to the size of the finite element in order to ensure the correct energy dissipation. In the case of the non-local approach the strain distribution within the FPZ can be obtained, requiring a high degree of mesh refinement and the use of appropriate non-local constitutive models.

The discretization strategy must also be related to the type of constitutive law. If spatially averaged constitutive laws are adopted for RC (such as the ones developed in Chapter 3) the finite element size can be taken larger than the crack spacing. However, if constitutive laws based exclusively upon fracture mechanics concepts are considered, a higher degree of mesh refinement is required for tracking the propagation of each individual crack. Using the crack band model and with proper mesh refinement, tension stiffening effects can be to some extent approximated without explicitly taking into account bond slip effects, as discussed by Cervenka [56].

4.2.4 Discussion

The strong discontinuity approach initiated by Simo *et al.* [220] and widely used over the last years offers the possibility of merging continuous constitutive models for the bulk response and a cohesive model for the discontinuous part of the kinematics in the same formulation. This is certainly appealing from the physics of fracture point of view. Recent developments [173] enabled successful applications of this type of approach to RC problems exhibiting multiple cracks and concrete-reinforcement interaction [175]. However, as recognized by Oliver and Dias [172] these methods require a degree of sophistication that seems to place a limitation on their incorporation in commercial simulation codes and to their use in real scale civil engineering structures analyses. New developments [172] are being attempted to overcome these difficulties.

Non-local models were formulated for dealing with situations where failure is governed by the propagation of one or a few cracks. In these circumstances, the mesh induced directional bias¹ [199] and stress locking² [115; 197] exhibited by the classical local constitutive models, which use a description of the displacement field based on weak discontinuities, leads in some cases to poor estimates of the crack trajectories and of the

¹ Mesh induced directional bias can be defined as the tendency for the localization regions to follow the direction defined by the finite element sides.

² Stress locking is referred to the spurious stress transfer between the two sides of a crack resulting from the inability of the finite element interpolation to reproduce the discontinuous nature of the actual displacement field.

post-peak branches of force-displacement curves. However, besides some known shortcomings adhering to the nonlocal description of the continuum (see for instance [114; 221]), the use of very fine meshes and non-trivial parameters – in the sense that they cannot be experimentally determined – are required in the formulation of the non-local constitutive models, which still inhibits its practical application.

The models based on the concept of weak discontinuities are the most widespread in the analysis of civil engineering structures, still presenting the best compromise between accuracy, simplicity and economy of computer resources, and allowing the use of standard finite element formulations. Not only localized cracking problems can be analysed with sufficient accuracy for engineering purposes, see discussion by Cervenka [54], but also distributed cracking patterns in the presence of bonded reinforcement can be treated within the same framework. The use of spatially averaged constitutive laws allows the definition of very effective relationships for the reinforced concrete material, thus constituting the most efficient way for the analysis of large scale structural concrete elements. Therefore, this was the approach followed in this work.

4.2.5 Solution procedures for nonlinear systems

4.2.5.1 Incremental – iterative solution of the equilibrium equations

From a mathematical point of view the determination of the continuum displacement field \mathbf{u} of a body Ω in static equilibrium with external solicitations $\boldsymbol{\varphi}$, constrained by a set of boundary conditions and fulfilling the material constitutive laws, consists in the solution of a boundary value problem (BVP) of the form:

$$\mathbf{L}(\mathbf{u}) = \boldsymbol{\varphi} \quad (4.4)$$

with \mathbf{L} being a second order differential operator. As previously mentioned, the finite element method is the most commonly used method to solve this BVP. This being the case, static equilibrium can be most conveniently expressed in the integral (weak) form using the principle of virtual displacements:

$$\int_{\Omega} \delta \boldsymbol{\varepsilon}^T \boldsymbol{\sigma} dV = \int_{\Omega} \delta \mathbf{u}^T \mathbf{b} dV + \int_{\partial \Omega} \delta \mathbf{u}^T \mathbf{t} dS \quad (4.5)$$

In the equation above, $\delta \mathbf{u}$ is a kinematically admissible virtual displacement vector, $\delta \boldsymbol{\varepsilon}$ is the corresponding linearized¹ virtual strain vector, $\boldsymbol{\sigma}$ is the internal stress vector, \mathbf{b} are the external forces applied to the body Ω , and \mathbf{t} are the tractions defined on the boundary $\partial\Omega$. The left hand side of equation (4.5) represents the virtual work performed by the internal forces which must be equal to the virtual work of the external forces given in the right hand side.

In FEM the continuum is discretized in finite elements and the continuum displacement and strain fields are recovered from the vector of nodal displacements, \mathbf{a} , using the interpolation matrix \mathbf{N} , and the deformation matrix \mathbf{B} , respectively:

$$\mathbf{u} = \mathbf{N} \cdot \mathbf{a} \quad \boldsymbol{\varepsilon} = \mathbf{B} \cdot \mathbf{a} \quad (4.6)$$

Considering that the equality (4.5) must be fulfilled for every virtual displacement field, and taking into account (4.6) it can be shown [176] that in the context of FEM static equilibrium can be alternatively expressed by:

$$\mathbf{p} - \mathbf{f} = \mathbf{0} \quad (4.7)$$

with the internal forces given by:

$$\mathbf{p} = \int_{\Omega} \mathbf{B}^T \boldsymbol{\sigma} dV \quad (4.8)$$

and the external forces by:

$$\mathbf{f} = \int_{\Omega} \mathbf{N}^T \mathbf{b} dV + \int_{\partial\Omega} \mathbf{N}^T \mathbf{t} dS + \sum \mathbf{N}^T \mathbf{q} \quad (4.9)$$

with \mathbf{q} being the vector of point forces.

For problems governed by a nonlinear differential operator \mathbf{L} , the internal force vector \mathbf{p} is a nonlinear function of the nodal displacements \mathbf{a} and the solution to equation (4.7) can be found using an incremental-iterative procedure. The incremental nature of the solution procedure is reflected by the stepwise loading application, which can be thought as a discretization in the time domain. At a given stage $t+\Delta t$, the system of equilibrium equations to be solved reads:

$$\mathbf{p}(\mathbf{a}_{t+\Delta t}) - \lambda_{t+\Delta t} \mathbf{f}_0 = \boldsymbol{\psi}(\mathbf{a}_{t+\Delta t}) = \mathbf{0} \quad (4.10)$$

¹ Small deformations are assumed throughout this section

where $\boldsymbol{\psi}(\mathbf{a}) = \boldsymbol{\psi}$ is the vector of the unbalanced forces (or residuals), which must vanish within a prescribed accuracy, λ is a scalar load factor and \mathbf{f}_0 the reference external force vector. The equilibrium solution from the previous load stage t

$$\mathbf{a} = \mathbf{a}_t \quad \mathbf{f} = \lambda_t \cdot \mathbf{f}_0 \quad \boldsymbol{\psi}_t = \mathbf{0} \quad (4.11)$$

is altered when the next load step $\Delta\lambda_{t+\Delta t} \mathbf{f}_0$ is applied,

$$\mathbf{f}_{t+\Delta t} = \mathbf{f}_t + \Delta\lambda_{t+\Delta t} \mathbf{f}_0 \quad (4.12)$$

The Newton-Raphson method, which will be used throughout this thesis, can be derived performing the linearization of (4.10) in a neighbourhood of the current state:

$$\boldsymbol{\psi}_{t+\Delta t}^{i+1} = \boldsymbol{\psi}_{t+\Delta t}^i + \left(\frac{\partial \boldsymbol{\psi}}{\partial \mathbf{a}} \right)_{t+\Delta t}^i \delta \mathbf{a}_{t+\Delta t}^{i+1} = \mathbf{0} \quad (4.13)$$

The equation above is solved iteratively, see Figure 4.2. The superscript i is the iteration counter and

$$\left(\frac{\partial \boldsymbol{\psi}}{\partial \mathbf{a}} \right)_{t+\Delta t}^i = \left(\frac{\partial \mathbf{p}}{\partial \mathbf{a}} \right)_{t+\Delta t}^i = \mathbf{K}_{t+\Delta t}^i \quad (4.14)$$

where \mathbf{K} is the assembled (or structural) tangential stiffness matrix. The iterative update to the nodal displacement vector is readily obtained from (4.13):

$$\delta \mathbf{a}_{t+\Delta t}^{i+1} = -\left(\mathbf{K}_{t+\Delta t}^i \right)^{-1} \boldsymbol{\psi}_{t+\Delta t}^i \quad (4.15)$$

After a series of iterations the incremental nodal displacement vector is given by:

$$\Delta \mathbf{a}_{t+\Delta t}^{i+1} = \sum_{k=1}^{i+1} \delta \mathbf{a}_{t+\Delta t}^k \quad (4.16)$$

In the context of FEM, the structural tangential stiffness matrix is obtained from

$$\mathbf{K}_{t+\Delta t}^i = \int_{\Omega} \mathbf{B}^T \mathbf{D}_{t+\Delta t}^i \mathbf{B} dV \quad (4.17)$$

where the matrix

$$\mathbf{D}_{t+\Delta t}^i = \left(\frac{\partial \boldsymbol{\sigma}}{\partial \boldsymbol{\varepsilon}} \right)_{t+\Delta t}^i \quad (4.18)$$

is the constitutive tangent stiffness matrix, which is evaluated at each integration point using the appropriate constitutive model.

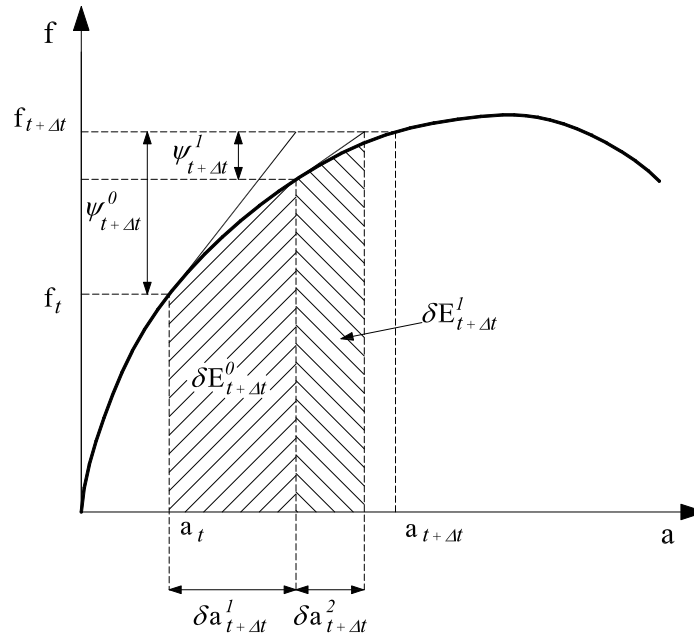


Figure 4.2 – Newton – Raphson iteration. Notation.

4.2.5.2 Line-search technique

The Newton-Raphson method is shown not to be globally convergent. The method is based on reasonable predictions of the iterative correction to the nodal displacement vector such that the iteration process converges to an equilibrium solution. However, the iterative predictions may sometimes be too far from the equilibrium path and convergence cannot be found. This can happen in processes with strong nonlinearities, such as cracking or constitutive laws involving softening (see Section 4.2.5.5), which is usually the case in concrete structures. In these circumstances, *line search algorithms* can significantly enhance the robustness of the Newton-Raphson method.

In the line search technique, the search direction at a given iteration is defined by the iterative update of the nodal displacement vector $\delta \mathbf{a}_{t+\Delta t}^{i+1}$. The updated displacement vector is now written as

$$\mathbf{a}_{t+\Delta t}^{i+1,j} = \mathbf{a}_{t+\Delta t}^i + \eta^{i,j} \delta \mathbf{a}_{t+\Delta t}^{i+1} \quad (4.19)$$

where the superscript j is the counter of line searches, and η is the line search factor which scales the iterative update to the displacement field in order to bring it closer to the equilibrium path. The scalar η is determined such that the projection of the residuals in the search direction is smaller than a predefined tolerance by solving the scalar inequality

$$\left| \left(\delta \mathbf{a}_{t+\Delta t}^{i+1} \right)^T \boldsymbol{\psi} \left(\mathbf{a}_{t+\Delta t}^i + \eta^{i,j} \delta \mathbf{a}_{t+\Delta t}^{i+1} \right) \right| \leq \psi \left| \left(\delta \mathbf{a}_{t+\Delta t}^{i+1} \right)^T \boldsymbol{\psi} \left(\mathbf{a}_{t+\Delta t}^i \right) \right| \quad (4.20)$$

through a local iterative method. The tolerance that was used in the examples presented in this thesis is defined by setting the scalar $\psi = 0.8$, which is the default value implemented in DIANA and was found to be sufficient to stabilize the global iteration process. For details and more references regarding this technique refer to [70; 76; 135; 256].

4.2.5.3 Constrained Newton-Raphson

With the standard load control method described above, in which the incremental load factor $\Delta \lambda_{t+\Delta t}$ is kept constant during the equilibrium iterations, the softening branch of the structural response cannot be obtained. Moreover, this method also fails at local peaks of the force-deformation curve. This deficiency can be overcome by using the *arc-length method* [69]. This method adds a new constraint equation to the system of nonlinear equations given by (4.10), which considers $\Delta \lambda_{t+\Delta t}$ as an additional variable,

$$f(\Delta \lambda_{t+\Delta t}, \Delta \mathbf{a}_{t+\Delta t}) = 0 \quad (4.21)$$

thus introducing the possibility of overcoming local limit points by iterating in the load-displacement space. In this work, the update normal plane constraint [191] was adopted,

$$\left(\Delta \mathbf{a}_{t+\Delta t}^i \right)^T \delta \mathbf{a}_{t+\Delta t}^{i+1} = \mathbf{0} \quad (4.22)$$

which sets an orthogonality condition between the incremental and the iterative update nodal displacement vectors. In order to determine the incremental load factor from the equation above, the iterative update to the nodal displacement vector is split in two parts:

$$\begin{aligned} \delta \mathbf{a}_{t+\Delta t}^{i+1} &= -\left(\mathbf{K}_{t+\Delta t}^i \right)^{-1} \boldsymbol{\psi}_{t+\Delta t}^i \\ &= -\left(\mathbf{K}_{t+\Delta t}^i \right)^{-1} \left(\mathbf{p}_{t+\Delta t}^i - \mathbf{f}_t - \Delta \lambda_{t+\Delta t}^{i+1} \mathbf{f}_0 \right) \\ &= \left(\mathbf{K}_{t+\Delta t}^i \right)^{-1} \left(\mathbf{f}_t - \mathbf{p}_{t+\Delta t}^i \right) + \Delta \lambda_{t+\Delta t}^{i+1} \left(\mathbf{K}_{t+\Delta t}^i \right)^{-1} \mathbf{f}_0 \\ &= \delta^I \mathbf{a}_{t+\Delta t}^{i+1} + \Delta \lambda_{t+\Delta t}^{i+1} \delta^{II} \mathbf{a}_{t+\Delta t}^{i+1} \end{aligned} \quad (4.23)$$

The first part, $\delta^I \mathbf{a}_{t+\Delta t}^{i+1}$, is obtained from the difference between the external forces at the end of the last converged load step and the internal forces after iteration i . The second part, $\Delta \lambda_{t+\Delta t}^{i+1} \delta^{II} \mathbf{a}_{t+\Delta t}^{i+1}$, is related to the external load increment being applied in the current load step. After substitution of Eq. (4.23)₄ into the constraint equation (4.22), the incremental load factor is determined:

$$\Delta \lambda_{t+\Delta t}^{i+1} = - \frac{(\Delta \mathbf{a}_{t+\Delta t}^i)^T \delta^I \mathbf{a}_{t+\Delta t}^{i+1}}{(\Delta \mathbf{a}_{t+\Delta t}^i)^T \delta^{II} \mathbf{a}_{t+\Delta t}^{i+1}} \quad (4.24)$$

In cases of strong localization of deformations leading to very brittle responses, it can be more efficient to use a reduced set of active degrees of freedom in the nodal displacement vector. In these circumstances, the vectors $\Delta \mathbf{a}$ and $\delta \mathbf{a}$ used in the constraint equation (4.22) are obtained from a modified displacement vector defined as

$$\mathbf{a} = \{0 \quad \dots \quad \mathbf{a}_p \quad \dots \quad 0\} \quad (4.25)$$

with \mathbf{a}_p being a subset of \mathbf{a} . In the extreme situation where only one degree of freedom is chosen to be active, this method is also called *indirect displacement control*. The active degrees of freedom must be selected with engineering judgement. In this work, this procedure is only adopted when the regular arc-length control method fails. For a more complete description and more references concerning the arc-length method refer to [29; 76; 135; 256].

4.2.5.4 Convergence criterion

The Newton-Raphson iterative process described above is stopped when the solution is sufficiently close to the equilibrium path, in which case a convergence criterion established using an appropriate metrics is fulfilled. In this thesis, the metrics based on the so called energy norm [256]

$$\left| \frac{\delta E_{t+\Delta t}^i}{\delta E_{t+\Delta t}^0} \right| = \left| \frac{(\delta \mathbf{a}_{t+\Delta t}^{i+1})^T (\mathbf{p}_{t+\Delta t}^{i+1} + \mathbf{p}_{t+\Delta t}^i)}{(\delta \mathbf{a}_{t+\Delta t}^0)^T (\mathbf{p}_{t+\Delta t}^1 + \mathbf{p}_{t+\Delta t}^0)} \right| \leq tol \quad (4.26)$$

was adopted, see Figure 4.2. This norm is more versatile than the usual Euclidean norm of the out-of-balance force vector, especially in the cases where the structural response

exhibits a yielding plateau. The convergence criterion was defined by setting the tolerance $tol = 10^{-4}$.

4.2.5.5 Some comments on the uniqueness of the solution

According to the definition first presented by Hadamard [93], a BVP is said to be *well-posed* if: (1) a solution exists; (2) the solution is unique; and (3) the solution depends continuously on the data. Mathematically, the *ellipticity* of the differential operator \mathbf{L} is a necessary condition for the desired property of well-posedness of a BVP in the form of Eq. (4.4). In the context of finite element analyses, the existence of a unique solution for the problem at hand and the fact that the solution does not involve discontinuities practically ensures a smooth convergence of the numerical iterative methods and the independence of the solution with respect to the adopted finite element mesh, i.e., *mesh objectivity* of the results.

Considering the adopted incremental solution procedure, equilibrium at the infinitesimal scale can be re-written in rate form as:

$$\dot{\boldsymbol{\sigma}} = \mathbf{D} \dot{\boldsymbol{\varepsilon}} \quad (4.27)$$

where \mathbf{D} is the tangent constitutive stiffness matrix as defined in Eq. (4.18). It can be shown [35; 116; 254] that loss of ellipticity of the local BVP occurs when there is a normal unit vector \mathbf{n} such that:

$$\det(\mathbf{n}\mathbf{n}^T \mathbf{D}) = 0 \quad (4.28)$$

which also defines the necessary condition for the onset of localization of deformations along the surface defined by \mathbf{n} [113; 116; 254]. In constitutive models involving softening or perfectly plastic behaviour, condition (4.28) is satisfied at the onset of the softening or yielding regimes, respectively. In these circumstances, deformations tend to localize in narrow regions of the structure, in spite of the fact that the external actions continue to follow a monotonic loading programme. This effect is more severe in constitutive models exhibiting softening. According to what was stated above, if there is a vector \mathbf{n} that satisfies Eq. (4.28), the solution ceases to be unique. In these circumstances, it is not guaranteed that the solution found through the above described nonlinear solution

procedures is the one corresponding to the global minimum of the system elastic potential energy. As mentioned in Section 4.2.4 the solutions may also be strongly dependent on the adopted finite element mesh, which is an inherent shortcoming of the traditional local constitutive models based on the concept of weak discontinuities. Objectivity of the results with respect to the size of the finite elements can be achieved by introducing the localization band length into the constitutive laws, as in the crack band model. However, mesh induced directional bias cannot be as easily removed. Non-local constitutive models are shown to restore the well-posedness of the local BVP. Another way of circumventing the problem is to perform a bifurcation analysis using the localization tensor $\mathbf{nn}^T \mathbf{D}$, and adding a deformation mode affine with the lowest (negative) eigenvalue. This procedure is described in detail in reference [29] and constitutes the basis of the modern strong discontinuity approaches. For a detailed discussion on this topic refer to references [29; 254].

4.3 Total strain based model

The total strain smeared crack model developed within this work is implemented in the user supplied subroutine USRMAT in the finite element code DIANA. A set of state variables continuously monitor the damage evolution in concrete and enable establishing suitable loading/unloading/reloading conditions. The flowchart of the subroutine is presented in Figure 4.3. The objective is to determine the updated vector $\boldsymbol{\sigma}$ of the internal stresses, to update the state variables vector \mathbf{k} and to determine the tangent constitutive matrix \mathbf{D} in each iteration of the incremental-iterative procedure. The remaining operations described in Section 4.2.5 are performed by DIANA.

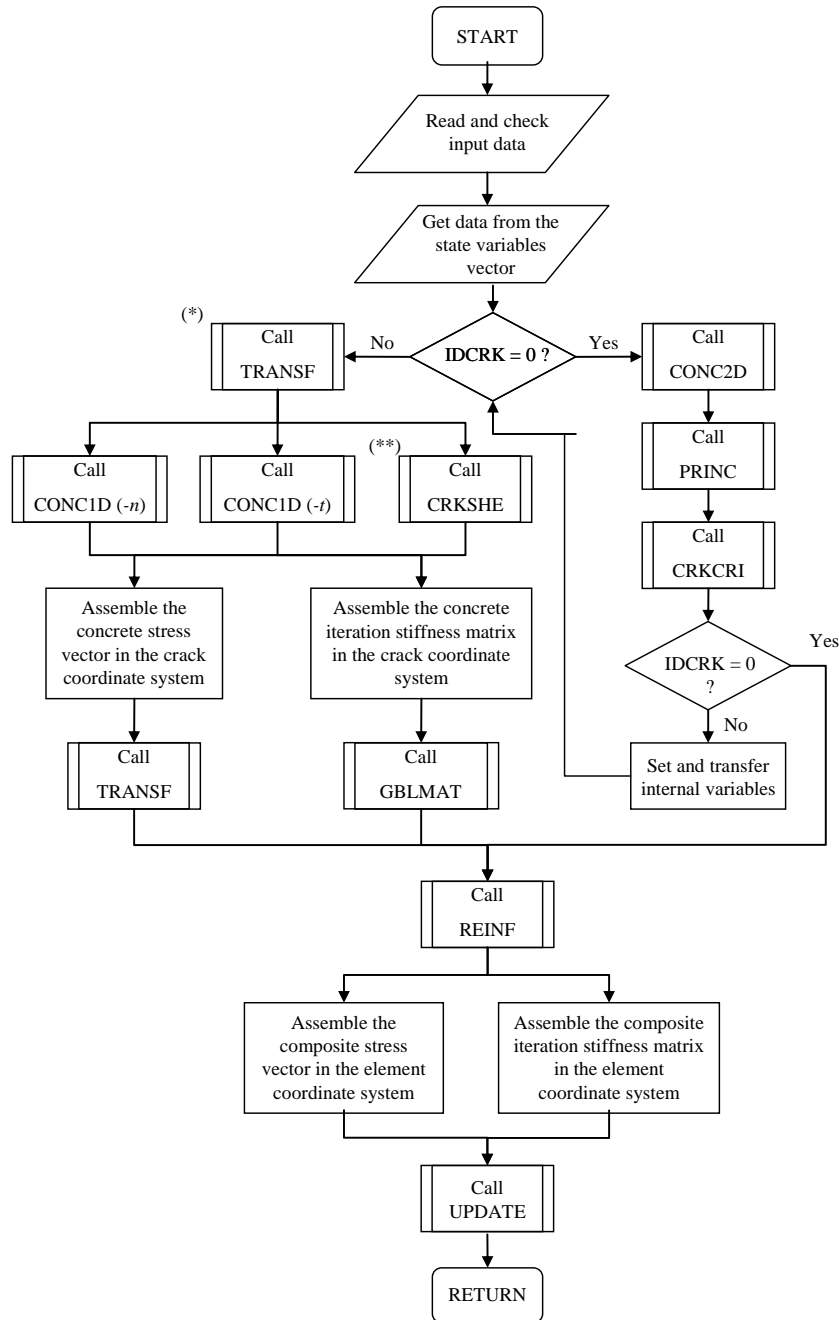


Figure 4.3 – Flow chart of the subroutine.

The relevant input data consists of the user defined model parameters, the total strain vector in the last converged load step, the current incremental strain, the vector of the state variables, and the current stress vector. After reading and checking the input data, the state variables values are assigned to a set of internal variables, which are used and modified throughout the subroutine. The indicator IDCRK monitors the cracking condition: IDCRK = 1 or = 0 whether cracking has or not occurred in the past history, respectively. If concrete is uncracked, the CONC2D subroutine is invoked for calculation of the concrete stresses and concrete iteration stiffness matrix. The concrete principal stresses and the principal

stress direction are calculated (subroutine PRINC) and the violation of the crack detection envelope during the current iteration is checked by the subroutine CRKCRI, which updates the indicator IDCRK. If cracking has not occurred during the current iteration, the calculation proceeds and the reinforcement subroutine (REINF) is called for evaluating the reinforcement stresses. If cracking has occurred during the current iteration, the internal variables required for the cracked concrete subroutines are set and, in the case of the fixed crack model, the principal stress direction is assigned to an internal variable defining the directions of the crack coordinate system. The cracked concrete subroutines are then invoked.

If cracking has occurred (IDCRK=1), the total strains are transformed into the crack coordinate system. In the case of the fixed crack model a tensorial transformation is made using the fixed crack angle (subroutine TRANSF), while in the case of the rotating crack model the principal total strains are calculated instead (subroutine PRINC), since they coincide with the total strains in the rotating crack coordinate system. The two normal stresses and the shear stress in the crack coordinate system are evaluated by the CONC1D and CRKSHE subroutines, respectively. These subroutines also compute the corresponding components of the iteration stiffness matrix. In the case of the fixed crack model, the CRKSHE subroutine also computes the dilatancy stresses normal to the crack lips. In the case of the rotating crack model there is no shear stress in the crack coordinate system and only the normal stresses are calculated. The local stress vector and the local iteration stiffness matrix are assembled using the outputs of the previously mentioned subroutines and are subsequently transformed back to the element coordinate system by the TRANSF and GBLMAT subroutines, respectively.

After having computed the stresses in the concrete material, the REINF subroutine is called for calculating reinforcement stresses and corresponding iteration stiffness matrix. The composite stresses and stiffness matrix are determined simply by adding the contribution of the reinforcements to the respective concrete components. Finally, the UPDATE subroutine is called for updating the state variables array, which is saved only when convergence is achieved.

The outputs of the subroutine are the updated stress and state variables vectors, and the stiffness matrix at the integration point level, which is going to be used in the iterative solution procedure.

4.3.1 Uncracked concrete

In this section, the theory and the algorithm behind the CONC2D subroutine are described. For uncracked concrete, an efficient isotropic damage like formulation is adopted, requiring only one state variable for tracing the damage evolution and establishing the loading/unloading/reloading conditions.

4.3.1.1 Equivalent stress

The equivalent stress S is here defined as a scalar measure of the applied stress level under biaxial plane stress conditions. For $S = 0$ concrete is totally unloaded while for $S = 1$ the biaxial failure envelope has been reached. As proposed by Maekawa [136], the equivalent stress can be defined as a function of the two invariants of the stress tensor,

$$S = \sqrt{\left(\frac{a}{f'_c} \sigma_m\right)^2 + \left(\frac{b}{f'_c} \tau_d\right)^2} \quad \begin{array}{l} a = 0.61 \\ b = 1.27 \end{array} \quad (4.29)$$

with σ_m and τ_d being, respectively, its mean and deviatoric invariant components:

$$\begin{aligned} \sigma_m &= \frac{\sqrt{2}}{2} (\sigma_1 + \sigma_2) \\ \tau_d &= \frac{\sqrt{2}}{2} (\sigma_1 - \sigma_2), \quad \sigma_1 \geq \sigma_2 \end{aligned} \quad (4.30)$$

The two parameters a and b in Eq. (4.29) were determined from experimental data for the uniaxial compression and equal biaxial compression stress trajectories. In these cases the principal stresses at failure are given by $\sigma_1 : \sigma_2 = 0 : -f'_c$ and $\sigma_1 : \sigma_2 = -1.16f'_c : -1.16f'_c$, respectively. In Figure 4.4 the resulting failure envelope ($S=1$) is presented in the σ_1 - σ_2 plane and it is compared to the Kupfer and Gerstle [128] failure criteria, which was adopted by the CEB in the Model Code 1990 [40]. The crack detection envelope represented in the figure is used for detecting if cracking has occurred. When this envelope is violated, the cracked concrete subroutines are invoked.

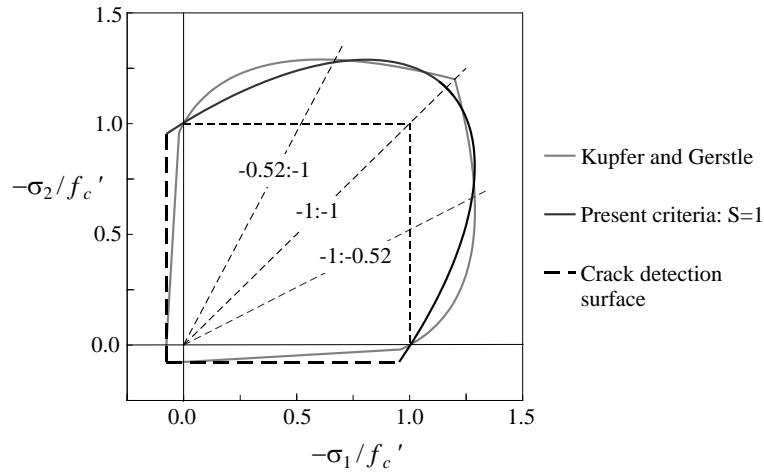


Figure 4.4 – Proposed failure criterion in the σ_1 - σ_2 stress plane.

4.3.1.2 Equivalent total strain

The equivalent total strain E is a scalar measure of the current biaxial total strain level. Similar to the equivalent stress, for $E=0$ concrete is unloaded while for $E=1$ the failure envelope is reached. The equivalent total strain is also defined as a function of the two invariants of the total strain tensor [136],

$$E = \sqrt{\left(\frac{c}{\varepsilon'_0} \varepsilon_m\right)^2 + \left(\frac{d}{\varepsilon'_0} \gamma_d\right)^2} \quad \begin{array}{l} c = 0.62 \\ d = 1.10 \end{array} \quad (4.31)$$

with ε_m and γ_d being, respectively, its mean and deviatoric invariant components:

$$\varepsilon_m = \frac{\sqrt{2}}{2}(\varepsilon_1 + \varepsilon_2) \quad (4.32)$$

$$\gamma_d = \frac{\sqrt{2}}{2}(\varepsilon_1 - \varepsilon_2), \quad \varepsilon_1 \geq \varepsilon_2$$

The two parameters c and d in Eq. (4.31) were derived such as to fit the peak strains obtained in the uniaxial compression and equal biaxial compression tests.

4.3.1.3 Stress-strain relationships and loading/unloading determination

In a monotonic loading process it is assumed that the equivalent stress S can be univocally obtained from the equivalent total strain E through the following nonlinear relationship:

$$S = \begin{cases} \frac{kE - E^2}{1 + (k-2)E} & , E \leq 1 \\ \frac{1}{1 + \frac{\eta}{2}(1 - 2E + E^2)} & , E > 1 \end{cases} \quad (4.33)$$

For the ascending branch, $E \leq 1$, the Sargin's law was adopted [84], while for the descending (post-peak) branch a modified version of the function proposed by Krätzig and Pölling [125] was defined, ensuring a smooth transition between the two branches. The parameter k determines the shape of the curve in the ascending branch. With $k=2$, a parabolic relationship is obtained. In general,

$$k = \frac{E_{ci}}{f'_c / \varepsilon'_0} \quad (4.34)$$

with E_{ci} being the initial tangential modulus of elasticity in a uniaxial compressive test. The parameter η controls the shape of the curve in the descending branch. The post-peak response must be regularized according to the dimension of the strain localization band, h_C , which is related to the finite element size. It is proposed to use

$$\eta = \frac{1}{2} \left(\frac{\pi f'_c \varepsilon'_0}{G_C / h_C - f'_c \varepsilon'_0 / 2} \right)^2 \quad (4.35)$$

where G_C is the compressive fracture energy. Unless stated otherwise, G_C is estimated using the Compressive Damage Zone (CDZ) model proposed by Markeset and Hillerborg [144] considering $k = 3$, $r = 1.25$ mm, $w_c = 0.6$ mm and $L = 2.5 \cdot e$, being e the element thickness:

$$G_C = 1500 G_F e + 0.0003 f'_c \quad (4.36)$$

In Figure 4.5, the resulting uniaxial stress-strain curves for an element with length/width/thickness of $0.25 \times 0.25 \times 0.10 \text{ m}^3$ are presented for 5 different uniaxial concrete strengths. The fracture energy G_F , the Young modulus E_{ci} and the peak uniaxial strain ε'_0 were calculated according to the equations given in Chapters 2 and 3.

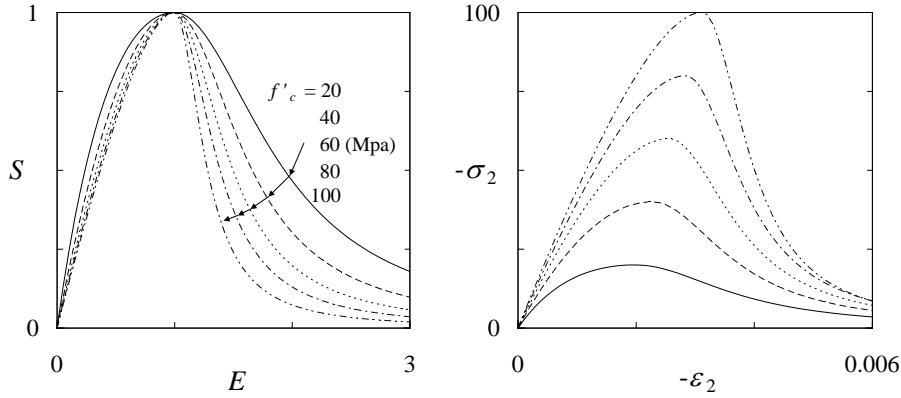


Figure 4.5 – Graphical representation of the proposed stress-strain curve in the uniaxial compression case for 5 different concrete strengths: (a) Equivalent stress vs. equivalent strain; (b) Resulting uniaxial stress-strain curves.

In the present model, a loading step always leads to damage evolution while in an unloading/reloading step damage remains constant. The variable that is used to monitor damage evolution is the maximum equivalent total strain, E_{\max} , which by definition is a non-decreasing variable. A given E_{\max} value bounds a region in the total strain space where no damage evolution occurs – the reversible process domain. This region expands as the maximum total strain increases and can never contract.

The implemented algorithm is given in Box 4.1. A value of $r < 1$ corresponds to an unloading or to a reloading step, while $r = 1$ corresponds to a loading step.

Box 4.1 – Algorithm for loading/unloading determination and calculation of the current equivalent stress.

1 – Calculate the current equivalent total strain $E^{t+\Delta t}$ from the current total strain tensor $\boldsymbol{\varepsilon}^{t+\Delta t}$

$$E^{t+\Delta t} = f(\boldsymbol{\varepsilon}^{t+\Delta t}) \quad \text{Eq. (4.31)}$$

2 – Calculate the current maximum equivalent total $E_{\max}^{t+\Delta t}$ strain and the strain ratio r .

$$E_{\max}^{t+\Delta t} = \max\{E_{\max}^t, E^{t+\Delta t}\} \quad \% \text{ State variable}$$

$$r = \frac{E^{t+\Delta t}}{E_{\max}^{t+\Delta t}}$$

3 – Calculate the equivalent stress corresponding to $E_{\max}^{t+\Delta t}$.

$$S_{\max}^{t+\Delta t} = f(E_{\max}^{t+\Delta t}) \quad \text{Eq. (4.33)}$$

4 – Calculate the current equivalent stress $S^{t+\Delta t}$

$$S^{t+\Delta t} = r S_{\max}^{t+\Delta t}$$

4.3.1.4 Constitutive and iteration stiffness matrices

So far, only a scalar relationship between the equivalent stress and equivalent total strain was defined. To complete the formulation, a directional relationship between the total strain and stress tensors is required. In the present model, before cracking, concrete is treated as an isotropic material. At higher loading levels this is a simplifying assumption, as shown in reference [136]. Nonetheless, it greatly simplifies the model while the error that is introduced is small and has little significance on the overall response of a RC member under biaxial stress conditions. The secant constitutive matrix relating concrete stresses with the total strains is derived in the form of a nonlinear elasticity matrix

$$\begin{Bmatrix} \sigma_{cx} \\ \sigma_{cy} \\ \tau_{cxy} \end{Bmatrix} = \frac{E_{c,sec}}{1-\nu^2} \begin{bmatrix} 1 & \nu & 0 \\ \nu & 1 & 0 \\ 0 & 0 & \frac{1-\nu}{2} \end{bmatrix} \begin{Bmatrix} \varepsilon_x \\ \varepsilon_y \\ \gamma_{xy} \end{Bmatrix} \quad (4.37)$$

$$E_{c,sec} = \frac{f'_c}{\varepsilon_0} \frac{S}{\sqrt{\left(\frac{a}{f'_c} \frac{\varepsilon_m}{1-\nu}\right)^2 + \left(\frac{b}{f'_c} \frac{\gamma_d}{1+\nu}\right)^2}}$$

where $E_{c,sec}$ is the secant Young modulus and ν is the Poisson ratio for which a constant value $\nu = 0.2$ may be taken. The expression for $E_{c,sec}$ is directly obtained from the definitions of equivalent stress and equivalent strain given by Eqs. (4.29) and (4.31), respectively.

The secant stiffness matrix of Eq. (4.37) is used to calculate stresses for the given strain state. The tangent stiffness matrix \mathbf{D}_c is used for construction of an element stiffness matrix for the iterative solution at the structural level. This matrix can readily be obtained in the global coordinate system replacing $E_{c,sec}$ in Eq. (4.37)₁ by the tangential modulus $E_{c,tan}$, which is the slope of the equivalent stress-strain curve at a given total strain:

$$E_{c,tan} = \begin{cases} \frac{f'_c}{\varepsilon_0} \frac{k - 2E - (k-2)E^2}{[1 + (k-2)E]^2} \geq E_{c,tan}^{MIN} & , E \leq 1 \\ E_{c,tan}^{MIN} & , E > 1 \end{cases} \quad (4.38)$$

The tangent modulus as defined in Eq. (4.38) is always positive. Whenever the slope of the curve is less than the minimum $E_{c,tan}^{MIN}$ the value of the tangent modulus is set to

$E_{c,\tan} = E_{c,\tan}^{MIN}$. This occurs in the softening range and near the compressive peak. Strictly speaking, in these situations the stiffness matrix ceases to be tangent.

The resulting algorithm is simple and is given in Box 4.2. Both the stresses and tangent stiffness matrix are determined explicitly from total strains.

Box 4.2 – Algorithm for computation of the stresses and tangent stiffness matrix

1 – Calculate the current equivalent total strain $E^{t+\Delta t}$ and the current equivalent stress $S^{t+\Delta t}$ using the algorithm in Box 4.1.

2 – Calculate the current value of the secant modulus $E_{c,\sec}^{t+\Delta t}$

$$E_{c,\sec}^{t+\Delta t} = f(\boldsymbol{\varepsilon}^{t+\Delta t}, S^{t+\Delta t}) \quad \text{Eq. (4.37)}_2$$

3 – Calculate the concrete stresses from the total strains using Eq. (4.37)₁

4 – Calculate the current value of the tangent modulus $E_{c,\tan}^{t+\Delta t}$

IF $r = 1$ % Loading step

$$E_{c,\tan}^{t+\Delta t} = f(E^{t+\Delta t}, S^{t+\Delta t}) \quad \text{Eq. (4.38)}$$

ELSE % Unloading/reloading step

$$E_{c,\tan}^{t+\Delta t} = E_{c,\sec}^{t+\Delta t} \geq E_{c,\tan}^{MIN}$$

END

5 – Assemble the stiffness matrix \mathbf{D}_c directly in the global coordinate system using $E_{c,\tan}^{t+\Delta t}$ in Eq. (4.37)₁

4.3.1.5 Examples

Biaxial compression - comparison with the experimental results of Kupfer and Gerstle

In Figure 4.6 the results from the analytical model are compared to a classical set of experimental data [128] with three compressive biaxial stress trajectories (see also Figure 4.4). The agreement is quite good in view of the simplifications considered in the model, such as the isotropy assumption and the constant value for the Poisson coefficient.

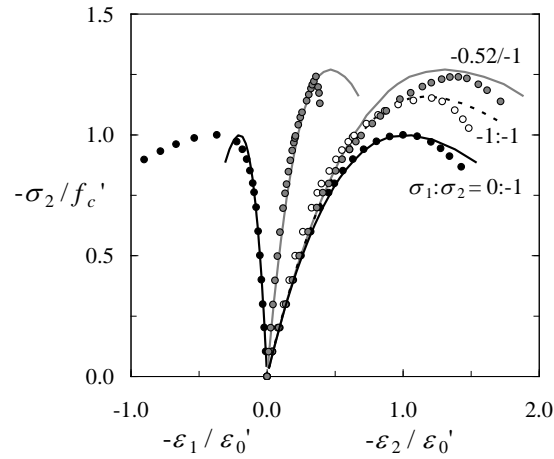


Figure 4.6 – Comparison of analytical model ($k=2.375$, $\nu=0.2$) with experimental data from reference [128].

Loading/unloading/reloading tests

In Figure 4.7 the model response for the case of non-proportional loading under biaxial compression stress states is presented. In a first stage, a uniaxial compression loading was applied till the equivalent stress reached $S = 0.7$, after which followed an unloading stage. Then a biaxial compression loading path was applied following the stress trajectory $\sigma_1:\sigma_2 = -0.52:-1$ till the equivalent stress reached $S = 0.85$. After unloading, a biaxial compression loading path was finally applied following the stress trajectory $\sigma_1:\sigma_2 = -1:-1$. The stress trajectories are represented in Figure 4.7 (a) and the corresponding strain trajectories in Figure 4.7 (b). Due to the adoption of a constant Poisson ratio, the strain trajectories are straight lines. A given value of the maximum equivalent strain bounds the domain of reversible stress states, as discussed in Section 4.3.1.3. In Figure 4.7 (c) the equivalent stress-equivalent strain relationship is depicted. The loading/unloading/reloading behaviour of the model can be clearly perceived. The points corresponding to the boundary of the reversible process at the end of each loading stage are represented by symbols. The normalized principal stress-principal strain curves are shown in Figure 4.7 (d). The points corresponding to the boundary of the reversible process are represented by the same symbols as in Figure 4.7 (c). It can be seen that the unloading/reloading portions of the stress-strain curves are straight lines, corresponding to stress and strain trajectories inside the boundaries delimiting the reversible process.

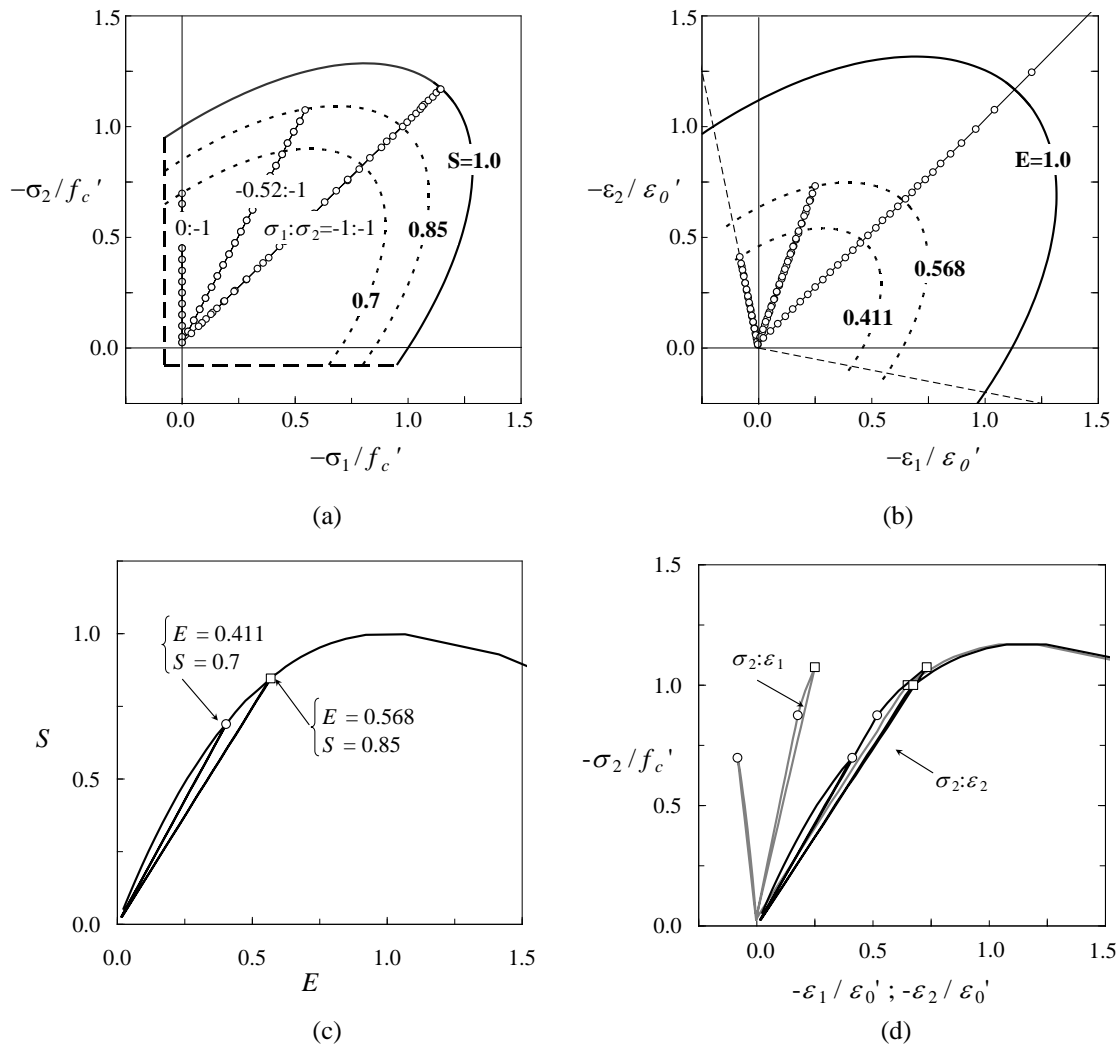


Figure 4.7 – Model behaviour under non-proportional biaxial compression loading paths: (a) Load paths in the principal stress space and (b) corresponding principal strain trajectories; (c) equivalent stress-equivalent strain relationship; (d) minimum compressive stress ratio versus the two principal strain ratios.

4.3.2 Cracked concrete

After cracking, concrete is treated as an orthotropic material and a local coordinate system is introduced (n - t coordinates) where the constitutive laws are established. The total strains in the global coordinate system are transformed into the local coordinate system through the usual strain transformation relationship:

$$\boldsymbol{\varepsilon}_{nt} = \mathbf{T}_{\varepsilon} \boldsymbol{\varepsilon}_{hv} \Leftrightarrow \begin{Bmatrix} \varepsilon_n \\ \varepsilon_t \\ \gamma_{nt} \end{Bmatrix} = \begin{bmatrix} c^2 & s^2 & sc \\ s^2 & c^2 & -sc \\ -2sc & 2sc & c^2 - s^2 \end{bmatrix} \begin{Bmatrix} \varepsilon_h \\ \varepsilon_v \\ \gamma_{hv} \end{Bmatrix}, \quad \begin{matrix} s = \sin \theta \\ c = \cos \theta \end{matrix} \quad (4.39)$$

where the subscripts $(\cdot)_h$ and $(\cdot)_v$ refer to the horizontal and vertical axis of the global coordinate system, respectively, and θ is the angle between the h -axis and the normal to the cracks.

Once cracking occurs, two uniaxial stress fields are assumed along the two orthogonal n - t directions and the Poisson effect in the cracked concrete is neglected. In the case of rotating crack models, the local coordinate system rotates and the n -direction is aligned with the direction of the maximum principal total strain, i.e., $\theta = \theta_\varepsilon$. In the case of fixed crack models, the crack direction is determined by the principal tensile direction of the concrete stress tensor at impending cracking. The crack angle θ remains fixed and is kept in memory as a state variable.

4.3.2.1 Compression model parallel to crack direction

The compressive stress parallel to the crack direction is determined from the total strain along the respective local axis using the base curve (4.33) already adopted in the uncracked stage. However, as the compressive strength of cracked concrete is reduced with increasing tensile strains in the orthogonal direction ε_\perp , the compressive strength f'_c must be replaced by the effective compressive strength $f_{c,ef} = \zeta_f \zeta_e f'_c$. In the case of the fixed crack model, the peak uniaxial strain is also reduced to $\varepsilon_{0,ef} = \zeta_f \zeta_e \varepsilon'_0$. Both the equivalent stress and the equivalent strain of cracked concrete are calculated according to Eqs. (3.27). It is remarked that instead of using the current tensile strain ε_\perp , the maximum tensile strain in the past history $\varepsilon_{\perp,max}$ is used for computing the softening coefficient ζ_e .

$$\zeta_e = \frac{1}{C_m (1.08 + 81\varepsilon_{\perp,max})} \quad (4.40)$$

This is required in order to ensure thermodynamic consistency, i.e., that energy cannot be generated during an arbitrary loading/unloading/reloading cycle.

In the case of cracked concrete, the parameter η_{cr} replaces η in Eq. (4.33)₂ and controls the shape of the compression curve in the post-peak branch, being calculated by:

$$\eta_{cr} = \eta \left(\frac{f_{c,ef}}{f'_c} \right)^2 \left(\frac{\varepsilon_{0,ef}}{\varepsilon'_0} \right)^2 \quad (4.41)$$

4.3.2.2 Tension model normal to crack direction

Depending on the material model formulation, the tension model can either relate the crack bridging stresses with the smeared crack opening, being in this case a *tension softening* model, or the average concrete tensile stresses in the reinforced concrete domain with the average strains, i.e., a *tension stiffening* model. In the present formulation, the material model relates the stresses at the cracks with the average strains and, therefore, only a tension softening formulation is included. The selected crack bridging stress law is the one described in Section 3.6.2.

In the case of plain concrete, tensile fracture is a localized phenomenon and some kind of regularization of the strain field must be employed. As previously discussed, the crack band model is considered here and, therefore, the crack opening w and the total tensile strain ε_{\perp} are related by

$$w = \varepsilon_{\perp} h_t \quad (4.42)$$

with h_t being the crack band width, which is a function of the finite element size and type, integration rule and crack orientation. A correct definition of the crack band width is very important in the case of unreinforced or poorly reinforced structures in order to ensure the correct amount of energy dissipation during the fracture process. The propagation of a vertical crack parallel to the element sides and an inclined crack is schematically depicted in Figure 4.8.

In the case of linear quadrilateral elements, and if the crack propagates parallel to the sides of the finite elements, the crack band width equals the size of the element side. However, if the crack propagates diagonally, the crack band width can be larger than the projection of the element side along the normal to the cracks due to the fact that cracks also occur in the neighbouring elements. This introduces an orientation effect in the calculation of the crack band width. In the present implementation this effect is taken into account following the proposal of Cervenka *et al* [57] by increasing the crack band width according to Eq.(4.43), in which h is the projection of the finite element dimensions along the normal to the cracks and h_t is the corrected crack band width. According to Eq. (4.43), it can be easily seen that $0 \leq h_t \leq 1.5 \cdot h$.

$$h_t = h \cdot \left(1 + \frac{\alpha}{\pi/2} \right) \quad , \quad \alpha \in [0; \pi/4] \quad (4.43)$$

If quadratic finite elements are used instead, cracks may localize on some of the integration points. In the case of a 2x2 reduced integration scheme, the propagation of both vertical and diagonal cracks is schematically depicted in Figure 4.8 (c) and (d), respectively. In this case, h is the projection of the gauss point tributary length along the normal to the cracks.

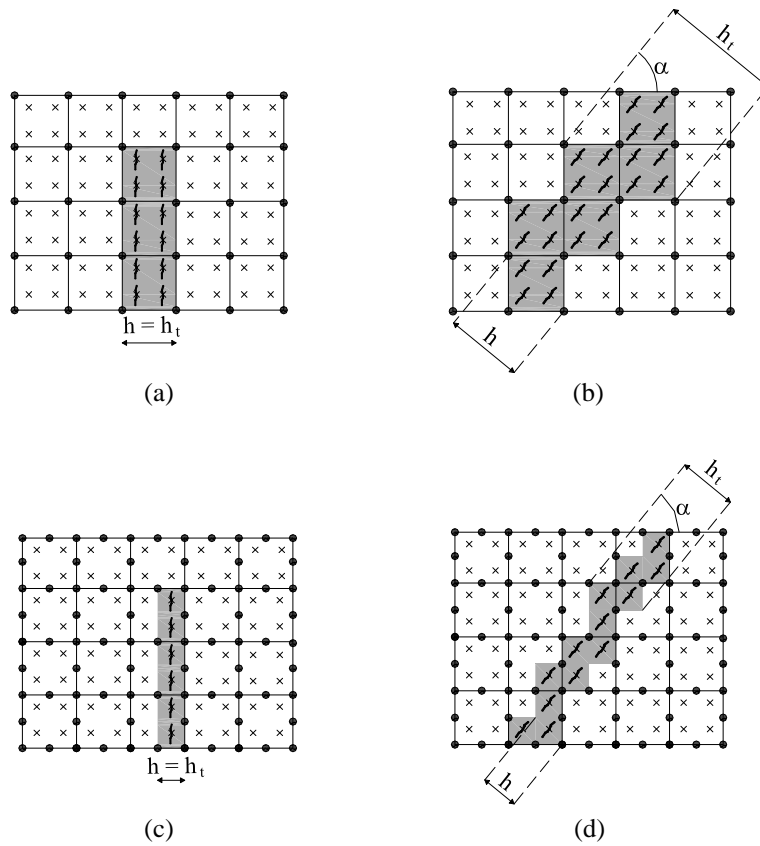


Figure 4.8 – Calculation of the crack band width: (a) propagation of a vertical crack in linear quadrilateral elements; (b) propagation of an inclined crack in linear quadrilateral elements; (c) propagation of a vertical crack in quadratic quadrilateral elements; (d) propagation of an inclined crack in quadratic quadrilateral elements.

4.3.2.3 Coupled tension-compression model

The combination of the compression and tension models results in a path-dependent model, which is required in case of non-proportional or reversed loading paths. Note that, even in the case of proportional monotonic loading, stress redistributions within the structure may lead some regions to unload. The unloading/reloading is performed secant to the origin. For reproducing this type of behaviour two state variables are required for each direction of the local coordinate system: the maximum and minimum total strain experienced in the past history. In the present implementation, instead of the minimum compressive strain, the state variable governing the compressive behaviour is the maximum equivalent total strain in the past history. Immediately after cracking, the state variable E_{\max}^t from the uncracked subroutines is transferred to the cracked subroutines:

$$E_{n,\max}^t = E_{t,\max}^t = E_{\max}^t \quad (4.44)$$

which is equivalent to assuming an isotropic damage evolution prior to cracking.

The loading/unloading determination is made independently for the n - and t -directions according to the algorithm described in Box 4.3. Similarly to the uncracked concrete subroutines, a value of $r < 1$ corresponds to an unloading or to a reloading step while $r = 1$ corresponds to a loading step. Once concrete is cracked, the biaxial confinement effects cannot be recovered.

Box 4.3 – Algorithm for loading/unloading determination and current normal stress calculation (cracked state)

1 – Transform the total strains from the global to the local coordinate system.

$$\boldsymbol{\varepsilon}_{nt}^{t+\Delta t} = \mathbf{T}_\varepsilon(\theta) \boldsymbol{\varepsilon}_{hv}^{t+\Delta t} \quad \text{Eq. (4.39)}$$

Note that θ is either a state variable, in the case of fixed crack models, or is calculated from the current total strain tensor, in the case of rotating crack models. In this last case the notation $\theta^{t+\Delta t}$ should have been used.

2 – Calculate the current normal stress $\sigma_n^{t+\Delta t}$ in the n -direction:

i. Evaluate the softening coefficient $\zeta_f \zeta_e$:

$$\varepsilon_{t,\max}^{t+\Delta t} = \max(\varepsilon_{t,\max}^t, \varepsilon_t^{t+\Delta t}) \quad \% \text{ State variable}$$

$$\text{IF } \varepsilon_{t,\max}^{t+\Delta t} > 0$$

$$\varepsilon_\perp = \varepsilon_{t,\max}^{t+\Delta t} \quad \text{with } \zeta_f \text{ and } \zeta_e \text{ given by Eqs. (3.24).}$$

ELSE

$$\zeta_f \zeta_e = 1$$

END

ii. For compressive stress states, $\varepsilon_n^{t+\Delta t} < 0$

$$E_n^{t+\Delta t} = -\frac{\varepsilon_n^{t+\Delta t}}{\varepsilon_{0,ef}}, \quad \text{with } \varepsilon_{0,ef} = \zeta_f \zeta_e \varepsilon_0' \quad \text{in the case of the fixed crack model}$$

$$E_{n,\max}^{t+\Delta t} = \max(E_{n,\max}^t, E_n^{t+\Delta t}) \quad \% \text{ State variable}$$

$$r = \frac{E_n^{t+\Delta t}}{E_{n,\max}^{t+\Delta t}}$$

$$S_{\max}^{t+\Delta t} = f(E_{\max}^{t+\Delta t}) \quad \text{Eq. (4.33)}$$

$$S^{t+\Delta t} = r S_{\max}^{t+\Delta t}$$

$$\sigma_n^{t+\Delta t} = -\zeta_f \zeta_e f_c' S^{t+\Delta t}$$

iii. For tensile stress states, $\varepsilon_n^{t+\Delta t} > 0$

$$\varepsilon_{n,\max}^{t+\Delta t} = \max(\varepsilon_{n,\max}^t, \varepsilon_n^{t+\Delta t}) \quad \% \text{ State variable}$$

$$r = \frac{\varepsilon_n^{t+\Delta t}}{\varepsilon_{n,\max}^{t+\Delta t}}$$

$$\sigma_{\max}^{t+\Delta t} = f(\varepsilon_{n,\max}^{t+\Delta t}) \quad \text{Eqs. (4.42) and (3.32)}$$

$$\sigma_n^{t+\Delta t} = r \sigma_{\max}^{t+\Delta t}$$

iv. For $\varepsilon_n^{t+\Delta t} = 0 \Rightarrow \sigma_{c,n}^{t+\Delta t} = 0$

3 – Calculate the normal stress $\sigma_t^{t+\Delta t}$ in the t -direction repeating the previous steps i-iv and changing the subscripts $(\cdot)_n$ and $(\cdot)_t$ where appropriate.

4.3.2.4 Shear transfer model in the crack coordinate system

In the case of rotating crack models, the local axes of orthotropy constitute a principal system of the concrete stress tensor and no shear transfer model is required. However, in the case of fixed crack models, an additional shear transfer model must be supplied for calculation of the shear stress in the local coordinate system. In most fixed crack models, the shear stress transfer is crudely modelled considering a secant formulation, in which the cracked concrete shear stiffness $G_{c,nt}$ is obtained from the elastic stiffness G_c as

$$G_{c,nt} = \mu G_c \quad , \quad 0 \leq \mu \leq 1 \quad (4.45)$$

where μ is the so called shear retention factor, which is usually taken either as a constant or as a function of the normal tensile strain. The shear stress is then calculated by $\tau_{c,nt} = G_{c,nt} \gamma_{nt}$. In this type of formulations the crack dilatancy stresses are not considered. In the present model, a more detailed and realistic formulation is implemented according to what has been exposed in Section 3.6.3.

One active crack in the local coordinate system

The crack shear and crack dilatancy stresses are calculated from the normalized shear strain $\beta = \gamma_{nt} / \varepsilon_{n,max}$, where γ_{nt} is the current shear strain and $\varepsilon_{n,max}$ is the maximum normal strain, the latter being a state variable. For loading/unloading states in the positive side of the normalized shear strain, $\beta > 0$, the shear and dilatancy stresses are given by Eqs.(3.33). In the negative side of the normalized shear strain, $\beta < 0$, a minus sign must be placed in the τ_{agg} expression. The state variable $\varepsilon_{n,max}$ is used instead of the current normal strain ε_n in the determination of the normalized shear strain, β . This is required for ensuring the algorithm stability in the unloading/reloading regimes and a smooth transition from loading to unloading states.

For simplicity of the resulting algorithm, especially when two cracks arise in the same integration point, loading and unloading are performed following the same expression. Considering the fact that the present model relates stresses and strains, and not stress and strain rates (see discussion in 4.2.2), in the case of complex loading histories the thermodynamic requirement that energy cannot be generated during an arbitrary loading/unloading/reloading cycle requires the formulation of the crack shear stress capacity as a non increasing variable. Therefore, the g function must be defined as,

$$g(\varepsilon_{n,\max}, s_{rm\theta}) = \frac{0.5}{0.31 + 200 s_{rm\theta} \varepsilon_{n,\max}} \leq 1 \quad (4.46)$$

where the state variable $\varepsilon_{n,\max}$ is used instead of the current normal strain ε_n .

In cases where strain localization phenomena govern the structural behaviour, either because reinforcement is not present or is not capable of ensuring multiple crack formation, mesh objectivity of the results must be guaranteed. It can be easily shown that the normalized shear strain β is mesh independent. In fact, β is calculated as the ratio between two strain components which are obtained by smearing crack opening and slip displacements over the same length. In order to ensure mesh objectivity of the crack shear stress capacity, and whenever a single crack governs the behaviour, the g function is modified to:

$$g(\varepsilon_{n,\max}, h_t) = \frac{0.5}{0.31 + 200 h_t \varepsilon_{n,\max}} \leq 1 \quad (4.47)$$

This expression is obtained from Eq. (4.46) replacing the average crack spacing $s_{rm\theta}$ by the crack band width h_t in the calculation of the crack width.

Equilibrium and compatibility for two orthogonal cracks

A robust material model must deal with situations where at least two cracks arise in the same integration point. In the present formulation, post-cracking stresses are evaluated in the local orthotropy axes, which are, by definition, orthogonal. Therefore, only two orthogonal cracks are allowed. In the case of the fixed crack model, the orthotropy directions may not coincide with the principal concrete stress directions, and the violation of the concrete tensile strength may not be strictly verified. This may occur in the case of non-proportional or cyclic loading paths, where non-orthogonal cracks are observed in real structures. However, even under proportional loading, internal stress redistributions may lead to the formation of non-orthogonal cracks. This occurs, for example, in webs of girders where flexural cracks are sometimes crossed by diagonal shear cracks, which have formed later during the loading process. If these diagonal cracks govern the failure mode, less accuracy is to be expected from the fixed crack model.

In an RC element containing two cracks, the total shear strain γ_{nt} must be distributed by each crack (see Figure 4.9) so that the corresponding shear and dilatancy stresses can be

calculated. Equilibrium requires that the shear stress transmitted along both cracks is the same. Therefore, the problem is governed by the two following conditions:

$$\tau_{agg} = \tau_{agg}(\beta_1) = \tau_{agg}(\beta_2) \quad (4.48)$$

$$\gamma_{nt} = \gamma_{nt,1} + \gamma_{nt,2}$$

with $\beta_1 = \gamma_{nt,1} / \varepsilon_{n,\max}$ and $\beta_2 = \gamma_{nt,2} / \varepsilon_{t,\max}$.

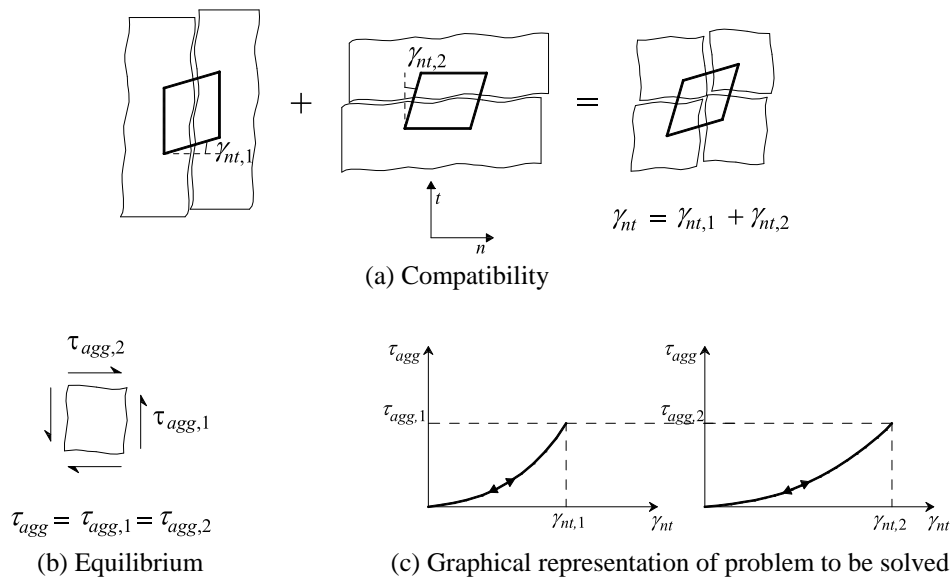


Figure 4.9 – Equilibrium and compatibility for two-way orthogonal cracks.

It can be shown that the determination of the shear strains fulfilling the equilibrium and compatibility conditions (4.48) can be reduced to the problem of finding the roots of a fourth degree polynomial. Since only one real root exists in the interval, $\gamma_{nt,1} \in [0, \gamma_{nt}]$, the bisection method, which can be shown to be unconditionally convergent, was implemented for finding the solution. The algorithm starts by checking how many active cracks exist. An active crack is defined as having tensile normal strains, otherwise is considered to be closed or inactive. The algorithm is presented in Box 4.4.

After having determined the active cracks and obtained the shear strains for each crack in the local coordinate system, the crack shear and dilatancy stresses are calculated using the algorithm indicated in Box 4.5.

Box 4.4 – Algorithm for determining the active cracks

1 – Check which cracks are active

```

IF  $idcrk = 1$                                      %Only one crack in the coordinate system.  $idcrk$  is
a state indicator with the number of times the crack detection envelope was violated in the past history

 $\gamma_{nt,1} = \gamma_{nt}$       ;       $\gamma_{nt,2} = 0$ 

IF  $\varepsilon_n < tol$                                % Closed crack
   $idshea = 0$ 
ELSE                                               % Active crack normal to  $nn$ 
   $idshea = 1$       ;       $\tau_{LIM,1} = 3.83f_c^{1/3} g(\varepsilon_{n,max}, S_{rm\theta})$ 
END IF
ELSE IF  $idcrk = 2$                                %Two cracks in the coordinate system
  IF  $\max(\varepsilon_n, \varepsilon_t) < tol$            % Closed cracks
     $idshea = 0$       ;       $\gamma_{nt,1} = \gamma_{nt}$       ;       $\gamma_{nt,2} = 0$ 
  ELSE IF  $\varepsilon_n \geq tol$  AND  $\varepsilon_t < tol$    % Active crack normal to  $nn$ 
     $idshea = 1$       ;       $\gamma_{nt,1} = \gamma_{nt}$       ;       $\gamma_{nt,2} = 0$ 
     $\tau_{LIM,1} = 3.83f_c^{1/3} g(\varepsilon_{n,max}, S_{rm\theta})$ 
  ELSE IF  $\varepsilon_n < tol$  AND  $\varepsilon_t \geq tol$    % Active crack normal to  $tt$ 
     $idshea = 2$       ;       $\gamma_{nt,1} = 0$       ;       $\gamma_{nt,2} = \gamma_{nt}$ 
     $\tau_{LIM,2} = 3.83f_c^{1/3} g(\varepsilon_{t,max}, S_{rm\theta})$ 
  ELSE                                           % Two active cracks
     $idshea = 3$ 
     $\tau_{LIM,1} = 3.83f_c^{1/3} g(\varepsilon_{n,max}, S_{rm\theta})$       ;       $\tau_{LIM,2} = 3.83f_c^{1/3} g(\varepsilon_{t,max}, S_{rm\theta})$ 

    Call the subroutine with the bisection method for determining  $\gamma_{nt,1}$ 
    and  $\gamma_{nt,2}$  fulfilling the conditions (4.48).
  END IF
END IF
END IF

```

Box 4.5 – Algorithm for determining the crack shear and dilatancy stresses

- 1 – Closed cracks: $idshea = 0$ % Secant formulation of an orthotropic material
 $E_n = \sigma_n / \varepsilon_n$; $E_t = \sigma_t / \varepsilon_t$; $G_{nt} = 0.25(E_n + E_t)$
 $\tau_{agg} = G_{nt} \cdot \gamma_{nt}$; $\sigma_{dil,1} = 0$; $\sigma_{dil,2} = 0$
- 2 – One active crack normal to the nn axis: $idshea = 1$
 i. $\beta = \gamma_{nt} / \varepsilon_{n,max}$
 ii. Calculate the crack shear stress τ_{agg} and dilatancy stress σ_{dil} from Eq. (3.33)
 iii. $\sigma_{dil,1} = \sigma_{dil}$; $\sigma_{dil,2} = 0$
- 3 – One active crack normal to the tt axis: $idshea = 2$
 i. $\beta = \gamma_{nt} / \varepsilon_{t,max}$
 ii. Calculate the crack shear stress τ_{agg} and dilatancy stress σ_{dil} from Eq. (3.33)
 iii. $\sigma_{dil,1} = 0$; $\sigma_{dil,2} = \sigma_{dil}$
- 4 – Two orthogonal active cracks: $idshea = 3$ % Note that $\tau_{agg,1} = \tau_{agg,2}$.
 4.1. For the first crack
 i. Perform steps 2-i to 2-ii using $\gamma_{nt,1}$ instead of γ_{nt} ;
 ii. $\sigma_{dil,1} = \sigma_{dil}$
- 4.2. For the second crack:
 i. Perform steps 3-i to 3-ii using $\gamma_{nt,2}$ instead of γ_{nt} ;
 ii. $\tau_{agg,2} = \tau_{agg}$; $\sigma_{dil,2} = \sigma_{dil}$

4.3.2.5 Assembly of the concrete stress vector

The concrete stress vector is finally assembled as follows:

$$\begin{aligned}\sigma_{c,n} &= \sigma_n + \sigma_{dil,1} \\ \sigma_{c,t} &= \sigma_t + \sigma_{dil,2} \\ \tau_{c,nt} &= \tau_{agg}\end{aligned}\tag{4.49}$$

It must be noted that in the case of the rotating crack model the stresses $\sigma_{dil,1}$, $\sigma_{dil,2}$ and τ_{agg} are all null.

4.3.2.6 Iteration concrete stiffness matrix

After cracking, a diagonal concrete stiffness matrix is adopted for the iteration procedure. In the local crack coordinate system the matrix has the form:

$$\mathbf{D}_{c,nt} = \begin{bmatrix} D_{11} & 0 & 0 \\ 0 & D_{22} & 0 \\ 0 & 0 & D_{33} \end{bmatrix} \quad (4.50)$$

In the case of the rotating crack model, the cross term D_{21} , which is related to the influence of the normal tensile strains on the compressive behaviour, is disregarded. In the case of the fixed crack model, also the additional cross terms D_{13} and D_{31} , related to the influence of the shear strains on the crack dilatancy stresses (normal to the cracks) and the influence of the normal tensile strains on the crack shear stress, respectively, are neglected. The adoption of a diagonal stiffness matrix neglecting the effect of the cross terms weakens the convergence characteristics of the algorithm if a fully Newton-Raphson procedure is adopted for the incremental-iterative solution procedure. Nonetheless, this effect was found not to be severe and good convergence rates can still be achieved.

Normal stiffness terms D_{11} and D_{22}

The stiffness coefficients for the normal directions are determined independently and following the same algorithm. If the uniaxial state of stress is compressive, and similarly to the procedure adopted for the uncracked concrete subroutines, the stiffness coefficient is given by the derivative of the equivalent stress-equivalent strain curve:

$$D_{11} = \begin{cases} \frac{f_{c,ef}}{\varepsilon_{0,ef}} \frac{k - 2E - (k - 2)E^2}{[1 + (k - 2)E]^2} \geq D_{comp}^{MIN} & , E \leq 1 \\ D_{comp}^{MIN} & , E > 1 \end{cases} \quad (4.51)$$

Again, the tangent modulus defined in (4.51) is always positive. Whenever the slope of the curve is less than the minimum value D_{comp}^{MIN} , the value of the tangent modulus is set to $D_{11} = D_{comp}^{MIN}$. This occurs near the peak stress and in the post peak range.

If the uniaxial state of stress is tensile, a secant value is adopted, which must always be greater than the limit value D_{tens}^{MIN} . The resulting algorithm is presented in Box 4.6 and is performed in the sequence of the algorithm given in Box 4.3.

Box 4.6 – Algorithm for calculation of the normal stiffness terms in the crack coordinate system

1 – Calculate the current stiffness term D_{11} corresponding to the n -direction:

- i. For compressive stress states, $\varepsilon_n^{t+\Delta t} < 0$, calculate the current value of the tangent modulus:

IF $r = 1$ % Loading step

D_{11} given by Eq. (4.51)

ELSE % Unloading/reloading step

$$D_{11} = \max \left(\frac{f_{c,ef}}{\varepsilon_{o,ef}} \frac{S_{\max}^{t+\Delta t}}{E_{n,\max}^{t+\Delta t}}, D_{comp}^{MIN} \right)$$

END

- ii. For tensile stress states, $\varepsilon_n^{t+\Delta t} > 0$, calculate the current value of the secant modulus:

$$D_{11} = \max \left(\frac{\sigma_{\max}^{t+\Delta t}}{\varepsilon_{n,\max}^{t+\Delta t}}, D_{tens}^{MIN} \right)$$

- iii. For $\varepsilon_n^{t+\Delta t} = 0$, $D_{11} = E_{ci}$

2 – Calculate the current stiffness term D_{22} corresponding to the t -direction repeating the previous steps i-iii and changing the subscripts $(\cdot)_n$ and $(\cdot)_t$ where appropriate.

Shear stiffness coefficient D_{33}

As shown, for example, in reference [71], in the case of the rotating crack model, the tangent shear stiffness coefficient is given by:

$$D_{33} = \frac{1}{2} \frac{\sigma_{c,1} - \sigma_{c,2}}{\varepsilon_1 - \varepsilon_2} \geq D_{shear}^{MIN} \quad (4.52)$$

where the subscripts $(\cdot)_1$ and $(\cdot)_2$ are equivalent to $(\cdot)_n$ and $(\cdot)_t$ since the nt coordinate system is a principal system of both concrete stresses and average strains. The shear stiffness is made always greater than a small limit value D_{shear}^{MIN} in order to avoid numerical instabilities.

In the case of the fixed crack model, the tangent stiffness term is obtained differentiating the crack shear stress expressions with respect to the shear strain. For the positive side of the shear strain, $\gamma_{nt} > 0$, it is given by:

$$D_{33,i} = \frac{\tau_{LIM,i}}{\varepsilon_{i,\max}} \frac{2\beta_i}{(1 + \beta_i^2)^2} \quad (4.53)$$

where the subscript $(\cdot)_i$ can take the values 1 or 2, identifying the two cracks that can be present. For the negative side of the shear strain, $\gamma_{nt} < 0$, the expression is similar and a minus sign must be introduced in Eq. (4.53).

In the case of only one active crack, then $D_{33} = D_{33,1}$ or $D_{33} = D_{33,2}$, depending on which crack is active. If there are two active cracks then the shear stiffness is obtained from:

$$\frac{1}{D_{33}} = \frac{1}{\frac{1}{D_{33,1}} + \frac{1}{D_{33,2}}} \quad (4.54)$$

The shear stiffness calculation is performed jointly with the algorithm presented in Box 4.5.

4.3.2.7 Examples

Loading/unloading/reloading test

In this single element test, a linear quadrilateral element was subjected to uniaxial loading conditions according to Figure 4.10 (a). The adopted concrete strength was $f'_c = 30\text{MPa}$, the tensile strength $f_{ct} = 2.6\text{MPa}$, and the crack band width $h_t = h_c = 0.20\text{m}$. All the remaining material properties were determined from f'_c according to the exposed in the previous sections. The obtained stress-strain curve is depicted in Figure 4.10 (b). The numbers indicate the loading sequence, thus illustrating the loading/unloading/reloading behaviour of the model.

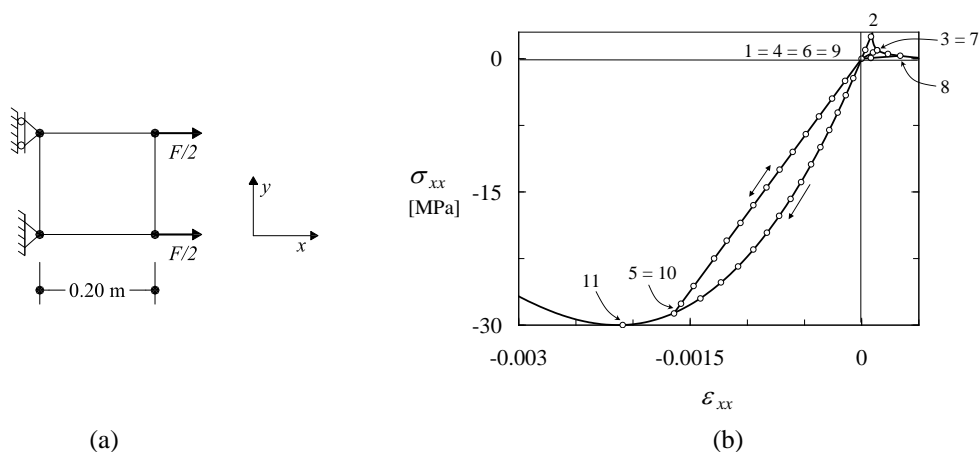


Figure 4.10 – Uniaxial loading/unloading/reloading test. The loading sequence is identified by the numbers indicated in the figure.

Crack shear transfer model

Two single element tests are shown to illustrate the behaviour of the crack shear transfer model. The adopted concrete strength was $f'_c = 30\text{MPa}$. In a first test, the element was pre-cracked by prescribing an initial vertical displacement, according to Figure 4.11 (a). The shear forces were then applied maintaining the initial crack opening. In a second test, two orthogonal cracks were introduced previously to the application of the shear deformations, according to Figure 4.11 (b). Like the first test, the initial crack openings were maintained constant during the shear deformation.

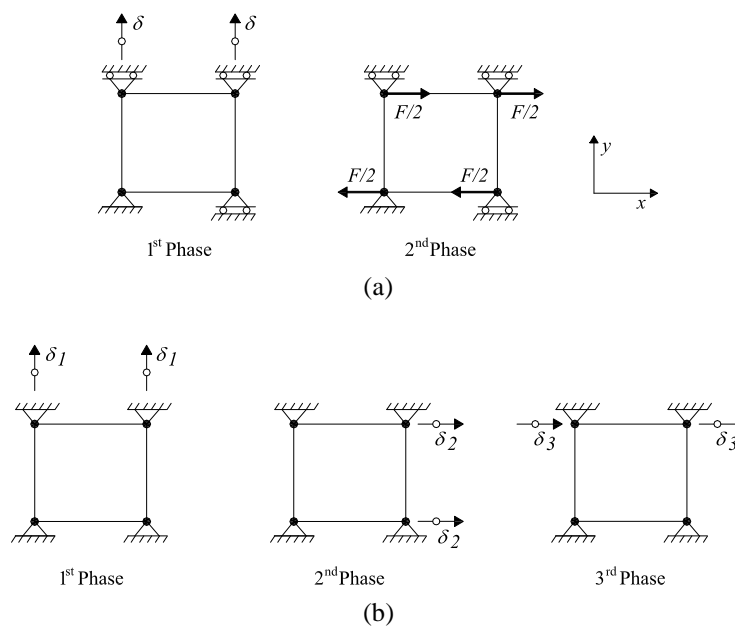


Figure 4.11 – Crack shear stress transfer model: (a) single crack test; (b) test with two orthogonal cracks.

The results of the tests are presented in Figure 4.12. Each plot corresponds to an initial crack opening value. Both shear and dilatancy stresses are shown for the positive and negative side of the shear deformation. Since the crack openings were maintained constant during shear loading, the loading/unloading/reloading curves coincide.

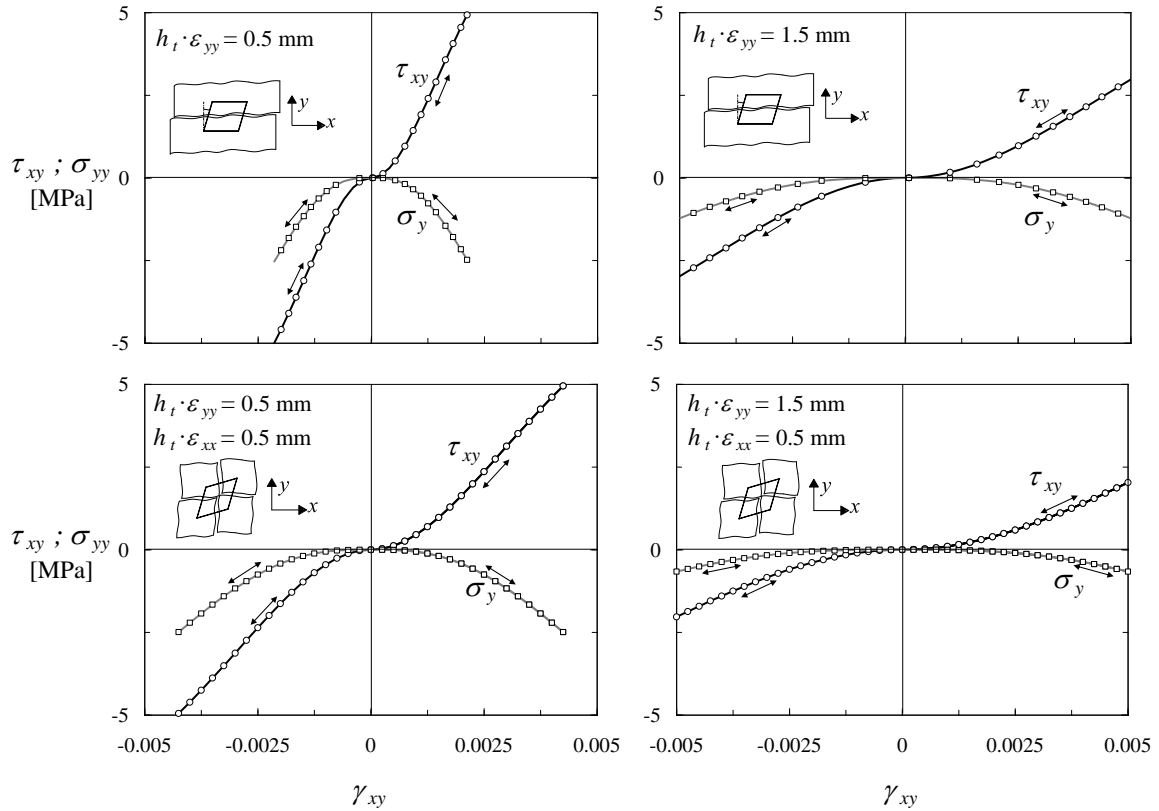


Figure 4.12 – Crack shear stress transfer model: results of the single element validation tests.

4.3.3 Reinforcement steel

4.3.3.1 Behaviour for non-proportional loading paths

In the present model reinforcement stresses at the cracks are calculated from the average strains, as described in Section 3.6.4. For implementation in a finite element code, the formulation of suitable loading/unloading/reloading conditions is required. These can be derived considering a rigid-plastic behaviour for the bond shear stress-slip law as depicted in Figure 4.13 (a). In the unloading stage, it is hereby assumed that bond shear stress drops to zero. In reality, the bond shear stress may reverse sign and, although a rapid degradation of bond is usually seen, negative bond shear stresses are expected in the unloading stage. This may be important for an accurate modelling of the cracks widths in service conditions and should be subject of future generalization of the present model.

If reversed bond action is neglected, and when the unloaded length is equal to the crack spacing, the stresses in the reinforcement are equal to $\sigma_{s,min}$, see Figure 4.13 (b). From that point on, the naked bar stress-strain relation is adopted. A linear relationship is assumed until the unloaded length is equal to the crack spacing. It can be shown that the

unloading/reloading stiffness in this region is twice the steel young modulus E_s if the steel stresses along the tension chord are all above or below the yielding stress f_{sy} . In these cases the following equalities hold (see Figure 4.13 (c)):

$$\Delta\sigma_{sr} = \sigma_{sr} - \sigma_{s,min} = 2(\sigma_{sr} - \sigma_{sm}) \quad (4.55)$$

$$\frac{\Delta\sigma_{sr}}{\Delta\varepsilon_{sm}} = 2E_s \quad (4.56)$$

In Figure 4.13 (c) the resulting loading/unloading/reloading behaviour is illustrated. The determination of the notable points of the unloading/reloading $\sigma_{sr}(\varepsilon_{sm})$ curve, i.e. the points where the unloading/reloading slope changes from $2 \cdot E_s$ to E_s , is made using the equilibrium conditions of the differential element as discussed in Section 2.2.1, as well as the constitutive laws for the reinforcement steel and bond shear stress.

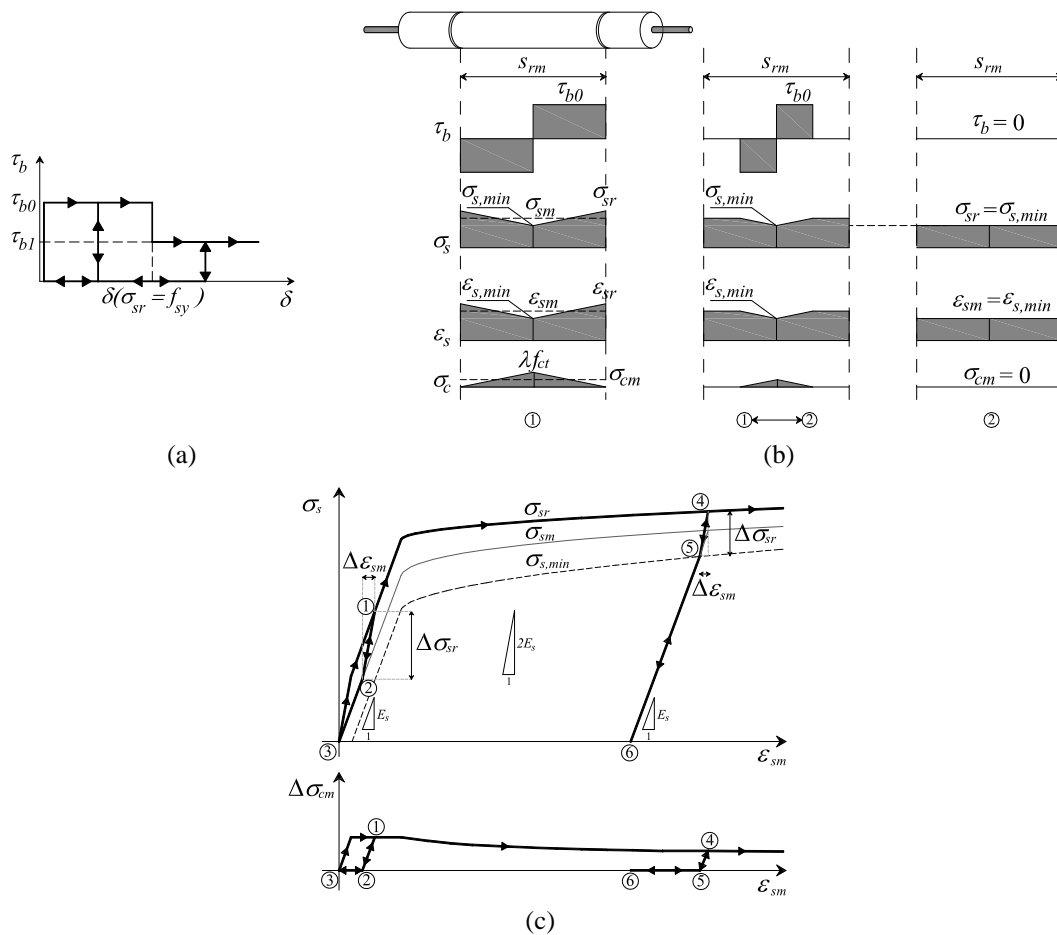


Figure 4.13 – Formulation of the reinforcement model under non-proportional loading: (a) Bond stress-slip law; (b) Stress and strain distributions between the cracks (pre-yielding stage); (c) Resulting stress-strain laws for the steel and corresponding average stresses in the concrete.

In the cases where partial yielding has occurred along the tension chord, i.e. $\sigma_{s,\min} < f_{sy} < \sigma_{sr}$, the equalities (4.55) and (4.56) are only good approximations of the real solution. These were still considered for simplicity of the resulting algorithm.

The naked bar stress-strain law is adopted when the stresses go into the compressive side. The plastic strains are used as offsets of the steel response, as depicted in Figure 4.14. The algorithm for the one-dimensional reinforcing bar is shown in Box 4.7.

Box 4.7 – Algorithm for calculation of the stresses in one reinforcement direction

```

1 – Calculate the elastic strain:  $\varepsilon_{sm,el} = \varepsilon_{sm} - \varepsilon_{p-} - \varepsilon_{p+}$            %  $\varepsilon_{p-}$  and  $\varepsilon_{p+}$  are state variables
2 – IF  $\varepsilon_{sm,el} \leq 0$                                            % Reinforcement is on the compressive side
    Calculate the effective compressive strain:  $\varepsilon_{sm,ef} = \varepsilon_{sm} - \varepsilon_{p+}$ 
    IF  $\varepsilon_{sm,ef} < \varepsilon_{sm,\min}$                                % Loading in compression.  $\varepsilon_{sm,\min}$  is a state variable
        Calculate  $\sigma_{sr}$  according to the naked bar stress-strain relationship
    ELSE                                                         % Unloading/reloading in compression
         $\sigma_{sr} = E_s \cdot \varepsilon_{sm,el}$                        % Elastic unloading/reloading behaviour
    END IF
3 – IF  $\varepsilon_{sm,el} > 0$                                            % Reinforcement is on the tensile side
    Calculate the effective tensile strain:  $\varepsilon_{sm,ef} = \varepsilon_{sm} - \varepsilon_{p-}$ 
    IF  $\varepsilon_{sm,ef} > \varepsilon_{sm,\max}$                            % Loading in tension.  $\varepsilon_{sm,\max}$  is a state variable
        Calculate  $\sigma_{sr}$  from  $\varepsilon_{sm}$  according to Eqs. (3.37) – (3.39)
    ELSE                                                         % Unloading/reloading in tension
        Calculate  $\sigma_{sr,\max}$  and  $\sigma_{sm,\max}$  using  $\varepsilon_{sm,\max}$  in Eq. (3.37) – (3.39)
         $\varepsilon_{sm,ref} = \varepsilon_{sm,\max} - (\sigma_{sr,\max} - \sigma_{sm,\max}) / E_s$  % Strain at which the unloading/reloading
        slope changes from  $2 \cdot E_s$  to  $E_s$ 
        IF  $\varepsilon_{sm,ef} > \varepsilon_{sm,ref}$                          % The unloaded length is smaller than the average crack spacing
             $\sigma_{sr} = \sigma_{sr,\max} - 2 \cdot (\sigma_{sr,\max} - \sigma_{sm,\max}) + 2 \cdot E_s \cdot (\varepsilon_{sm,ef} - \varepsilon_{sm,ref})$ 
        ELSE
             $\sigma_{sr} = E_s \cdot \varepsilon_{sm,el}$  % The unloaded length equals the average crack spacing. Elastic behaviour
        END IF
    END IF
END IF

```

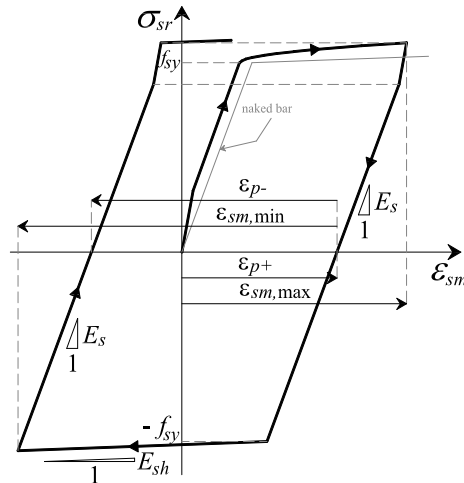


Figure 4.14 – Reinforcement stresses under non-proportional loading.

4.3.3.2 Calculation of the crack spacing

For two-dimensional stress conditions, the crack spacing along each orthogonal reinforcement direction is calculated according to Section 3.6.4.2. The resulting algorithm is presented in Box 4.8. It is remarked that when the cracks are oriented at very acute angles to the reinforcement, the calculation of the crack spacing according to Eq. (3.45) may lead to unrealistic solutions. In fact, when cracks are almost parallel to the reinforcement, the bond stresses are not totally mobilized and are overestimated if calculated according to the rigid plastic bond shear stress-slip law of Figure 3.10 (a). In these circumstances, a simple interpolation is performed between the solution corresponding to the case where the cracks are inclined at $\theta_{r,\text{lim}} = 25^\circ$ with respect to the reinforcements, for which a total mobilization of the bond shear stress is assumed to occur, and the limiting case corresponding to uniaxial stress conditions.

Box 4.8 – Algorithm for calculation of crack spacing along each reinforcement direction

1 – Calculate the uniaxial crack spacings s_{rmx0} and s_{rmy0} for the x- and y- directions, respectively, according to Eqs. (3.43). If the reinforcement content is null in one of the directions, assume a large uniaxial crack spacing in that direction.

2 – Calculate the angle $\theta_r \in [-\pi/2 ; \pi/2]$ between the n - direction and the x -reinforcement.

3 – If $\theta_{r,\text{lim}} \leq |\theta_r| \leq \pi/2 - \theta_{r,\text{lim}}$:

- i. Calculate the diagonal crack spacing s_{rm} solving Eq. (3.45);
- ii. Calculate the crack spacing in the reinforcement directions s_{rmx} and s_{rmy} from Eq. (3.41).

4 – If $|\theta_r| < \theta_{r,\text{lim}}$:

- i. Calculate the diagonal crack spacing s_{rm} solving Eq. (3.45) for $\theta_r = |\theta_{r,\text{lim}}|$;
- ii. Calculate λ'_x and λ'_y from Eq. (3.42) using $\theta_r = |\theta_{r,\text{lim}}|$;
- iii. Calculate λ_x and λ_y from

$$\lambda_x = 1 + \frac{|\theta_r|}{\theta_{r,\text{lim}}} (\lambda'_x - 1) \quad \lambda_y = \frac{|\theta_r|}{\theta_{r,\text{lim}}} \lambda'_y$$

- iv. Calculate the crack spacing in the reinforcement directions:

$$s_{rmx} = \lambda_x \cdot s_{rmx0} \quad s_{rmy} = \lambda_y \cdot s_{rmy0}$$

5 – If $|\pi/2 - \theta_r| < \theta_{r,\text{lim}}$:

- i. Calculate the diagonal crack spacing s_{rm} solving Eq. (3.45) using $\theta_r = |\pi/2 - \theta_{r,\text{lim}}|$;
- ii. Calculate λ'_x and λ'_y from equation (3.42) Eq. $\theta_r = |\pi/2 - \theta_{r,\text{lim}}|$;
- iii. Calculate λ_x and λ_y from

$$\lambda_x = \frac{|\pi/2 - \theta_r|}{\theta_{r,\text{lim}}} \lambda'_x \quad \lambda_y = 1 + \frac{|\pi/2 - \theta_r|}{\theta_{r,\text{lim}}} (\lambda'_y - 1)$$

- iv. Calculate the crack spacing in the reinforcement directions:

$$s_{rmx} = \lambda_x \cdot s_{rmx0} \quad s_{rmy} = \lambda_y \cdot s_{rmy0}$$

6 – Transform the total strains from the global h - v coordinate system to the reinforcement x - y coordinate system.

4.3.3.3 Assembly of the composite stress vector and iteration stiffness matrix

In the reinforcement coordinate system, the composite stress vector can be assembled according to Eqs. (3.2) and the iteration stiffness matrix of the reinforcement is expressed by the diagonal matrix:

$$\mathbf{D}_{s,xy} = \begin{bmatrix} \rho_x D_x & 0 & 0 \\ 0 & \rho_y D_y & 0 \\ 0 & 0 & 0 \end{bmatrix} \quad (4.57)$$

The D_x and D_y terms are computed by differentiation of the σ_{sr} expression with regard to ε_{sm} . This is performed jointly with the algorithm presented in Box 4.7. After transformation back to the global coordinate system, the composite stiffness matrix is obtained by adding the steel and concrete stiffness matrices.

4.3.3.4 Examples

Tensile tests

In this numerical test, a single finite element was subjected to uniaxial tension with varying reinforcement angles with respect to the external force. The results are depicted in Figure 4.15 for $\alpha = 0$ and 45° . The adopted steel properties are $f_{sy,x} = f_{sy,y} = 500\text{MPa}$, $f_{su,x} = f_{su,y} = 625\text{MPa}$, $\varepsilon_{su,x} = \varepsilon_{su,y} = 50\%$ and $E_s = 200\text{GPa}$. The concrete tensile strength is $f_{ct} = 2.6\text{MPa}$. The curves corresponding to $\lambda = 0$ are equivalent to disregarding the tension stiffening effects, while the curves with $\lambda = 1$ correspond to the maximum crack spacing. The loading/unloading behaviour of the reinforcement model is shown in Figure 4.15 (c).

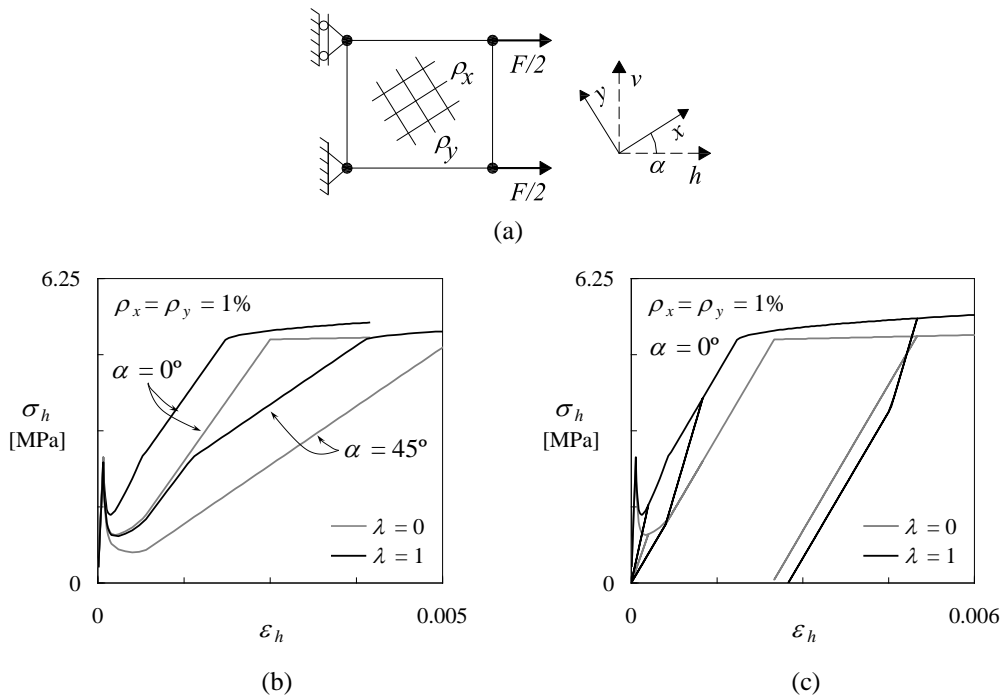


Figure 4.15 – Reinforcement model: (a) notation; (b) results for $\alpha = 0^\circ$ and $\alpha = 45^\circ$; (c) loading/unloading/reloading test.

Mesh objectivity

Whenever the reinforcement steel content is less than the minimum, the strain averaging concept implied in the formulation of the RC cracked membrane element described in Chapter 3 is no longer valid. In this case, the formation of a stabilized array of regularly spaced cracks does not occur, and the structural behaviour is governed by the propagation of one, or a few cracks. As discussed in Section 4.2, this has implications in the formulation of the constitutive laws used within finite element models. Similarly to the unreinforced concrete case, deformations tend to localize in a single finite element and some kind of localization limiter must be introduced in the constitutive laws to ensure objectivity of the results with regard to the finite elements size. According to the TCM, the averaging of the reinforcement strains is performed along a length equal to the average crack spacing s_{rm} (see Figure 3.10). For consistency with the description of the strain field based on the concept of “weak discontinuities”, and whenever the strains are localized in the crack band h_t , the regularization of the average reinforcement strains is performed according to Eq. (4.58) in order to enforce mesh objectivity of the results.

$$\boldsymbol{\varepsilon}'_{xy} = \frac{h_t}{s_{rm}} \boldsymbol{\varepsilon}_{xy} \quad (4.58)$$

In order to illustrate this aspect, a tensile test was simulated using three different meshes, as depicted in Figure 4.16. The material properties are the same as in the previous numerical test. The concrete tensile strength of the hatched finite elements is 5% lower than that of the neighbouring elements to ensure that the first crack would occur in that predefined location. If the reinforcement is less than the minimum, the post-cracking stresses are lower than the cracking stress and the deformations localize in one finite element. This is shown in the deformed shapes of Figure 4.16 (b), where it can be seen that only the central element is stretched while the others are practically not deformed. In order to obtain the same elongation, different post cracking strains develop in each of the stretched elements. These deformed shapes correspond to a tensile test with a reinforcement content of $\rho = 0.314\%$.

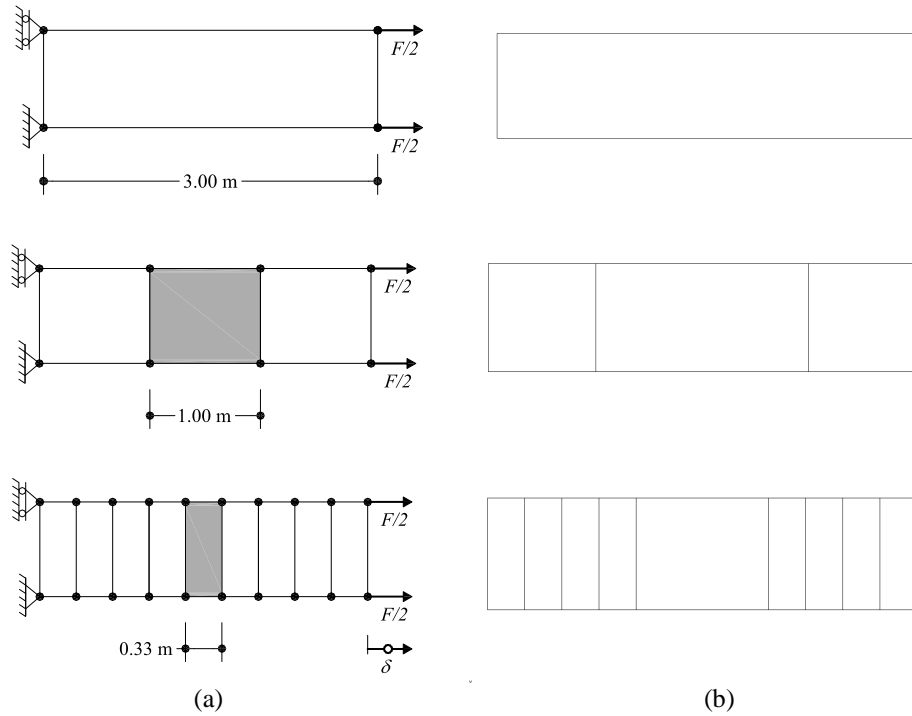


Figure 4.16 – Tensile tests with different meshes: (a) adopted finite element meshes; (b) deformed shapes (x100) after concrete cracking for $\rho = 0.314\%$.

The corresponding stress-elongation curves are depicted in Figure 4.17. The strain regularization procedure expressed by Eq. (4.58) leads to coincident post-cracking branches for all the three meshes, which is a crucial aspect if mesh independent deformation capacity estimates are to be obtained. Moreover, as the average crack spacing s_{rm} depends on the rebar diameter \emptyset , the proposed model is capable of retrieving different post-cracking branches and consequently different deformation capacities with varying \emptyset . A similar conclusion was presented by Soltani *et al* [223] using a more complex material model.

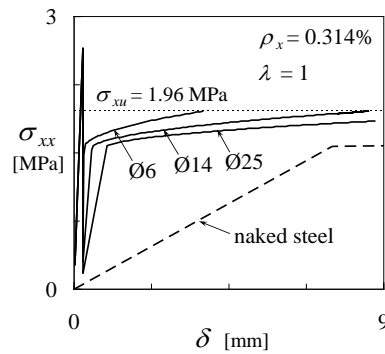


Figure 4.17 – Stress-elongation curves for a tensile chord reinforced with lower than minimum reinforcement ratio.

If the reinforcement content is larger than the minimum, the strains in the post-cracking stage no longer localize in one single finite element. A tensile test was again simulated using the three meshes of Figure 4.16 (a), but this time using a reinforcement ratio of $\rho = 1\%$. The tensile strength was randomly distributed along the mesh (with a mean value of $f_{ct} = 2.6\text{MPa}$) in order to avoid simultaneous formation of cracks in all the finite elements, thus reflecting the real crack pattern development more closely.

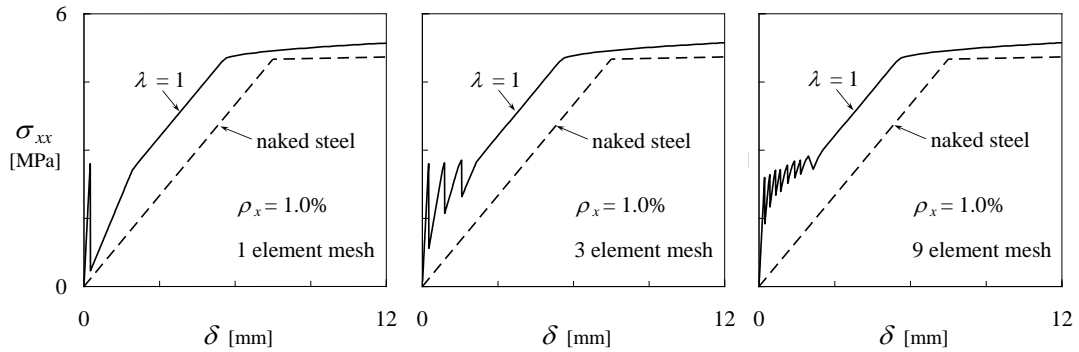


Figure 4.18 – Stress-elongation curves for a tensile chord reinforced with higher than minimum reinforcement ratio.

The results of the simulations are presented in Figure 4.18. A brittle tensile concrete behaviour was adopted in order to emphasize the effect of the reinforcement model. During the crack formation stage, the curves differ amongst the three meshes. The saw-toothed aspect of the stress-elongation curves is due to the sequential formation of cracks. The number of teeth equals the number of finite elements in the mesh. As expected, in the stabilized cracking stage all the three curves coincide. In this case, the rebar diameter exerts no influence of the post-cracking curves.

Push off tests with passive confinement

In this numerical test, the combined behaviour of both the crack shear stress transfer and reinforcement models is evaluated. A uniaxially reinforced quadrilateral element was firstly pre-cracked in uniaxial tension and stretched until reaching $\varepsilon_{xx} = 0.371 \times 10^{-3}$. This corresponds to the end of the first phase of loading, as indicated in Figure 4.19. In a second phase, shear forces were applied. In this case, confinement is only exerted by the reinforcement steel. Due to shear dilatancy, the reinforcement stresses increase with the applied shear forces. The adopted material properties are the same as above, that is $f'_c = 30\text{MPa}$, $f_{ct} = 2.6\text{MPa}$, $f_{s,y,x} = f_{s,y,y} = 500\text{MPa}$, $f_{su,x} = f_{su,y} = 625\text{MPa}$, $\varepsilon_{su,x} = \varepsilon_{su,y} = 50\%$ and $E_s = 200\text{GPa}$.

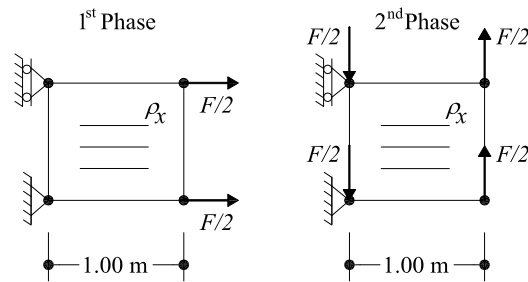


Figure 4.19 – Push-off tests with passive confinement (variable crack opening).

Several analyses were performed and the results are presented in Figure 4.20. The influence of the rebar diameter, reinforcement content and crack spacing on the crack shear behaviour is illustrated. In all the presented analyses, shear failure occurred after reinforcement yielding.

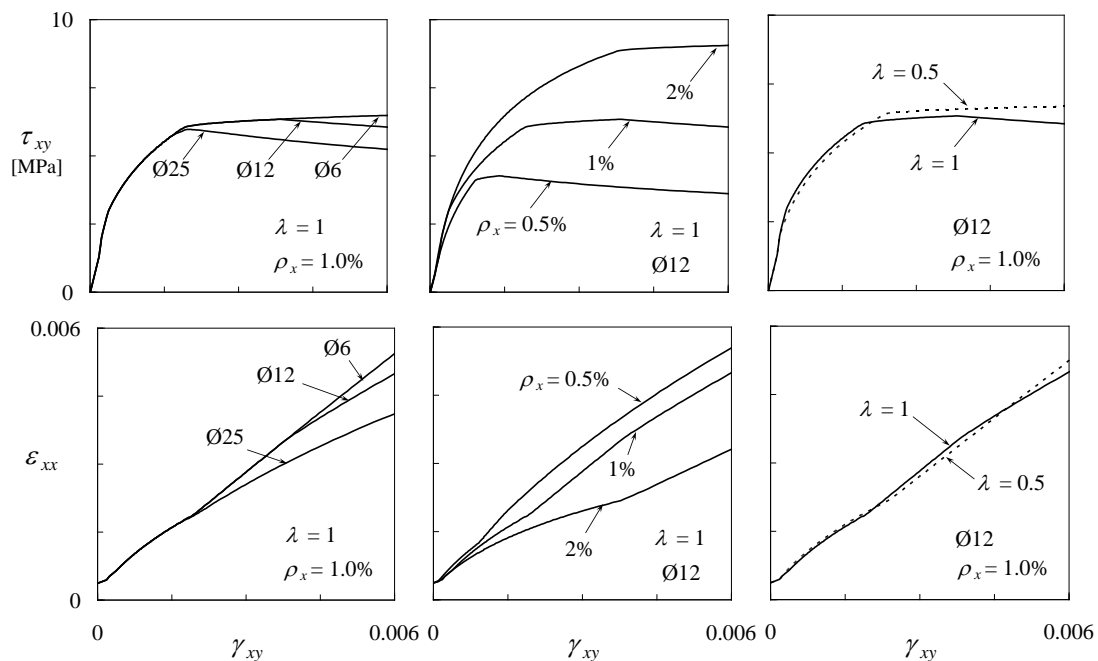


Figure 4.20 – Push off tests with passive confinement: (a) effect of the rebar diameter; (b) effect of the reinforcement content; (c) effect of the crack spacing.

Another test was additionally performed consisting in the application of reversed cyclic shear loading in phase 2 with increasing cycling amplitude. The results are depicted in Figure 4.21, where the numbers indicate the loading sequence. It can be seen that the proposed formulation renders physically consistent results.

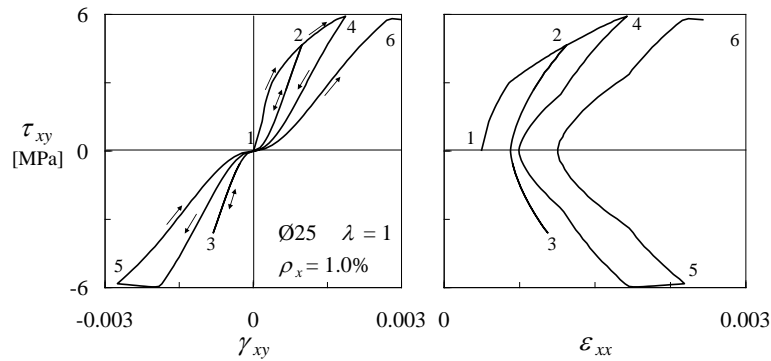


Figure 4.21 – Cyclic push off tests with passive confinement.

4.4 Extension to shell elements

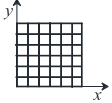

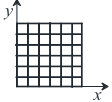
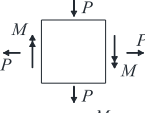
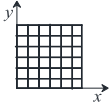
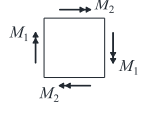
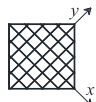
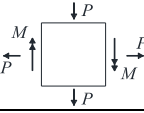
The extension of the proposed algorithm from plane stress to shell elements substantially enlarges the range of applicability of the proposed model to more general structural forms. In the present formulation, the shell element is assumed as a series of juxtaposed layers subjected to in-plane forces. This means that out-of-plane shear nonlinear effects are not accounted for and only out-of-plane bending is considered besides the in-plane shear and axial stresses. If out-of-plane shear is suspected to govern the behaviour, the Critical Shear Crack Theory [81; 164; 166; 196] can be used together with the proposed models to determine the shear resistance and corresponding deformation capacity, as outlined in the report [82]. This theory can make use of the bending deformations for determining the shear and punching strengths of slabs and beams. However, the analysis of out-of-plane shear effects is out of scope of the present work.

Polak and Vecchio [188] undertaken a test program to investigate the behaviour of shell elements subjected to biaxial bending and in-plane load conditions. The four test specimens were panels 1524x1524x316 mm in dimension reinforced with two layers of deformed bars in each of the two orthogonal directions. The specimens were subjected to various combinations of biaxial bending and in-plane loads using the “Shell-Element Tester” at the University of Toronto. Details regarding the test parameters are given in Table 4.1.

Specimen SM1 was loaded in pure uniaxial bending along the stronger reinforcement direction. The loading of SM2 involved uniaxial bending coupled with in-plane tensile forces in-line with the stronger reinforcement. Specimen SM3 was tested in pure biaxial bending. Of particular interest are the results of test SM4 because of the skew direction of

the reinforcement with respect to the applied bending and in-plane tensile forces. Significant reorientation of the stress fields was reported when the weaker reinforcement yielded.

Table 4.1 – Test parameters

Name	f'_c [MPa]	Reinforcement pattern	ρ_x^c [%]	ρ_y^c [%]	Loading pattern	Loading ratio
SM1	47		1.25 ^a	0.42 ^b		-
SM2	62		1.25 ^a	0.42 ^b		M/P = 0.25 m
SM3	56		1.25 ^a	0.42 ^b		M ₁ /M ₂ = 3.2
SM4	64		1.32 ^a	0.44 ^b		M/P = 0.25 m

^a $f_{sx} = 425\text{MPa}$, $\varnothing_x = 19.5\text{ mm}$

^b $f_{sy} = 430\text{MPa}$, $\varnothing_y = 11.3\text{ mm}$

^c per layer

Since a uniform state of stress and strain was applied to the specimens, these were modelled using one single finite element with four nodes. Five layers were used and the Simpson integration rule is used along the layer thickness. Five integration points were used in the inner layer while only three were used in the others. Predicted and observed moment-curvature responses are compared in Figure 4.22. Good correlation is observed, thus providing further validation to the proposed model. In the tensioned layers of specimen SM4 two orthogonal cracks developed and shear stresses were induced due to the skew direction of the reinforcement. In this case, stiffness degradation is more gradual. Even in this demanding situation the proposed algorithm revealed good convergence characteristics.

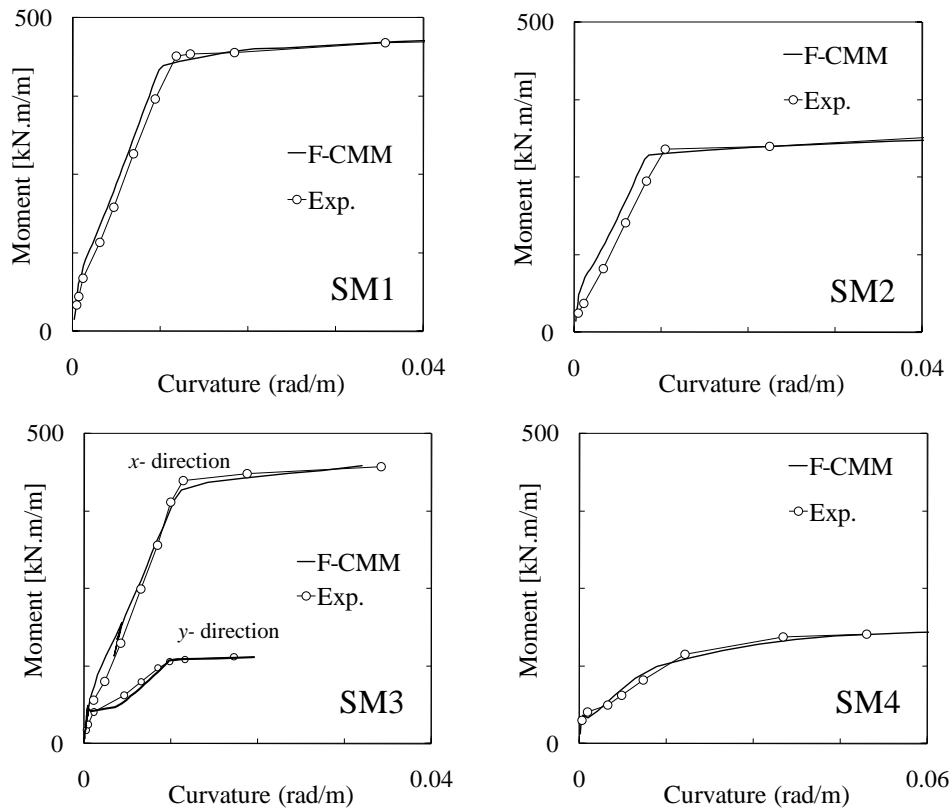


Figure 4.22 – Moment vs. curvature relationships for the panels of the SM series

4.5 Concluding remarks

The basic concepts behind the computational models for nonlinear analysis of structural concrete elements were presented and a total strain constitutive model for accommodating the RC cracked membrane element constitutive laws devised in Chapter 3 was developed. The implemented algorithm was described in detail and some simple validation examples were presented to illustrate the model response. The implementation was extended to shell elements and good agreement was obtained when comparing the calculated results with experimental data collected on RC shell elements subjected to bending and membrane loads. Good convergence characteristics were exhibited in the analysed examples. The validation of the proposed model at the structural level is presented in the following chapter.

5 Analysis of shear critical elements

5.1 General

Following the previously performed validation at element level, which included the extensive set of RC panels analysed in Chapter 3, in this chapter the validation at the structural level of the proposed constitutive model is presented. This validation is made using a set of experimental tests on large scale structural elements, which were criteriously selected to provide a stringent test to the capabilities of the model. In general, the validation presented here was targeted at evaluating the accuracy of the model in the: (1) calculation of shear failure loads and corresponding failure mechanisms; (2) determination of the load-deformation curves and of the deformation capacity of large scale beams; (3) simulation of the observed cracking patterns and calculation of the corresponding crack widths. Each of the selected test series represents a specific feature of the structural behaviour that should be properly modelled in order to allow improved structural analyses of existing concrete bridges. Where appropriate, comparisons with codes of practice are presented for reference.

All the required concrete related parameters are calculated automatically from f'_c according to what has been exposed previously. Therefore, f'_c is the only concrete related parameter that needs to be specified. The only remark goes to the parameter f_{c0} . In Chapter 3, f_{c0} was taken equal to 20MPa. However, in the following examples better estimates of the effective concrete compressive strength $f_{c,ef}$ were obtained with $f_{c0} = 30$ MPa. This fact can be attributed to some degree of out of plane confinement that is present in the critical regions of the webs, thereby delaying the splitting failure mode.

The structural elements were modelled with 8 node plain stress finite elements using the default 2x2 Gaussian integration rule. The reinforcement contribution is directly taken into account in the constitutive laws. Therefore, there is no need for using dedicated finite elements for modelling the reinforcements. However, embedded truss elements are required for modelling the post-tensioning cables or prestressing strands, for which the available elements in the DIANA element library are used.

5.2 Shear in continuity regions

5.2.1 Description and objectives

The goal of the VN test series presented in this section was to investigate the behaviour of webs of structural concrete girders with no plastic deformation in the chords, having low shear reinforcement ratios ($\rho_w=0.335\%$) and correspondingly flat inclinations of the concrete compressive struts at failure. The state of stress is similar to that observed outside the support regions of a continuous girder (Figure 5.1). These specimens can be assumed to reproduce the behaviour of typical continuity, or B-, regions. For that purpose a dedicated testing facility was developed by Kaufmann and Marti at ETH Zürich, allowing the investigation of elements of beams rather than entire girders. For further details refer to test report [119].

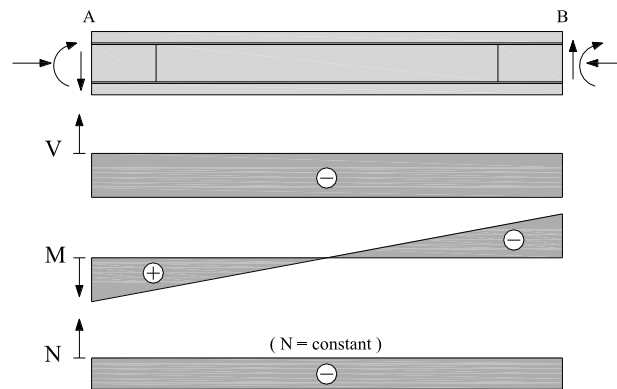


Figure 5.1 – Internal forces in the beams of the VN series.

The VN series is constituted by four identical 5.84m long and 0.78m high I-shaped beam segments. These were monotonically loaded in shear until failure with zero moment at midspan, as shown in Figure 5.1. The longitudinal reinforcement was designed to remain elastic during the test. The specimens VN1 and VN3 were pre-cracked in tension before the application of the shear forces and are not analysed here. The specimen VN4 differs from VN2 because it was subjected to a constant compressive axial force of $N = 1 \text{ MN}$ (which is equivalent to an initial uniform compressive stress of 3.2MPa). The geometry and reinforcement content of the beams are presented in Figure 5.2 together with the adopted finite element mesh. The shaded elements in Figure 5.2 (c) were included to reproduce the real external force eccentricities with respect to the beam. The material

properties are given in Table 5.1. The zones corresponding to different material properties are identified in Figure 5.2 (c).

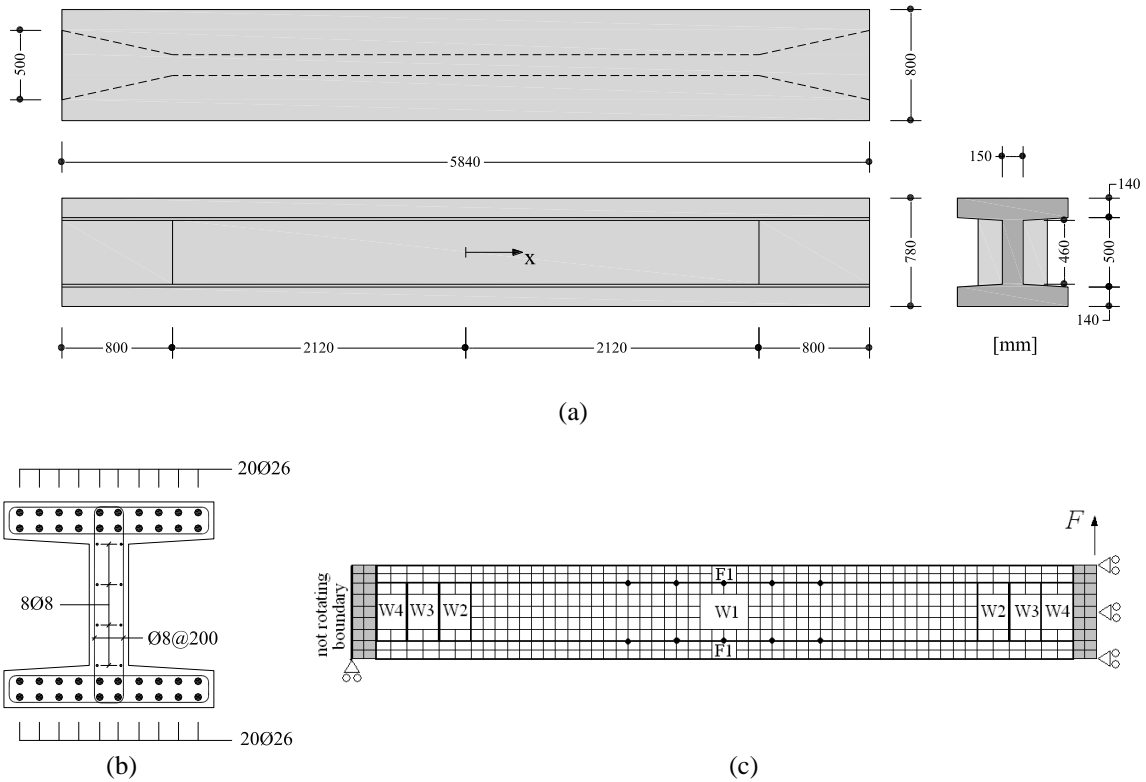


Figure 5.2 – VN series: (a) Geometry; (b) Reinforcement content; (c) Finite element mesh. The black dots indicate the nodes whose displacements were used for calculating the average web deformations.

Table 5.1 – Material properties of the beams VN2 and VN4

Zone	t [m]	f'_c [MPa]	λ	ρ_x [%]	ϕ_x [mm]	$f_{sy,x}$ [MPa]	$f_{su,x}$ [MPa]	$\epsilon_{su,x}$ [‰]	ρ_y [%]	ϕ_y [mm]	$f_{sy,y}$ [MPa]	$f_{su,y}$ [MPa]	$\epsilon_{su,y}$ [‰]
F1	0.80		1	8.849	26	539	644	118	0.126	8	510	604	53
W1	0.15	52.6 (VN2)	0.5	0.558	8	510	604	53	0.335	8	510	604	53
W2	0.258		0.5	0.682	8	510	604	53	0.628	8	510	604	53
W3	0.475	61.9 (VN4)	0.5	0.370	8	510	604	53	0.352	8	510	604	53
W4	0.692		0.5	0.254	8	510	604	53	0.242	8	510	604	53

Due to the small amount of stirrups, large web crack spacings could be expected if these were only governed by the web reinforcement content. In the webs, the crack spacing is often governed not only by the web reinforcement but also by the crack spacing in the tension chord. Therefore, in the analyses presented in this chapter different values were adopted for the parameter λ in the flanges and in the webs. Unless otherwise stated, the maximum crack spacing ($\lambda = 1$) was considered in the flanges and the minimum crack spacing ($\lambda = 0.5$) was adopted in the webs. Although some fine tuning could be performed,

reasonable estimates of the crack spacing and crack widths were generally obtained. In the case of beam VN4, the axial force was applied in the first loading step. Afterwards the shear force F was incremented until failure, see Figure 5.2 (c).

5.2.2 Results

5.2.2.1 Failure loads and failure mechanisms

Collapse was governed by failure of the web in the central portion of the girders in all the tests. In girder VN2, collapse was triggered by stirrup rupture with some spalling of the web concrete cover. Specimen VN4 exhibited a web crushing failure. These failure modes were accurately predicted by the F-CMM. The R-CMM predicts web crushing failures for both VN2 and VN4. The failure loads and failure modes are summarized in Table 5.2. It can be seen that the limitation on the inclination of the web struts governs the ultimate loads predicted by the EC2 [46] variable angle truss model. The F-CMM provides the best estimates of the failure loads.

Table 5.2 – Comparison between experimental and calculated failure loads and failure modes

	N [kN]	Experimental		F-CMM			R-CMM			EC2		
		V_u [kN]	Mode (1)	V_u [kN]	Mode (1)	Rat. (2)	V_u [kN]	Mode (1)	Rat. (2)	V_u [kN]	Mode (3)	Rat. (2)
VN2	0	548	SF	537	SF	1.02	565	WC	0.97	404	S	1.36
VN4	1000	564	WC	566	WC	1.00	604	WC	0.93	404	S	1.40

⁽¹⁾Failure mode: SF – Stirrup failure; WC – web crushing failure; WS – web sliding failure

⁽²⁾Failure load ratio: $V_{u,exp} / V_{u,calculated}$

⁽³⁾Failure mode according to the EC2 variable angle truss model: S – failure governed by the stirrups (in this case, the limitation on the inclination of the struts to $\cot\theta = 2.5$ governs); C – failure governed by crushing of the web.

In the case of cracked concrete, the state variable $E_{max} = -\varepsilon_t / \varepsilon_{0,ef}$ is an indicator of whether concrete crushing has or not occurred. If $E_{max} > 1$ the post-peak branch of the stress strain curve has been achieved. In this stage of the curve, signs of concrete cover spalling or concrete delamination are to be expected in real specimens. The contour levels with the values of E_{max} at failure are presented in Figure 5.3. It can be seen that the F-CMM predicts only minor signs of web cover spalling near the flanges for beam VN2. Similarly to the test, collapse was triggered by rupture of the vertical reinforcement. This can be confirmed in Figure 5.4, where the contour levels with the vertical reinforcement stresses at the cracks are presented. The red colour corresponds to regions where the tensile strength of the

stirrups ($f_{su} = 604 \text{ MPa}$) was exceeded. In the case of the R-CMM, the stresses in the vertical reinforcement are well below this value.

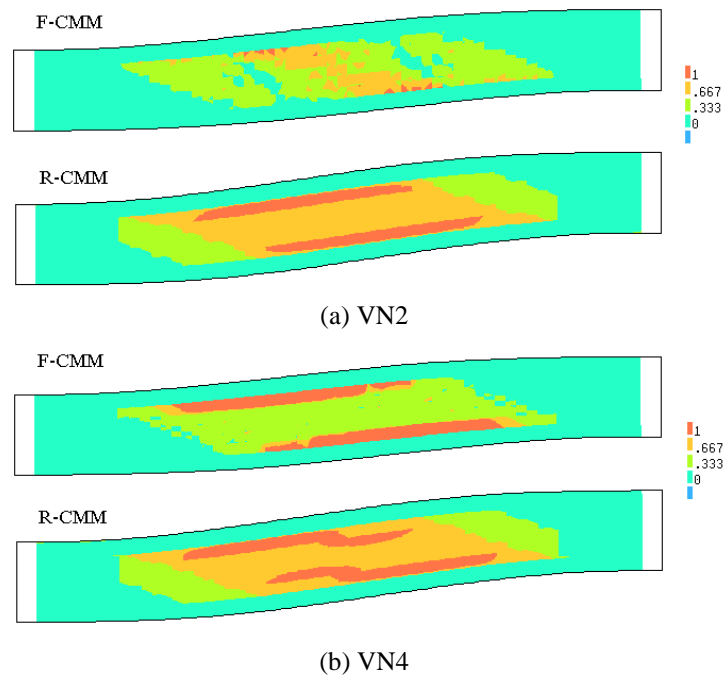


Figure 5.3 – Deformed shape (x10) with the E_{max} contour levels at failure.

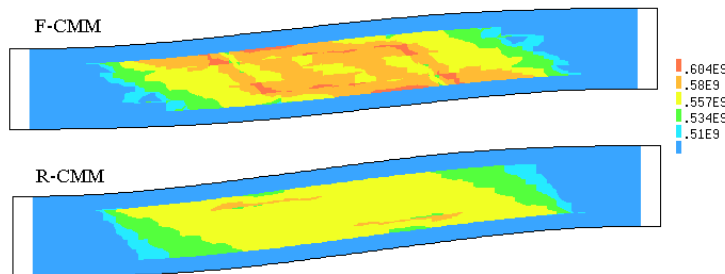


Figure 5.4 – Beam VN2: deformed shape (x10) at peak load with the contour levels representing stirrup stresses at the cracks (in Pa).

5.2.2.2 Force-deformation curves

In Figure 5.5 the calculated and the measured average deformations in a 1.60m (from $x = -0.80 \text{ m}$ to $x = +0.80\text{m}$) long web segment at the centre of the beams are compared. In the test, the average deformations were obtained from the relative displacements between targets positioned in the webs or in the flanges of the beams, which explains the two curves for the experimental results presented in each plot. The values corresponding to the numerical results were determined from the displacements of the nodes indicated in Figure

5.2. Parameter ε_y is the average vertical strain within the measuring domain, ε_2 is the average principal compressive strain and α_e is the angle of the principal average compressive strain with the beam longitudinal axis. The agreement between the calculated and the measured force-deformation curves is good, especially for the F-CMM. The R-CMM tends to overestimate the stiffness after stirrup yielding. In the case of beam VN2, stirrup failure is predicted by the F-CMM, but for an average vertical strain that is smaller than that observed in the test. This can be attributed to the fact that the model cannot reproduce bond slip occurring across several cracks. A close inspection to the picture of beam VN2 at failure presented in Figure 5.6 (a) reveals that stirrup debonding is likely to have occurred in the test. Therefore, conservative estimates of the stirrups deformation capacity are to be expected in similar cases. The angle α_e is accurately predicted, which is an indication that both the crack kinematics and inclination of the struts are well reproduced. At failure, α_e values down to 15° were obtained.

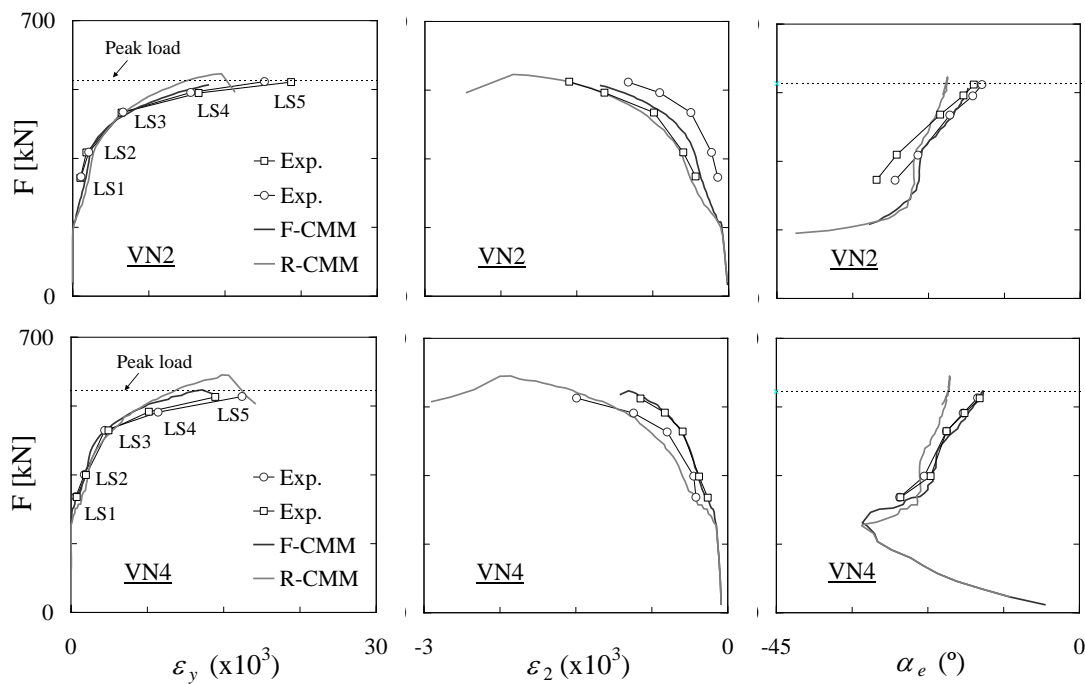


Figure 5.5 – Force vs. average deformation related parameters. Manual measurements were made at the load steps LS_i.

5.2.2.3 Cracking patterns

The experimental and calculated cracking patterns at failure are presented in Figure 5.6 and Figure 5.7. The calculated cracking patterns are represented by lines with the direction of the crack. Its thickness is proportional to the crack opening using a three level scale.

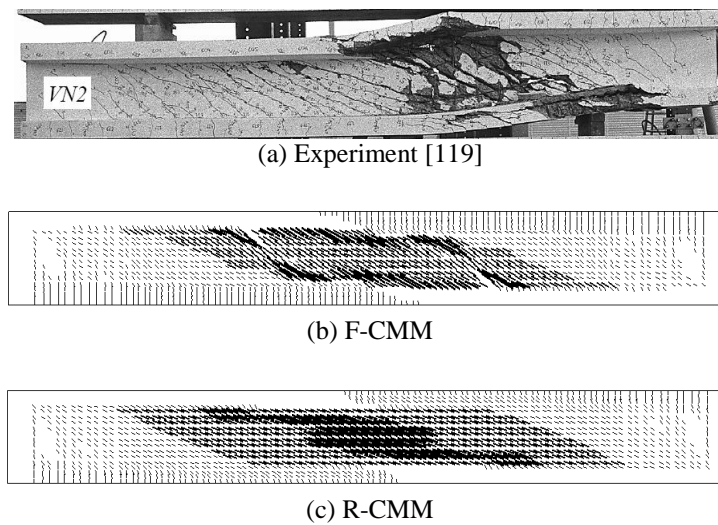


Figure 5.6 – Beam VN2: cracking patterns at failure.

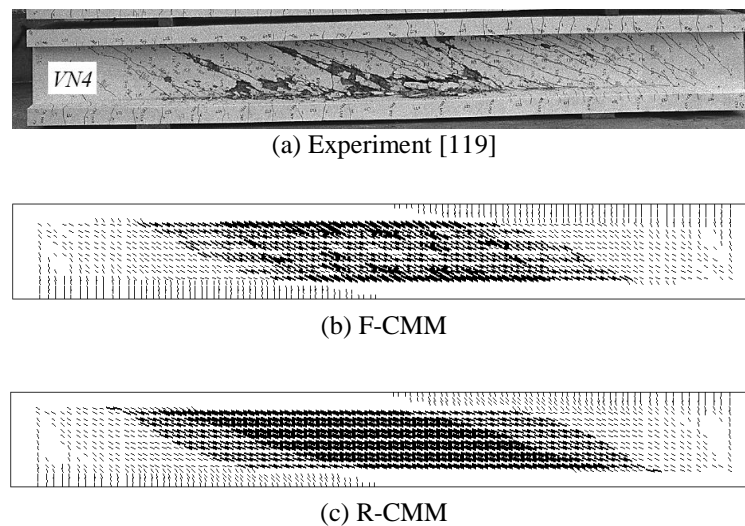


Figure 5.7 – Beam VN4: cracking patterns at failure.

The crack angles and the crack widths are presented in Figure 5.8. The load steps LS_i are identified in Figure 5.5. The crack angles are better predicted by the F-CMM. By allowing continuous crack rotation, the crack angles calculated with the R-CMM tend to deviate from the measured ones as loading progresses. The crack width predictions in the webs are reasonably fitted to the measurements, although some underestimation of the maximum crack width is observed in the first load stages. However, in these stages the cracking pattern is not yet stabilized and increased scatter must be expected.

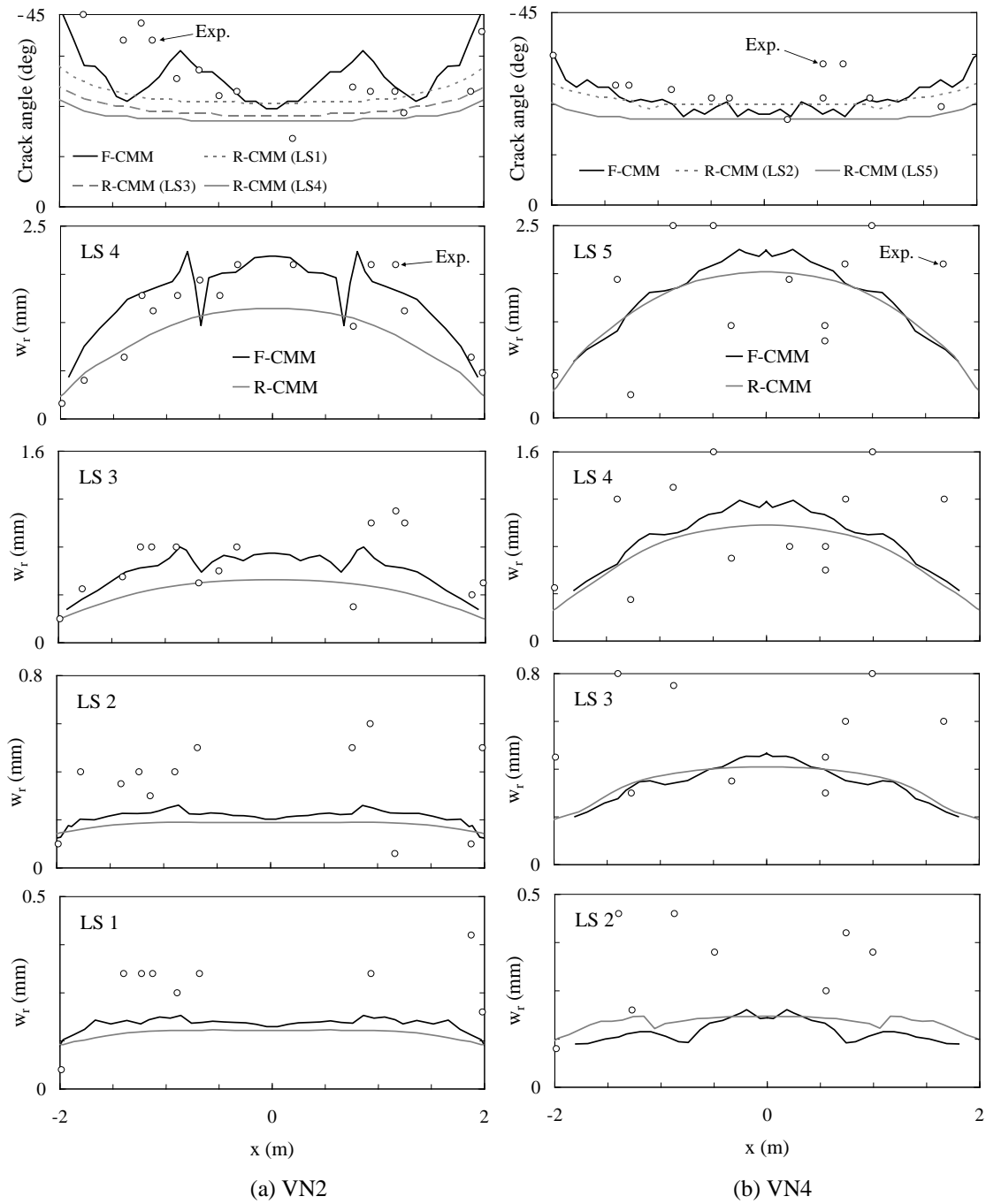


Figure 5.8 – Crack angles and crack widths compared to experimental evidence: (a) VN2; (b) VN4.

5.3 Shear in discontinuity regions with plastic reinforcement strains

5.3.1 Description and objectives

The four beams of the series MVN have the same geometry and the same shear reinforcement content as the ones from the series VN. However, in contrast to series VN, an additional vertical jack was installed at midspan. The loading procedure simulated the behaviour of an (inverted) intermediate support of a continuous girder, see Figure 5.9. In this case, bending moments may have a significant influence on the behaviour of the girder and usually chords are plastically deformed. Note that this bending-shear interaction is not directly taken into account in the lower bound limit analysis methods specified in codes of practice. Contrary to the series VN, in these specimens failure is expected to occur in a typical discontinuity, or D-, region.

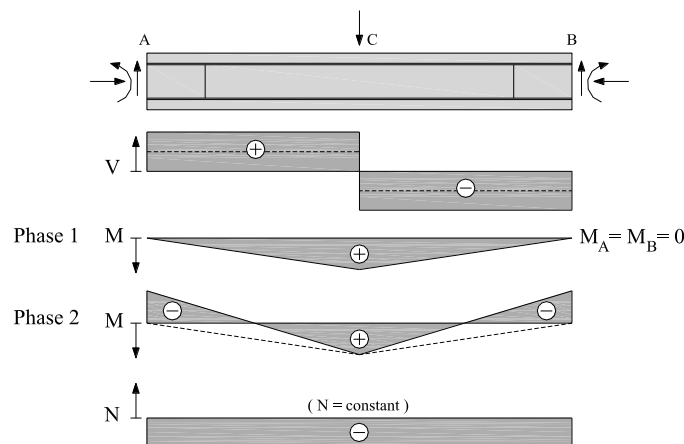


Figure 5.9 – Internal forces in the beams of the MVN series.

In the first phase of the test, horizontal forces were controlled such that moments at the element ends were null. In the second phase, after reaching the yield moment at midspan, rotations at the element ends were prevented. This second phase of the test simulated a redistribution of moments from the support region (midspan) to the span (element ends) of a continuous girder. The forces applied at the element ends were controlled so that normal forces remained constant throughout the test and shear forces on either side of the concentrated load were of equal magnitude.

All the girders contained the same amount of web reinforcement: $\rho_w=0.335\%$, equal to the one adopted in the series VN. Regarding the longitudinal reinforcement, specimens MVN1

to 3 were designed to reach the yield moment at midspan under the same net web shear (i.e. total shear minus the contribution of the inclined post-tensioning cable as shown below). MVN4 was designed not to yield at midspan during the entire test. Specimens MVN2 and MVN4 were subjected to axial compression of 1.30 MN before being loaded in shear and the axial force was held constant during the test. Specimens MVN3 and MVN4 were post-tensioned with a bonded VSL 6-7 cable ($P_u = 1.85$ MN) with an initial target force of 1.30 MN. Therefore, the initial horizontal compressive stresses in the beams were null for MVN1, 4.2MPa for MVN2 and MVN3, and 8.4MPa for MVN4. The cable layout and the reinforcement content of the beams are presented in Figure 5.10.

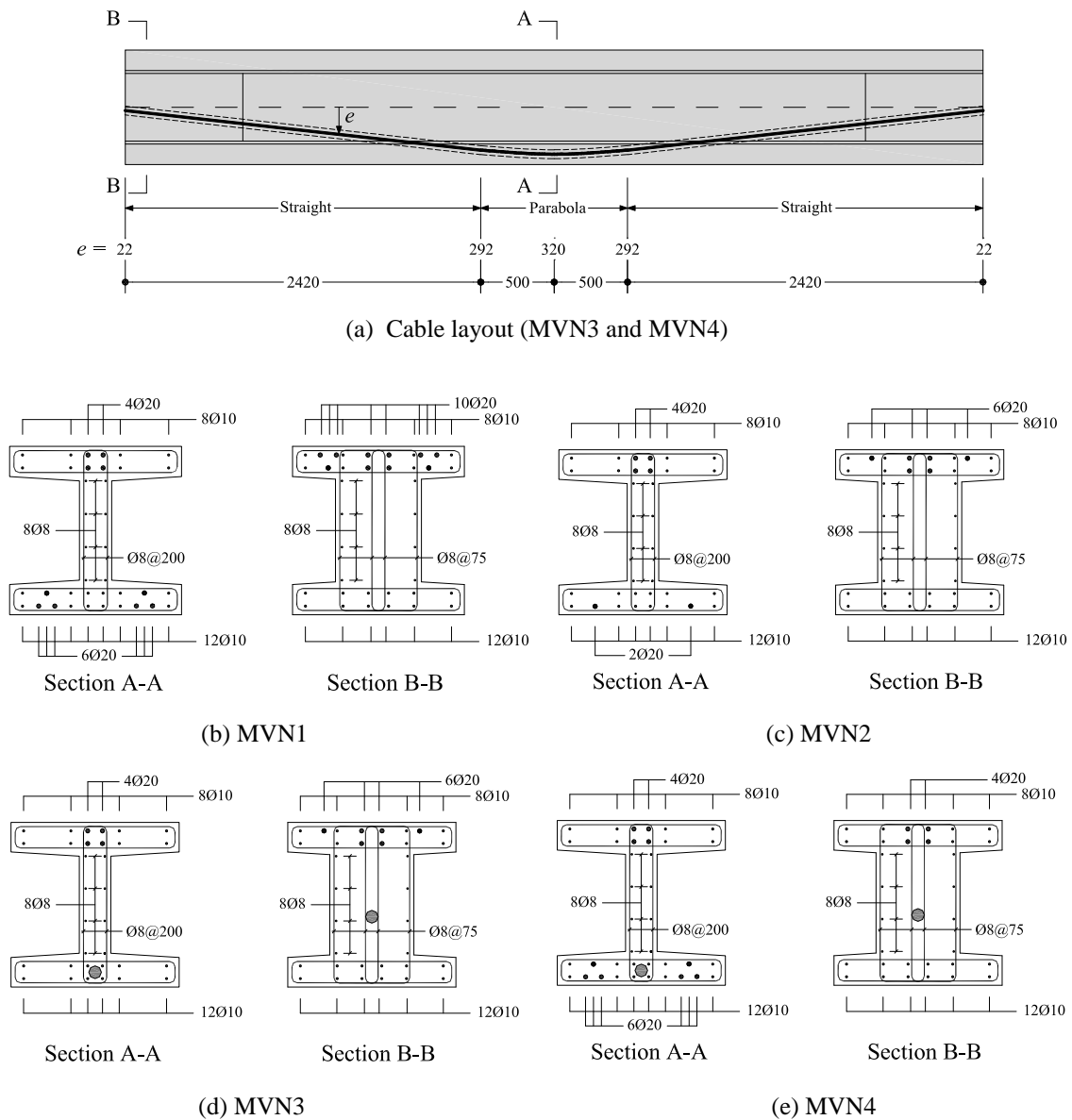


Figure 5.10 – MVN series: (a) Cable layout of beams MVN3 and MVN4; (b) reinforcement content.

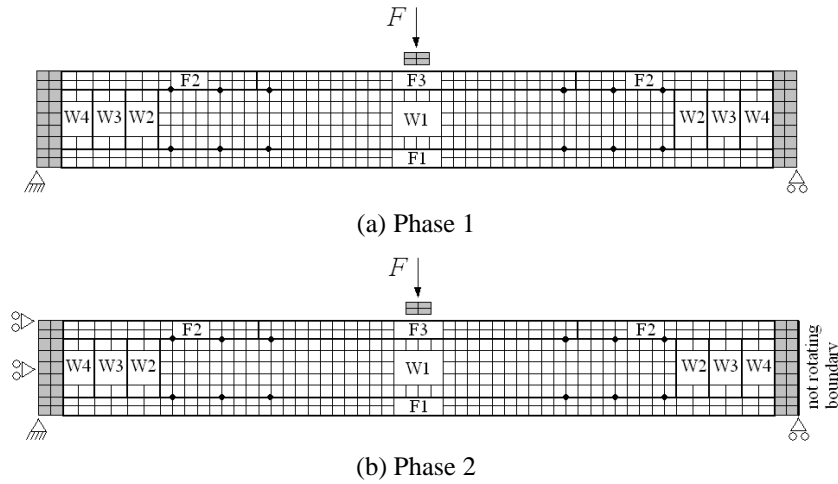


Figure 5.11 – MVN series: finite element mesh. The black dots indicate the nodes whose displacements were used for calculating the average web deformations.

Table 5.3 – Material properties of the beams MVN1 to MVN4

Zone	t [m]	f'_c [MPa]	λ	ρ_x [%]	$\varnothing_x^{(2)}$ [mm]	$f_{sy,x}^{(2)}$ [MPa]	$f_{su,x}^{(2)}$ [MPa]	$\varepsilon_{su,x}^{(2)}$ [‰]	ρ_y [%]	\varnothing_y [mm]	$f_{sy,y}$ [MPa]	$f_{su,y}$ [MPa]	$\varepsilon_{su,y}$ [‰]
MVN1													
F1	0.80	62.8	1	2.356	16	524	652	128	0.126	8	461	580	87
F2				3.142	16	528	660	127	0.378				
F3				1.571	16	524	653	130	0.126				
MVN2													
F1	0.8	58.8	1	1.309	16	518	642	128	0.126	8	461	580	87
F2				2.094	16	526	656	127	0.378				
F3				1.571	16	524	653	130	0.126				
MVN3													
F1	0.8	62.2	1	0.785	10	508	625	131	0.126	8	461	580	87
F2				2.094	16	526	656	127	0.378				
F3				1.571	16	524	653	130	0.126				
MVN4													
F1	0.8	64.3	1	2.356	16	524	652	128	0.126	8	461	580	87
F2				1.571	16	524	653	130	0.378				
F3				1.571	16	524	653	130	0.126				
MVN1 to MVN4													
W1	0.15	(1)	0.5	0.558	8	461	580	87	0.335	8	461	580	87
W2	0.258		0.5	0.682					0.628				
W3	0.475		0.5	0.370					0.352				
W4	0.692		0.5	0.254					0.242				

(1) For each beam, the uniaxial cylinder strength of the web concrete is the same adopted for the flanges.

(2) In the case of rebars with different diameters and steel properties, a weighted average value was adopted.

The adopted finite element mesh is depicted in Figure 5.11. The compatibility of the vertical displacements between the loading platen and the upper flange elements was enforced while the corresponding relative horizontal displacements were allowed. The

prestressing tendon was modelled using embedded reinforcement elements [256]. A bilinear stress-strain law was adopted with $f_{py} = 1713$ MPa, $f_{pu} = 1866$ MPa, $\varepsilon_{pu} = 60\%$ and $E_p = 190$ GPa. The adopted material properties are presented in Table 5.3. The zones corresponding to distinct reinforcement contents and element thicknesses are identified in Figure 5.11. In the first step the self-weight, the axial force and the post-tensioning force were applied. Only after the force F was incrementally increased. When the bottom longitudinal reinforcement started yielding, the boundary conditions were modified according to Figure 5.11 for the second phase of the test.

5.3.2 Results

5.3.2.1 Failure loads and failure mechanisms

The failure loads and the failure modes are summarized in Table 5.4. The calculated ultimate loads are in good agreement with the observed ones. The effect of the applied normal and prestressing forces significantly influenced the failure mode and failure loads experienced by the tested specimens. The limitation on the inclination of the web struts governs the ultimate loads predicted by the EC2 [46] variable angle truss model. Three different failure modes were observed in the tests. The contour levels of the state variable E_{max} at peak load are presented in Figure 5.12 for the MVN1 and MVN4 specimens.

Table 5.4 – Comparison between experimental and calculated failure loads and failure modes

			Experimental		F-CMM			R-CMM			EC2		
	N [kN]	P ₀ [kN]	F _u [kN]	Mode (1)	F _u [kN]	Mode (1)	Rat. (2)	F _u [kN]	Mode (1)	Rat. (2)	F _u [kN]	Mode (3)	Rat. (2)
MVN1	0	0	1063	SF	1040	SF	1.02	1157	WC	0.92	730	S	1.46
MVN2	1300	0	1208	WS	1206	WS/WC	1.00	1202	WC	1.00	730	S	1.65
MVN3	0	1300	1760	WS	1627	WC	1.08	1594	WC	1.10	1020	S	1.73
MVN4	1300	1250	1950	WC	1787	WC	1.09	1731	WC	1.13	1020	S	1.91

⁽¹⁾Failure mode: SF – Stirrup failure; WC – web crushing failure; WS – web sliding failure.

⁽²⁾Failure load ratio: $F_{u,exp} / F_{u,calculated}$.

⁽³⁾Failure mode according to the EC2 variable angle truss model: S – failure governed by the stirrups (in this case, the limitation on the inclination of the struts to $\cot\theta = 2.5$ governs); C – failure governed by crushing of the web.

The collapse of beam MVN1 was initiated by the rupture of a stirrup after some spalling of the web concrete cover. Once again, this failure mode was accurately predicted by the F-CMM, while the R-CMM predicted a web crushing failure.

The specimens MVN2 and MVN3 failed in a similar manner: half of the girder shifted over the remaining part of the element along an inclined failure surface made up of existing web shear cracks, with crushing of concrete in the flange. Spalling of the concrete cover in the web was observed, notably in specimen MVN3, which indicates crushing of the concrete in the web. This failure mode is here classified as a web sliding failure. By definition, this failure mode cannot be reproduced by the R-CMM and this model predicts web crushing failures for both specimens. As it was shown in the previous chapter, the F-CMM can reproduce such type of failure in RC panels. However, the web compressive stresses are rather high and crushing ends up to govern the computed failure mode. Nonetheless, in the case of MVN2 collapse occurred after concrete crushing in the top flange, near the loading platen. This can be confirmed by the incremental deformed shape in the post peak branch of the load-deformation curves, see Figure 5.13, which is an indication of the occurrence of a sliding shear failure. Although the localization of the crack shear strains γ_{nt} along an inclined band can be seen in Figure 5.13, this localization is not sharp enough to properly reproduce the sliding movement along the failure crack.

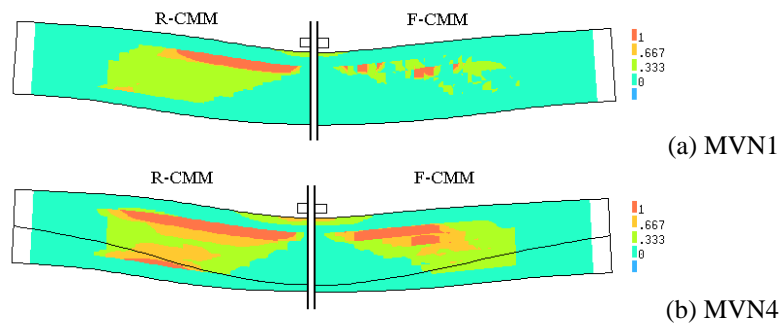


Figure 5.12 – Deformed shape (x10) after peak load with the contour levels of the state variable E_{max} .

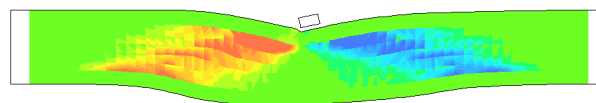


Figure 5.13 – Failure mode of beam MVN2 as calculated with the F-CMM: incremental deformed shape (x1000) after the peak load with the contour levels of the crack shear strains γ_{nt} .

The specimen MVN4 exhibited a web crushing failure. Failure was more ductile and the web concrete crushed progressively on both sides of the girder. This failure mode was correctly predicted by both the F-CMM and R-CMM. However, in both numerical analyses strain localization is observed in the web near the upper flange, see Figure 5.12 (b). This localization of the compressive strains is much more pronounced than the observed in the

experiment, where the crushing failure progressed in several regions of the web. This is an intrinsic limitation of the adopted kinematic description of the displacement field based on the weak-discontinuities concept.

5.3.2.2 Force-deformation curves

The calculated and measured average deformations are compared in Figure 5.14. Deformations were averaged over two symmetrically located and 0.80 m long web segments (from $x = \pm 1.20$ m to $x = \pm 2.00$ m). The numerical results were calculated from the relative displacements of the nodes indicated in Figure 5.11.

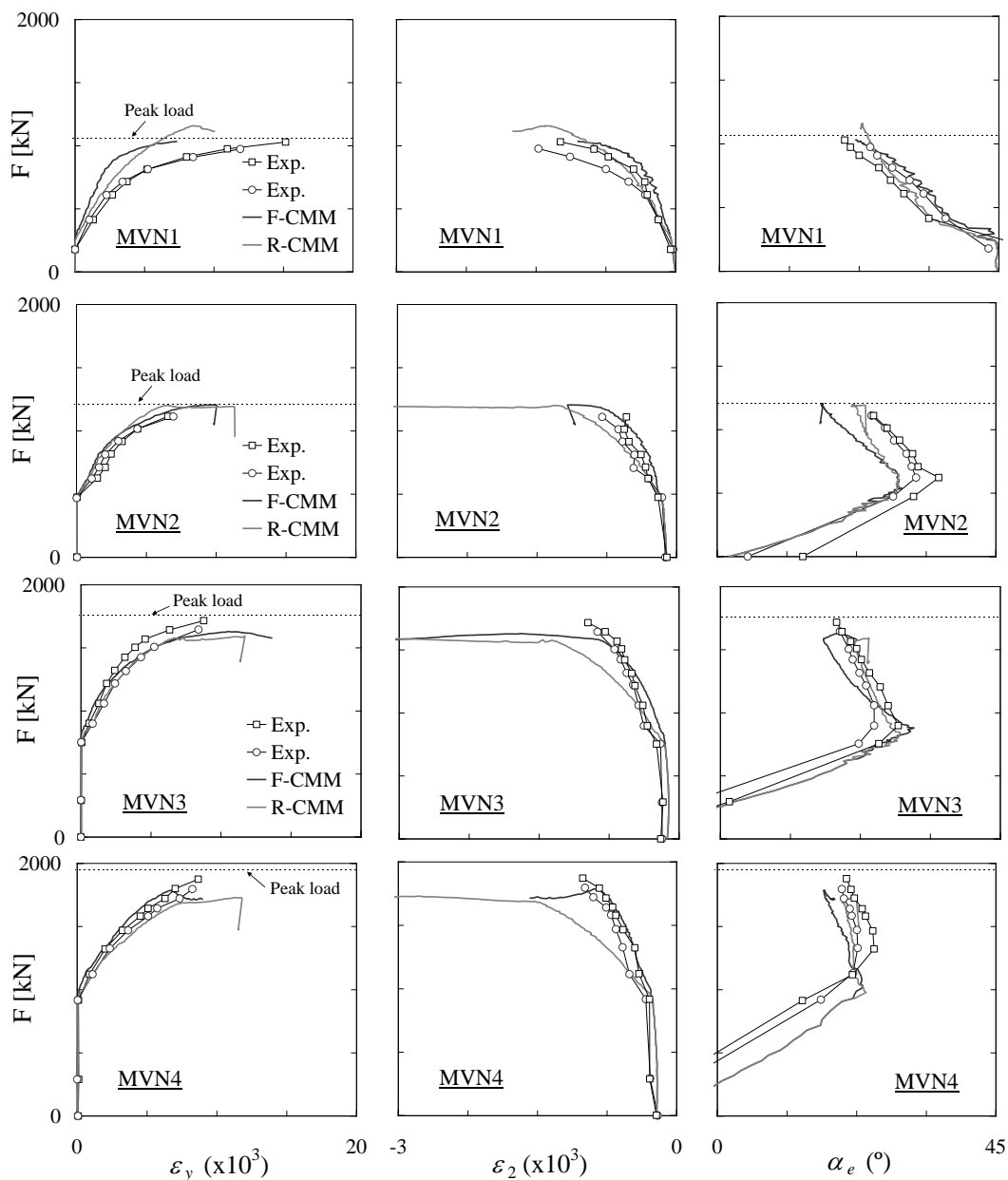


Figure 5.14 – Force vs. average deformation related parameters.

In general, the agreement between the measurements and the calculations is good. It must be remarked that these are average web strains which are directly related with the shear behaviour. Usually, a good fit between numerical and experimental results is easier to obtain if flexure related parameters (midspan displacements, for instance) are compared. The exception lies in the fit between the predicted and measured average vertical strains ε_y for specimen MVN1, which is rather poor. An overly stiff F - ε_y curve is computed with the F-CMM. This might be due to the fact that, in the test, the shear cracks in the vicinity of the vertical jack propagate through previously formed vertical flexural cracks. As discussed previously, this cannot be modelled by the F-CMM because only orthogonal cracks are allowed. In the other three tests this phenomenon was not observed and the agreement is significantly better. Still regarding specimen MVN1, the overestimation of the stiffness of the F - ε_y curve exhibited by the R-CMM is somewhat more difficult to explain. A similar behaviour was observed in the analysis of the panel PP1 (see Chapter 3) and of the beams VN2 and VN4. Although not so evident as in this case, it was then noticed that the R-CMM over-predicted both the stiffness and the ultimate shear stress of elements exhibiting significant crack shear slip in the experimental tests.

The analysis of the curves in Figure 5.14 also shows that the principal compressive strains are systematically overestimated with R-CMM. This is more noticeable in the cases where less crack shear slip is expected due to the external axial forces. In these cases, the use of a softened peak uniaxial strain in the cracked concrete stress-strain relationship could improve the results. However, this would worsen the performance in the other cases, since in the rotating crack model the crack shear slip is not independently modelled.

5.3.2.3 Cracking patterns

The experimental and calculated cracking patterns at failure are presented in Figure 5.15 to Figure 5.18. In general, the calculated crack patterns provide a good picture of the real ones. The shear failure plane of specimens MVN2 and MVN3 is not clearly evidenced in the numerical simulations due to the fact that crushing of the web concrete governed the computed failure mode, as described above.

The crack angles are compared in Figure 5.19. The F-CMM provides good estimates of the crack inclination and the effect of normal stresses is well reproduced. Similarly to what has been observed in the VN series, the crack angles predicted by the R-CMM tend to deviate from the measured ones as the loading progresses.

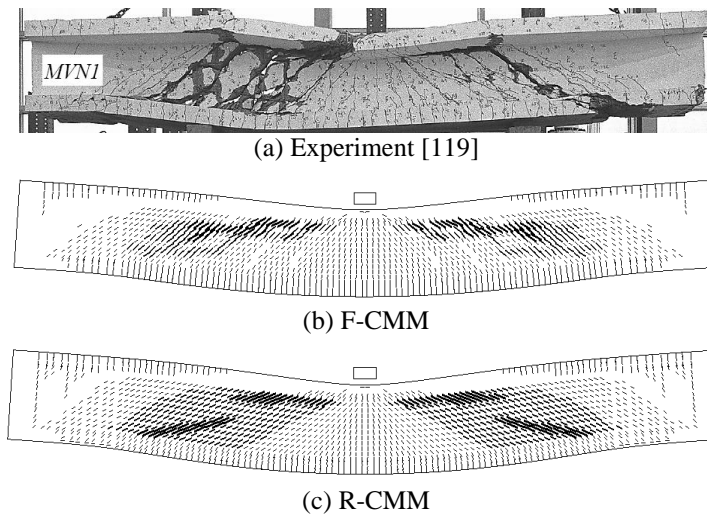


Figure 5.15 – Beam MVN1: cracking patterns at failure.

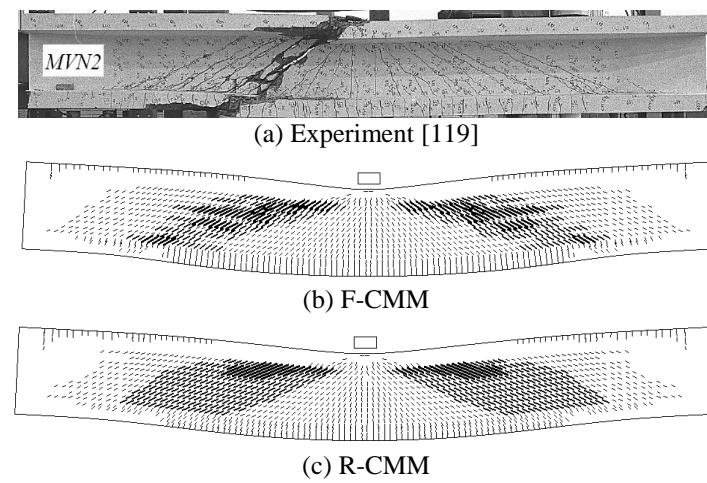


Figure 5.16 – Beam MVN2: cracking patterns at failure.

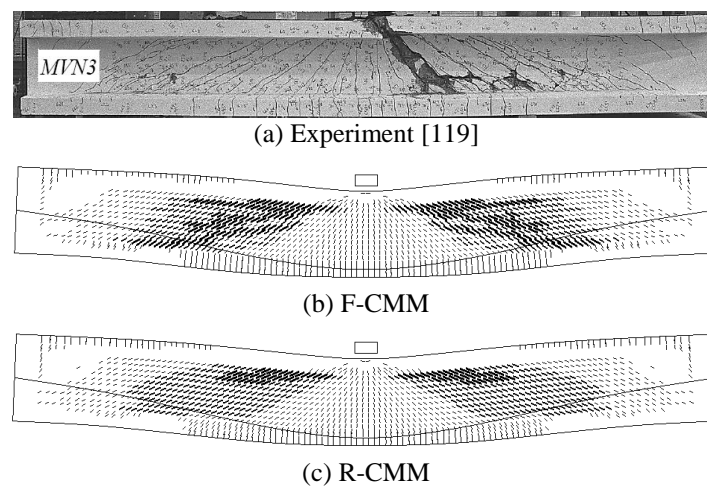


Figure 5.17 – Beam MVN3: cracking patterns at failure.

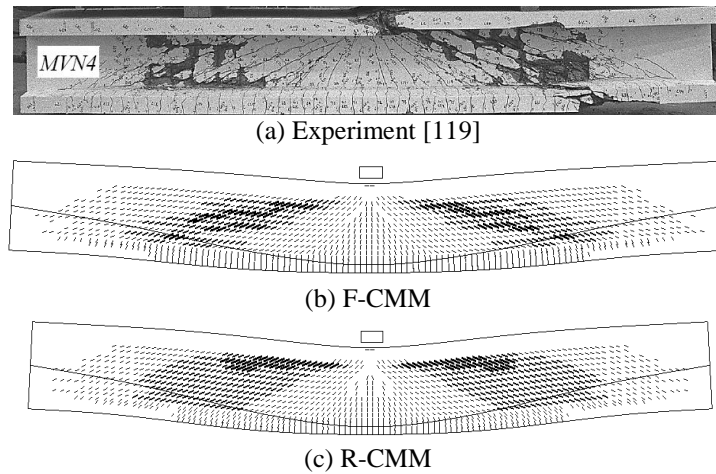


Figure 5.18 – Beam MVN4: cracking patterns at failure.

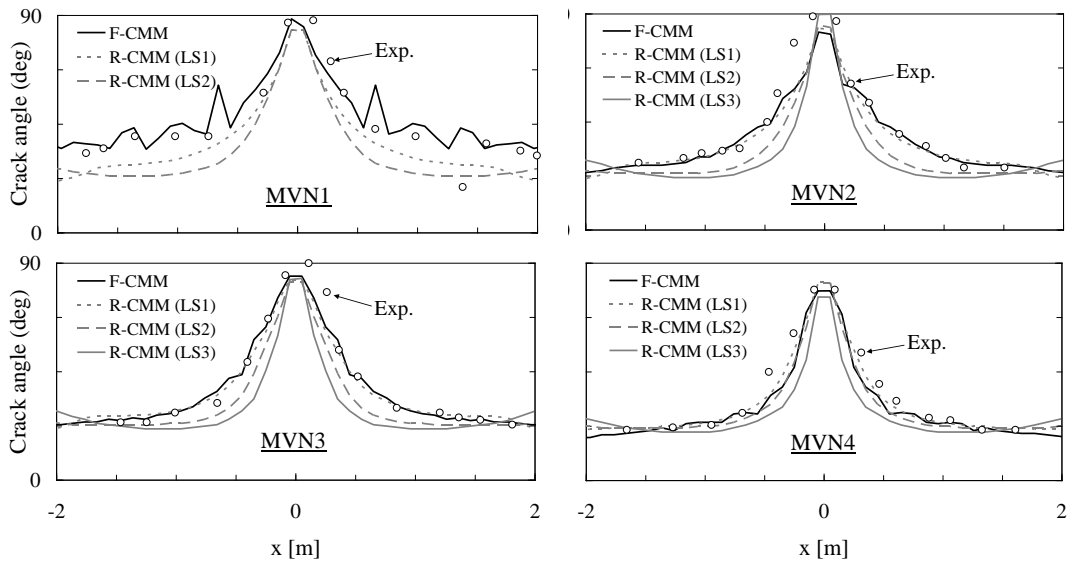


Figure 5.19 – Web crack angles for specimens MVN1 to MVN4.

5.3.2.4 Shear force carried by the various elements of the girders

It is interesting to evaluate the contribution of each element of the girder – web, flanges, and prestressing tendons – for the shear load carrying capacity. The numerical analyses allow performing such investigation. The results obtained with the F-CMM are plotted in Figure 5.20. The important role of the upper flange can be noted in the beams of the MVN series in the regions closer to mid-span, while in the beam VN4 this contribution is not so significant, as should be expected in a continuity region.

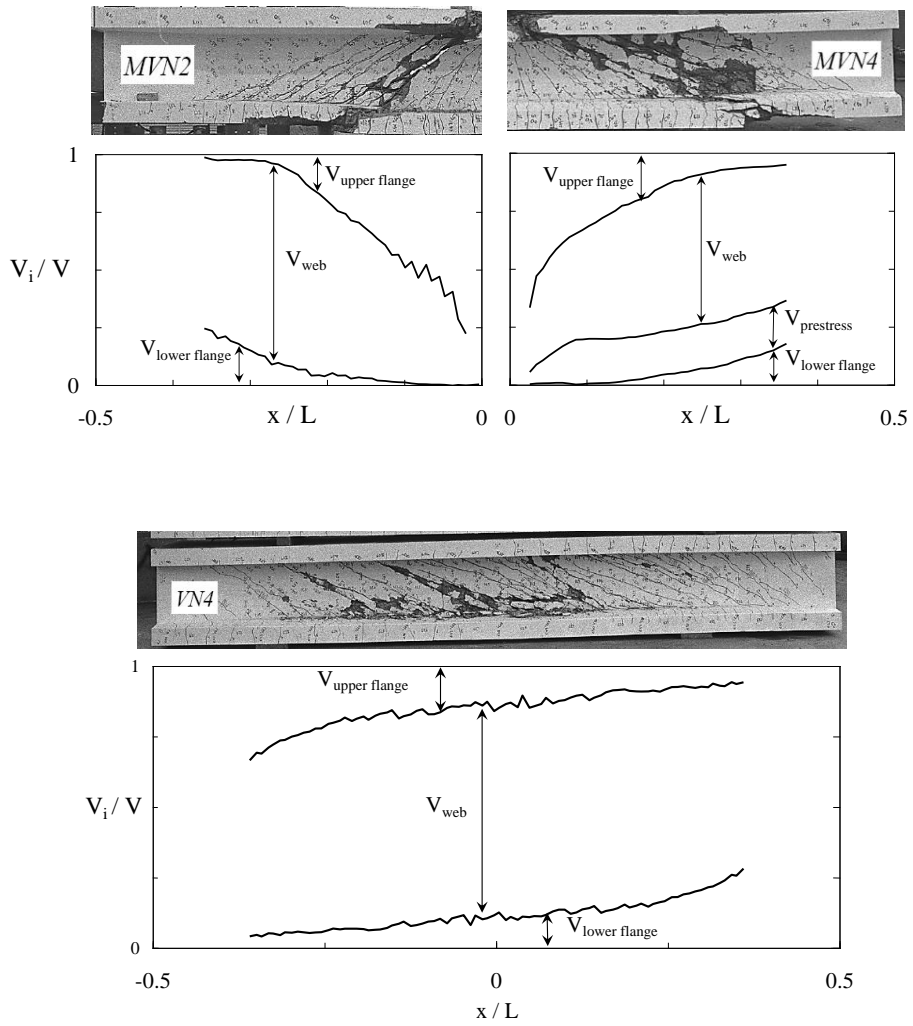


Figure 5.20 – Shear forces carried by the various elements of the girders.

5.4 High strength concrete girders critical in shear

5.4.1 Description and objectives

This testing program was performed for the NCHRP at the University of Illinois under the supervision of Hawkins and Kuchma [94]. The study aimed at extending the applicability of the shear provisions of the AASHTO LFRD Bridge Design Specifications [1] to reinforced and prestressed concrete structures with concrete strengths above 70 MPa. A total of twenty experiments on ten 1.85 m deep and 15.85 m long bulb-tee girders were performed. The girders were simply supported with a span of 15.24 m and were subjected to a uniformly distributed load over the central 13.41 m of their length. A 0.25 m deep slab was cast over each girder. The overall geometry of the tested girders is presented in Figure 5.21.

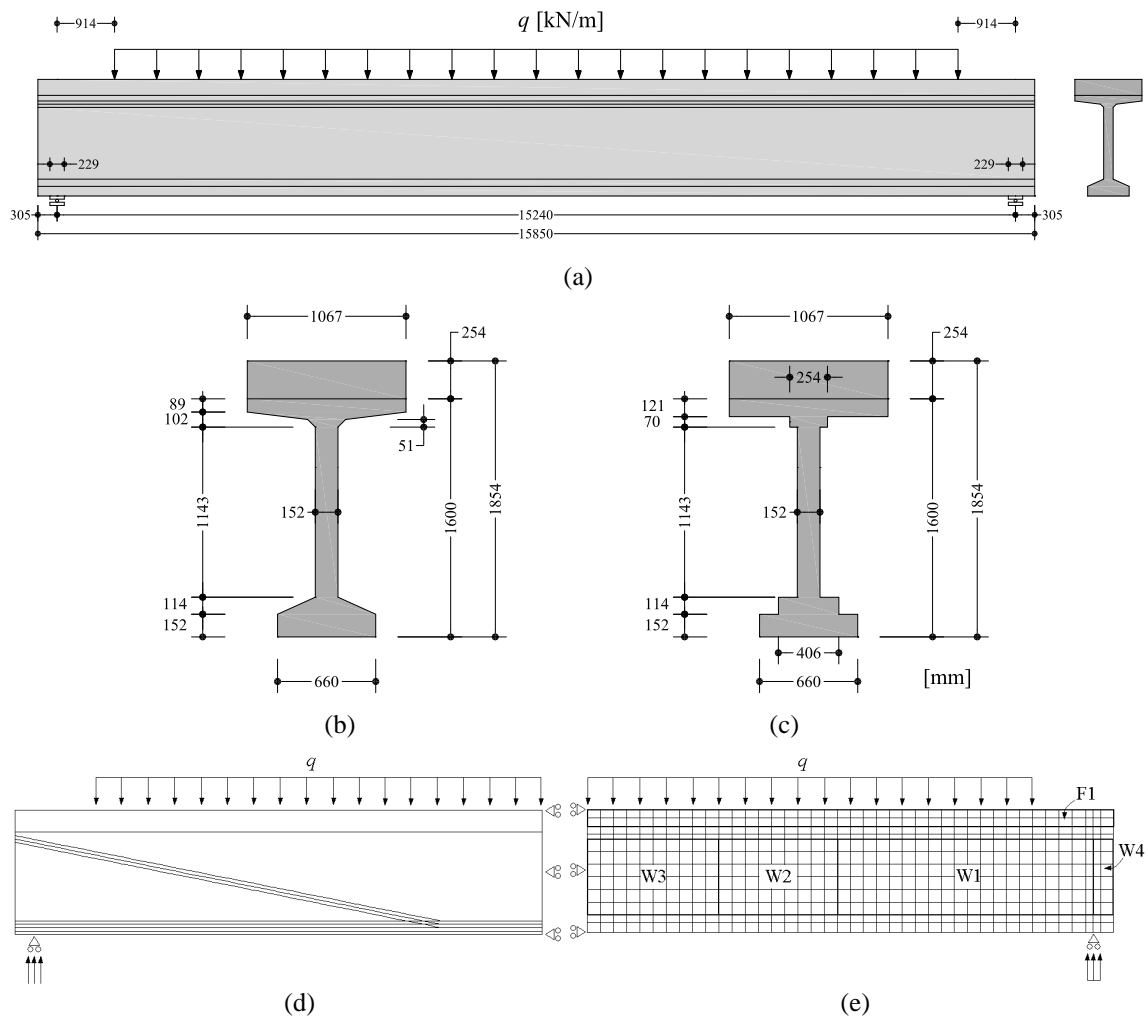


Figure 5.21 – Geometry of the tested girders: (a) Elevation; (b) Cross-section; (c) Cross-section as modelled; (d) West half of beam G1 with draped strands; (e) Finite element mesh.

Each half of each girder (designated as East and West) was designed to be different so as to obtain two test results from each girder. This was accomplished by reconstructing and strengthening the half of the girder that failed first and then reloading the girder until the other half failed. Here, only the girders G1, G2 and G5 are analysed. These girders have vertical web reinforcement ratios in the failure zone of $\rho_w = 0.56$, 0.94 and 0.18%, respectively. In girders G1 and G2, six prestressing strands were draped in the West end, thus increasing the shear strength due to the vertical component of the prestressing force. In girder G5, the difference between the East and West ends was the adoption of welded wire reinforcement in the East end, while maintaining the diameters and the spacing between the rebars.

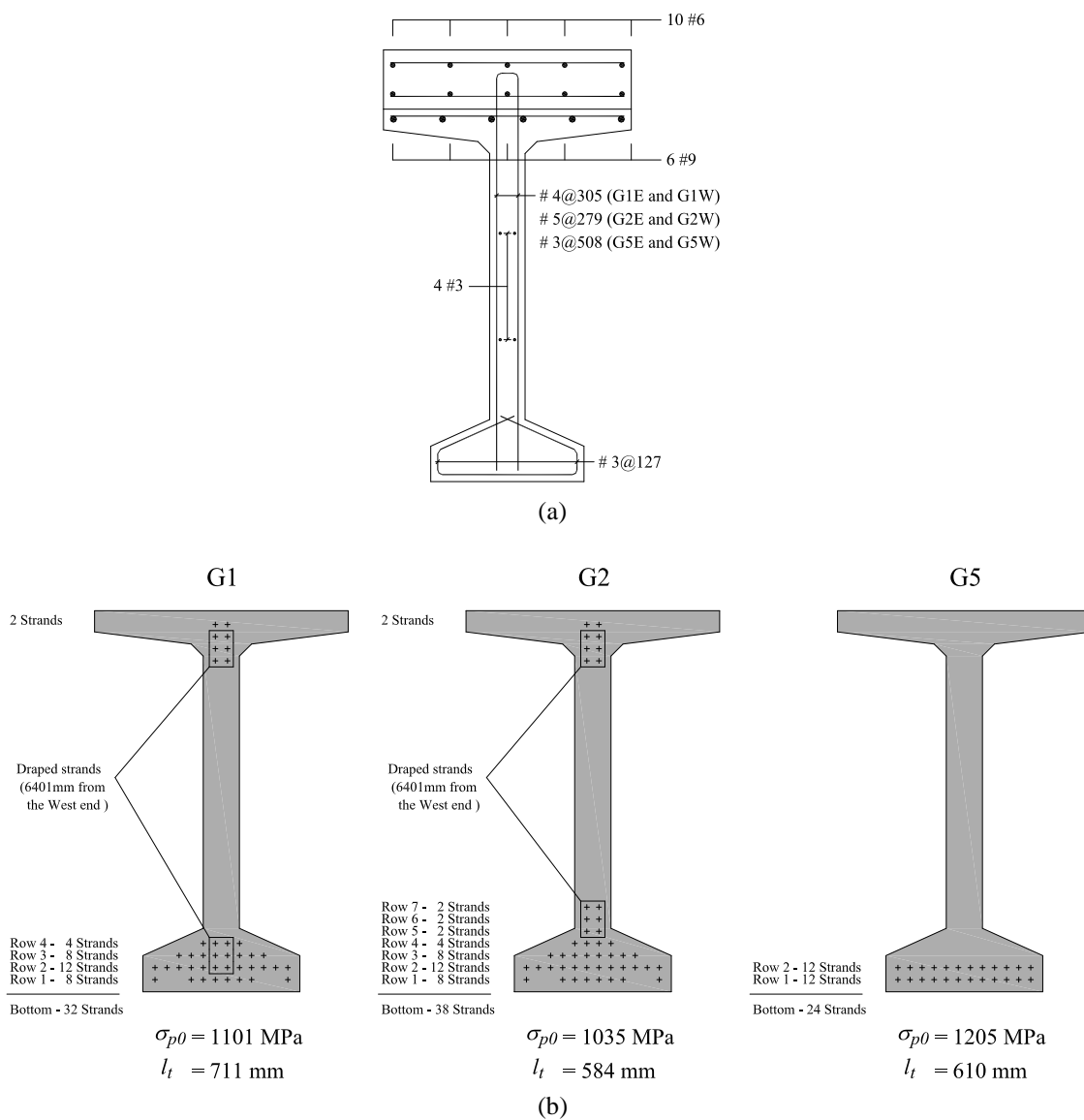


Figure 5.22 – Cross-section: (a) Reinforcement content in the critical region; (b) Location of prestressing strands.

The reinforcement arrangement within the cross-section and the location of the prestressing strands are presented in Figure 5.22. The spacing between the strands layers equals 50.8 mm. The measured effective initial prestress, σ_{p0} , and the corresponding transfer lengths, l_t , of the prestressing force are also indicated in the figure. In all the analyses, the initial prestress was assumed to vary linearly from zero up to σ_{p0} along the transfer length. A bilinear stress-strain law was adopted for the prestressing steel with $f_{py} = 1675$ MPa, $f_{pu} = 1860$ MPa, $\varepsilon_{pu} = 50\%$ and $E_p = 195$ GPa. The remaining material properties are indicated in Table 5.5. It is remarked that reasonable estimates of the web crack spacing for G5 were only obtained with $\lambda = 0.3$. The length of the web regions with different amounts of stirrups is indicated in Table 5.6.

Table 5.5 – Material properties of the analysed beams belonging to the G series

Zone	t [m]	f'_c [MPa]	λ	ρ_x [%]	\emptyset_x [mm]	$f_{sy,x}$ [MPa]	$f_{su,x}$ [MPa]	$\varepsilon_{su,x}^{(1)}$ [%]	ρ_y [%]	\emptyset_y [mm]	$f_{sy,y}$ [MPa]	$f_{su,y}$ [MPa]	$\varepsilon_{su,y}^{(1)}$ [%]
G1E and G1W													
F1	1.067	31.0	1	1.040	19	547	820	150	0.0	-	-	-	-
W1	0.152	83.4	0.5	0.166	9.5	527	775	150	0.555	12.7	483	752	150
W2									0.278				
W3									5.160	15.9	547	820	150
W4													
G2E and G2W													
F1	1.067	59.3	1	1.040	19	547	820	150	0.0	-	-	-	-
W1	0.152	86.8	0.5	0.166	9.5	527	775	150	0.939	15.9	547	820	150
W2									0.608				
W3									0.303	12.7	483	752	150
W4									5.160	15.9	547	820	150
G5E													
F1	1.067	42.0	1	1.040	19	547	820	150	0.0	-	-	-	-
W1	0.152	122.7	0.3	0.166	9.5 ⁽²⁾	637	732	100	0.183	9.5 ⁽²⁾	637	732	100
W2													
W3									5.160	15.9	547	820	150
W4													
G5W													
F1	1.067	42.0	1	1.040	19	547	820	150	0.0	-	-	-	-
W1	0.152	122.7	0.3	0.166	9.5	527	775	150	0.183	9.5	527	775	150
W2													
W3									5.160	15.9	547	820	150
W4													

⁽¹⁾ Not indicated in the test report. Typical value for steel currently used in the US was adopted;

⁽²⁾ Welded wire reinforcement.

Table 5.6 – Length of the web regions with different amounts of stirrups

Girder	Length [m]		
	W1	W2	W3
G1	3.658	3.963	-
G2	3.658	2.438	1.524
G5	7.620	-	-

The analyses were divided in two phases. In the first phase, only the finite elements corresponding to the beam were activated. In this stage, the self weight and the prestressing forces were applied matching the effective prestress and the transfer lengths l_t indicated in Figure 5.22 (b). In the second phase, the finite elements corresponding to the slab were activated and the vertical load was incremented until failure.

5.4.2 Results

5.4.2.1 Failure loads and failure mechanisms

Collapse occurred in a similar manner for specimens G1E, G1W, G2E and G2W. Concrete crushing occurred in the web immediately above the bottom bulb. This failure mode was accurately predicted both by the F-CMM and the R-CMM. Representative pictures of this failure mode are depicted in Figure 5.23 (a) and (b). The corresponding contour levels with the state variable E_{max} in the post-peak stage are presented in Figure 5.23 (c). Although a band of crushed finite elements can be seen, concrete crushing started immediately above the support and then progressed until the formation of the band depicted in Figure 5.23 (c). This failure mode is largely influenced by support dimensions and reinforcement detailing in the end region of the beams.

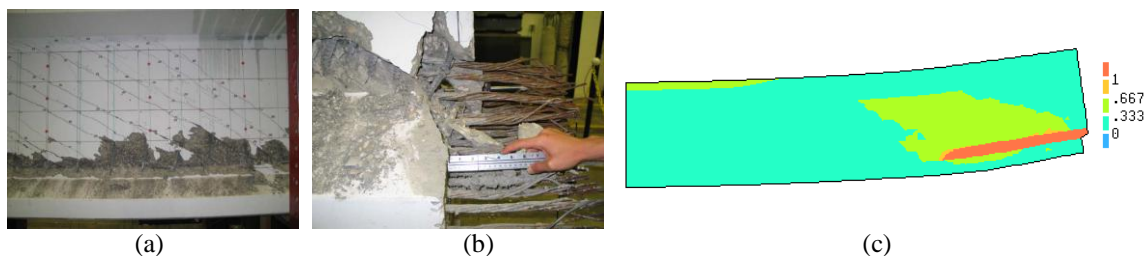


Figure 5.23 – Typical web crushing failure observed in the girders G1E, G1W, G2E and G2W: (a) East half of girder G2 at failure [95]; (b) Detail of the end region [95]; (c) F-CMM analysis of the half girder G2E - deformed shape (x10) with the E_{max} contour levels in the post-peak stage.

In the case of specimens G5E and G5W, a wide open shear crack dominated the behaviour. In the East half, which was reinforced with welded wire mesh, a diagonal tension failure occurred due to stirrup rupture, as depicted in Figure 5.24 (a). Both the F-CMM and the R-CMM correctly predicted this failure mode, as can be observed from the contour levels with the calculated stirrup stresses at the cracks presented in Figure 5.24 (b). The red colour corresponds to regions where the tensile strength of the stirrups ($f_{su} = 732$ MPa) was exceeded. The West half collapsed with local web concrete crushing above the support and with significant sliding along the dominant web shear crack.

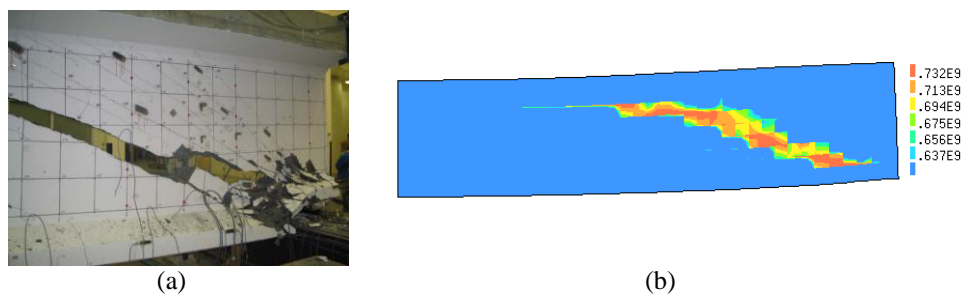


Figure 5.24 – Diagonal tension failure of girder G5E: (a) East half of girder G5 at failure [95]; (b) F-CMM analysis - deformed shape (x10) with the vertical reinforcement stress contour levels at peak load (values in Pa and between f_{sy} and f_{su}).

The failure loads and failure modes are summarized in Table 5.7. The F-CMM supplies once again the best predictions of the failure loads. The failure load of the specimen G5E is underpredicted with both models. However, it must be remarked that no information regarding the ultimate tensile strain of the reinforcement was given in the test report and that the failure mode is sensitive to this parameter. Although exhibiting good agreement with the failure loads of girders G1 and G2, the precision of the Eurocode 2 [46] variable angle truss model decays significantly when very low shear reinforcement ratios are used. Nonetheless, the use of sectional models in this case is debatable as failure was governed by local conditions at the ends of the specimens.

Table 5.7 – Comparison between experimental and calculated failure loads and failure modes

	Experimental		F-CMM			R-CMM			EC2		
	q_u [kN/m]	Mode ⁽¹⁾	q_u [kN/m]	Mode ⁽¹⁾	Rat. ⁽²⁾	q_u [kN/m]	Mode ⁽¹⁾	Rat. ⁽²⁾	q_u [kN/m]	Mode ⁽³⁾	Rat. ⁽²⁾
G1E	380	WC	371	WC	1.02	333	WC	1.14	371	S	1.02
G1W	439	WC	423	WC	1.04	374	WC	1.17	414	S	1.06
G2E	493	WC	489	WC	1.01	461	WC	1.07	515	B	0.96
G2W	565	WC	515	WC	1.10	468	WC	1.21	515	B	1.10
G5E	346	SF	300	SF	1.15	282	SF/WC	1.23	185	S	1.87
G5W	291	WC/WS	291	WC/WS	1.00	279	WC	1.04	153	S	1.90

⁽¹⁾ Failure mode: SF – Stirrup failure; WC – web crushing failure; WS – web sliding failure; ⁽²⁾ Failure load ratio: $F_{u,exp} / F_{u,calculated}$; ⁽³⁾ Failure mode according to the EC2 variable angle truss model: S – failure governed by the stirrups; C – failure governed by crushing of the web; B – bending failure.

5.4.2.2 Force-deformation curves

The force vs. midspan displacement curves for all the analysed beams are depicted in Figure 5.25 and in general good agreement can be found between the calculated and the measured curves.

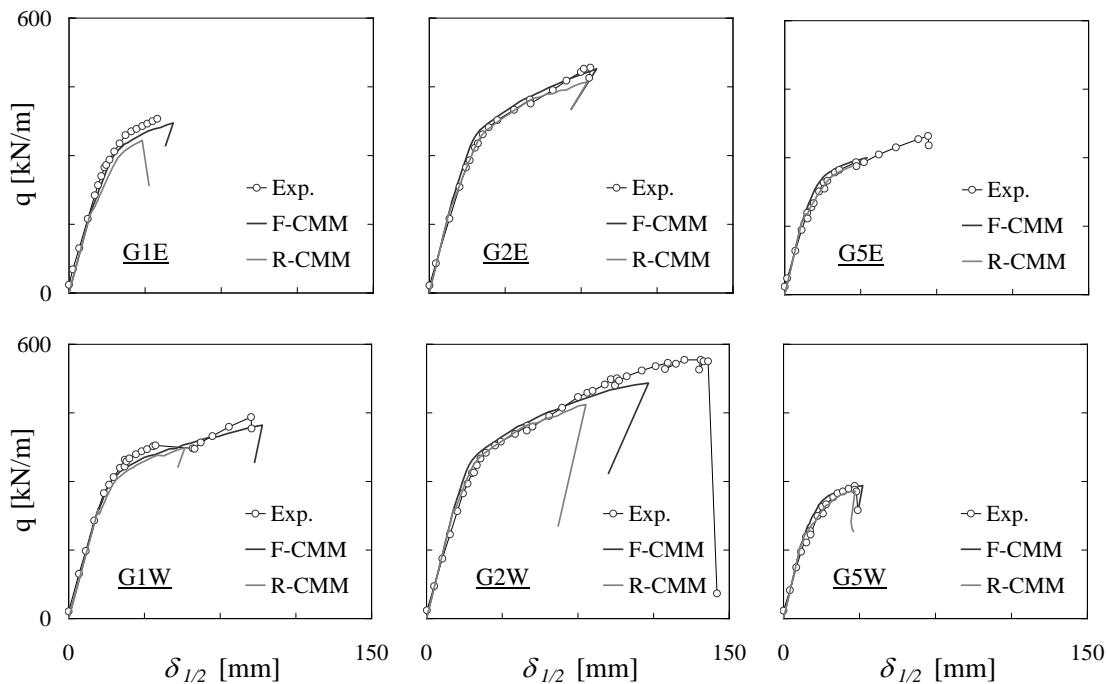


Figure 5.25 – Distributed force vs. midspan displacement.

It can be shown that - with the adopted value for the yielding stress of the prestressing steel - the yielding moment at midspan is reached when $q = 432, 515$ and 340 kN/m for beams G1, G2 and G5, respectively. In the G2W experiment the theoretical yielding force is

exceeded by 10%, which seems to indicate that the real yielding strength of the prestressing strands is somewhat higher than the considered in the analyses.

The average force vs. average web shear strain curves are depicted in Figure 5.26. The average web shear strains were determined from the measurements of two LVDTs with an inclination of $\pm 45^\circ$ and with a base length of 1.219 m. The centre of the measuring area was located at 1.778 m from the support of the girders G1 and G2 and at 1.219 m for girder G5. The values corresponding to the numerical analyses were determined from the displacements of the nodes located closest to the real location of the LVDTs. Similarly to the RC panels analysed in Chapter 3, the curves present three distinct branches. Prior to cracking, the behaviour is essentially linear. After cracking and until stirrup yielding, the slope of the curves is flatter and depends on the amount of shear reinforcement. After stirrup yielding, the slope becomes even more flat. Although the cracking load is somewhat underestimated for beams G1 and G2, the F-CMM provides a good approximation to the measured curves. The R-CMM tends to underestimate not only the failure loads but also the shear stiffness of the cracked webs.

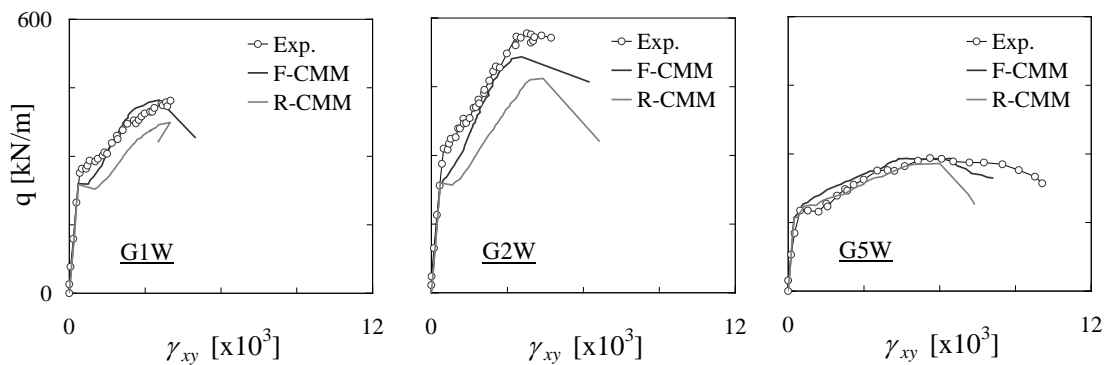


Figure 5.26 – Distributed force vs. average shear strain.

5.4.2.3 Cracking patterns

The calculated and observed cracking patterns are depicted in Figure 5.27 to Figure 5.29. The crack angles are compared in Figure 5.30 and good agreement can be found. The developed models can also predict the crack spacing. The calculated and the measured average spacing of the shear cracks in zone W1 (see Table 5.6 and Figure 5.21 (d)) are compared in Table 5.8. In the case of girder G5, $\lambda = 0.3$ was adopted in the webs in order to obtain a reasonable estimate of the crack spacing. Note that this parameter determines the deformation capacity of the stirrups.

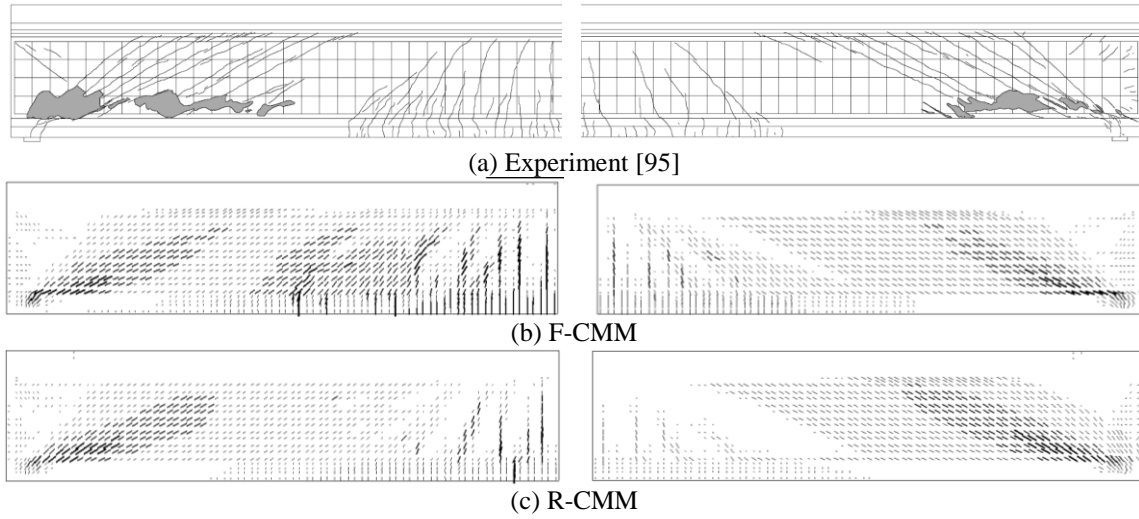


Figure 5.27 – Beams G1W (left) and G1E (right): cracking patterns at failure.

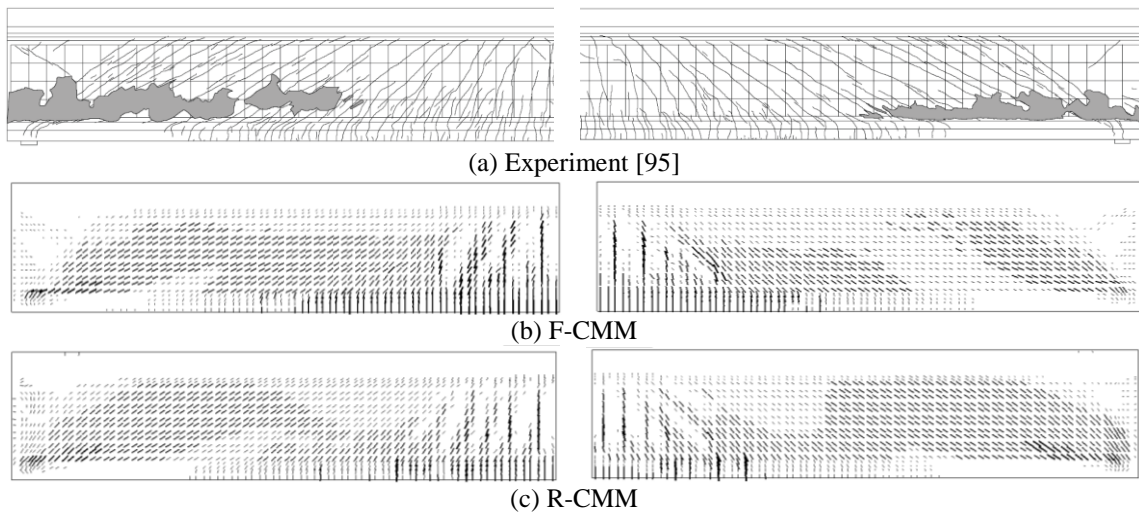


Figure 5.28 – Beams G2W (left) and G2E (right): cracking patterns at failure.

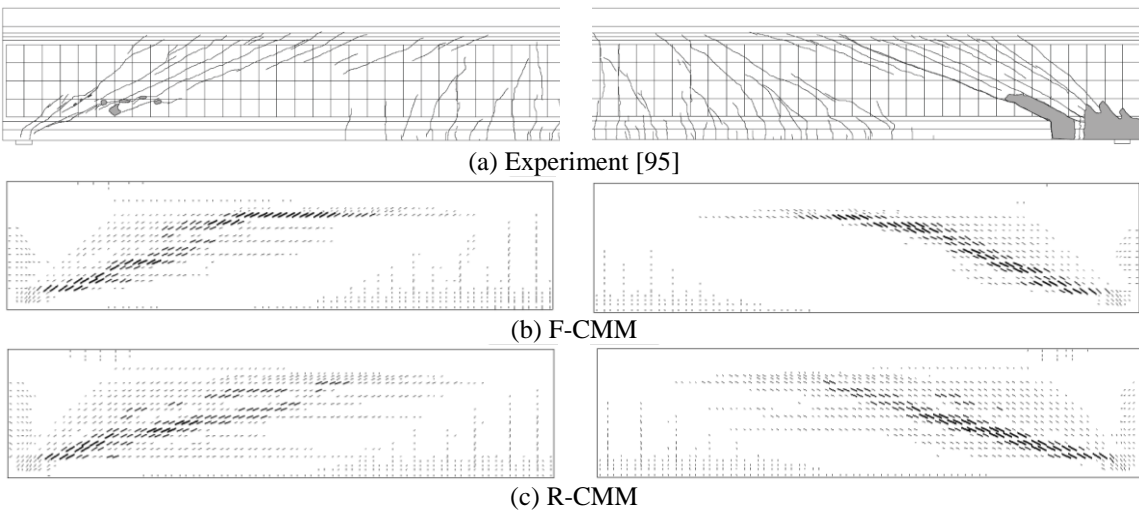


Figure 5.29 – Beams G5E and G5W: cracking patterns at failure.

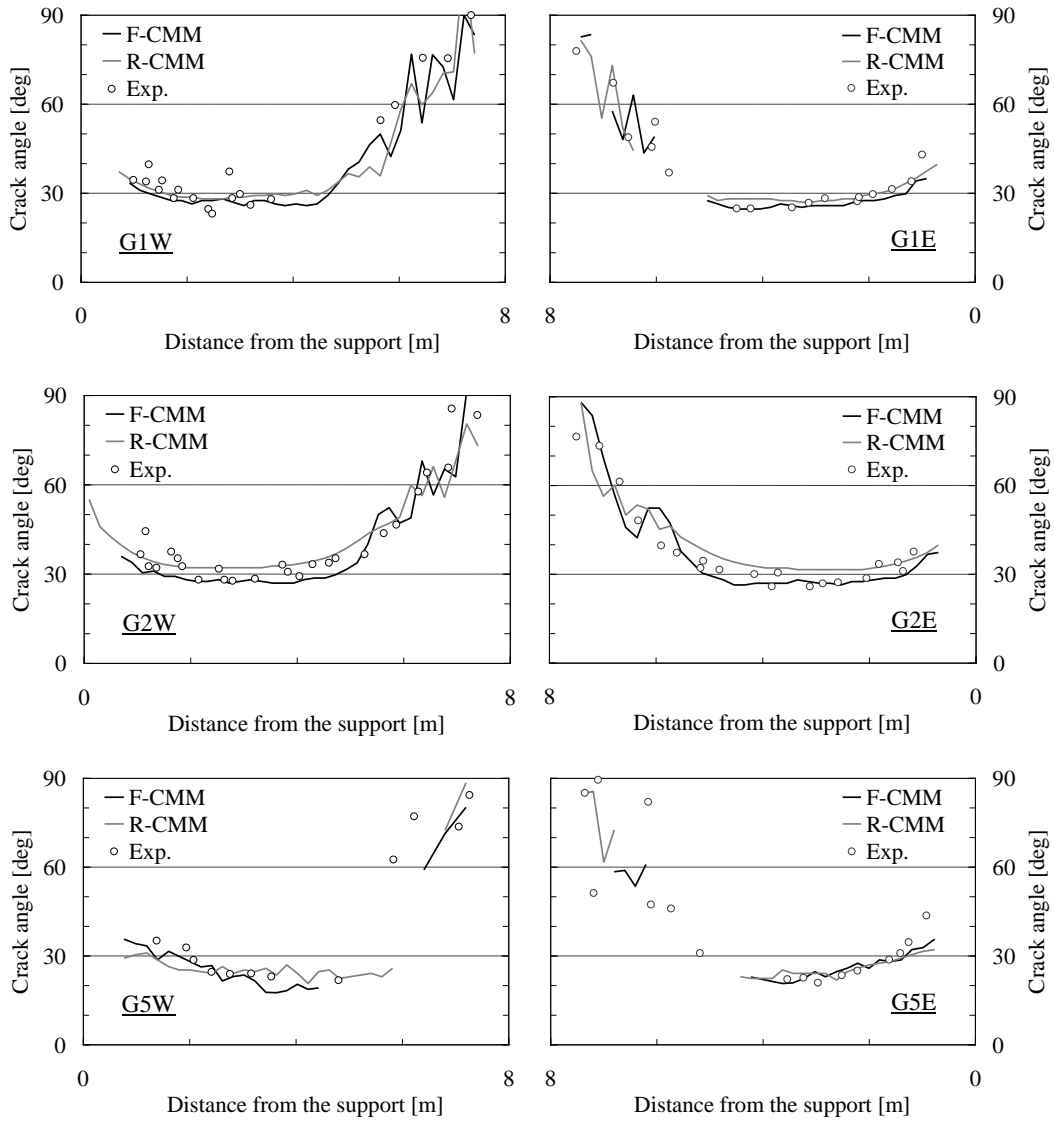


Figure 5.30 – Web crack angles for specimens G1, G2 and G5.

Table 5.8 – Measured and calculated average spacing of the web shear cracks

Girder	Average web shear crack spacing [mm]		
	Measured	F-CMM	R-CMM
G1E	148	140	140
G1W	94	140	140
G2E	130	111	109
G2W	106	112	110
G5E	144	150	150
G5W	154	150	150

5.5 Analysis of the deformation capacity of plastic hinges with high shear stresses

5.5.1 Description and objectives

The experiments in this test series aimed at investigating the influence of some major parameters on the deformation capacity of conventionally reinforced and prestressed concrete girders [218]. In particular, the tests were planned to study the development of plastic hinges in regions subjected to high bending moments and shear forces using large scale specimens. Although a total of six girders were tested (T1 to T6), here only three girders will be analysed (T1, T2 and T4).

The girders are simply supported and have an overhang on one side (Figure 5.31). Each girder was subjected to a single load at the free end of the overhang and a uniformly distributed load in the span between the supports. In a first phase, the specimens were subjected to proportionally increasing loads with $Q = 1.6 \cdot P$. After onset of yielding of the longitudinal reinforcement in the negative moment region (over support B) the vertical displacement at the free end of the overhang was blocked and the distributed force Q was increased until failure. In the second phase the girders become statically indeterminate.

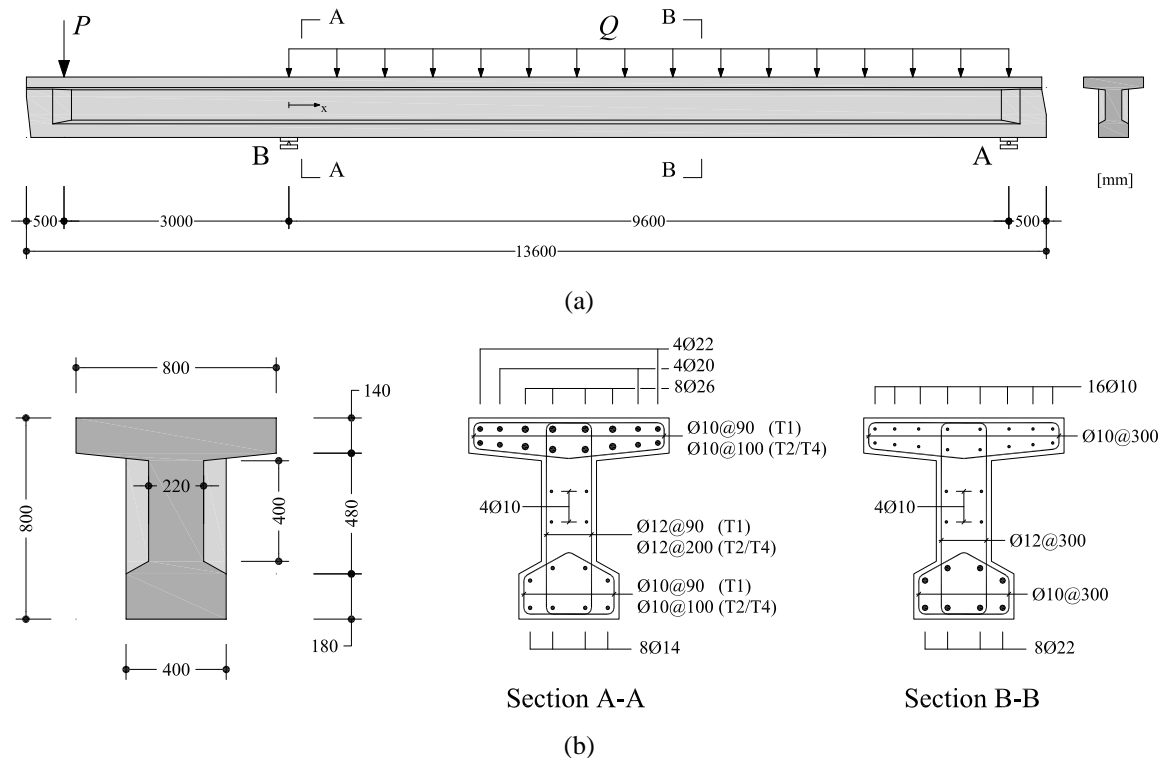


Figure 5.31 – Geometry and reinforcement content of the analysed girders.

The specimens T1, T2 and T4 have the same amount of longitudinal reinforcement in the critical regions, see Figure 5.31. Therefore, the theoretical bending mechanism with two plastic hinges leads to the same collapse load in all the three girders. The dimensioning of the shear reinforcement was made assuming a discontinuous stress field with different inclinations of the diagonal compressive struts. As can be seen in Figure 5.31 (b), this leads to significantly different amounts of stirrups in girders T2/T4 when compared to girder T1. The longitudinal reinforcement of beams T1 and T2 was curtailed according to the tension chord forces given by the corresponding discontinuous stress field. The longitudinal reinforcement in specimen T4 was not curtailed. For details regarding the reinforcement layout refer to the test report [218]. The concrete strength equals $f'_c = 46.5, 48.4$ and 45.8MPa for beams T1, T2 and T4, respectively. The steel properties are summarized in Table 5.9 and the adopted finite element mesh is depicted in Figure 5.32.

Table 5.9 – Steel properties

Rebar	Ø10	Ø12	Ø14	Ø20	Ø22	Ø26
f_{sy} [MPa]	506	498	482	502	563	511
f_{su} [MPa]	634	624	616	635	744	633
ε_{su} [‰]	129	144	132	128	105	139

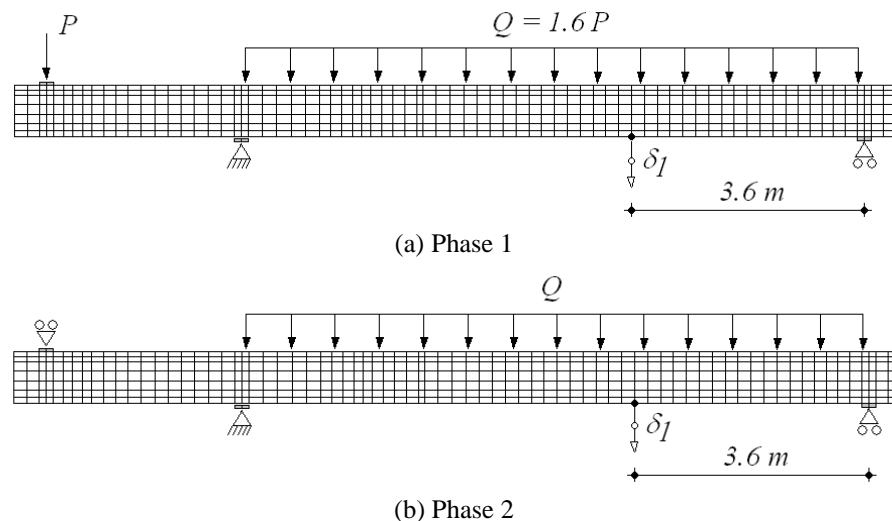


Figure 5.32 – Finite element mesh of girder T2.

The calculation of the rotation capacity of plastic hinges is highly dependent on the correct definition of the concrete ductility in the compressed flanges. In this case, concrete in the bottom flange of the overhang is confined by closely spaced stirrups and hoops, as

depicted in Figure 5.31. This confinement introduces a three-dimensional stress state responsible for both strength and ductility increase of the compressed concrete which cannot be directly modelled using a plane stress formulation. In the present work, a rational procedure was adopted for incorporating this three-dimensional behaviour into the constitutive laws, following the lines of the Compression Chord Model¹ (CCM) proposed by Sigrist [218]. The confined compressive strength is given by expression (2.23), where the confining stresses are assumed to be mobilized by yielding of the transversal reinforcement. Taking into account the fact that the confinement is provided at discrete locations spaced of s_c , see Figure 5.33 (a), the average confined concrete strength is given by

$$f_{c3} = f'_c \left[1 + 4 \omega_s \left(1 - \frac{s_c}{a_c} \right) \left(1 - \frac{s_c}{b_c} \right) \right] \quad (5.1)$$

where the mechanical reinforcement ratio ω_s is given by (see Figure 5.33 (a) for notation):

$$\omega_s = \min(\omega_y ; \omega_z) \quad (5.2)$$

$$\omega_y = \frac{A_{sy} f_{sy}}{a_c s_c f'_c} ; \quad \omega_z = \frac{A_{sz} f_{sz}}{b_c s_c f'_c}$$

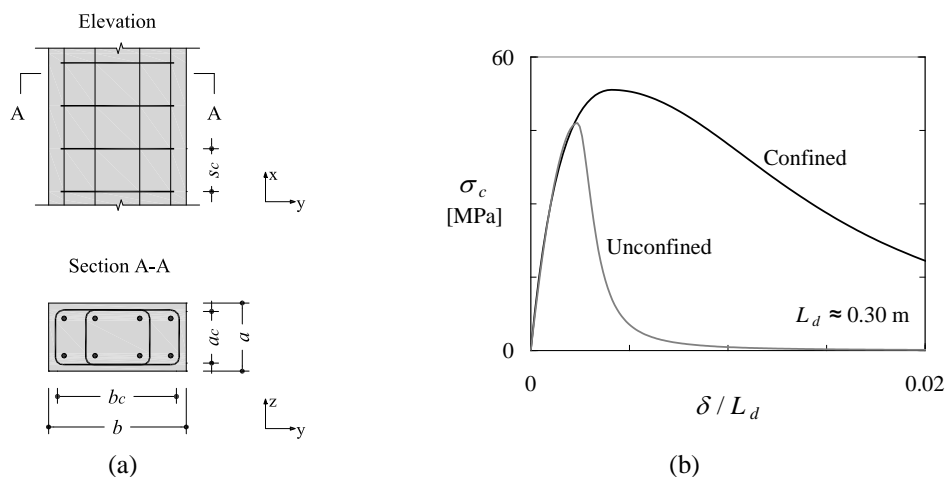


Figure 5.33 – Compression chord model: (a) notation; (b) comparison between the confined and unconfined stress-strain diagrams for the bottom flange of beam T1.

The strain at peak stress is calculated from:

¹ Translated from the German *Druckgurtmodell*.

$$\varepsilon_{c3} = \varepsilon'_0 \left(5 \frac{f_{c3}}{f'_c} - 4 \right) \quad (5.3)$$

As discussed in 2.4.2, with increasing confinement the post-peak branch of the concrete stress-strain curve experiences a gradual transition from softening to ductile behaviour. In the post-peak regime, it is assumed in the CCM that the deformations localize along a length $L_d = 2 \cdot a_c$ (with $a_c \leq b_c$). The displacement δ_{50} corresponding to a post peak stress equal to $0.5 \cdot f_{c3}$ is here conservatively estimated from:

$$\frac{\delta_{50}}{L_d} = \varepsilon_{c3} + 0.1(\omega_y + \omega_z) \left(1 - \frac{s_c}{2a_c} \right) \quad (5.4)$$

Although this procedure can be automated, in the present formulation the user must define a modified compressive fracture energy G_C that fits the post-peak strains given by (5.4). The adopted stress-strain curves for confined and unconfined concrete are compared in Figure 5.33 (b) for the case of the bottom flange of girder T1. Objectivity of the results with respect to the finite element size is guaranteed by performing the regularization of the post-peak branch along the lines of the crack band model. It is remarked that the effect of cover spalling due to buckling of the longitudinal reinforcement is not included in the formulation.

5.5.2 Results

5.5.2.1 Failure loads and failure mechanisms

Girder T1 failed by crushing of the bottom flange after the formation of two plastic hinges in the regions of maximum bending moments. This can be considered a bending failure motivated by the exhaustion of the rotation capacity of the plastic hinge over the support region. Girders T2 and T4 experienced a web crushing failure in a typical discontinuity region. However, girder T2 exhibited a yielding plateau in the force-displacement curve, whereas girder T4 experienced a brittle failure. The failure loads and failure modes are summarized in Table 5.10. According to the Eurocode 2 variable angle truss model, girder T1 is not shear critical while girders T2 and T4 are shear critical and do not achieve the failure load corresponding to the bending mechanism.

Table 5.10 – Comparison between experimental and calculated failure loads and failure modes

	Experimental		F-CMM			R-CMM			EC2		
	Q_u [kN]	Mode ⁽¹⁾	Q_u [kN]	Mode ⁽¹⁾	Rat. ⁽²⁾	Q_u [kN]	Mode ⁽¹⁾	Rat. ⁽²⁾	Q_u [kN]	Mode ⁽³⁾	Rat. ⁽²⁾
T1	1892	FC	1939	FC	0.98	1945	FC	0.97	1893	B	1.00
T2	1805	WC	1774	WC	1.02	1763	WC	1.02	1825	C/S	0.99
T4	1716	WC	1752	WC	0.98	1762	WC	0.97	1759	C/S	0.98

⁽¹⁾ Failure mode: FC – bottom flange compressive failure; WC – web crushing failure

⁽²⁾ Failure load ratio: $Q_{u,exp} / Q_{u,calculated}$

⁽³⁾ Failure mode according to the EC2 variable angle truss model: S – failure governed by the stirrups; C – failure governed by crushing of the web; B – Bending failure with two plastic hinges.

The pictures of the failure region and the contour levels of the state variable E_{max} at peak load are presented in Figure 5.34 through Figure 5.36. It can be seen that both models correctly reproduce the observed failure modes. However, and as previously noticed, crushing of the web concrete tends to appear localized in the finite elements close to the compressed flange. In these cases, failure was initiated by crushing of the web concrete in the vicinities of the support, which seems to be consistent with the experimental failure mode.

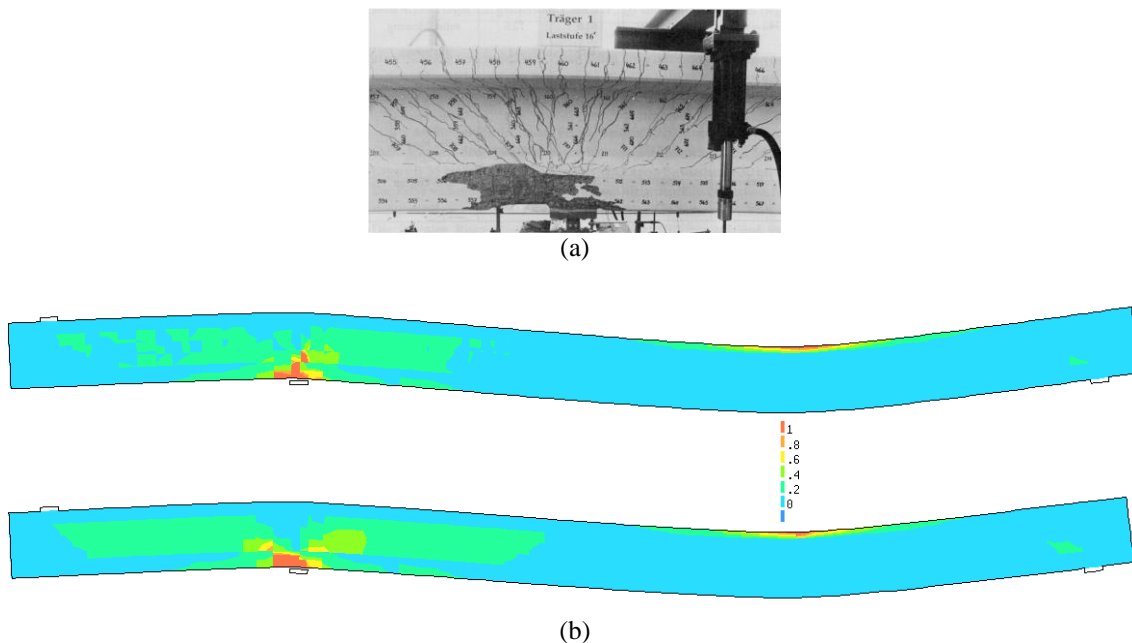


Figure 5.34 – Girder T1 at failure: (a) detail of the failure region; (b) E_{max} contour levels in the post-peak stage for the F-CMM (top) and R-CMM (bottom).

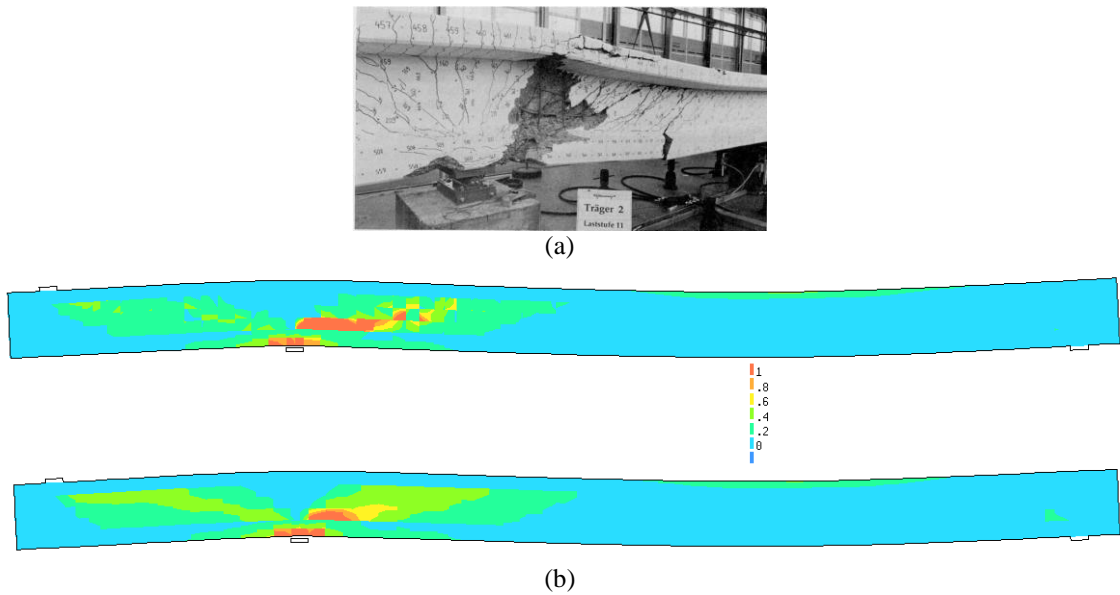


Figure 5.35 – Girder T2 at failure: (a) detail of the failure region; (b) E_{max} contour levels in the post-peak stage for the F-CMM (top) and R-CMM (bottom).

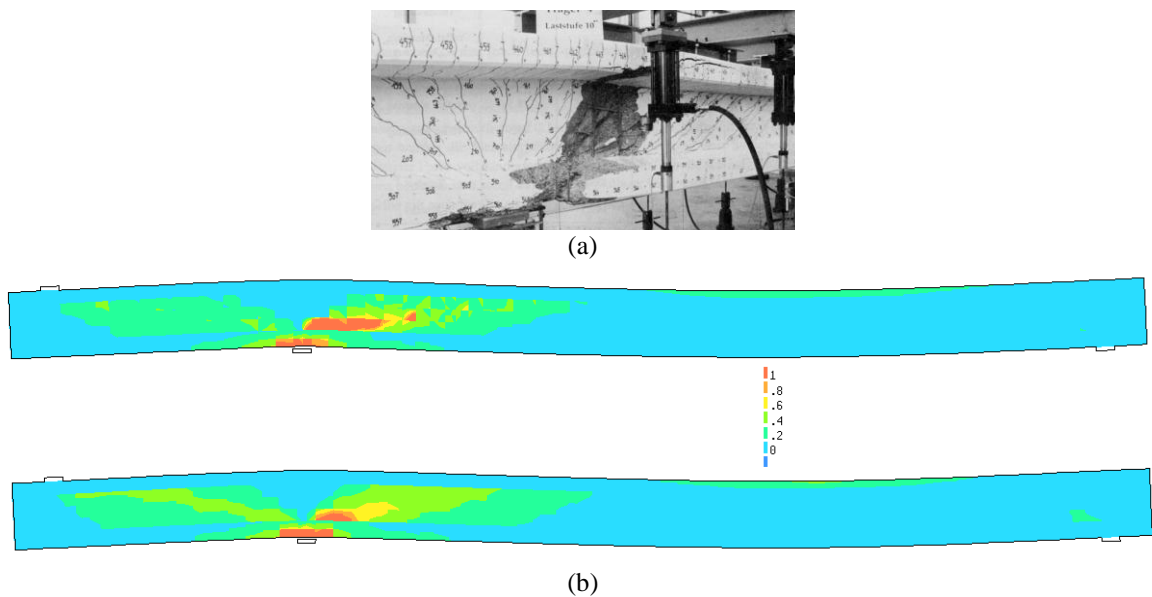


Figure 5.36 – Girder T4 at failure: (a) detail of the failure region; (b) E_{max} contour levels in the post-peak stage for the F-CMM (top) and R-CMM (bottom).

5.5.2.2 Force-deformation curves

The force deformation curves are depicted in Figure 5.37. Regarding specimen T1, which failed with the formation of the two plastic hinges, a good estimate of the deformation capacity could be obtained, thus validating the procedure described above for taking into account the confinement provided to the bottom flange concrete in the region of the continuous support. The ultimate deformation of girder T2 is clearly underestimated. In the

numerical analysis, failure occurs shortly after longitudinal steel yielding in the span and no yielding plateau could be obtained. Nonetheless, the brittle behaviour of girder T4 is accurately reproduced. It is recalled that these beams contained the same amount of stirrups and that T2 had curtailed reinforcement. Considering the fact the concrete strength of girder T2 was only marginally higher than that of girder T4, it can be concluded that the delayed crushing of the web concrete in girder T2 with respect to that of girder T4 can be explained by the inherent scatter of the cracked concrete compressive strength.

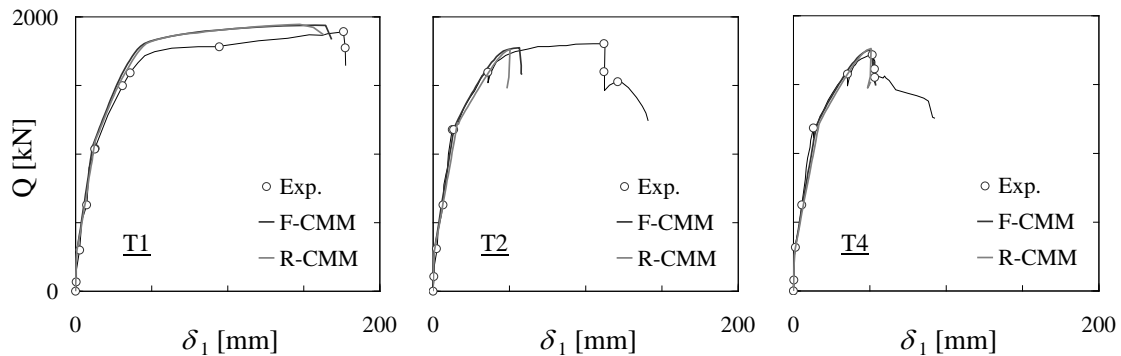


Figure 5.37 – Force-deformation curves for beams T1, T2 and T4.

The longitudinal strains obtained by measuring the relative displacements of targets located in the top and bottom fibres of beam T1, as well as the corresponding curvature distribution along the beam longitudinal axis, are presented in Figure 5.38. A good match with the numerical values is observed, namely in what concerns the length of the plastic hinges, which is an important feature in order to get accurate estimates of its rotation capacity. The results correspond to a loading step where the displacement at the span equals $\delta_1 = 95\text{mm}$ (approximately half-way through the yielding plateau observed in Figure 5.37).

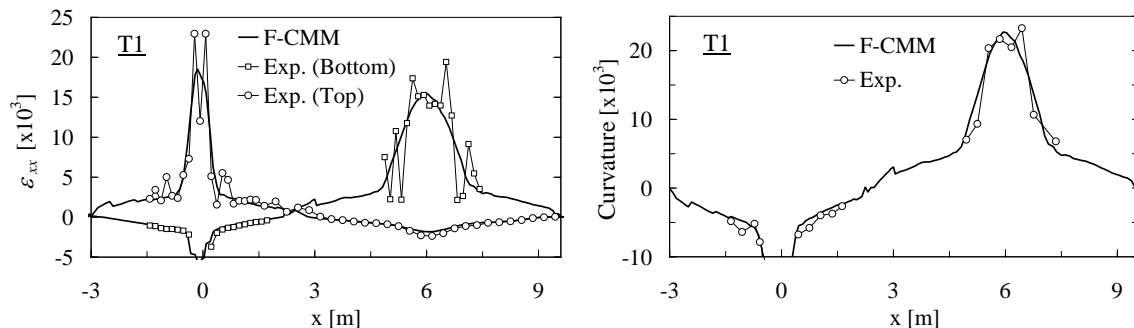


Figure 5.38 – Average longitudinal strains (left) and curvatures (right) for beam T1 corresponding to a vertical displacement in the span of $\delta_1 = 95\text{mm}$.

5.5.2.3 Cracking patterns

The observed and calculated cracking patterns at failure are depicted in Figure 5.39 through Figure 5.41. Once again the calculated cracking patterns provide a good picture of the real cracking pattern.

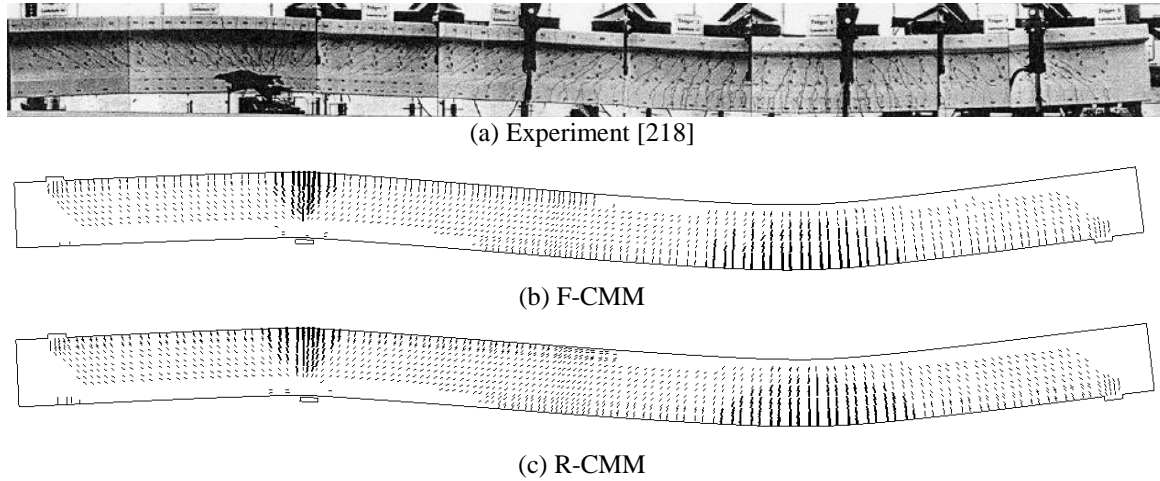


Figure 5.39 – Beam T1: cracking patterns at failure.

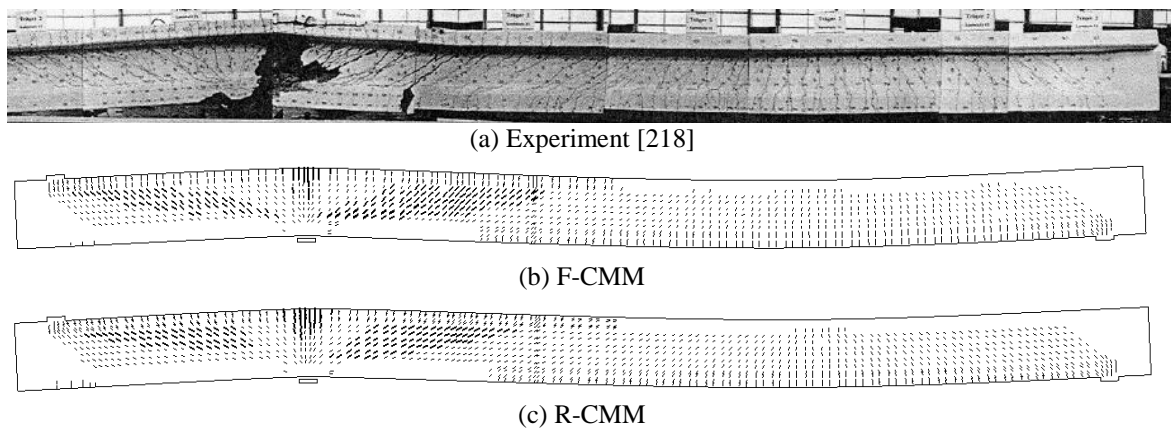


Figure 5.40 – Beam T2: cracking patterns at failure.

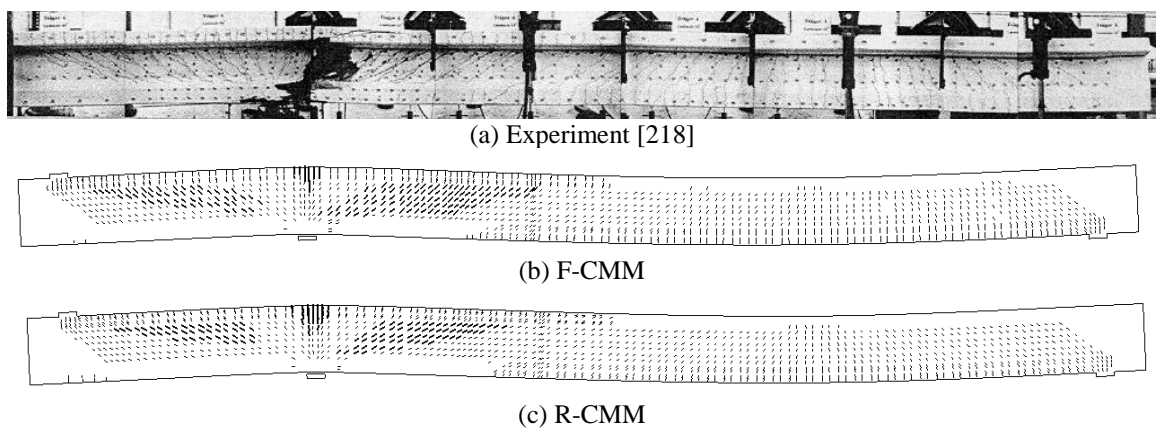


Figure 5.41 – Beam T4: cracking patterns at failure.

5.6 Concluding remarks

A validation campaign was undertaken using a set of experimental tests on large scale shear critical structural elements. Both continuity and discontinuity regions were analysed. The models proved capable of reproducing shear failures in demanding situations, such as the ones involving plastic strains in the longitudinal reinforcement. The effect of normal forces on the shear behaviour was dully modelled. Although both the rotating and fixed crack models performed well, the F-CMM provided better estimates of the failure modes, failure loads and cracking patterns. The implementation of both models proved robust and the force-deformation responses could be computed in the post-peak range, thus allowing a clear identification of the failure mechanisms. When compared to the Eurocode 2 provisions based on the variable angle truss model, the numerical analysis allowed a significant improvement in the estimates of shear failure load of beams containing low amounts of shear reinforcement. Although the focus was driven to the modelling of the shear failures in shear reinforced concrete girders, an example was presented of a concrete girder failing in bending. In this case, both models allowed good estimates of the deformation capacity and an accurate sizing of the plastic hinge regions.

In spite of the overall good results, some limitations were found. (1) Although not severe, the deformation capacity of the stirrups is somewhat underestimated whenever failure is governed by stirrup rupture. This can be attributed to the fact that the model cannot reproduce bond slip occurring across several cracks; (2) Despite the fact that the F-CMM can reproduce the associated crack kinematics, the shear sliding failure mode that occurred in girders MVN2 and MVN3 could not be clearly evidenced due to anticipated crushing of web concrete. It seems that the adopted softening law, which is based on the results obtained on RC panels, gives somewhat conservative estimates of the effective compressive strength in discontinuity regions. Nonetheless, the failure loads and the force-deformations curves were still in good agreement with the observed ones and the failure region is correctly identified; (3) Finally, due to the kinematic description of the displacement field based on the concept of weak discontinuities, web crushing failure is systematically localized along a row of finite elements instead of spreading throughout the whole web. Although this effect has almost no implications in the calculation of the peak load, it may influence the computation of the load carrying mechanisms in the post-peak regime. The well-posedness recovery using a regularization of the compressive strain field based on a non-local approach might be a possible remedy for this situation.

6 Simplified models for engineering practice

6.1 General

In the previous chapters a numerical model was developed for NLFEA of structural concrete elements allowing detailed examinations of the structural behaviour. Besides enabling the determination of the complete force-deformation curves, also cracking patterns and crack widths can be estimated with good accuracy. However, in the course of a structural examination of an existing bridge such a detailed structural analysis may not always be required. Even if this is not the case, in early stages of the structural assessment simpler methods should be employed to provide a first estimate of the determinant failure modes and corresponding failure loads. The advantage of a stepwise procedure in the safety evaluation of existing structures is widely recognized [36; 66; 259] and has been adopted in the recent *fib* model code [87]. However, it is also important that the successive methods are somehow related. The simpler methods should preferably be based on the more detailed ones through transparent simplifying assumptions in order to keep clarity and consistency between the results obtained in the successive levels of analysis. In the present chapter the focus is driven on the shear strength assessment of structural elements containing at least the minimal amount of shear reinforcement and plasticity theory concepts are adopted in the formulation of simplified models. It is shown how plasticity based structural analysis methods relate to the models developed in the previous chapters and how those can be used in intermediate stages of assessment.

Based on the equilibrium equations of the cracked membrane element and on the work of Kaufmann [117; 118], considering the simplifying assumptions mentioned in Section 3.4 and the constitutive equation (3.24) for the effective concrete compressive strength $f_{c,ef}$, in Section 6.2 a simplified analytical model is derived for shear strength assessment of RC panels which can be considered as an extension of the classical limit analysis equations. This formulation is then used at the structural level for obtaining continuous stress fields at failure conditions through a simplified nonlinear analysis model. It is also shown how the same set of equations can be used for the strength assessment of general structural concrete

elements using discontinuous stress fields, thus establishing a link between the developed NLFEA models and the analytical engineering methods of limit analysis for structural concrete elements. Finally, in Section 6.3 a sectional analysis method is developed for continuity (or B-) regions which results in a set of expressions similar to those of the well known variable angle truss model. The proposed model can be used in an intermediate assessment stage and has the advantage of being formally similar to the shear design provisions used in the recent European codes of practice.

6.2 Limit analysis methods for structural concrete elements subjected to in-plane forces

6.2.1 Overview and general considerations

Limit analysis methods result from the application of the theory of plasticity to structural concrete, allowing a unified treatment of the design methods of beams, walls, slabs and shells [150; 163; 169]. Concrete and steel are treated as rigid-plastic materials and therefore only ultimate loads can be calculated. These methods have been built on a sound physical basis through the establishment of the lower-bound (or static) and upper-bound (or kinematic) theorems of limit analysis.

The lower-bound theorem states that any load corresponding to a statically admissible state of stress everywhere at, or below, yield is not higher than the ultimate load. Therefore, in the lower-bound methods an internal force flow in equilibrium with the external loads is assumed. This admissible stress field can be idealized as a discontinuous stress field [146; 147; 149; 167; 169; 217], or simply as a system of struts and ties [149; 208; 209] in which the stresses are replaced by its static equivalent resultants – a strut and tie model can be regarded as a discrete representation of the associated discontinuous stress field. While these methods are applicable to general geometric and loading configurations, simple section-by-section analysis procedures can be derived for linear members – beams and columns – in which all static and geometric quantities vary only gradually along the structural axis. The shear design method based on the variable angle truss model proposed in the Eurocode 2 [46] is an example of such an analysis procedure.

The lower bound methods are powerful analysis and design tools that permit visualising the force flow throughout the structure, allowing for consistent dimensioning and detailing.

However, a certain degree of expertise is necessary for the application of these methods in cases of structures with complex geometry since the choice of an appropriate stress field may not be straightforward. In these cases, rather than determining the reinforcement from a discontinuous stress field solution, admissible stress fields can be obtained from linear elastic finite element analysis. The yield conditions for membrane elements [168; 169] allow dimensioning the reinforcement in such cases [134]. Although this may have the advantage of restoring uniqueness to the problem, the resulting reinforcement layouts can be inadequate for practical use. Moreover, in the evaluation of an existing structure this procedure can be too conservative since the adoption of a linear elastic stress field is incoherent with the assumed plastic behaviour and may deviate considerably from the actual stress field at failure conditions. Consistent admissible continuous stress fields can still be established with the aid of the finite element method by using appropriate elastic-plastic constitutive relationships [79]. Good agreement with experimental findings has been reported [80] and this method is suitable for refined checks of a previous design or of an existing structure.

The upper-bound methods are also suited for checking a previous design or an existing structure. These methods involve the consideration of an admissible failure mechanism and the determination of the corresponding work W done by the external forces, as well as the internal energy dissipation D at lines of kinematic discontinuity [100; 149; 169; 217]. The failure load corresponding to a given mechanism is determined from condition $W = D$. The upper-bound theorem states that any load resulting from the consideration of a kinematically admissible state of deformation is not lower than the ultimate load. Therefore, the most critical mechanism is the one providing the lowest failure load and can be found either through a minimization procedure or by trial and error considering a discrete number of admissible failure mechanisms.

As concrete is a strain softening and brittle material, its idealization as a perfectly plastic material can be debatable. However, this limited material ductility can be taken into account by choosing an appropriate reduced value for the effective concrete compressive strength $f_{c,ef}$. The analysis and design with limit analysis methods also requires a certain amount of structural ductility enabling the mobilization of the assumed admissible stress field or failure mechanism. In general, in order to guarantee the required structural ductility, besides a suitable value for the concrete compressive strength, these methods should be applied in conjunction with a well distributed minimum reinforcement in the regions where no main reinforcement is required. As the compatibility conditions are not explicitly

verified, design codes usually limit the inclination of the compressive stress field so that the plastic stress field is not so far off from the elastic solution. This limitation is also imposed to avoid failures governed by steel rupture, excessive softening of concrete or sliding through a dominant crack. Rooted on the models developed in Chapter 3 and following the work of Kaufmann [117], a different approach is proposed in this chapter, whereby the limits to the inclination of the compression field are removed and replaced by rationally derived expressions based on a simplified strain compatibility analysis.

6.2.2 Yield conditions of reinforced concrete membranes

The yield conditions for RC membranes under in-plane stress conditions can be derived to determine its load carrying capacity according to the lower-bound theorem of limit analysis. Reinforced concrete is treated as a composite material containing concrete and reinforcing bars, both considered as rigid-plastic materials. Concrete is assumed to obey the modified Coulomb criterion with zero tensile cut-off [169], that is, the tensile strength is neglected. In plane stress conditions, this criterion corresponds to two conical surfaces described by the equations $\tau_{xy}^2 = \sigma_x \sigma_y$ and $\tau_{xy}^2 = (f_{c,ef} + \sigma_x)(f_{c,ef} + \sigma_y)$. In the principal stress space (σ_1, σ_2) the criterion comes down to the square yield locus defined by the vertices $(0,0)$, $(0, -f_{c,ef})$, $(-f_{c,ef}, -f_{c,ef})$, $(-f_{c,ef}, 0)$.

In the present work, and according to what has been exposed in Chapters 2 and 3, the effective compressive strength $f_{c,ef}$ is considered proportional to $f_c'^{2/3}$. This being the case, the mechanical reinforcement ratios in the x - and y - directions are defined as:

$$\omega_x = \frac{\rho_x f_{sy,x} - \sigma_x}{f_c'^{2/3}} \quad \omega_y = \frac{\rho_y f_{sy,y} - \sigma_y}{f_c'^{2/3}} \quad (6.1)$$

Although formal derivations can be made starting from the basic assumptions of plasticity theory, the yield condition for RC membranes can be easily derived from the simplified form of the general equilibrium equations given by (3.16). Using the notation above and defining

$$\zeta = f_{c,ef} / f_c'^{2/3} = \zeta_e \zeta_f f_c'^{1/3} \quad (6.2)$$

the yield conditions and the corresponding angle θ can be expressed in the following form:

$$\begin{aligned}
 Y_1 : \quad \frac{\tau_{xy}}{f_c'^{2/3}} &= \sqrt{\omega_x \omega_y} & \tan \theta &= \sqrt{\frac{\omega_x}{\omega_y}} \\
 Y_2 : \quad \frac{\tau_{xy}}{f_c'^{2/3}} &= \sqrt{\omega_y (\zeta - \omega_y)} & \tan \theta &= \sqrt{\frac{\zeta - \omega_y}{\omega_y}} \\
 Y_3 : \quad \frac{\tau_{xy}}{f_c'^{2/3}} &= \sqrt{\omega_x (\zeta - \omega_x)} & \tan \theta &= \sqrt{\frac{\omega_x}{\zeta - \omega_x}} \\
 Y_4 : \quad \frac{\tau_{xy}}{f_c'^{2/3}} &= \frac{\zeta}{2} & \tan \theta &= 1
 \end{aligned} \tag{6.3}$$

In the precedent expressions, the yield conditions Y_1 to Y_4 correspond to the four failure modes that can be distinguished in limit analysis, respectively: (1) x- and y-reinforcement yielding; (2) concrete crushing with elastic x-reinforcement; (3) concrete crushing with elastic y-reinforcement; and (4) concrete crushing with both reinforcements in the elastic range.

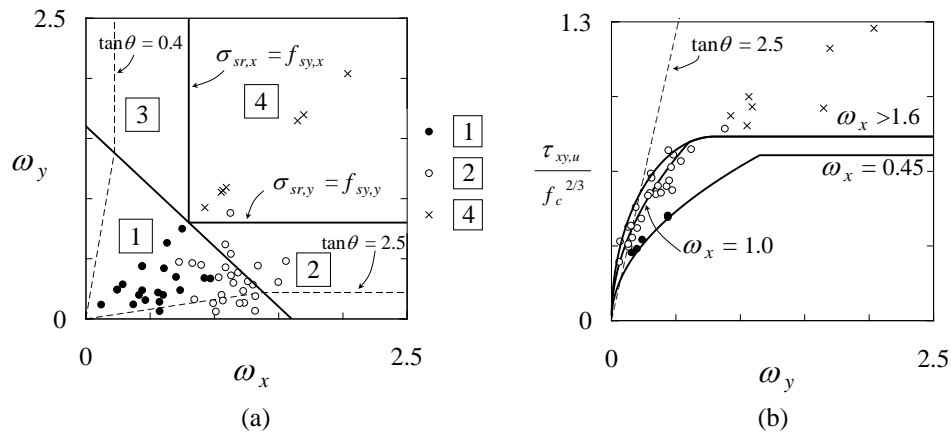


Figure 6.1 – Limit analysis. Comparison with experimental results: (a) failure modes; (b) shear strength.

Muttoni [163; 167] proposed to use $\zeta=1.6$ to calculate the effective concrete strength under moderate transverse strains, and therefore $f_{c,ef} = 1.6f_c'^{2/3}$. If $f_{c0} = 20\text{MPa}$ is taken in Eq. (6.2), this is equivalent to considering $\zeta_e \approx 0.6$. With this constant value for $f_{c,ef}$, the predicted boundaries of the 4 failure regimes are depicted in Figure 6.1(a) together with the experimental failure modes of the same set of 54 RC panels introduced in Chapter 3. The thin dashed lines correspond to the limitation that is imposed in the Eurocode 2 [46], per

example, regarding the maximum inclination of the diagonal compressive field. Two sections of the failure surface are presented in Figure 6.1(b). Although the shear strength of the panels can be fairly predicted, the agreement between calculated and experimental failure modes is rather poor. In limit analysis, shear failures due to sliding across wide open cracks, or stirrup rupture due to exhaustion of the steel deformation capacity must also be included in the web crushing failure mode. Since an overestimation of the shear strength of panels lightly reinforced in the y -direction and failing in regime 2 is obtained with $\zeta_e \approx 0.6$, some kind of limitation to angle θ is essential if a constant value for ζ is adopted.

6.2.3 Yield conditions accounting for compression softening

6.2.3.1 Formulation

A further improvement on limit analysis methods was made by Kaufmann [117] by incorporating the softened compressive strength relationship (3.24) into the yield conditions for membrane elements, thereby eliminating the need for *ad hoc* upper limits to $\tan\theta$.

From the Mohr circle of strains it is possible to show that:

$$\varepsilon_1 = \varepsilon_x + (\varepsilon_x - \varepsilon_y) \tan^2 \theta \quad (6.4)$$

The inclusion of the softened compressive strength into the yield conditions of regimes 2, 3 and 4 can be achieved making two additional assumptions: (1) when concrete crushes the principal compressive average strain is $\varepsilon_2 = -0.002$; (2) a conservative estimate of the softening coefficient can be made considering that the non-yielding reinforcements are about to yield, which results in an average strain approximately given by $\varepsilon_{x/y} = 0.8f_{sy,x/y}/E_s \approx 0.002$. In these circumstances the strain softening coefficient of Eq. (3.24) simplifies to

$$\zeta_e = \frac{1}{1.248 + 0.326 \tan^2 \theta} \quad (6.5)$$

where the parameter C_m , see Eq. (3.24), was taken as 1.0 for consistency with the remarks made in 3.6.1 regarding the effects of the explicit modelling of crack shear slip in the softening coefficient. Noting that $\tan\theta$ is given by Eqs. (6.3) in each of the four failure

regimes, and after some algebraic manipulation, the yield conditions can be expressed in the following form:

$$\begin{aligned}
 Y_1 : \quad \frac{\tau_{xy}}{f_c^{2/3}} &= \sqrt{\omega_x \omega_y} & \tan \theta &= \sqrt{\frac{\omega_x}{\omega_y}} \\
 Y_2 : \quad \frac{\tau_{xy}}{f_c^{2/3}} &= \omega_y \tan \theta & \tan \theta &= \sqrt{-2.417 + \sqrt{2.0 + \frac{3.07 f_{c0}^{1/3}}{\omega_y}}} \quad (6.6) \\
 Y_4 : \quad \frac{\tau_{xy}}{f_c^{2/3}} &= 0.318 f_{c0}^{1/3} & \tan \theta &= 1
 \end{aligned}$$

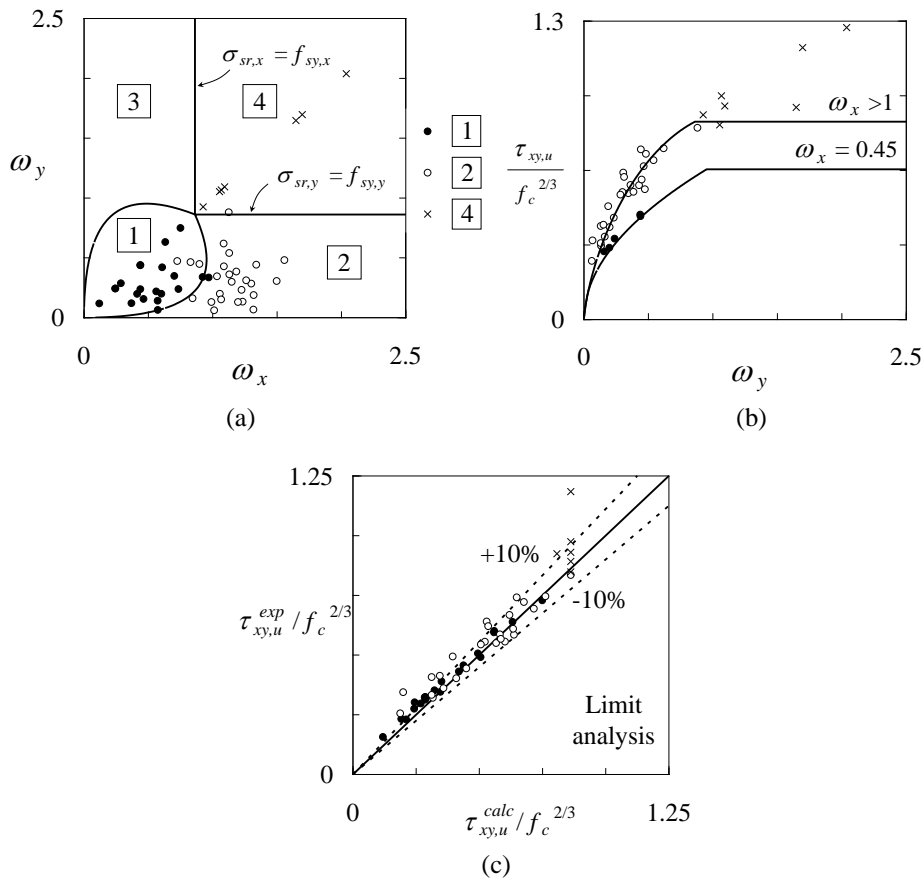


Figure 6.2 – Limit analysis accounting for compression softening. Comparison with experimental results: (a) failure modes; (b) and (c) shear strength.

The expression for yield condition Y_3 can be obtained from Y_2 by exchanging indexes and by using $\theta' = 90 - \theta$ instead of θ . The predicted boundaries of the 4 failure regimes are depicted in Figure 6.2 (a) together with the experimental failure modes of the same 54 RC panels that were already used in Chapter 3. In Figure 6.2 (b) the theoretical failure surface is compared to the experimental shear strengths of panels with $\omega_x \approx 0.45$ and $\omega_x > 1$. Good agreement can be found, demonstrating the suitability of this formulation for the design, capacity evaluation and identification of the mode of failure of RC membrane elements. A summary of the results of the validation campaign is presented in Table 3.3 and in Figure 6.2 (c). The average value of the $\tau_{u,exp}/\tau_{u,calc}$ ratio is 1.10 and the coefficient of variation equals 14.7%. A value of $f_{c0} = 20\text{MPa}$ was adopted in the calculations.

6.2.3.2 Comparison to the R-CMM and F-CMM

It is interesting to confirm that the precision level increases with the complexity of the model. As should be expected, the data summarized in Table 3.3 reveals that the dispersion of the $\tau_{u,calc}/\tau_{u,exp}$ ratio obtained with the limit analysis formulation accounting for compression softening is somewhat larger than the obtained with the F-CMM or R-CMM. However, by not considering the hardening behaviour of reinforcement steel and by adopting conservative estimates of the compression softening coefficient, the limit analysis formulation is generally on the safe side when compared to the previously mentioned models, even in the cases of failure due to transverse steel rupture or due to sliding along the shear cracks (the latter can only be predicted by the F-CMM). This can be confirmed in the failure envelope sections depicted in Figure 6.3. It can thus be concluded that the limit analysis formulation accounting for compression softening is a suitable method for a stepwise procedure for the shear safety assessment of existing structures culminating, if necessary, with a nonlinear analysis using the models developed in Chapters 3 and 4.

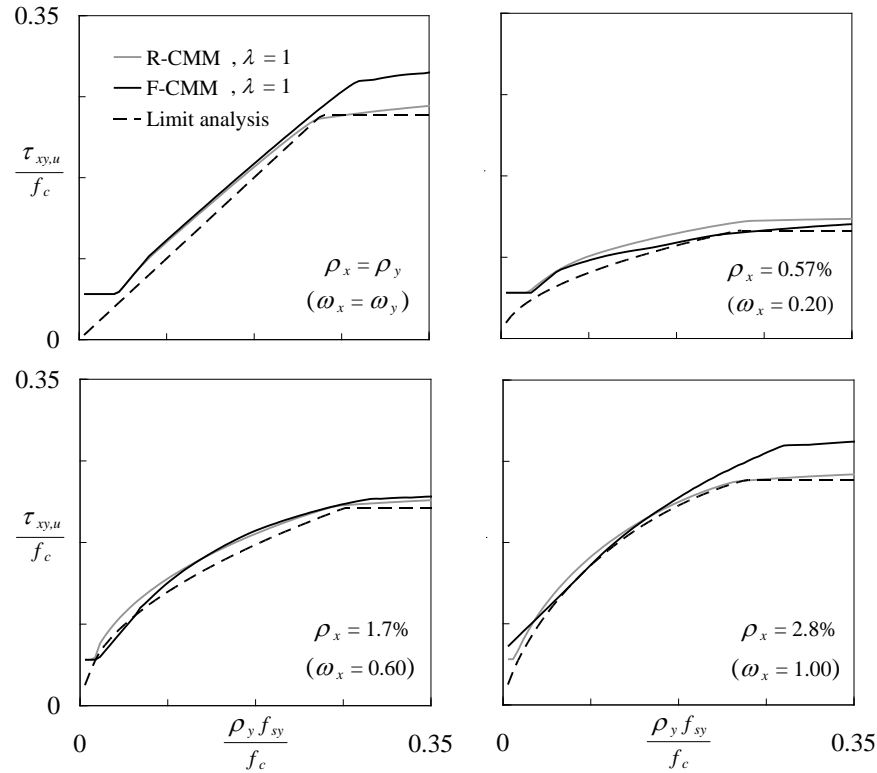


Figure 6.3 – Sections of the F-CMM, R-CMM and limit analysis with compression softening failure envelopes. Calculations were made using: $f'_c = 45$ MPa, $f_{sy} = 450$ MPa, $f_{su} = 580$ MPa, $\varepsilon_{su} = 50\text{‰}$ and $\varnothing = 16$ mm.

6.2.3.3 Effect of the strains in the stronger reinforcement

The yield conditions (6.6) were derived assuming $\varepsilon_x = 0.002$, which is equivalent to assuming that the stronger reinforcement is about to yield. In some cases this assumption can be inadequate: in prestressed concrete structures longitudinal strains below the yielding strain can usually be found in shear critical regions; on the other hand, in statically indeterminate structures, notably in the hogging moment region of continuous beams, plastic reinforcement strains can be found in shear critical zones. In these circumstances, a refined shear strength assessment can be made using the equations (6.7) where the condition $\varepsilon_x = 0.002$ was removed:

$$Y_2 : \frac{\tau_{xy}}{f_c'^{2/3}} = \omega_y \tan \theta$$

$$\tan \theta = \sqrt{\frac{-0.46 - 60 \varepsilon_x + \sqrt{0.1156 + \frac{44.21 f_{c0}^{1/3}}{\omega_y} (\varepsilon_x + 0.002)}}{0.12 + 60 \varepsilon_x}} \quad (6.7)$$

$$Y_4 : \frac{\tau_{xy}}{f_c'^{2/3}} = \frac{f_{c0}^{1/3}}{2.497 + 325.7 \varepsilon_x} \quad \tan \theta = 1$$

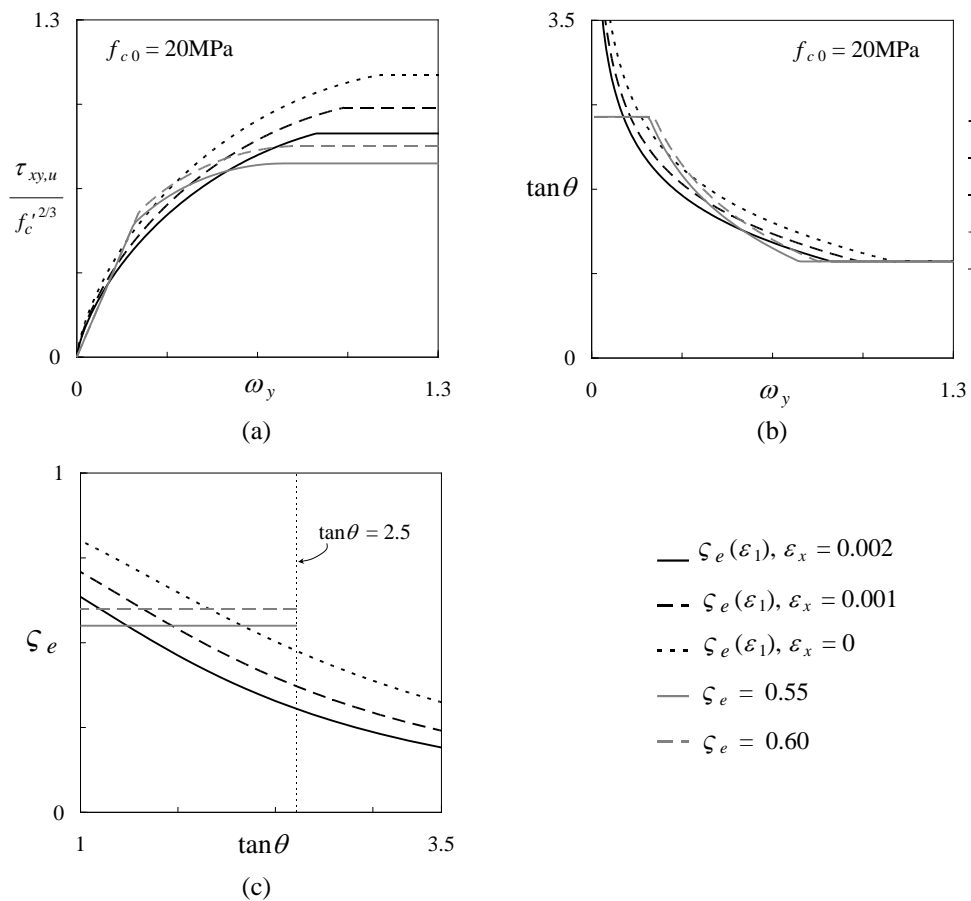


Figure 6.4 –Limit analysis: (a) sections to the failure envelope; (b) evolution of $\tan \theta$ with the mechanical reinforcement ratio ω_y ; (c) relation between the strain softening coefficient ζ_e and $\tan \theta$. The amount of stronger reinforcement is such that failure occurs in the regimes 2 and 4.

The failure envelope sections and the corresponding values of $\tan\theta$ are depicted in Figure 6.4 and compared to the results obtained with traditional limit analysis considering constant $f_{c,ef}$. In the latter, the limitation $\tan\theta \leq 2.5$ was considered. According to Eq. (6.1), and for very low amounts of vertical reinforcement, $\tan\theta$ can assume values up to 3.5. Beyond this limit it is likely that the minimum vertical steel requirements govern, and limit analysis methods cease to be applicable, as discussed in Section 6.2.1. The relation between the softening coefficient ζ_e and $\tan\theta$ is also presented in the figure and a comparison can be made with the constant values $\zeta_e = 0.55 \dots 0.60$ adopted when the influence of ε_1 is not explicitly taken into account.

6.2.4 Continuous stress fields

The equilibrium equations (3.16) used in the development of the yield conditions can be implemented in a finite element code following the same formalism adopted in the implementation of the R-CMM. This offers the possibility of migration from the membrane level - in which a uniform state of equilibrium is assumed - to the structural level of analysis. The previously derived expressions can be then applied in the automatic generation of stress fields expressing the stress flow at failure conditions of structural concrete elements. The stress fields obtained through the procedure described in this section are designated as continuous in opposition to the traditional discontinuous stress fields, see Section 6.2.5.

6.2.4.1 Constitutive laws

Simple constitutive laws are adopted here, observing more closely limit analysis assumptions and current engineering practice than in the case of the detailed models developed in Chapters 3 and 4. An elastic-perfectly plastic stress-strain law is adopted both for concrete and the reinforcements. Likewise the yield conditions accounting for compression softening, the compressive strength of cracked concrete is reduced according to Eq. (3.24). The biaxial compression effects are disregarded and the square yield locus mentioned in Section 6.2.2 is adopted. The simplified constitutive laws are summarized in Figure 6.5.

Since bond effects and concrete tensile strength are neglected, the deformations are in general overestimated. If accurate load-deformation curves are of interest, the F-CMM or the R-CMM models should be used. However, if only an estimate of the ultimate load is of interest, this simplified formulation can be most useful, namely due its close relation to

limit analysis methods. Moreover, the required input variables reduce to the concrete strength and steel yielding stress, which is quite adequate for a simplified model.

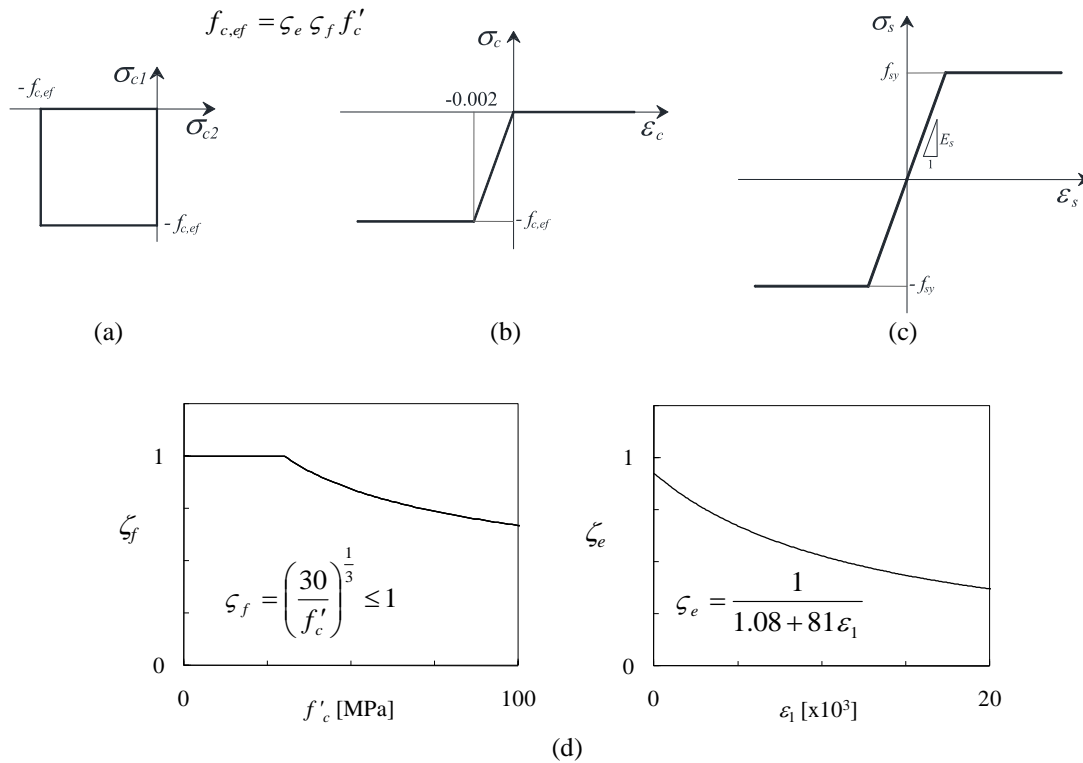


Figure 6.5 –Continuous stress field analysis: (a) Yield criterion; (b) and (c) Elastic-plastic constitutive laws; (d) Softened compressive strength

6.2.4.2 Examples

Shear in continuity regions – Beams VN2 and VN4 tested by Kaufmann and Marti [119]

These beams have already been analysed in the previous chapter and represent a typical situation where shear failure occurs in a continuity region, that is, away from stress disturbances caused by the introduction of point loads. They are here re-analysed using the simplified model described above.

In the case of beam VN2, the calculated shear strength is $V_{u,cal} = 505$ kN, leading to the ratio $V_{u,exp}/V_{u,cal} = 1.09$. The struts are computed to be 19.4° inclined with respect to the horizontal axis, which is equivalent to consider $\tan\theta = 2.84$, and concrete crushes for $f_{c,ef} = 16.4$ MPa. The stress field at failure is depicted in Figure 6.6. In the contour levels with the compressive stresses at failure, an inclined parallel stress band with compressive stresses below -16MPa is clearly identified, as expected in a B-region subjected to

constant shear force. Stirrups are yielding through the entire length of the web. The computed stress field gives a clear indication of the force flow in the structural element.

In the case of beam VN4, the calculated shear strength is $V_{u,cal} = 537$ kN, leading to the ratio $V_{u,exp}/V_{u,cal} = 1.05$. The struts are computed to be 18.5° inclined with respect to the horizontal axis, which is equivalent to consider $\tan\theta = 2.98$, and concrete crushes for $f_{c,ef} = 18.2$ MPa. The stress field is very similar to that obtained for beam VN2, and is not presented here.

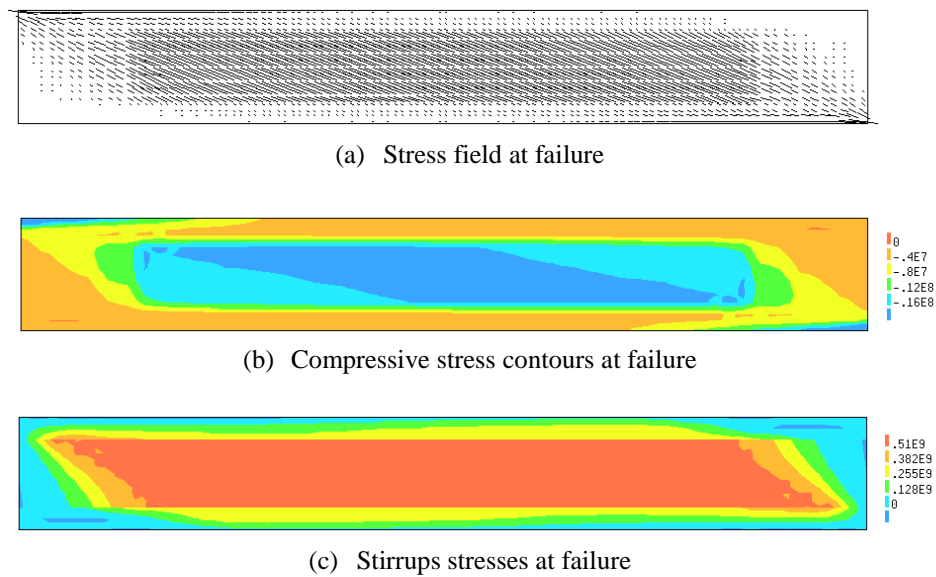


Figure 6.6 – Continuous stress field analysis of beam VN2.

As expected in a lower bound solution, the computed failure loads in both specimens are on the safe side. Nevertheless, only a minor decrease in accuracy is obtained compared to the results presented in Chapter 5.

Shear in discontinuity regions - Beams G2E and G5W tested by Kuchma et al. [94; 127]

As examples of shear failures occurring in a typical discontinuity region, the beams G2E and G5W (see Chapter 5) were selected for analysis. The stirrup ratios equal $\rho_w = 0.94$ and 0.18% respectively.

In the continuous stress field analysis, both beams failed with local crushing of the concrete in the web immediately above the support. The ultimate loads were $q_u = 435$ and 235 kN/m for G2E and G5W, respectively, which leads to $q_{u,exp}/q_{u,cal}$ ratios of 1.23 and 1.13 . The computed stress fields are depicted in Figure 6.7. Compressive stresses close to the effective compressive strength are only obtained in a localized region above the support,

providing clear evidence that failure is governed by local conditions at the ends of the specimens. Although stirrup yielding is computed for both beams, in the case of G2E, the yielding zone is very limited.

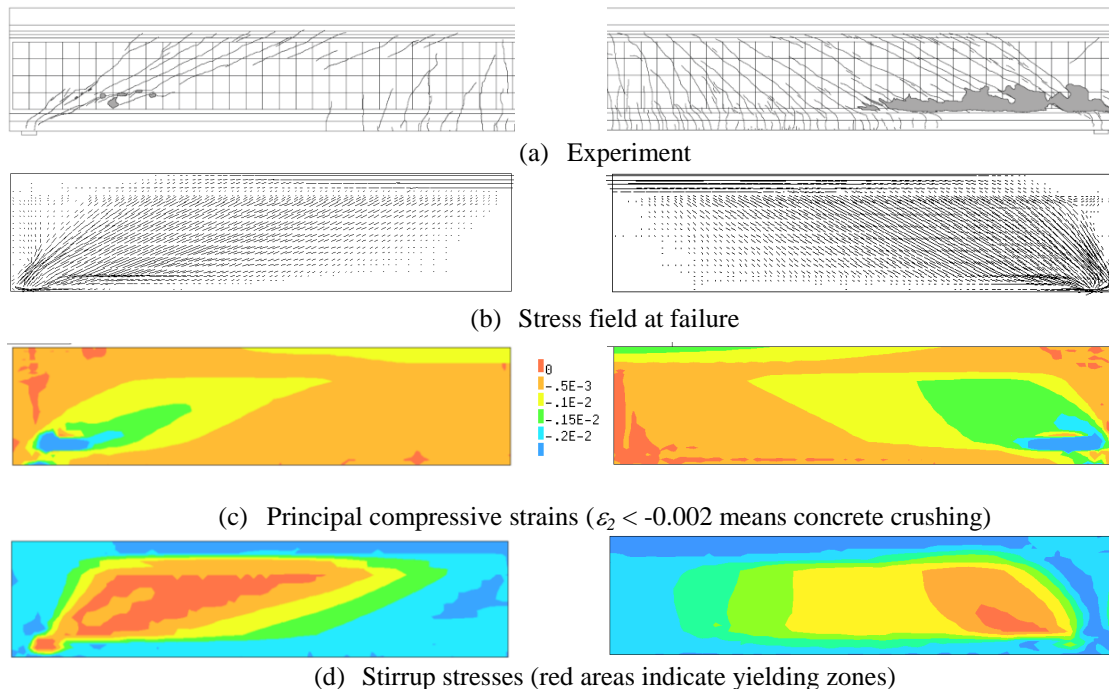


Figure 6.7 – Continuous stress field analysis of beams G5W (left) and G2E (right).

The computed stress fields provide useful information about the stress flow and the identification of the critical zone. As expected, lower bound estimates of the failure load were again calculated. The continuous stress field analysis results deviate more from those obtained in the previous chapter in the case of the beam with the lowest amount of stirrups. In this case, tensile stresses in between the cracks and the post yielding behaviour of reinforcing steel have a more important contribution for the load carrying capacity.

6.2.5 Discontinuous stress fields

6.2.5.1 Basic concepts

Within the framework of the theory of plasticity, discontinuous stress fields offer the possibility of migrating from the membrane element level to the structural level of analysis without using finite element techniques to solve the boundary value problem. A given discontinuous stress field solution represents one statically admissible stress field, which in light of the lower-bound theorem of limit analysis represents a solution on the safe side as long as an appropriate value for the effective concrete compressive strength is chosen.

As schematically depicted in Figure 6.8, lines of stress discontinuity are assumed in virtue of the underlying rigid-plastic material behaviour. It can be shown [169] that the satisfaction of the equilibrium equations implies the continuity of the shear stress $\tau_{nt}^I = \tau_{nt}^{II}$ and of the normal stress $\sigma_n^I = \sigma_n^{II}$, where the local $n-t$ axes are defined normal and tangential to the discontinuity line, respectively. However, no claims for the sake of equilibrium are made regarding the axial stress parallel (or tangential) to the discontinuity line σ_t . Therefore, only axial stresses acting parallel to the discontinuity line may exhibit a jump across the stress discontinuity.

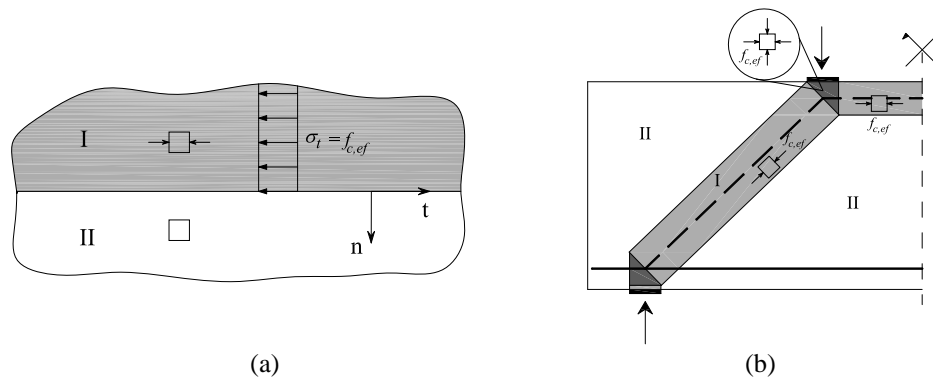


Figure 6.8 – Stress discontinuity lines: (a) notation; (b) discontinuous stress field for direct strut action.

Although more general stress fields can be derived, in practice it is convenient to use struts (Figure 6.8(b)), fans and parallel stress bands as basic stress field components, see Figure 6.9. The state of stress in each of these basic elements has been thoroughly established in several works, mostly developed at the Swiss Federal Institute of Technology, Zurich, as per example in references [117; 145; 162; 216; 228].

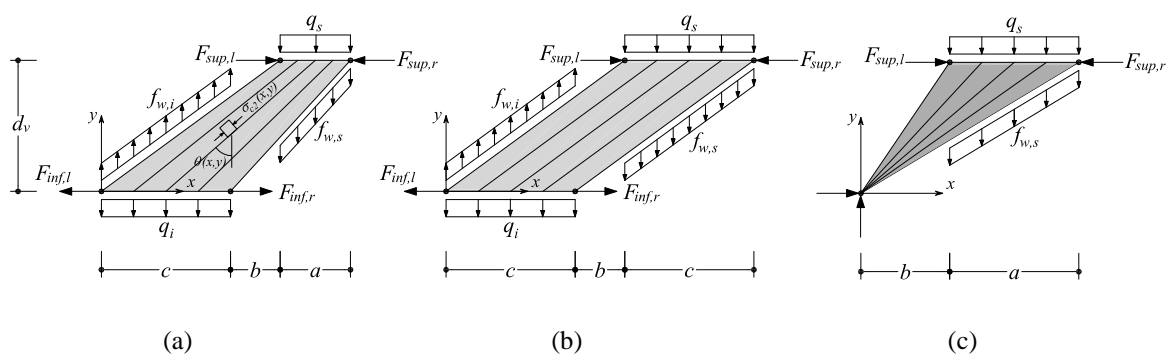


Figure 6.9 – Basic discontinuous stress field elements: (a) centred fan with intersection point away from the chords; (b) parallel stress band; (c) centred fan with intersection point in the bottom chord (note that in this case the forces in the upper chord have sign opposite to the represented).

Taking once again the simplified form of the equilibrium equations of the cracked membrane element (3.16), and assuming a membrane element with uniform thickness b_w , it is possible to conclude that

$$-\sigma_{c2} = \frac{q_v}{b_w} (1 + \tan^2 \theta) \quad (6.8)$$

with $q_v = q + f_w$ being the resultant vertical force, $q = -b_w \sigma_y$ the external vertical load and $f_w = b_w \rho_y \sigma_{sy}$ the stirrup force (all these forces per unit length). In the simplest case of the parallel stress band, the principal compressive stresses in concrete σ_{c2} are constant if both the external load and the stirrup force distributions are uniform. The fans presented in Figure 6.9 are called centred because the stress trajectories meet in one point. In this case the concrete stresses vary hyperbolically along the stress trajectories and can still be calculated with Eq. (6.8), but noting that q_v and θ cease to be constant along the fan [228]:

$$q_v = (q_s + f_{w,s}) \frac{a d_v + y(c-a)}{c d_v} \quad \tan \theta = \frac{c(c+b) - x(c-a)}{c d_v - y(c-a)} \quad (6.9)$$

In the expression above, the coordinates x and y define a point in the rectangular coordinate system represented in Figure 6.9, where all the remaining variables are identified. The force distribution in the chords can be derived from the translational equilibrium equations of the infinitesimal strut section represented in Figure 6.10:

$$\frac{dF_{\text{inf}}}{dx} = (f_{w,i} - q_i) \tan \theta \quad (6.10)$$

$$\frac{dF_{\text{sup}}}{dx'} = (q_s + f_{w,s}) \tan \theta \quad , \quad x' = x - c - b$$

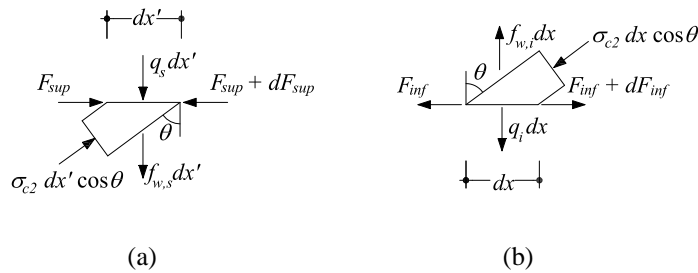


Figure 6.10 – Equilibrium of forces acting in the top (a) and bottom (b) chords.

According to the previous expressions, the chord forces vary linearly along parallel stress bands since θ has a constant value and uniform distributions of stirrup and external forces are usually assumed. In the centred fans the variation is parabolic and can be obtained by integration of Eqs. (6.10) with proper consideration of Eq. (6.9):

$$F_{\text{inf}}(x) - F_{\text{inf},l} = (f_{w,i} - q_i) \frac{2(c+b)cx - x^2(c-a)}{2cd_v} \quad (6.11)$$

$$F_{\text{sup}}(x') - F_{\text{sup},l} = (f_{w,s} + q_s) \frac{2(c+b)ax' - x'^2(c-a)}{2d_v a}$$

The expressions above were derived assuming that the chords are straight and parallel to the x -axis, see Figure 6.9. More general expressions can be derived for curved chords [228], which are suited for cases where the stress field is deviated by a curved prestressing tendon.

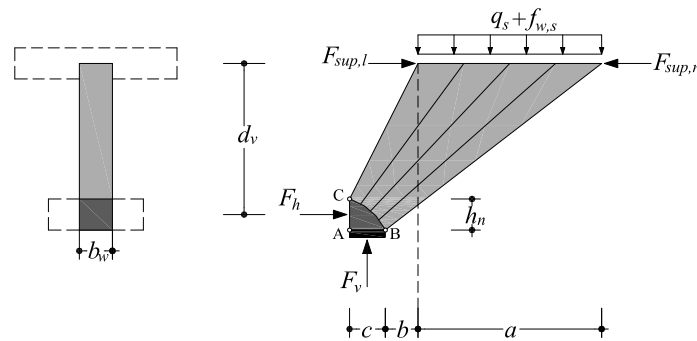


Figure 6.11 – Non-centred fan with nodal region (a) and detail of the node (b).

Infinitely high compressive stresses result at the centre of the fan depicted in Figure 6.9(c). In reality supports or loading plates have a finite dimension and more detailed admissible stress fields can be considered adopting non-centred fans with nodal region, as illustrated in Figure 6.11. Since a reasonable approximation of the stresses in the vicinity of the chord opposite to the node can be obtained with the centred fan, the non-centred fan can be used mainly for checking the state of stress in the vicinity of concentrated loads. The equation describing the boundary of the nodal region can be determined assuming that concrete is yielding in biaxial compression – that is, the concrete stresses along lines AB, AC and BC equal $f_{c,ef}$ – and solving the differential equation of equilibrium for the vertical forces. For constant $f_{c,ef}$ and b_w it can be shown [217] that the boundary line is hyperbolic and that

$$c = \frac{(q_s + f_{w,s})a}{f_{c,ef}b_w} \quad h_n = \frac{(a + 2b + c)c}{2d_v} \quad (6.12)$$

which allows checking the minimum node dimensions. The expressions above are valid for flanged or hollow-box beams in which the flange regions adjacent to the web are assumed to carry the compressive chord forces. For details refer to [118; 217].

6.2.5.2 The effective compressive strength

As thoroughly discussed in Chapter 3, the effective concrete compressive strength $f_{c,ef}$ can be conveniently expressed by Eq. (3.24). When a constant value for the softening coefficient ζ_e is adopted, the best fit to the shear strength of RC panels is obtained with $f_{c0} = 20\text{MPa}$ and $\zeta_e = 0.6$, as shown in Section 6.2.2. However, for structural concrete elements other than uniformly stressed RC panels, the results from the numerical analyses of Chapter 5 show that better agreement between the calculated and observed shear strength is obtained using $f_{c0} = 30\text{MPa}$. This fact was attributed to the partial restraint to laminar splitting provided by the intact concrete surrounding the failure zone, with particular emphasis on the flanges. This seems to be confirmed in the most recent draft of the CEB-FIP Model Code 2010 [87] wherein $f_{c,ef}$ is defined similarly to (3.24) with $f_{c0} = 30\text{MPa}$ and $\zeta_e = 0.55^1$. The latter is somewhat more conservative, and therefore more appropriate to be specified in a code, than the best fit value of $\zeta_e = 0.6$ referred above. Not surprisingly, it is interesting to confirm that this definition of $f_{c,ef}$ renders practically the same values in the range $f'_c \in [0; 100]$ (MPa) as the one proposed in the Eurocode 2 [46] using $\zeta_e = 0.6$ and ζ_f given by (2.20).

As discussed in Section 6.2.3, more accurate shear strength assessments can be made if a strain compatibility analysis is made such that the dependence of ζ_e on the principal tensile average strains ε_1 is explicitly taken into account. This is exemplified in the following examples.

6.2.5.3 Examples

Beams VN2 and VN4 tested by Kaufmann and Marti [119]

The adopted stress field is depicted in Figure 6.12. The similarity with the stress field obtained using the continuous stress field approach is evident. The critical value of $\tan\theta$ is

¹ This value of ζ_e is proposed for the case of compressive stress fields with the reinforcement running obliquely to the direction of compression, as is typically the case in the web of a beam.

determined in regime 2 using the corresponding Eq. (6.7), for which ε_x and ω_y must be defined. Since failure occurs in the parallel stress band – note that $\tan\theta$ is maximum in this region – , it is here proposed to use the most unfavourable value of the average longitudinal strain ε_x occurring in this region, having in mind that the conditioning value must be located in the web. This corresponds to the locations indicated in the figure, which yield the same value for ε_x due to the antisymmetric loading conditions. A trial and error procedure is required since $\tan\theta$ depends on ε_x , and the critical location for the determination of ε_x depends on $\tan\theta$. However, great precision is not necessary in the determination of ε_x and a couple iterations are usually enough to achieve a reasonable estimate. For beam VN4 the applied compression force is assumed to be carried exclusively by the chords.

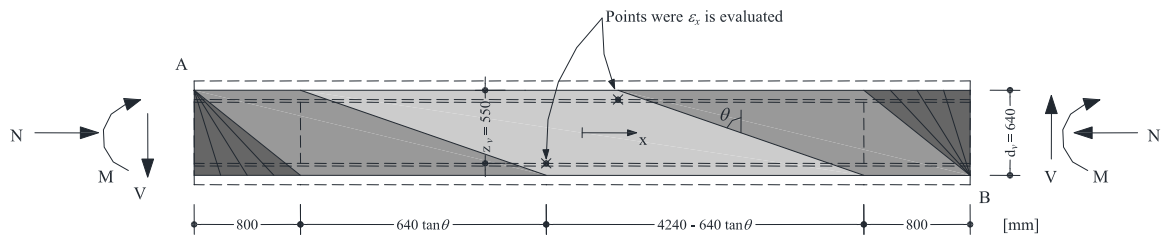


Figure 6.12 – Discontinuous stress-field for the beams VN2 and VN4.

Defining the lever arm $d_v = 0.64\text{m}$ as the distance between the centres of the flanges, the force in the tensile chord can be determined from the bending moment diagram as $F_T = M / d_v$. Knowing the amount of longitudinal steel in the flange $A_s = 106\text{cm}^2$ and assuming a linear variation of ε_x throughout the cross-section height, the critical average strain is estimated as:

$$\varepsilon_x = 0.8 \frac{z_v}{d_v} \frac{F_T}{A_s E_s} \quad (6.13)$$

where z_v is defined in Figure 6.12.

Beam VN2 failed for $V = 548\text{kN}$, which corresponds to extreme bending moments of $M = 548 \cdot 5.840 / 2 = 1600\text{kN.m}$. Using the appropriate expressions (6.11) the tensile chord force at the critical location is found to be $F_T = 1193\text{ kN}$ and the average strain can be estimated as $\varepsilon_x = 0.8 \cdot 0.55 / 0.64 \cdot F_T / A_s \cdot E_s = 0.39\text{e-}03$. Considering $f'_c = 52.6\text{ MPa}$, $\omega_y = 0.122$ (see the material properties in Table 5.1) and the estimated value of ε_x , the value $\tan\theta = 2.89$ is determined from Eq. (6.7). Substituting $\tan\theta$ and ε_x in Eq. (3.24), it is

possible to conclude that $f_{c,ef} = 16.0\text{MPa}$. As should be expected, this value is quite close to that obtained in the continuous stress field analysis. As failure occurs in the parallel stress band, the corresponding ultimate shear force can be calculated from Eq. (6.8) as $V_{u,cal} = 473\text{ kN}$, leading to the ratio $V_{u,exp}/V_{u,cal} = 1.16$.

Beam VN4 failed for $V = 564\text{kN}$, corresponding to $M = 1647\text{kN.m}$. Performing calculations identical to the ones described in the previous paragraph, but noting the applied compressive force $N = 1000\text{kN}$, it can be found that $\varepsilon_x = 0.23\text{e-}03$, $\tan\theta = 3.04$, $f_{c,ef} = 17.6\text{MPa}$ and $V_{u,cal} = 498\text{ kN}$. This leads to a ratio $V_{u,exp}/V_{u,cal} = 1.13$.

Compared to the failure loads calculated using a constant value for $f_{c,ef}$, an improvement is achieved due to the fact that the angle θ is no longer limited by the condition $\tan\theta \leq 2.5$. The failure loads that are obtained with constant $f_{c,ef}$ are identical to the ones calculated using the Eurocode 2 provisions and are given in Table 5.1. This shows the benefits that can be gained from performing a more detailed analysis using the proposed procedure. Moreover, the effects of the compressive axial force could be taken into account. As should be expected, even better correlation with the experimental failure loads could be obtained with NLFEA models.

Beam CM2 tested by Cerruti and Marti [53]

Let us consider the beam CM2 tested by Cerruti and Marti [53], see Figure 6.13. Besides the self weight W , this large scale beam was subjected to a uniform load Q in the span and to a point load P in the overhang. The test was aimed at verifying the adequacy of the staggering concept in a specimen with curtailed longitudinal reinforcement. The beam failed at $Q = 1711\text{kN}$ and $P = 904.7\text{kN}$ owing to crushing of the web concrete after extensive yielding of the stirrups in the interior span adjacent to support B. Prior to failure, yielding of the longitudinal bars in the top and bottom flanges was also observed.

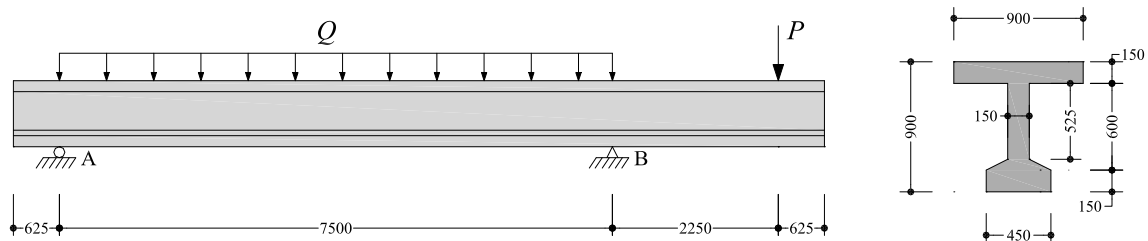


Figure 6.13 –Beam CM2 tested by Cerruti and Marti [53]. Dimensions in mm.

One possible discontinuous stress field is presented in Figure 6.14. The lever arm d_v was defined as the distance between the centres of the flanges. The stirrups are uniformly distributed along the distances indicated in the figure, leading to the provided stirrup forces $f_{w,r}$. The stirrup content in the interior span adjacent to support B equals $\rho_w = 0.895\%$ with $f_{sy} = 457\text{MPa}$. Considering the compressive strength $f'_c = 44.7\text{MPa}$, the mechanical reinforcement ratio $\omega_y = 0.325$ can be calculated.

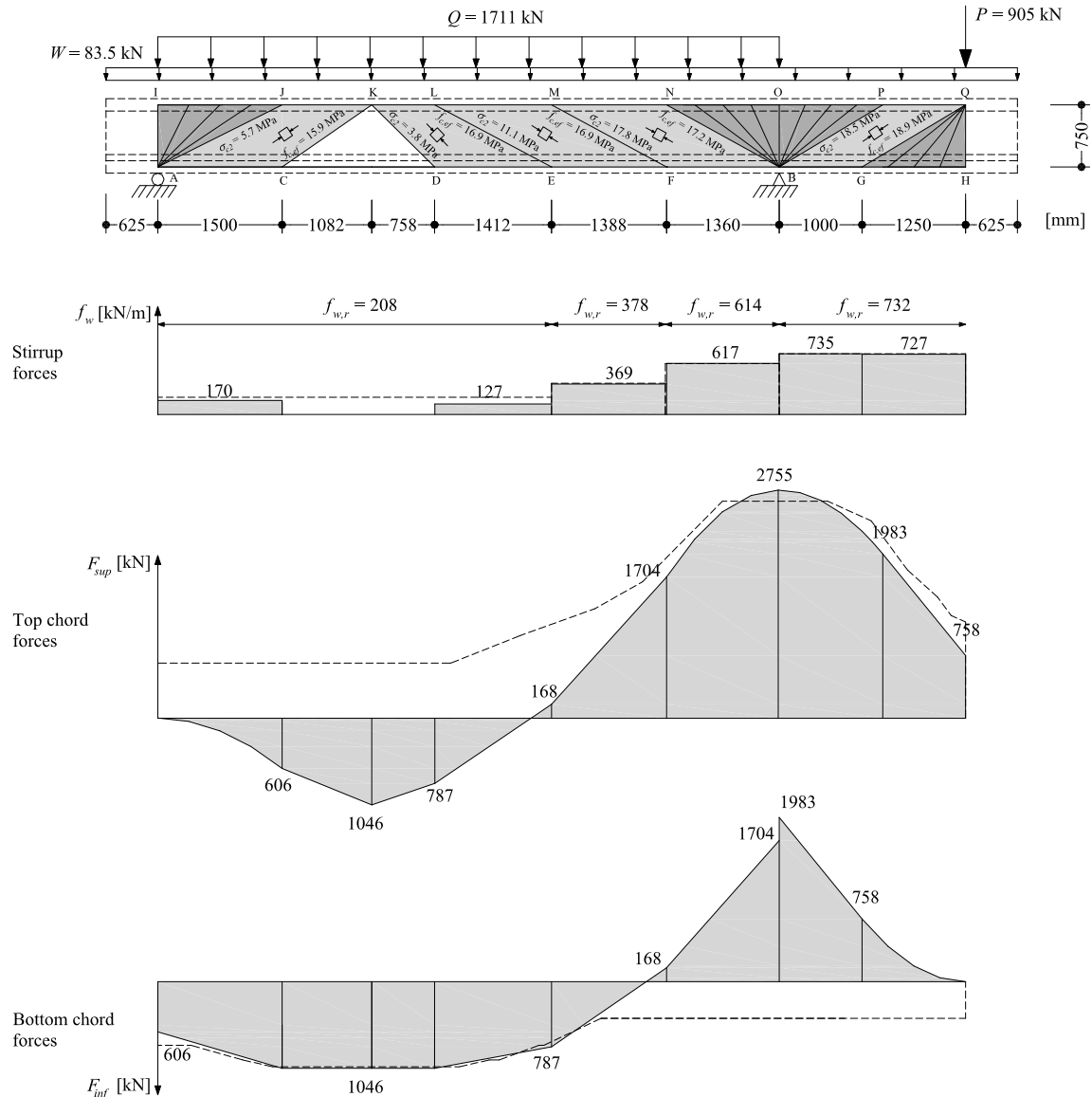


Figure 6.14 – Stress field analysis of beam CM2. The dashed lines indicate yielding forces provided by the existing reinforcement.

Admitting in a first iteration that $\varepsilon_x = 0.002$ in the top chord, the value $\varepsilon_x = 0.675/0.75 = 0.0018$ can be calculated in the web immediately below the chord. It is recalled that

$\varepsilon_x = 0.002$ already accounts for the tension stiffening effects, being approximately 80% of the reinforcement yielding strain. Substituting this value in the expression for $\tan\theta$ corresponding to the failure regime 2 given in (6.7), and considering $f_{co} = 30\text{MPa}$, one obtains $\tan\theta = 1.81$. This angle defines the critical inclination for the fan BON over support B. The stirrup content is constant in a length of about 1375mm, of which only $d_v \cdot \tan\theta = 1360\text{mm}$ were mobilized by the fan BNMF. In the adjacent 1388mm segment the spacing is changed such that $\rho_w = 0.546$ and $\omega_y = 0.198$. Still considering that $\varepsilon_x = 0.0018$ in this region, the maximum value of $\tan\theta = 2.17$ is determined. Having defined the successive critical values of $\tan\theta$ corresponding to the different segments with uniform stirrup spacing, the stress field can be constructed. In this case, the critical value of $\tan\theta$ is only attained in the fans BNMF and BON, which means that these are the critical regions for the web crushing failures. The resulting stirrup and chord forces in equilibrium with the external ultimate load, as determined by Eq. (6.11), are also depicted in Figure 6.14. The dashed lines indicate the corresponding forces provided by the existing reinforcement. The resistance of a longitudinal bar was assumed to increase linearly along its development length and account was made for the additional length required for the bars placed in the flanges outside the web. For details regarding the reinforcement layout refer to [53].

The adequacy of the adopted value for ε_x can now be assessed. Observing the forces in the upper chord in the region of the support B, it is possible to confirm that the longitudinal bars are about to yield. In fact these bars were curtailed to fit the demand in the tensioned chords. Although some fine tuning could be made, the adopted value of ε_x can be considered a reasonable one. Therefore, adopting $\varepsilon_2 = -0.002$, $\varepsilon_x = 0.0018$ and $\tan\theta = 1.81$ in expression (6.4), the principal average tensile strain in the critical region of the web can be estimated as $\varepsilon_l = 0.014$ for the fan BNMF, which agrees very well with the measured strains reported in [53]. The principal compressive stresses in the web can be calculated from Eq. (6.8) and are shown in Figure 6.14 jointly with the corresponding effective compressive strength $f_{c,ef}$. As discussed previously, the concrete stresses are not constant within the fans. The presented values refer to the locations near the tension chord with maximum absolute value of σ_{c2} (note that $f_{c,ef}$ increases as ε_x decreases towards the compression chord). It can be concluded that web crushing occurred in the fan BNMF, since $\sigma_{c2} > f_{c,ef}$. The analysis of the required vs. provided stirrup forces per unit length (f_w vs. $f_{w,r}$) indicates that stirrups are yielding at the critical locations. From the analysis of the forces in the chords it can also be concluded that the longitudinal steel is yielding both in the span and in the hogging moment region. This is in total agreement with the

experimental observations, thus validating the adopted stress field and the procedure for determining $f_{c,ef}$ and $\tan\theta$. In this case, the calculated value of $f_{c,ef}$ in the critical fan BNMF is obtained with $\zeta_e = 0.44$, which is lower than the constant value of $\zeta_e = 0.55$ mentioned in Section 6.2.5.2. This is clearly evidenced in Figure 6.4(c), where it can be seen that $\zeta_e \leq 0.55$ when ε_x is close to 0.002 and $\tan\theta \geq 1.35$. Some minor violations of the chord yielding forces are observed which can be explained by the gross estimation of the lever arm and by the fact that perfectly plastic behaviour is assumed for the reinforcing steel, thus neglecting the hardening branch.

In the previous analysis the concrete stresses in the discontinuity region corresponding to fan BON were not analysed. To do so, a non-centred fan with nodal zone such as the one depicted in Figure 6.11 must be used. Such type of analysis is thoroughly discussed by Kaufmann in [117]. It is concluded that in most typical cases it is sufficient to evaluate the stresses at the boundary of the nodal zone and at the top end of the fan, where the effective compressive strength is lower, particularly if there are plastic strains in the chord. In the present case it is possible to show that the nodal zone must be located inside the bottom flange in order to make use of the enlarged concrete section. At each support the specimen was placed on a 5 x 200 x 450 mm steel plate [53]. This being the case, from expressions (6.12) and using $\zeta_e = 1.0$ in the definition of $f_{c,ef}$ in the nodal region (according to Eq. (3.24) this is equivalent to assuming that $\varepsilon_x < -0.0017$), it is easily concluded that $c = 111\text{mm}$, $h_n = 101\text{mm}$ and the required thickness of the nodal zone is $b_w = 267\text{mm}$, which is larger than the web thickness. This means that the non-centred fan has variable thickness and an additional verification of the stresses in the fan must be made at the interface between the bottom flange and the web. The detailed examination of σ_{c2} and $f_{c,ef}$ throughout the fan involves the estimation of ε_x . Since plastic strains are expected in this region, the average values of ε_x in the web can be calculated from σ_{sr} at the tensile chord using the TCM relations (3.37) to (3.39) and assuming a linear variation towards the compressive chord. Such a detailed calculation is not presented here.

6.2.6 Section-by-section analysis for continuity regions

A sectional analysis procedure can be derived for the so called continuity regions considering a uniform shear stress distribution along the cross-section height, that is $\tau_{xy} = V / b_w \cdot d_v$. This being the case, and noting that $(\sin\theta \cdot \cos\theta)^{-1} = \cot\theta + \tan\theta$, the last equation of (3.16) can be elaborated to:

$$\sigma_{c2} = -\frac{V}{b_w d_v} (\cot \theta + \tan \theta) \quad (6.14)$$

which allows determining the minimum concrete stresses in the web. Taking Eq. (6.14), considering $\sigma_y = 0$ and the stirrup force per unit length $f_w = b_w \cdot \rho_y \cdot \sigma_{sy}$ in Eq. (3.16)₂, one obtains

$$V = f_w d_v \tan \theta \quad (6.15)$$

which allows checking the shear reinforcement. This shows how the results obtained in Section 6.2.3 can be applicable in shear assessment and design.

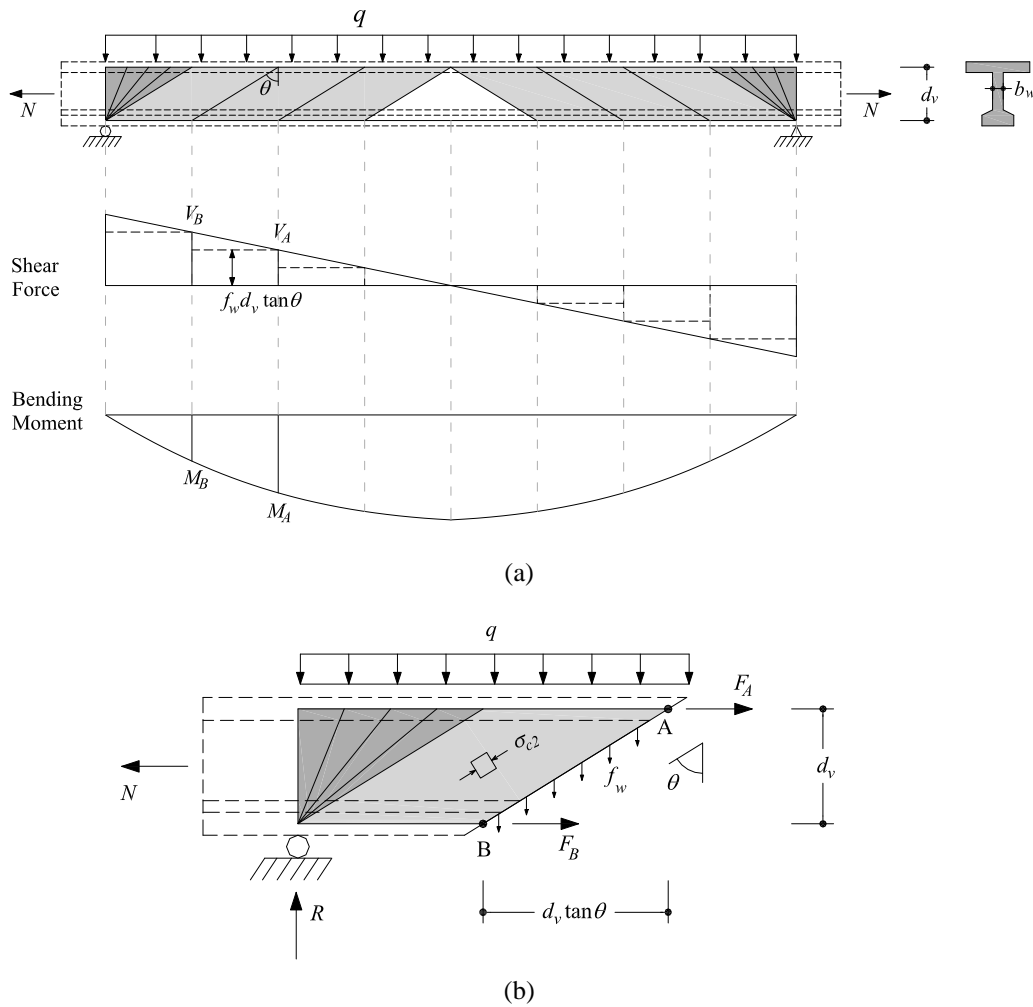


Figure 6.15 –Development of the sectional analysis procedure: (a) discontinuous stress field and adopted notation; (b) free body diagram.

This simple section-by-section analysis procedure can also be developed based on the discontinuous stress field analysis concept. Figure 6.15(a) shows a simply supported beam

and the adopted discontinuous stress field. In order to determine the chord forces F_A and F_B , and the required stirrup force per unit length f_w , the free-body diagram of Figure 6.15(b) can be used from which the results given in Eqs. (6.16) and (6.17) are found.

$$V_A = f_w d_v \tan \theta \quad (6.16)$$

$$F_A = -\frac{M_A}{d_v} + \frac{V_A}{2} \tan \theta + \frac{N}{2} \quad F_B = \frac{M_B}{d_v} + \frac{V_B}{2} \tan \theta + \frac{N}{2} \quad (6.17)$$

Starting from Eq. (6.8) it is easily found that the web concrete stresses σ_{c2} are given by

$$\sigma_{c2} = -\frac{V_B}{b_w d_v} (\cot \theta + \tan \theta) \quad (6.18)$$

The expressions above show how the chord forces can be determined and that the shear force at a given section is balanced by the stirrups within the distance $d_v \tan \theta$ from that section. Generally speaking, this means that for beams uniformly loaded on the top chord the stirrup reinforcement required within the length $d_v \tan \theta$ may be determined using the lowest value of V that occurs within this length. However, the same cannot be done in the determination of diagonal compression in the web, see Eq. (6.18). This is known as the “staggering effect” [148] and puts in evidence that, in a strict sense, sectional analysis procedures are inadequate for shear analysis and design.

6.3 Code-like formulation

In many cases, a code-like formulation based on the section-by-section procedure outlined in Section 6.2.6 may suffice for performing the shear safety evaluation of an existing concrete bridge. The formulation suggested herein is proposed as part of a stepwise approach to the shear safety evaluation of members containing at least the minimum amount of shear reinforcement. In the first level of analysis, shear design equations based on the variable angle truss model with constant $f_{c,ef}$ can be used with the inherent limits on the angle θ . In a second level, $f_{c,ef}$ is defined according to Section 6.2.3 and the limits on the angle θ are replaced by Eq. (6.7). In a third level of analysis, the use of continuous/discontinuous stress fields is suggested. Finally, and if required, NLFEA using the models developed in Chapters 3 and 4 is proposed as the most accurate method.

6.3.1 Proposed expressions

The maximum shear force is governed by crushing of the web concrete and can be elaborated directly from (6.18) substituting σ_{c2} by $f_{c,ef} = \zeta_e \zeta_f f_{cd}$, with f_{cd} being the design value of the uniaxial compressive strength in cylinders:

$$V_{R,max} = \frac{b_w d_v \zeta_e \zeta_f f_{cd}}{\tan \theta' + \cot \theta'} \quad (6.19)$$

The angle $\theta' = 90 - \theta$ is adopted instead of θ since in this context it is more common to use the inclination of the compression field, θ' , instead of the angle θ defining the normal to the cracks. Eq. (6.16) allows checking the amount of stirrups and can be elaborated to

$$V_{R,s} = \frac{A_{sw}}{s} f_{ywd} d_v \cot \theta' \quad (6.20)$$

with A_{sw}/s being the stirrup area per unit length, s the stirrup spacing and f_{ywd} the design value of the steel yielding stress. Not surprisingly, these expressions are formally identical to the ones of the variable angle truss model.

6.3.1.1 Definition of the control sections

Notwithstanding the remarks made in Section 6.2.6 regarding the adequacy of sectional analysis methods for shear design and assessment, the development of a practical methodology requires the definition of control sections wherein the shear strength provided by Eqs. (6.19) and (6.20) is compared to the shear demand. According to the lower bound limit analysis methods, the compression stress field in the web rotates to a lower inclination after yielding of the shear reinforcement in order to activate more stirrups, thus extending the failure zone. This rotation leads to an increase of the compressive concrete stresses in the web and, provided that flexural failures are prevented, can only continue until concrete crushing occurs. If $f_{c,ef}$ is defined according to Section 6.2.3, an unambiguous definition of the location wherein the strain ε_x is evaluated is crucial. The occurrence of a shear failure after stirrup yielding involves yielding of this reinforcement over a length of beam of $d_v \cot \theta'$. Hence, the sectional analysis can be taken as representing a length of beam $d_v \cot \theta'$ long with the control section being in the middle of this length, see Figure 6.16 (a). As exemplified in Section 6.2.5.3, ε_x is conservatively evaluated in the most unfavourable region of the web, that is, near the tensile chord. Considering that the flanges supply some kind of out-of-plane confinement to the web, in

flanged sections with thin webs ε_x can be calculated at a distance z_x from the tensile reinforcement, see Figure 6.16(a). In general, this point can be considered to be located at b_w from the edge of the flange. For simplicity, a linear variation of the strain can be adopted considering $\varepsilon_x = 0$ at the centre of the compression chord, as depicted in Figure 6.16 (a).

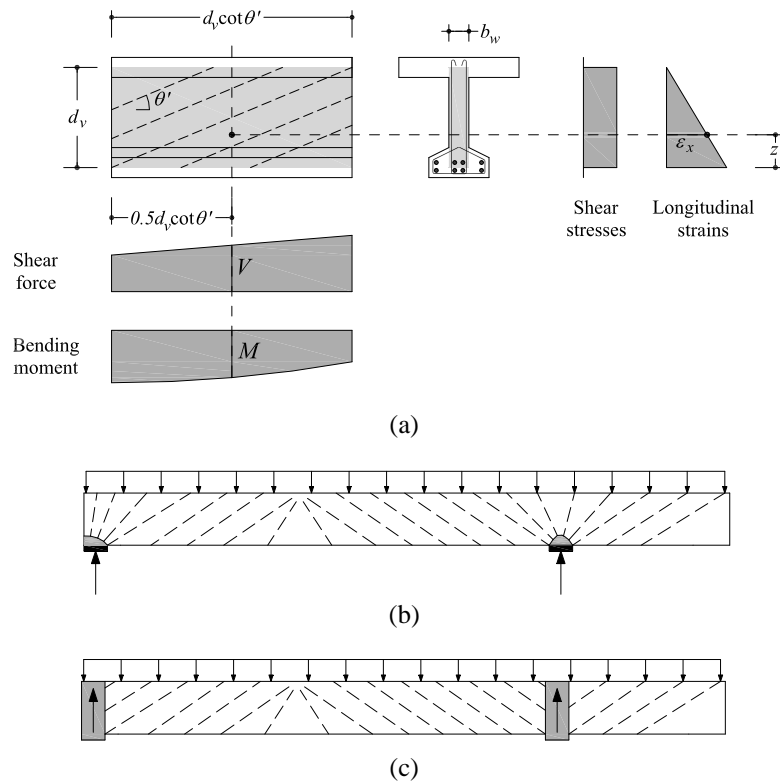


Figure 6.16 – Control section: (a) Definition and location of the point where ε_x is evaluated (b) Beam on direct supports; (c) Beam supported by cross-girders.

The cross-sections with maximum shear are usually located near the supports. These are typical discontinuity regions where the applicability of sectional analysis methods may be questionable. Nevertheless, due to the fanning effect the adopted procedure is conservative since it does not take into account the variation of θ' occurring in the fans, as schematically illustrated in Figure 6.16 (b). The same occurs in beams subjected to point loads. In most practical cases beams are supported through cross-girders, see Figure 6.16 (c). In this case, the reactions feed in over the member depth, the fanning action is not so pronounced, and the states of stress and strain within the control section are closer to the sectional analysis assumptions. However, it must be remarked that whenever the end regions of a bridge girder are not cast integral with the supports, local crushing may occur in the support region, as evidenced in Chapter 5. As this failure mode is governed mainly by the support

dimensions and reinforcement detailing, a detailed verification using stress field models or NLFEA is advised.

6.3.1.2 Level I analysis

In the first level of analysis, the effective compressive concrete strength to be adopted in Eq. (6.19) is determined using a constant softening coefficient given by

$$\zeta_e \zeta_f = 0.55 \left(\frac{f_{c0}}{f'_c} \right)^{1/3} \quad (6.21)$$

with $f_{c0} = 30\text{MPa}$ if $f'_c \geq 30\text{MPa}$, and $f_{c0} = f'_c$ otherwise. The angle θ' in Eqs. (6.19) and (6.20) is limited by

$$1 \leq \cot \theta' \leq \sqrt{\frac{0.55 f_{c0}^{1/3} - \omega_y}{\omega_y}} \quad (6.22)$$

where the upper limit comes from Eq. (6.3)₂ and corresponds to the situation $V_{R,s} = V_{R,\max}$. The mechanical shear reinforcement ratio ω_y is defined as

$$\omega_y = \frac{A_{sw} f_{yw}}{s b_w f_c^{2/3}} \quad (6.23)$$

As discussed in Section 6.2.2, the adoption of a constant value for ζ_e overestimates the shear strength in the case of lightly shear reinforced beams and an additional upper limit to $\cot \theta'$ must be obeyed:

$$\cot \theta' \leq 2.5 \quad (6.24)$$

6.3.1.3 Level II analysis

In the second level of analysis, a refined assessment can be made using

$$\zeta_e \zeta_f = \frac{1}{1.08 + 81 \varepsilon_1} \left(\frac{f_{c0}}{f'_c} \right)^{1/3} \quad \varepsilon_1 = \varepsilon_x + (\varepsilon_x + 0.002) \cot^2 \theta' \quad (6.25)$$

The limits for $\cot \theta'$ are directly obtained from Eq. (6.7)₂,

$$1 \leq \cot \theta' \leq \sqrt{\frac{-0.46 - 60 \varepsilon_x + \sqrt{0.1156 + \frac{44.21 f_{c0}^{1/3}}{\omega_y} (\varepsilon_x + 0.002)}}{0.12 + 60 \varepsilon_x}} \quad (6.26)$$

and the average longitudinal strain can be estimated as

$$\varepsilon_x \approx 0.8 \left(1 - \frac{z_x}{d_v} \right) \frac{|M|/d_v + 0.5|V| \cot \theta' + 0.5N}{E_s A_s + E_p A_p}, \quad \varepsilon_x \geq 0$$

$$\varepsilon_x \approx 0.8 \left(1 - \frac{z_x}{d_v} \right) \frac{|M|/d_v + 0.5|V| \cot \theta' + 0.5N}{E_s A_s + E_p A_p + E_c A_{ct}}, \quad \varepsilon_x < 0$$
(6.27)

where A_{ct} is the area of the corresponding tensile chord and the bending moment M , the shear force V and the axial force N are assumed to include the effects of prestressing. The demand $|M|/d_v + 0.5|V| \cot \theta'$ is limited by the force at the location of maximum bending moment due to moment alone. In the absence of a more detailed analysis, the reinforcing and prestressing steel areas A_s and A_p , respectively, to be used in Eqs. (6.27) refer to bars or tendons which are fully anchored in the $d_v \cot \theta'$ long beam segment which the control section is representing.

6.3.2 Sample calculations

The practical application of the Level II analysis requires an iterative procedure because the location of the critical section depends on ε_x , which on its turn depends on the location of the critical section where it is being determined. A simple algorithm that can be easily performed on a spreadsheet or pocket calculator is proposed in Box 6.1. In the following some calculation examples are presented.

Box 6.1 – Algorithm for shear strength calculation according to the Level II sectional analysis.

- 1 – Estimate θ' from Eq. (6.26) using a trial value for ε_x , for instance $\varepsilon_x = 1.0\text{e-}3$;
- 2 – Define de control section according to Figure 6.16 and determine the corresponding sectional forces V and M ;
- 3 – Update ε_x using Eqs. (6.27);
- 4 – New estimate for $\cot \theta'$ using Eq. (6.26);
- 5 – Check if the solution is acceptable: $|\varepsilon_{x,i} - \varepsilon_{x,i-1}| < tol$?
- 6 – If the solution is acceptable compute V_R with Eqs. (6.19) or (6.20), else return to point 2.

Beams tested by Higgins et al [98]

In 2004 a major research study was completed at the Oregon State University by Higgins et al. [98] that investigated the shear capacity of 44 full sized reinforced bridge girders. Here only a subset of the investigated girders will be analysed, in which the only significant variable was the amount of shear reinforcement.

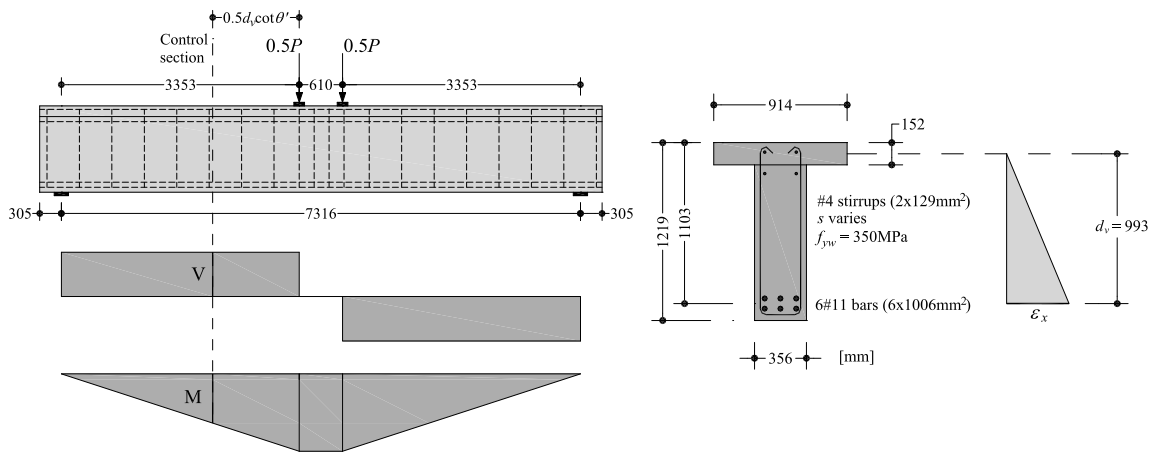


Figure 6.17 –Beams tested by Higgins et al. [98].

The diagrams with the internal forces are depicted in Figure 6.17. The critical section is located $0.5 \cdot d_v \cdot \cot \theta'$ away from the applied forces as indicated in the figure. Since the shear force diagram is approximately constant, – the self-weight is almost negligible when compared to the applied forces –, another possibility would be to consider the control section located $0.5 \cdot d_v \cdot \cot \theta'$ away from the supports. However, in the latter the corresponding tensile chord forces are lower, which according to Eqs. (6.26) and (6.27) leads to non conservative estimates of the ultimate shear force. This is confirmed by the experimental observations. In fact, the shear cracks that led to collapse were located closer to the considered control section. The strain ϵ_x was determined at the level of the longitudinal reinforcement, that is, considering $z_x = 0$ in Eqs. (6.27).

The analysis results are summarized in Table 6.1. Two of the beams exhibited flexural failures, which are correctly predicted by the sectional analysis method. It is noted that whenever $\cot \theta'$ is higher than the ratio between the shear span and the lever arm, L/d_v , combined strut and fan action must be occurring and, provided that the longitudinal steel is properly anchored, a portion of the applied force is being directly transmitted to the support. If advantage is to be taken of this mixed load carrying mechanism, the sectional

method ceases to be applicable and proper attention must be paid to the detailing of the anchorage region and to the concrete stresses in the vicinity of the support trough NLFEA or stress fields. However, if the strut action is neglected, applying the sectional method is still conservative. In this case, it is reasonable to limit $\cot \theta' \leq L/d_v \approx 3.38$. This is illustrated in Figure 6.18. The calculation results plotted in this figure were obtained using $f'_c = 26.7\text{MPa}$. This value was calculated by averaging the compressive strength values of the five beams failing in shear. It can be seen that the Level II approach successfully reproduces the shear strength evolution with increasing shear reinforcement. For very low amounts of shear reinforcement, the condition $\cot \theta' = 3.38$ governs the shear strength. However, even if this condition was not used realistic estimates could still be attained. The minimum amount of shear reinforcement indicated in the figure was determined according to $\rho_{w,\min} = 0.08\sqrt{f'_c}/f_{yw}$ [46; 87].

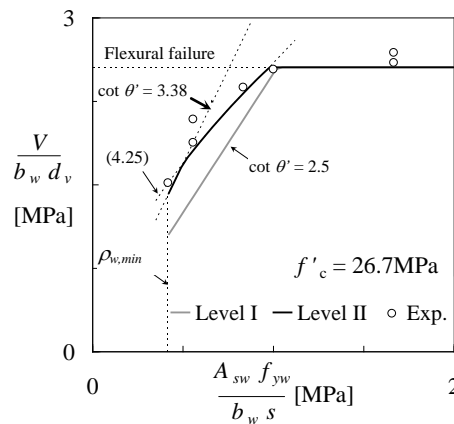


Figure 6.18 – Effect of adding shear reinforcement.

Beam T1 tested by Leonhardt and Walther [131]

This test was aimed at evaluating the shear strength of a specimen failing in shear by crushing of the web concrete prior to yielding of the stirrups. The geometry and reinforcement of the beam are depicted in Figure 6.19. The failure mode is correctly predicted both by Level I and II sectional approaches. However, the shear strength is largely underestimated by the simpler method, as can be confirmed in Table 6.1. The control section was defined similarly to the previous example and the strain ε_x was determined using $z_x = 175\text{mm}$, that is, b_w above the edge of the bottom flange.

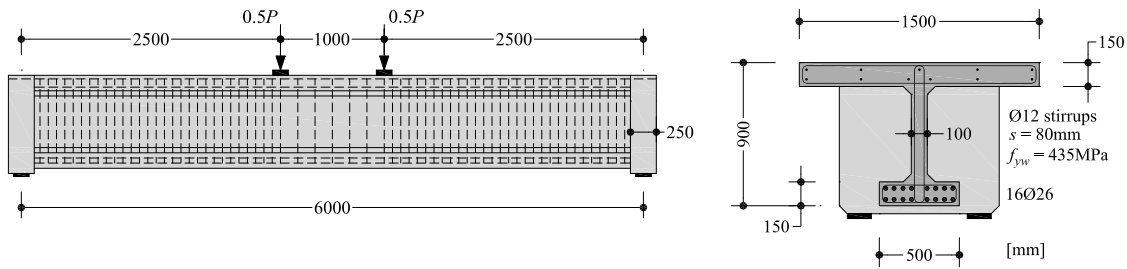
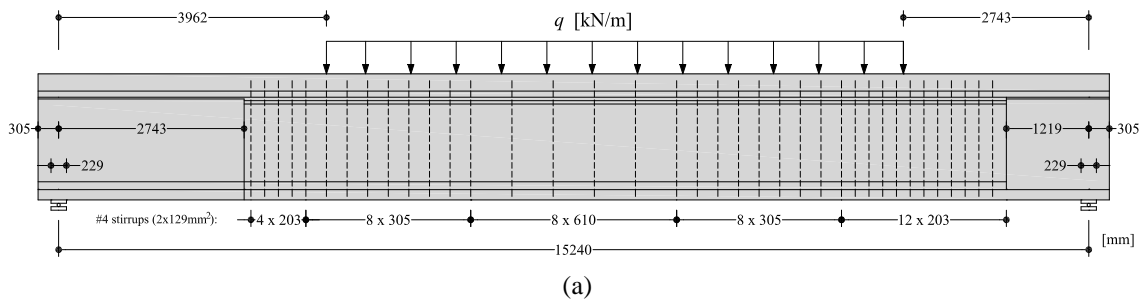


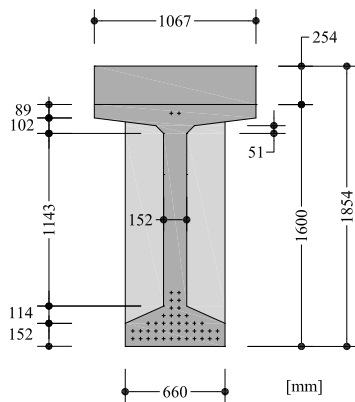
Figure 6.19 – Geometry and reinforcement of the beam T1 tested by Leonhardt and Walther [131].

Beam G8E tested by Kuchma et al. [94; 127]

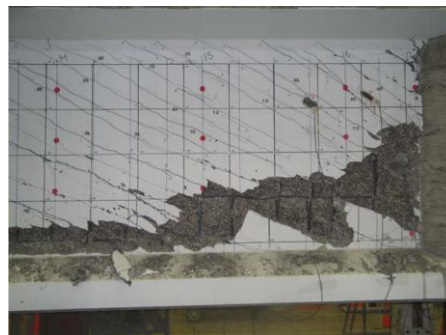
This beam belongs to the same series already presented in Section 5.4. However, this specimen was strengthened with transversely post-tensioned concrete diaphragms in order to prevent failure of the end regions and thereby drive the failure zone from a typical discontinuity region to a continuity region. In this specimen, the longitudinal prestressing strands were anchored through special devices aimed at eliminating strand slip at the element ends. The specimen geometry and reinforcement content are depicted in Figure 6.20 together with a picture of the failure zone located in the vicinity of the right support. The beam failed by web concrete crushing after stirrup yielding.



(a)



(b)



(c)

Figure 6.20 – Beam G8E tested by Kuchma et al. [94; 127]: (a) Elevation and distribution of the #4 (2x129mm²) stirrups; (b) cross section with the 42+2 prestressing strands; (c) picture of the failure zone.

The sectional method implies activation of the stirrups within the length $d_v \cdot \cot \theta'$. These stirrups are represented by thicker lines in Figure 6.21. It can be seen that the stirrup spacing is not constant within this length which means that the shear reinforcement ratio to be adopted in the calculations depends on $\cot \theta'$ and must be adapted accordingly during the iterative process described in Box 6.1. The location of the control section and the point where ε_x is evaluated are indicated in Figure 6.21. The prestressing force was determined based on the test data and corresponds to a prestressing steel stress of 1093MPa. The bending moment due to the prestressing force M_p was determined considering that the centroid of the composite section is located at 1178mm from the extreme bottom fiber.

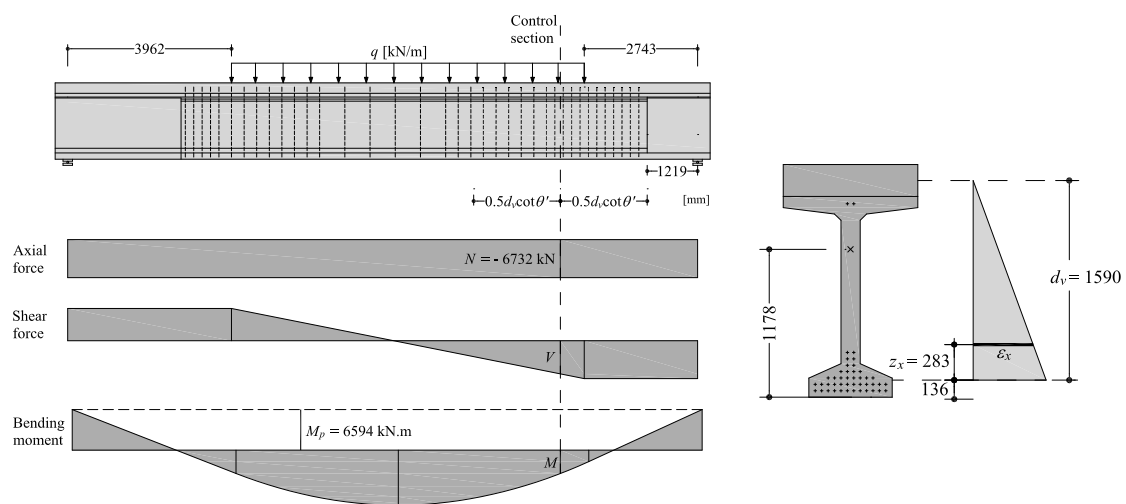


Figure 6.21 – Analysis of the beam G8E: location of the control section and determination of ε_x .

The analysis results are summarized in Table 6.1. The failure mode is correctly predicted by the Level II approach. The shear strength calculated by the simpler method is limited by $\cot \theta' = 2.5$. In this case only a marginally better prediction of the shear strength is obtained with the Level II approach.

Table 6.1 – Summary of the analyses

Beam	Ref.	f'_c [MPa]	d_v [cm]	s [cm]	A_{sv}/s [cm ² /m]	ω_y [MPa ^{1/3}]	Level II				Level I		
							ϵ_x [%]	$\cot\theta'$	$V_{R,calc}$ [kN]	Ratio ₍₁₎	$\cot\theta'$	$V_{R,calc}$ [kN]	Ratio ₍₁₎
40		23.6		61.0	4.23	0.051	1.112	3.38 ⁽²⁾	497	1.08	2.50	368	1.46
11		27.4		45.7	5.64	0.061	1.438	3.28	642	1.04	2.50	490	1.36
3		34.0		45.7	5.64	0.053	1.483	3.38 ⁽²⁾	662	1.12	2.50	490	1.51
7	[98]	24.3	99.3	30.5	8.48	0.099	1.784	2.71	797	1.05	2.50	735	1.14
5		24.5		25.4	10.16	0.118	1.995	2.53	891	1.01	2.50	882	1.02
1		32.4		15.2	16.93	0.164	2.000 ⁽³⁾	2.31	903 ⁽⁴⁾	1.02	2.50	903 ⁽⁴⁾	1.02
25		30.4		15.2	16.93	0.171	2.000 ⁽³⁾	2.28	903 ⁽⁴⁾	1.05	2.50	903 ⁽⁴⁾	1.05
T1	[131]	25.3	75	8.0	28.30	1.427	0.825	1.00	686	1.14	1.00	522	1.50
G8E	[94]	86.2	159	Var.	10.67 ⁽⁵⁾	0.171 ⁽⁵⁾	0.141	2.63	2125	1.21	2.50	2093	1.26

⁽¹⁾ $Ratio = V_{R,exp} / V_{R,calc}$

⁽²⁾ Some degree of direct strut action predicted. The angle θ' is limited by shear span: $d_v \cdot \cot\theta' \leq 3.353m$

⁽³⁾ Longitudinal steel is yielding or about to yield at the control section. This value was adopted for simplicity.

⁽⁴⁾ Flexural failure. V_R is limited by the flexural capacity.

⁽⁵⁾ Only valid for Level II approach. For level I, $A_{sv}/s = 11.03\text{cm}^2/\text{m}$ and $\omega_y = 0.177$.

6.4 Concluding remarks

The F-CMM is a compressive stress field approach that allows detailed calculations of the force deformation curves, crack widths, crack spacing, steel deformation capacity and that exhibits a good accuracy in describing the shear failure modes of both concrete panels and shear critical beams. The R-CMM can be obtained from the F-CMM by imposing an additional constraint related with the coincidence of the principal axes of concrete stress at the cracks and average strain. The equilibrium equations and the constitutive laws are simplified at the cost of some decrease in accuracy. The limit analysis formulation presented in this chapter can be obtained from the R-CMM by neglecting the concrete tensile strength and the bond stress transfer effects. It is simpler to use and, in the case of RC panels, comes down to a set of closed form expressions for the yield conditions. However, in the case of a structural analysis, the relevant outcomes are simply the stress fields expressing the equilibrium at failure conditions and the corresponding ultimate load. A simple sectional analysis method can be derived directly from the yield conditions considering a constant shear stress distribution along the cross-section height. The resulting expressions are formally similar to those of the variable angle truss model adopted in the recent European codes. By allowing the exploitation of a wider range of values for the inclination of the struts and the incorporation of the effect of the longitudinal

reinforcement/prestressing steel strains in the definition of $f_{c,ef}$, the proposed method is suitable for an intermediate shear strength assessment of an existing concrete bridge.

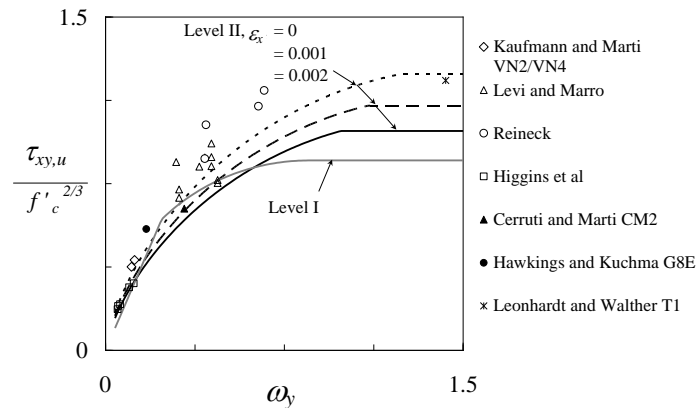


Figure 6.22 – Summary of all the validation examples. Only beams failing in shear are included.

Figure 6.22 summarizes the results obtained in a preliminary validation campaign, which should now be extended. Besides the beams presented in this chapter, also the specimens tested by Reineck [192] (2 reinforced + 2 prestressed girders) and Levi and Marro [132] (7 reinforced + 3 prestressed girders) are included, which allowed the examination of a wide range of mechanical shear reinforcement ratios ω_y . It is clear that the level II approach is more accurate, but still conservative. In fact, this aspect was carefully evaluated during the derivation of the method. The comparison presented in Section 6.2.3.2 between the shear strength envelope according to the F-CMM, R-CMM and limit analysis accounting for compression softening shows that the latter is generally on the safe side. Moreover, also some conservative assumptions were made in the definition of the control section, see Section 6.3.1.1, namely by neglecting the fanning action in the vicinity of the supports and by calculating the reference average longitudinal strain near the tension chord. Finally, as shown in Chapter 5 and also discussed in [80], the shear stresses are not carried exclusively in the web. In some cases the contribution of the flanges is not negligible, though it is disregarded in the sectional analysis method.

7 Case study: N. S. da Guia Bridge

7.1 Description of the bridge and problem statement

The N. S. da Guia Bridge (see Figure 7.1) is a prestressed concrete bi-cellular box-girder bridge with a total length of 250m, divided in 5 spans of 38-3x58-38m. The cross-section height varies parabolically from 1.45m at the spans to 2.9m at the intermediate supports with a resulting slenderness ranging between $L/40$ and $L/20$. The deck is 11.84m wide holding one carriageway with two traffic lanes and being supported by laminated neoprene bearing pads which rest on lightly reinforced concrete piers. At the abutments the bearings have a Teflon layer.

This was one of the first bridges designed and built in Portugal according to the balanced cantilever construction method. Although the original design dates back to 1973, the construction only began in 1978 and the bridge was opened to traffic in 1980. This bridge is located on the EN 201 national road, which was once part of the main route connecting the Spanish region of Galicia with the North-western part of Portugal. In 1998 a new motorway connecting these two regions was built and nowadays the bridge is crossed mainly by local traffic.

Still during the construction and with the bridge almost complete, a design error was detected which led to an underestimation of the upper deck slab transverse flexural reinforcement. Only after a load test was the bridge opened to traffic without axle load restrictions. A consistent and stabilized cracking pattern developed in the bottom face of the upper slab. This cracking pattern has been observed ever since and, notwithstanding the low reinforcement content, it remains stabilized even after 30 years in service. In 1999, a slab portion was strengthened with different CFRP systems as part of a research program conducted by the Laboratory for the Concrete Technology and Structural Behaviour (LABEST) of the Faculty of Engineering of the University of Porto [88]. More recently (February 2005), during a routine inspection aimed at evaluating the efficiency of the CFRP systems, several cracks were detected in the webs [68]. These cracks were not reported in previous inspections and, apparently, neither were they related with the slab damage.

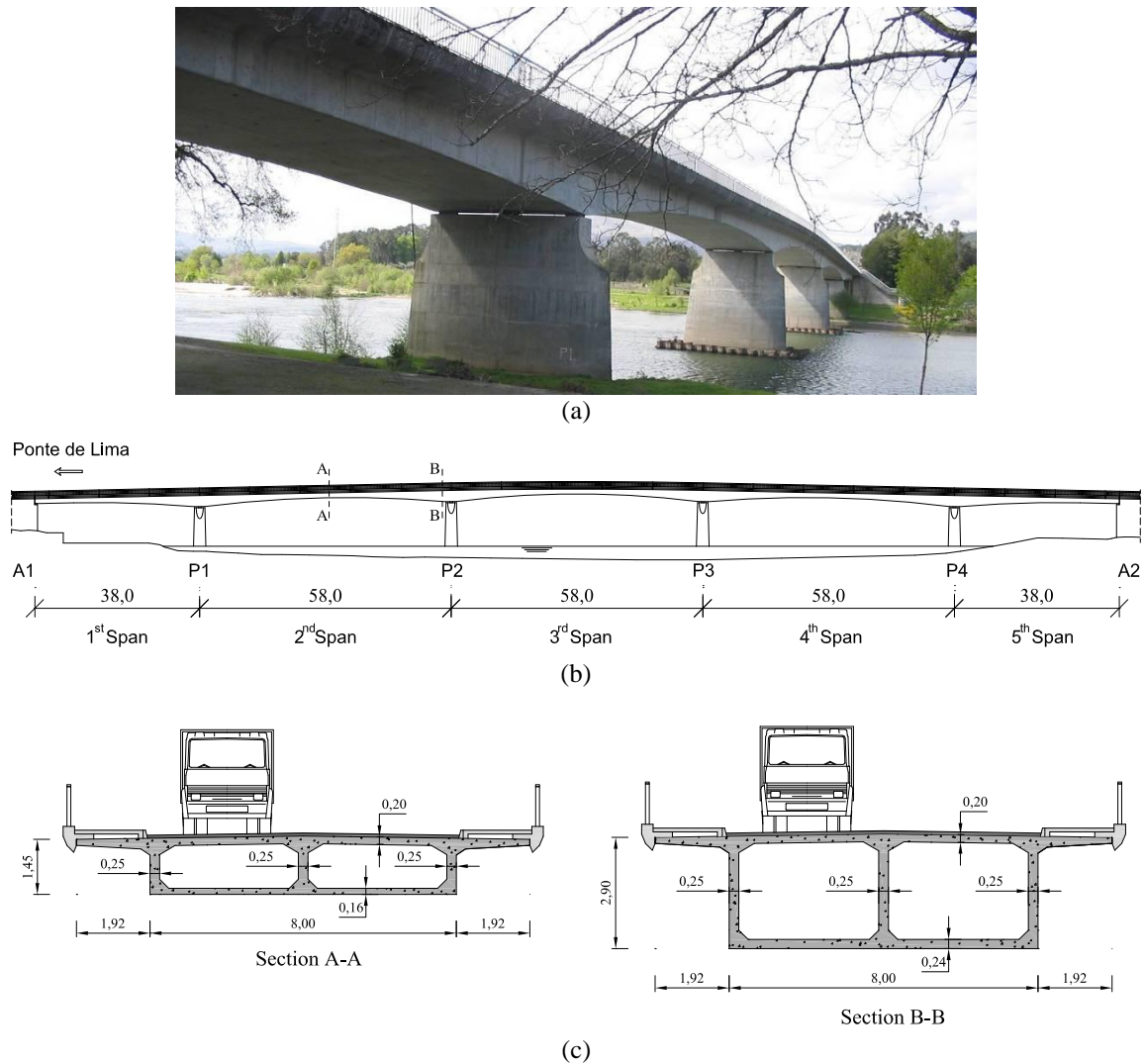


Figure 7.1 – N. S. da Guia Bridge: (a) view of the bridge; (b) side elevation and notation; (c) typical cross-sections.

In this chapter the working program developed to perform the condition examination of the bridge and to evaluate the urgency of eventual strengthening actions is described. This program included a detailed inspection campaign, some material characterization studies, and monitoring the bridge response during a load test and under daily temperature variations. It is also found important to determine whether the observed cracking patterns can be expected with the prestress steel in good conditions, or are an indication of ongoing corrosion leading to a decrease of the effective prestressing force. For this purpose the bridge is analysed with both 2D and 3D finite element models taking into account the construction sequence and the time-dependent evolution of the sectional forces due to the effects of creep, shrinkage and prestressing steel relaxation. In all the numerical analyses presented in this chapter the viscoelastic constitutive models for concrete available in the

software DIANA are adopted. The ultimate limit state safety evaluation of the bridge is presented in Chapter 8. The particular issue of the deck slab cracking will not be discussed here since it has been studied elsewhere [67].

7.2 Available data

The work presented in this chapter began in the second half of 2006. At the time, the available documentation consisted of:

- The original 1973 design, including design drawings (see Figure 7.2) and calculation reports;
- Construction site log book where the supervision team documented the events that occurred in each day of the construction period;
- Reports with the results of 159 compressive tests on 20x20x20cm cubes tested at the age of prestress application (3, 4, 5 and 7 days);
- The bill of quantities and corresponding budget estimate presented by the contractor;
- Non-destructive testing results of the top slab concrete which were obtained before the experimental strengthening with CFRP.

Regarding the prestress, only the long-term prestressing force required in each cross-section was specified in the original design. Definition and detail of the tendon layout were left for the contractor to draw accordingly with the adopted post-tensioning system. According to the bridge owner, the corresponding construction drawings and calculation reports were lost. Only three drawings were available corresponding to the midspan segments of the 2nd, 3rd and 4th spans. Therefore, the reconstitution of the real tendon layout and the determination of the corresponding effective prestressing force were subject to considerable error due to the following facts:

- Apart from the bottom slab continuity tendons, the anchorages are not visible and accessible to confirm the assumptions that inevitably had to be made;
- A close observation of the formwork marks on the concrete surface inside the box-girder and the information contained in the construction log book reveals that the construction sequence defined in the original design was not strictly followed. Therefore, the prestressing forces calculated in the original design may not constitute a reliable basis;

- The use of precast concrete segments was defined in the original design. In these circumstances the time dependent alteration of the sectional forces due to concrete creep is lower than in the adopted cast in-situ segmental cantilever construction method. It was unclear if a re-calculation of the bridge had been made in order to account for the different construction sequence and procedure.

Much of the work presented here, namely the inspection campaign and the load test, was performed considering the above mentioned uncertainty regarding the installed prestress. However, in 2009 the post-tension construction drawings were made available and the information they contained was taken into account in the subsequent work presented both in this Chapter and in Chapter 8. All the conclusions and exploratory numerical analyses that have been made before 2009 are documented in references [184-187; 203-205]

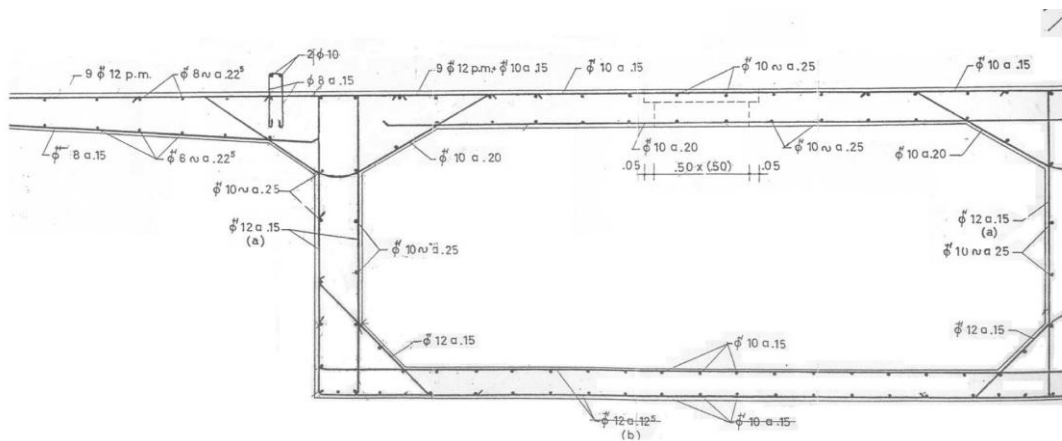


Figure 7.2 – Ordinary reinforcements according to the original design.

7.3 Inspection

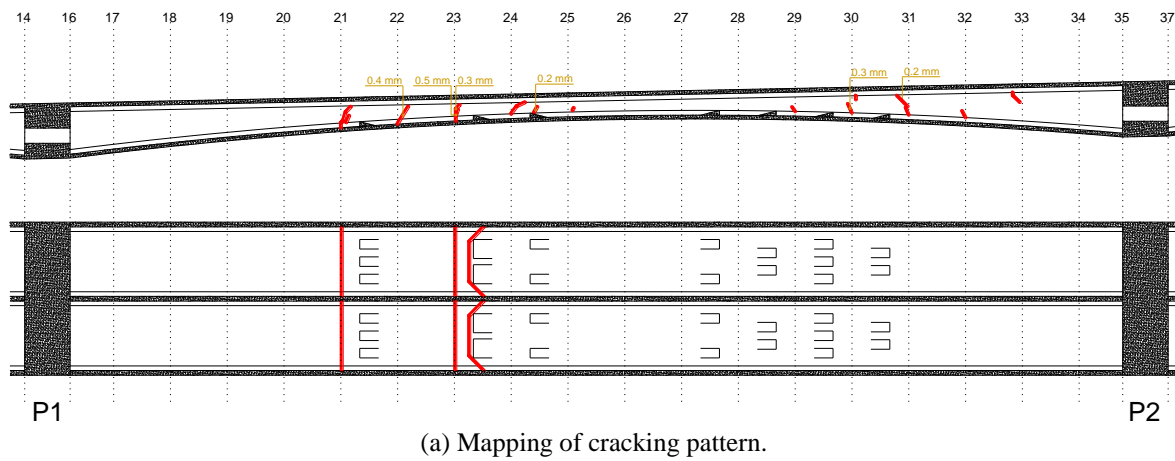
7.3.1 Mapping of the cracking patterns

A detailed visual inspection campaign was carried out, see Figure 7.3, enabling a complete mapping of the cracking patterns and other anomalies of the bridge deck. Both internal and external inspections were performed. An exhaustive description of the inspection results can be found in the inspection report [204]. In the following, a brief description of the main observations is presented. The spans, piers and abutments are numbered according to Figure 7.1 b).

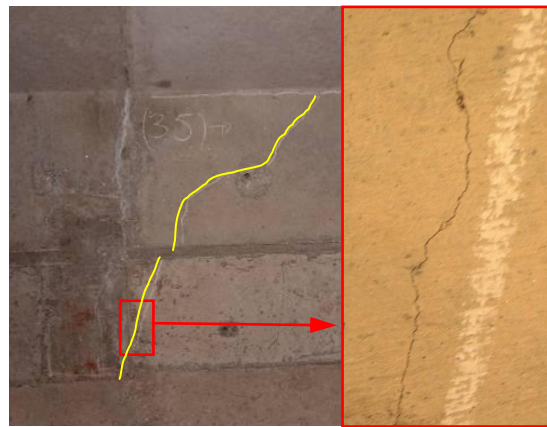


Figure 7.3 – View of the special vehicle used in the external inspection of the deck.

Consistent cracking patterns were observed in the webs and in the bottom slab, exhibiting both longitudinal and transversal symmetry, as depicted in Figure 7.4 to Figure 7.6. No systematic cracking patterns were identified in the 1st and 5th spans. In the webs, cracks are generally inclined and crack widths up to 0.3mm were measured. These cracks are usually more noticeable near the tendon anchorages. Apart from only one crack (Figure 7.5, 3rd span, section 55), the web cracks do not cross the joints of segmental construction. The cracking pattern is similar amongst the three webs, although slightly more pronounced in the central web. For clarity, only the central web is presented for representing each individual span. In the bottom slab the cracks generally have a transversal orientation and are mostly observed in the 2nd and 4th spans. In these two spans the cracking pattern is symmetric. A polygonal cracking pattern was observed around the anchorages of the continuity tendons (Figure 7.4). The cracks at sections n°21 and n°23 are continuous to the webs, as well as the symmetric ones at sections n°70 and n°72. These cracks occur in the vicinity of the anchorages of the bottom continuity tendons. In the 3rd span, no cracks were observed in the bottom slab inside the box-girder.



(b) Crack detail at section n°21

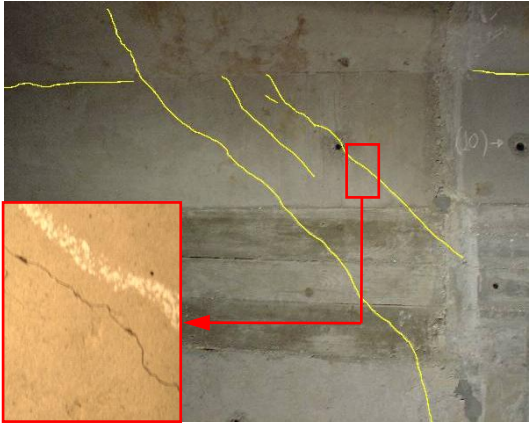
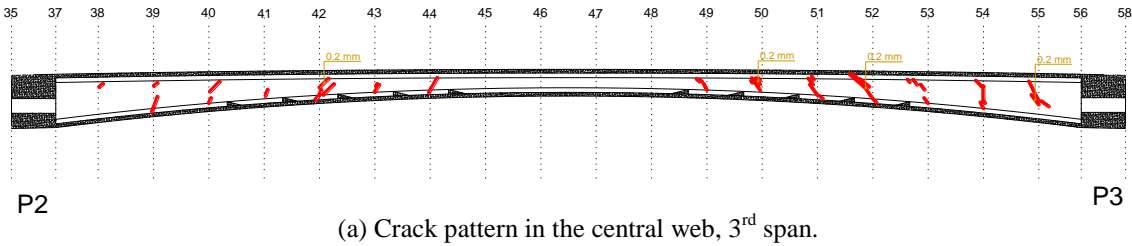


(c) Crack detail at section n°24



(c) Detail of the crack development at section n°23.

Figure 7.4 – Cracking pattern in the 2nd span.



(b) Crack detail at section n° 52.



(c) Crack detail at section n° 55.

Figure 7.5 – Cracking pattern in 3rd span.

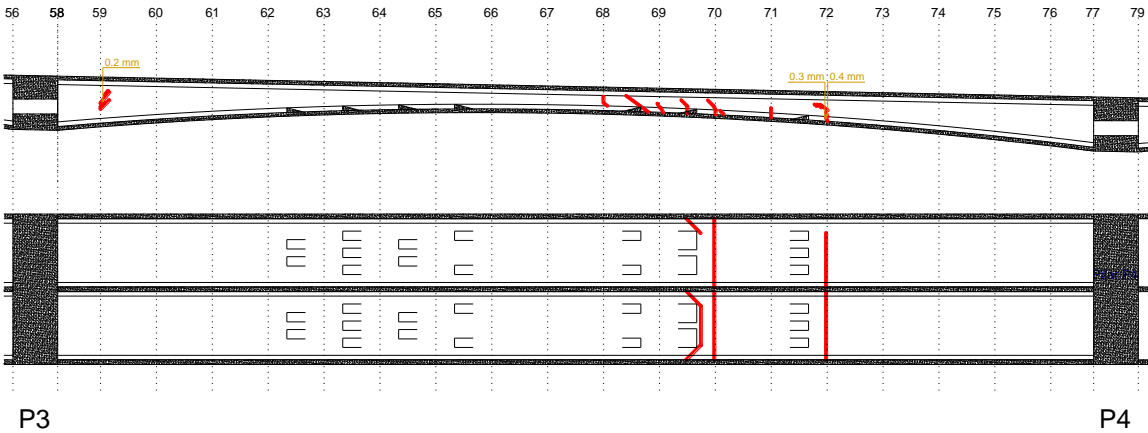
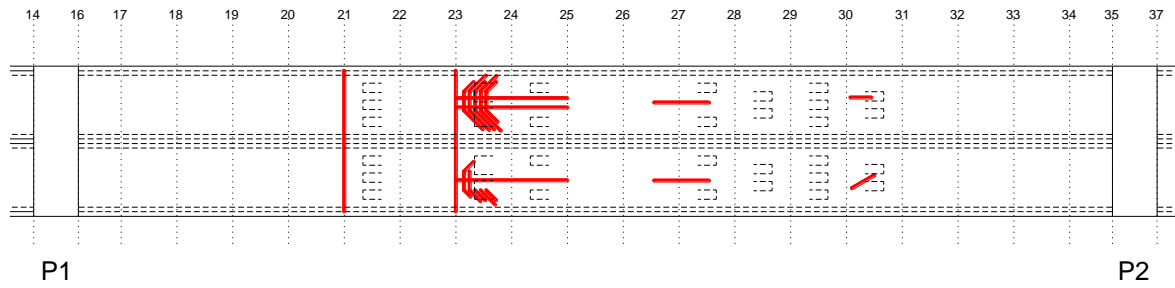
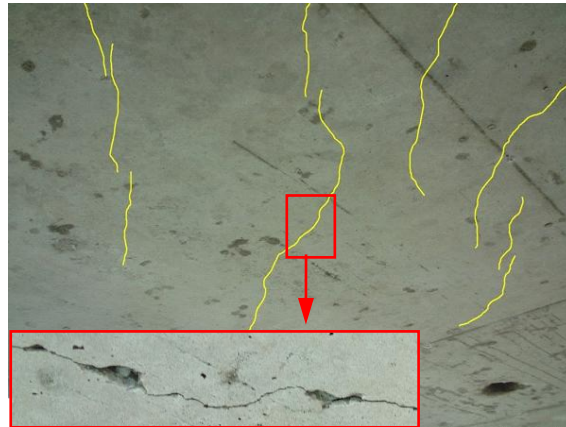


Figure 7.6 – Cracking pattern in 4th span.

As the surface of the top face of the bottom slab is highly irregular and covered by dust, the identification of the cracks was difficult. This may explain the fact that in the external inspection more cracks were observed. In fact, in the bottom face an array of cracks was identified developing around the anchorages of the bottom slab continuity tendons (see Figure 7.7).

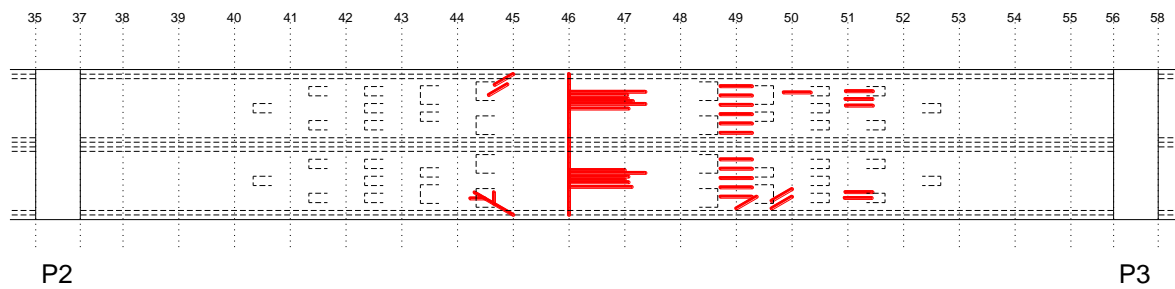


(a) Bottom view of the bottom slab.

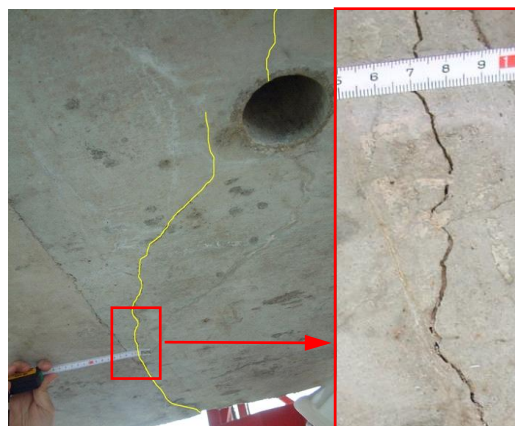


(b) Detail of the cracks between sections n° 23 and n°24.

Figure 7.7 – Cracking pattern observed in the bottom slab of the 2nd span.



(a) Bottom view of the bottom slab.



(b) Detail of the cracks at section n° 45.

Figure 7.8 – Cracking pattern observed in the bottom slab of the 3rd span.

In the 3rd span, although not so developed, a similar cracking pattern was observed. In this span, no continuous cracks between the webs and the bottom slab were detected. However, longitudinal cracks were systematically observed on the bottom face (Figure 7.8), forming an array of regularly spaced cracks that extended through several joints of segmental construction. The longitudinal cracking development represented in Figure 7.8 is merely indicative. In posterior inspections inside the box-girder these cracks could not be detected on the top face of the bottom slab.

7.3.2 Corrosion evidence

Besides minor signs of corrosion in confined areas, mainly related with drainage problems of the deck, and some stirrups not properly protected by an adequate concrete cover, the main concern is related to the state of the embedded prestressing tendons. The holes allowing the attachment of traveller form equipment to the deck were not filled with concrete and, in some of them, it is possible to observe corroded metallic ducts containing the bottom continuity tendons, as depicted in Figure 7.9. It is also known that, at the time of the construction, grouting of the ducts was a problematic issue and it is likely that it was not properly executed. As these ducts were locally exposed during almost 30 years, the state of the prestressing tendons is, at the present time, unknown.



Figure 7.9 – Prestressing ducts exposed at the bottom slab.

7.3.3 Verification of the reinforcement layout

In a limited number of predefined locations, a covermeter was used to check if the reinforcement layout coincided with the prescribed in the original design. The agreement was found to be good. Only the most superficial reinforcements, and not the post-tensioning ducts, could be detected with this method (Figure 7.10).

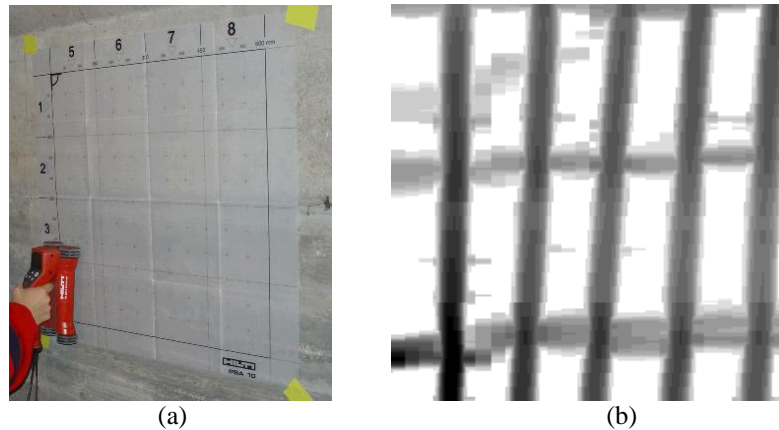


Figure 7.10 – Reinforcement detection using the Hilti PS200 Ferroskan: (a) grid positioning in the web; (b) corresponding scan results. The vertical bars correspond to 12mm stirrups (12.5cm spacing) and the horizontal ones to the 10mm longitudinal web reinforcement (25cm spacing).

7.3.4 Trial test using gamma rays

7.3.4.1 General

Owing to the corrosion signs observed in some exposed ducts, the condition of the post-tensioned tendons is uncertain and a special inspection is sought essential for clarifying this issue. Moreover, at the time this inspection work was being performed, no information regarding the prestress installed in the bridge was available due to the fact that the construction drawings with the real tendon layout were assumed to be lost. If performed with resource to destructive methods a complete examination of the tendons would be unfeasible. Therefore, the use of NDT methods was pursued.

NDT is playing an increasingly important role in the condition examination of existing concrete bridges. Reviews of the existing methods can be found in references [39; 65; 153; 258]. When focusing on a specific case, it can be noted that in most instances NDT methods provide only partial answers. In these cases, the contribution of a second technique must necessarily uphold the diagnosis and the use of complimentary NDT techniques is advised [138]. The development of data fusion techniques for combining the information retrieved by different NDT methods constitutes a promising research topic in this field. In the particular case of post-tensioning tendons, a set of complementary technologies have been developed which retrieve different levels of information:

- Impulse Radar (or Ground Penetrating Radar - GPR) – This method is based on the emission of high frequency electromagnetic pulses. A receiving antenna records the GPR impulse signals that contain echoes from the reflections

generated when the emitted waves meet boundaries between materials with different dielectric constants. In the case of post-tensioned construction, this technology is mainly used for detecting the position of tendon ducts, reinforcing bars and concrete delamination at depths up to 50cm. The GPR pulses operate over too in the low frequency domain to obtain rebar diameters. It is also physically unfeasible to test inside the metallic ducts. Its main advantage lies in the high speed and relatively inexpensive NDT of structures.

- Impact-echo (IE) technique – This method is based on the propagation characteristics of transient stress waves generated by elastic impact. A small instrumented impulse hammer is used to hit the surface of a structure at a given location and the reflected energy is recorded with an accelerometer mounted adjacent to the impact location. The reflected signals are then analysed in the frequency domain. The presence of voids in an element under the testing point will result in changes in the frequency spectrum. This method is targeted at the detection of voids, such as of grouting voids in post-tension ducts. Its advantages lie on the simplicity of the experimental setup and on being relatively inexpensive. Knowledge of the position of the tendons is required previous to its application and no further information besides the existence of voids can be obtained.
- Remanent magnetism (RM) method or Magnetic leakage flux measurement [156; 252] – This technique uses the ferromagnetic properties of the prestressing steel. The strands are magnetized by suitable magnets and, at fracture areas of magnetized prestressing steels, magnetic stray fields are generated which can be detected at the concrete surface by means of suitable sensors. Due to the different magnetic behaviour, the signal component of the non-stressed reinforcement can be filtered out during signal analysis. The characteristic magnetic flux leakage field can be detected even if the fractured wire is screened by other wires or by the metal sheathing and even if the fracture width is negligible. However, only wire fractures can be detected with this method and the position of the tendons has to be determined a priori.
- Radiographic methods – In these methods, X- or gamma radiation is used to produce images of the interior of the irradiated elements. These radiations have a very short wave length and are capable of traversing solid media, being detected and recorded with appropriate films or phosphor image plates. Therefore, access to both faces of the element is required. Steel attenuates the radiation much more

than concrete does, while air attenuates much less effectively than concrete. These differences yield a photographic image of the internal structure of the analysed specimen. In X-radiography, an electric powered linear accelerator is used to generate the X-rays. On the other hand, gamma-rays are emitted naturally from the nucleus of radioactive atoms. The most common radioisotope sources are Cobalt (^{60}Co) and Iridium (^{192}Ir), the latter being the one with the least intensity¹ and thus the most portable because it requires the least amount of shielding material to meet the radiological protection standards. The radiographic methods are acknowledged to be powerful diagnostic tools allowing the detection of grouting voids and, in certain circumstances, tendon corrosion and wire fractures [73; 141; 142]. Gammagraphy has enjoyed somewhat greater success than X-ray radiography in field applications. Recent developments [90; 142; 143; 230] related to tomographic analysis led to promising results regarding the extraction of quantitative information from the gammagraphies.

In this particular case, not only the evaluation of the tendons condition was required but also the characterization of the strand type, duct size and number of strands per tendon was of interest. It can be concluded that a combination of at least two techniques is advised: the GPR to locate the tendons and to define the tendons coordinates; and a gammagraphic study on selected zones in order to evaluate the tendons condition, to perform the tendons characterization and to solve eventual ambiguities regarding the tendon layout raised during the GPR inspection. In the context of the present work it was possible to perform a preliminary gammagraphic study on some selected spots of the deck. This study was aimed at evaluating the logistics required for such an operation, so that a complete inspection could be planned. The work was a collaborative project of LABEST and of the Argentina based company THASA (Tomografia de Hormigon Armado, S.A.). In this preliminary campaign the field work duration was restricted to one day.

7.3.4.2 Experimental setup

In order to reduce the required safety measures, the in-situ application of gamma-rays in most practical cases is only viable in case low intensity and low activity² ^{192}Ir sources are

¹ The intensity of a radioisotope is related to the energy being emitted and is a characteristic of the atomic structure of the material. Iridium and Cobalt emit radiation in two and three discrete wavelengths, respectively: ^{60}Co emits 1.33 and 1.17 MeV, and ^{192}Ir emits 0.31, 0.47, and 0.60 MeV gamma rays. From a radiation safety point of view, this difference in intensity is important because the ^{60}Co has more material penetrating power and, therefore, requires more shielding.

² The strength of a source is called its activity, which is defined as the rate at which the isotope decays. The activity is usually measured in Curies ($1\text{Ci} = 3.7 \times 10^{10}$ disintegrations/sec).

used. However, there is a balance between source activity, intensity, exposure times, maximum thickness of the analysed elements and contrast of the obtained images. In the present case the maximum thickness of the cross-section elements is 25 cm, which made the use of a portable ^{192}Ir source with only 20Ci feasible.

The source is kept inside a special container where it is encapsulated by a Uranium shield. To perform an irradiation, the source is placed at the tip of the guide tube by remote control (Figure 7.11). Conventional films were still used because no local provider for a computed radiography (CR) system could be found. The required exposure times led to the fact that only 7 gammagraphies could be taken in one working day, including the necessary time for their chemical development in laboratory. Using the same source and employing a portable CR system up to 20-25 gammagraphies could have been obtained. The films were placed inside flexible cassettes which contained thin lead foils designed to improve image contrast by filtering the scattered radiation. Care was taken at all times to meet radiological protection and safety requirements in accordance to the International Atomic Energy Agency (IAEA) regulations. A collimator was used in order to reduce the safety perimeter, see Figure 7.11 (a). Acceptable radiation dose rates were achieved at a distance of approximately 10 meters. Outside the box-girder, dose rates well below the acceptable levels for general public were measured. It is to be noted that gamma radiation from radioactive sources induces no radioactivity on the irradiated elements nor does it produce any unwanted effects on them.

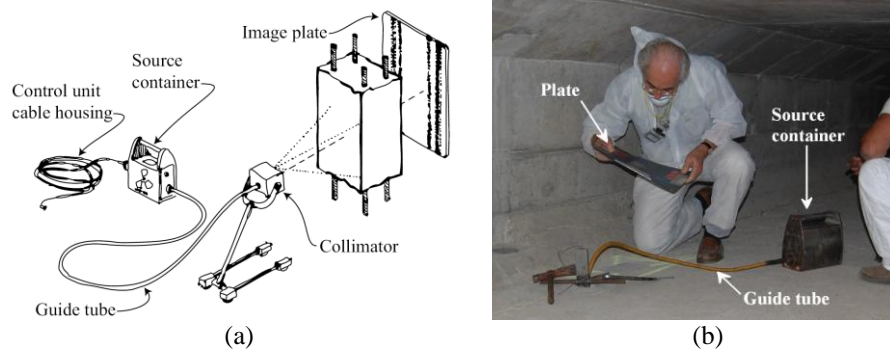


Figure 7.11 – Gamma-ray testing: (a) Schematic representation of a typical experimental arrangement (b) View of the source container, guide tube and image plate during the test.

In Figure 7.12 and Figure 7.13 the sectors where the measurements were taken are identified. Each measurement covers an area of 45 x 35 cm, which is defined by the dimensions of the film. Sectors 1-4 and 7 are located in the bottom slab and sectors 5 and 6 in the central web.

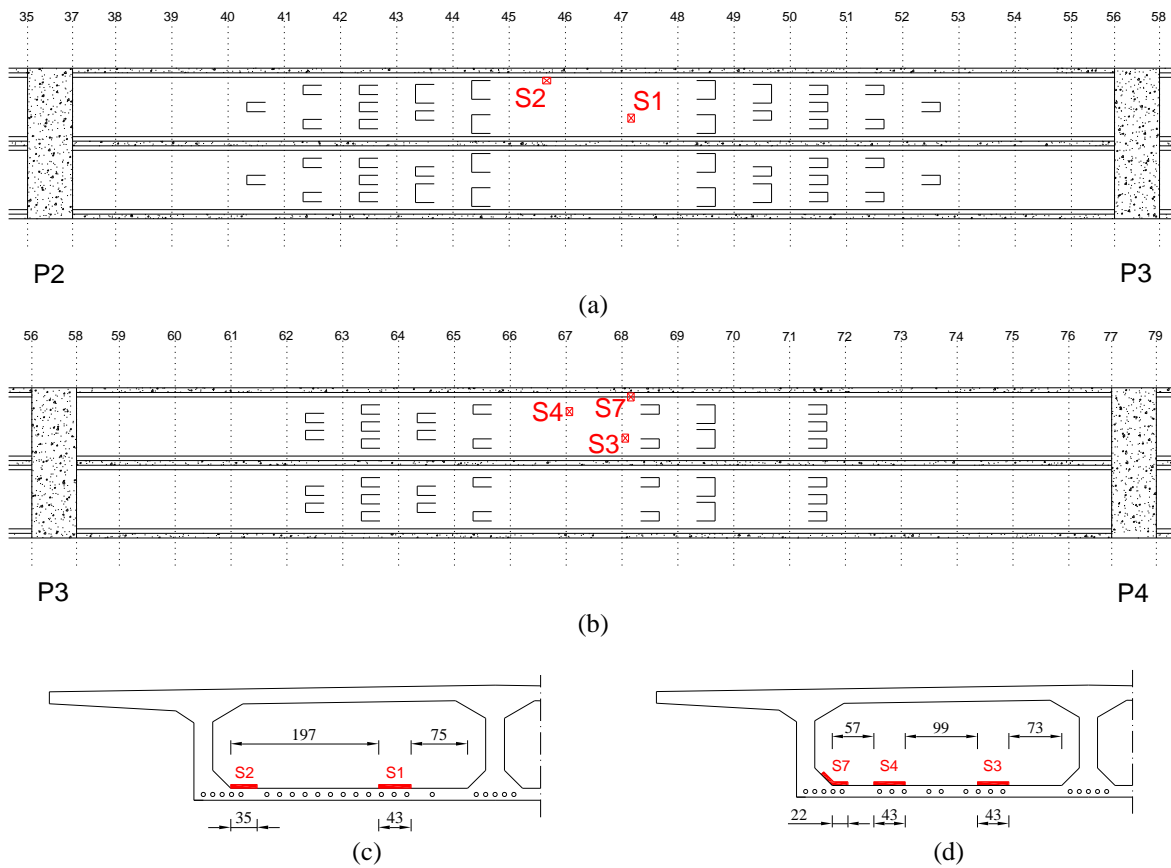


Figure 7.12 – Sectors where measurements were taken: (a) sectors 1 and 2 in the bottom slab of the 3rd span; (b) sectors 3, 4 and 7 in the bottom slab of the 4th span; (c) and (d) corresponding positioning in the box-girder with the expected cables location..

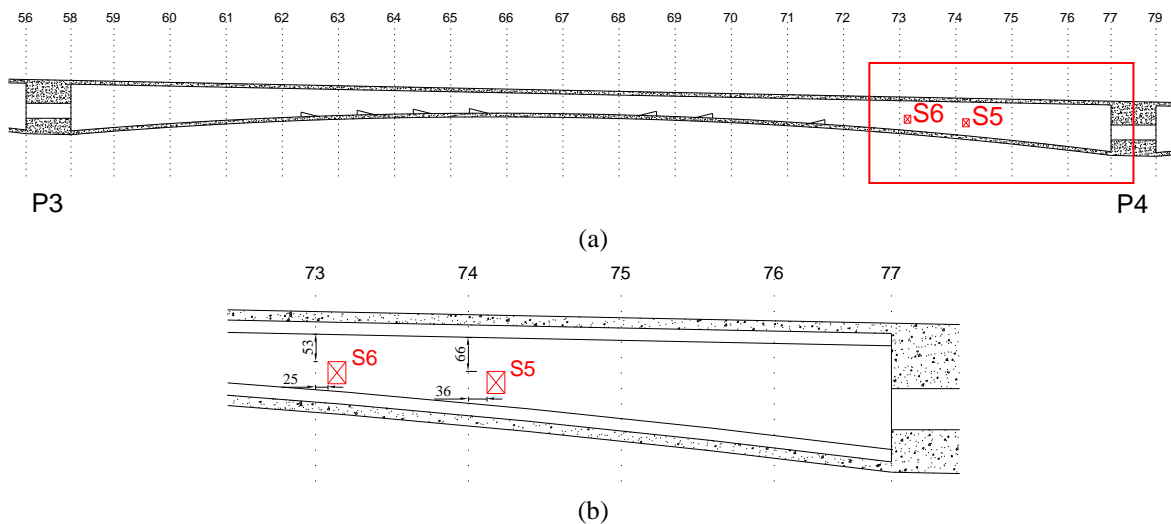


Figure 7.13 – Location of the sectors where measurements were taken: (a) sectors 5 and 6 in the central web; (b) corresponding positioning in the box-girder.

For the web measurements, thin wires inserted through existent holes were used as reference for the correct positioning of source and plate on each side of the web, as

depicted schematically in Figure 7.14 (a). In the case of the bottom slab measurements, an especially designed tool, see Figure 7.14 (b), was used in conjunction with the existing $\varnothing 90\text{mm}$ holes. This tool made it possible to position the source beneath the floor in a very inexpensive way when compared to the alternative of costly scaffoldings or other heavy equipment.

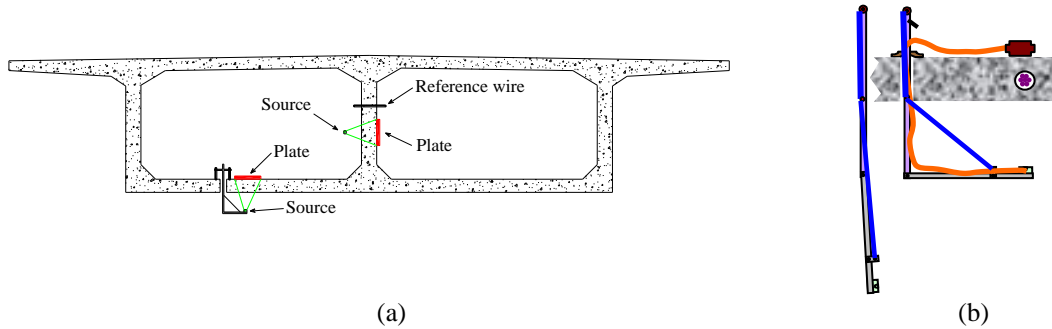


Figure 7.14 – Experimental setup: (a) Bridge cross section showing the two source-plate arrangements used in this work; (b) Sketch of the tool designed to position the source beneath the bottom slab using pre-existing holes.

The application of mathematical algorithms for the quantitative analysis of the data extracted from the gammagraphies requires special hardware for a precise characterization of the relative positions of the source, object being analysed and recording means. This type of hardware has been developed and patented by THASA [143]. Due to budget constraints and to the preliminary character of this work, this hardware was not brought from Argentina. Therefore, the relative positions were hand measured, which increases the error involved in the determination of the coordinates of the observed elements.

7.3.4.3 Results

All the obtained gammagraphies show one or more ducts with cables inside plus various ordinary reinforcing bars. The quality of the images makes it possible to see details such as the duct edges, individual strands and even individual wires. The image quality of the photographs shown here is necessarily reduced with respect to the original gammagraphies. These photographs were obtained with a pocket digital camera and with the gammagraphies placed on back lit translucent plates. Image parameters have been adjusted to improve some features of these photographs at the expense of others, to improve image contrast.

In all the 7 gammagraphies no grouting defects were observed nor signs of wire breaks or section loss due to corrosion. According to the THASA report [140] where the quantitative

analysis of the obtained gammagraphies is performed, the ducts are 55 mm in diameter and the strands were confirmed to be 0.5". Regarding the number of strands per duct, not all the strands could be identified due to their relative positioning in the duct. In Figure 7.15 the gammagraphy corresponding to sector S3 is depicted. Three tendons can be identified together with upper and bottom reinforcement grids. In Figure 7.16 the gammagraphies of the web sectors are depicted and one cantilever tendon is identified in each gammagraphy. The bright rectangle near the centre of the gammagraphies corresponds to the image of an external element used for ID purposes.

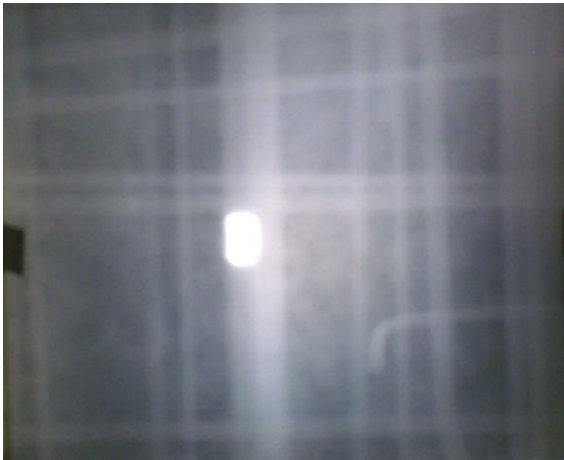


Figure 7.15 – Gammagraphy of sector S3 located in the bottom slab.



(a) Sector S5



(b) Sector S6

Figure 7.16 – Gammagraphies of the web sectors.

7.4 Material characterization

7.4.1 Concrete

Chloride content and depth of carbonation

During cement hydration, a highly alkaline pore solution is formed in concrete. In this alkaline environment, ordinary reinforcing steel forms a very thin oxide film – the passive film – that protects the steel from corrosion. This passive film remains stable as long as the pore water composition remains constant and is destroyed when sufficient chloride ions have penetrated to the reinforcement or when the pH of the pore solution drops to values below 9 due to carbonation. In these circumstances the reinforcing steel is depassivated and thus vulnerable to corrosion attack. In the present case, the chloride content was evaluated using the rapid chloride test. Very low chloride concentration was detected – always less than 0.06% of the cement content – which is well below the critical chloride content of 0.3-0.5% [4; 193]. The depth of carbonation was measured by spraying exposed surfaces with the phenolphthalein indicator. The indicator turned pink immediately below the surface, which means that the pH of the alkaline environment is always higher than 9.2. From these tests it could be concluded that the concrete is in good condition and supplies an adequate protective environment to the (not exposed) embedded cables and reinforcements.

Concrete strength

In the evaluation of the concrete compressive strength of an existing structure, the conventional compressive strength and the in-situ compressive strength must be distinguished. The conventional compressive strength is determined on the basis of normalized tests using standardized cylinder concrete specimens, which were cast with fresh concrete and cured under specified conditions. Its average value is usually denoted by f_{cm} . The average in-situ compressive strength, here denoted by $f_{cm, is}$, is the compressive strength of the concrete in the structure and can either be determined directly, i.e., on the basis of compressive tests on cores drilled from the structure, or indirectly by measuring a certain quantity that can be empirically correlated to the compressive strength. The most commonly used indirect methods are the rebound hammer test (or sclerometer test), the ultrasonic pulse velocity test and the pull-off test. While the latter is classified as a semi-destructive test, the former two are purely NDT techniques. Despite being less expensive

and eliminating the introduction of damage in the structure, the indirect methods are mostly used to check the uniformity of the concrete quality due to the uncertainty in the correlation process. The combination of both direct and preferably several indirect methods is advised when a precise estimate of the in-situ compressive strength is required. In the norm dealing with the assessment of in-situ compressive strength in structures [49] the use of both direct [44] and/or indirect methods [45; 47; 48] is regulated.

Several studies [6; 28; 38; 92; 183] point towards the fact that the strength of drilled cores is lower than that of the standard cylinder. In fact, the quality of the concrete in the structure may differ from that of the standard cylinder because the compaction and/or curing of the in-situ material may not be well represented by the standard test specimens. Amongst other parameters, the $f_{cm, is}/f_{cm}$ ratio depends on the type of structural element from which the cores were drilled [92] and even on their location within the element [7]. The value $f_{cm, is}/f_{cm} = 0.85$ was adopted in the European norms [49]. In general, cores drilled from slabs present the lowest $f_{cm, is}/f_{cm}$ ratios and average values below 0.85 are reported in the literature [28; 38].

In the present case, drilling of concrete cores was kept to a minimum so as not to damage the bridge. Therefore, only two cores were drilled from the deck bottom slab. The samples were cylinders with $\varnothing 100\text{mm}$ and 230mm height. The cores were rectified and tested in uniaxial compression. The mean compressive strength was 41MPa (the compressive strength in each of the tests was 40.20 and 41.80MPa). The uniformity of the concrete quality in the webs was evaluated both using the sclerometer test and the ultrasonic pulse velocity method and no significant variation in the concrete strength was detected throughout the deck. Similar conclusions have been taken from a previous NDT campaign on the top slab.

In the construction documents, the specified concrete class was B350. According to the code in force at the time of construction, this meant that, at 28 days, the characteristic strength (95% percentile) in $0.20 \times 0.20 \times 0.20$ cubes should be 350 kgf/cm^2 . Assuming a normal distribution with a coefficient of variation of 13% [96; 255] it can be concluded that the specified average compressive strength in 20 cm cubes is 44 MPa. Using the expression proposed by L'Hermite [129], which relates the compressive strength of 20cm cubes $f_{cube,20}$ with that of standard cylinders f_{cyl} ,

$$\frac{f_{cyl}}{f_{cube,20}} = 0.502 + 0.2 \log f_{cube,20} \quad (f_{cube,20} \text{ in MPa}) \quad (7.1)$$

the specified average compressive strength in cylinders at 28 days, $f_{cm,28} = 36$ MPa, is calculated. It can be concluded that the specified concrete class is similar to the C30/37 class of the Eurocode 2 [46].

Amongst the available documentation from the construction period were the results of 159 compressive tests on 0.20x0.20x0.20m³ concrete cubes. These tests were performed at 3, 4, 5 and 7 days of age in order to evaluate the concrete strength at the time of application of the prestressing forces. The results are summarized in Table 7.1. The calculated coefficients of variation are in agreement with the values that can be found in the literature [96; 255].

Table 7.1 – Standard cylinder compressive strength statistics determined from tests performed during the construction

<i>t</i> (days)	Mean values (MPa)	COV (%)	Number of specimens	95% confidence interval for the mean
3	19.4	11.7	48	[18.8 ; 20.1]
4	21.7	14.7	54	[20.8 ; 22.5]
5	23.6	11.3	45	[22.8 ; 24.4]
7	27.2	6.3	12	[26.2 ; 28.2]

At the time of construction slow-hardening (low fineness) cements were commonly used in Portugal. In this particular case, this can be confirmed from the analysis of the cement dosage that was used. Assuming that the development of the concrete strength in time is given by the equation,

$$f_{cm}(t) = f_{cm,28} \cdot \beta_{cc}(t) \quad ; \quad \beta_{cc}(t) = e^{s(1-\sqrt{28/t})} \quad (t \text{ in days}) \quad (7.2)$$

where $s = 0.38$ [40] for slow hardening cements, and that $f_{cm,28}$ is the specified value determined above, the thin dashed curve of Figure 7.17 is obtained. However, if a nonlinear regression is performed varying the parameters $f_{cm,28}$ and s of Eq. (7.2), the best fit to the measured strengths at 3, 4, 5 and 7 days is given by the solid curve. The best fit curve was obtained with $s = 0.323$ and $f_{cm,28} = 37.2$ MPa. Even though the data points used for curve fitting are too close to each other, the fitted parameters are reasonably close to those initially assumed. It can be seen that both curves exhibit good agreement with the 30 years conventional compressive strength $f_{cm}(30\text{years})$ which can be estimated from the in-situ compressive strength determined from the two cores. Taking into account the considerations above and that the cores extracted from the bottom slab represent a lower

bound concerning the concrete quality, the average in-situ compressive strength $f_{cm, is}(30 \text{ years}) = 41 \text{ MPa}$, corresponding to $f_{cm}(30 \text{ years}) = 48 \text{ MPa}$, can be considered as an estimate on the safe side. Therefore, these were the values adopted in the structural analysis and subsequent safety checks.

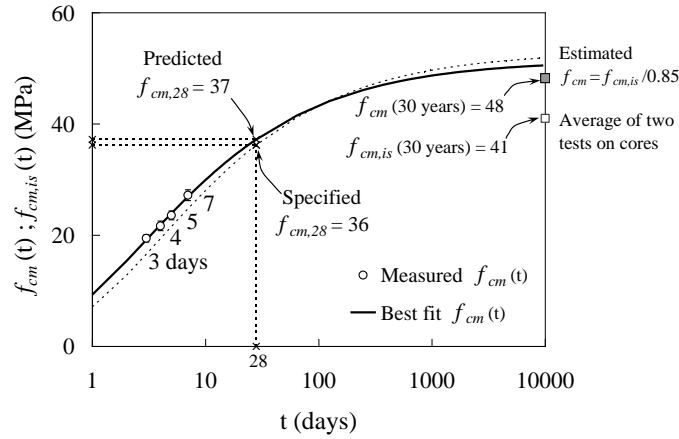


Figure 7.17 – Development of the concrete strength with time.

Concrete Young modulus

In order to reproduce the structural response during the load test, an estimate of the concrete Young modulus is required. Empirical relationships such as the one of Eq. (3.30) are usually used to derive the Young modulus from the conventional compressive strength at 28 days and from the aggregate type (in this case quartzitic aggregates were used). The evolution of the Young modulus with time is given by

$$E_{cm}(t) = E_{cm,28} \cdot \beta_{cc}(t)^a \quad (t \text{ in days}) \quad (7.3)$$

with $a = 0.3$ or 0.5 according to [46] or [40; 84], respectively.

Similarly to the compressive strength, it is most likely that the in-situ Young modulus $E_{cm, is}$ differs from the conventional value E_{cm} . However, it is not clear if the empirical relationship (3.30) still yields reasonable estimates of the in-situ Young modulus when the $f_{cm, is}(28)$ is used instead of $f_{cm,28}$. For lack of a better alternative, this was the adopted approach yielding $E_{cm, is}(28) = 32 \text{ GPa}$. At the age of 30 years, and assuming $s = 0.323$ according to the curve fitting performed above, a stiffness increase of 10 to 17% is calculated using expression (7.3) with $a = 0.3$ or 0.5 , respectively. According to this reasoning the value $E_{cm, is}(30 \text{ years}) \approx 37 \text{ GPa}$ is adopted.

7.4.2 Reinforcing steel

The specified type of steel was the SNT 40, which according to the code in force at the time corresponds to a nominal yield strength of $f_{yk} = 400\text{MPa}$ (5% percentile). The reinforcing bars used in the deck are 10 and 12mm diameter. Two rebar segments were taken from the pier P4 and from the abutment E2. Six 20cm length samples ($4\text{Ø}10 + 2\text{Ø}12$) were prepared and tested in the laboratory. The obtained stress-strain diagrams are typical of cold worked high-strength steel not exhibiting a defined yield plateau. The mean values of the steel properties obtained in the tests are given in Table 7.2.

Table 7.2 – Reinforcing steel properties. Mean values from 6 samples

$f_{0.2\%}$ (MPa)	f_t (MPa)	ϵ_u (%)	Es (GPa)
478	571	3.2	200

The bias factor $\lambda_s = f_{ym}/f_{yk}$ is defined as the ratio between the average yield strength and the nominal yield strength for the steel of a given class. Values of λ_s around 1.20 are referred in literature reviews for the steel produced at the time [96; 255], which agrees well with the value of $\lambda_s = 478/400 = 1.19$ determined from the tested samples.

7.4.3 Prestressing steel

No information regarding the prestressing steel type could be found in the available documentation. However, it is most likely that the adopted steel was of the class corresponding to $f_{pu,k} = 1770\text{MPa}$. From the construction drawings made available in 2009 it can be confirmed that VSL Type-E anchorages were adopted. The gammagraphic study revealed that seven wire 0.5” strands were used. However, it was not possible to discern if these strands had 100mm^2 or 93mm^2 nominal area. Conservatively, the latter was used throughout the calculations.

7.5 Monitoring campaign

The bridge was monitored during a controlled load test and during 4 days under normal traffic and environment excitations. The monitoring campaign aimed at evaluating the linearity of the bridge response as well as the crack movements under controlled traffic loads and daily thermal variations. The full description of the monitoring system design, including all the instrumentation, data acquisition systems, testing procedures, data post-processing and an exhaustive list of the obtained results can be found in the test report [203]. Here only the most significant results will be discussed. The measured

displacements and rotations are presented in Figure 7.18, the location of the thermal sensors in indicated in Figure 7.19 and the monitored cracks are schematically shown in Figure 7.20.

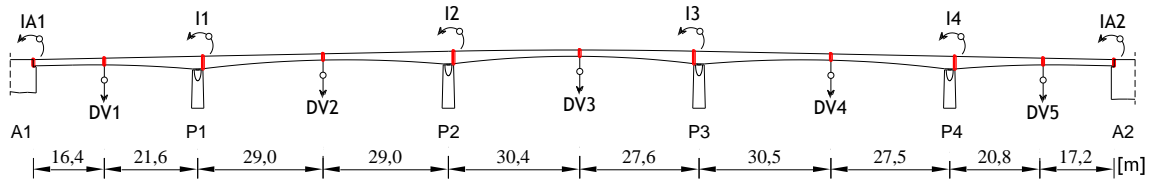


Figure 7.18 – Measured displacements and rotations.

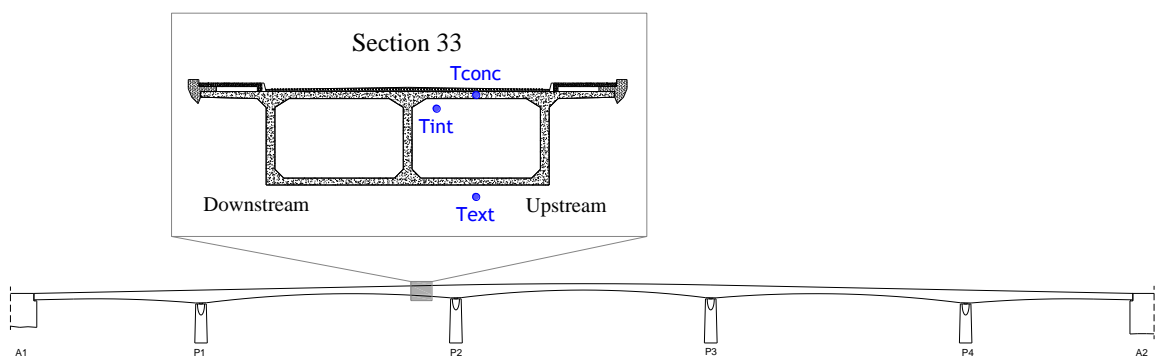


Figure 7.19 – Location of the thermal sensors

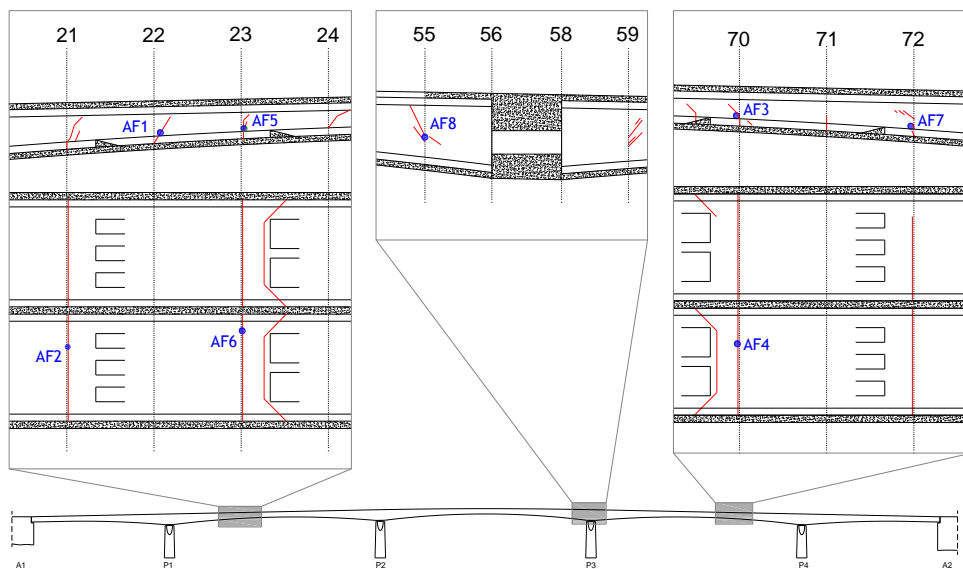


Figure 7.20 – Measured crack opening variations.

The midspan vertical displacements were measured with a hydrostatic levelling system, constituted by 3 hydraulic circuits with fixed reservoirs placed at the abutment A1 and

piers P2 and P4. The deck rotations at the intermediate supports were measured with clinometers while the rotations at the abutments were measured with lvdt's, so the deck longitudinal movements could also be obtained. The crack width variations were measured using either lvdt's or clip-gages crossing the selected cracks. Three thermometers were used to measure the air temperature inside and outside the box-girder and immediately below the bituminous layer. Whenever relevant, the experimental results were compared with the corresponding numerical values calculated with a linear elastic finite element bridge model. The bridge was modelled with 3 node Timoshenko beam elements. Each element is numerically integrated with a 2-point Gaussian quadrature along the bar axis, while in the area of the cross-section the Simpson rule is adopted (see Figure 7.21). The longitudinal reinforcements and the post-tensioning cables were modelled using embedded bar elements. An equivalent spring was used to model the longitudinal stiffness of the bearing/pier system. As expected, the spring stiffness is mostly dictated by the longitudinal bearing pad stiffness, which is much lower than that of the pier. The concrete Young modulus was calculated as described in Section 7.4.1. The vehicle loading was modelled as distributed load acting on the bridge axis. The weight of each vehicle was distributed along 7.0m. The model uses two-dimensional finite elements and therefore the torsional effects cannot be reproduced.

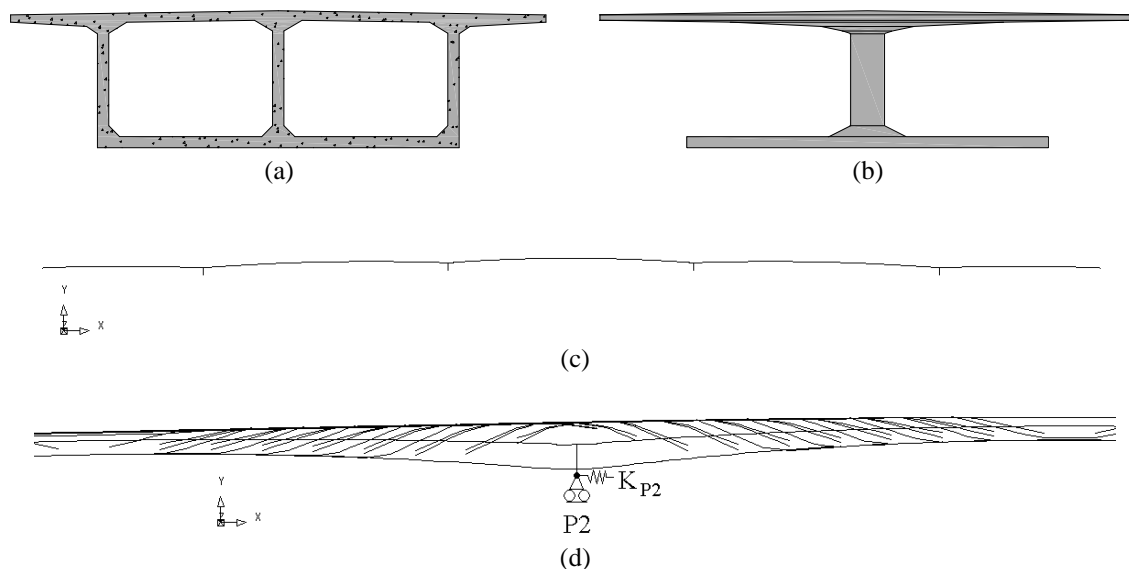


Figure 7.21 – Finite element model: (a) Real cross-section and (b) corresponding layered discretization; (c) global view of the model represented by the centroid axis; (d) detail of the model in the region of pier P2 with the representation of the post-tensioning tendons and longitudinal reinforcements.

7.5.1 Load test

The bridge was loaded by four 26ton trucks, with similar geometry and axle weights, see Figure 7.22. The test was divided in two stages. In the first stage the readings were taken with the four vehicles stopped at 9 consecutive positions on the deck (load cases LC1 to LC9). In order to evaluate the repeatability of the measurements, these 9 positions were repeated with 5 different transversal vehicle arrangements, as depicted in Figure 7.23.

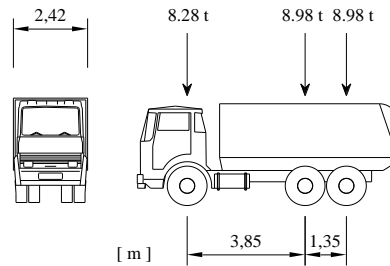


Figure 7.22 – Vehicle geometry and average axle weight. Average total weight of 26.24 tonnes/vehicle.

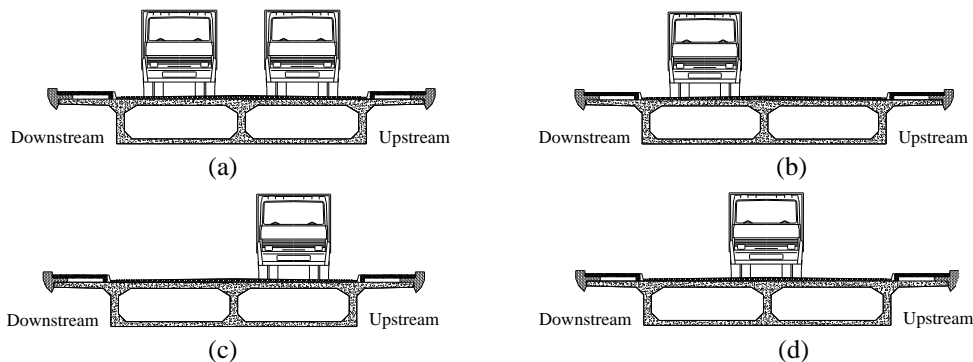


Figure 7.23 – Transversal vehicle arrangements: (a) side-by-side (with 2 and 4 vehicles); (b) downstream (2 vehicles) ; (c) upstream (2 vehicles) ; (d) centred (2 vehicles).

During the test, the maximum positive bending moments reached 60% of the bending moment envelope due to the characteristic value of the traffic load prescribed by the current Portuguese code [200]. According to the same code, the frequent value of the traffic load is assumed be 40% of the characteristic value. In the second stage of the load test, measurements were taken with the vehicles moving at different speeds, so that both static and dynamic experimental influence lines could be obtained. The presented experimental results were post-processed. The effect of the increasing temperature during the period of testing was removed and a low-pass filter was applied for eliminating some of the noise present in the original signals [203]. In cases of high noise/signal ratio some artificial low amplitude oscillation is seen in the filtered results.

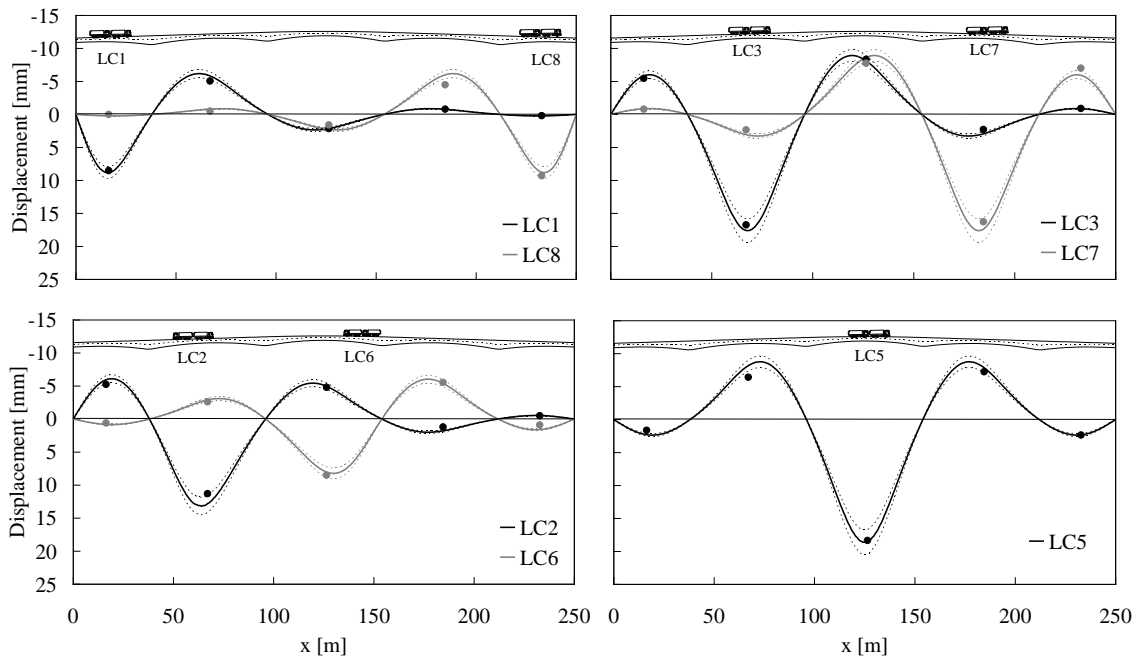


Figure 7.24 – Calculated (lines) versus measured (dots) vertical displacements for different load cases. The dashed lines represent the $\pm 10\%$ interval around the calculated values.

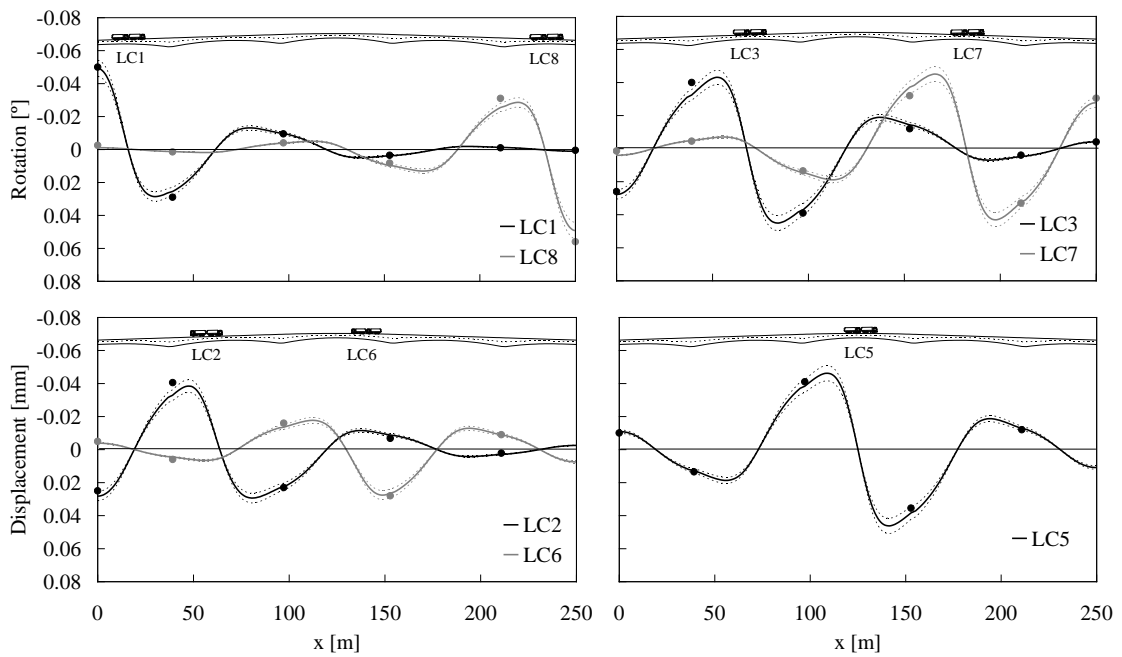


Figure 7.25 – Calculated (lines) versus measured rotations (dots) for different load cases. The dashed lines represent the $\pm 10\%$ interval around the calculated values.

The vertical deck displacements and rotations are presented in Figure 7.24 and Figure 7.25, respectively, for the static load cases in which four trucks were used. The static influence lines obtained with two vehicles crossing the bridge side by side are depicted in Figure 7.26. With the systematic exception of fifth span, the measured displacements are generally lower than calculated. This tendency cannot be observed for the rotations, with the values measured in some of the sensors being consistently higher than calculated. In general the differences between the calculated and measured values are within the $\pm 10\%$ interval delimited by the thin dashed lines. The displacement and rotation influence lines presented in Figure 7.26 seem to confirm the observations made above. The displacement measured in the 5th span and the rotations measured by the sensors I1, I2, I4 and IA2 are consistently higher than the corresponding calculated values.

During the load test all the monitored cracks exhibited opening and closing movements around the unloaded state. A strong correlation between the bending moment and crack movements influence lines was detected in the measurements provided by sensors located in the bottom slab (AF2, AF4 and AF6). In the cases where the cracks were continuous to the webs, the correlation was still reasonable with the crack movements measured in the webs, e.g. sensors AF3 and AF5. This is illustrated in Figure 7.27 (a)-(c) for the sensors AF2 to AF6. The movements of the crack monitored by the sensor AF8 are related with the shear force, as can be inferred from Figure 7.27 (d). A maximum crack opening variation of 0.13mm was measured by AF6 during LC2, with four trucks positioned on the deck. In the figures, an opening movement corresponds to a negative value.

Despite the measured crack activity, the bridge response was linear elastic. No discernable deviation from linearity was observed in the tests with simultaneous loading by 1, 2 and 4 trucks.

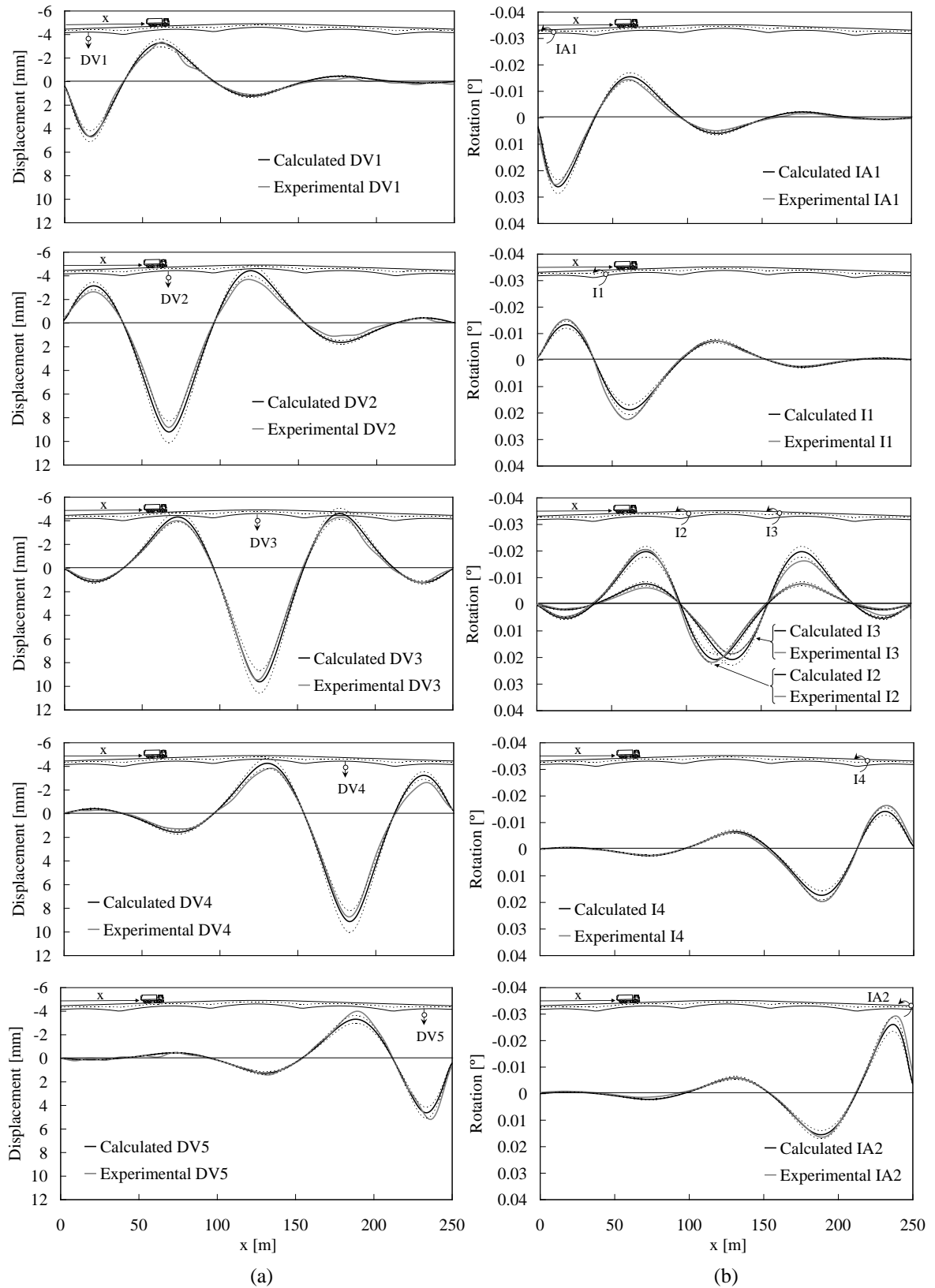


Figure 7.26 – Calculated versus measured influence lines: (a) vertical displacements; (b) rotations. The influence lines refer to a pair of 26ton trucks crossing the bridge side by side.

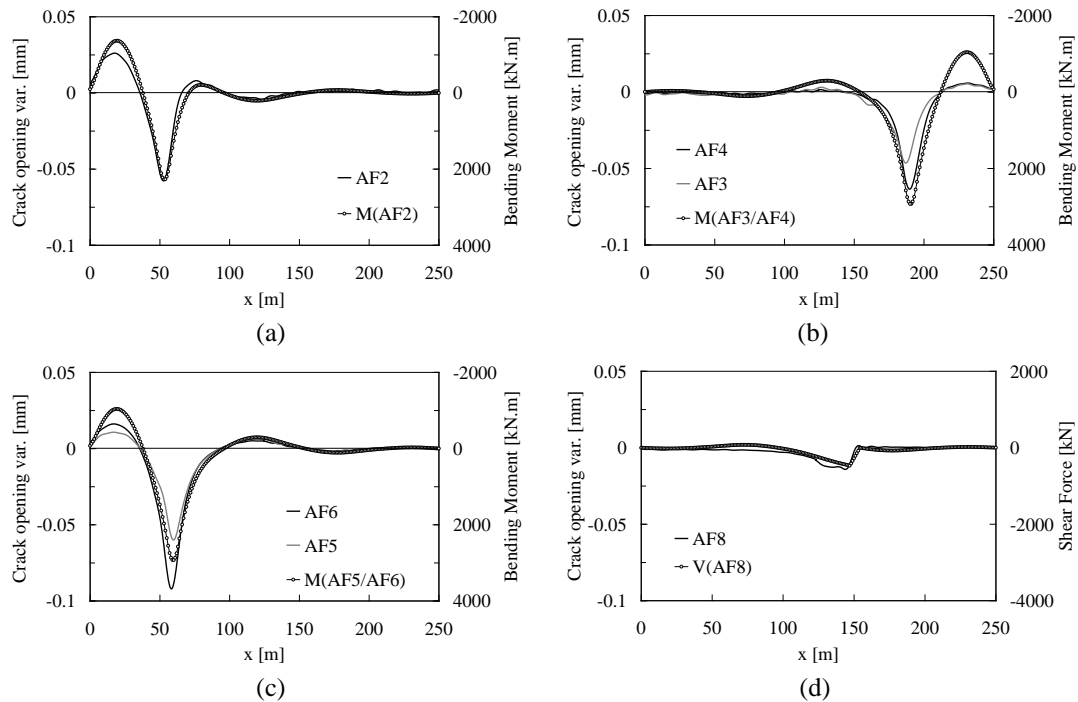


Figure 7.27 – Comparison of the crack movement influence lines (2 trucks side by side) with the: (a)-(c) corresponding bending moment influence lines; (d) shear force influence line.

7.5.2 Response to temperature variations

In the four days subsequent to the load test, sensors AF1 to AF4 were continuously read every 15 minutes, together with the temperatures indicated in Figure 7.19. The results are presented in Figure 7.28. All the cracks were active, exhibiting both closing and opening movements around the unloaded state. It can be seen that the total crack movement (opening and closing) is larger than the obtained with two 26 ton trucks side by side.

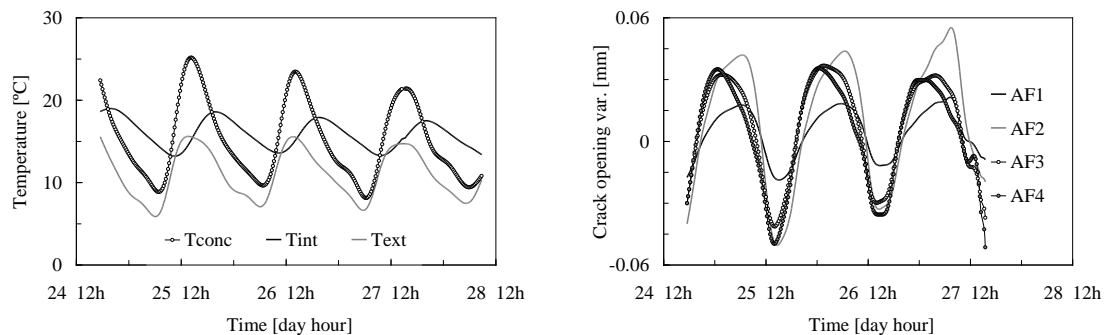


Figure 7.28 – Evolution of the measured temperatures and crack movements during four days.

7.6 Investigation of the causes for the observed cracking patterns

7.6.1 Stress analysis in serviceability conditions

Due to the time-dependent effects of creep and differential shrinkage, in continuous bridges built by the balanced cantilever method bending moments continue to build up after casting of the closing segment. As the time-dependent behaviour of concrete is associated to great uncertainty, the long term bending moment distribution can only be estimated. These uncertainties are partially reflected in the significant differences that can be found between several creep and shrinkage models. Although attempts have been made to bring the models in line with fundamental theoretical principles [11; 19], most practical models are still empirical formulations. In most practical cases, information about the actual water/cement ratio and about the real drying, moisture and thermal conditions is generally unavailable which makes the application of more sophisticated formulations difficult.

The literature regarding time-dependent effects in this type of bridges focuses mainly on the development of the long-term deflections [126; 194; 229]. Less examples of long term strain monitoring are reported, see for instance the works of Santos [206] and Félix [78]. In general, the calculated deflection or strain evolution can only match the measured values after some kind of scaling of the creep compliance functions, either by adopting multiplicative factors [83; 194; 206] or by modifying the standard input parameters [15]. In the present case no long term monitoring data is available and no fitting of the creep and shrinkage constitutive laws can be made. Therefore, considering the available data, the long term stress distribution that is going to be calculated must be considered as one possible estimate.

In this section, a stress analysis is carried out using the beam element model of the bridge already described in section 7.5. Each segment of the bridge deck is divided in two Timoshenko beam elements with three nodes each. Embedded truss elements are adopted for the reinforcements and post-tension tendons. The layout of the latter was as determined from the post-tension construction drawings, see Figure 7.21. As the model is two-dimensional, only the in-plane coordinates of the tendons are defined. The length of continuity tendons located in the bottom slab is reduced in an attempt to reproduce the transmission of the prestressing force to the webs, as schematically depicted in Figure 7.29.

This effect is only properly analysed with the three-dimensional model described in section 7.6.2.1.

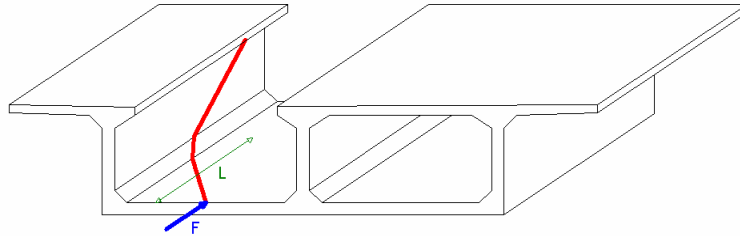


Figure 7.29 – Transmission to the web of the prestressing force due to a tendon anchored in the bottom slab.

7.6.1.1 Construction sequence

The construction sequence of the bridge was determined based on the information contained in the construction site log book and differs from that specified in the original 1973 design. With the exception of the pier table and the end portions of the 1st and 5th spans, the deck was divided in 3 meter length cast in-situ segments. Therefore, each cantilever comprised 8 segments with the closing segment being the 9th. The construction stages can be divided in the following 7 distinct phases, which are not necessarily in chronological order:

- Phase 1. Simultaneous balanced cantilever construction of the segments over Piers 1 and 2. In this phase the rotation of the cantilevers is restricted by means of stabilizing vertical prestressed cables. Not considering the period corresponding to the construction of the pier tables, this phase has the approximate duration of 87 days.
- Phase 2. Closing of the 2nd span and release of the stabilizing cables of piers 1 and 2.
- Phase 3. Construction of the remaining portion of the first span. Following the original design, an additional 3.0m length segment is still cast by the cantilevering method.
- Phase 4. Simultaneous balanced cantilever construction of the segments over Piers 3 and 4. In this phase the rotation of the cantilevers is restricted by means of stabilizing vertical prestressed cables. This phase has the approximate duration of 60 days.
- Phase 5. Closing of the 4th span and release of the stabilizing cables of piers 3 and 4.

Phase 6. Construction of the remaining portion of the first span, with an additional 3.0m length segment still cast by the cantilevering method.

Phase 7. Casting of the closing segment in the central span.

The construction sequence was modelled as indicated in Figure 7.30. In the balanced cantilever stage, each segment cycle was subdivided in 3 distinct stages: (1) placement of the traveller form – in this stage the loads equivalent to traveller form weight are applied on the precedent segment; (2) casting – the loads equivalent to the weight of the new segment are added to those of the traveller form; (3) post-tensioning of the tendons – the post-tension forces are applied, the elements corresponding to the new segment are initialized and the previously applied loads equivalent to its self-weight are removed. With the exception of the first segments of the cantilevers over piers 1 and 2, prestressing was mostly applied 3 days after casting. Therefore, every new element at a given phase is initialized with 3 days of age. Previous to grouting, tendon elements are considered unbonded and do not share the displacement field of the embedding concrete elements. Grouting of the tendons in segment i is made to coincidet with the first operation of the cycle corresponding to segment $i+1$. Following the indication of the original design, a total weight of 170kN was considered for the traveller form, which is roughly equivalent to 1/3 of the heaviest segment. The resulting phased numerical analysis comprised a total of 60 distinct stages.

The construction site log book contained the casting dates of every segment, allowing a detailed reproduction of the construction stages. However, no information is given on the stressing sequence of the cables. This is more significant in the case of the continuity cables, since the hiperstatic effect of the prestressing depends on the structural configuration at the time of stressing. The calculations were made considering that the continuity cables were stressed immediately after closure of the corresponding span.

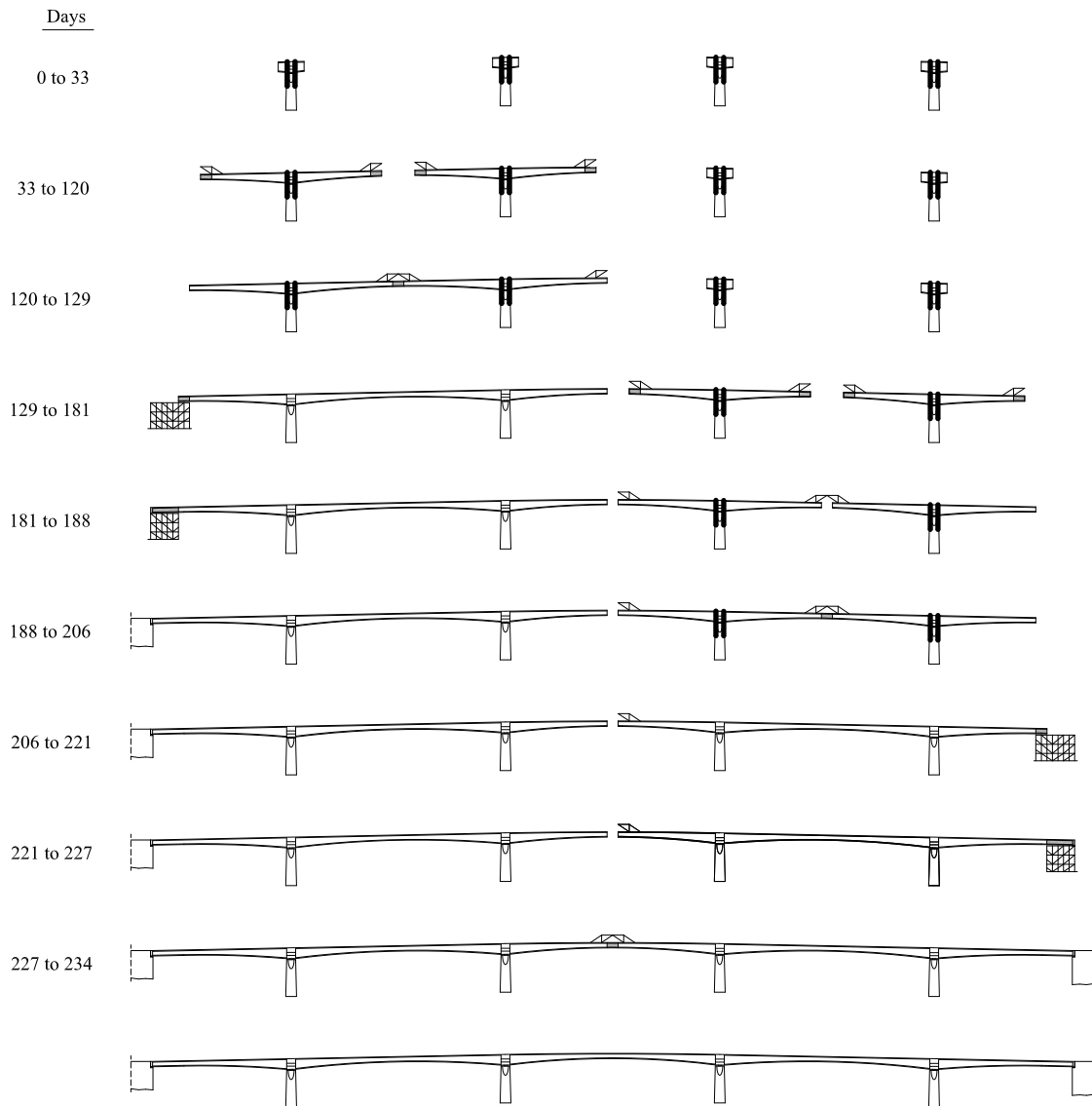


Figure 7.30 – Construction sequence as modelled.

7.6.1.2 Modelling of the prestressing force

The prestressing force in the tendon varies along the tendon axis and with time. In post-tensioned systems the initial prestressing force applied at the anchor is reduced by prestress losses resulting from friction, anchor slip, steel relaxation and shortening of the concrete due to elastic, creep and shrinkage deformations.

Immediate losses due to friction and anchor slip are calculated automatically by DIANA [231] 7 considering the adopted tendon layout. After post-tensioning, the prestressing force at a distance x of the anchorage is given by (see Figure 7.31):

$$P(x) = P_0' e^{-(\mu\alpha + kx)} \quad (7.4)$$

where

- P'_0 is the applied prestressing force at the active anchorage during tensioning;
- μ is the Coulomb friction coefficient;
- α is the total cumulative angular variation over the length x [rad];
- k is the wobble friction coefficient [1/m].

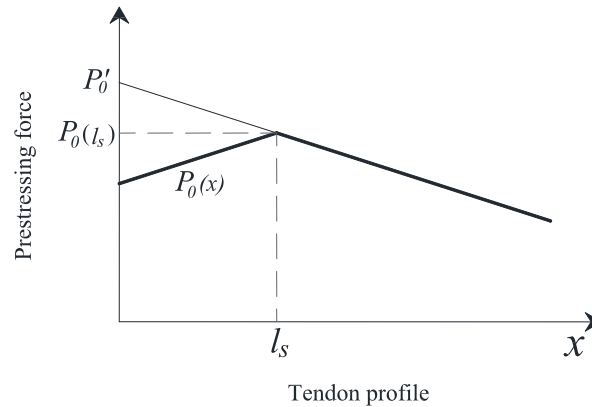


Figure 7.31 – Prestressing force after immediate losses.

The values of μ and k vary considerably depending on several factors. For strands in metal sheathing, and in the absence of more accurate values, the CEB-FIP Model Code 1990 [40] recommends the use of 0.20 for μ and $0.005\mu \div 0.01\mu$ per meter for k . The value of the wobble friction coefficient can be higher in segmentally constructed structures due to the additional wobble effect at the location of the segment interfaces. Since the out-of-plane curvature of the tendons is not considered in this two-dimensional model, increased friction and wobble factors were considered in order to compensate for that, see Table 7.4. The losses due to anchor slip are determined considering that the anchor slip s is equal to the shortening of the tendon over the length l_s , as expressed by the equation

$$s = \frac{2}{E_p A_p} \int_0^{l_s} (P(x) - P(l_s)) dx \quad (7.5)$$

In the context of finite element analysis, the unknown length l_s can be determined by the numerical procedure described in reference [231], after which the effective prestressing force after immediate losses can be calculated over the length l_s as

$$P_0(x) = 2P(l_s) - P(x) \quad (7.6)$$

Beyond the length of l_s anchor slip has no influence and $P_0(x) = P(x)$, the latter given by Eq. (8.6).

The losses due to prestressing steel relaxation are quantified according to the model included in EN 1992-1-1 [46]. This model was implemented in a user-supplied subroutine for DIANA by Sousa and Neves [225]. Three classes of relaxation are defined:

- Class1: wire or strand – ordinary relaxation
- Class2: wire or strand – low relaxation
- Class3: hot rolled and processed bars

The calculation of the losses due to relaxation is based on the value of the relaxation loss at 1000 hours after tensioning, at a mean temperature of 20°C, represented by ρ_{1000} . The value of ρ_{1000} is expressed as a percentage ratio of the initial stress, and is obtained for a initial stress equal to $0.7 f_p$, where f_p is the actual tensile strength of the prestressing steel samples (for design calculations the characteristic tensile strength f_{pk} is used). The recommended values of ρ_{1000} are given in Table 7.3. In the present analyses, ordinary relaxation steel was assumed (Class 1).

Table 7.3 – Parameters for calculation of relaxation losses.

Class	ρ_{1000} (%)	A	B
1	8.0	5.39	6.7
2	2.5	0.66	9.1
3	4.0	1.98	8.0

If the elongation of the prestressing steel is kept constant over time, the relaxation loss is determined from the expression

$$\frac{\Delta\sigma_{pr}}{\sigma_{pi}} = A \cdot \rho_{1000} \cdot e^{B \cdot \mu} \cdot \left(\frac{t}{1000} \right)^{0.75(1-\mu)} \cdot 10^{-5} \quad (7.7)$$

$\Delta\sigma_{pr}$ is the absolute value of the relaxation loss at time t ;

σ_{pi} is the absolute value of the prestress at the beginning of time interval;

$\mu = \sigma_{pi} / f_{pk}$;

A, B are parameters defined in Table 7.3;

t is the time after tensioning, in hours.

If the prestressing tendon is subjected to instantaneous stress variations, the relaxation losses are calculated for different time intervals using the Equivalent Time Method, according to the Annex D of EN1992-1-1, to which the reader is referred. With this method it is possible to quantify the relaxation loss $\Delta\sigma_{pr,i}$ that occurs in a given time interval $\Delta t_i = t_{i+1} - t_i$. However, in a real situation, the deformation imposed to the prestressing tendon is neither kept constant over time nor varies only instantaneously. In fact, concrete delayed deformations caused by creep and shrinkage lead to a gradual variation of strain over time. This way, at a given time interval Δt_i , a strain variation $\Delta\varepsilon_i$ takes place. This situation is not explicitly dealt with in the EN 1992-1-1. In this subroutine, the proposal of Hernandez and Gamble [97] quoted by Póvoas [189] was followed. The stress $\sigma_{p,i+1}^-$ at the end of a given time interval Δt_i is given by

$$\sigma_{p,i+1}^- = \sigma_{p,i}^+ + E_p \cdot \Delta\varepsilon_i - \Delta\sigma_{pr,i} \quad (7.8)$$

where

$\Delta\sigma_{pr,i}$ is the relaxation loss of the time interval considered quantified according to Equivalent Time Method;

$\sigma_{p,i}^+$ is the tensile stress in the tendon at the beginning of the current time interval (just after t_i)

7.6.1.3 Concrete time-dependent behaviour

The time-dependent concrete strains are usually expressed by the sum of two strain components

$$\boldsymbol{\varepsilon}_c(t, t_0, t_s) = \boldsymbol{\varepsilon}_{c\sigma}(t, t_0) + \boldsymbol{\varepsilon}_{cs}(t, t_s) \quad (7.9)$$

where

$\boldsymbol{\varepsilon}_{c\sigma}(t, t_0)$ is the stress-dependent strain vector at time t of a concrete member loaded at time t_0 ;

$\boldsymbol{\varepsilon}_{cs}(t, t_s)$ is the stress-independent strain vector at time t , which is here considered equal to the shrinkage strain. This strain is assumed to start to occur when drying begins, after the end of curing, at time t_s .

If concrete is considered as an aging linear viscoelastic material, the stress-dependent strain vector of a concrete member loaded with a variable stress $\sigma_c(t)$ may be written as

$$\boldsymbol{\varepsilon}_{c\sigma}(t, t_0) = \boldsymbol{\sigma}_c(t_0)J(t, t_0) + \int_{t_0}^t J(t, \tau) \mathbf{C} \frac{\partial \boldsymbol{\sigma}_c}{\partial \tau} d\tau \quad (7.10)$$

where $J(t, \tau)$ is the creep function or creep compliance, representing the strain response at time t due to a sustained constant unit stress applied at time τ , and \mathbf{C} is a dimensionless matrix depending only on the Poisson ratio [32]. The creep function is usually written as:

$$J(t, \tau) = \frac{1}{E_c} \left(\frac{1}{\beta_E(\tau)} + \varphi_0(\tau)\beta_c(t - \tau) \right) \quad (7.11)$$

where

$\varphi_0(\tau)$ is the notional creep coefficient for concrete loaded at the age τ

$\beta_E(\tau)$ is a coefficient which depends on the age of concrete, τ

$\beta_c(t - \tau)$ is the coefficient to describe the development of creep with time after loading.

In the present analyses, the creep and shrinkage models proposed in the CEB-FIB Model Code 1990 were adopted. These models were reviewed in the 1999 *fib* bulletin [84], reflecting the progresses made in the research of high-strength concrete, and the revised versions were adopted in the EN-1992-1-1. For normal strength concrete, both the original and revised versions yield the same results and the original CEB-FIB Model Code 1990 formulation was still considered in this work since it was readily available in DIANA. The adopted parameters are summarized in Table 7.4.

Table 7.4 – Material properties for the time-dependent phased analysis.

<i>Parameter</i>	<i>Symbol</i>	<i>Value</i>
Concrete		
Average compressive strength	f_{cm}	38 MPa
Average Young modulus	E_{cm}	34 GPa
Cement type	-	S
Notional size	h_0	235 mm
Relative humidity	RH	80%
Average temperature	T	20°C
Age at first loading	t_0	3 days
Age when drying begins	t_s	3 days
Prestressing steel		
Tensile strength	f_{puk}	1770 MPa
Tensioning stress	$\sigma_{p'0}$	1260 MPa
Young modulus	E_p	195 GPa
Relaxation loss at 1000 hours after tensioning	ρ_{1000}	8%
Data for calculation of immediate prestressing losses		
Coulomb friction coefficient	μ	0.3
Wobble coefficient	k	0.01μ
Anchor slip	s	6 mm

The development of creep and shrinkage is significantly affected by the dimensions of the structural member through drying. The average size of a cross-section with arbitrary shape is characterized by the notional size h_0 :

$$h_0 = \frac{2A_c}{u} \quad (7.12)$$

where A_c is the cross-sectional area and u is the perimeter exposed to drying. In the beam element model the notional size was taken constant not only within the cross-section but also throughout the deck. Therefore, uniform creep and shrinkage rates are considered.

However, the different thickness of individual parts of the box-girder, as well as the different exposure conditions, result in non-uniform creep and shrinkage rates. The additional curvature development due to non-uniform creep and shrinkage within the cross-section has been shown to be significant in cases of bridges with high thickness contrasts between the elements of the cross-section [15; 126; 139], where typically the bottom slab is several times thicker than the remaining elements. In the present case, the thickness of the bottom slab varies from 160mm at midspan to 240mm close to the supports. The thicknesses of the webs and top slab are constant and equal to 250mm and 200mm, respectively. Due to the small thickness difference, the adoption of uniform creep and shrinkage rates within the cross-section is still acceptable. The application of Eq. (7.12) to the 1.45m high cross-section at midspan and to the 2.9m high cross-section in the vicinity of the supports leads to $h_0 = 225\text{mm}$ and $h_0 = 252\text{mm}$, respectively. Again, due to the small variation, a constant value of 235mm is adopted throughout the deck.

For general structural computations the integral of Eq. (7.10) must be evaluated using numerical methods. Time is discretized in finite time increments and the integrals are replaced by finite sums. Still, such a formulation has the inconvenient feature that the strain increment at any new time step is calculated as a function of the entire previous stress (or strain) history. This makes the formulation impractical for large computations because the entire stress (or strain) history must be stored for each computation point. In the context of finite element analysis rate-type formulations are preferred instead, which have the advantage of expressing the relationship between the stress and strain increments over a time step with a small number of state variables [32]. The creep function is written as a truncated Dirichlet series, which can be interpreted as a chain of simple units corresponding to the Kelvin rheological model. DIANA automatically generates the chain components to fit the selected creep compliance based on a non-linear least squares regression. Details can be found in [231].

7.6.1.4 Loading

Besides the prestressing, the permanent loads consist of self weight and the weight of the finishings. The latter are shown in Figure 7.32 (a). Regarding the traffic loading, the load models of the current Portuguese code RSAEP [200] were adopted. For the N. S. Guia Bridge the conditioning load model consists of a uniformly distributed load $q_k = 4\text{kN/m}^2$ and a “knife” load $Q_k = 50\text{kN/m}$, both distributed along the width of the traffic lane, see Figure 7.32 (b). Considering a 8 m wide traffic lane, the loads shown in Table 7.5 are obtained. This traffic load model was developed in the early 60-ties for the former

Portuguese code RSEP [201] and it is still in force today. Nonetheless, it can be considered obsolete due to the large infrastructure development and consequent increase of the traffic intensities and maximum gross weight of the heavy vehicles that occurred in the last 50 years. Still, it can be more representative of the actual traffic crossing the N. S. da Guia Bridge than the new load models of the Eurocode 1 [43], which were developed based on traffic data recorded on very busy French motorways connecting the main industrialized regions of central Europe.

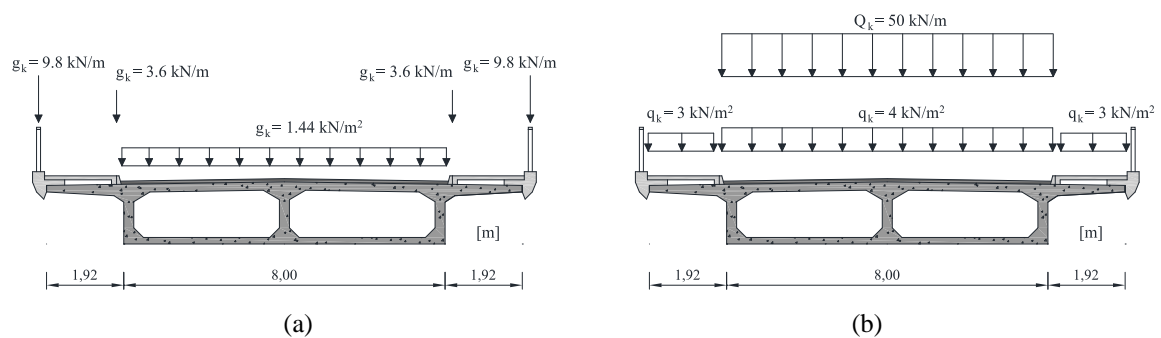


Figure 7.32 – Loads: (a) Remaining permanent loads; (b) Traffic and pedestrian loads.

Table 7.5 – Loads considered in the analysis

<i>Permanent loads</i>	<i>Nominal value</i>			
Self weight	$\gamma_c = 25\text{kN/m}^3$			
Prestress	See 7.6.1.2			
Remaining permanent loads	38 kN/m			
<i>Live loads</i>	<i>Characteristic value</i>	ψ_0	ψ_1	ψ_2
Traffic	32 kN/m + 400 kN	0.6	0.4	0.2
Pedestrian	11.5 kN/m	0.6	0.4	0.2
Differential temperature component	10°C		0.5	0.5

Thermal effects play an important role in bridge analysis and design. The temperature distribution within a given cross-section can be divided in uniform, differential and nonlinear temperature components. The uniform component is associated to the seasonal temperature variations and is normally used to evaluate the longitudinal deck movements. If the deck is not continuous with the piers, and if the bearings are properly designed, negligible stresses arise due to this effect. Due to the poor thermal conductivity of concrete,

the daily temperature variations lead to a complex temperature distribution within the cross-section. This distribution can be sought as the sum of the differential and nonlinear components. In hyperstatic structures, the former gives rise to bending moments and corresponding longitudinal stresses, while the later is responsible for a self-equilibrated stress distribution irrespective of the static scheme. The differential temperature component was defined based on the recommendations given by Mirambell *et al* and by Silveira [158; 219]. According to these references, and considering a box-girder cross-section size similar to that of the N. S. Guia Bridge and the specific location of the bridge in the northern part of the Iberian peninsula, the characteristic value of differential temperature component is $\Delta T_k = 10^\circ\text{C}$. This value coincides to that recommended in the national annex of the NP EN 1991-5 [50].

The self-equilibrated stress distribution arising due to the nonlinear component is determined according to the nonlinear temperature distribution proposed in the NP EN 1991-5 and is illustrated in Figure 7.33 for the cross-section at the intermediate supports. Similar stress distributions were calculated for the other cross-sections. The calculated values are in reasonable agreement with the values reported by Silveira [219] for concrete box-girder bridges with similar cross-section dimensions and considering the climatic conditions in Northern Portugal. Moreover, the stress distribution throughout the cross-section height is similar to those obtained by Mirambell and Aguado [157] in concrete box-girder bridges.

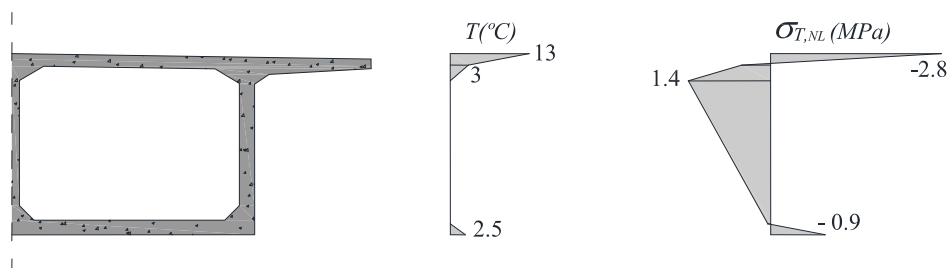


Figure 7.33 – Self-equilibrated stress distribution arising due to the nonlinear temperature component.

7.6.1.5 Results

The time evolution of the vertical displacements at the center of the closing segments of each of the five spans is presented in Figure 7.34. The presented values correspond to the displacement variation with respect to the theoretical level at the time of casting. The operations leading to the highest displacement variations are marked by dashed lines and correspond to the following events:

- $t = 135$: stressing of the continuity tendons of the 2nd span and release of the stabilizing cables in piers P1 and P2;
- $t = 164$: stressing of the cantilever tendons corresponding to the 9th segment of the first span;
- $t = 181$: stressing of the continuity tendons in the first span;
- $t = 206$: stressing of the continuity tendons in the 4th span, release of the stabilizing cables in piers P3 and P4, and stressing of the cantilever tendons corresponding to the 9th segment of the fifth span;
- $t = 221$: stressing of the continuity tendons in the 5th span;
- $t = 233$: stressing of the continuity tendons in the 3rd span;
- $t = 450$: remaining permanent loads.

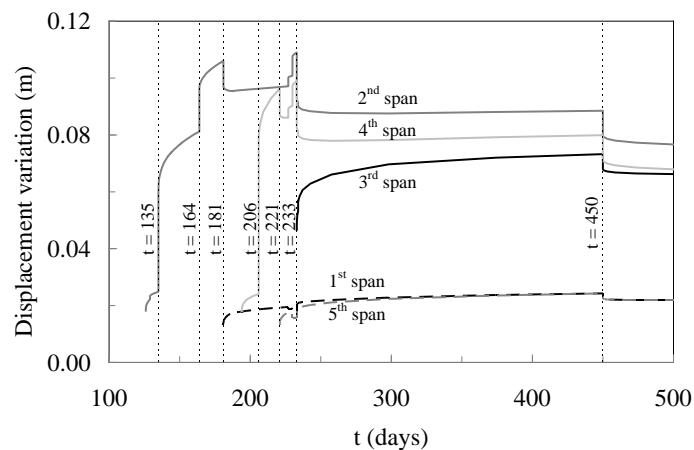


Figure 7.34 – Displacements at the center of the closing segment of each span.

The calculated axial force is depicted in Figure 7.35(a) and is compared to the prestressing force referred both in the original design and in the prestress design documents. Due to creep, shrinkage and prestressing steel relaxation, the long term axial force is lower than that estimated neglecting the time dependent effects. The long term axial force, here determined for $t = 30$ years, is generally below that considered in the tendons design, which means that the long term losses might have been slightly underestimated at the design stage.

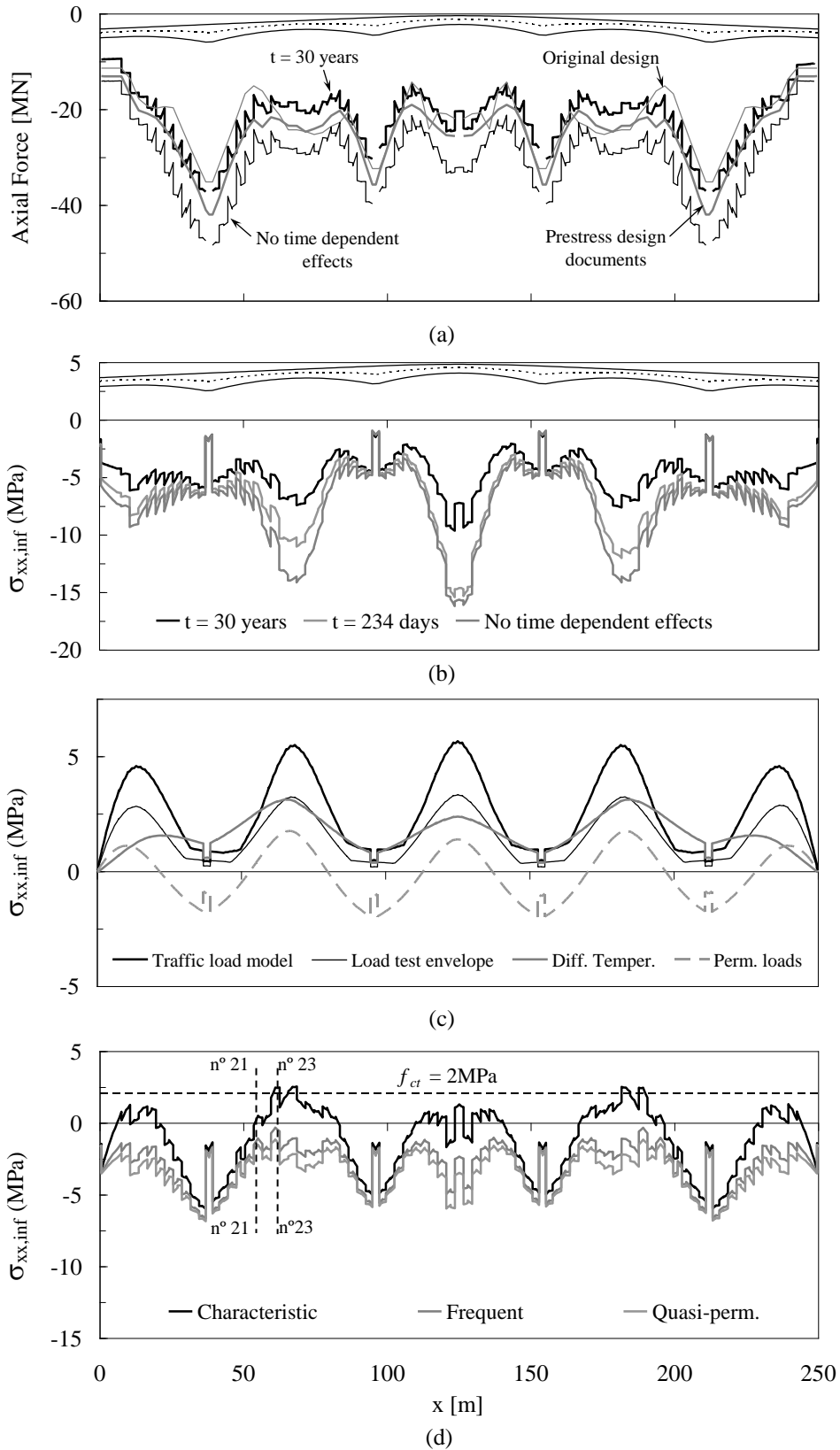


Figure 7.35 – (a) Long term axial force; Stresses in the bottom fibre: (b) due to self-weight and prestress; (c) due to the remaining permanent loads and characteristic values of differential temperature and live loads; (d) for serviceability load combinations

The concrete stresses in the extreme bottom fibre of the cross-section are presented in Figure 7.35(b) to (d). The long term effects are responsible for a significant stress variation, as can be seen in Figure 7.35 (b). Immediately after casting the final segment and stressing the corresponding continuity tendons at day 233, the concrete stresses already exhibit some differences with respect to those calculated neglecting the time dependency of the constitutive laws. Nonetheless, the major stress variations occur after the bridge is complete.

The concrete stresses due to the characteristic values of the traffic loads, differential temperature and nominal values of the remaining permanent loads are presented in Figure 7.35 (c). Also the stress envelope due to the four 26 ton trucks used during the load test is shown for reference. It can be seen that the stress variation due to the long term effects is higher than that due to the characteristic traffic action.

The stresses corresponding to the serviceability load combinations are presented in Figure 7.35 (d). Considering the tensile strength given by Eq. (2.2) it can be concluded that cracking should be expected in the characteristic load combination. However, the region where the computed stresses are near, or above, f_{ct} does not match the region where transversal cracks were seen in the bottom slab. Sections n°21 and 23 correspond to two of the sections where cracks propagated from the bottom slab towards the webs, see Figure 7.4. Although tensile stresses above f_{ct} are computed in section n°23, in section n°21 the stresses only reach 0.23 MPa in the characteristic load combination.

In the CEB-FIP Model Code 1990 it is mentioned that the coefficients of variations (COV) for creep compliance and shrinkage strains are 20% and 35%, respectively. It is also stated that the normal distribution can be adopted in probabilistic calculations. Given their importance to the final stress distribution, a sensitivity analysis is performed to assess the influence of creep and shrinkage variability on the calculated long term concrete stresses. Two separate analyses were performed where the standard creep or shrinkage functions were scaled in order to fit the corresponding 95% percentile. While the scaled creep compliance was introduced via a user supplied sub-routine for DIANA [226], the scaled shrinkage function was defined by adjusting the relative humidity parameter in the embedded shrinkage model. Beyond the uncertainties related to creep and shrinkage, also the effectively installed prestressing force cannot be precisely determined. Therefore, a third analysis was performed considering a 10% decrease of the initial post-tensioning force in all the tendons. The stress variations in the bottom fibre with respect to that of the analysis with standard parameters are shown in Figure 7.36. Stress variations due to

increased creep and shrinkage and decreased prestressing force tend to achieve its maximum values at the same regions of the deck. From the magnitude of the obtained stresses it can be concluded that, even considering the 95% percentiles of creep and shrinkage and a decrease of 10% of the initial prestressing force, the tensile stresses in the characteristic load combination reach only 0.83 MPa at section n°21, which is well below the tensile strength.

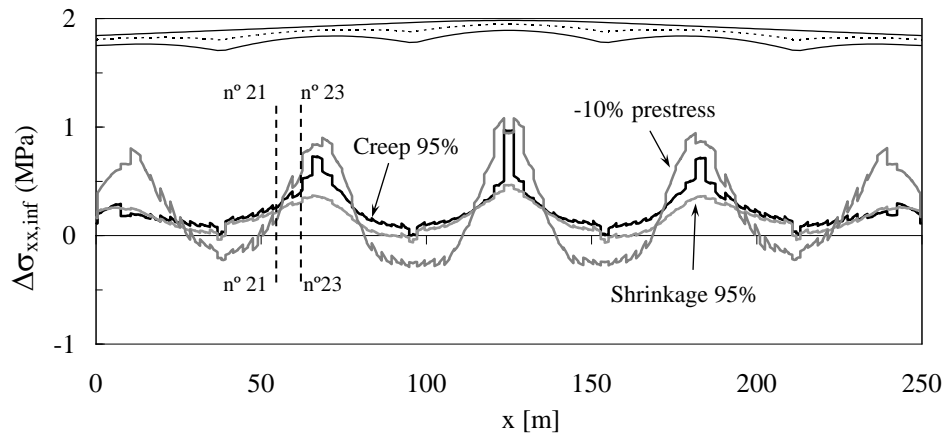


Figure 7.36 – Stress variation in the bottom fibre for $t = 30$ years with respect to the analysis with standard average parameters: Creep 95% - analysis with 95% percentile values of creep; Shrinkage 95% - analysis with 95% percentile values of shrinkage; -10% prestress – analysis considering a 10% decrease of the initial prestressing force.

7.6.2 Effect of local stress conditions

Since the origin of the observed cracks could not be clearly explained by the results obtained with the 2D beam model, a three-dimensional model of the bridge was developed in order to evaluate the influence of nonlinear stress distributions arising in discontinuity regions. As will be shown later on, these discontinuities occur mostly in the vicinity of the anchorages of both cantilever and slab continuity tendons.

7.6.2.1 Model description

The bridge deck was discretized into 8 node curved shell elements, see Figure 7.37. Integration is performed with 2×2 Gaussian quadrature in the in-plane directions and with the Simpson rule along the element thickness. The ordinary reinforcements were modelled with embedded shell elements with null shear stiffness. In order to avoid stiffness and mass duplication in the connection between the slabs and the webs, special linking elements were used as indicated in Figure 7.37 (b). These elements have negligible axial stiffness in

the X direction and large shear stiffness in the ZX plane, ensuring that no relative displacements exist between the slabs and the webs. As shown in Figure 7.38, only half the bridge was modelled by taking into account the symmetry plan perpendicular to the longitudinal bridge axis. Special attention was paid to the reproduction of the tendon layout. The tendons can be divided into four distinct families and were modelled by embedded truss elements sharing the displacement field of the embedding shell elements. The three-dimensional tendon coordinates were carefully determined from the post-tension design drawings.

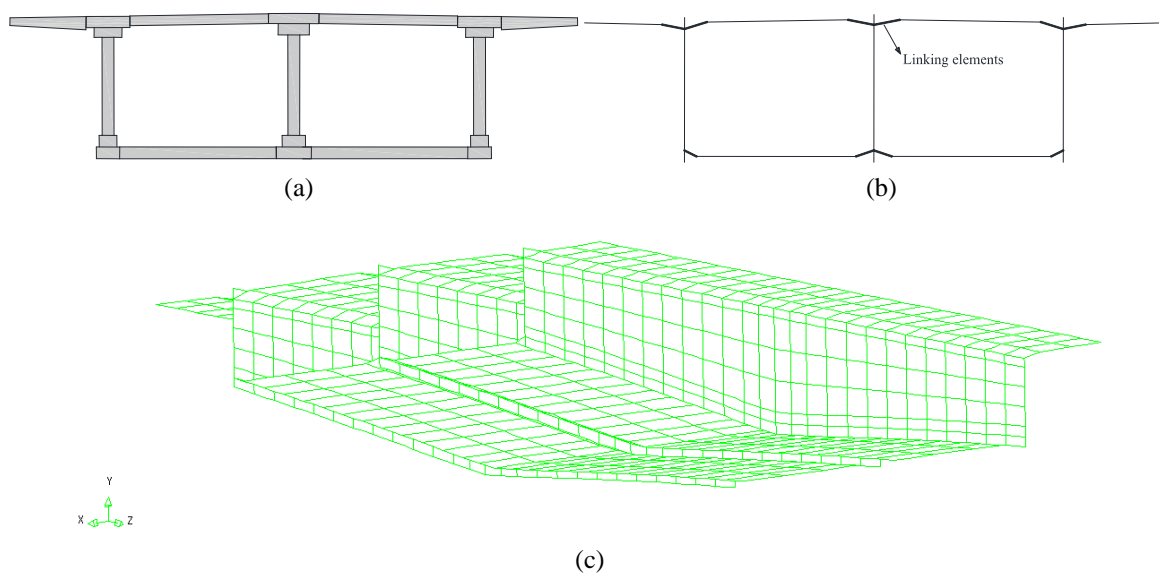


Figure 7.37 – 3D model: (a) thickness modelling; (b) axis of the curved shell elements; (c) partial view showing the finite element mesh.

The construction sequence, load cases, prestressing force modeling strategy, and constitutive models accounting for the time dependent behavior are the same already used in the previous two-dimensional analysis. The only difference is that the notional size h_0 is here determined based on the actual thickness of the elements, instead of considering an average value throughout the deck. Therefore, differential shrinkage and differential creep effects are taken into account.

One additional analysis was performed considering the possibility of crack formation. In this case, besides the time dependent behaviour, the *multi-directional fixed crack* model [231] following the formulation described in references [34; 197; 199] was adopted. This smeared crack model belongs to the suite of constitutive models implemented in DIANA

and considers the decomposition of the strain tensor into elastic, creep, shrinkage and fracture strains, see [30]. The tensile strength $f_{ct} = 2.1$ MPa and the fracture energy $G_F = 75$ N/m were estimated by Eqs. (2.2) and (2.6), respectively. Tension stiffening effect was neglected. After cracking, the shear stiffness is reduced using a constant shear retention factor $\beta = 0.2$. As discussed in Section 4.3.2.4, this is the simplest way to model shear stress transfer through rough cracks.

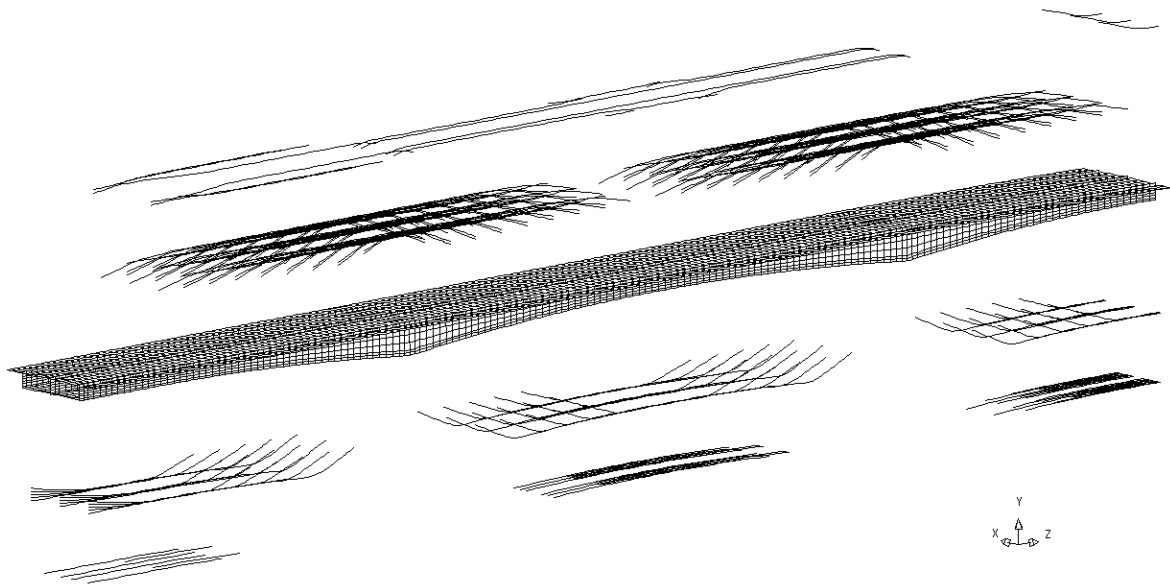


Figure 7.38 – Isometric view of the 3D model. From top to bottom: top slab continuity tendons; cantilever tendons; finite element mesh of the deck; web continuity tendons; bottom slab continuity tendons.

The model comprises 24000 nodes and 8160 shell elements. A total of 36 phases were defined to model the construction sequence, requiring the definition of more than 200 time steps. The live loads are applied for $t=30$ years and, in the case of the analyses where cracking was allowed, the standard Newton-Raphson iterative procedure is adopted to solve the nonlinear problem.

7.6.2.2 Results

Linear viscoelastic analysis

The computed longitudinal stresses due to the permanent loads (self-weight + finishings + prestress) are depicted in Figure 7.39 for different instants. Due to the localized action of the post-tension tendons, the regions immediately behind the anchorages exhibit considerably smaller compressive stresses than in the surrounding regions. This occurs

both in the webs and in the bottom slab where the cantilever and continuity tendons are anchored, respectively. The time evolution of the stress distribution is also noticeable.

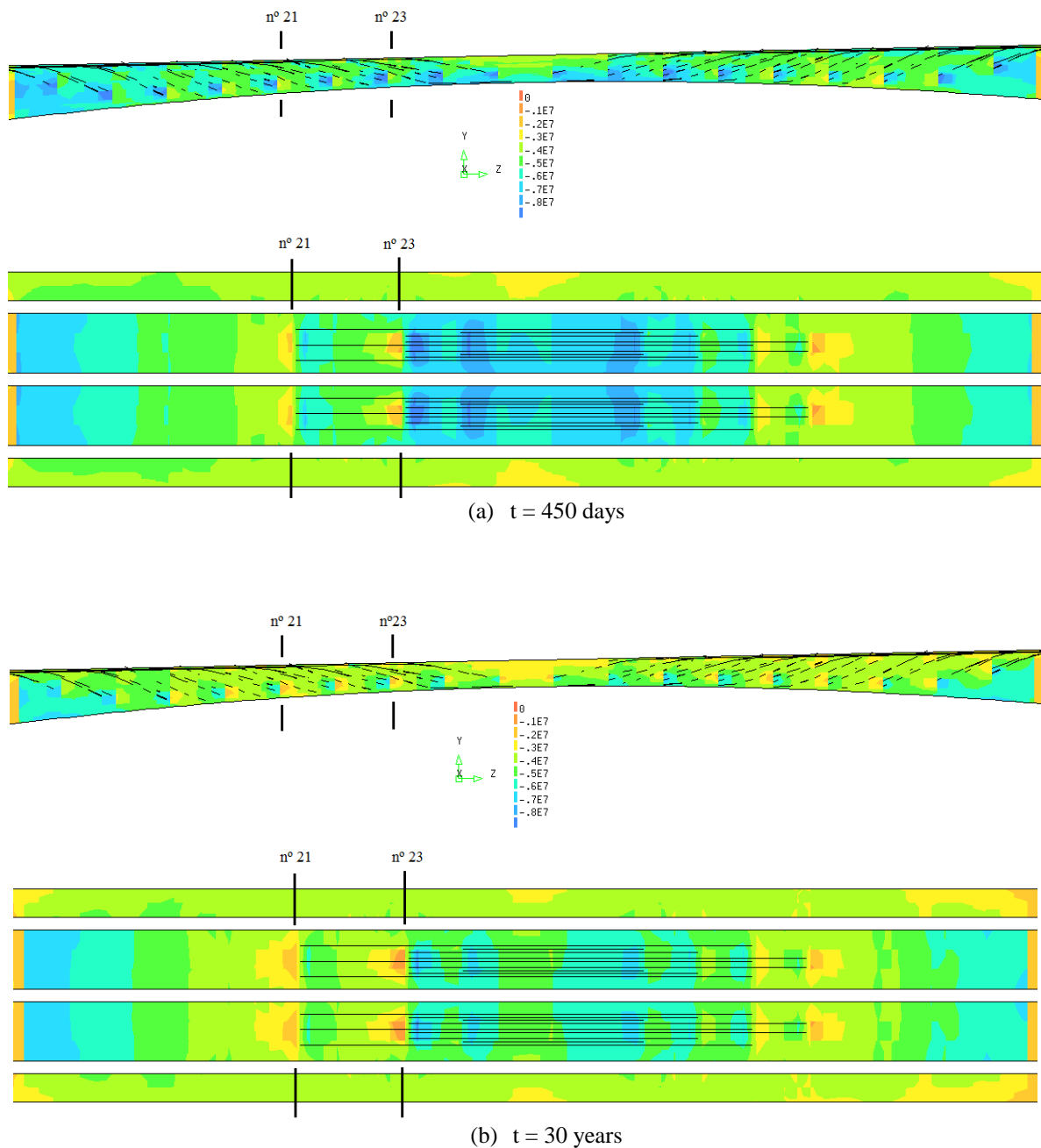


Figure 7.39 – Time evolution of the longitudinal stresses in the web and in the bottom slab for the action of the self weight, prestress and remaining permanent loads.

In the case of the webs, the cantilever tendons are stressed before casting the adjacent segment. Nonetheless, due to the different creep rates between the highly compressed concrete facing the anchorage and the less stressed concrete in the adjacent segment, the

long term stress state immediately behind the anchorages tends towards the tensile side. In the case of the bottom slab, the tendons are stressed with the span already closed. This means that, immediately behind the anchorages and already at the time of stressing, a tensile stress state is added to the existing compressive stress state.

The longitudinal stress distributions along sections n°21 and n°23 are shown in Figure 7.40 and Figure 7.41, respectively. The stresses computed with the 2D beam model are shown for reference and to display the effect of the local stress conditions. In the web, both sections were defined passing immediately behind the anchorage of the cantilever tendons. In the bottom slab, the sections are located immediately behind the anchorages of the continuity tendons, as indicated in Figure 7.39.

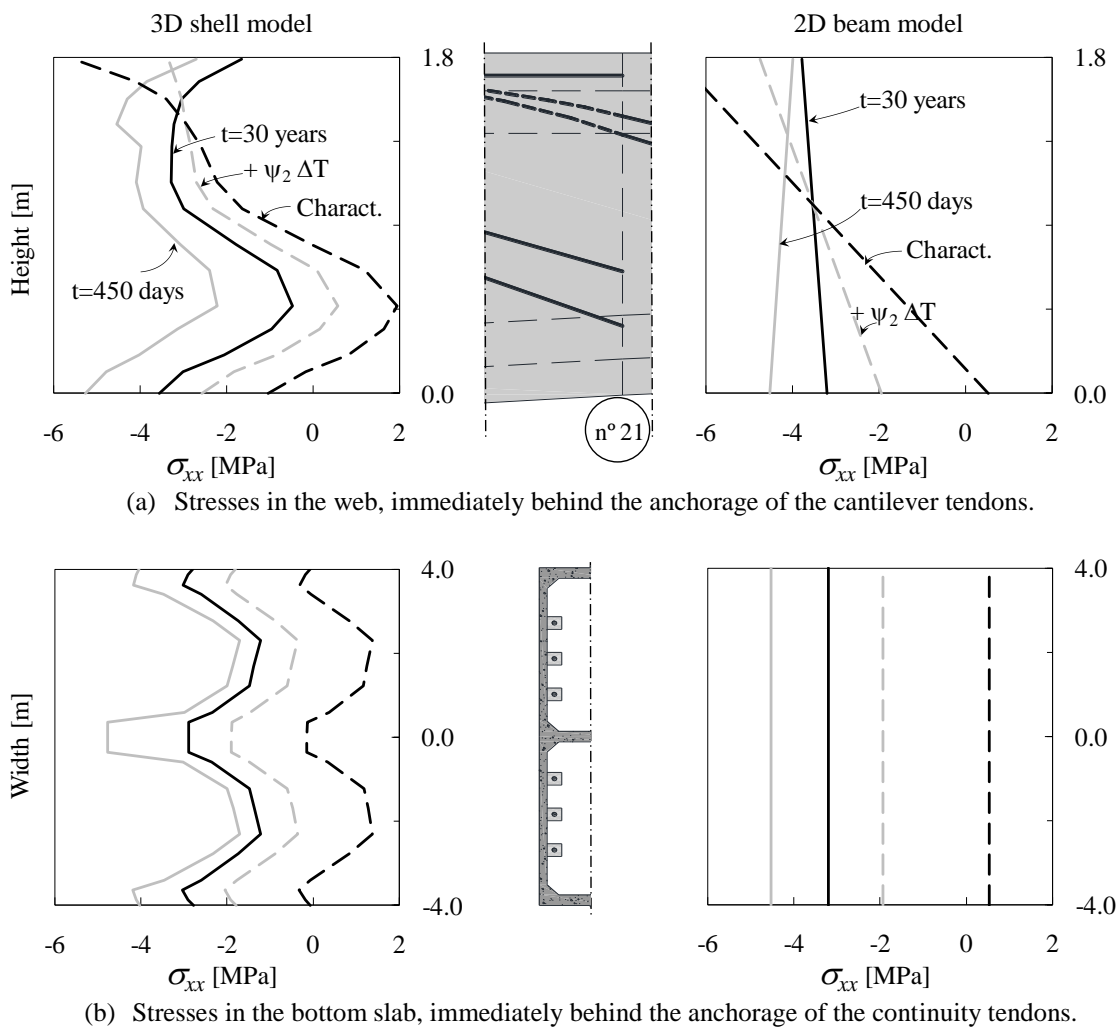


Figure 7.40 – Evolution of the longitudinal stresses at section n°21.

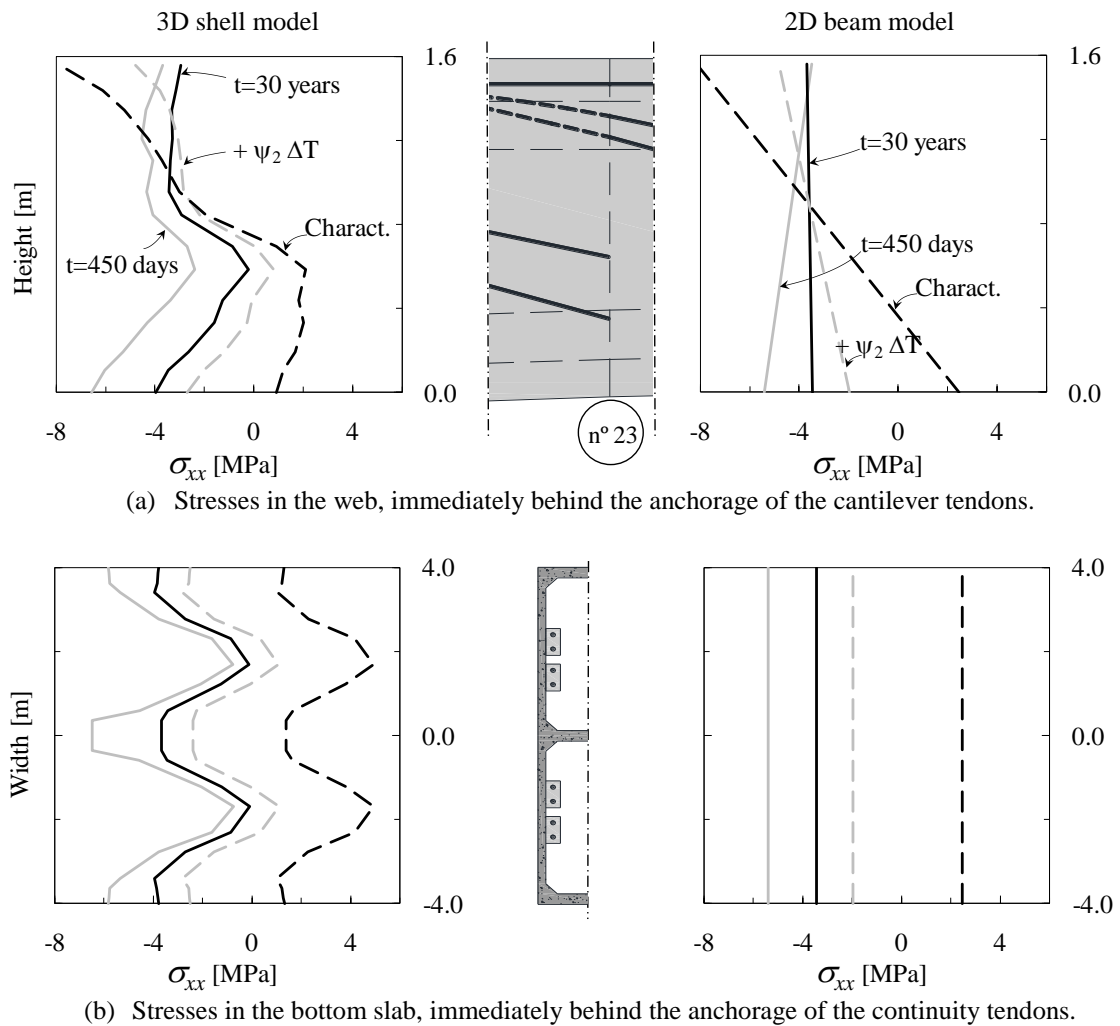


Figure 7.41 – Evolution of the longitudinal stresses at section n°23 according to both the 3D (right) and 2D models (left).

Analysing primarily the stresses due to the permanent actions for instants $t = 450$ days and $t = 30$ years, which are given by the solid lines in the figures above, the effect of the anchorages is noticeable both in the bottom slab and in the web. In fact, the stress distribution due to the permanent loads is far from being linear as assumed in the beam model. Considering this nonlinear stress distribution, it can be seen that the decompression limit state is almost attained in the webs and in the bottom slab at section n°23 due to the sole action of the permanent loads.

The stresses due to the permanent loads plus the quasi-permanent value of the thermal action are represented by the dashed grey lines. In this case, tensile stresses are computed in the webs and, in the case of section n°23, also in the bottom slab. It is noted that in the case of the 3D model the thermal stresses include the nonlinear self-equilibrated component while in the case of the 2D beam model only the differential component is

considered. The stresses under the characteristic load combination are given by the black dashed lines. In this case, tensile stresses reaching $f_{ct} \approx 2$ MPa are computed in both sections. In section n°23, the stresses in the bottom slab reach 4 MPa. Considering that the tensile strength in the interface between two segments is certainly lower than that of the surrounding concrete, these results show that cracking should be expected in serviceability conditions in both sections.

Since the bridge was observed under load levels well below the characteristic load combination, it is important to evaluate the magnitude of the residual crack openings that can be expected. Laurencet [130] has shown that the residual crack opening is mainly a function of the maximum previously applied tensile stress, of the magnitude of permanent compressive stress and of the reinforcement steel ratio. Based on the guidelines resulting from Laurencet's work, given the permanent compressive stresses between -0.5 and 0.0 MPa, the small amount of ordinary reinforcement (longitudinal reinforcement ratio in the bottom slab, $\rho \approx 0.5\%$), and the stress amplitude due to live loads around 4 MPa, average values of the residual crack opening exceeding 0.3 mm may be expected. In the bottom slab of section n°21 the live load stress amplitude is only 2 MPa and the average residual crack width is reduced to about $0.15 \div 0.2$ mm. In the case of the webs, the longitudinal reinforcement ratio is 0.25%, see Figure 7.2. In this case, and considering a live load stress amplitude of 2 MPa, the average residual crack opening may be expected to be around 0.25 mm. These values agree reasonably well with the observed crack widths in both sections n°21 and n°23 and seem to indicate that the observed crack patterns may occur even with the prestress steel in good conditions and are mainly due to a deficient layout of the prestress tendons and to the low ordinary reinforcement content.

Visco-elastic analysis with cracking

Considering now the results of the analysis where cracking was allowed and observing the cracking pattern calculated for the characteristic load combination, some similarities with the observed cracks can be identified, see Figure 7.42. In this analysis only one loading configuration was considered and the knife load was applied between sections n°23 and 24.

Transversal cracks in the bottom slab are mainly computed at the location where the bottom slab continuity tendons are anchored. This fact confirms that these tendons are in fact too short and should have been anchored further away from mid-span. In some regions of the deck these cracks propagate to the webs producing a cracking pattern similar to that observed in situ. Moreover, some of the cracks in the webs do not connect with cracks in

the bottom slab, – see the crack between sections n°21 and 23 –, which also agrees with the in-situ observations.

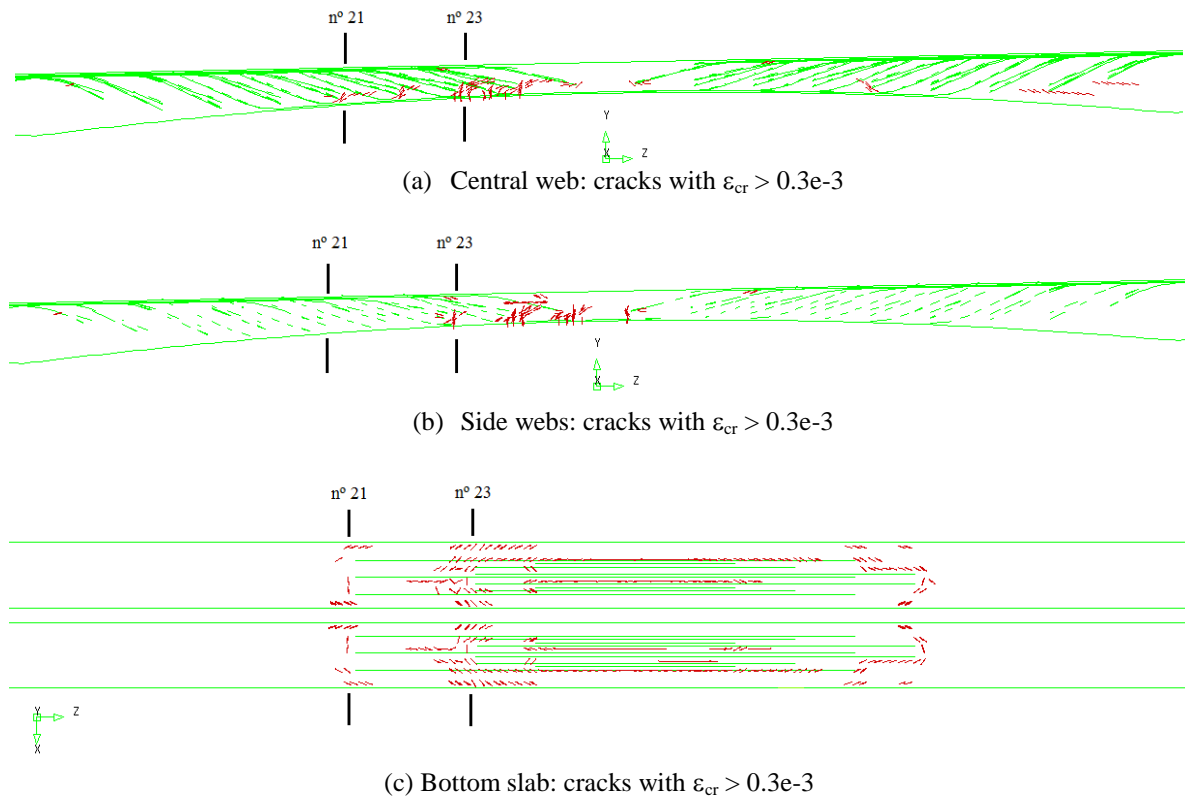


Figure 7.42 – Calculated crack patterns in the second span for the characteristic load combination.

Longitudinal cracks are computed in the bottom surface of the lower slab. These cracks are caused by the downward thrust due to the lower slab continuity tendons. In fact, in bridge decks with variable depth, the longitudinal compression in the lower slab creates a radial thrust due to the curvature of the slab which leads to transverse bending of this slab [8], see Figure 7.43. Assuming the lower slab as a cylindrical shell, the radial upward thrust q_σ can be approximated by

$$q_\sigma = \sigma_{slab} \frac{t}{R} \quad (7.13)$$

where σ_{slab} is the mean stress in the lower slab, t is the slab thickness and R is the radius of the mean axis of the slab. The presence of prestress tendons in curved slabs generates similar forces q_P but in the opposite (downward) direction:

$$q_P = \frac{P}{b \cdot R} \quad (7.14)$$

where P is the prestress force due to the tendons located in the slab and b is the slab width. If the slab was disconnected from the webs these effects would cancel each other: σ_{slab} would be equal to $P/b \cdot t$ and no resulting radial thrust would be obtained. Not being the case, the action of the tendons can be preponderant in regions where compressive stresses in the slab stresses are lower, that is, near midspan. This effect is reproduced in the analysis. The longitudinal cracks propagate when the load factor equals 0.5, that is, when the live load is slightly higher than the frequent value and when the transversal cracks around the bottom slab continuity tendons propagate towards the webs.

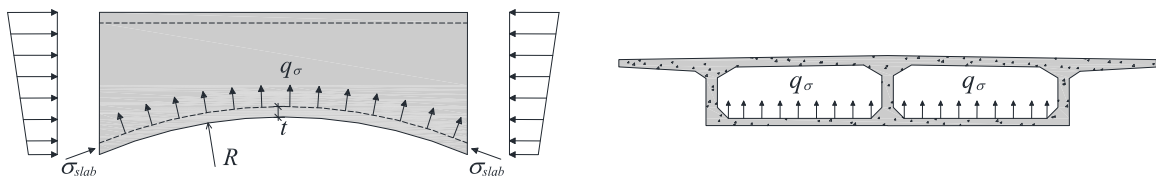


Figure 7.43 – Vertical thrust in a curved slab: (a) longitudinal section; (b) transversal section.

The load-displacement diagram depicted in Figure 7.44 shows a noticeable decrease in the stiffness of the deck after the frequent load combination is attained. For $LF=0.5$, the propagation of the transversal cracks from the bottom slab towards the webs is responsible for the observed stiffness decrease. In the load test the bridge was tested in the unloading/reloading branch of load-displacement curve, which usually exhibits higher stiffness than that of the virgin loading branch. This may explain why the load test results can be reasonably reproduced by a model considering the stiffness of the uncracked state.

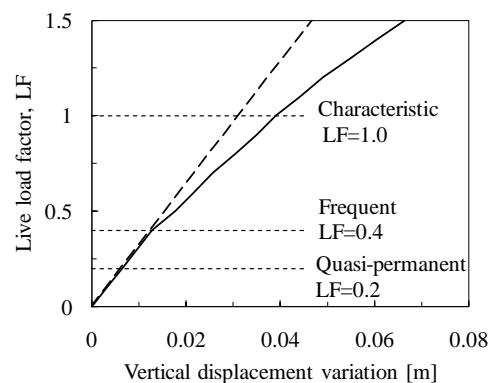


Figure 7.44 – Variation of the vertical displacement at the middle of the 2nd span with the stepwise application of the live load.

7.7 Discussion

A 30 year-old post-tensioned concrete box-girder bridge exhibiting consistent cracking patterns throughout the deck was examined in detail. Cracks were observed in the webs, mainly at the joints of segmental construction, and in the bottom slab. Besides a detailed visual inspection and some material characterization studies, a preliminary non-destructive inspection using gamma-rays was undertaken in order to evaluate the feasibility of an exhaustive inspection campaign using this technology. This was motivated by the uncertainty regarding the condition of post-tension tendons. The obtained gammagraphies revealed no grouting defects or corrosion signs in the wires. This study should now be completed in order to collect more data in different locations of the deck.

The bridge was also monitored during a controlled load test and along 4 days under normal traffic and environment excitations. The monitoring campaign aimed at evaluating the linearity of the bridge response as well as the crack movements under controlled traffic loads and daily thermal variations. Crack opening variations of 0.13mm were measured with four loaded trucks on the deck producing a live-load bending moment approximately 65% of that produced by the load model of the Portuguese code used in the original design and still in force today. Due to the daily thermal variations in a 4 days measuring period, the crack width variations reached 0.1mm. In spite of the measured crack activity, the bridge exhibited linear elastic behaviour during the load test. Although the measured response in some sensors was systematically more flexible than that calculated, the response to vehicle loading compared reasonably well with that calculated considering the uncracked stiffness of the deck. Since no baseline condition is available, no definite conclusions could be drawn from this set of results. In fact, stiffness changes due to localized cracks are expected to be small and difficult to evaluate without a direct and careful comparison with previous measurements - it must be noted that only the cracks that are continuous between the bottom slab and the webs effectively decrease the bending stiffness. Still, the obtained results can serve as a comparison basis for future tests and show that the structural condition of the bridge does not require immediate intervention.

In order to explain the origin of the observed cracking patterns, the bridge was analysed with both two 2D and 3D finite element models taking into account the construction sequence and the time-dependent evolution of the sectional forces due to the effects of creep, shrinkage and prestress steel relaxation. The obtained results indicate that the observed cracking patterns are not linked to prestress steel corrosion and are mainly due to

an inadequate layout of the prestress tendons together with the adoption of a very low ordinary reinforcement ratio in the longitudinal direction. In this respect, the 3D analysis proved essential to confirm that the decompression limit state both in the bottom slab and in the webs is almost reached in the long-term considering only the action of permanent loads.

It can be concluded that the anchorage of the cantilever tendons in the webs and in the middle of the bottom slab was responsible for the observed cracks. The bottom slab continuity tendons revealed too short and should have been extended a few more meters in order to ensure an adequate transmission of the stresses towards the webs in the regions where the live load stresses are higher. In the present circumstances, average residual crack widths larger than 0.3 mm are to be expected, which agrees well with the mapped crack widths.

8 Safety evaluation of the N. S. da Guia Bridge

8.1 General

Current design and assessment procedures for the ultimate limit state are based on the verification of the following inequality:

$$R_d \geq S_d \quad (8.1)$$

where S_d is the design value of the inner force at the cross-section being analysed and R_d is the corresponding design value of the resistance. While the inner forces are usually calculated using a linear elastic analysis, nonlinear behaviour is taken into consideration in the determination of the resistance. Such a subdivision of the design process results in an artificial, yet convenient, separation between the determination of the inner forces and the design/assessment of the cross-sections. This process usually involves the following steps:

1. Linear elastic analysis of the structure considering all possible load combinations for determining the inner forces. Their design values can be written as:

$$S_d = \gamma_G G_k + \gamma_Q \left(Q_{k,j} + \sum_{i \neq j} \psi_{0,i} Q_{k,i} \right) \quad (8.2)$$

where G_k and Q_k are the characteristic values of the permanent and variable loads, respectively, γ_G and γ_Q are the corresponding partial safety factors and ψ_0 is a combination factor. The previous expression includes safety provisions, in which nominal action effects are amplified by appropriate partial safety factors. The combination factor reflects the unlikelihood of having the extreme values of several independent variable actions occurring simultaneously.

2. Determination of the design resistance of a cross-section, which is calculated using the design values of the material properties:

$$R_d = R(f_d, a_{nom}), \quad f_d = f_k / \gamma_{Rd,m} \quad (8.3)$$

The safety provision for resistance is applied at the material level. The design values of the material properties f_d are obtained from the characteristic values f_k by reduction with an appropriate partial safety factor $\gamma_{Rd,m}$. The random variability of the material properties is covered by the partial safety factors of each material. The geometrical properties are taken as nominal values a_{nom} and its variability is accounted for in the partial safety factors γ_m .

3. Safety check of the considered limit state by evaluation of the design condition expressed by (8.1).

The safety format outlined above is tailored for linear elastic analyses, beam models and local section safety checks. Since the inequality (8.1) is only evaluated at the cross-sections, this can be considered as a *member level* (or local) assessment. On the other hand, a nonlinear analysis constitutes a *system level* (or global) assessment in which all structural parts interact leading to a generalization of the notions of resistance and action effect presented above. In general, system resistance is a function of the material parameters f , geometrical data a and loading pattern S :

$$R = R(f, a, S) \quad (8.4)$$

The loading pattern S encloses the notions of load type, location, combination and history.

If the reliability of global, or system, resistance is to be evaluated, the effects of the random variation of the basic variables must be taken into account. However, in this case the use of the partial safety factor format is questionable. Design values of the material properties are extremely low and do not represent a real material. A realistic simulation of structural behaviour should be based on mean values for the material properties and the safety provision should be referred to it. Analysis based on extremely low material properties may result in an unrealistic redistribution of forces, which may not be on the conservative side, and may also change the failure mode. In this context, and still adopting the design condition (8.1), the design resistance can be obtained by division of the resistance calculated using the mean values of the material properties f_m and nominal geometrical parameters a_{nom} by a global resistance safety factor γ_R :

$$R_d = \frac{R(f_m, a_{nom}, S)}{\gamma_R} \quad (8.5)$$

In this chapter it is shown how to define a global resistance factor based on a semi-probabilistic approach that can capture the system resistance sensitiveness to the random variation of the input variables. The basic reliability concepts are introduced and the theoretical background behind the semi-probabilistic approach is summarized. In Section 8.3, the safety evaluation of the N. S. da Guia Bridge is presented. In a first step, a member level assessment using partial safety factors is performed considering the inner sectional forces determined from the linear viscoelastic beam model described in Chapter 7. The shear safety evaluation is made with resource to the sectional analysis model described in Chapter 6. Finally, a detailed nonlinear analysis is performed using the F-CMM implementation described in Chapter 4. In the system level assessment, the safety format based on the global resistance factor is adopted.

8.2 Safety format for nonlinear analysis of existing bridges

8.2.1 Basic reliability concepts

The safety requirements of a given structure can be brought into the form of a so called *limit state condition*, which can generally be written as:

$$G(\mathbf{X}) \geq 0 \quad (8.6)$$

In the expression above $G(\mathbf{X})$ is the limit state function and \mathbf{X} the vector of random variables governing the problem. In the simplest case, the limit state function can be defined as the difference between the generalized structural resistance R and the generalized action effect S :

$$G(\mathbf{X}) = R - S \quad (8.7)$$

in which case G is equal to the safety margin.

In a full probabilistic approach, the satisfaction of the safety requirement is expressed by the condition $p_f \leq p_0$, where p_0 is the target probability of failure and the probability of failure p_f , or probability of limit state violation, is defined as:

$$p_f = \text{Prob}[G(\mathbf{X}) < 0] \quad (8.8)$$

In general, the limit state function can be a function of many variables and a direct calculation of p_f is not possible. Stochastic simulation techniques, such as the Monte Carlo method, can be used to get a reliable estimate of the probability of failure. This method requires the knowledge of the distribution functions of all random variables, the evaluation of the limit state function for each realisation of the random variable vector and a posterior statistical evaluation of the results. However, even considering the use of variance reduction techniques, such as the Latin Hypercube sampling, or importance sampling techniques [96; 250], the number of limit state function evaluations required to evaluate small probabilities of failure is generally very large, entailing the corresponding consequences in terms of computational time whenever NLFEA is involved in the process.

Second Moment Reliability Methods

In most circumstances, alternative approximate methods are preferred instead, such as the Second Moment Reliability Methods. In these methods the distributions of the basic variables defining R and S are described solely by two properties, namely their expected values and their variances. In this context, it is convenient to measure structural safety in terms of a reliability index β , which is related to the probability of failure:

$$\beta = -\Phi^{-1}(p_f) \quad (8.9)$$

In the expression above, Φ^{-1} is the inverse of the standard normal probability distribution function. It follows immediately from this definition that the reliability index can also be expressed by

$$\beta = \frac{\mu_G}{\sigma_G} \quad (8.10)$$

with μ_G being the mean value of the limit state function and σ_G the corresponding standard deviation. This last equation shows that the reliability index indicates how many times the standard deviation of the random variable G may be placed between zero and the mean value of G .

In this context, the safety requirement is expressed as $\beta \geq \beta_n$, where β_n is the target reliability index, see Section 8.2.3. As for β , there are various procedures available for its calculation, see for instance reference [211]. The simplest case involves the limit state

function as expressed by Eq. (8.7). If both R and S are independent normal random variables, the reliability index is simply given by,

$$\beta = \frac{\mu_R - \mu_S}{\sqrt{\sigma_R^2 + \sigma_S^2}} \quad (8.11)$$

where μ_R = mean of R , μ_S = mean of S , σ_R = standard deviation of R and σ_S = standard deviation of S . In this particular case, the probability of failure can be exactly calculated from Eq. (8.9).

On the other hand, if both R and S are independent lognormal random variables, the reliability index is given by¹,

$$\beta \approx \frac{\ln(\mu_R/\mu_S)}{\sqrt{v_R^2 + v_S^2}} \quad (8.12)$$

where v_R and v_S are the coefficients of variation of R and S , respectively.

If the variables R and S are neither normal nor lognormal, or if the limit state function cannot be expressed by Eq. (8.7), the reliability index can be calculated using an iterative procedure, such as the *First Order Reliability Method* (FORM) or the *Second Order Reliability Method* (SORM) [211]. The main difference between these two methods resides on the order of the Taylor expansion used to approximate the limit state function in the neighbourhood of the design point. These methods require an analytical definition of the limit state function. As in most cases this is not possible, a so called *response surface* can be fitted to the numeric results obtained through a simulation procedure and used in the FORM/SORM algorithms. The number of required limit state function evaluations is smaller than in the case of pure simulation techniques and is generally in the order of tens.

Semi-probabilistic methods

In most practical applications, simpler semi-probabilistic methods may suffice to perform the safety evaluation. For this purpose, the second moment reliability methods can be easily developed into the design condition (8.1) with R_d and S_d being the design values of the generalized resistance and action effect, respectively. Although in the semi-probabilistic approach the reliability index is not explicitly evaluated, the determination of

¹ It is remarked that this expression is approximated and supplies almost exact results if the coefficients of variation are below 0.20.

the design values is still based on reliability concepts. In fact, if both R and S are independent normal variables, their design values can be obtained from Eq. (8.11). Using simple algebra it is easily shown [211] that:

$$R_d = \mu_R(1 - \alpha_R \beta_n \sigma_R) \quad S_d = \mu_S(1 + \alpha_S \beta_n \sigma_S) \quad (8.13)$$

with $\alpha_R = \sigma_R / (\sigma_R^2 + \sigma_S^2)^{1/2}$ and $\alpha_S = \sigma_S / (\sigma_R^2 + \sigma_S^2)^{1/2}$ being the so-called sensitivity factors expressing the importance of each variable in the determination of the probability of failure. On the other hand, if both R and S are independent lognormal variables, Eq. (8.12) can be elaborated to:

$$R_d = \mu_R \exp(-\alpha_R \beta_n v_R) \quad S_d = \mu_S \exp(\alpha_S \beta_n v_S) \quad (8.14)$$

with $\alpha_R = v_R / (v_R^2 + v_S^2)^{1/2}$ and $\alpha_S = v_S / (v_R^2 + v_S^2)^{1/2}$.

In the FORM/SORM context, the design values of the basic variables can be defined as the coordinates of the point in the failure surface ($G = 0$) closest to the average point. The sensitivity factors are the direction cosines of the vector defined by the average and design points and are calculated iteratively. In a semi-probabilistic approach it is advantageous to separate the *action side* from the *resistance side* of the problem. In this case, it is generally conservative to assume the sensitivity factors $\alpha_R = 0.8$ and $\alpha_S = 0.7$ [42; 211].

8.2.2 Global resistance safety factor

One of the simplest stochastic models for the resistance considers R as the product of the nominal resistance R_m by three factors F , G and M :

$$R = R_m \cdot F \cdot G \cdot M \quad (8.15)$$

in which:

- F – factor related to the uncertainty in the material properties f ;
- G – factor related to the uncertainty in the geometrical parameters a ;
- M – factor related to the uncertainty in the model adopted to determine the nominal value R_m .

The factors F , G and M are ratios of actual to nominal values and are considered as random variables having their own distribution properties. If the bias (systematic variation) is

neglected and R_m is taken as the mean value of the resistance, F , G and M may be assumed as having an average value equal to unity. Since it appears as a product of variables, R tends to a lognormal distribution. Besides, negative resistances are hardly possible. Therefore, the design value of the resistance can be expressed by Eq. (8.14)₁ where the coefficient of variation is given by

$$v_R = \sqrt{v_F^2 + v_G^2 + v_M^2} \quad (8.16)$$

with v_F , v_G and v_M being the coefficients of variation of F , G and M , respectively. It is assumed in the expression above that these variables are statistically independent.

Based on the assumption of a lognormal distributed resistance, it follows immediately from Eqs. (8.5) and (8.14)₁ that the global resistance safety factor γ_R is given by:

$$\gamma_R = \exp(\alpha_R \beta_n v_R) \quad (8.17)$$

8.2.2.1 Estimate of the coefficient of variation of the resistance

It remains now to define the procedure to determine the coefficient of variation of the resistance v_R . At the structural level, the scatter in the resistance depends on the structural system and failure mode. In fact, the coefficients of variation of the material and geometrical parameters differ from those of variables F and G : $v_F \neq v_f$ and $v_G \neq v_a$. This means that v_R is case dependent. As in most cases of practical interest no explicit formulation is available for F and G , their coefficients of variation can only be estimated.

Material uncertainty

If a lognormal distribution for R is assumed, the component of v_R concerned to the scatter in the material properties can be expressed as proposed by Cervenka [55; 87]:

$$v_F = \frac{1}{1.65} \ln \left(\frac{R_m}{R_k} \right) \quad (8.18)$$

The mean value of the resistance is assumed to be determined from

$$R_m = R(f_{cm, is}, f_{ym}, \dots, a_{nom}, S) \quad (8.19)$$

where the mean values of the in-situ material strength parameters are adopted. The characteristic value R_k is determined as indicated in Eq. (8.19) but using the 5% percentile

values of the in-situ material strength parameters. These can be determined from their mean values as:

$$f_k = f_m \exp(-1.65v_f) \quad (8.20)$$

As discussed in Chapter 7, the in-situ concrete compressive strength is approximately 85% of that of the standard cylinder. This procedure requires only two nonlinear analysis to estimate the coefficient of variation v_F .

In general, reliable data regarding the scatter of the material properties is only available for the concrete compressive strength and the steel yield strength. However, a detailed nonlinear analysis model may have many input material parameters, which can be determined from $f_{cm, is}$ and f_{ym} using empirical correlations. If the variability of these parameters is not accounted for, this remaining uncertainty is assumed to be part of the (material) model uncertainty.

An alternative definition is proposed by Schlune *et al* [210]. In this case, the coefficient of variation v_F is determined from a perturbation analysis around the mean value of the resistance in order to capture its sensitivity to variations in the input parameters:

$$v_F \approx \frac{1}{R_m} \sqrt{\sum_i^n \left(\frac{R_m - R_{\Delta f_i}}{\Delta f_i} \sigma_{f_i} \right)^2} \quad (8.21)$$

In the expression above, R_m and $R_{\Delta f_i}$ are the resistances determined using the mean material parameters and reduced material parameter f_i , respectively; Δf_i are the step sizes to decrease the material parameters f_i ; and σ_{f_i} is the standard deviation of f_i . This procedure requires $n + 1$ nonlinear analysis to estimate v_F , where n is the number of material parameters included in the sensitivity analysis. This proposal is more adequate whenever it is suspected that other material parameters besides the concrete compressive strength and the steel yielding stress may have a decisive influence on the failure load.

Geometrical uncertainty

It is usually considered [210] that $v_G = 0.05$ is a conservative estimate for structures that are insensitive to geometrical imperfections. In these cases, it is here proposed that a refined estimate of the geometrical uncertainty can be achieved defining the modified characteristic values of the material strength parameters as

$$f_k' = f_m \exp\left(-1.65\sqrt{v_f^2 + v_a^2}\right) \quad (8.22)$$

in which case

$$\sqrt{v_F^2 + v_G^2} = \frac{1}{1.65} \ln\left(\frac{R_m}{R_k'}\right) \quad (8.23)$$

The last expression has the advantage of enabling the consideration of differentiated uncertainties in the geometrical parameters, such as the reinforcement and prestress steel cross-sectional area, thickness of different parts of the structure, etc. Moreover, it reflects the system sensitivity to the uncertainty in both material and geometrical parameters instead of simply assuming a pre-defined value for v_G .

Model uncertainty

There is little data available to quantify the model uncertainty for nonlinear analysis. In the guideline document [212] coefficients of variation $v_M = 0.04$, 0.06 and 0.09 are recommended for good, normal and poor computational models.

8.2.2.2 Comparison with the partial safety factor method – member level

At the member level, it should be expected that both the global safety factor and the partial safety factor approach lead to equivalent results. In order to compare both approaches, two cases are analysed: a short reinforced concrete column subjected to compressive axial forces and a rectangular cross-section in bending with reinforcements only on the tensile side. In order to achieve comparable results, the coefficients of variation adopted in derivation of the partial safety factors in Eurocodes were selected. For concrete $v_f = 0.15$, $v_a = 0.05$ and $v_M = v_m = 0.05$, where v_m is the coefficient of variation associated with the model uncertainty at the member (or local) level. For steel $v_f = 0.04$, $v_a = 0.05$ and $v_M = v_m = 0.025$. An average concrete compressive strength $f_{cm} = 38\text{MPa}$ was considered, which corresponds to an average in-situ compressive strength $f_{cm,is} = 38/1.15 = 33\text{MPa}$ [51]. The characteristic yield strength of the reinforcing steel was taken equal to $f_{yk} = 500\text{MPa}$. The target reliability index is set equal to 3.8. Since 2nd order effects are not relevant, Eqs. (8.22) and (8.23) were adopted to determine the effects of the uncertainties in the material and geometrical parameters.

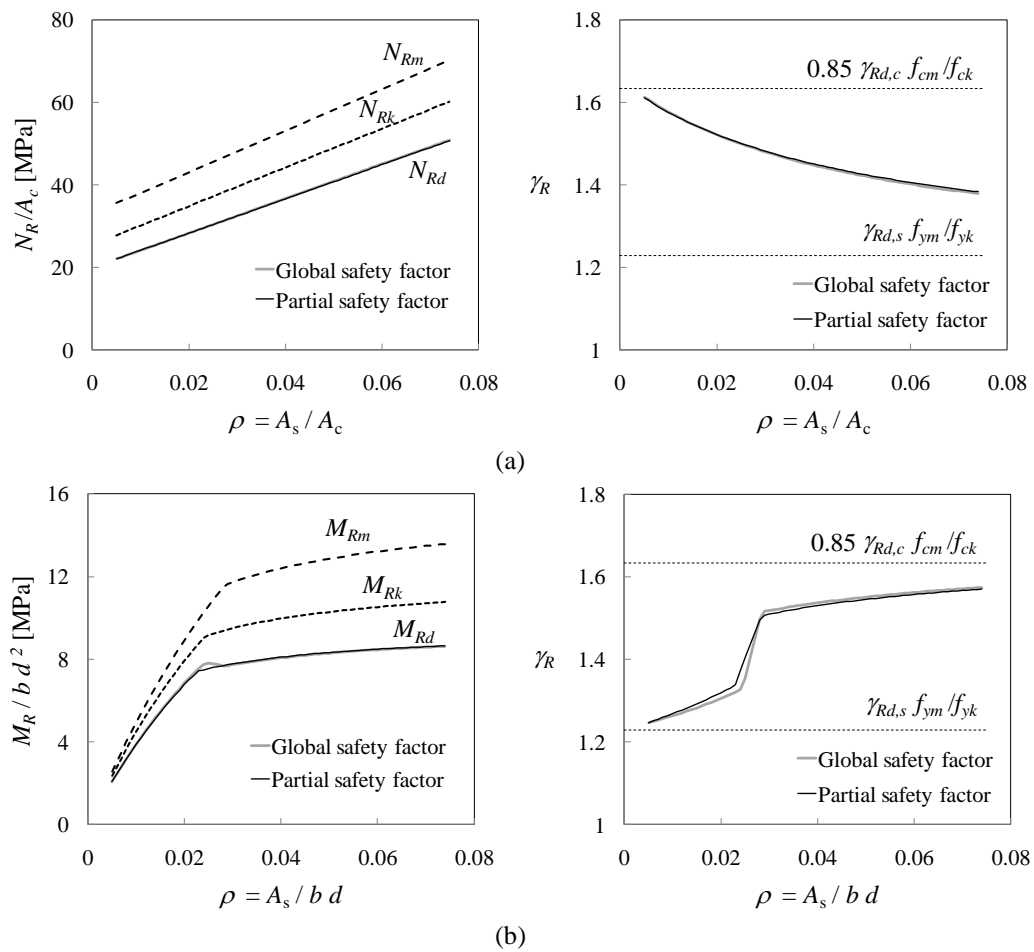


Figure 8.1 – Comparison between the partial and global safety factor approaches.

The results obtained with both approaches are shown in Figure 8.1. It can be confirmed that the design values of the axial and bending resistance remain practically unchanged, irrespective of the adopted safety format. In the case of the partial safety factor format, the corresponding global safety factor can be computed from the ratio R_m/R_d . The global safety factor determined using both approaches is also shown in the figure. In the case of the short column, γ_R decreases as the reinforcement ratio increases, tending asymptotically to $\gamma_{Rd,s} f_{yk} / f_{yk}$. In the case of the cross section in bending, both approaches reproduce the increase in the required global safety factor when the failure mode goes from ductile to brittle.

8.2.3 Target reliability index

The target reliability index is defined to ensure acceptable safety and depends on several factors such as the failure consequences arising from a given hazard scenario, the importance and value of the structure, the cost of measures to increase safety and other socio-economic factors. The safety requirements supporting the establishment of the target reliability levels for new and existing bridges are not the same and more conservative criteria are usually adopted in the design standards for new structures. The main differences are due to [227]:

- *economic considerations*: the incremental cost between acceptance and upgrading an existing bridge can be very large whereas the cost increment of increasing safety of a new structure is generally small;
- *social considerations*: the execution of replacement/strengthening works in an existing bridge usually causes serious problems to the circulation of goods and persons, leading to a disruption of the socio-economic activities; in the analysis of an existing structure heritage values may have to be considered;
- *environmental considerations*: waste reduction considerations and control of environmental impacts are more prevalent in the rehabilitation of existing structures.

In reference [227] it is proposed that the safety level under which a repair intervention is required can be obtained from:

$$\beta_{n,exist} = \beta_{n,new} - \Delta\beta \quad (8.24)$$

where $\beta_{n,new}$ is the target reliability index adopted in the design of a new structure with similar characteristics and $\Delta\beta = 0.5$.

In references [66; 255] an extensive comparison is made between the target reliability levels of various codes and standards currently in use. In some cases, the target reliability index refers to a reference period of one year, and the corresponding failure probability is actually a failure probability rate. In other cases, the target reliability index refers to the remaining working life of the structure. Whenever the main uncertainty comes from actions that have statistically independent maxima in each year, both values are related by the expression:

$$\Phi(\beta_n) = [\Phi(\beta_1)]^n \quad (8.25)$$

with β_1 the annual target reliability index and β_n being the lifetime target reliability indexes for a reference period of n years. A comparison between common values of β_1 and β_n is presented in Table 8.1.

Table 8.1 – Comparison between β_1 and β_n for two common reference periods

β_1	3.7	4.2	4.4	4.7	5.2
β_{50}	2.6	3.2	3.5	3.8	4.4
β_{100}	2.3	3.0	3.3	3.7	4.3

In the new SIA 269 [215], and similarly to what is proposed in the Joint Committee on Structural Safety publication devoted directly to existing structures [109], the annual target reliability indexes are defined as a function of the consequences of failure and of the relative costs of the safety measures (or effectiveness of the intervention), see Table 8.2. In the norm SIA 269, the failure consequences are determined based on the ratio between the costs associated to failure and the costs associated to the repair or substitution of the structure. The effectiveness of the intervention is evaluated based on the ratio between the risk reduction and the costs attributed to the rehabilitation component dedicated to increase the structural safety.

Table 8.2 – SIA 269 and JCSS: Annual target reliability index β_1

<i>Effectiveness of the intervention</i>	<i>Failure consequences</i>		
	Minor	Moderate	Large
Small	3.1	3.3	3.7
Normal	3.7	4.2	4.4
Large	4.2	4.4	4.7

A different approach is followed in the Nordic Committee on Buildings Regulations (NKB) Report No. 35 [170], which was later adopted in the Danish guideline document for reliability based-classification of the load carrying capacity of existing bridges [212]. In this proposal, the target reliability index is defined as a function of the failure consequences and of the failure type, see Table 8.3.

Table 8.3 – NKB Report No. 36: Annual target reliability index β_1

Failure type	Failure consequences		
	Less serious	Serious	Very serious
Ductile with extra carrying capacity	3.1	3.7	4.2
Ductile without extra carrying capacity	3.7	4.2	4.7
Brittle	4.2	4.7	5.2

In the EN1990 [42], the target reliability indexes $\beta_1 = 4.2, 4.7$ and 5.2 are recommended for the reliability classes RC1, RC2 and RC3, which are associated with the economic, environmental and social consequences of failure and foreseen losses of human life. These values are recommended for the design of new structures and are mentioned here for reference. The partial safety factors were calibrated for the reliability class RC2 and for a reference period of 50 years, leading to $\beta_{50} = 3.8$.

8.2.4 Application to NLFEA of existing bridges

In a nonlinear analysis, resistance can be most conveniently expressed as a scalar multiplier, or load factor LF , by which the loading pattern S is multiplied to reach the limit state. As discussed in Chapter 4, external loads must be applied in a sequential and incremental manner. In some cases, time dependent effects must be accounted for. In general, the self weight and the prestressing force must be applied first, followed by the remaining permanent loads due to the surfacing and finishing. The live loads can then be applied until the characteristic load combination is achieved. Afterwards, both permanent and variable loads are incremented until failure, in which case the following equality holds:

$$R_m = G_k + P + \frac{\gamma_Q}{\gamma_G} \left(Q_{k,j} + \sum_{i \neq j} \psi_{0,i} Q_{k,i} \right) + (LF_m - 1) \left[G_k + \frac{\gamma_Q}{\gamma_G} \left(Q_{k,j} + \sum_{i \neq j} \psi_{0,i} Q_{k,i} \right) \right] \quad (8.26)$$

where P is the prestress effect and LF_m is the total load factor at failure. It follows from the previous equation that:

$$LF_m = \gamma_G \frac{R_m - P}{S_d} \quad (8.27)$$

The subscript $(\cdot)_m$ indicates that the mean values of the material properties were adopted in the analysis. Considering the global resistance factor as defined in 8.2.2, the safety requirement can be expressed by

$$LF_m \geq LF_{req} = \gamma_R \cdot \gamma_G \quad (8.28)$$

The estimate of the coefficient of variation of resistance given by Eq. (8.16) can be rewritten as:

$$v_R = \sqrt{\left[\frac{1}{1.65} \ln \left(\frac{LF_m}{LF_k} \right) \right]^2 + v_G^2 + v_M^2} \quad (8.29)$$

where LF_k is the total load factor at failure in a nonlinear analysis conducted with the characteristic values of the material and geometrical properties. If 2nd order effects are negligible, the uncertainty in the geometrical properties can be included in the characteristic values of the strength parameters, in which case it is advantageous to use:

$$v_R = \sqrt{\left[\frac{1}{1.65} \ln \left(\frac{LF_m}{LF_k'} \right) \right]^2 + v_M^2} \quad (8.30)$$

The above defined procedure to estimate the global safety factor requires only two separate nonlinear analyses to estimate the sensitiveness of the structural resistance to the random variability of the input parameters. If the failure mode is sensitive to the tensile strength, fracture energy, or other, the procedure proposed by Schlune *et al.* [210] is recommended, see section Section 8.2.2.1.

8.3 Structural safety evaluation of the N. S. da Guia Bridge

8.3.1 Definition of the target reliability index

In the proposed semi-probabilistic framework, updated examination values of the material parameters and action effects must be determined based on a pre-defined target-reliability index. This allows performing reliability differentiation based on risk analysis concepts and on the expected remaining service life.

The N. S. da Guia Bridge crosses the Lima River, connecting the two sides of the Ponte de Lima village and plays a very important role in local social-economic activities: the closest toll-free crossings of the river are located 20 km East in the village of Ponte da Barca and 30 km West in the city of Viana do Castelo. During the period spent at the site, it could be confirmed that the average daily traffic crossing the bridge is rather high. According to the Swiss norm SIA 269 [215], the failure consequences can be classified as “Large” whenever the ratio between the costs associated to failure and the cost of re-construction is larger than 5. Considering the cost of a 250 m long bridge with a 12 m wide deck located in a scenic setting to be around 5 million €, and estimating the cost of a human life at 2.5 million € [215], this means that the failure consequences are large if more than 10 casualties occur. Assuming the hazard scenario of collapse of the bridge deck, it is reasonable to assume that more than 10 casualties are likely to occur. This means that, considering human safety as the governing factor, the failure consequences are large.

Based on the conclusions of a detailed study undertaken by Costeira [67], a strengthening intervention to the deck slab is already being planned. Besides, the inspection campaign described shortly in Chapter 7 and detailed in reference [204] has shown that, irrespective of the current safety conditions, the deck requires a light intervention in order to ensure proper durability conditions: local drainage problems were found; some stirrups are not protected by an adequate concrete cover; corroded prestress ducts were detected in some holes in the bottom slab; some of the neoprene bearings are damaged; the safety barriers in the sidewalks are rusted and fractured at the welding spots. Moreover, in a post tensioned structure such as the N. S. da Guia Bridge, and according to current practice, the existence of cracks such as the ones observed in the bottom slab and in the webs is not acceptable due to concerns regarding to tendon durability. Therefore, the marginal cost of an intervention aimed at reducing the risk of collapse (per example, the installation of an external prestressing system) can be considered to be low since the gross part of intervention is justified by serviceability conditions. Considering this aspect and the large failure consequences, according to the recommendations of the SIA 269 expressed in the Table 8.2 the annual target reliability index can be set to $\beta_1 = 4.7$.

According to the recommendations of the Nordic Committee on Building Regulations expressed in Table 8.3, the adoption $\beta_1 = 4.7$ corresponds to a scenario of a ductile failure with very serious failure consequences, which can be considered to suit the present case. In the EN1990 [42], $\beta_1 = 5.2$ is recommended for design of new bridges such as the N. S. da Guia Bridge, confirming the remarks made in Section 8.2.3 regarding the differences between the target reliability indexes for design and for assessment. Given the agreement between the examined proposals, the annual target reliability index $\beta_1 = 4.7$ was adopted.

In this particular case it is reasonable to admit an extension of the bridge service life for at least 50 years. Therefore, the lifetime target reliability index to be used in the calculations can be determined from Eq. (8.25): $\beta_{50} = 3.8$.

8.3.2 Updated examination values

During the inspection campaign described in Chapter 7, several destructive and non destructive tests were performed for determining the in-situ mean values of both concrete and steel strengths. The characteristic values of the uniaxial concrete compressive strength, of the steel yielding and tensile strengths, and of the prestress steel tensile strength are here determined from the corresponding mean values using Eq. (8.20). The design values are determined from the characteristic values using partial safety factors as determined from:

$$\gamma_d = \exp\left(\alpha_R \beta_n \sqrt{v_f^2 + v_a^2 + v_m^2} - 1.65v_f\right) \quad (8.31)$$

The coefficients of variation recommended in the Eurocodes [51] were adopted, see Table 8.4. In the case of prestress steel, v_f was defined according to the recommendations given in reference [255]. It is remarked that the design values of the material properties were only used in the member level approach. In the nonlinear analysis, the remaining concrete model parameters were assumed to be perfectly correlated with the uniaxial compressive strength through the correlations presented in Chapters 3 and 4.

Table 8.4 – Updated examination values of the material properties.

Concrete		Steel				Prestress steel	
v_f	0.15	v_f		0.04		v_f	0.025
v_a	0.05	v_a		0.05		v_a	0.05
v_m	0.05	v_m		0.025		v_m	0.025
$f_{cm, is}$	41.0	f_{sym}	478	f_{sum}	571	f_{pum}	1845
$f_{ck, is}$	32.0	f_{syk}	447	f_{suk}	535	f_{puk}	1770
f_{cd}	24.8	f_{syd}	388	f_{sud}	463	f_{pud}	1530

Stresses given in MPa; For the prestress steel the yield strength is taken as 90% of the corresponding tensile strength;

According to the semi-probabilistic framework, the design value of the action effect is determined from Eq. (8.2). In the safety examination of existing bridges, and whenever available, use of updated information regarding the real loads should be made. This can be achieved through the adoption of site-specific traffic load models and updated values of the

permanent loads resulting from in-situ measurements. If both the mean values and standard deviations are available, partial safety factors can also be updated using the semi-probabilistic approach described in Section 8.2.1. The permanent action effect is usually described by a normal distribution and its design value can be determined from Eq. (8.13)₂. The extreme traffic action effects are usually associated to a Gumbel distribution. For details refer to [215]. In the present case, the focus was driven to the resistance side of the problem. Therefore, the permanent and traffic loads referred in section 7.6.1.4 were adopted and the partial safety factors $\gamma_G = 1.35$ and $\gamma_Q = 1.5$ were considered.

8.3.3 Linear elastic analysis – member level approach

In a first stage, a traditional member level assessment is always recommended. The results of such an assessment are presented in Figure 8.2. The actions effects were determined with resource to the 2D beam model described in Chapter 7. The internal forces were calculated taking into account the time-dependent behaviour of concrete and prestress steel and correspond to the long term ($t = 30$ years) distribution.

Regarding the bending moment envelope, it can be seen that the critical zones are located in the 2nd span, in the vicinities of section n°21, and in the hogging moment region of the 3rd span, near pier P2. In the latter, the inclination of the compression struts in the webs has to be limited to $\cot \theta' = 1.4$ so that the resisting bending moment envelope is not violated.

The shear strength was determined taking into account the interaction between the shear forces and transverse bending of the webs. This was made following the recommendations given by Menn [154] and Gaspar and Stucchi [91]. In this case, the maximum transverse bending moment in the webs amounts to 32 kN.m/m [67; 205]. This transverse moment can be equilibrated by shifting the resultant vertical compressive force in the web by 55mm with respect to the web axis, requiring a negligible increase in the stirrup forces. Assuming a rectangular (rigid-plastic) distribution of the compressive stresses along the web thickness, the effective web width $b_{w,ef}$ was taken as $250 - 2 \times 55 = 140$ mm. Since the transverse bending demand acts only on two webs at a time, this effective width was only considered in two of the webs. Due to the existence of prestressing tendons with duct diameters $\emptyset_D \geq b_w/8$ the ultimate resistance of the compression struts was calculated using a nominal web width:

$$b_{w,nom} = \zeta_D b_{w,ef} \quad , \quad \zeta_D = 1 - k_D \frac{\phi_D}{b_{w,ef}} \quad (8.32)$$

where $k_D = 0.5$ for grouted steel ducts [46; 87]. As illustrated in Figure 8.2, shear strength is not governed by diagonal crushing of concrete in the web, but by the limitation to $\cot\theta'$ coming from the flexural analysis. Even using the simpler Level I procedure described in Chapter 6, shear safety is verified. The Level II procedure reveals an extra safety margin in regard to web crushing.

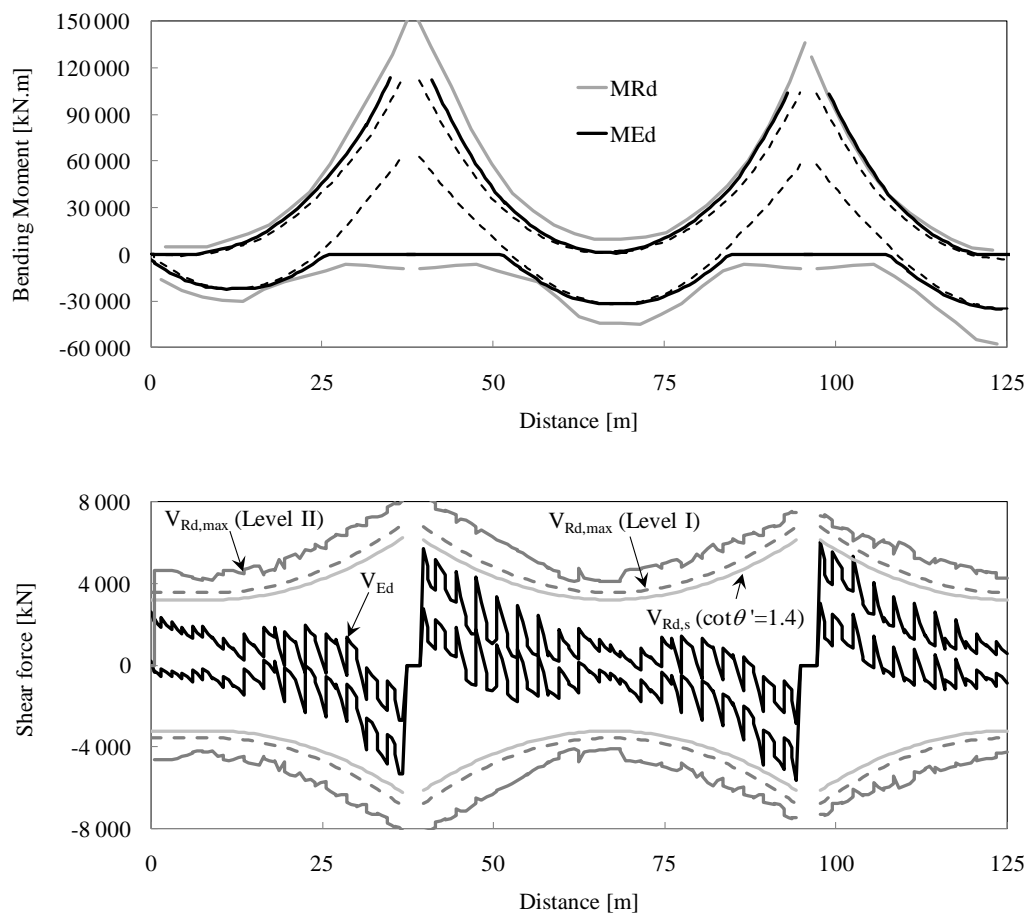


Figure 8.2 – Bending moment and shear force envelopes for $\cot\theta' = 1.4$.

8.3.4 Nonlinear analysis

Based on the results of the precedent member level analysis and on the cracking patterns observed in-situ, four traffic load cases were selected for the nonlinear analysis, see Figure 8.3:

- Load combination LC1: maximum bending moment at section n°23 where some of the bottom slab continuity tendons are anchored, see Figure 7.4;
- Load combination LC2: maximum bending moment at section n°21 where the remaining bottom slab continuity tendons of the 2nd span are anchored. According to the member level assessment, this section is critical;
- Load combination LC3: maximum hogging bending moment in the region of pier P2. According to the member level assessment this region is critical;
- Load combination LC4: maximum shear force in the 3rd span. In order to avoid direct force transmission towards the support, the “knife load” was applied 8m away from pier P2.

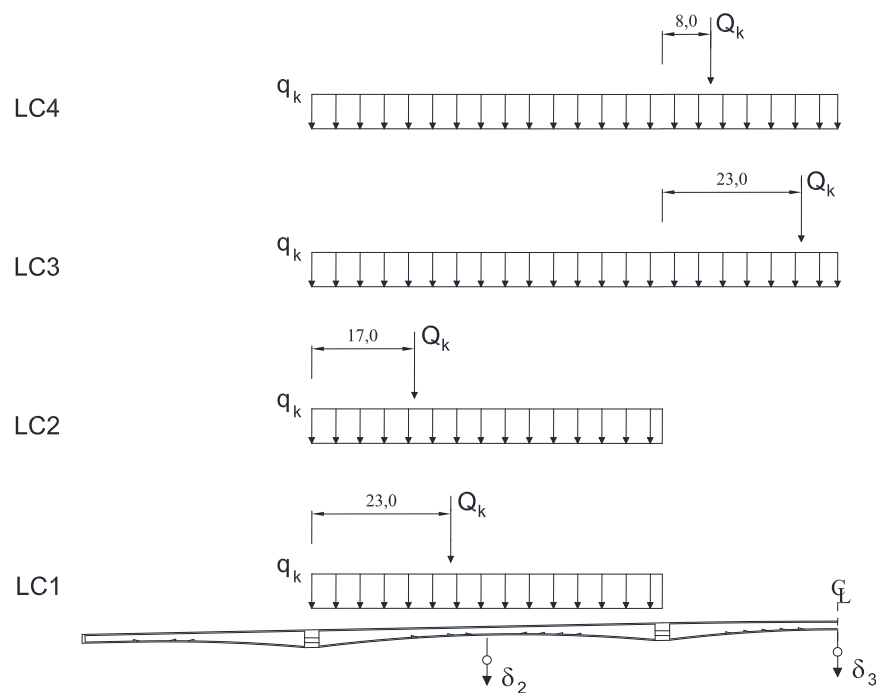


Figure 8.3 – Load cases considered in the nonlinear analysis: LC1 – maximum bending moment at section n°23; LC2 – maximum bending moment at section n°21; LC3 – maximum hogging bending moment over pier P2; LC4 – Maximum shear force in the 3rd span.

The position of the “knife” load was determined with the help of the elastic influence lines. The loads were transversely distributed along the deck width according to Figure 7.32. The “knife” load was also distributed longitudinally by a 3m length in order to avoid unrealistic stress concentrations and premature slab failure. The pedestrian loads and thermal effects

were considered as accompanying actions. The latter were applied before the traffic load whenever its effect is unfavourable, that is, together with load cases LC1 and LC2.

The material properties were determined according to Table 8.4 and using the correlations presented in Chapters 2 and 3. Like in section 3.8.2, and according to Eq. (8.32), an extra compression strength reduction factor $\zeta_D = 0.9$ was adopted in the webs in order to take into account the presence of the tendon ducts. As for the ultimate strain of the prestressing steel, and lacking experimental data, a tentative value of $\varepsilon_{pu} = 0.05$ was adopted. The crack spacing factor λ was taken equal to 0.7, corresponding to an intermediate situation between the extremes 0.50 and 1.0.

The load-displacement relationships corresponding to each of the analysed load combinations are depicted in Figure 8.4. As indicated in Figure 8.3, the displacements δ_2 and δ_3 refer to the monitoring points located in the middle of the 2nd and 3rd spans, respectively. The ratio $r_u = LF_u/LF_{req}$ presented in the graphs indicates the safety margin.

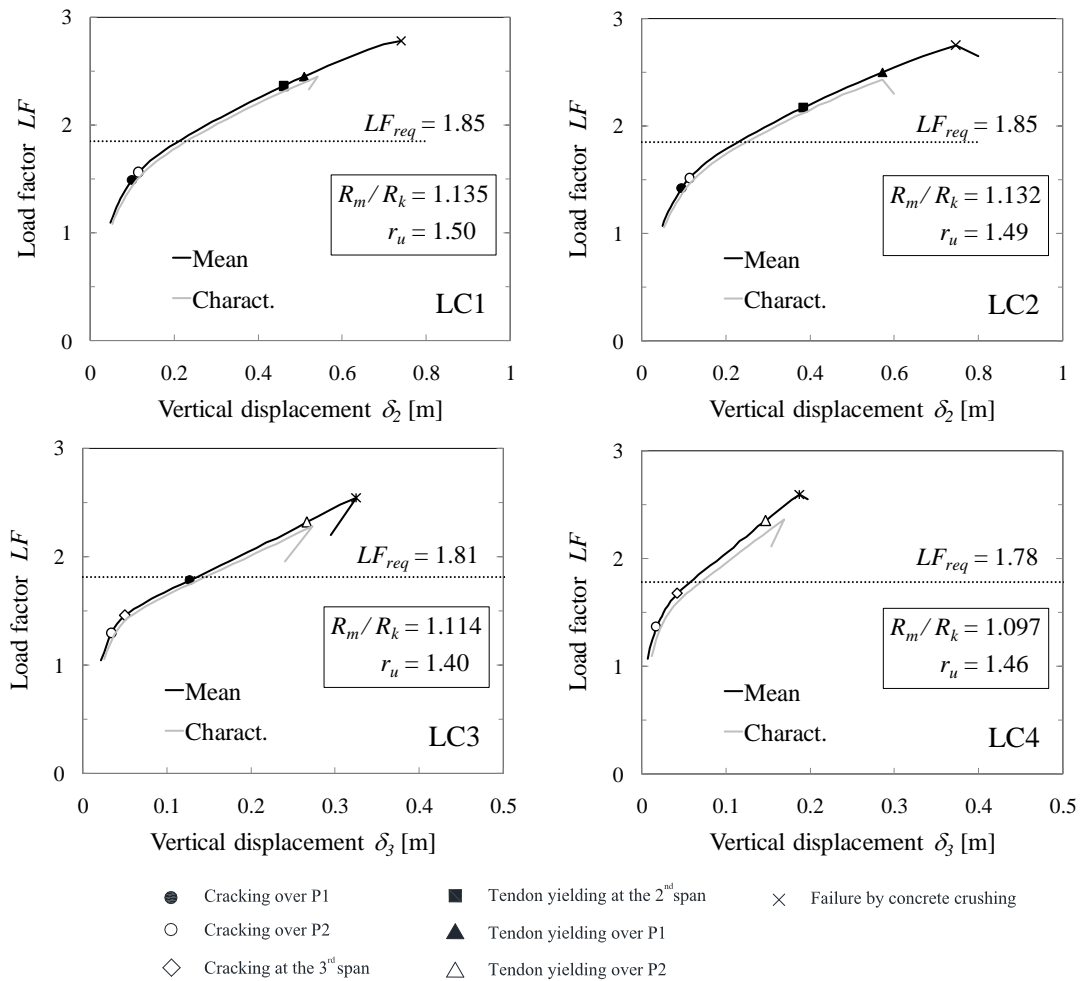


Figure 8.4 – Load-displacement curves for the each of the analysed load combinations.

Irrespective of the load combination and of adopting mean or characteristic values for the material parameters, failure was always triggered by concrete crushing in the bottom slab in the vicinities of pier P1 (load combinations LC1 and LC2) or pier P2 (load combinations LC3 and LC4). Prestress steel yielding was always observed in the hogging moment region where crushing occurred. Since there is no marked change of slope in the force displacement curves attributable to longitudinal steel yielding, it can be concluded that failure occurred in the transition from fragile to ductile behaviour. Nevertheless, and as it will be shown later, crack patterns are well developed at impending failure conditions and failure can be assumed to occur with warning.

The required, or target, load factor LF_{req} was determined for each load combination using Eqs. (8.28) and (8.29). The reference values were determined considering $v_G = 0.05$ and $v_M = 0.06$. The sensitivity of LF_{req} to the assumed values for v_G and v_M is illustrated in Figure 8.5. It can be seen that even considering very large values for these two coefficients of variation, safety could be proven for all the studied load combinations. For the extreme cases of brittle and ductile failures, the values that could be expected for LF_{req} using the coefficients of variation adopted in the Eurocodes are also represented.

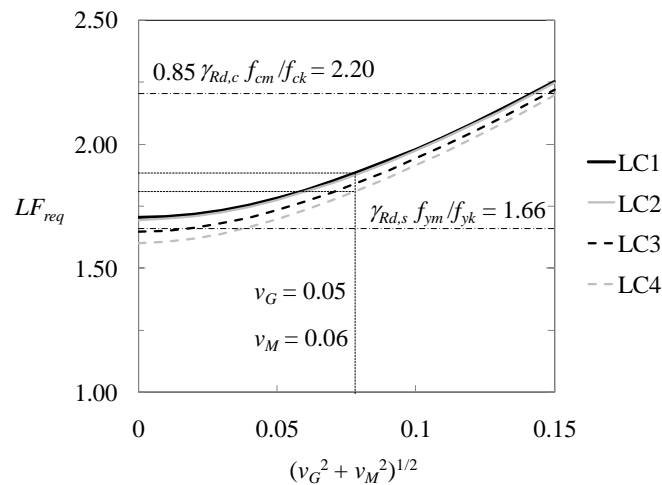


Figure 8.5 – Variation of the required load factor LF_{req} with the assumed values for v_G and v_M .

In the following, the results obtained for each of the load combinations are discussed. The results of load combination LC2 are very similar to those of LC1 and were, therefore, omitted.

Load combination LC1

Failure occurred for $LF_u = 2.78$ by crushing of the concrete in the bottom slab near pier P1. The biaxial strength envelope is first reached for $LF = 2.55$, after which concrete in the bottom slab enters the softening regime. At peak load, significant stress release is observed, as can be confirmed in Figure 8.6. The contour levels with the state variable E_{max} (see Chapter 4) clearly indicate the extent of the region in the softening regime.

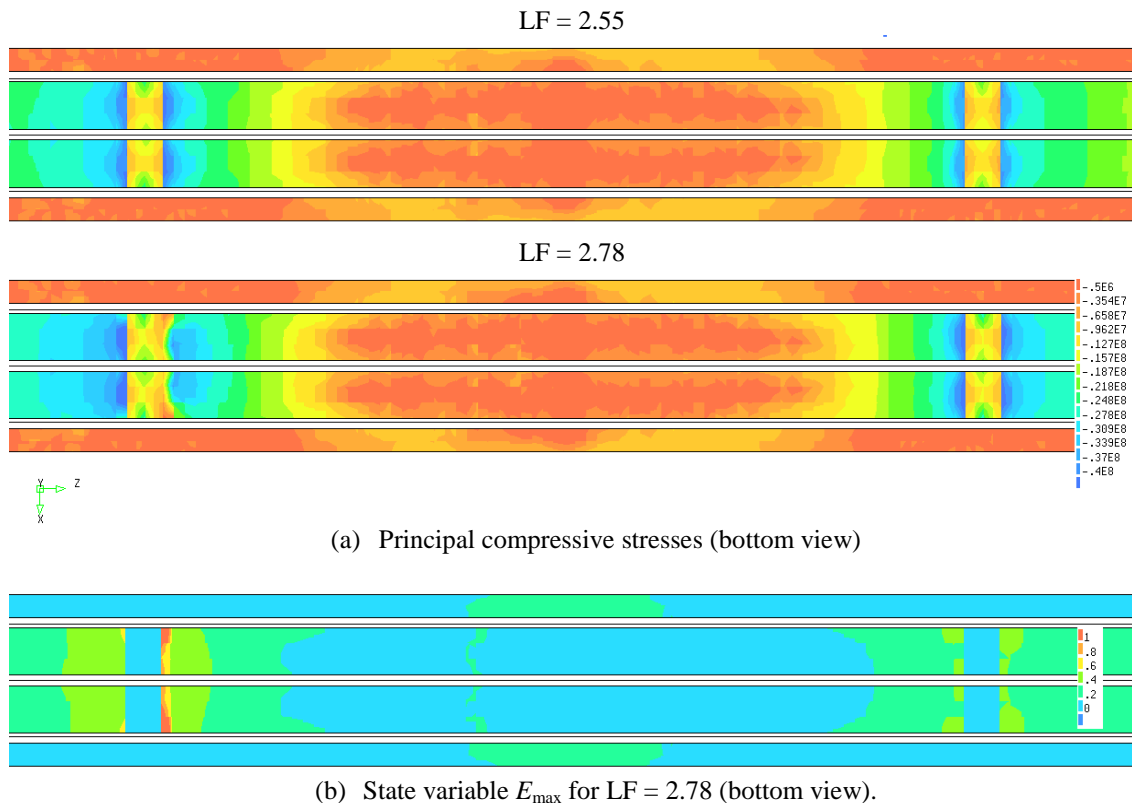
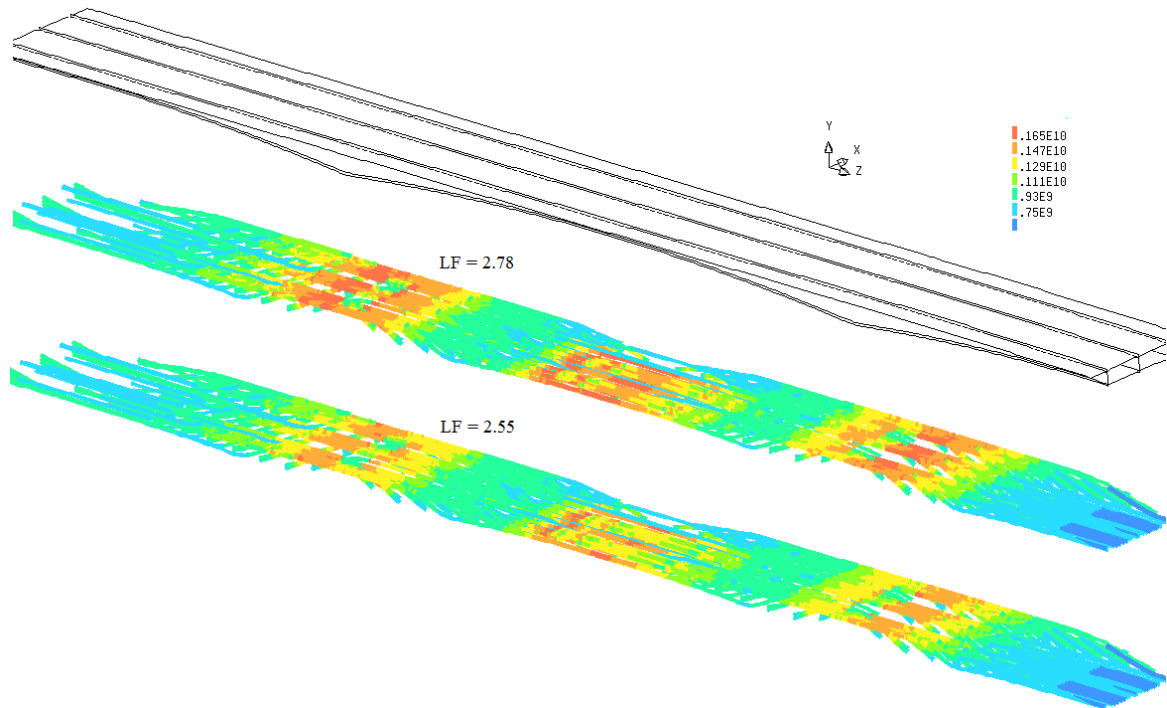
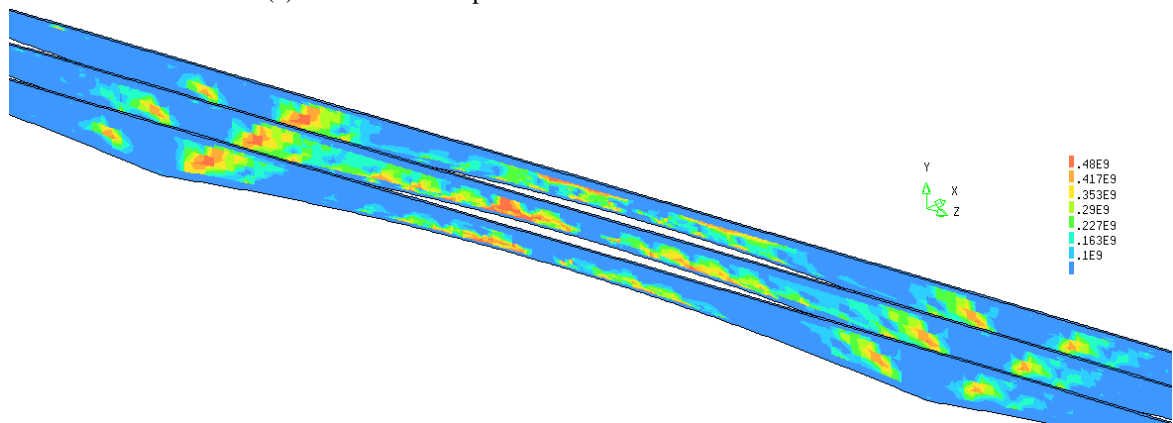


Figure 8.6 – Contour levels with: (a) the principal compressive stresses; (b) state variable E_{max} .

Although not clearly evidenced in the force-displacement relationship, yielding of the prestress tendons is calculated both at the span and at the pier sections. First yielding occurs in the 2nd span for $LF = 2.36$. At the piers, the first signs of yielding are observed for $LF = 2.45$. However, and as can be seen in Figure 8.7, yielding over piers P1 and P2 is only generalized for $LF = 2.78$. The maximum stresses in the prestress steel occur at the bottom slab and amount to 1765 MPa, which indicates that the margin against tendon failure is low. As for the stirrup stresses, the corresponding contour levels are depicted in Figure 8.7 (b). The first signs of stirrup yielding were detected in the 2nd span, near the “knife load” application point, for $LF = 2.00$. Steel stresses reaching 543 MPa were computed at failure, meaning that stirrup rupture was close.



(a) Stresses in the post-tension tendons for $LF = 2.55$ and 2.78 .



(b) Stirrup stresses at failure ($LF = 2.78$).

Figure 8.7 – Contour levels with the steel stresses.

The calculated cracking patterns are illustrated in the following figures, jointly with a detail of the deformed shape of the 2nd span. The middle of the 2nd span is already cracked in serviceability conditions. The first cracks over piers P1 and P2 appear for $LF = 1.44$ and 1.55 , respectively. The cracking pattern for $LF = 1.9$, which is approximately equal to the required load factor, is depicted in Figure 8.8. The cracks presenting the highest openings are located in the 2nd span. Horizontal cracks in the webs due to transverse bending can be clearly identified. The cracking pattern at failure is shown in Figure 8.9. Cracks wider than 1 mm are computed for the spans and over the piers. Both the webs and the top and bottom slabs are extensively cracked, which indicates that failure is not brittle.

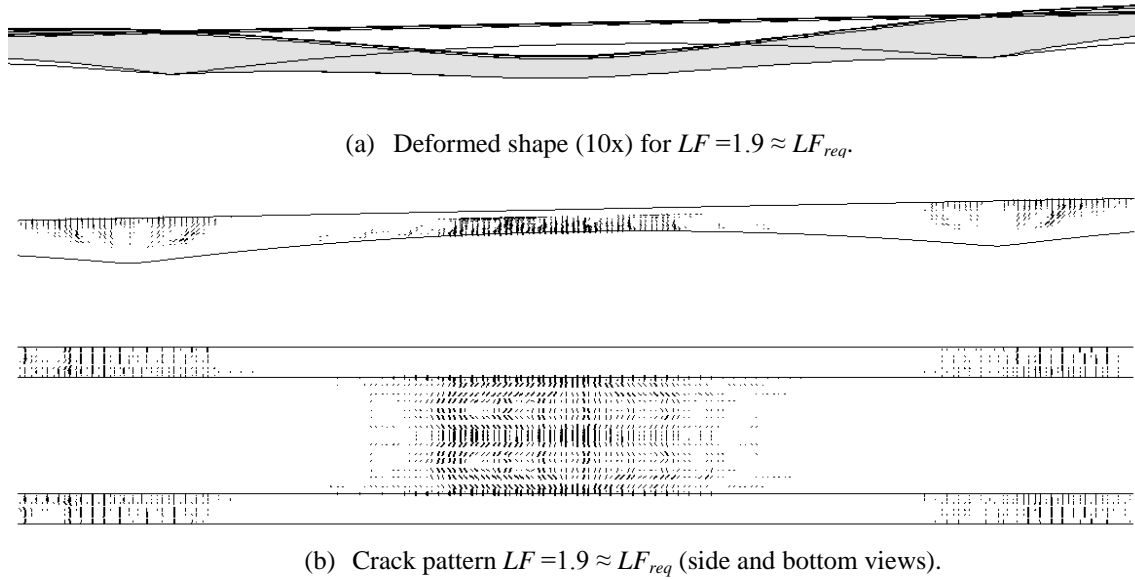


Figure 8.8 – Deformed shape and crack pattern for $LF = 1.9 \approx LF_{req}$. Cracks are presented in a three level scale: thicker lines correspond to crack larger than 0.5 mm; cracks thinner than 0.1 mm are not displayed.

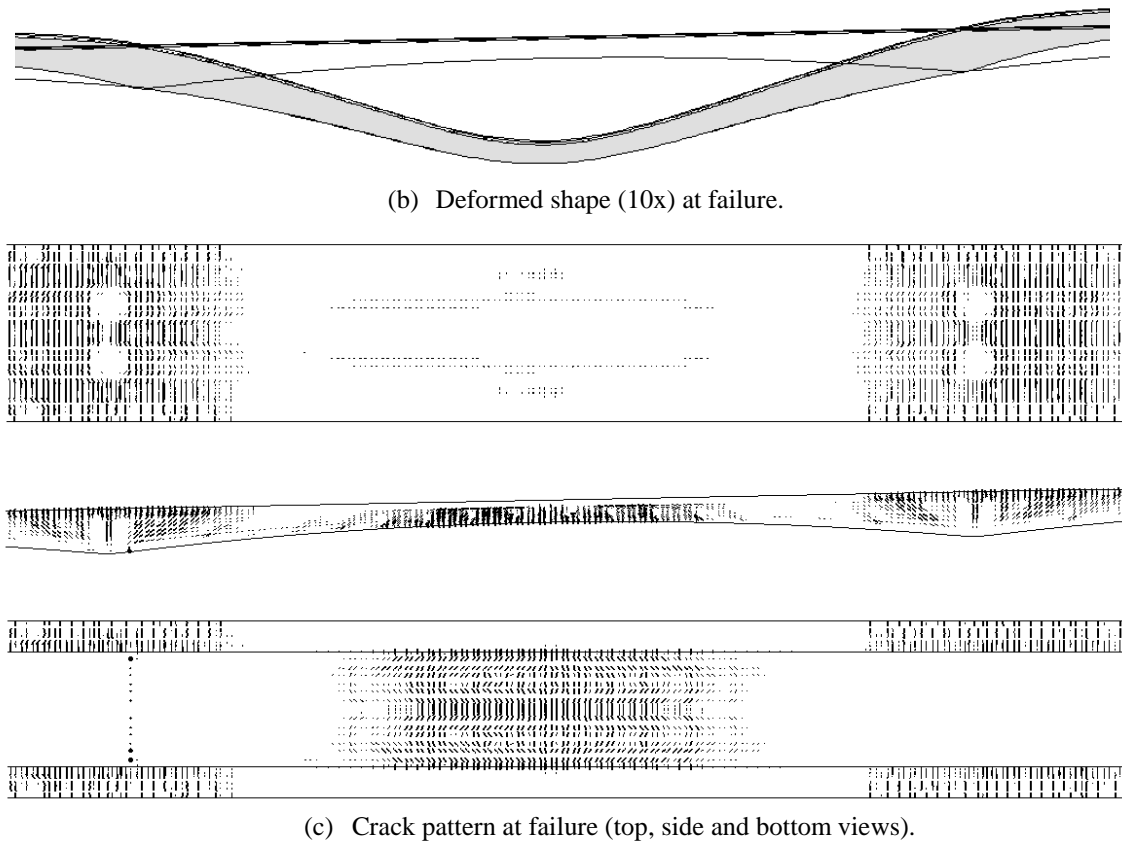


Figure 8.9 – Deformed shape and crack pattern at failure ($LF_u = 2.78$). Cracks are presented in a three level scale: thicker lines correspond to crack larger than 1.0 mm; cracks thinner than 0.3 mm are not displayed.

Cracks larger than 2mm are represented in Figure 8.10. These very wide cracks are mostly located at mid-span. In the bottom slab, the cracks circumventing the tendon anchorages presented the largest openings.

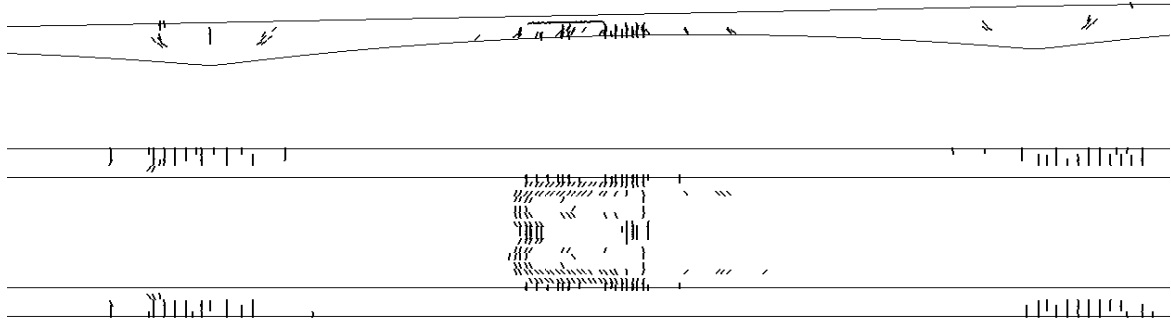


Figure 8.10 – Cracks with crack widths larger than 2 mm at failure: side and bottom views.

Load combination LC3

Also in this case the middle of the 2nd span is already cracked in the serviceability stage. The first cracks over pier P2, in the 3rd span and over pier P1 appear for $LF = 1.30, 1.46$ and 1.80 , respectively. First yielding of the prestress tendons occurs for $LF = 2.32$, and coincides both with first stirrup yielding at a shear crack in the hogging moment region and with the first Gauss point reaching the compressive strength envelope. Failure occurs for $LF_u = 2.54$ due to concrete crushing in the bottom slab of the 3rd span, near P2.

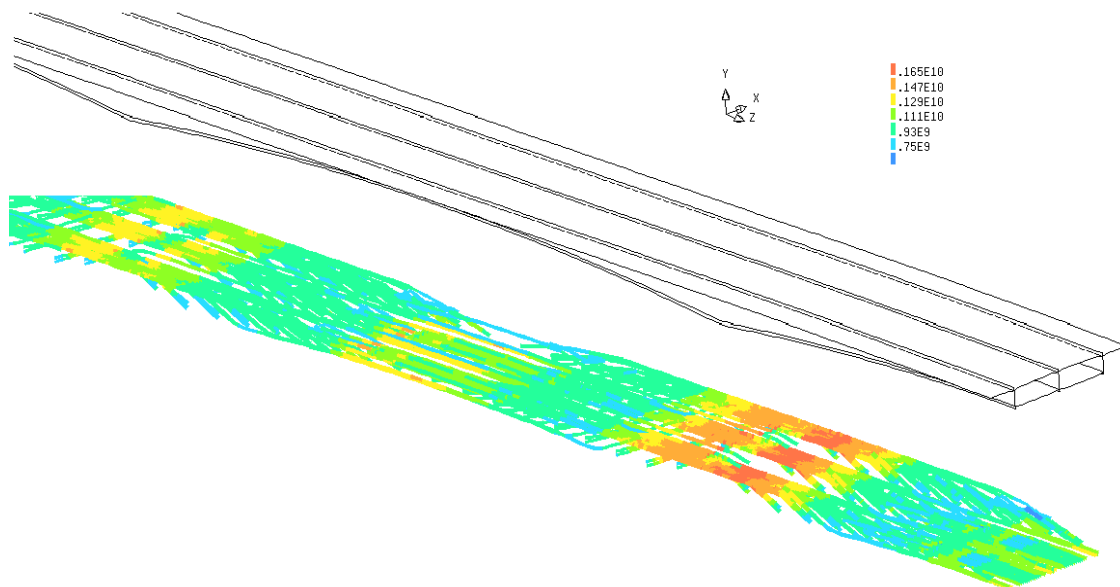


Figure 8.11 – Contour levels with the stresses in the post-tension tendons at failure ($LF_u = 2.54$)

The stresses in the tendons at impending failure are depicted in Figure 8.11. It can be seen that yielding is generalized over pier P2. No yielding is obtained in the bottom slab continuity tendons of the 3rd span and only localized yielding zones are computed in the 2nd span. The stirrup stresses are depicted in Figure 8.12. The maximum stirrup stress was computed at 501 MPa, which means that there is still some reserve available till stirrup failure.

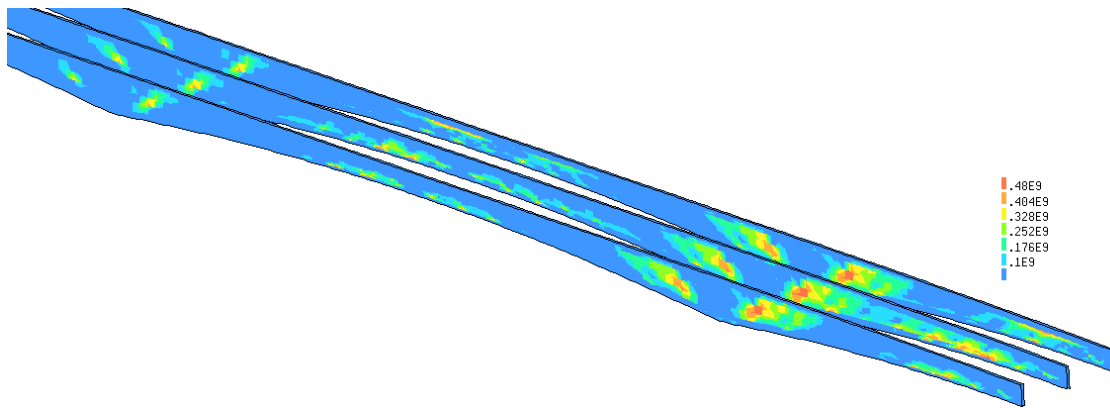
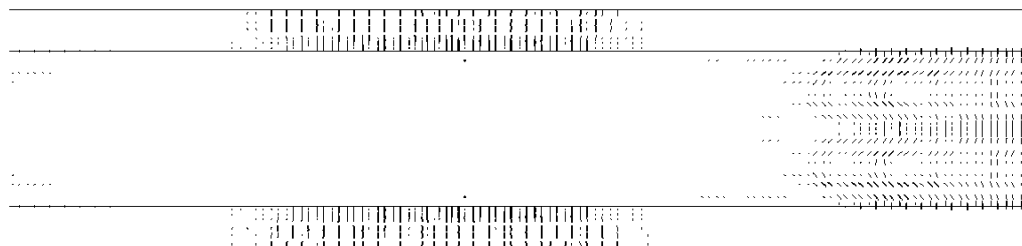


Figure 8.12 – Contour levels with the stirrup stresses at failure ($LF_u = 2.54$)



(a) Deformed shape (10x) at failure.



(a) Crack pattern at failure (side and bottom views).

Figure 8.13 – Detail of the deformed shape and crack pattern at failure ($LF_u = 2.54$). Cracks are presented in a three level scale: the thicker lines correspond to crack widths larger than 1.0 mm; cracks thinner than 0.3 mm are not displayed.

The cracking pattern at impending failure is shown in Figure 8.13. The region over pier P2 exhibits the widest cracks and cracks wider than 1 mm are obtained in a 10 m long segment of the deck. Once again, failure occurs with the structure exhibiting clear signs of distress.

Load combination LC4

The results for this load combination are not very different from those of LC3. While the first cracks over pier P2 appear for $LF = 1.37$, cracking over pier P1 and in the bottom slab of the 3rd span occur at the same load step, $LF = 1.68$. As for the stirrups, yielding at the shear crack located in the hogging moment region of the 3rd span is first observed for $LF = 1.90$. The prestress tendons start yielding simultaneously with the first gauss point reaching the biaxial strength envelope for $LF = 2.35$. Failure occurs for $LF_u = 2.59$ in the same way as in the previous case, that is, due to concrete crushing in the bottom slab of the 3rd span, near P2. The maximum stirrup stress is computed to be 502 MPa.

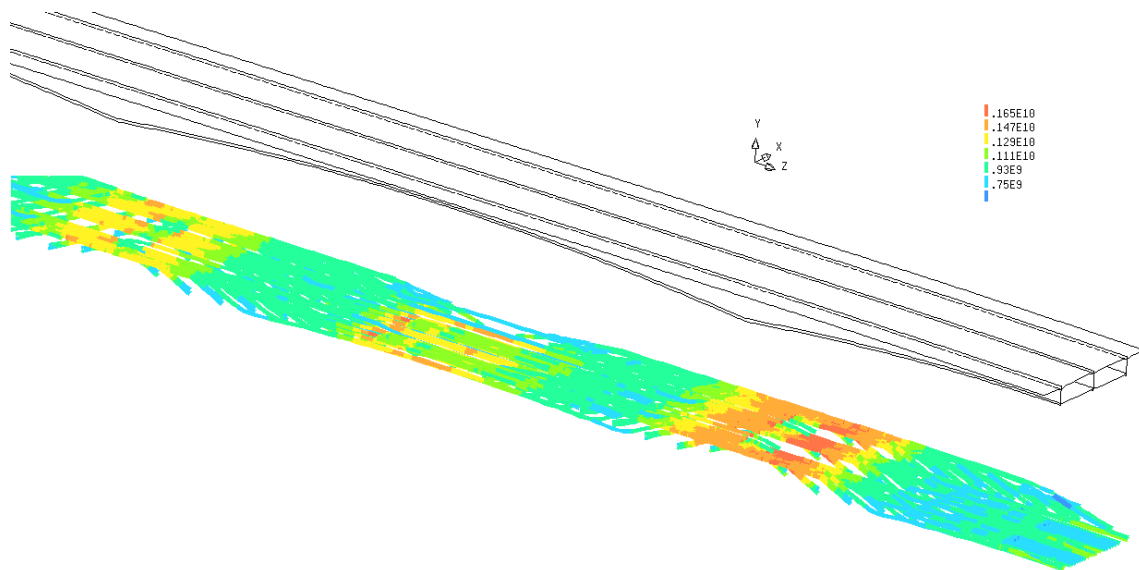


Figure 8.14 – Contour levels with the tendon stresses at failure ($LF_u = 2.54$)

The tendon stress contours at impending failure are depicted in Figure 8.14. It can be seen that yielding of the prestress tendons over pier P1 is not as generalized as in the load combination LC3. As for the stirrup stresses, see Figure 8.15, the results are quite similar. The deformed shape and the cracking pattern at impending failure are shown in Figure 8.16. Similar comments as those made for the analysis corresponding to load combination LC3 apply.

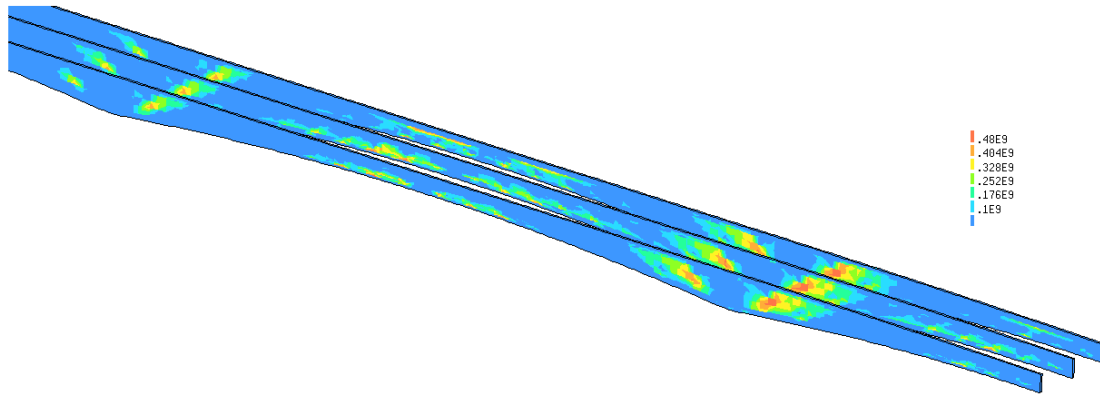
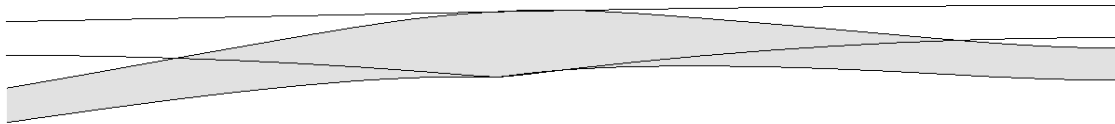
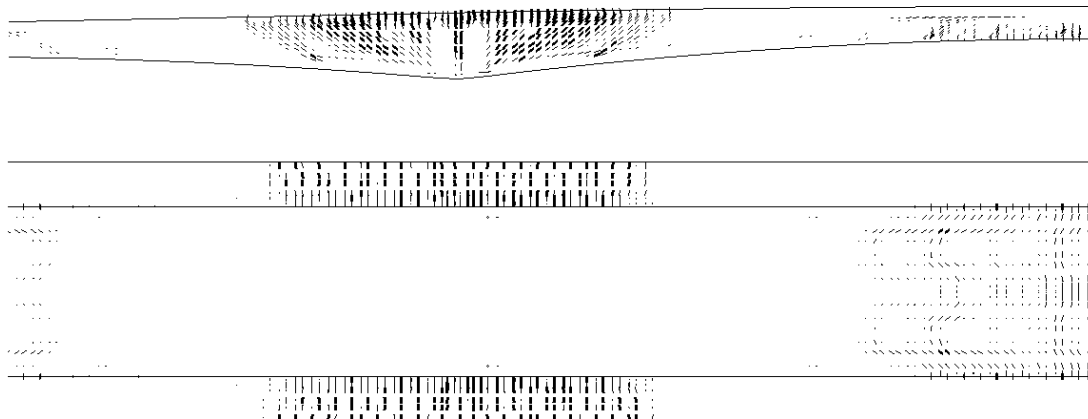


Figure 8.15 – Contour levels with the stirrup stresses at failure ($LF_u = 2.54$)



(b) Deformed shape (10x) at failure.



(b) Crack pattern at failure (side and bottom views).

Figure 8.16 – Detail of the deformed shape and crack pattern at failure ($LF = 2.54$). Cracks are presented in a three level scale: the thicker lines correspond to crack widths larger than 1.0 mm; cracks thinner than 0.3 mm are not displayed.

8.3.5 Continuous stress field analysis

An additional set of analyses was performed using the continuous stress field approach (CSFA) as described in Chapter 6. Once elastic-perfectly plastic stress strain curves are adopted for steel and for concrete, additional strain limitations must be imposed in order to

avoid an overestimation of the structural capacity. This way, failure is assumed to occur when the first of the following events takes place: the tensile strains in the reinforcing steel exceed 15‰; the strains in the prestressing steel exceed 20‰; or the compressive concrete strains exceed 4‰ (which is equivalent to having $E_{\max} \leq 2$). In cases where the ultimate load is strongly dependent on these strain limits and the safety margin is low, a refined calculation of the deformation capacity using the F-CMM is recommended.

Although the calculation of force-deformation curves is not the purpose of the CSFA, the calculated curves for load combinations LC1 and LC3 are compared to those obtained with the F-CMM, see Figure 8.17. The dashed portion of the curves corresponds to equilibrium states beyond the theoretical failure load determined on the basis of the strain limitation criteria. The events marked in the curves were defined in accordance to the strain limits defined above.

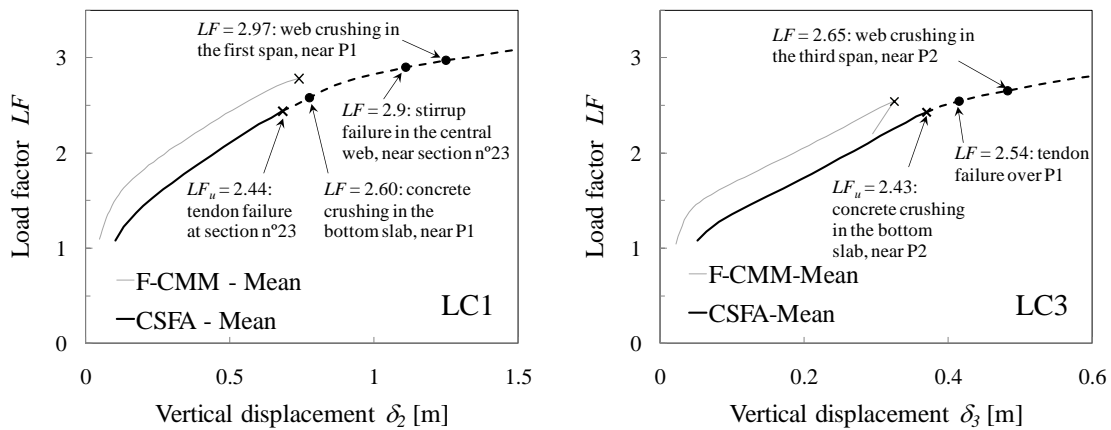


Figure 8.17 – Force-displacement curves.

The continuous stress field in the central web of the 3rd span at impending failure is depicted in Figure 8.18 for load combination LC3. Due to the contribution of the inclined tendons, a slightly deviated stress field develops [80]. The average inclination of the compressive stress field is such that $\cot\theta'$ varies between 1.35 and 1.40, which agrees remarkably well with what has been considered in the member level assessment. If a large ductility for the compressed concrete in the bottom slab is assumed, shear failure is predicted to occur for $LF = 2.65$.

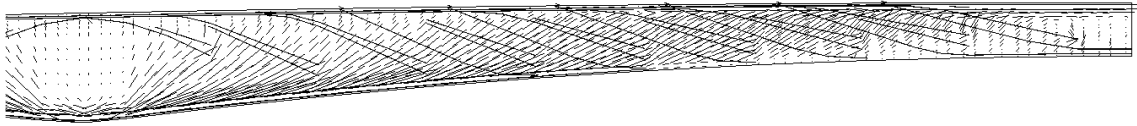


Figure 8.18 – Continuous stress fields in the central web of the 3rd span for load combination LC3.

8.4 Concluding remarks

In this chapter it was shown how to define a global resistance factor based on a semi-probabilistic approach that can capture the system resistance sensitiveness to the random variation of the input variables. A simple safety format that is compatible with NLFEA assumptions was formulated, following closely what is being proposed by Cervenka [55] and the new CEB-FIP Model Code 2010 [87]. Besides enabling the use of updated information regarding the material properties, the proposed procedure allows performing reliability differentiation based on risk analysis considerations and on the expected remaining service life of the structure, being therefore suitable for the safety examination of existing bridges.

A traditional safety assessment at the member level led to the conclusion that the bridge fulfils the safety requirements without any safety margin. The bridge was predicted to be critical in bending, namely in the hogging moment regions of the 3rd span and in the region of the 2nd span where the bottom slab continuity tendons are anchored. The system level assessment using the F-CMM revealed that the bridge has, in fact, an appreciable safety margin, which can be explained by its redistribution capacity. Failure was predicted to occur by concrete crushing in the hogging bending moment regions irrespective of the load combination being considered. The results obtained for the load combinations LC1 and LC2, in which the traffic load was positioned so as to maximize the bending moment in the sections where the bottom continuity tendons are anchored, revealed that tendon and stirrup failure were about to occur. If the safety margin had not turned out so comfortable, the analysis should proceed to a sensitivity study varying the parameters defining the ductility of the steel.

A set of analyses was also performed using the continuous stress field model developed in Chapter 6. As elastic-perfectly plastic stress-strain relations are used, in statically indeterminate structures additional strain limits are required in order to avoid overestimations of the load carrying capacity. This way notional failure loads were

obtained for each load combination. These compared favourably with the more accurate estimates using the F-CMM, which is an indicator of the adequacy of the adopted strain limits.

Since the bridge safety is not at risk, the installation of a surveillance system, constituted by a set of sensors monitoring the activity of some selected cracks, and remotely transmitting the information for periodic or continuous assessment, could provide valuable information to the bridge owner, enabling increasing the period between periodic visual inspections while the planned intervention is scheduled. This intervention is justified by the concerns related to the durability of the bridge.

9 Summary and conclusions

This thesis was oriented towards the development of a harmonised set of models enabling a stepwise approach to the safety assessment of existing concrete bridges. Nonlinear finite element analysis (NLFEA) was adopted as the reference tool for the accurate assessment of the load-carrying capacity. Since many structural elements can be idealized as an assembly of membrane elements, special attention was paid to the analysis of RC panels subjected mainly to in-plane shear and axial forces. Based on the detailed models developed for NLFEA, simplified formulations were derived for shear strength assessment of structural elements containing at least the minimal amount of shear reinforcement and a case study was presented aimed at illustrating the applicability of the developed tools. In the following, a brief summary of the work developed in each chapter is presented.

Chapter 2

In Chapter 2, the main features of concrete behaviour when subjected to short term loading conditions were examined. Four basic phenomena were identified at the macro-level governing the behaviour of structural concrete elements: tensile fracture; bond shear stress transfer between the reinforcements and the surrounding concrete; shear stress transfer through rough cracks; and compressive behaviour under uniaxial or multiaxial stress conditions. The experimental procedures, and corresponding theoretical models, aimed at providing a description of each of the above mentioned phenomena were discussed in some detail. The concepts and terminology introduced in this chapter were thoroughly used throughout the thesis.

Chapter 3

In Chapter 3, a new model considering fixed and interlocked cracks, the F-CMM, was proposed for the analysis of RC panels subjected to in-plane shear and axial stresses. The model complements the Cracked Membrane Model of Kaufmann and Marti (here designated as R-CMM) by extending its concept to the case of fixed and interlocked cracks capable of transferring shear and normal stresses. This enabled a more consistent reproduction of shear sliding failures in orthotropically reinforced panels, a better fit to the observed deformational behaviour and improved calculations of the shear strength.

Equilibrium is formulated in terms of stresses at the cracks and compatibility is formulated in terms of average strains. The consideration of the local mechanical effects that take place at the cracks, - such as aggregate interlock, crack bridging and softened compressed concrete behaviour - , together with the bond stress transfer mechanics described according to the Tension Chord Model (TCM), allowed a rational derivation of both local and average stress/strain fields and a deeper understanding of the complex mechanics governing the behaviour of cracked RC membranes. Nevertheless, the model was kept sufficiently simple for implementation in a robust finite element formulation for structural analysis. A validation campaign was carried out using a database with the experimental results of 54 RC panels tested under in-plane shear and axial stress conditions. Good agreement was found between the predicted and the observed shear strengths, failure modes and deformational behaviour. The database covered a wide range of reinforcement ratios and concrete strengths ensuring that the model is generally applicable.

Chapter 4

In Chapter 4, the basic concepts behind the computational models for nonlinear analysis of structural concrete elements were presented and a total strain constitutive model for accommodating the RC cracked membrane element constitutive laws devised in Chapter 3 was developed. The model comprises a set of state variables that continuously monitor damage evolution in concrete and enable the establishment of suitable loading/unloading conditions. Strain localization issues were dealt with using a description of the displacement field based on the “weak discontinuities” concept, which was still found to present the best compromise between accuracy, simplicity and economy of computer resources. Uncracked concrete nonlinear behaviour in biaxial compression was formulated in a very efficient way using the concepts of equivalent stress and equivalent strain. Due to the adoption of a dedicated phenomenological model for shear stress-transfer between rough cracks, which includes both shear and dilatancy stresses, special attention was paid to the equilibrium and compatibility conditions in cases of two orthogonal cracks arising in the same integration point. The model for reinforcing steel was formulated according to the Tension Chord Model and clear physical assumptions were used for establishing the loading/unloading conditions and the behaviour under reversed loading paths. The implemented algorithms were described in detail and some simple validation examples were presented for illustrating the model response. The implementation was extended to shell elements and good agreement was obtained when comparing the calculated results

with experimental data. Good convergence characteristics were exhibited in the analysed examples.

Chapter 5

In Chapter 5, a validation campaign was undertaken using a set of experimental tests on large scale shear critical structural elements. Both continuity and discontinuity regions were analysed. The model proved capable of reproducing shear failures in demanding situations, such as the ones involving plastic strains in the longitudinal reinforcement. Good estimates of the failure modes, failure loads, cracking patterns and crack widths were achieved. The implementation proved robust and the force-deformation responses could be computed in the post-peak range, thus allowing the identification of the failure mechanisms. Although the focus was driven to modelling of shear failures in shear reinforced concrete girders, an example was presented of a concrete girder failing in bending. In this case, good estimates of the deformation capacity in the post-yield stage and an accurate sizing of the plastic hinge regions were obtained. In spite of the overall good results, some limitations were found. (1) Although not severe, the deformation capacity of the stirrups is somewhat underestimated whenever failure is governed by stirrup rupture. This is attributed to the fact that the model cannot reproduce bond slip occurring across several cracks; (2) Despite the fact that the F-CMM can reproduce the associated crack kinematics, the shear sliding failure mode could not always be clearly evidenced due to anticipated crushing of web concrete. In fact, localization of the shear displacements along a well defined crack could not be obtained in cases where the compressive stresses in the web were high and plastic strains in the tensile reinforcement were observed (specimens MVN2 and MVN3). This seems to indicate that the adopted softening law, which is based on the results obtained on RC panels, gives conservative estimates of the effective compressive strength in discontinuity regions similar to those of specimens MVN2 and MVN3. Nonetheless, the failure loads and the force-deformations curves were still in good agreement with the observed ones and the failure region is correctly identified; (3) Finally, due to the kinematic description of the displacement field based on the concept of weak discontinuities the web crushing failure is systematically localized along a row of finite elements, instead of spreading throughout the whole web. Although this effect has almost no implications in the calculation of the peak load, it influences the computation of the load carrying mechanisms in the post-peak regime.

Chapter 6

In Chapter 6 simplified models for engineering practice were presented. Given the fact that flexural strength can be considered to be satisfactorily predicted in current design methods, the focus of these simplified formulations was driven to shear dominated problems. In Chapter 3 it was shown that the R-CMM can be obtained from the F-CMM by imposing an additional constraint related with the coincidence of the principal axes of concrete stress at the cracks and average strain. The equilibrium equations and the constitutive laws are simplified at the cost of some decrease in accuracy. The R-CMM can be further simplified by neglecting the concrete tensile strength and the bond stress transfer effects, resulting in a limit analysis formulation following more closely the assumptions usually adopted in engineering practice. It is simpler to use and, in the case of RC panels, comes down to a set of closed form expressions for the yield conditions. However, in the case of a structural analysis, the relevant outcomes are simply the stress fields expressing the equilibrium at failure conditions and the corresponding ultimate load. This tool can be extremely useful whenever the choice of an appropriate discontinuous stress field is not trivial and establishes the link between limit analysis methods and the numerical models developed in the previous chapters. For the case of continuity regions, a simple sectional analysis method was derived directly from the yield conditions considering a constant shear stress distribution along the cross-section height. The resulting expressions are formally similar to those of the variable angle truss model adopted in the recent European codes. However, by allowing the exploitation of a wider range of values for the inclination of the struts and the incorporation of the effect of the longitudinal reinforcement/prestressing steel strains in the definition of $f_{c,ef}$, the proposed method is suitable for an intermediate shear strength assessment of an existing concrete bridge.

Chapter 7

In Chapter 7 a 30 year-old post-tensioned concrete box-girder bridge exhibiting consistent cracking patterns throughout the deck was examined in detail. Cracks were observed in the webs, mainly at the joints of segmental construction, and in the bottom slab. Besides a detailed visual inspection and some material characterization studies, a preliminary non-destructive inspection using gamma-rays was undertaken in order to evaluate the feasibility of an exhaustive inspection campaign using this technology. This was motivated by the uncertainty regarding the condition of post-tension tendons. The obtained gammagraphies

revealed no grouting defects or corrosion signs in the wires. This study should now be completed in order to collect more data in different locations of the deck.

The bridge was also monitored during a controlled load test and along 4 days under normal traffic and environment excitations. The monitoring campaign aimed at evaluating the linearity of the bridge response as well as the crack movements under controlled traffic loads and daily thermal variations. Crack opening variations of 0.13mm were measured with four loaded trucks on the deck producing a live-load bending moment approximately 65% of that produced by the load model of the Portuguese code used in the original design and still in force today. Due to the daily thermal variations in a 4 days measuring period, the crack width variations reached 0.1mm. In spite of the measured crack activity, the bridge exhibited linear elastic behaviour during the load test. Although the measured response in some sensors was systematically more flexible than that calculated, the response to vehicle loading compared reasonably well with that calculated considering the uncracked stiffness of the deck. Since no baseline condition is available, no definite conclusions could be drawn from this set of results. In fact, stiffness changes due to localized cracks are expected to be small and difficult to evaluate without a direct and careful comparison with previous measurements - it must be noted that only the cracks that are continuous between the bottom slab and the webs effectively decrease the bending stiffness. Still, the obtained results can serve as a comparison basis for future tests and show that the structural condition of the bridge does not require immediate intervention.

In order to explain the origin of the observed cracking patterns, the bridge was analysed with both 2D and 3D finite element models taking into account the construction sequence and the time-dependent evolution of the sectional forces due to the effects of creep, shrinkage and prestress steel relaxation. The obtained results indicate that the observed cracking patterns are not linked to prestress steel corrosion and are mainly due to an inadequate layout of the prestress tendons together with the adoption of a very low ordinary reinforcement ratio in the longitudinal direction. In this respect, the 3D analysis proved essential to confirm that the decompression limit state both in the bottom slab and in the webs is almost reached in the long-term considering only the action of permanent loads. The analysis of the local stress conditions around the tendon anchorages was crucial in order to understand the origin of the observed cracking patterns. In these circumstances, average residual crack widths larger than 0.3 mm are to be expected, which agrees well with the mapped crack widths.

Chapter 8

In Chapter 8 it was shown how to define a global resistance factor based on a semi-probabilistic approach that can capture the system resistance sensitiveness to the random variation of the input variables. A simple safety format that is compatible with NLFEA assumptions was formulated, following closely what is being proposed by Cervenka [55] and in the new CEB-FIP Model Code 2010 [87]. Besides enabling the use of updated information regarding the material properties, the proposed procedure allows performing reliability differentiation based on risk analysis considerations and on the expected remaining service life of the structure, being therefore suitable for the safety examination of existing bridges.

A traditional safety assessment at the member level led to the conclusion that the bridge fulfils the safety requirements without any safety margin. The bridge was predicted to be critical in bending, namely in the hogging moment regions of the 3rd span and in the region of the 2nd span where the bottom slab continuity tendons are anchored. The system level assessment using the F-CMM revealed that the bridge has, in fact, an appreciable safety margin, which can be explained by its redistribution capacity. Failure was predicted to occur by concrete crushing in the hogging bending moment regions irrespective of the load combination being considered. The results obtained for the load combinations in which the traffic load was positioned so as to maximize the bending moment in the sections where the bottom continuity tendons are anchored revealed that tendon and stirrup failure were about to occur. If the safety margin had not turned out so comfortable, the analysis should proceed to a sensitivity study varying the parameters defining the ductility of the steel.

A set of analyses was also performed using the continuous stress field model developed in Chapter 6. As elastic-perfectly plastic stress-strain relations are used, in statically indeterminate structures additional strain limits are required in order to avoid overestimations of the load carrying capacity. In this way notional failure loads were obtained for each load combination. These compared favourably with the more accurate estimates using the F-CMM, which is an indicator of the adequacy of the adopted strain limits.

9.1 Recommendations for future research

RC cracked membrane element

As shown by Alvarez [3], refined calculations of the steel stresses at the cracks in the post-yielding stage can be made if more realistic stress-strain laws are adopted for the rebars instead of the simplified bi-linear law adopted in this work. This requires the generalization of the TCM expressions (3.38) and (3.39) and may improve the estimates of the deformation capacity whenever the reinforcement ratio is low. The influence of the reinforcement ductility class on the failure modes and failure loads of both RC panels and structural concrete elements should be investigated.

The crack shear stress transfer model must be generalized for high strength concrete. Also a dowel action model can be included in the formulation, thereby allowing the examination of the dowel action effects on the shear strength and on the reduction of the apparent yielding stress of the reinforcement. The RC cracked membrane element formulation presented in Chapter 3 could be also extended to accommodate non-orthogonal reinforcement meshes.

Following the works of Vecchio [241], Bentz [24] and Mohr *et al* [161], both the F-CMM and the R-CMM can be implemented in a layered beam finite element formulation. This would enable a more efficient study of the shear response in beam continuity regions and would allow tracing accurate (N, M, V) interaction diagrams for different types of cross-sections. Moreover, this type of elements is widely used in commercial finite element codes dedicated to bridge analysis and design and would enhance the applicability of the developed models in engineering practice.

NLFEA model based on the RC cracked membrane element

The use of a non-local formulation for improving mesh objectivity with regard to compression failures should be attempted. This could enhance the predictions of the deformation capacity of plastic hinge regions as well as a more accurate reproduction of web crushing or web sliding failures.

It is also advised to extend the validation campaign. Similarly to what has been performed with RC cracked membrane element, the database of analysed shear reinforced girders should be increased in order to cover a broader range of reinforcement and prestressing ratios. Moreover, other structural elements should be included, the most typical being shear walls, deep beams and elements subjected to torsion. Much is learned during these

validation analyses, eventually leading to the improvement of some features of the model. This would also be important to establish the model uncertainty parameter to be adopted in the safety format described in Chapter 8.

The interaction between out-of-plane bending and in-plane shear should also be evaluated and compared to experimental evidence. As evidenced in Chapter 8, this interaction occurs in the webs of box-girder bridges and may govern the shear capacity.

The application of the developed NLFEA model in serviceability calculations requires the generalization of the formulation so that residual crack openings can be determined with good accuracy. Although previous overloading may cause crack development, it is the residual crack opening at a pre-determined operating load level that should be compared to the target value. Therefore, reversed bond action and re-contact stress at crack closing should be introduced in the model. Moreover, concrete time dependent effects, such as shrinkage and creep, should be also included. This is an important feature for realistic serviceability analyses of segmental bridges, such as the one analysed in Chapter 7.

Simplified models for engineering practice

The model for continuous stress field analysis of structural elements developed in Chapter 6 revealed great potential both for academic and practical engineering purposes. Since simple constitutive laws are used, the model can be used as an introductory tool in courses concerned to NLFEA. Moreover, it can serve as an auxiliary tool in advanced structural concrete courses treating discontinuous stress fields/strut-and-tie models. In engineering practice, this model can be used in the analysis, design and assessment of discontinuity regions with complex geometry by structural engineers with no relevant expertise in NLFEA. However, and as remarked in Chapter 8, due to the adoption of elastic-perfectly plastic stress-strain laws, additional strain limits must be imposed in order to avoid overestimation of the load carrying capacity of statically indeterminate structures. Although tentative values have been adopted in the analysis of the N.S da Guia Bridge, these limits should be confirmed after comparison with experimental evidence and/or numerical analyses with the F-CMM.

As for the simplified analytical model for continuity regions, its extension to problems involving torsion should be made. The applicability of this model in the analysis of the interaction between out-of-plane bending and in-plane shear should be evaluated.

Safety formats for NLFEA

The safety format for NLFEA described in Chapter 8 should be thoroughly evaluated through comparison with the results obtained with higher order reliability or simulation methods. A clear set of recommendations could then be issued in future codes of practice, which would certainly contribute to increasing use of more advanced analysis tools in the safety examination of existing concrete bridges.

References

- [1] AASHTO. (2004). *AASHTO LFRD Bridge Design Specifications*, Washington D. C.
- [2] Alfaiate, J. M. V. (1992). "Estudo e Modelação do Comportamento do Betão Fissurado," Tese de Doutoramento, Instituto Superior Técnico, Lisboa.
- [3] Alvarez, M. (1998). "Einfluss des Verdunverhaltens auf das Vermormungsvermögen von Stahlbeton," Doctoral Thesis, Swiss Federal Institute of Technology Zurich, Zurich.
- [4] Angst, U., Elsener, B., Larsen, C. K., and Vennesland, O. (2009). "Critical chloride content in reinforced concrete — A review " *Cement and Concrete Research*, 39(12), 1122-1138.
- [5] Aspiotis, J. (1993). "Compression Softening of High Strength Reinforced Concrete Elements," Master Thesis, University of Toronto, Toronto.
- [6] Barlett, F. M., and MacGregor, J. G. (1996). "Statistical Analysis of the Compressive Strength of Concrete in Structures." *ACI Materials Journal*, 93(2), 158-168.
- [7] Barlett, F. M., and MacGregor, J. G. (1999). "Variation of In-Place Concrete Strength in Structures." *ACI Materials Journal*, 96(2), 261-271.
- [8] Barras, P., Matteis, D., Derais, J.-F., Duviard, M., Guillot, D., Lacombe, J.-M., Ojeda, V., Paillusseau, P., and Reinhardt, J.-M. (2003). *Design guide - Prestressed concrete bridges built using the cantilever method*, Sétra.
- [9] Bazant, Z. P. (1986). "Mechanics of distributed cracking." *Appl Mech Rev, ASME*, 39(5), 675-705.
- [10] Bazant, Z. P. (1991). "Why Continuum Damage is Nonlocal: Micromechanics Arguments." *Journal of Engineering Mechanics*, 117(5), 1070-1087.
- [11] Bazant, Z. P., and Baweja, S. (1995). "Creep and shrinkage prediction model for analysis and design of concrete structures - model B3." *Materials and Structures*, 28(6), 357-365.
- [12] Bazant, Z. P., and Gambarova, P. G. (1980). "Rough crack models in reinforced concrete." *Journal of Structural Engineering*, 106(4), 819-842.
- [13] Bazant, Z. P., and Gambarova, P. G. (1984). "Crack Shear in Concrete: Crack Band Microplane Model." *Journal of Structural Engineering*, 110(9), 2015-2035.
- [14] Bazant, Z. P., and Jirasek, M. (2002). "Nonlocal Integral Formulations of Plasticity and Damage: Survey of Progress." *Journal of Engineering Mechanics*, 128(11), 1119-1149.
- [15] Bazant, Z. P., Li, G.-H., Yu, Q., Klein, G., and Kristek, V. (2009). "Explanation of Excessive Long-Time Deflections of Collapsed Record-Span Box Girder Bridge in Palau - Preliminary Structural Engineering Report No. 08-09/A222e." Infrastructure Technology Institute, McCormick School of Engineering and Applied Science, Northwestern University, Evanston, Illinois.
- [16] Bazant, Z. P., and Lin, F. B. (1989). "Nonlocal Smeared Cracking Model for Concrete Fracture." *Journal of Structural Engineering*, 114(11), 2493-2511.
- [17] Bazant, Z. P., and Oh, B. H. (1983). "Crack band theory for fracture of concrete." *Materials and Structures*, 16(1), 155-177.
- [18] Bazant, Z. P., and Yu, Q. (2005). "Designing Against Size Effect on Shear Strength of reinforced Concrete Beams Without Stirrups: 2. Verification and Calibration." *Journal of Structural Engineering*, 131(12), 1886-1896.
- [19] Bazant, Z. P., and Yu, Q. (2010). "Modelling of concrete creep and hygrothermal deformations, and computation of their structural effects." *Computational Modelling of Concrete Structures: EURO-C 2010*, Rohrmoos/Schladming.

- [20] Belarbi, A. (1991). "Stress-Strain Relationships of Reinforced Concrete in Biaxial Tension-Compression," Doctoral Thesis, University of Houston, Houston.
- [21] Belarbi, A., and Hsu, T. T. C. (1994). "Constitutive Laws of Concrete in Tension and Reinforcing Bars Stiffened by Concrete." *ACI Structural Journal*, 91(4), 465-474.
- [22] Belarbi, A., and Hsu, T. T. C. (1995). "Constitutive Laws of Softened Concrete in Biaxial Tension-Compression." *ACI Structural Journal*, 92(5), 562-573.
- [23] Belletti, B., Cerioni, R., and Ivori, I. (2001). "Physical Approach for Reinforced-Concrete (PARC) Membrane Elements." *Journal of Structural Engineering*, 127(12), 1412-1426.
- [24] Bentz, E. C. (2000). "Sectional Analysis of Reinforced Concrete Members," Doctoral Thesis, University of Toronto, Toronto.
- [25] Bentz, E. C. (2005). "Explaining the Riddle of Tension Stiffening Models for Shear Panel Experiments." *Journal of Structural Engineering*, 131(9), 1422-1425.
- [26] Bentz, E. C., and Collins, M. P. (2006). "Development of the 2004 Canadian Standards Association (CSA) A23.3 shear provisions for reinforced concrete." *Canadian Journal of Civil Engineering*, 33, 521-534.
- [27] Bhide, S. B., and Collins, M. P. (1989). "Influence of Axial Tension on the Shear Capacity of Reinforced Concrete Members." *ACI Structural Journal*, 86(5), 570-581.
- [28] Bloem, D. L. (1968). "Concrete Strength in Structures." *ACI Journal*, 65(3), 176-187.
- [29] Borst, R. (1986). "Nonlinear Analysis of Frictional Materials," Doctoral Thesis, Technical University of Delft, Delft.
- [30] Borst, R. (1987). "Smearred cracking, plasticity, creep and thermal loading - A unified approach." *Computer Methods in Applied Mechanics and Engineering*, 62(1), 89-110.
- [31] Borst, R. (1993). "A generalization of J2-flow theory for polar continua." *Computer Methods in Applied Mechanics and Engineering*, 103, 347-362.
- [32] Borst, R., and Boogaard, A. H. (1994). "Finite-Element Modeling of Deformation and Cracking in Early-Age Concrete." *Journal of Engineering Mechanics*, 120(12), 2519-2534.
- [33] Borst, R., and Mühlhaus, H.-B. (1992). "Gradient-dependent plasticity: Formulation and algorithmic aspects." *International Journal for Numerical Methods in Engineering*, 35, 521-539.
- [34] Borst, R., and Nauta, P. (1985). "Non-orthogonal cracks in a smeared finite element model." *Engineering Computations*, 2, 35-46.
- [35] Borst, R., Sluys, L. J., Mühlhaus, H.-B., and Pamin, J. (1993). "Fundamental issues in finite element analyses of localization of deformation." *Engineering Computations*, 10, 99-121.
- [36] BRIME. (2001). "Deliverable D14 - Final Report." Available from: <http://www.trl.co.uk/brime/deliver.htm>.
- [37] Bujadham, B., and Maekawa, K. (1992). "The Universal Model for Stress Transfer Across Cracks in Concrete." *Proc. of the JSCE*, 17, 277-287.
- [38] Campbell, R. H., and Tobin, R. E. (1967). "Core and Cylinder Strengths of Natural and Lightweight Concrete." *ACI Journal*, 64(4), 190-195.
- [39] Carino, N. J., and Malhotra, V. M. (2004). "Handbook on Non-destructive Testing of Concrete." CRC Press, Boca Raton.
- [40] CEB. (1993). *CEB-FIP Model Code 1990*, Thomas Telford, London.
- [41] CEB. (1996). "RC elements under cyclic loading. State-of-the-art report.", Thomas Telford, London.
- [42] CEN. (2002). *EN 1990 - Eurocode: Basis of structural design*, European Committee for Standardization, Brussels.
- [43] CEN. (2003). *EN 1991-2 Eurocode 1: Actions on structures - Part 2: Traffic loads on bridges*, European Committee for Standardization, Brussels.

-
- [44] CEN. (2003). *NP EN 12504-1:2003 Ensaios do betão nas estruturas - parte 1: Carotes. Extração, exame e ensaio à compressão*, IPQ.
- [45] CEN. (2003). *NP EN 12504-2:2003 Ensaios do betão nas estruturas - parte 2: Ensaio não destrutivo. Determinação do índice esclerométrico.*, IPQ.
- [46] CEN. (2004). *Eurocode 2: Design of concrete structures - Part 1-1: General rules and rules for buildings*, European Comitee for Standardization, Brussels.
- [47] CEN. (2007). *NP EN 12504-2:2007 Ensaios do betão nas estruturas - parte 3: Determinação da força de arranque*, IPQ.
- [48] CEN. (2007). *NP EN 12504-2:2007 Ensaios do betão nas estruturas - parte 4: Determinação da velocidade de propagação dos ultra-sons*, IPQ.
- [49] CEN. (2008). *NP EN 13791 - Avaliação da resistência á compressão do betão nas estruturas e em produtos pré-fabricados*, IPQ.
- [50] CEN. (2009). *NP EN 1991-5:2009. Eurocódigo 1 - Acções em estruturas. Parte 1-5: Acções gerais. Acções térmicas.* , IPQ.
- [51] CEN TC 250/SC2. (2008). *Eurocode 2 Commentary*, European Concrete Platform, Brussels.
- [52] Cerioni, R., Iori, I., Michelini, E., and Bernadi, P. (2008). "Multi-directional modeling of crack pattern in 2D R/C members." *Engineering Fracture Mechanics*, 75, 615-628.
- [53] Cerruti, L. M., and Marti, P. (1987). "Staggered shear design of concrete beams: large-scale tests." *Canadian Journal of Civil Engineering*, 14, 257-268.
- [54] Cervenka, J., and Cervenka, V. (2010). "On the uniqueness of numerical solutions of shear failure of deep concrete beams: Comparison of smeared and discrete crack approaches." *EURO-C 2010: Computational modelling of concrete structures*, 281-290.
- [55] Cervenka, V. (2008). "Global Safety Factor for Nonlinear Calculation of Reinforced Concrete." *Beton- und Stahlbetonbau*, 103, 37-42.
- [56] Cervenka, V., and Cervenka, J. (1996). "Computer simulation as a design tool for concrete structures." *ICCE-96 - Second International Conference in Civil Engineering on Computer Applications, Research and Practice*, Bahrain.
- [57] Cervenka, V., Pukl, R., Ozbolt, J., and Eligehausen, R. (1995). "Mesh sensitivity effects in smeared finite element analysis of concrete fracture." *Fracture Mechanics of Concrete structures (FRAMCOS II)*, Zurich, 1387-1396.
- [58] Chen, W. F. (1982). *Plasticity in Reinforced Concrete*, McGraw-Hill.
- [59] Chintrakarn, R. (2001). "Minimum Shear Steel and Failure Modes Diagram of Reinforced Concrete Membrane Elements," Master Thesis, University of Houston, Houston.
- [60] Collins, M. P. (1978). "Towards a Rational Theory for RC Members in Shear." *Journal of the Structural Division ASCE*, 104(4), 649-666.
- [61] Collins, M. P. (1998). "Procedures for Calculating the Shear Response of Reinforced Concrete Elements: A Discussion." *Journal of Structural Engineering*, 124(12), 1485-1488.
- [62] Collins, M. P., and Kuchma, D. (1999). "How Safe Are Our Large, Lightly Reinforced Concrete Beams, Slabs, and Footings?" *ACI Structural Journal*, 96(4), 482-490.
- [63] Collins, M. P., Mitchell, D., Adebar, P., and Vecchio, F. J. (1996). "A General Shear Design Method." *ACI Structural Journal*, 93(1), 36-45.
- [64] Cornelissen, H. A. W., Hordijk, D. A., and Reinhardt, H. W. (1986). "Experimental determination of crack softening characteristics of normal weight and lightweight concrete." *Heron*, 31(2).
- [65] COST-345. (2004). "Procedures Required for Assessing Highway Structures - Joint report of Working Groups 2 and 3: methods used in European States to inspect and assess the condition of highway structures." European Commission - Directorate General Transport and Energy. Available from: http://cost345.zag.si/final_reports.htm.

- [66] COST-345. (2004). "Procedures Required for the Assessment of Highway Structures - Final report." European Commission - Directorate General Transport and Energy. Available from: http://cost345.zag.si/final_reports.htm.
- [67] Costeira Silva, P. (2008). "Comportamento de Estruturas de Betão Reforçadas por Colagem Exterior de Sistemas CFRP," Doctoral Thesis, Faculty of Engineering of the University of Porto, Porto.
- [68] Costeira Silva, P., Juvandes, L., and Figueiras, J. A. (2005). "Inspeção Visual das Paredes do Caixão do Tabuleiro da Ponte de N. S. da Guia - Relatório Interno." LABEST, Universidade do Porto, Faculdade de Engenharia, Porto.
- [69] Crisfield, M. A. (1981). "A fast incremental/iterative solution procedure that handles snap-through." *Computer & Structures*, 13, 55-62.
- [70] Crisfield, M. A. (1991). *Non-linear Finite Element Analysis of Solids and Structures, vol. 1: Essentials*, John Wiley & Sons, Chichester.
- [71] Crisfield, M. A., and Wills, J. (1989). "Analysis of R/C Panels Using Different Concrete Models." *Journal of Engineering Mechanics*, 115(3), 578-597.
- [72] CSA. (2004). *Design of Concrete Structures, CSA A23.3-04*, Canadian Standards Association.
- [73] Dérobert, X., Aubagnac, C., and Abraham, O. (2002). "Comparison of NDT techniques on a post-tensioned beam before its autopsy." *NDT&E international*, 35, 541-548.
- [74] Dias da Silva, V. (1995). *Mecânica e Resistência dos Materiais*, EDILIBER Editora, Coimbra.
- [75] Elices, M., and Planas, J. (1989). "Material Models." *Fracture Mechanics of Concrete Structures*. Report of the RILEM Comitee 90-FMA, L. Elfgren, ed., Chapman and Hall, London, 16-66.
- [76] Feenstra, P. H. (1993). "Computational Aspects of Biaxial Stress in Plain and Reinforced Concrete," Doctoral Thesis, Delft University of Technology, Delft.
- [77] Feenstra, P. H., Borst, R., and Rots, J. G. (1991). "Numerical Study on Crack Dilatancy. II: Applications." *Journal of Engineering Mechanics*, 117(4), 754-769.
- [78] Félix, C. (2004). "Monitorização e análise do comportamento de obras de arte," Doctoral Thesis, Faculdade de Engenharia da Universidade do Porto, Porto.
- [79] Fernández-Ruiz, M., and Muttoni, A. (2007). "On Development of Suitable Stress Fields for Structural Concrete." *ACI Structural Journal*, 104(4), 495-502.
- [80] Fernández-Ruiz, M., and Muttoni, A. (2008). "Shear Strength of Thin-Webbed Post-Tensioned Beams." *ACI Structural Journal*, 105(3), 308-317.
- [81] Fernández-Ruiz, M., and Muttoni, A. (2009). "Applications of Critical Shear Crack Theory to Punching of Reinforced Concrete Slabs with Transverse Reinforcement." *ACI Structural Journal*, 106(4), 485-494.
- [82] Fernández-Ruiz, M., Rodrigues, R. V., and Muttoni, A. (2009). "Dimensionnement et vérification des dalles de roulement des ponts routiers." Ecole Polytechnique Fédérale de Lausanne (EPFL), Laboratoire de Construction en Béton (IS-BETON), Office fédéral des routes (OFROU), Lausanne.
- [83] Ferraz, M. (2010). "Modelo para avaliação do comportamento estrutural de obras de arte," Doctoral Thesis, Faculdade de Engenharia da Universidade do Porto, Porto.
- [84] fib. (1999). "Bulletin nº1: Structural Concrete. Text book on Behaviour, Design and Performance. Vol.1." fib, Lausanne.
- [85] fib. (2000). "Fib bulletin 10: Bond of reinforcement in concrete - State-of-art report." fib, Lausanne.
- [86] fib. (2008). "A Practitioner's Guide to Computer-Based Modelling of Structural Concrete (bulletin 45)." fib, Lausanne.
- [87] fib. (2010). *Model Code 2010 - First complete draft*, fib, Lausanne.
- [88] Figueiras, J., Juvandes, L., and Oliveira, L. (1999). "Reforço Experimental da Laje do Tabuleiro da Ponte de N. S. da Guia em Ponte de Lima - Relatório Técnico." LABEST, Universidade do Porto, Faculdade de Engenharia, Porto.

- [89] Figueiras, J. A. (1983). "Ultimate Load Analysis of Anisotropic and reinforced Concrete Plates and Shells," Doctoral Thesis, University College of Swansea, Swansea, Wales.
- [90] Frigerio, T., Mariscotti, M. A. J., Ruffolo, M., and Thieberger, P. (2004). "Development and application of computed tomography in the inspection of reinforced concrete." *Insight*, 46(12).
- [91] Gaspar, R., and Stucchi, F. R. (2009). "Dimensionamento das almas de pontes celulares." *Revista Portuguesa de Engenharia de Estruturas*, Série II(6), 41-46.
- [92] Gonçalves, A. F. (1987). "Resistência do betão nas estruturas," Doctoral Thesis, Laboratório Nacional de Engenharia Civil, Lisboa.
- [93] Hadamard, J. (1902). "Sur les problèmes aux dérivées partielles et leur signification physique." *Princeton University Bulletin*, 49-52. .
- [94] Hawkins, N. M., and Kuchma, D. A. (2007). "NCHRP Report 579 - Application of LFRD Bridge design Specifications to High-Strength Structural Concrete: Shear Provisions." Transportation Research Board, Washinton, D.C.
- [95] Hawkins, N. M., and Kuchma, D. A. (2007). "NCHRP Report 579 - Application of LFRD Bridge design Specifications to High-Strength Structural Concrete: Shear Provisions (Appendices)." Transportation Research Board, Washington, D.C.
- [96] Henriques, A. A. (1998). "Aplicação de Novos Conceitos de Segurança no Dimensionamento do Betão Estrutural," Doctoral Thesis, Faculdade de Engenharia da Universidade do Porto, Porto.
- [97] Hernandez, H. D., and Gamble, W. L. (1975). "Time-dependent losses in prestressed concrete construction." University of Illinois.
- [98] Higgins, C., Miller, T. H., Rosowsky, D. V., Solomon, C. Y., Potistouk, T., Daniels, T. K., Nicholas, B. S., Robelo, M. J., Lee, A.-Y., and Forrest, R. W. (2004). "Assessment methodology for diagonally cracked reinforced concrete deck girders - Final Report SPR 350, SR 500-091." Oregon Department of Transportation (ODOT) and Federal Highway Administration (FHWA).
- [99] Hillerborg, A., Modéer, M., and Petersson, P. E. (1976). "Analysis of crack formation and crack growth in concrete by means of fracture mechanics and finite elements." *Cement and Concrete Research*, 6, 773-782.
- [100] Hoang, L. C., and Nielsen, M. P. (1998). "Plasticity Approach to Shear Design." *Cement and Concrete Composites*, 20, 437-453.
- [101] Hordijk, D. A. (1992). "Tensile and tensile fatigue behaviour of concrete: experiments, modelling and analyses." *Heron*, 37(1), 1-79.
- [102] Hordijk, D. A., Van Mier, J. G. M., and Reinhardt, H. W. (1989). "Material Properties." Fracture Mechanics of Concrete Structures. Report of the RILEM Comitee 90-FMA, L. Elfgren, ed., Chapman and Hall, London, 67-127.
- [103] Hsieh, S.-S. (1981). "Elastic-plastic-fracture analysis of concrete structures," Doctoral Thesis, Purdue University.
- [104] Hsu, T. T. C., and Zhang, L. (1996). "Tension Stiffening in Reinforced Concrete Membrane Elements." *ACI Structural Journal*, 93(1), 108-115.
- [105] Hsu, T. T. C., and Zhang, L. X. (1997). "Nonlinear Analysis of Membrane Elements by Fixed-Angle Softened-Truss model." *ACI Structural Journal*, 94(5), 483-492.
- [106] Hsu, T. T. C., and Zhu, R. R. H. (2002). "Softened Membrane Model for Reinforced Concrete Elements in Shear." *ACI Structural Journal*, 99(4), 460-469.
- [107] Ingraffea, A., and Saouma, V. (1985). "Numerical modelling of discrete crack propagation in reinforced and plain concrete." Engineering Application of Fracture Mechanics, G. C. Sih and A. D. Tommaso, eds., Martinus Nijhoff Publishers, Dordrecht, The Netherlands.
- [108] Jansen, D. C., and Shah, S. P. (1997). "Effect of Length on Compressive Strain Softening of Concrete." *Journal of Engineering Mechanics*, 123(1), 25-35.

- [109] JCSS. (2001). "Probabilistic Assessment of Existing Structures - JCSS Report." D. Diamantidis, ed., RILEM Publications SARL
- [110] Jirasek, M. (1998). "Nonlocal Models for Damage and Fracture: Comparison of Approaches." *International Journal of Solids and Structures*, 35(31), 4133-4145.
- [111] Jirasek, M. (2000). "Comparative study on finite elements with embedded discontinuities " *Computer Methods in Applied Mechanics and Engineering*(188), 307-330.
- [112] Jirasek, M. (2002). "Plasticity, Damage and Fracture." Technical University of Catalonia (UPC), Barcelona.
- [113] Jirasek, M., and Horák, M. (2010). "Localization properties of damage models." *EURO-C 2010: Computational modelling of concrete structures*, 327-336.
- [114] Jirasek, M., Rolshoven, S., and Grassl, P. (2004). "Size effect on fracture energy induced by non-locality " *International Journal for Numerical and Analytical Methods in Geomechanics*, 28(7-8), 653-670.
- [115] Jirasek, M., and Zimmerman, T. (1998). "Analysis of Rotating Crack Model." *Journal of Engineering Mechanics*, 124(8), 842-851.
- [116] Kang, H. D., and Willam, K. (1999). "Localization Characteristics of Triaxial Concrete Model." *Journal of Engineering Mechanics*, 125(8), 941-950.
- [117] Kaufmann, W. (1998). "Strength and Deformations of Structural Concrete Subjected to In-Plane Shear and Normal Forces," Doctoral Thesis, Swiss Federal Institute of Technology Zurich, Zurich.
- [118] Kaufmann, W. (2002). "Analysis and design of structural concrete elements subjected to in-plane forces." *Structural Concrete, Journal of the fib*, 3(3), 155-159.
- [119] Kaufmann, W., and Marti, P. (1996). "Versuche an Stahlbetonträgern unter Normal- und Querkraft." Swiss Federal Institute of Technology Zürich, Zürich.
- [120] Kaufmann, W., and Marti, P. (1998). "Structural Concrete: Cracked Membrane Model." *Journal of Structural Engineering*, 124(12), 1467-1475.
- [121] Kenel, A. (2002). "Biegetragverhalten und Mindestbewehrung von Stahlbetonbauteilen," Doctoral Thesis, Swiss Federal Institute of Technology Zurich, Zurich.
- [122] Kenel, A., Nellen, P., Frank, A., and Marti, P. (2005). "Reinforcing Steel Strains Measured by Bragg Grating Sensors." *Journal of Materials in Civil Engineering*, 17(4), 423-431.
- [123] Kirschner, U. (1986). "Investigating the behaviour of reinforced concrete shell elements," Doctoral Thesis, University of Toronto, Toronto.
- [124] Kotsovos, M. D., and Pavlovic, M. N. (1995). *Structural Concrete. Finite element analysis for limit-state design.*, Thomas Telford, London.
- [125] Krätzig, W. B., and Pölling, R. (2004). "An elasto-plastic damage model for reinforced concrete with minimum number of material parameters." *Computer & Structures*, 82, 1201-1215.
- [126] Kristek, V., Bazant, Z. P., Zich, M., and Kohoutkova, A. (2005). "Why is the Initial trend of Deflections of Box Girder Bridges Deceptive?" *Creep, Shrinkage and Durability of Concrete Structures: CONCREEP 7*, Nantes.
- [127] Kuchma, D., Kim, K. S., Nagle, T., Sun, S., and Hawkins, N. M. (2008). "Shear Tests on High-Strength Prestressed Bulb-Tee Girders: Strengths and Key Observations." *ACI Structural Journal*, 105(3), 358-367.
- [128] Kupfer, H. B., and Gerstle, K. H. (1973). "Behaviour of Concrete Under Biaxial Stresses." *Journal of Engineering Mechanics Division*, 99(EM4), 853-866.
- [129] L'Hermite, R. (1955). *Idées actuelles sur la technologie du béton*, Documentation Techniq. Batiment Et Travaux Publics, Paris.
- [130] Laurencet, P. (1999). "Précontrainte et armature pour contrôler l'ouverture résiduelle des fissures," Doctoral Thesis, École Polytechnique Fédérale de Lausanne (EPFL), Lausanne.

-
- [131] Leonhardt, F., and Walther, R. (1962). "Versuche an Plattenbalken mit hoher Schubbeanspruchung." Deutscher Ausschuss für Stahlbeton (Heft 152), Berlin.
- [132] Levi, F., and Marro, P. (1989). "Shear tests up to failure of beams made with normal and high strength concrete." *Bulletin d'Information 193 - Design Aspects of High Strength Concrete*, CEB, Lausanne.
- [133] Li, B., Maekawa, K., and Okamura, H. (1989). "Contact Density Model for Stress Transfer across Cracks in Concrete." *Journal of the Faculty of Engineering of Tokyo*, XL(1), 9-52.
- [134] Lourenço, P., and Figueiras, J. A. (1993). "Automatic Design of Reinforcement in Concrete Plates and Shells." *Engineering Computations*, 10(6).
- [135] Lourenço, P. B. (1996). "Computational strategies for masonry structures," Doctoral thesis, Technische Universiteit Delft, Delft.
- [136] Maekawa, K., and Okamura, H. (1983). "The Deformational Behavior and Constitutive Equation of Concrete Using the Elasto-Plastic and Fracture Model." *Journal of the Faculty of Engineering of Tokyo*, XXXVII(2).
- [137] Maekawa, K., Pimanmas, A., and Okamura, H. (2003). *Nonlinear Mechanics of Reinforced Concrete*, Spoon Press, London.
- [138] Maierhofer, C., Krause, M., Mielentz, F., Streicher, D., Milmann, B., Gardei, A., Kohl, C., and Wiggerhauser, W. (2007). "Complementary Application of Radar, Impact-Echo, and Ultrasonics for Testing Concrete Structures and Metallic Tendon Ducts " *Transportation Research Record: Journal of the Transportation Research Board*, 1892, 170-177.
- [139] Malm, R., and Sundquist, H. (2010). "Time-dependent analyses of segmentally constructed balanced cantilever bridges " *Engineering Structures*, 32(4), 1038-1045
- [140] Mariscotti, M. A. J. (2008). "Gammagraphic Study of the N.S. da GUIA bridge." THASA, Buenos Aires.
- [141] Mariscotti, M. A. J., Jalinoos, F., Frigerio, T., Ruffolo, M., and Thieberger, P. (2008). "Gamma-ray imaging for void and corrosion assessment in PT girders." *NDE/NDT for Highways and Bridges - Structural Materials Technology (SMT)*, Oakland.
- [142] Mariscotti, M. A. J., Jalinoos, F., Frigerio, T., Ruffolo, M., and Thieberger, P. (2009). "Gamma-Ray Imaging for Void and Corrosion Assessment " *Concrete International*(November 2009), 48-53.
- [143] Mariscotti, M. A. J., Thieberger, P., Frigerio, T., and Ruffolo, M. (2007). "Method and device for improving tomographic determinations, particularly suitable for inspection of steel reinforcement bars in concrete structures." Tomografia De Hormigon Armado S.A., US patent office, application number PCT-US2007/2286.
- [144] Markeset, G., and Hillerborg, A. (1995). "Softening of concrete in compression - Localization and size effects." *Cement and Concrete Research*, 25(4), 702-708.
- [145] Marti, P. (1980). "Zur plastischenberechnung von stahlbeton," Doctoral Thesis, Swiss Federal Institute of Technology Zurich, Zurich.
- [146] Marti, P. (1985). "Basic Tools for Reinforced Concrete Design." *ACI Journal*, 82(1), 46-56.
- [147] Marti, P. (1985). "Truss models in detailing." *Concrete International*, 7(12), 66-73.
- [148] Marti, P. (1986). "Staggered Shear Design of Simply Supported Concrete Beams." *ACI Journal*, 83(1), 36-42.
- [149] Marti, P. (1991). "Dimensioning and Detailing." *IABSE Colloquium Stuttgart 1991: Structural Concrete*, IABSE, Stuttgart.
- [150] Marti, P. (1999). "How to Treat Shear in Structural Concrete." *ACI Structural Journal*, 96(3), 408-415.
- [151] Marti, P., Alvarez, M., Kaufmann, W., and Sigrist, V. (1998). "Tension Chord Model for Structural Concrete." *Structural Engineering International*, 98(4), 287-298.
- [152] Marti, P., and Meyboom, J. (1992). "Response of Prestressed Concrete Elements to In-Plane Shear Forces." *ACI Structural Journal*, 89(5), 503-514.

- [153] McCann, D. M., and Forde, M. C. (2001). "Review of NDT methods in the assessment of concrete and masonry structures." *NDT&E international*, 34, 71-84.
- [154] Menn, C. (1990). *Prestressed Concrete Bridges*, Birkhäuser Verlag, Basel.
- [155] Middleton, C. (2004). "Bridge Management and Assessment in the UK (Invited keynote lecture)." *Austroroads 5th Bridge Conference*, Hobart, Australia.
- [156] Mietz, J., and Fischer, J. (2007). "Evaluation of NDT methods for detection of prestressing steel damage at post-tensioned concrete structures." *Materials and Corrosion*, 58(10), 789-794.
- [157] Mirambell, E., and Aguado, A. (1990). "Temperature differences and stress distributions in concrete box-girder bridges." *Journal of Structural Engineering*, 116(9), 2388-2409.
- [158] Mirambell, E., Aguado, A., Mendes, P. A., and Branco, F. A. (1991). "Design Temperature Differences for Concrete Bridges." *Structural Engineering International*, 1(3), 36-40.
- [159] Mitchell, D., and Collins, M. P. (1974). "Diagonal Compression Field Theory - A Rational Model for Structural Concrete in Pure Torsion." *ACI Journal*, 71(8), 396-408.
- [160] Miyahara, T., Kawakami, T., and Maekawa, K. (1988). "Nonlinear Behavior of Cracked reinforced Concrete Plate Element under Uniaxial Compression." *Concrete Library International, JSCE*, 11, 303-319.
- [161] Mohr, S., Bairán, J., and Marí, A. (2010). "A frame element model for the analysis of reinforced concrete structures under shear and bending." *Engineering structures*, 32(12), 3936-3954
- [162] Müller, P. (1978). "Plastische Berechnung von Stahlbetonscheiben und -balken," Doctoral Thesis, Swiss Federal Institute of Technology Zurich, Zurich.
- [163] Muttoni, A. (1990). "Die Anwendbarkeit der Plastizitätstheorie in der Bemessung von Stahlbeton " *Bericht Nr. 176*, Swiss Federal Institute of Technology Zürich, Zurich.
- [164] Muttoni, A. (2008). "Punching Shear Strength of Reinforced Concrete Slabs without Transverse Reinforcement." *ACI Structural Journal*, 105(4), 440-450.
- [165] Muttoni, A., Burdet, O., and Hars, E. (2006). "Effect of Duct Type on Shear Strength of Thin Webs." *ACI Structural Journal*, 103(5), 729-735.
- [166] Muttoni, A., and Fernández-Ruiz, M. (2008). "Shear Strength of Members Without Transverse Reinforcement as Function of Critical Shear Crack Width." *ACI Structural Journal*, 105(2), 163-172.
- [167] Muttoni, A., Schwartz, J., and Thurlimann, B. (1997). *Design of Concrete Structures with Stress Fields*, Birkhäuser Verlag, Basel.
- [168] Nielsen, M. P. (1971). "On the strength of reinforced concrete discs." *Acta Polytechnica Scandinavica, Civil Engineering and Building Construction series*, No. 70, Copenhagen.
- [169] Nielsen, M. P. (1984). *Limit Analysis and Concrete Plasticity*, Prentice-Hall, New Jersey.
- [170] Nordisk Komité for Bygningsbestemmelser. (1978). "Retningslinier for last- og sikkerhedsbestemmelser for bærende konstruktioner, NKB-rapport nr. 35."
- [171] Okamura, H., and Maekawa, K. (1991). *Nonlinear Analysis and Constitutive Models of Reinforced Concrete*, Gihodo-Shuppan Co., Tokyo.
- [172] Oliver, J., and Dias, I. F. (2010). "Strong discontinuities, mixed finite element formulations and localized strain injection, in fracture modelling of quasi-brittle materials." *EURO-C 2010: Computational modelling of concrete structures*, 381-389.
- [173] Oliver, J., and Huespe, A. E. (2004). "Continuum approach to material failure in strong discontinuity settings." *Computer Methods in Applied Mechanics and Engineering*(193), 3195-3220.
- [174] Oliver, J., Huespe, A. E., and Sánchez, P. J. (2006). "A comparative study on finite elements for capturing strong discontinuities: E-FEM vs X-FEM." *Computer Methods in Applied Mechanics and Engineering*(195), 4732-4752.

- [175] Oliver, J., Linero, D. L., Huespe, A. E., and Manzoli, O. L. (2008). "Two-dimensional modeling of material failure in reinforced concrete by means of a continuum strong discontinuity approach." *Computer Methods in Applied Mechanics and Engineering*, 197, 332-348.
- [176] Oñate, E. (1995). *Calculo de estructuras por el metodo de elementos finitos: análisis estático lineal* CIMNE - Centro Internacional de Métodos Numéricos en Ingeniería, Barcelona.
- [177] Ottosen, N. S. (1977). "A failure criterion for concrete." *Journal of Engineering Mechanics Division - ASCE*, 103(527-535).
- [178] Pang, X. (1991). "Constitutive Laws of Reinforced Concrete in Shear," Doctoral Thesis, University of Houston, Houston.
- [179] Pang, X., and Hsu, T. T. C. (1995). "Behaviour of Reinforced Concrete Membrane Elements in Shear." *ACI Structural Journal*, 92(6), 665-679.
- [180] Pang, X., and Hsu, T. T. C. (1996). "Fixed Angle Softened Truss Model for Reinforced Concrete." *ACI Structural Journal*, 93(2), 197-207.
- [181] Papanikolaou, V. K., and Kappos, A. J. (2007). "Confinement-sensitive plasticity constitutive model for concrete in triaxial compression." *International Journal of Solids and Structures*, 44, 7021-7048.
- [182] Peerlings, R. H. J., Borst, R., Brekelmans, W. A. M., and Vree, J. H. P. (1996). "Gradient enhanced damage for quasi-brittle materials." *International Journal for Numerical Methods in Engineering*, 39, 3391-3403.
- [183] Petersons, N. (1968). "Should standard cube test specimens be replaced by test specimens taken from structures?" *Materiaux et Constructions*, 1(5), 425-435.
- [184] Pimentel, M., Mariscotti, M. A. J., and Figueiras, J. (2009). "Inspeção não destrutiva dos cabos de pré-esforço da Ponte de N. S. da Guia através da tomografia por raios gama " *ASCP'09 – 1º Congresso de Segurança e Conservação de Pontes*, Lisboa.
- [185] Pimentel, M., Santos, J., and Figueiras, J. (2007). "Monitoring and Detailed Modelling for extending the Lifespan of a 30 years Old Prestressed Concrete Bridge." *Structural Faults & Repair 2008: 12th International Conference*, Edinburgh.
- [186] Pimentel, M., Santos, J., and Figueiras, J. (2008). "Inspeção, monitorização e avaliação de segurança da Ponte de N. S. da Guia." *Betão Estrutural 2008*, Guimarães.
- [187] Pimentel, M., Santos, J., and Figueiras, J. (2008). "Safety appraisal of an existing bridge via detailed modelling." *International fib Symposium 2008*, Amsterdam.
- [188] Polak, M. A., and Vecchio, F. J. (1994). "Reinforced Concrete Shell Elements Subjected to Bending and Membrane Loads." *ACI Structural Journal*, 91(3), 261-268.
- [189] Póvoas, R. H. C. P. (1991). "Modelos não-lineares de análise e dimensionamento de estruturas laminares de betão incluindo os efeitos diferidos," Tese de Doutoramento, Faculdade de Engenharia da Universidade do Porto, Porto.
- [190] Pramono, E., and Willam, K. (1989). "Fracture Energy-Based Plasticity Formulation of Plain Concrete." *Journal of Engineering Mechanics*, 115(6), 1183-1204.
- [191] Ramm. (1981). "Strategies for tracing the nonlinear response near limit points." *Nonlinear Finite Element Analysis in Structural Mechanics*, Bochum, 63-83.
- [192] Reineck, K.-H. (1989). "Theoretical considerations and experimental evidence on web compression failures of high strength concrete beams." *Bulletin d'Information 193 - Design Aspects of High Strength Concrete*, CEB, Lausanne.
- [193] RILEM. (1994). "Draft recommendation for repair strategies for concrete structures damaged by reinforcement corrosion." *Materials and Structures*, 27, 415-436.
- [194] Robertson, I. N. (2005). "Prediction of vertical deflections for a long-span prestressed concrete bridge structure." *Engineering Structures*, 27(12), 1820-1827.
- [195] Robinson. (1961). "Essais a l'effort tranchant de poutres a ame mince en beton arme." *Annales de Ponts et Chaussées*, 131(2), 225-255.

- [196] Rodrigues, R. V., Muttoni, A., and Fernandez-Ruiz, M. (2010). "Influence of Shear on Rotation Capacity of Reinforced Concrete Members Without Shear Reinforcement." *ACI Structural Journal*, 107(5), 516-525.
- [197] Rots, J. G. (1988). "Computational Modelling of Concrete Fracture," Doctoral Thesis, Technical University of Delft, Delft.
- [198] Rots, J. G., and Blaauwendraad, J. (1989). "Crack models for concrete: Discrete or smeared? Fixed, multi-directional or rotating." *Heron*, 34(1).
- [199] Rots, J. G., Nauta, P., Kusters, G. M. A., and Blaauwendraad, J. (1985). "Smeared crack approach and fracture localization in concrete." *Heron*, 30(1).
- [200] RSAEP. (1983). *Regulamento de Segurança e Acções para Estruturas de Edifícios e Pontes: D.L. 235/83 de 31 de Maio*, Lisboa.
- [201] RSEP. (1961). *Regulamento de Solicitações em Edifícios e Pontes: Decreto n.º 44041, de 18 de Novembro de 1961, e Portaria n.º 713/71, de 23 de Dezembro*, Imprensa Nacional, Lisboa.
- [202] SAMARIS. (2006). "Deliverable D30 - Guidance for the optimal assessment of highway structures." Available from: www.fehrl.org/?m=32&id_directory=356.
- [203] Santos, J., Dimande, A., Pimentel, M., and Figueiras, J. (2007). "Inspeção Ensaio de Carga e Modelação do Comportamento da Ponte de N. S. da Guia em Ponte de Lima - Parte 2: Ensaio de Carga." LABEST, Universidade do Porto, Faculdade de Engenharia, Porto.
- [204] Santos, J., Figueiras, H., and Figueiras, J. (2007). "Inspeção Ensaio de Carga e Modelação do Comportamento da Ponte de N. S. da Guia em Ponte de Lima - Parte 1: Relatório de Inspeção." LABEST, Universidade do Porto, Faculdade de Engenharia, Porto.
- [205] Santos, J., Pimentel, M., and Figueiras, J. (2007). "Inspeção Ensaio de Carga e Modelação do Comportamento da Ponte de N. S. da Guia em Ponte de Lima - Parte 3: Modelação e Análise da Segurança Estrutural." LABEST, Universidade do Porto, Faculdade de Engenharia, Porto.
- [206] Santos, L. O. (2001). "Observação e Análise do Comportamento Diferido de Pontes de Betão," Doctoral Thesis, Instituto Superior Técnico, Lisboa.
- [207] Sato, Y., and Fuji, S. (2002). "Local Stresses and Crack Displacements in Reinforced Concrete Elements." *Journal of Structural Engineering*, 128(10), 1263-1271.
- [208] Schlaich, J., and Schafer, K. (1991). "Design and Detailing of Structural Concrete Using Strut-and-Tie Models." *The Structural Engineer*, 69(6), 113-125.
- [209] Schlaich, J., Schafer, K., and Jennewein, M. (1987). "Towards a consistent design of structural concrete." *PCI-Journal*, 32(3), 74-150.
- [210] Schlune, H., Plos, M., and Gylltoft, K. (2011). "Safety formats for nonlinear analysis tested on concrete beams subjected to shear forces and bending moments." *Engineering structures*, (Article in press, doi: 10.1016/j.engstruct.2011.04.008).
- [211] Schneider, J. (2006). *Introduction to Safety and Reliability of Structures*, IABSE, Zurich.
- [212] Scholten, C., Enevoldsen, I., Arnbjerg-Nielsen, T., Randrup-Thompsen, S., Sloth, M., Englund, S., and Faber, M. (2004). *Reliability-Based Classification of the Load Carrying Capacity of Existing Bridges - Guideline Document (Report 291)*, Road Directorate, Copenhagen.
- [213] Selby, R. G., Vecchio, F. J., and Collins, M. P. (1996). "Analysis of Reinforced Concrete Members Subjected to Shear and Axial Compression." *ACI Structural Journal*, 93(3), 306-315.
- [214] Shima, H., Chou, L., and Okamura, H. (1987). "Micro and Macro Models for Bond in Reinforced Concrete." *Journal of the Faculty of Engineering of Tokyo*, XXXIX(2), 133-194.
- [215] SIA269. (2010). *SIA 269 - Bases pour la maintenance des structures porteuses*, SIA, Zurich.
- [216] Sigrist, V. (1995). "Zum Verformungsvermögen von Stahlbetonträgern," Doctoral Thesis, Swiss Federal Institute of Technology Zurich, Zurich.

-
- [217] Sigrist, V., Alvarez, M., and Kaufmann, W. (1995). "Shear and Flexure in Structural Concrete Beams." *Bulletin d'Information 223 - Ultimate Limit State Design Models*, CEB, Lausanne.
- [218] Sigrist, V., and Marti, P. (1993). "Versuche zum Verformungsvermögen von Stahlbetonträgern." Swiss Federal Institute of Technology Zürich, Zürich.
- [219] Silveira, A. (1996). "A Influência das Acções Térmicas no Comportamento de Pontes de Betão Armado e Pré-esforçado," Doctoral thesis, Laboratório Nacional de Engenharia Civil (LNEC), Lisboa.
- [220] Simo, J. C., Oliver, J., and Armero, F. (1993). "An analysis of strong discontinuities induced by strain-softening in rate-independent inelastic solids." *Computational Mechanics*, 12(5), 277-296.
- [221] Simone, A., Askes, H., and Sluys, L. J. (2004). "Incorrect initiation and propagation of failure in non.local and gradient enhanced media." *International Journal of Solids and Structures*, 41(2), 351-363
- [222] Soltani, M., An, X., and Maekawa, K. (2004). "Cracking response and local stress characteristics of RC membrane elements reinforced with welded wire mesh." *Cement & Concrete Composites*, 26(4), 389-404.
- [223] Soltani, M., An, X., and Maekawa, K. (2005). "Localized nonlinearity and size-dependent mechanisms of in-plane RC element in shear." *Engineering Structures*, 27, 891-908.
- [224] Soltani, M., and Maekawa, K. (2003). "Computational model for post cracking analysis of RC membrane elements based on local stress-strain characteristics." *Engineering Structures*, 25, 993-1007.
- [225] Sousa, C., and Neves, A. (2009). "DIANA user-supplied subroutine for computation of prestress losses due to steel relaxation." LABEST/FEUP, Porto.
- [226] Sousa, C., and Neves, A. (2009). "DIANA user-supplied subroutine for concrete creep modelling." LABEST/FEUP, Porto.
- [227] Steenbergen, R. D. J. M., and Vrouwenvelder, A. (2010). "Safety philosophy for existing structures and partial factors for traffic loads on bridges." *Heron*, 55(2), 123-139.
- [228] Stoffel, P. (2000). "Zur Beurteilung der Tragsicherheit bestehender Stahlbetonbauten," Doctoral Thesis, Swiss Federal Institute of Technology Zurich, Zurich.
- [229] Takács, P. F. (2002). "Deformations in Concrete Cantilever Bridges: Observations and Theoretical Modelling," Doctoral Thesis, The Norwegian University of Science and Technology, Trondheim.
- [230] Thieberger, P., Mariscotti, M. A. J., and Ruffolo, M. (2006). "Simulation Program for Reinforced Concrete Tomography with Gamma-Rays." *ASNT, NDE Conference on Civil Engineering.*, St. Louis.
- [231] TNO_DIANA_BV. (2008). *DIANA User's Manual - Release 9.3*, TNO DIANA BV Delft.
- [232] Van Mier, J. G. M. (1986). "Fracture of concrete under complex stress." *Heron*, 31(3), 2-90.
- [233] Van Mier, J. G. M. (2009). "Mode II Fracture Localization in Concrete Loaded in Compression." *Journal of Engineering Mechanics*, 135(1), 1-8.
- [234] Vecchio, F. J. (1981). "The response of concrete to in-plane shear and axial stresses," Doctoral Thesis, University of Toronto, Toronto.
- [235] Vecchio, F. J. (1989). "Nonlinear Finite Element Analysis of Reinforced Concrete Membranes." *ACI Structural Journal*, 86(1), 23-35.
- [236] Vecchio, F. J. (1990). "Reinforced Concrete Membrane Element Formulations." *Journal of Structural Engineering*, 116(3), 730-750.
- [237] Vecchio, F. J. (2000). "Disturbed Stress Field Model for Reinforced Concrete: Formulation." *Journal of Structural Engineering*, 126(9), 1070-1077.
- [238] Vecchio, F. J. (2001). "Disturbed Stress Field Model for Reinforced Concrete: Implementation." *Journal of Structural Engineering*, 127(1), 12-20.

- [239] Vecchio, F. J., and Chan, C. C. L. (1990). "Reinforced Concrete Membrane Elements with Perforations." *Journal of Structural Engineering*, 116(9), 2344-2360.
- [240] Vecchio, F. J., and Collins, M. P. (1986). "The Modified Compression-Field Theory for Reinforced Concrete Elements Subjected to Shear." *ACI Journal*, 83(2), 219-231.
- [241] Vecchio, F. J., and Collins, M. P. (1988). "Predicting the Response of Reinforced Concrete Beams Subjected to Shear Using the Modified Compression Field Theory." *ACI Structural Journal*, 85(3), 258-268.
- [242] Vecchio, F. J., and Collins, M. P. (1993). "Compression Response of Cracked Reinforced Concrete." *Journal of Structural Engineering*, 119(12), 3590-3610.
- [243] Vecchio, F. J., Collins, M. P., and Aspiotis, J. (1994). "High-Strength Concrete Elements Subjected to Shear." *ACI Structural Journal*, 91(423-433).
- [244] Vecchio, F. J., and DeRoo, A. (1995). "Smear-Crack Modeling of Concrete Tension Splitting." *Journal of Engineering Mechanics*, 121(6), 702-708.
- [245] Vecchio, F. J., Gauvreau, P., and Liu, K. (2006). "Modeling of Unbonded Post-tensioned Concrete Beams Critical in Shear." *ACI Structural Journal*, 103(1), 57-64.
- [246] Vecchio, F. J., Lai, D., Shim, W., and Ng, J. (2001). "Disturbed Stress Field Model for Reinforced Concrete: Validation." *Journal of Structural Engineering*, 127(4), 350-358.
- [247] Vecchio, F. J., and Selby, R. G. (1991). "Toward Compression-Field Analysis of Reinforced Concrete Solids." *Journal of Structural Engineering*, 117(6), 1740-1758.
- [248] Vecchio, F. J., and Shim, W. (2004). "Experimental and Analytical Reexamination of Classic Concrete Beam Tests." *Journal of Structural Engineering*, 130(3), 460-469.
- [249] Vonk, R. A. (1993). "A micromechanical investigation of softening of concrete loaded in compression." *Heron*, 38(3), 3-90.
- [250] Waarts, P. H. (2000). "Structural Reliability using Finite Element Analysis," Doctoral Thesis, Technical University of Delft, Delft.
- [251] Walraven, J. C., and Reinhardt, H. W. (1981). "Theory and Experiments on the Mechanical Behaviour of Cracks in Plain and Reinforced Concrete Subjected to Shear Loading." *Heron*, 26(1A).
- [252] Walther, A., and Hillemeier, B. (2008). "Fast NDT localisation of prestressing steel fractures in post-tensioned concrete bridges." *Structural Faults & Repair - 2008*, Edinburgh.
- [253] Wang, J. (2006). "Constitutive Relationships of Prestressed Concrete Membrane Elements," Doctoral Thesis, University of Houston, Houston.
- [254] Willam, K. (2002). "Constitutive Models for Engineering Materials." *Encyclopedia of Physical Science and Technology*, Academic Press, 603-633.
- [255] Wisniewski, D. F., Cruz, P. J. S., Henriques, A. A., and Simões, R. A. D. (2009). "Probabilistic models for mechanical properties of concrete, reinforcing steel and pre-stressing steel." *Structure and Infrastructure Engineering*, doi: 10.1080/15732470903363164.
- [256] Witte, F. C. (2005). "DIANA User's Manual - Release 9." TNO DIANA, BV, Delft.
- [257] Witte, F. C., and Kikstra, W. P. (2005). "DIANA User's Manual - Material Library." TNO DIANA, BV, Delft.
- [258] WP3. (2007). "Sustainable Bridges - D3.15: Guideline for inspection and condition assessment of railway bridges." Available from: www.sustainablebridges.net.
- [259] WP4. (2007). "Sustainable Bridges - D4.2: Guideline for Load and Resistance Assessment of Existing European Railway Bridges - advices on the use of advanced methods." Available from: www.sustainablebridges.net.
- [260] Zhang, L. X. (1992). "Constitutive Laws of Reinforced Elements with Medium-High Strength Concrete," Master Thesis, University of Houston, Houston.

- [261] Zhang, L. X. (1995). "Constitutive Laws of Reinforced Membrane Elements with High Strength Concrete," Doctoral Thesis, University of Houston, Houston.
- [262] Zhang, L. X., and Hsu, T. T. C. (1998). "Behaviour and Analysis of 100MPa Concrete Membrane Elements." *Journal of Structural Engineering*, 124(1), 24-34.
- [263] Zhu, R. R. H. (2000). "Softened-Membrane Model of Cracked Reinforced Concrete Considering the Poisson Effect," Doctoral Thesis, University of Houston, Houston.
- [264] Zhu, R. R. H., and Hsu, T. T. C. (2002). "Poisson Effect in Reinforced Concrete Membrane Elements." *ACI Structural Journal*, 99(5), 631-640.
- [265] Zhu, R. R. H., Hsu, T. T. C., and Lee, J. Y. (2001). "Rational Shear Modulus for Smearred Crack Analysis of Reinforced Concrete." *ACI Structural Journal*, 98(4), 443-450.

Appendix – Detailed validation results

A1.1 – Isotropically reinforced concrete panels

A1.1.1 – Series A

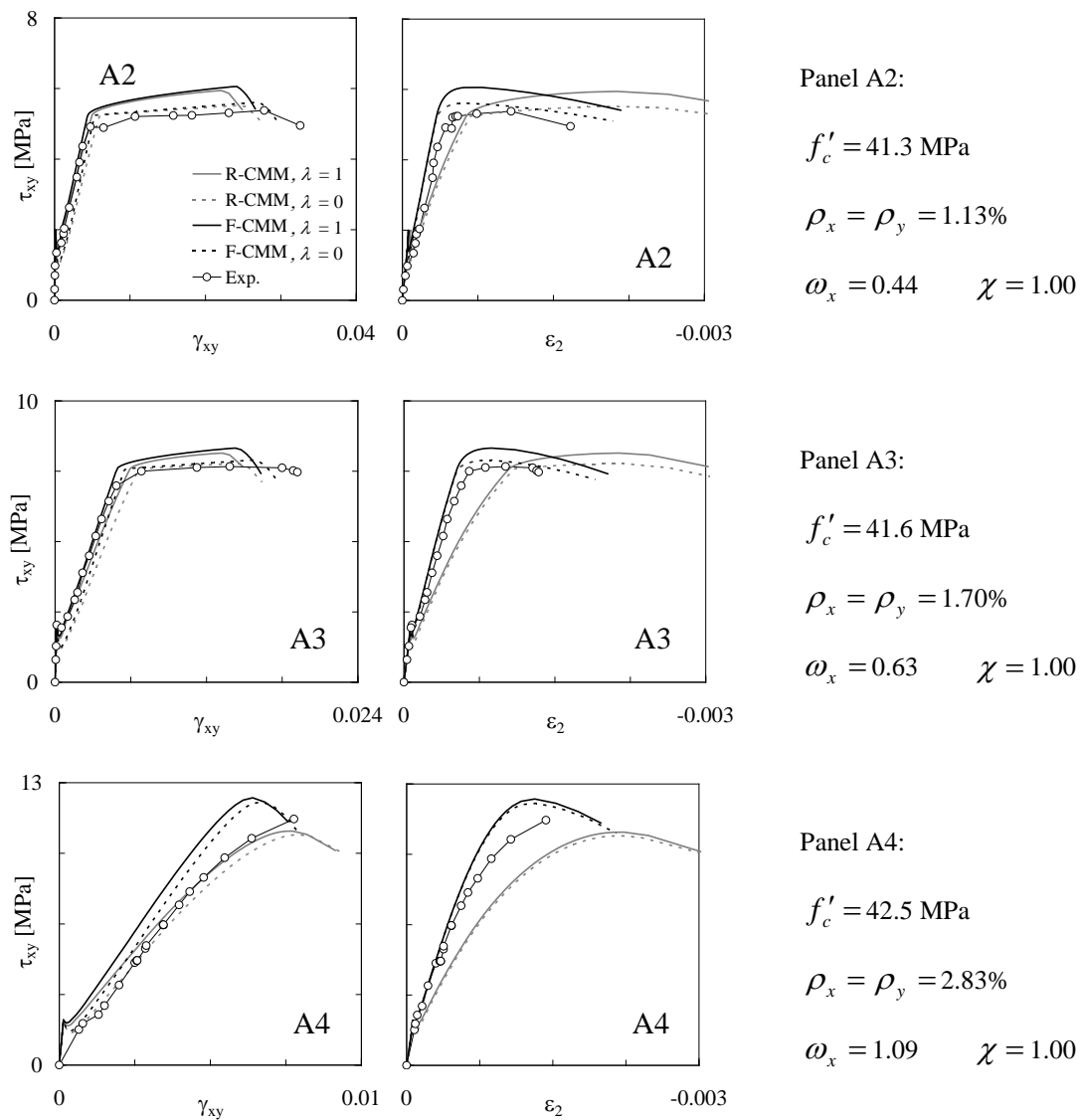


Figure A.1 – Comparison with experiments of Series A by Pang [178].

A1.1.2 – Series VA

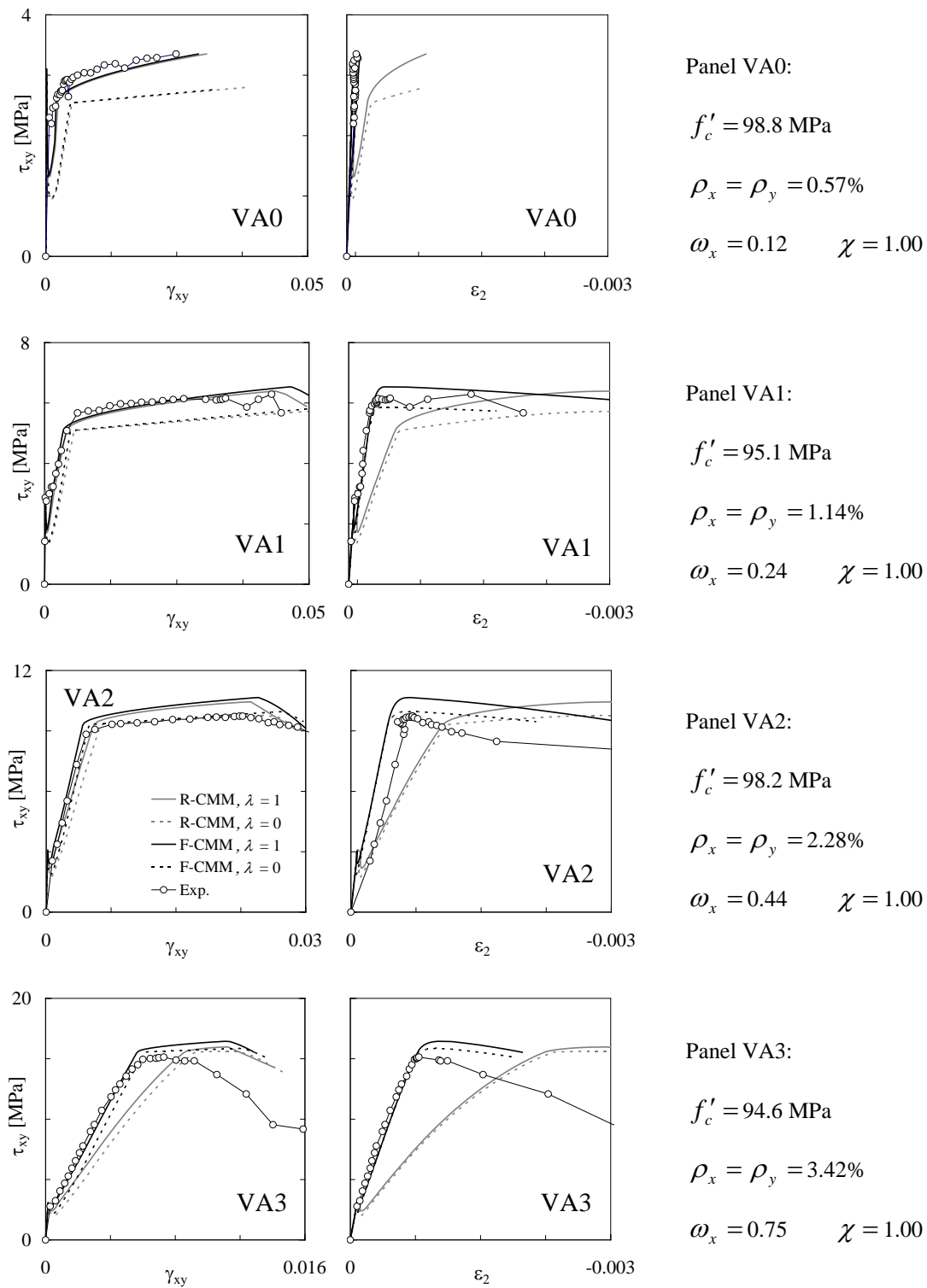


Figure A.2 – Comparison with experiments of Series VA by Zhang [261].

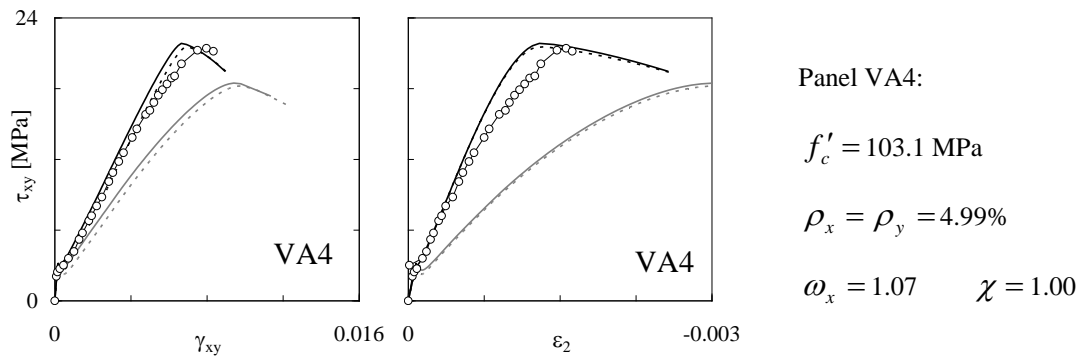


Figure A.2 – Comparison with experiments of Series VA by Zhang [261] (cont.).

A1.1.3 – Series PV

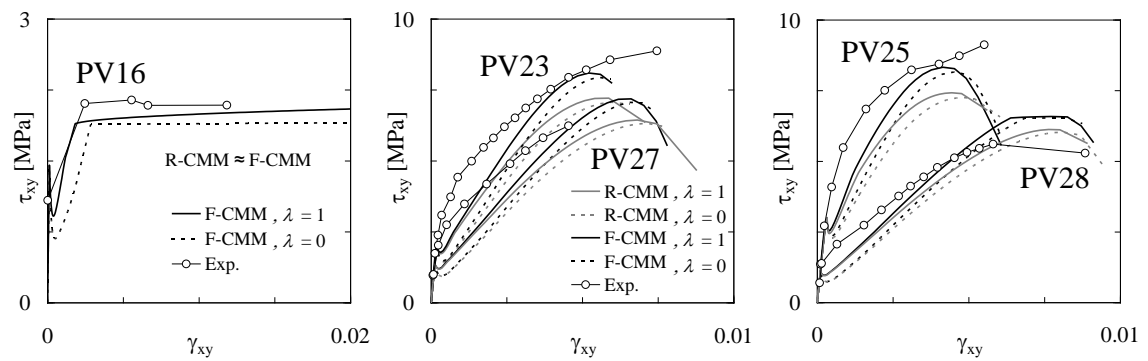


Figure A.3 – Comparison with experiments of Series PV by Vecchio [234].

A1.2 – Orthotropically reinforced concrete panels

A1.2.1 – Series B

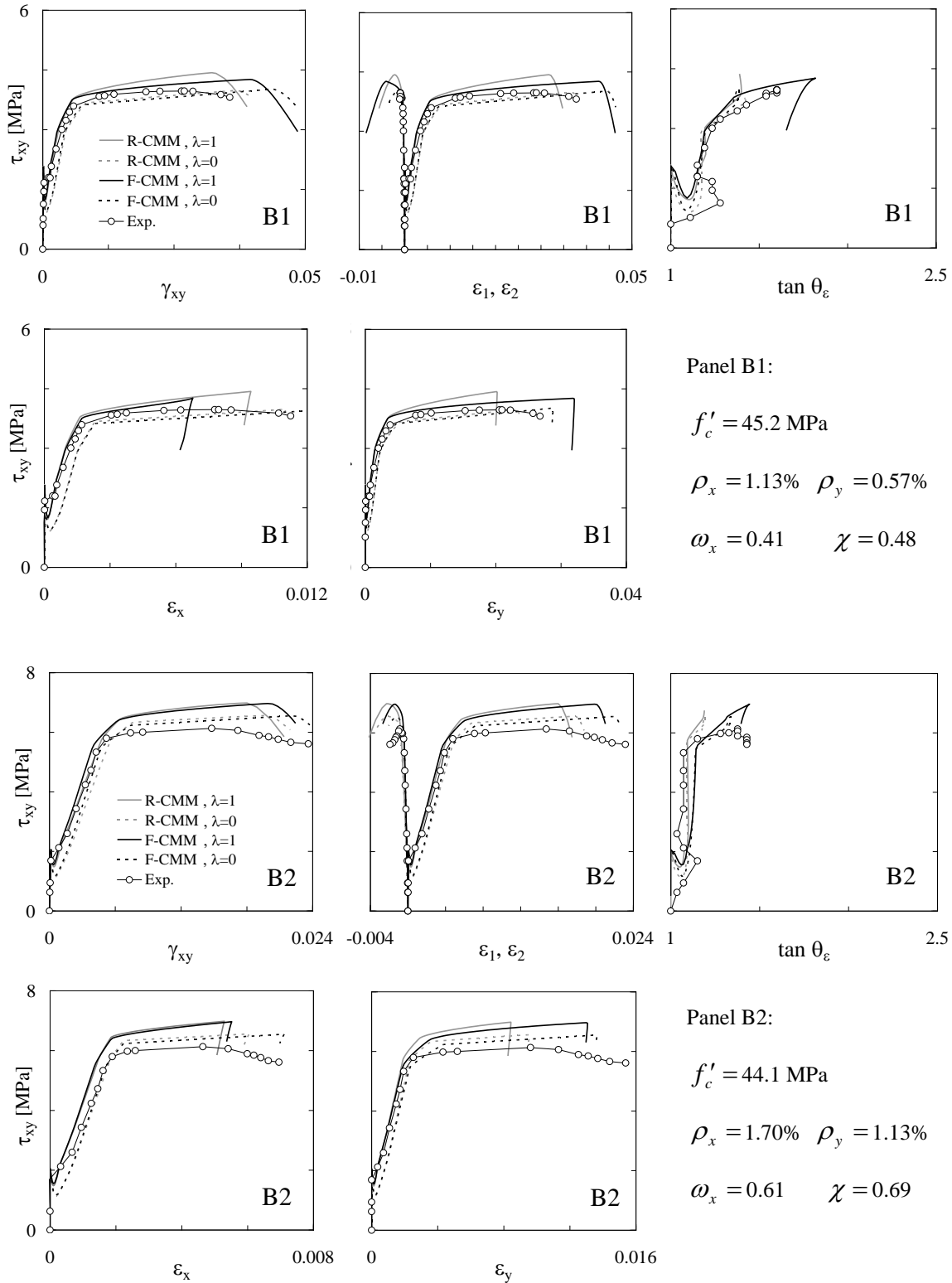


Figure A.4 – Comparison with experiments of Series B by Pang [178].

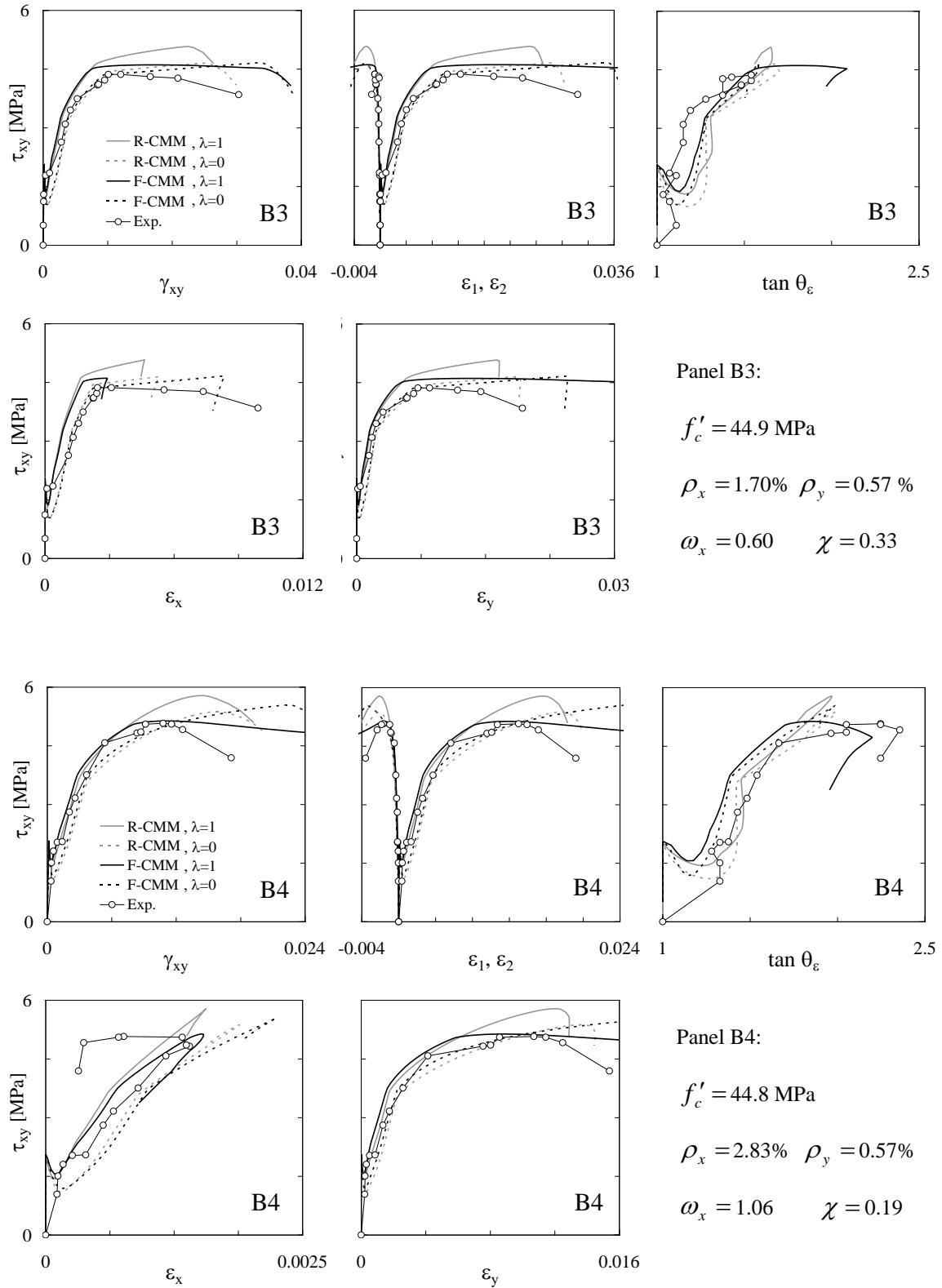


Figure A.4 – Comparison with experiments of Series B by Pang [178] (cont.).

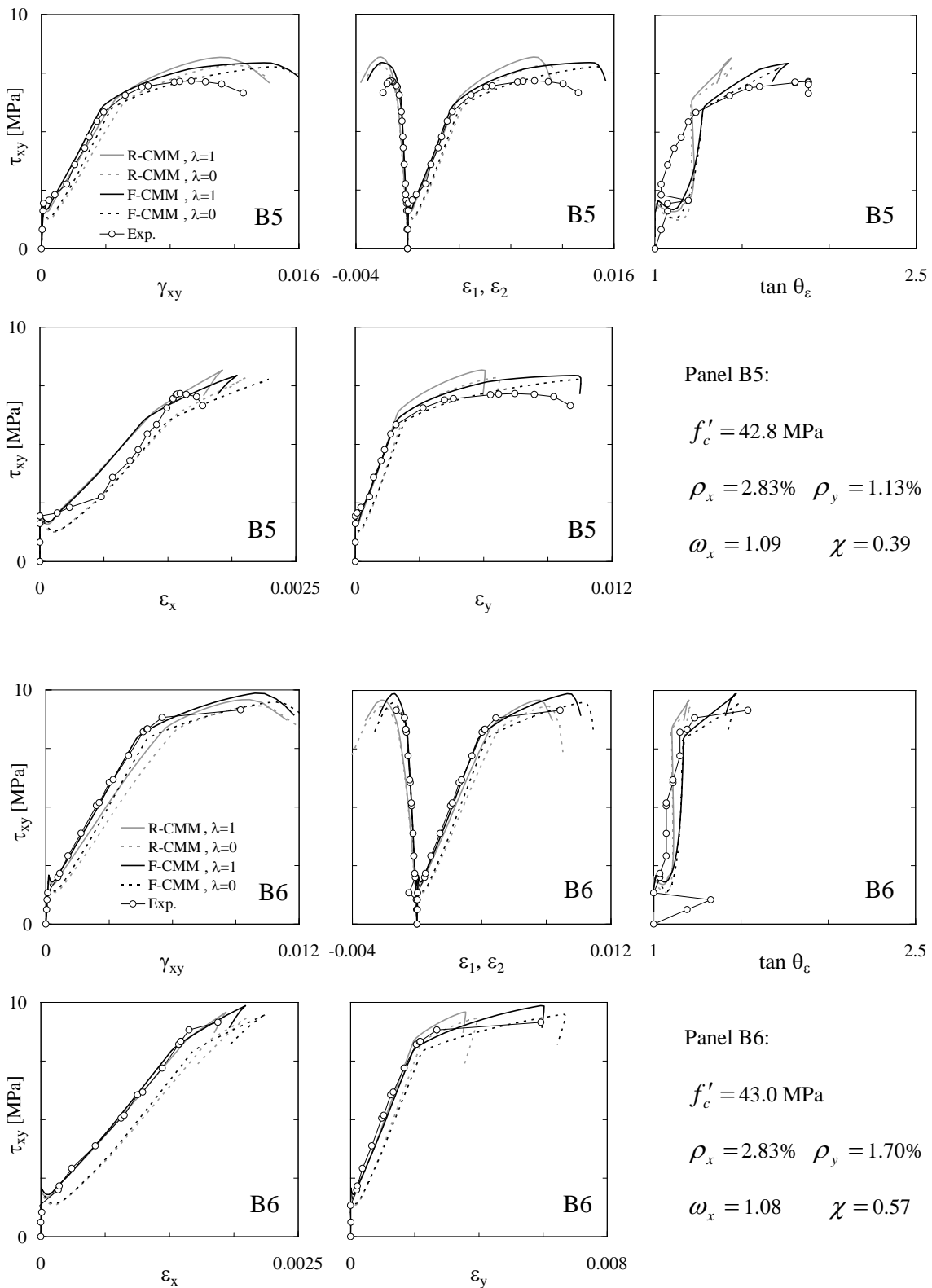


Figure A.4 – Comparison with experiments of Series B by Pang [178] (cont.).

A1.2.2 – Series PP

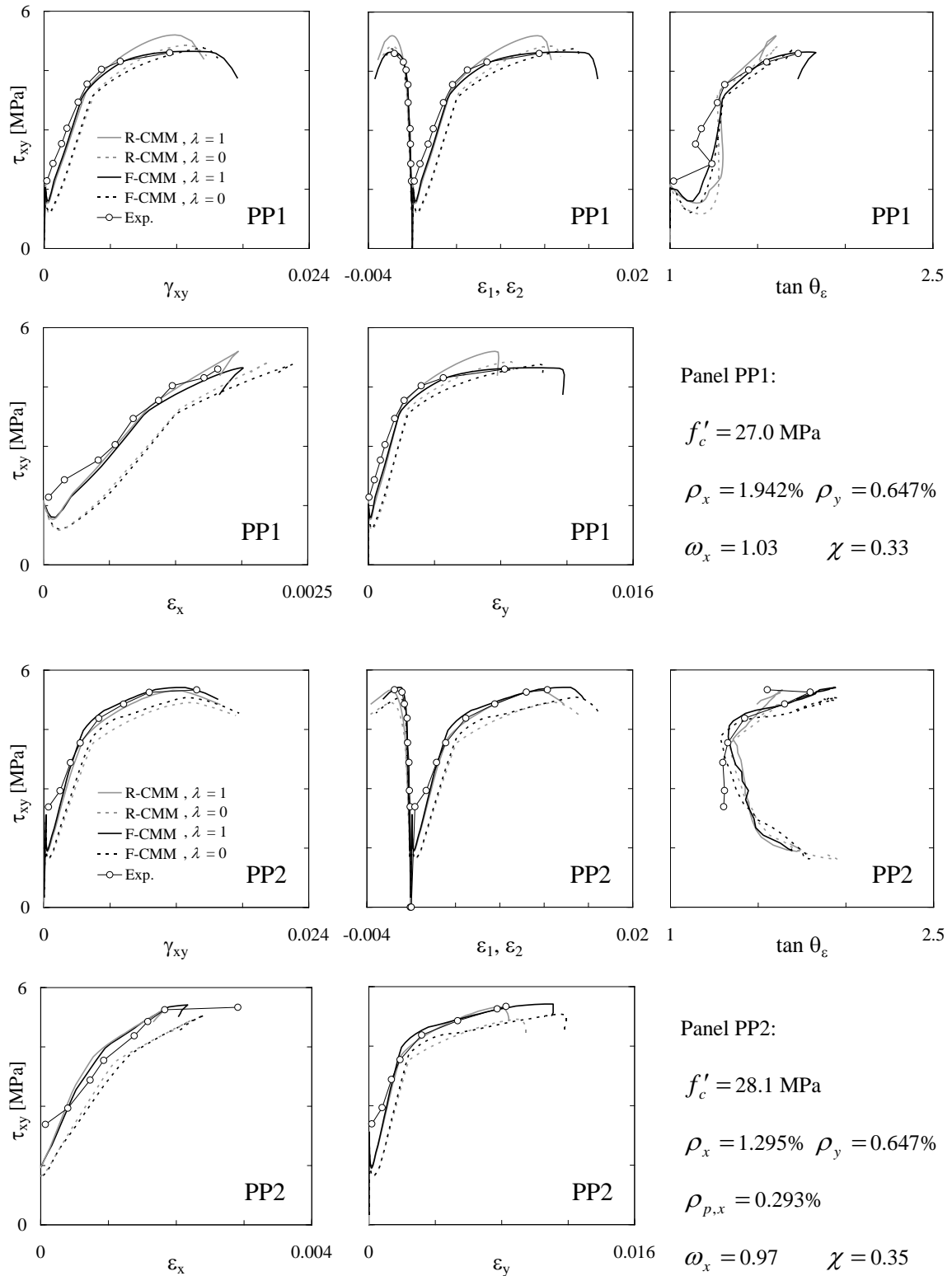


Figure A.5 – Comparison with experiments of Series PP by Marti and Meyboom [152]

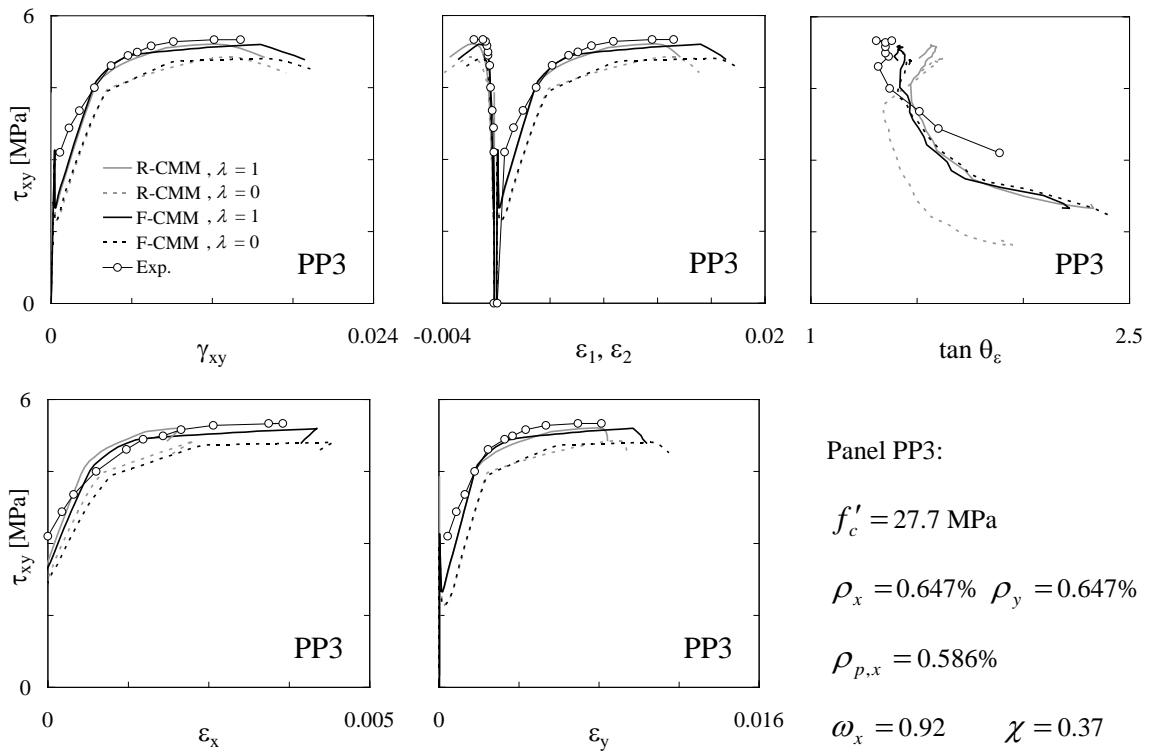


Figure A.5 – Comparison with experiments of Series PP by Marti and Meyboom [152] (cont.)

A1.2.3 – Series SE

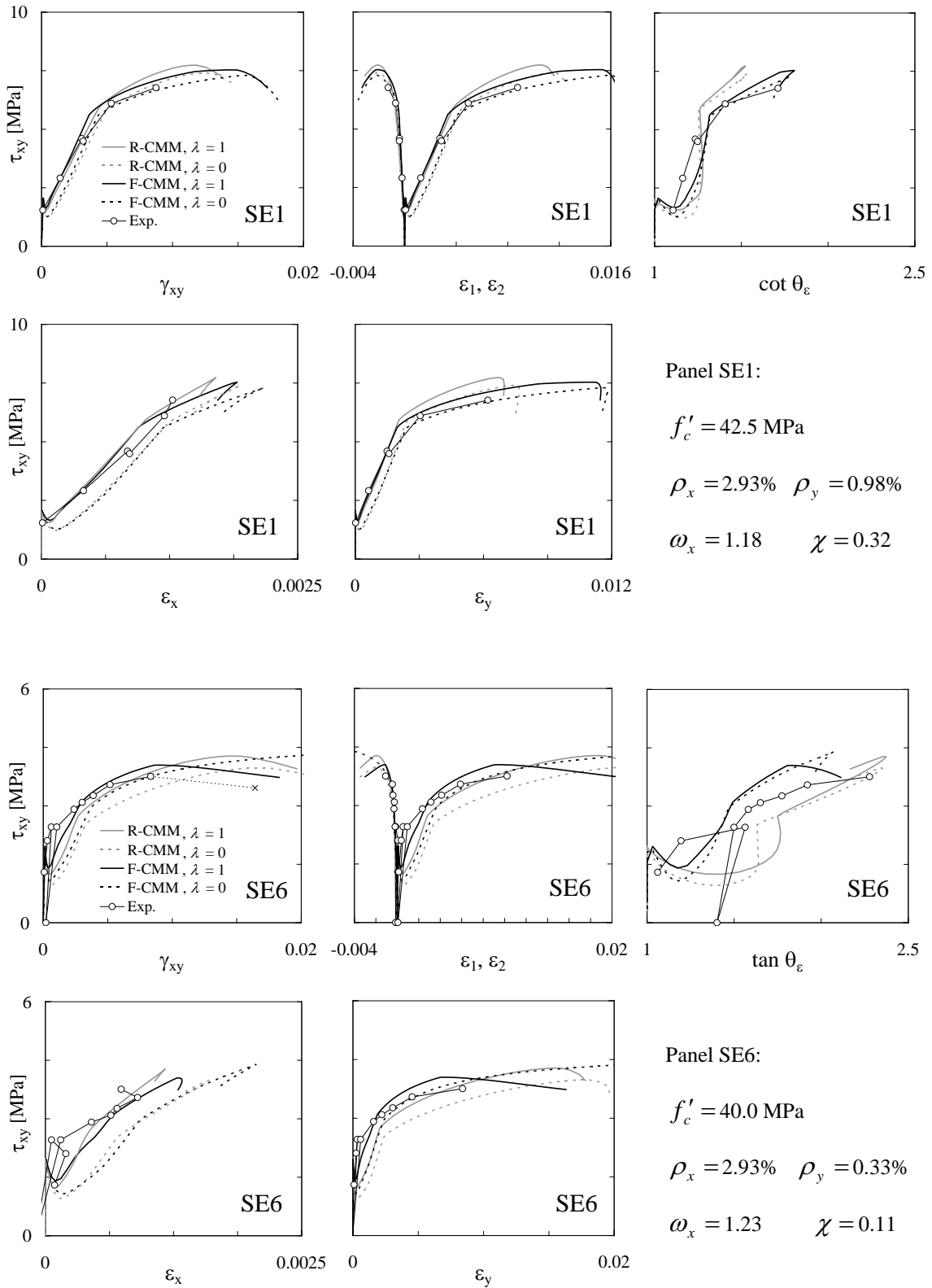


Figure A.6 – Comparison with experiments of Series SE by Kirschner [123].

A1.2.4 – Series VB

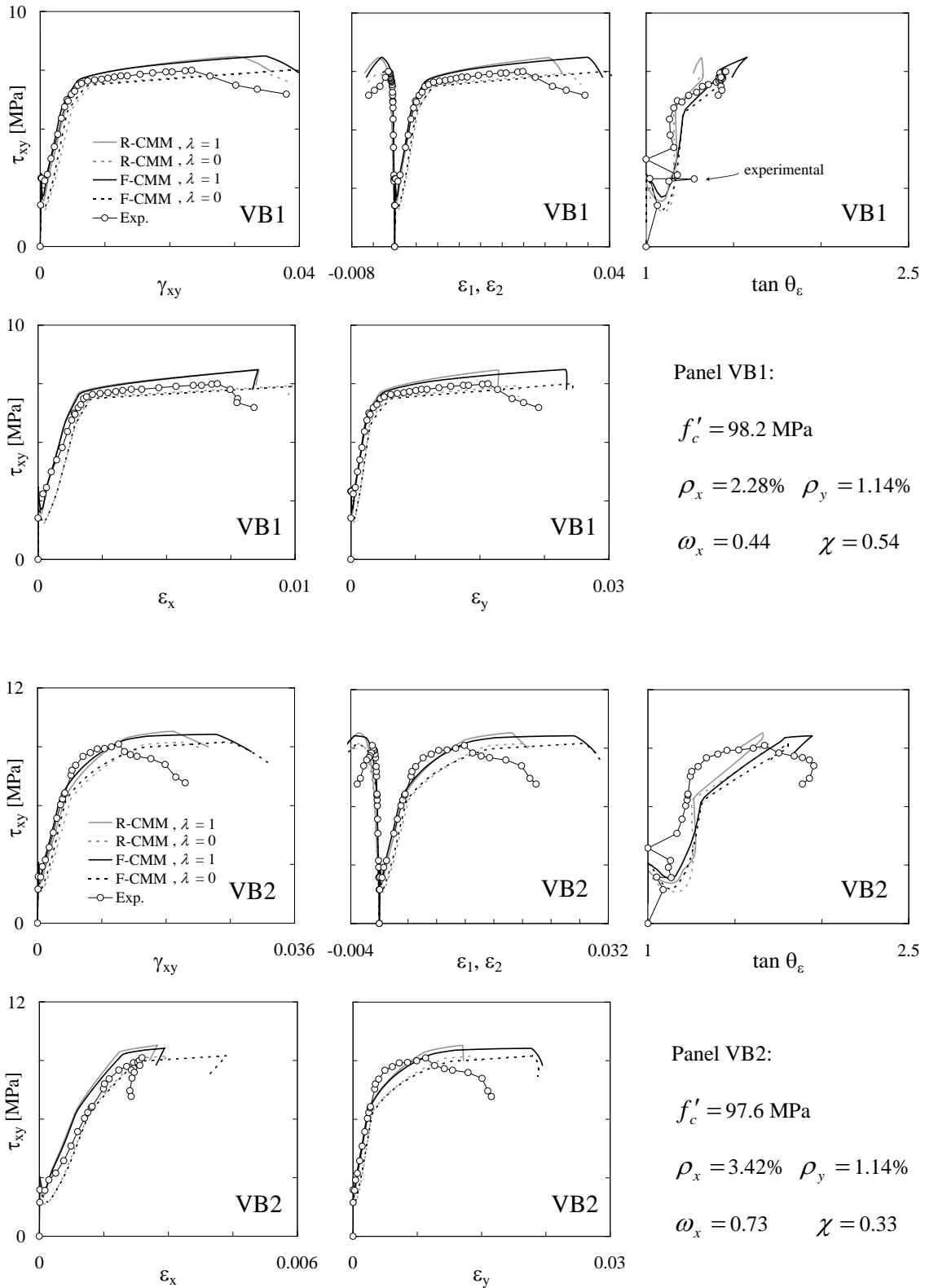


Figure A.7 – Comparison with experiments of Series VB by Zhang [261].

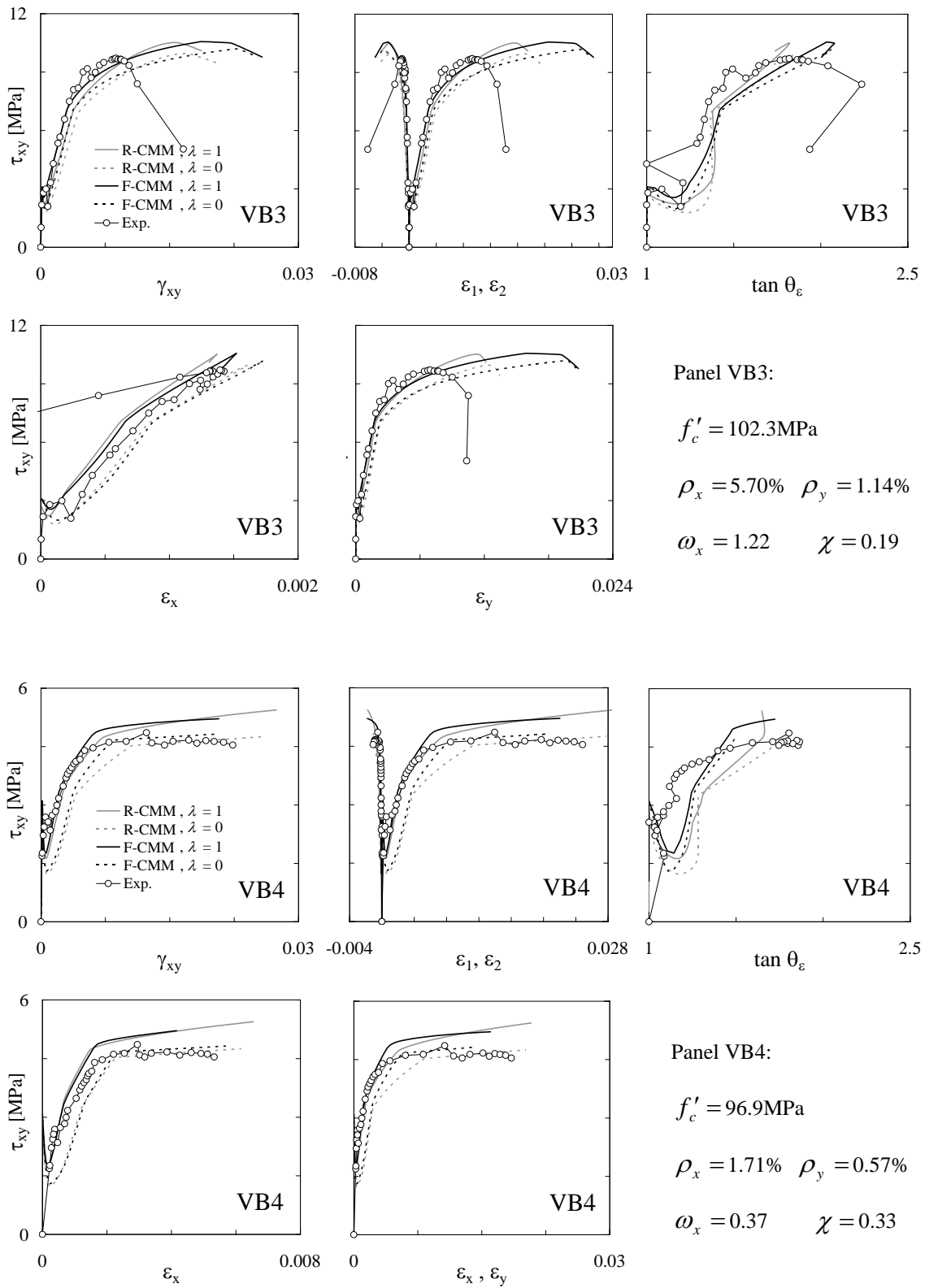


Figure A.7 – Comparison with experiments of Series VB by Zhang [261].

A1.2.5 – Series M

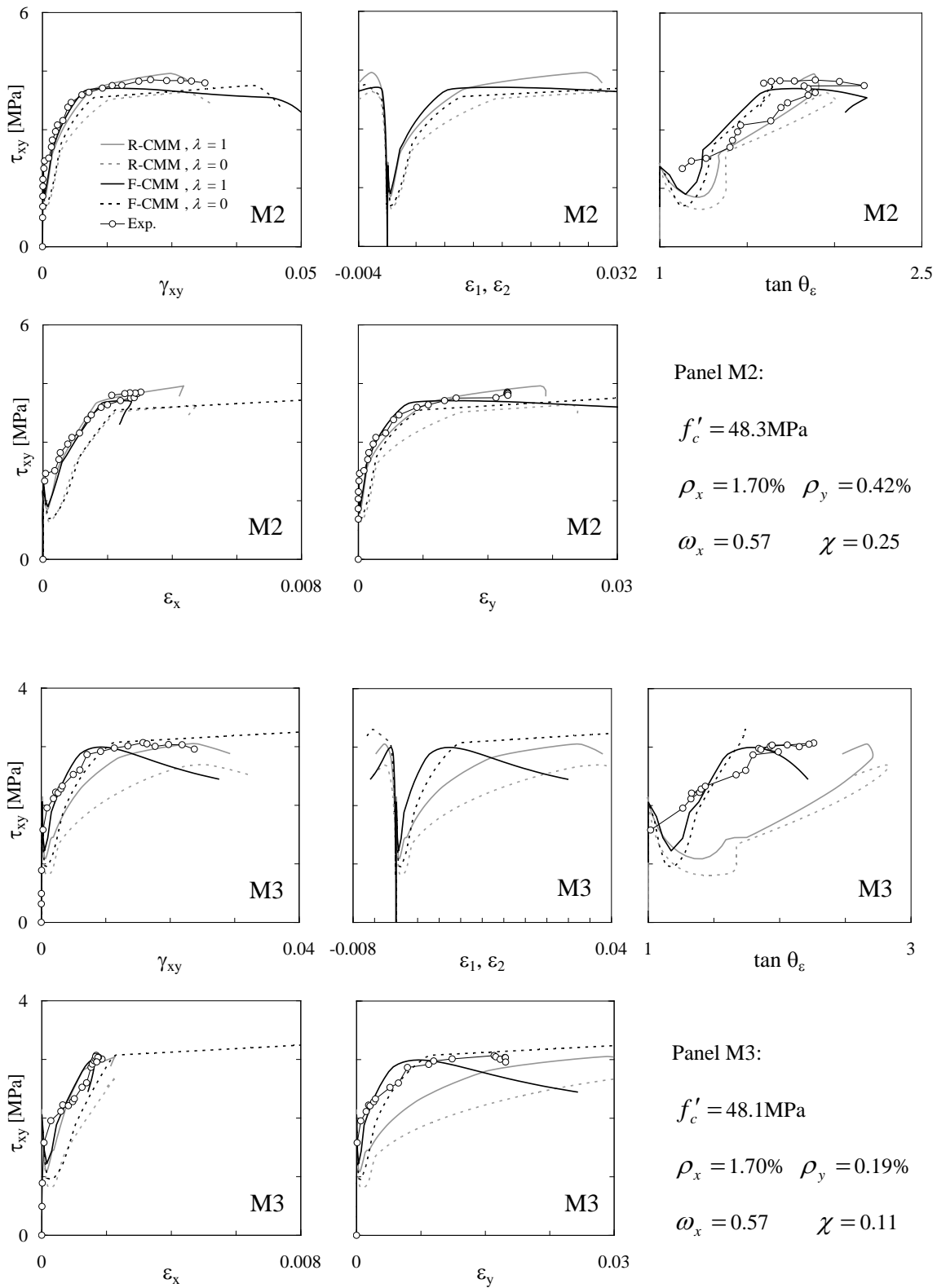


Figure A.8 – Comparison with experiments of Series M by Chintrakarn [253].

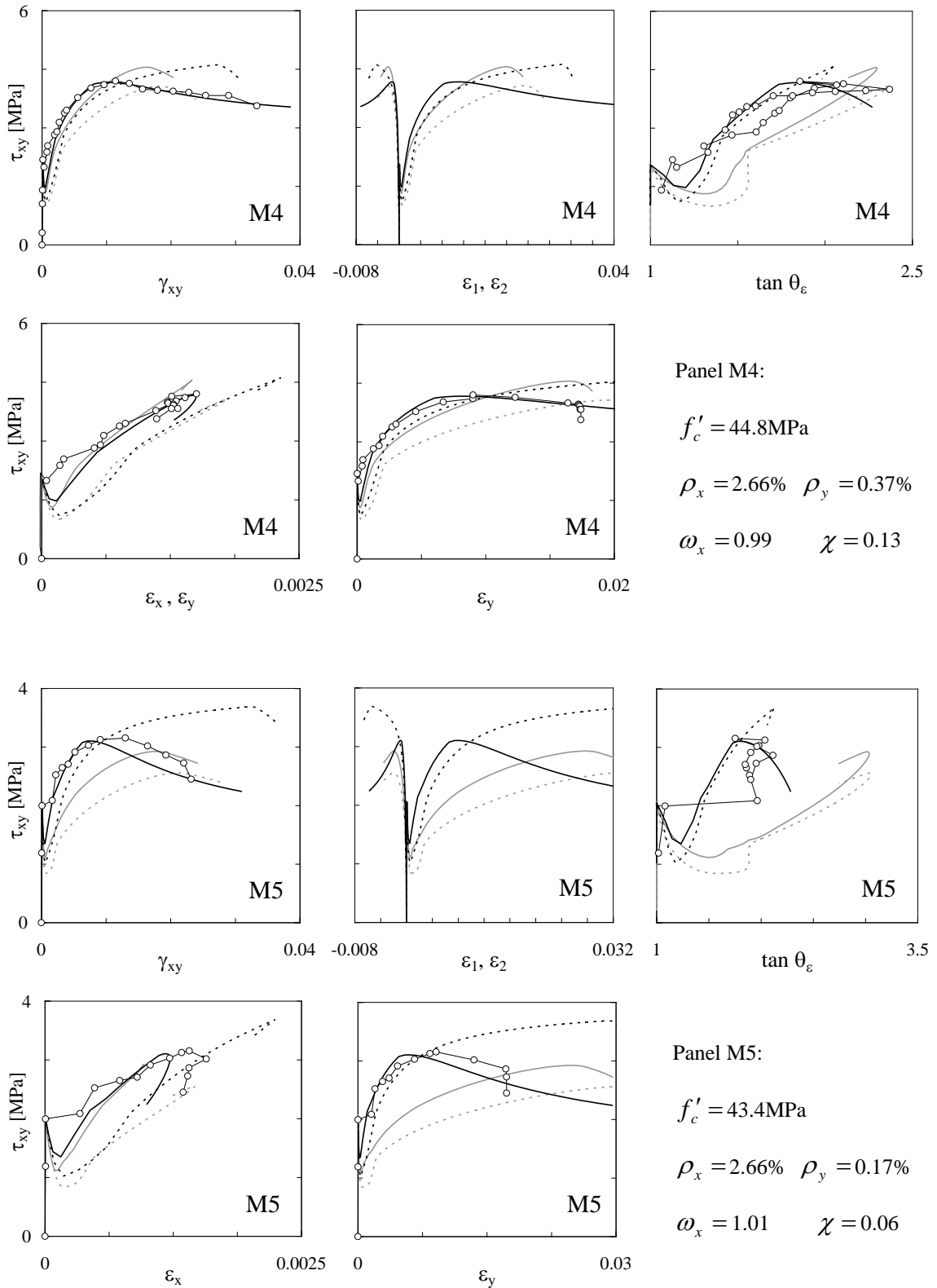


Figure A.8 – Comparison with experiments of Series M by Chintrakarn [253](cont.).

A1.2.6 – Series PV

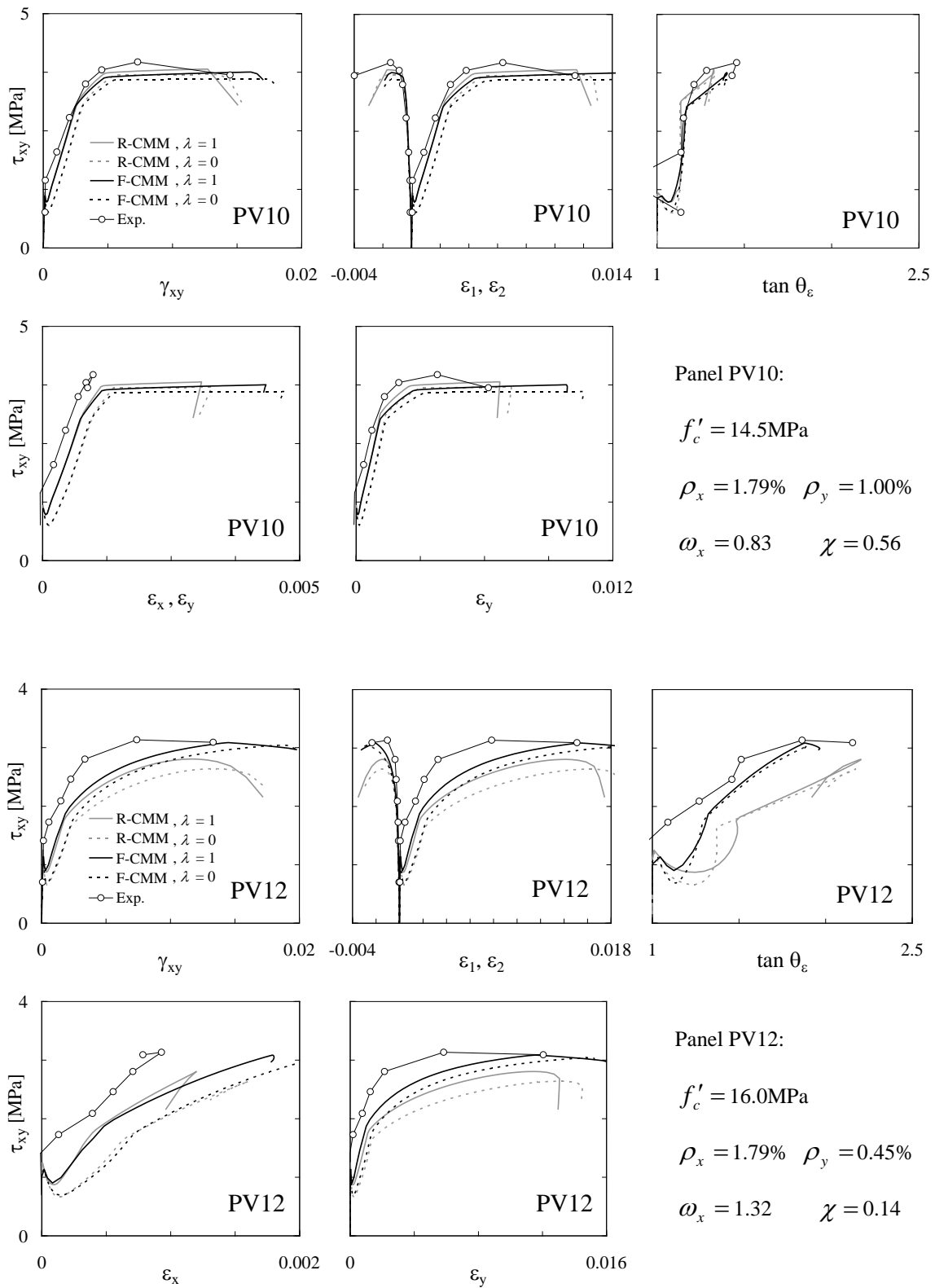


Figure A.9 – Comparison with experiments of Series PV by Vecchio [234].

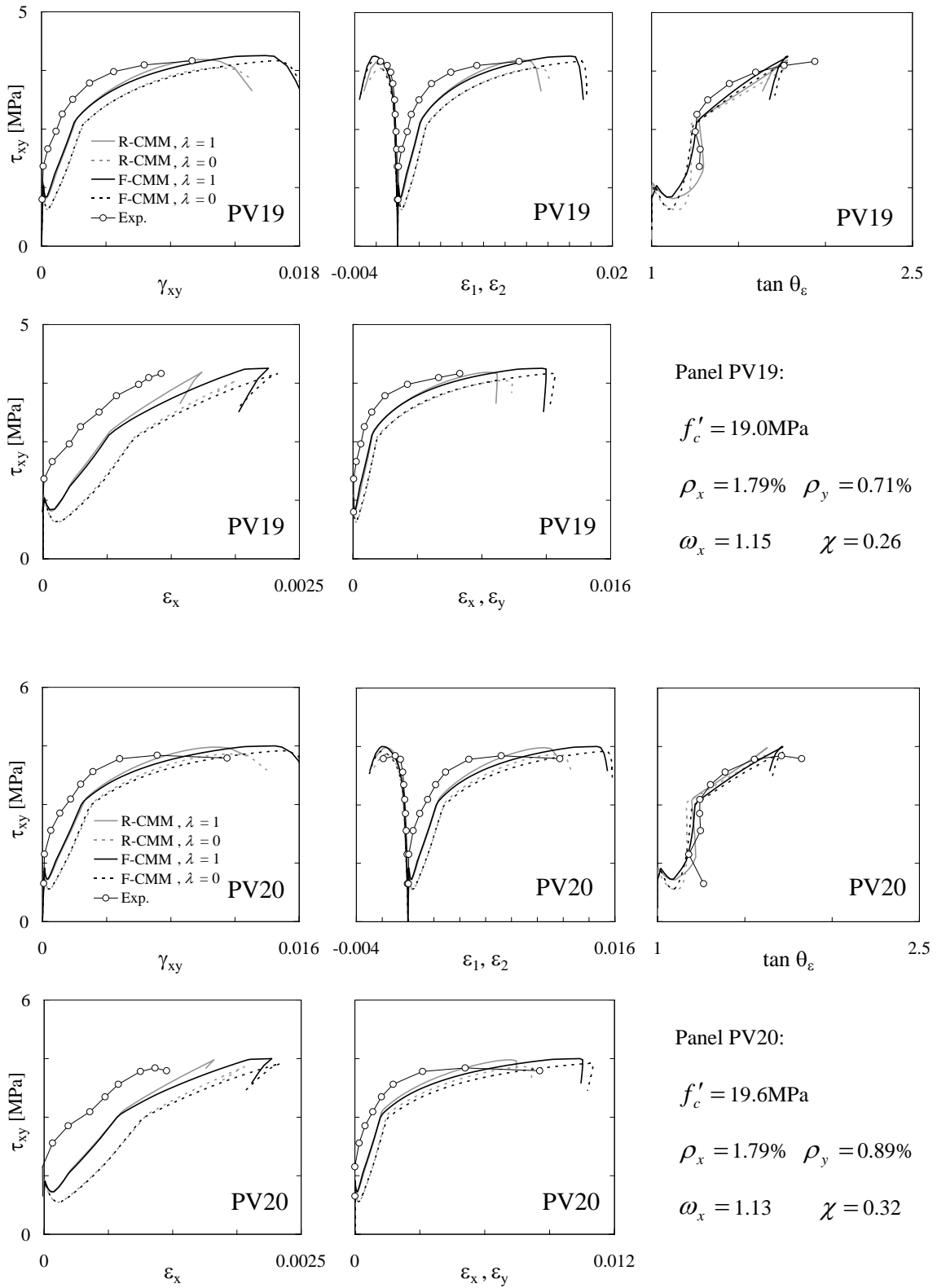


Figure A.9 – Comparison with experiments of Series PV by Vecchio [234] (cont.).

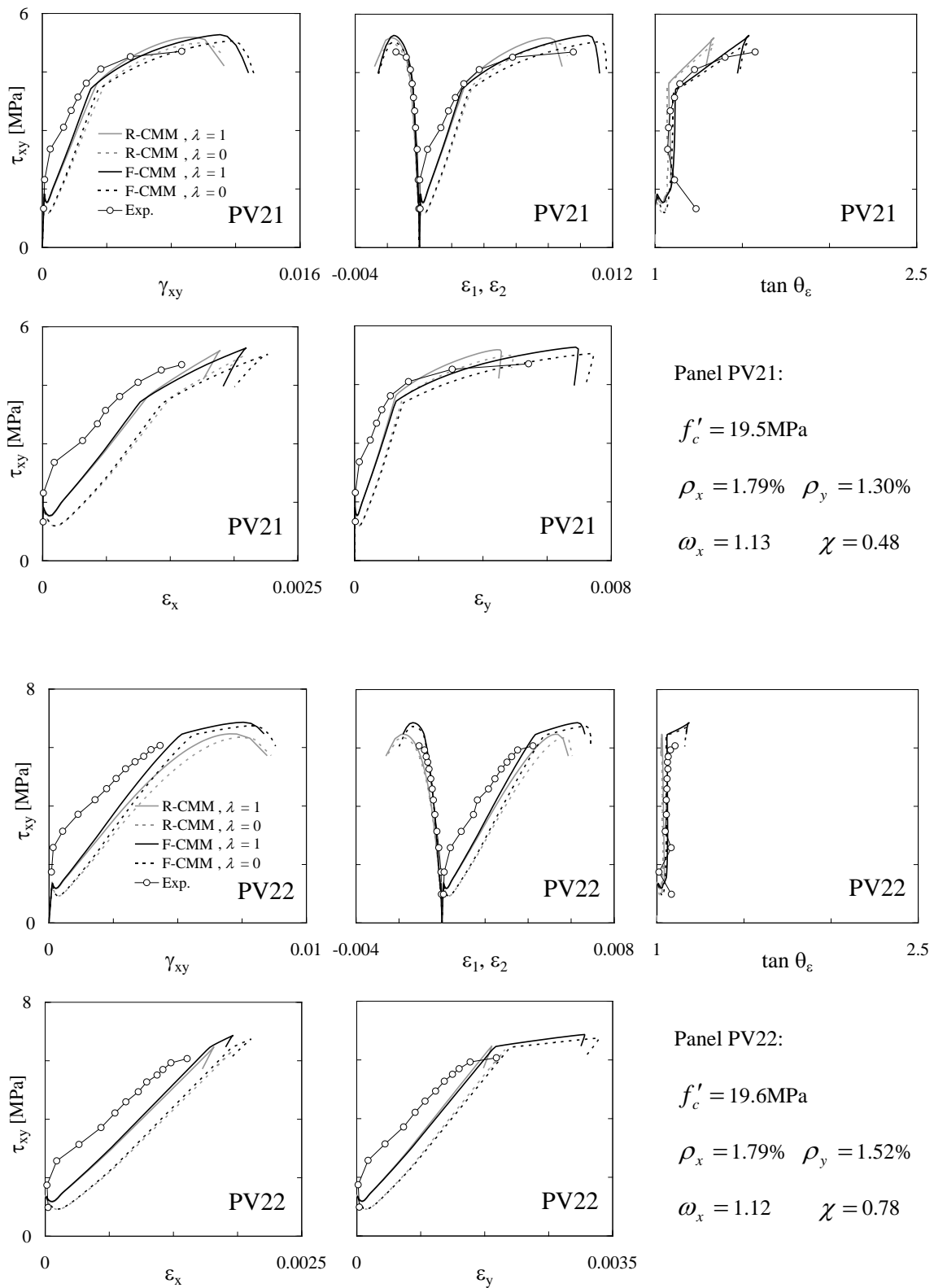


Figure A.9 – Comparison with experiments of Series PV by Vecchio [234] (cont.).

